Journal of Heat Transfer
Transactions of the ASME

Volume 129, Issue 2, pp. 101-243 , February 2007

MAX JAKOB AWARD PAPER

RESEARCH PAPERS

Conduction

Evaporation, Boiling, and Condensation

Forced Convection

Heat Pipes

TECHNICAL BRIEFS

Phase-Change Heat Transfer in Microsystems

Ping Cheng[1]
e-mail: mepcheng@yahoo.com

Hui-Ying Wu

Fang-Jun Hong

School of Mechanical and Power Engineering,
Shanghai Jiaotong University,
1954 Hua Shan Road,
Shanghai 200030, P.R. China

Recent work on miscroscale phase-change heat transfer, including flow boiling and flow condensation in microchannnels (with applications to microchannel heat sinks and microheat exchangers) as well as bubble growth and collapse on microheaters under pulse heating (with applications to micropumps and thermal inkjet printerheads), is reviewed. It has been found that isolated bubbles, confined elongated bubbles, annular flow, and mist flow can exist in microchannels during flow boiling. Stable and unstable flow boiling modes may occur in microchannels, depending on the heat to mass flux ratio and inlet subcooling of the liquid. Heat transfer and pressure drop data in flow boiling in microchannels are shown to deviate greatly from correlations for flow boiling in macrochannels. For flow condensation in microchannels, mist flow, annular flow, injection flow, plug-slug flow, and bubbly flows can exist in the microchannels, depending on mass flux and quality. Effects of the dimensionless condensation heat flux and the Reynolds number of saturated steam on transition from annular two-phase flow to slug/plug flow during condensation in microchannels are discussed. Heat transfer and pressured drop data in condensation flow in microchannels, at low mass flux are shown to be higher and lower than those predicted by correlations for condensation flow in macrochannels, respectively. Effects of pulse heating width and heater size on microbubble growth and collapse and its nucleation temperature on a microheater under pulse heating are summarized. [DOI: 10.1115/1.2410008]

Keywords: boiling, condensation, phase change, bubble, nucleation

Introduction

Advances in microelectronic fabrication technology have led to the miniaturization of silicon components. This coupled with the improved processing speed in clock frequencies from MHz to GHz has generated increasingly larger amount of heat in microprocessors. The large amount of heat, if not properly dissipated, will cause overheating of a chip, leading to its degrading performance and eventual damage. To cope with the demand for more efficient cooling technology for the next generation of high power electronics devices, various kinds of microheat exchangers and two-phase microchannel heat sinks [1,2] have been developed in recent years. For this reason, a great deal of recent work has been devoted to the study of boiling and condensation in microchannels [3–23].

Meanwhile, advances in microfabrication also led to many MEMS products such as thermal inkjet printheads [24] and microthermal bubble pumps [25]. For thermal inkjet application, microheaters under electrical pulse of several microseconds (μs) are used to generate a microbubble periodically. The microbubble will expel a small drop of ink through a nozzle at a high frequency to a specified position on a paper to compose the text and graphics. The quality of the print depends on the size of the drops and drop velocity, which are closely related to bubble nucleation. Recently, Deng et al. [26] found that if the pulse width applied to a microheater is increased from the microseconds to milliseconds level, the periods of bubble expansion and collapse are asymmetric. This characteristics can be used to design a thermal actuator or perturbator [26,27] and for DNA hybridization enhancement [28,29].

In this paper, we will review the most recent literature on boiling [4–18] and condensation [19–23] in microchannels with applications to microheat exchangers and microheat sinks, as well as bubble nucleation under pulse heating [25–31] with applications to microthermo-bubble actuators.

Classification of Microchannels

It is well known that the Bond number is an important parameter in phase change heat transfer [2,3]. The Bond number is defined as

$$\mathrm{Bo}_d = (D_h/\ell_c)^2 = g(\rho_\ell - \rho_v)D_h^2/\sigma \tag{1}$$

where $\ell_c=[\sigma/(\rho_\ell-\rho_v)g]^{1/2}$ is the capillary length; D_h is the hydraulic diameter of the channel; g is the gravitational acceleration; σ is the surface tension; and ρ_ℓ and ρ_v are density of the liquid and the vapor, respectively. Equation (1) shows that the Bond number is a ratio of the hydraulic diameter to the capillary length, which is also a measure of the relative importance of the buoyancy force to surface tension force. The classification of microchannels, minichannels, or macrochannel can be based on the Bond number as follows [2]:

1. Microchannel: if $\mathrm{Bo}_d<0.05$ where gravity effect can be neglected;
2. Minichannel: if $0.05<\mathrm{Bo}_d<3.0$ where surface tension effect becomes dominant and gravitational effect is small; and
3. Macrochannel: if $\mathrm{Bo}_d>3.0$ where surface tension is small in comparison with gravitational force.

It is relevant to point out that the Bond number, defined by Eq. (1), has taken into consideration the effects of temperature, pressure, and physical properties of the fluid. According to the above classification, a channel with its hydraulic diameter less than 490 μm (at 450 K) or 600 μm (at 300 K), respectively, is considered to be a microchannel for phase change heat transfer if water is used as the working medium.

[1]Corresponding author.

Contributed by the Heat Transfer Division of ASME for publication in the JOURNAL OF HEAT TRANSFER. Manuscript received August 4, 2006; final manuscript received September 20, 2006. Review conducted by Yogesh Jaluria. Paper presented at the International Heat Transfer Conference 2006. Max Jakob Award Lecture.

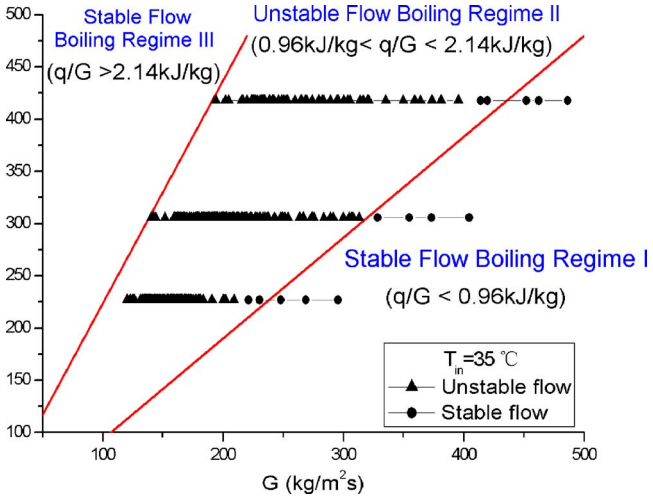

Fig. 1 Flow boiling regimes in microchanels [14]

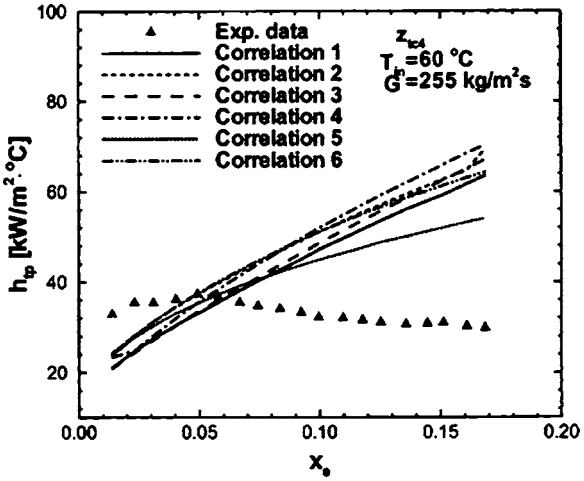

Fig. 2 Comparison of measurements of local heat transfer coefficient in flow boiling of water in microchannel with correlation equations for macrochannels [7]

Flow Boiling in Microchannel

UFlow Patterns. Hetsroni et al. [4] investigated flow boiling of water in silicon microchannels having hydraulic diameters of 103 μm and 129 μm, respectively, and observed periodic annular flow and periodic dry steam flow in the microchannels. In another paper, Hetsroni et al. [5] performed a flow boiling experiment on Vertrel XF fluid in silicon microchannels of triangular cross section, having a hydraulic diameter of 130.14 μm. They measured low-amplitude/short-period fluctuations in the pressure drop and outlet fluid temperature, which were attributed to the growth and collapse of vapor bubbles in the two-phase flow. Qu and Mudawar [6] performed a flow boiling experiment of water in a two-phase microchannel heat sink, and identified two types of instability in microchannels: severe pressure drop oscillation and mild parallel channel instability. They discussed the possibility of reverse vapor flow. Lee et al. [7] and Li et al. [8] found that reverse vapor flow exists in both single and multiple microchannels. Most recently, Hetsroni et al. [9] performed an experiment on flow boiling of water in a microchannel with a hydraulic diameter of 250 μm for mass flux in the range of 95–340 kg/mP^{2P} s and heat flux in the range of 80–330 kW/mP^{2P}. They observed explosive boiling with periodic wetting and dryout in the microchannels.

Wu et al. [10–12] carried out a series of experiments on the simultaneous visualization and measurements on flow boiling in parallel silicon microchannels having a hydraulic diameter ranging from 49.9 μm to 186 μm. It was found that large temperature and pressure fluctuations with long oscillation periods occurred under certain heat and mass flux conditions. Most recently, a more systematical investigation on flow boiling patterns has been carried out by Wang et al. [13], who show that stable and unstable flow patterns occur in microchannels, depending on the values of heat to mass flux ratio q/G and inlet subcooling. Note that the boiling number Bo_i is related to q/G by

$$\mathrm{Bo}_i = \frac{q}{Gh_{fg}} \tag{2}$$

Figure 1 shows that the following three flow boiling modes exist in microchannels having a hydraulic diameter of 186 μm at an inlet subcooling of 35°C:

1. Stable flow boiling mode I for $q/G<0.96$ J/g: This is a stable flow boiling regime with no temporal temperature and pressure variations. Isolated bubbles are generated near the inlet and are carried away downstream by the bulk flow.

Unstable flow boiling mode II for $0.96\ \mathrm{J/g}<q/G<2.14$ J/g: elongated bubbles expand upstream because of the limited transverse space in the microchannels. The elongated bubble may expand to near the inlet of the microchannels, which becomes an annular/mist flow. The incoming cooled liquid pushes the elongated bubbles back to downstream, and isolated bubbles being generated upstream are carried away to downstream by the cooler incoming liquid. Thus, isolated bubbles flow and annular/mist flow appear alternatively with time in the microchannels. This leads to cyclic variations of wall temperatures and inlet pressure. As a result, the inlet wall temperature is gradually increased until it reaches an equilibrium state, and no temporal temperature variation after a sufficiently long time. This is an unstable flow boiling mode.

3. Stable flow boiling mode III for $q/G>2.14$ J/g: This is a stable flow boiling regime with the inlet wall temperature near saturated condition, and no temporal temperature variation is observed. Annular flow and mist flow may appear alternatively with time in the microchannels. Small cyclic variations of inlet pressure with short periods occur in the microchannels.

UHeat Transfer CharacteristicsU. Qu and Mudawar [6] performed an experiment on flow boiling of water in microchannels with a hydraulic diameter of 0.349 mm. Figure 2 shows that the measured local heat transfer coefficient decreased with the vapor quality, and it was pointed out that this behavior was contradictory to existing correlations for macrochannels. Yen et al. [14] obtained the local heat transfer coefficient for flow boiling of water at a flow rate G of 295 kg/mP^{2P} s and a heat flux q in the range of 1–13 kW/mP^{2P} s in microchannels having a hydraulic diameter of 0.51 mm. They found that the local heat transfer coefficient is independent of mass flux, but is a strong function of heat flux. They also found that the local heat transfer coefficient decreases with vapor quality. The local boiling heat transfer coefficient decreasing with vapor quality was also confirmed by Hetsroni et al. [9], who performed an experiment on flow boiling of water in microchannels with triangular cross sections having a hydraulic diameter of 144 μm at $G=95-340$ kg/mP^{2P} s and $q=80-330$ kw/mP^{2P}. Sumith et al. [15] obtained heat transfer coefficient for flow boiling of water in minichannels with a hydraulic diameter of 1.45 mm at $G=23.4-152.7$ kg/mP^{2P} s, and $q=10-715$ kW/mP^{2P}. As shown in Fig. 3, their measured heat transfer coefficients for $q>200$ kW/mP^{2P} were in agreement with correlation equations for macrochannels. However, their measurements for $q<200$ kW/mP^{2P} were higher than those predicted by correlation equations for macrochannels.

Most recently, Lee and Mudawar [16] carried out an experimental investigation for flow boiling of R-134a in microchannels

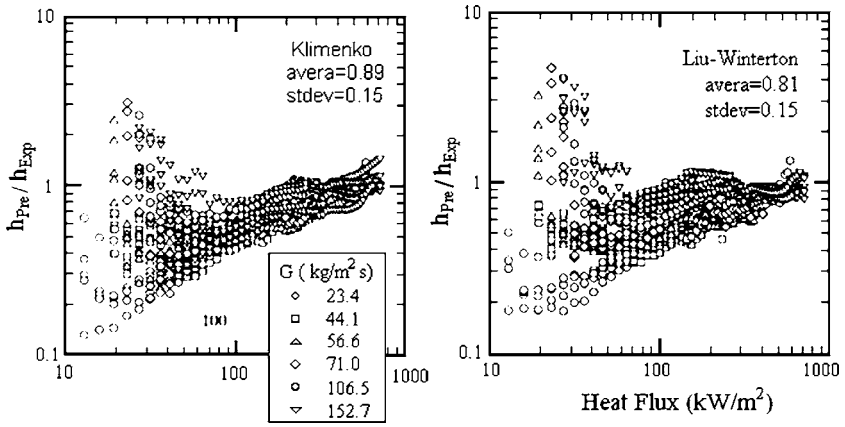

Fig. 3 Comparison of boiling heat transfer coefficient in minichannels with existing correlations for macrochannels [16]

having a hydraulic diameter of 0.349 mm. They found that boiling heat transfer coefficient of R-134a in microchannels cannot be predicted by existing correlation equations for flow boiling in macrochannels. Since boiling heat transfer mechanisms are different for low, medium, and high vapor qualities, they proposed different correlations for these three quality regimes. As in correlations for flow boiling in macrochannels, the Martinelli number is an important parameter in these three quality regimes in microchannels. However, whereas the Martinelli parameter is raised to a positive exponent in microchannel correlations, it was raised to a negative exponent in macrochannel correlation equations. In addition to the Martinelli parameter, they showed that the boiling number and the Weber number are also important parameters in the correlation of flow boiling heat transfer in the medium vapor qualities regime. It was found that their proposed correlations are in good agreement with their flow boiling heat transfer coefficient data in microchannels.

UPressure Drop Characteristics. In another paper, Lee and Mudawar [17] carried out an experiment for pressure drop in flow boiling of R-134a in a microchannel with a hydraulic diameter of 0.349 mm at $G=127-654$ kg/mP^{2P} s an $q=31.6-93.8$ W/cm P^{2P}. A comparison of their experimental data with existing correlation equations for pressure drop in macrochannels is presented in Fig. 4. It is shown that the pressure drop data in microchannels deviated greatly from those predicted by macrochannel correlations. Taking the surface tension effect into consideration, they proposed a modified Lockhart–Martinelli correlation with the additional parameters of Weber number and Reynolds number, which can predict their pressure drop data well.

Tran et al. [18] obtained pressure drop data in flow boiling of three refrigerants (R-134a, R-12, and R-113) in minichannels with hydraulic diameters of 2.46 and 2.92 mm, respectively. They compared their experimental data for minichannels with several existing correlations for macrochannels, and found that most of these existing correlations underpredicted the pressure drop in minichannels as shown in Fig. 5. They speculated that greater pressure drop in a microchannel may be due to additional friction relating to the movement of elongated bubbles. They proposed a modified B coefficient correlation taking into consideration the confinement of bubbles in microchannels. Their modified correlation for pressure drop in flow boiling of the three refrigerants agrees within ±20% of their measurements.

Condensation in Microchannels

UFlow Patterns. Chen and Cheng [19] performed the first flow visualization study on condensation of saturated steam in a silicon micorchannel with a hydraulic diameter of 75 μm. They found that mist flow with microwater droplets existed near the inlet of the microchannels and intermittent flow near the outlet. Subsequently, Wu and Cheng [20] carried out simultaneous visualization and measurement experiments on saturated steam condensing in parallel silicon microchannels with a length of 30 mm, having a trapezoidal cross section with a hydraulic diameter of 82.6 μm. They observed that mist flow, annular flow, slug/bubbly flow, and bubbly flow existed from upstream to downstream in the microchannels, as shown in Fig. 6. The transition from annular to slug/bubbly flow, which was clearly shown for the first time, is called the injection flow.

Most recently, Quan et al. [21] carried out a visualization study to investigate the effects of dimensionless condensation heat flux and Reynolds number of the saturated steam on the transition from annular flow to slug/bubbly flow in condensation in microchannels. The results are presented in Fig. 7 where Z/L is the

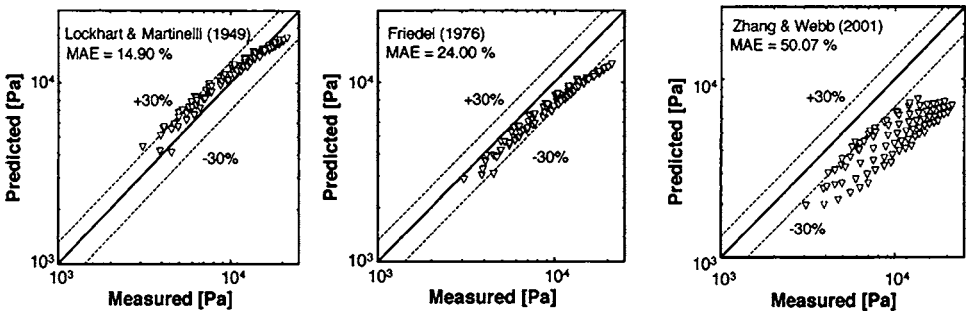

Fig. 4 Comparison of pressure drop data for flow boiling of R134a in microchannels with existing correlations for flow boiling in macrochannels [18]

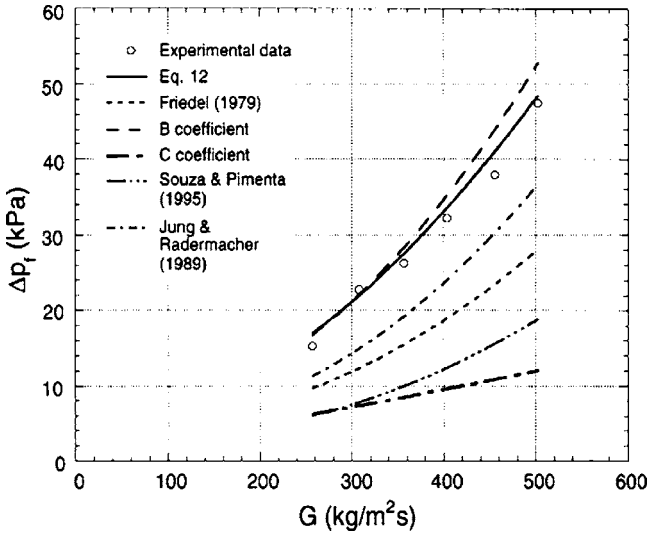

Fig. 5 Correlation of pressure drop of refrigerants in flow boiling in minichannels [19]

dimensionless location of the transition (with L denoting the length of the microchannels); Re is the Reynolds number of the steam; and $\tilde{q}=q_c/Gh_{fg}$ is the dimensionless condensation heat flux with q_c denoting the condensation heat flux. It is shown that the value of Z/L decreases (implying that injection flow occurs further upstream) with increasing $\tilde{q}$ or decreasing Re.

UHeat Transfer Characteristics. Shin and Kim [22] carried out an experiment on condensation of R134a in a microchanel with a hydraulic diameter of 0.493 mm. Figure 8 shows that their measured Nusselt numbers in the microchannels were higher than those predicted by the existing correlations for macrochannels at low mass fluxes ($G<200$ kg/mP^{2P} s). On the other hand, their measured Nusselt numbers at high mass flux ($G>200$ kg/mP^{2P} s) can be reasonably well predicted by existing correlations for macrochannels.

Pressure Drop Characteristics. Kim et al. [23] obtained pressure drop measurements for condensation flow of R134a in a microchannel having a hydraulic diameter of 0.691 mm. Figure 9 shows a comparison of their measurements with existing correlation equations for macrochannels. It is shown that at low mass flux ($G<200$ kg/mP^{2P} s), the pressure drop in condensation flow in a microchannel is lower than that predicted by Friedel's correlation for macrotubes. At higher mass fluxes ($G>200$ kg/mP^{2P} s), however, pressure drop in condensation flow in a microchannel can be predicted well by Friedel's correlation for macrotubes.

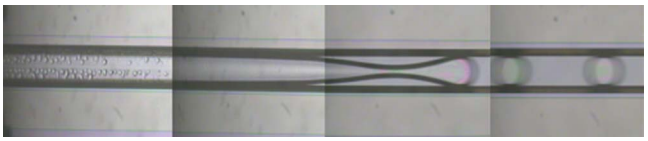

Fig. 6 Photos of condensation flow in microchannels with $DB_{hB}=82.6$ μm at $m=30.4$ g/cm^2 s [20]

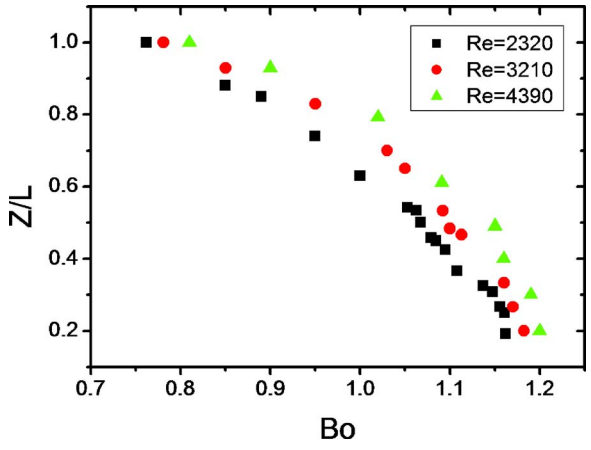

Fig. 7 Transition from annular to slug/bubbly flow in condensation of steam in microchannels [21]

Bubble Nucleation Under Pulse Heating

As mentioned in the Introduction s, microbubble nucleation under pulse heating has important applications to thermal inkjet printheads, vapor bubble pumps, and vapor bubble perturbators. Single bubbles can be generated periodically in these devices on a microheater under pulse heating with different pulse widths. For thermal inkjet printheads, bubbles are generated in the microsecond (μs) range. On the other hand, bubbles are generated in the millisecond (ms) range in vapor-bubble pumps and in vapor-bubble perturbators. Under rapid pulse heating, power densities equivalent to several megawatts per square meter can be generated. Bubble nucleation under an extremely high heat flux pulse differs from the usual nucleate boiling in many aspects. First, bubble nucleation is initiated at a higher temperature close to the theoretical superheat limit. Second, the boiling process is more explosive because the initial bubble pressure is very high. Third, the boiling process is more reproducible because its mechanism is governed by the property of the liquid (i.e., homogeneous nucleation) rather than by the surface characteristics (i.e., heterogeneous nucleation).

Effects of Pulse Width on Bubble Growth and Collapse. Deng et al. [26] performed an experiment to investigate the bubble growth and collapse on a nonuniform width microheater under pulse heating width in the millisecond range for the purpose of enhancing DNA hybridization [28–30]. Figure 10 shows the effect of pulse width τ on bubble growth and collapse on a nonuniform microheater with the slim part having a size of 10 $\times 3$ μm P^{2P}. It is shown that there is a rapid bubble expansion period followed by a slow bubble collapse period. The asymmetric bubble expansion and collapse periods lead to perturbation of the fluid. Moreover, a longer pulse width leads to a longer lifetime of a bubble. The case of $\tau=1.66$ ms was chosen for further study because this pulse width can lead to reasonable perturbation of fluid without introducing a large amount of heat.

Effects of Heater Size on Nucleation and Bubble Shape. Recently, Deng et al. [31] have performed an experiment to study effects of the heater size on bubble shape and onset of nucleation under a 1.66 ms pulse heating. Table 1 listed the dimensions of the submicron and micron heaters used in their experiments. Figure 11 shows the effect of heater size on nucleation temperature and nucleation time at a pulse width of 1.66 ms. It is shown that the nucleation temperature decreases while the nucleation time increases as the heater size is increased. This is because the temperature rise rate of the heater decreases with the heater size. It was also found that there existed a critical feature size of the heater, 10 μm, for this pulse width. The bubble shape for heaters with feature size below or above this critical value was quite different. Thus, the bubble generated by heaters can be classified into two groups as shown in Fig. 12. Single spherical bubble was generated periodically with Group I heaters (a)–(f) with the width of the slim part of the heater less than or equal to 10 μm, and an

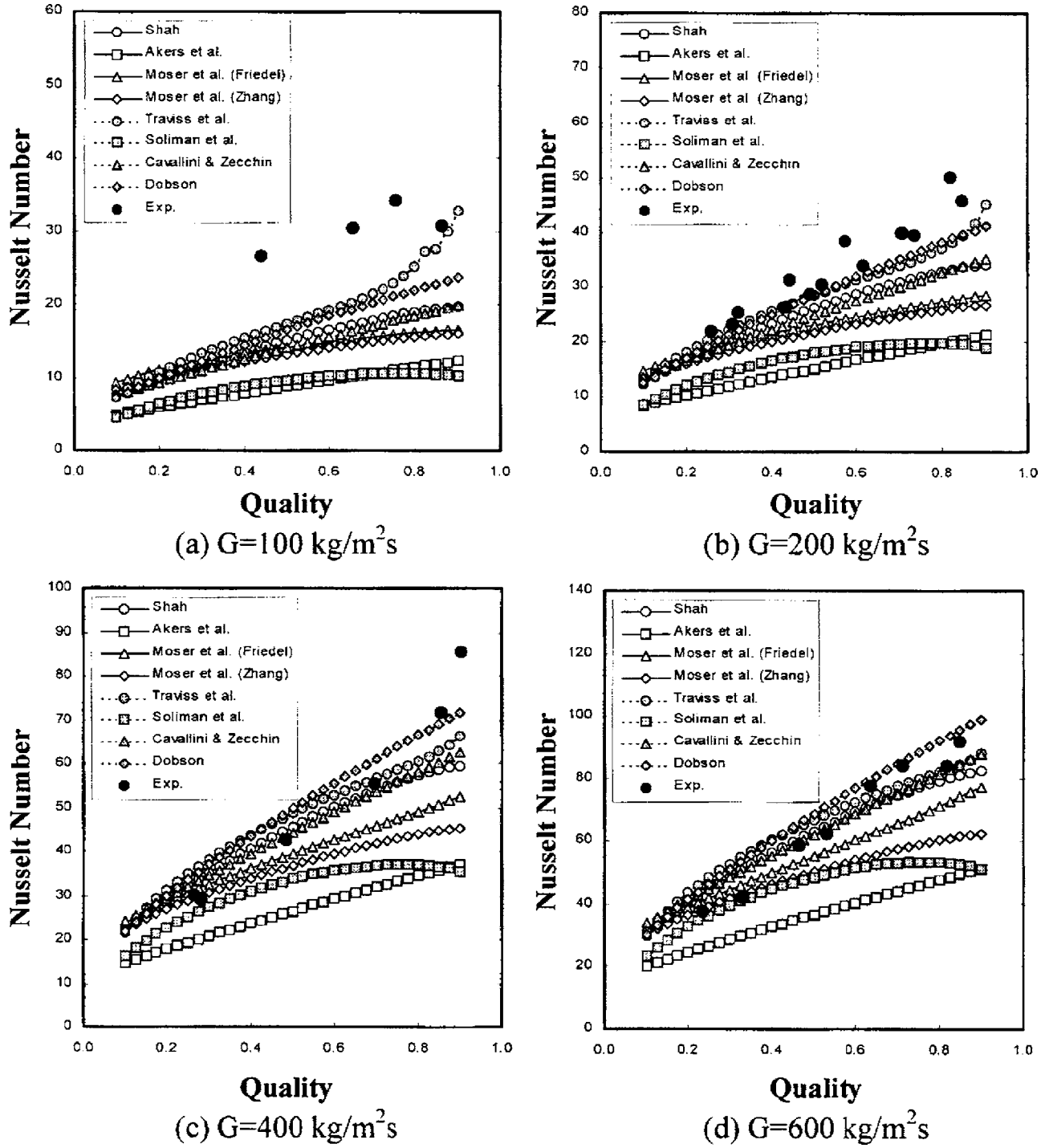

Fig. 8 Comparison of measured Nusselt number for condensation of R134a in microchannels with macrochannel correlation equation [23]

oblate vapor blanket was generated periodically with Group II heaters (g)–(k). The fact that the shape of the bubble and boiling pattern depends on the slim part of the heater can be explained as follows: after the occurrence of incipience of boiling, the water–vapor interface will try to form a spherical shape within the thin superheated liquid due to the surface tension effect, which is the dominant force at the microscale level. The spherical bubble begins to shrink when it grows near the outer edge of the thin superheated region because of the condensation effect. When the heater has exceeded a certain critical length, the spherical bubble cannot fit in the thin superheated region, and it grows to fit the thin superheated region as an elongated bubble on the heater. Because of the larger exposed area of the elongated bubble to outer cooled fluid, the condensation effect is much stronger than the spherical bubble. It then collapses immediately thereafter.

Concluding Remarks

Recent work on phase-change heat transfer processes in microsystems has been reviewed in this paper. The following conclusions can be drawn:

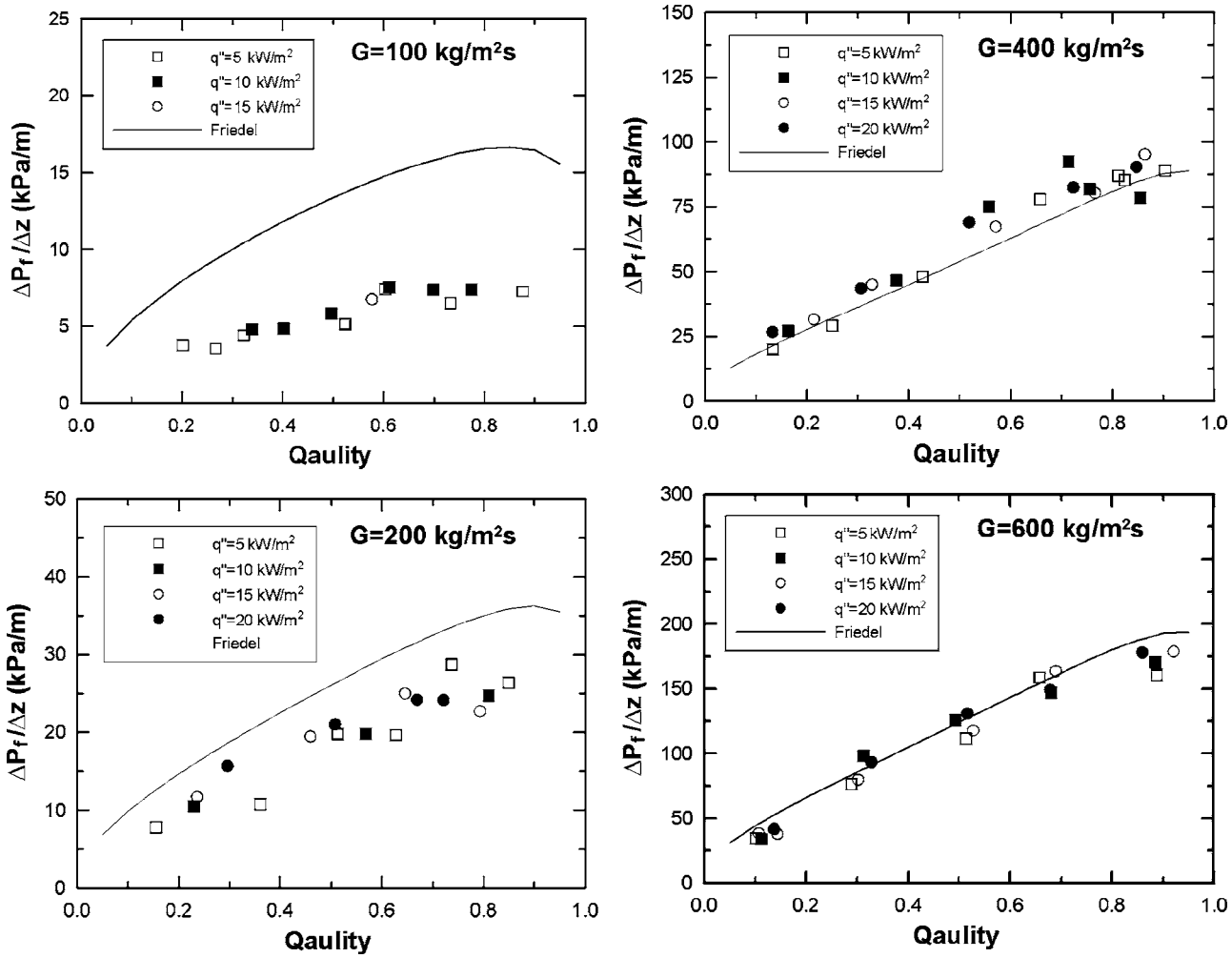

Fig. 9 Comparison of measured pressure drop versus quality for condensation flow of R-134a in a microchannel having D =0.691 mm with Friedel's correlation equation for macrochannels [24]

For Flow Boiling in Microchannels

1. Bubbly flow (isolated bubble), plug/slug flow (confined bubble), annular flow, and mist flow may exist in flow boiling in microchannels.
2. In the stable flow boiling mode I (see Fig. 1), vapor bubbles grow on the heated wall, elongated, and are carried away by the liquid to downstream. No temporal pressure and temperature variations have been observed in the microchannels under these conditions.
3. In the unstable flow boiling mode II (Fig. 1), cyclic variations of temperature and pressure have been observed. During one cycle, bubbly flow changes to annular/mist flow and then changes to bubbly flow again. The annular flow is formed when confined vapor bubbles expand in both up-

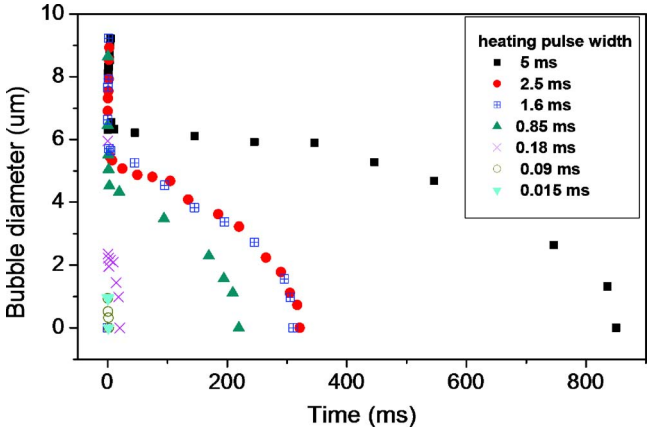

Fig. 10 Effects of pulse width on bubble growth and collapse on a 3×10 μm² microheater submerged in DI water [27]

Table 1 Dimensions of various submicron and micron heaters used in Deng et al.'s experiments [39]. The length and width are those of the slim part of the heater.

Heater ID	Length ±2% (μm)	Width ±3% (μm)
(a)	0.5	0.5
(b)	1	0.5
(c)	2	1
(d)	10	3
(e)	10	5
(f)	20	10
(g)	30	10
(h)	30	15
(i)	90	30
(j)	150	50
(k)	200	70

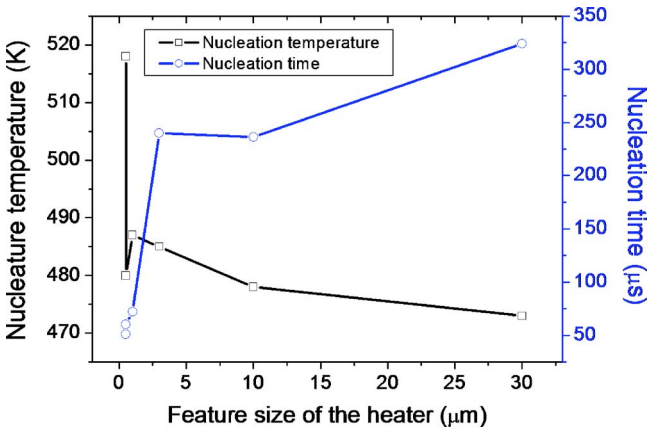

Fig. 11 Effects of heater size on nucleation temperature and nucleation time at pulse width of 1.66 ms [32]

stream and downstream directions, resulting in the increase of wall temperature and inlet water temperature. As a result, both wall temperature and inlet water temperature increase gradually with time, and amplitudes of oscillation decrease with time while the oscillation period increases with time. The oscillation flow becomes stable after an equilibrium condition is reached.

4. In the stable flow boiling mode III (Fig. 1), annular flow and mist flow appear, alternating in time in the microchannels. Periodic dryout and rewetting have been observed under these conditions. This is a stable flow boiling mode where no temperature oscillation has been observed although inlet pressure has small amplitude/short-period oscillations.
5. Both boiling heat transfer coefficient and pressure drop data in microchannels cannot be predicted by existing correlations obtained for macrochannels.

For Condensation Flow in Microchannels

1. There are four flow patterns in flow condensation in microchannels: mist flow, annular flow, slug/plug flow (confined bubble), and bubbly flow (isolated bubble).
2. The transition from annular flow to slug/plug flow during flow condensation takes place further downstream in the microchannels as the dimensionless heat transfer rate is increased, or as the Reynolds number is decreased.
3. At low mass fluxes ($G<200$ kg/mP^{2P} s), measured Nusselt numbers for condensation in microchannels are higher than predicted from correlations for macrochannels. At high mass fluxes ($G>200$ kg/mP^{2P} s), the measured Nusselt numbers in microchannels can be predicted well with existing correlations for macrochannels.
4. At low mass fluxes ($G<200$ kg/mP^{2P} s), measured pressure drop data for condensation flow in microchannels is lower those predicted by Friedel's correlation for macrotubes. At high mass fluxes ($G>200$ kg/mP^{2P} s), the measured pressure drop data can be predicted well with existing correlations for macrochannels.

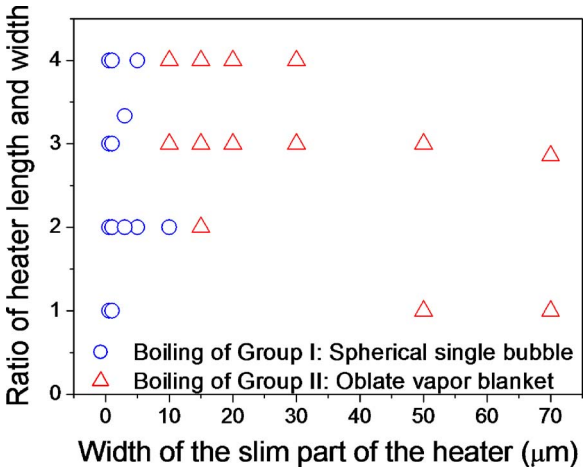

Fig. 12 Effect of heater size on bubble shapes at pulse width of 1.66 ms [32]

For Microbubble Generation Under Pulse Heating

1. A single microbubble can be generated periodically by a nonuniform width microheater under pulse heating.
2. When the pulse width of a microheater is in the microsecond range, the growth and collapse period of a microbubble is symmetric.
3. When the pulse width of a microheater is in the millisecond range, a rapid expansion period and a slow collapse period are observed. The rapid expansion period is pressure control while the slow collapse period is thermal control. The asymmetric expansion and collapse periods lead to flow perturbations.
4. Whether it is a spherical vapor bubble or oblate vapor blanket on the heater depends on the pulse width and heater size.

Acknowledgment

This work was supported by the National Natural Science Foundation of China through Grant No. 50536010 and 50476017, and by Shanghai Municipal Science and Technology Committee through Grant No. 05JC14025.

Nomenclature

Bo_d = Bond number
Bo_i = boiling number
DB_{hB} = hydraulic diameter (m)
g = gravity (m/sP^{2P})
G = mass flux (kg/mP^{2P} s)
h = enthalpy (J/kg)
hB_{fgB} = latent of heat of evaporation (J/kg)
L = length of the microchannel (m)
ℓB_{cB} = capillary length (m)
q = heat flux (kW/mP^{2P})
x = vapor quality
Z = distance from the inlet (m)

Greek Symbols

μ = dynamic viscosity (N s/mP^{2P})
ρ = density (kg/mP^{3P})
σ = surface tension (N/m)

References

[1] McGlen, R. J., Jachuck, R., and Lin, S., 2004, "Integrated Thermal Management Techniques for High Power Electronic Devices," Appl. Therm. Eng., **24**, pp 1143–116.
[2] Cheng, P., and Wu, H. Y., 2006, "Mesoscale and Microscale Phase-Change Heat Transfer," Adv. Heat Transfer, **39**, pp. 461–563.
[3] Kandlikar, S. G., 2004, "Heat Transfer Mechanism During Flow Boiling in Microchannels," J. Heat Transfer, **126**, pp. 8–16.
[4] Hetsronic, G., Mosyak, A., and Segal, Z., 2001, "Nonuniform Temperature Distribution in Electronic Devices Cooled by Flow in Parallel Microchannels," IEEE Trans. Compon. Packag. Technol., **24**, pp. 7–23.
[5] Hetsronic, G., Mosyak, A., Segal, Z., and Ziskind, G. A., 2002, "A Uniform Temperature Heat Sink for Cooling of Electronic Devices," Int. J. Heat Mass Transfer, **45**, pp. 3275–3286.
[6] Qu, W., and Mudawar, I., 2003, "Flow Boiling Heat Transfer in Two-Phase Microchannel Heat Sinks-I. Experimental Investigation and Assessment of Correlation Methods," Int. J. Heat Mass Transfer, **46**, pp. 2755–2771.
[7] Lee, P. C., Tseng, F. G., and Pan, C., 2004, "Bubble Dynamics in Microchannels. Part I: Single Microchannel," Int. J. Heat Mass Transfer, **47**, pp. 5575–5589.

[8] Li, H. Y., Tseng, F. G., and Pan, C., 2004, "Bubble Dynamics in Microchannels. Part II: Two Parallel Microchannels," Int. J. Heat Mass Transfer, **47**, pp. 5591–5601.
[9] Hetsroni, G., Mosyak, A., Pogrebnyak, and Segal, Z., 2005, "Explosive Boiling of Water in Parallel Microchannels," Int. J. Multiphase Flow, **31**, pp. 371–392.
[10] Wu, H. Y., and Cheng, P., 2003, "Visualization and Measurements of Periodic Boiling in Silicon Microchannels," Int. J. Heat Mass Transfer, **46**, pp. 2603–2614.
[11] Wu, H. Y., and Cheng, P., 2003, "Liquid/Two-Phase/Vapor Alternating Flow During Boiling in Microchannels at High Heat Flux," Int. Commun. Heat Mass Transfer, **30**, pp. 295–302.
[12] Wu, H. Y., and Cheng, P., 2004, "Boiling Instability in Parallel Silicon Microchannels at Different Heat Flux," Int. J. Heat Mass Transfer, **47**, pp. 3631–3641.
[13] Wang, G. D., Cheng, P., and Wu, H. Y., 2006, "Stable and Unstable Flow Boiling Regimes in Microchannels."
[14] Yen, T. H., Kasagi, N., and Suzuki, Y., 2003, "Forced Convective Boiling Heat Transfer in Microtubes at Low Mass and Heat Fluxes," Int. J. Multiphase Flow, **29**, pp. 1771–1792.
[15] Sumith, B., Kaminaga, F., and Matsumura, K., 2003, "Saurated Flow Boiling of Water in a Vertical Small Diameter Tube," Exp. Therm. Fluid Sci., **27**, pp. 789–801.
[16] Lee, J., and Mudawa, I., 2005, "Two-Phase Flow in High Heat Flux Microchannel Heat Sink for Refrigeration Cooling Applications: Part II-Heat Transfer Characteristics," Int. J. Heat Mass Transfer, **48**, pp. 941–955.
[17] Lee, J., and Mudawa, I., 2005, "Two-Phase Flow in High-Heat Flux Microchannel Heat Sink for Refrigeration Cooling Applications: Part I-Pressure Drop Characteristics," Int. J. Heat Mass Transfer, **48**, pp. 928–940.
[18] Tran, T. N., Chyu, M. C., Wambsganss, M. W., and France, D. M., 2000, "Two-Phase Pressure Drop of Refrigerants During Flow Boiling in Small Channels: An Experimental Investigation and Correlation Development," Int. J. Multiphase Flow, **26**, pp. 1739–1754.
[19] Chen, Y. P., and Cheng, P., 2005, "Condensation of Steam in a Silicon Microchannel," Int. Commun. Heat Mass Transfer, **32**, pp. 175–183.
[20] Wu, H. Y., and Cheng, P., 2005, "Condensation Flow Patterns in Silicon Microchannels," Int. J. Heat Mass Transfer, **48**, pp. 2186–2197.
[21] Quan, X. J., Cheng, P., and Wu, H. Y., 2006, Transition from Annular to Slug/Bubbly Flow in Convective Condensation in Microchannels, unpublished.
[22] Shin, J. S., and Kim, M. H., 2004, "An Experimental Study of Flow Condensation Heat Transfer Inside Circular and Rectangular Minichannels," *Proc. of* 2P^{ndP} *International Conference, on Microchannel and Microchannels*, pp. 633–640.
[23] Kim, M. H., Shin, J. S., Huh, C., Ki, T. J., and Seo, K. W., 2003, "A Study of Condensation Heat Transfer in a Single Mini-tube and a Review of Korean Micro-and Mini-Channel Studies," *Proceedings of* 1st *International Conference on Microchannel and Microchannels*, pp. 47–58.
[24] Kobayashi, H., Koumura, N., and Ohno, S., 1981, "Canon Kabushiki Kaisha Liquid Recording Medium," US Patent Specification No. 4243994.
[25] Yin, Z., Prosperetti, and Kim, J., 2004, "Bubble Growth on an Impulsively Powered Microheater," Int. J. Heat Mass Transfer, **47**, pp. 1053–1067.
[26] Deng, P. G., Lee, Y. K., and Cheng, P., 2003, "The Growth and Collapse of a Micro-bubble under Pulse Heating," Int. J. Heat Mass Transfer, **46**, pp. 4041–4050.
[27] Okamoto, T., Suzuki, T., and Yamamoto, N., 2000, "Microarray Fabrication With Covalent Attachment of DNA using Bubble Jet Technology," Nat. Biotechnol., pp. 438–441.
[28] Deng, P. G., Lee, Y. K., and Cheng, P., 2006, "Two-Dimensional Micro-Bubble Actuator Array to Enhance Efficiency of Molecular Beacon Based DNA Micro-Biosensors," Biosens. Bioelectron., **21**, pp. 1443–1450.
[29] Deng, P. G., Lee, Y. K., and Cheng, P., 2004, "Micro Bubble Dynamics in DNA Solutions," J. Micromech. Microeng., **14**, pp. 693–701.
[30] Deng, P. G., Lee, Y. K., and Cheng, P., 2005, "Measurements of Micro Bubble Nucleation Temperatures in DNA Solutions," J. Micromech. Microeng., **15**, pp. 564–574.
[31] Deng, P. G., Lee, Y. K., and Cheng, P., 2006, "An Experimental Study of Heater Size Effects on Microbubble Generation," Int. J. Heat Mass Transfer, **49**, pp. 2535–2544.

Multiquadric Collocation Method for Time-Dependent Heat Conduction Problems With Temperature-Dependent Thermal Properties

Somchart Chantasiriwan
Faculty of Engineering,
Thammasat University,
Pathum Thani 12121, Thailand
e-mail: somchart@engr.tu.ac.th

The multiquadric collocation method is a meshless method that uses multiquadrics as its basis function. Problems of nonlinear time-dependent heat conduction in materials having temperature-dependent thermal properties are solved by using this method and the Kirchhoff transformation. Variable transformation is simplified by assuming that thermal properties are piecewise linear functions of temperature. The resulting nonlinear equation is solved by an iterative scheme. The multiquadric collocation method is tested by a heat conduction problem for which the exact solution is known. Results indicate satisfactory performance of the method. [DOI: 10.1115/1.2401617]

Keywords: Kirchhoff transformation, meshless, radial basis function

Introduction

Multiquadrics is a radial basis function discovered by Hardy [1]. The multiquadric collocation method, also known as Kansa's method [2], has been used to solve various steady-state problems [3–6] and time-dependent problems [7–9] in mechanics. It has been shown that this method can yield satisfactory solutions to linear problems. Being a meshless method, this method has advantages over conventional numerical methods such as the finite element method and the finite difference method. However, before considering the multiquadric collocation method as a serious alternative to the finite element method and the finite difference method, this method must be tested with nonlinear time-dependent problems. There have been relatively few such problems solved by the multiquadric collocation method [10,11].

A well-known nonlinear time-dependent problem is the time-dependent heat conduction problem with temperature-dependent thermal properties. Several algorithms have been proposed to find its solution. Previous algorithms, however, depend on mesh-dependent methods such as the finite element method and the finite difference method. In this paper, an algorithm making use of the multiquadric collocation method is proposed. First, the problem is simplified by the Kirchhoff transformation. Then the multiquadric collocation method is formulated to deal with the problem in an iterative manner. The proposed algorithm is used to solve heat conduction problems in a fictitious material. Results show that solutions for problems in which heat capacities and thermal conductivities are piecewise linear functions of temperature are satisfactorily accurate.

Heat Conduction Problem

Heat conduction phenomena in which heat capacities and thermal conductivities depend on temperature are described by the following partial differential equation

$$\rho c_p(T)\frac{\partial T}{\partial t} = \nabla(k(T)\nabla T) + s(\boldsymbol{r},t) \quad \text{for } \boldsymbol{r} \text{ in } \Omega \tag{1}$$

Without the loss of generality, density is assumed to be constant. In addition, initial and boundary conditions are given by

$$T(\boldsymbol{r},0) = T_0(\boldsymbol{r}) \quad \text{for } \boldsymbol{r} \text{ in } \Omega \tag{2}$$

$$T(\boldsymbol{r},t) = T_b(\boldsymbol{r},t) \quad \text{for } \boldsymbol{r} \text{ on } \Gamma_1 \tag{3}$$

$$k(T)\frac{\partial T}{\partial n} = q_b(\boldsymbol{r},t) \quad \text{for } \boldsymbol{r} \text{ on } \Gamma_2 \tag{4}$$

Define u by using the Kirchhoff transformation

$$u(\boldsymbol{r},t) = \int_{T_r}^{T} k(T)\,dT \tag{5}$$

Transform the dependent variable in Eqs. (1)–(4) from T to u

$$\gamma(u)\frac{\partial u}{\partial t} = \nabla^2 u + s(\boldsymbol{r},t) \quad \text{for } \boldsymbol{r} \text{ in } \Omega \tag{6}$$

$$u(\boldsymbol{r},0) = u_0(\boldsymbol{r}) \quad \text{for } \boldsymbol{r} \text{ in } \Omega \tag{7}$$

$$u(\boldsymbol{r},t) = u_b(\boldsymbol{r},t) \quad \text{for } \boldsymbol{r} \text{ on } \Gamma_1 \tag{8}$$

$$\frac{\partial u}{\partial n} = q_b(\boldsymbol{r},t) \quad \text{for } \boldsymbol{r} \text{ on } \Gamma_2 \tag{9}$$

where $\gamma = \rho c_p/k$ is the reciprocal of thermal diffusivity α.

Discretization Scheme

Consider thermal properties of three materials shown in Tables 1–3. Thermal conductivities and heat capacities of materials A, B, and C are the same as those of zirconium, tungsten, and tantalum, respectively, which are obtained from Ref. [12]. However, the densities of materials A, B, and C are constant instead of temperature dependent as the actual densities of zirconium, tungsten, and tantalum are. It can be seen that thermal conductivities of these materials are not linear functions of T. Equation (5) indicates that $u(T)$ is a monotonically increasing function because $k(T)$ is al-

Contributed by the Heat Transfer Division of ASME for publication in the JOURNAL OF HEAT TRANSFER. Manuscript received June 13, 2005; final manuscript received April 30, 2006. Review conducted by A. Haji-Sheikh.

Table 1 Thermal properties of material A

T (K)	ρ (kg m^{-3})	k (W m^{-1} K^{-1})	c_p (J kg^{-1} K^{-1})
100	6570	33.2	205
200	6570	25.2	264
400	6570	21.6	300
600	6570	20.7	322
800	6570	21.6	342
1000	6570	23.7	362
1200	6570	26.0	344

ways positive, and an explicit function $u(T)$ can be found quite easily no matter how complicated $k(T)$ is. On the contrary, an explicit function of $T(u)$ is difficult to determine unless $k(T)$ is a linear function. Therefore, although it is possible to approximate $k(T)$ as a sixth-order polynomial function of T using data from seven temperatures, it is more efficient for computational purpose to approximate $k(T)$ as a piecewise linear function:

$$k(T) = k_{i-1} + \left(\frac{k_i - k_{i-1}}{T_i - T_{i-1}}\right)(T - T_{i-1}) \quad (T_{i-1} \le T < T_i) \tag{10}$$

where $T_1, T_2, \ldots, T_7$ are seven temperatures in Tables 1–3 in ascending order, and $k_1, k_2, \ldots, k_7$ are the corresponding thermal conductivities. Let $T_r = 100$ K. Substituting $k(T)$ from Eq. (10) into Eq. (5) yields

$$u(T) = u_{i-1} + k_{i-1}(T - T_{i-1}) + \frac{1}{2}\left(\frac{k_i - k_{i-1}}{T_i - T_{i-1}}\right)(T - T_{i-1})^2 \quad (T_{i-1} \le T < T_i) \tag{11}$$

from which the inversion formula for $T(u)$ can be obtained as follows

$$T(u) = T_{i-1} + \left(\frac{T_i - T_{i-1}}{k_i - k_{i-1}}\right)\left[-k_{i-1} + \sqrt{k_{i-1}^2 + 2\left(\frac{k_i - k_{i-1}}{T_i - T_{i-1}}\right)(u - u_{i-1})^2}\right] \quad (u_{i-1} \le u < u_i) \tag{12}$$

After values of u corresponding to seven temperatures in Tables 1–3 for each material are calculated, γ can be plotted as functions of u. Figure 1 shows that, for each material, γ does not vary rapidly with u, and can be approximated as a piecewise linear function. It is interesting to note that variations of γ with u for the three materials are quite different.

Table 2 Thermal properties of material B

T (K)	ρ (kg m^{-3})	k (W m^{-1} K^{-1})	c_p (J kg^{-1} K^{-1})
100	19300	208	87
200	19300	186	122
400	19300	159	137
600	19300	137	142
800	19300	125	145
1000	19300	118	148
1200	19300	113	152

Table 3 Thermal properties of material C

T (K)	ρ (kg m^{-3})	k (W m^{-1} K^{-1})	c_p (J kg^{-1} K^{-1})
100	16600	59.2	110
200	16600	57.5	133
400	16600	57.8	144
600	16600	58.6	146
800	16600	59.4	149
1000	16600	60.2	152
1200	16600	61.0	155

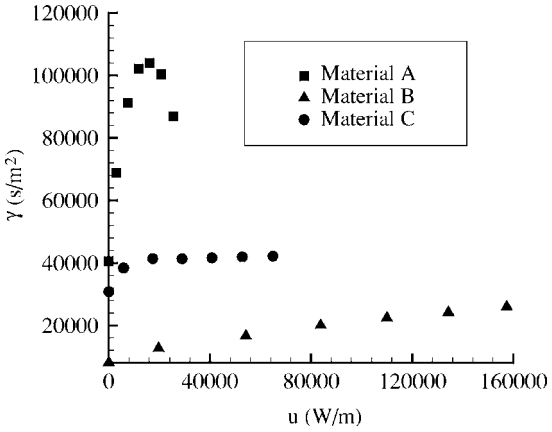

Fig. 1 Variations of the reciprocal of thermal diffusivities of materials A, B, and C with Kirchhoff transformation variable

Discretization of Eqs. (6)–(9) yields

$$\gamma^*\left(\frac{u_i^{(n)} - u_i^{(n-1)}}{\Delta t}\right) = \theta\nabla^2 u_i^{(n)} + (1-\theta)\nabla^2 u_i^{(n-1)} + s(\boldsymbol{r}_i, (n-1+\theta)\Delta t) \tag{13}$$

$$u_i^{(0)} = u_0(\boldsymbol{r}_i) \tag{14}$$

$$u_i^{(n)} = u_b(\boldsymbol{r}_i, n\Delta t) \tag{15}$$

$$\frac{\partial u_i^{(n)}}{\partial n} = q_b(\boldsymbol{r}_i, n\Delta t) \tag{16}$$

where

$$\gamma^* = \gamma(\theta u_i^{(n)} + (1-\theta)u_i^{(n-1)}) \tag{17}$$

Relaxation parameter θ must be greater than 0. In this study, $\theta = 0.5$.

Multiquadric Collocation Method

Let $\boldsymbol{r}_i$ $(i = 1, 2, \ldots, N_b)$ denote positions of boundary nodes and $\boldsymbol{r}_i$ $(i = N_b+1, N_b+2, \ldots, N_b+N_i)$ denote positions of interior nodes. The multiquadric collocation method approximates u as a linear combination of radial basis functions ϕ

$$u(\boldsymbol{r}, n\Delta t) = \sum_{j=1}^{N_b+N_i} a_j^{(n)} \phi(|\boldsymbol{r} - \boldsymbol{r}_j|) \tag{18}$$

where

$$\phi(r) = \sqrt{r^2 + c^2} \tag{19}$$

is known as multiquadrics. This function contains the shape parameter c. A suitable value of c is to be found by numerical experiments in this paper. Coefficients $a_j^{(0)}$ are determined directly from collocation using Eq. (14)

$$\sum_{j=1}^{N_b+N_i} a_j^{(0)} \phi(|\boldsymbol{r}_i - \boldsymbol{r}_j|) = u_0(\boldsymbol{r}_i) \quad (i = 1, 2, \ldots, N_b + N_i) \tag{20}$$

Coefficients $a_j^{(n)}$ $(n \ge 1)$ must be determined iteratively. First, Eq. (13) is rearranged

$$\theta\nabla^2 u_i^{(n)} - \left(\frac{\gamma^*}{\Delta t}\right)u_i^{(n)} = -(1-\theta)\nabla^2 u_i^{(n-1)} - \left(\frac{\gamma^*}{\Delta t}\right)u_i^{(n-1)} - s(\boldsymbol{r}_i, (n-1+\theta)\Delta t) \tag{21}$$

Next substitute $u_i^{(n)}$ and $u_i^{(n-1)}$ from Eq. (18) into Eqs. (21), (15), and (16)

$$\theta \sum_{j=1}^{N_b+N_i} a_j^{(n)} \nabla_i^2 \phi(|\boldsymbol{r}_i - \boldsymbol{r}_j|) - \left(\frac{\gamma^*}{\Delta t}\right) \sum_{j=1}^{N_b+N_i} a_j^{(n)} \phi(|\boldsymbol{r}_i - \boldsymbol{r}_j|)$$
$$= -(1-\theta) \sum_{j=1}^{N_b+N_i} a_j^{(n-1)} \nabla_i^2 \phi(|\boldsymbol{r}_i - \boldsymbol{r}_j|)$$
$$- \left(\frac{\gamma^*}{\Delta t}\right) \sum_{j=1}^{N_b+N_i} a_j^{(n-1)\phi}(|\boldsymbol{r}_i - \boldsymbol{r}_j|) - s(\boldsymbol{r}_i, (n-1+\theta)\Delta t)$$
$$(i = N_b+1, N_b+2, \ldots, N_b+N_i) \tag{22}$$

$$\sum_{j=1}^{N_b+N_i} a_j^{(n)} \phi(|\boldsymbol{r}_i - \boldsymbol{r}_j|) = u_b(\boldsymbol{r}_i, n\Delta t) \quad (i = 1,2, \ldots, N_{b1}) \tag{23}$$

$$\sum_{j=1}^{N_b+N_i} a_j^{(n)} \frac{\partial \phi}{\partial n} = q_b(\boldsymbol{r}_i, n\Delta t) \quad (i = N_{b1}+1, N_{b1}+2, \ldots, N_{b1}+N_{b2}) \tag{24}$$

Initially, it must be assumed that $a_j^{(n)} = a_j^{(n-1)}$ so that γ^* can be determined, and Eqs. (22)–(24) can be solved for $a_j^{(n)}$. After the determination of $a_j^{(n)}$, Eqs. (22)–(24) are solved for new values of $a_j^{(n)}$. The iteration process continues until the average difference between new and old values of $u_i^{(n)}$ is less than a tolerance number δ

$$\left[\frac{1}{N_i} \sum_{i=N_b+1}^{N_b+N_i} \left(1 - \frac{(u_i^{(n)})_{\text{new}}}{(u_i^{(n)})_{\text{old}}}\right)^2\right]^{1/2} < \delta \tag{25}$$

provided that no value of $u_i^{(n)}$ is zero. Otherwise, a new measure of the difference between new and old values of $u_i^{(n)}$ must be used. In this study, $\delta = 1.0 \times 10^{-5}$.

After converged values of $u_i^{(n)}$ have been found, $T_i^{(n)}$ can be determined from Eq. (12). If exact temperatures are known, average error in computed temperatures (ε) can be found from the average difference between computed temperatures and exact temperatures at N_t test nodes, of which locations are denoted by $\boldsymbol{\xi}_i$ ($i = 1,2, \ldots, N_t$).

$$\varepsilon = \left[\frac{1}{N_t} \sum_{i=1}^{N_t} \left(1 - \frac{T_i^{(n)}}{(T_i^{(n)})_{\text{exact}}}\right)^2\right]^{1/2} \tag{26}$$

where $T_i^{(n)}$ is determined from

$$u_i^{(n)} = \sum_{j=1}^{N_b+N_i} a_j^{(n)} \phi(|\boldsymbol{\xi}_i - \boldsymbol{r}_j|) \tag{27}$$

using Eq. (12), and $(T_i^{(n)})_{\text{exact}}$ is the exact solution at location $\boldsymbol{\xi}_i$ and time $n\Delta t$.

Results and Discussion

Consider a 0.12 m × 0.12 m square domain having the thermal properties of material A. Let N nodes be uniformly distributed in the domain so that there are $(\sqrt{N}-2)^2$ interior nodes and $(4\sqrt{N}-4)$ boundary nodes. The spacing between two adjacent nodes is, therefore, $0.12/(\sqrt{N}-1)$ m, which is denoted by Δ. Coordinates of N nodes are $((i-1)\Delta, (j-1)\Delta)$, where i and j run from 1 to $\sqrt{N}$. As shown in Fig. 2, the bottom, right, and top sides of the domain are subjected to the Dirichlet boundary condition, whereas the left side of the domain is subjected to the Neumann boundary condition. The exact solution is

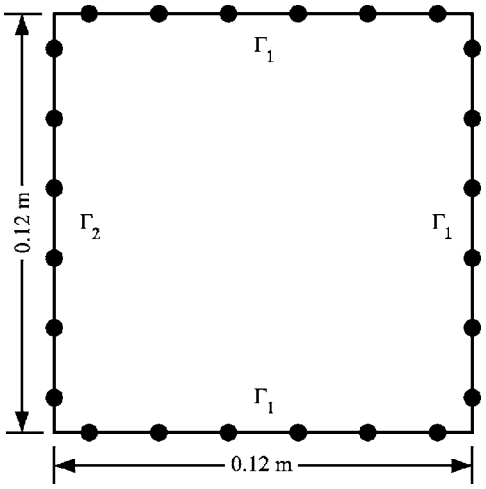

Fig. 2 Domain of test problem is a 0.12 m × 0.12 m square. The left side is the Neumann boundary and the other three sides are the Dirichlet boundary. Black circles indicate locations of 24 boundary test nodes.

$$T_{\text{exact}}(x,y,t) = [104.43 + 4.43 \cos(0.01t)] \exp[10(x+y)] \tag{28}$$

so that the minimum and maximum values are approximately 100 K and 1200 K, respectively, which are the lower and upper limits of the temperature range in Tables 1–3. This function is used to generate the initial value function $T_0(x,y)$, the Dirichlet boundary value function $T_b(x,y,t)$, the Neumann boundary value function $q_b(x,y,t)$ function, and the source function $s(x,y,t)$ according to

$$s(x,y,t) = \rho c(T) \frac{\partial T}{\partial t} - k(T)\left(\frac{\partial^2 T}{\partial x^2} + \frac{\partial^2 T}{\partial y^2}\right) - \frac{dk}{dT}\left[\left(\frac{\partial T}{\partial x}\right)^2 + \left(\frac{\partial T}{\partial y}\right)^2\right] \tag{29}$$

The multiquadric collocation method is then used to obtain an approximate solution, which can be compared with the exact solution to evaluate the performance of the method.

Effects of Shape Parameter. It is well known that the accuracy of the multiquadric collocation method is sensitive to the shape parameter, which may be chosen to optimize the performance of multiquadrics as an interpolating function. Although a variable shape parameter has been suggested [13,14], there is evidence that using a variable shape parameter does not always lead to a more accurate solution than using a constant shape parameter [7]. In order to investigate effects of the shape parameter on the solution by the proposed method, variations with time of average error are calculated for five values of the shape parameter (0.1, 0.11, 0.12, 0.13, and 0.14). Coordinates of 36 interior test nodes are $(0.02i - 0.01, 0.02j - 0.01)$, where i and j run from 1 to 6, $N = 49$, and $\Delta t = 0.5$ s. Figure 3 shows that average error depends on the shape parameter. It is obvious that there exists an optimum value of shape parameter as far as accuracy is concerned. For material A, the optimum value is around 0.11. It is also found that the optimum values for material B and C are 0.11 and 0.14, respectively. Instead of proposing an algorithm for finding the optimum value, it is proposed that the value of 0.12 is an appropriate value since this value gives a solution that is not much less accurate than the solution at the optimum value of shape parameter.

Convergence Test. Behaviors of solutions by the multiquadric collocation method as Δ and Δt decrease are investigated by using three values of N. With $\Delta t/\Delta^2$ kept constant at 1250 s/m^2, values of $(\Delta, \Delta t)$ corresponding to $N = 25$, 49, and 169 are

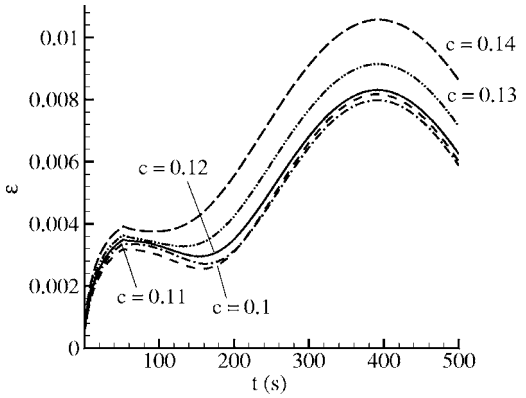

Fig. 3 Variations with time of average error for 36 interior test nodes corresponding to different shape parameters of multiquadrics

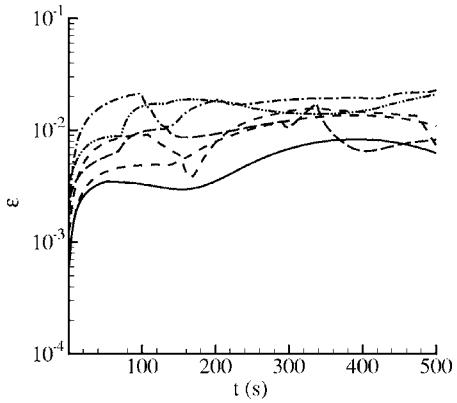

Fig. 5 Variations with time of average error for 36 interior test nodes corresponding to different node arrangements. The solid line represents the uniform arrangement, whereas five other lines represent five random arrangements.

(0.03 m, 1.125 s), (0.02 m, 0.5 s), and (0.01 m, 0.125 s), respectively. The shape parameter is varied according to $c/\Delta=6$. Wong et al. [8] and Fasshauer [15] also suggested that c should be proportional to Δ. Results in Fig. 4 indicate that reducing Δ and Δt in the multiquadric collocation method results in a more accurate solution.

Effects of Random Node Arrangement. The multiquadric collocation method does not require a uniform arrangement of nodes like the finite difference method. In fact, a random arrangement may be preferable if it makes the process of node placement easier. A random node arrangement results from distributing each interior node i randomly according to $(x_i, y_i)=(\bar{x}_i+d_1\Delta, \bar{y}_i+d_2\Delta)$, where $(\bar{x}_i, \bar{y}_i)$ is the position of node i in the uniform arrangement, and d_1 and d_2 are random numbers between −0.5 and 0.5. The result for the uniform arrangement is compared with results for five random arrangements with $N=49$, $\Delta t=0.5$ s, and $c=0.12$. Figure 5 shows that a random node arrangement does not significantly affect the accuracy of the solution.

Boundary solution. The boundary solution by a collocation method may be less accurate than interior solution. Figure 6 compares average error for the 36 interior test nodes used to obtain Figs. 3–5 with average error for six boundary test nodes on Γ_2 as shown in Fig. 2. It can be seen that the boundary solution is slightly less accurate than the interior solution. In addition, Fig. 6 shows variation of average error in the heat flux (ε_q) for 18 test nodes on Γ_1 as shown in Fig. 2

$$\varepsilon_q = \left[\frac{1}{N_t} \sum_{i=1}^{N_t} \left(1 - \frac{q_i^{(n)}}{(q_i^{(n)})_{\text{exact}}} \right)^2 \right]^{1/2} \tag{30}$$

where

$$q_i^{(n)} = \sum_{j=1}^{N_b+N_i} a_j^{(n)} \frac{\partial \phi}{\partial n}(|\boldsymbol{\xi}_i - \boldsymbol{r}_j|) \tag{31}$$

and $(q_i^{(n)})_{\text{exact}}$ is the exact heat flux at boundary location $\boldsymbol{\xi}_i$ and time $n\Delta t$. Average error in computed heat flux is about one order of magnitude larger than average error in computed temperatures.

Comparison With the Finite Difference Method. The finite difference method can be considered as a benchmark with which meshless methods such as the multiquadric collocation method should be compared. Although meshless methods have an advantage over the finite difference method in that an arbitrary problem geometry can be easily dealt with, this advantage should not mean solution accuracy has to be compromised. Figure 7 compares the solution to the test problem by the finite difference method having $N=169$ and $\Delta t=0.125$ s with the solution by the multiquadric collocation method having $N=169$, $\Delta t=0.125$ s, and $c=0.06$. Coordinates of the 121 test nodes used for computing both solutions are $(0.01i, 0.01j)$, where i and j run from 1 to 11. It is evident that both methods yield solutions of comparable accuracy. It is interesting to note, however, that comparison performed using a

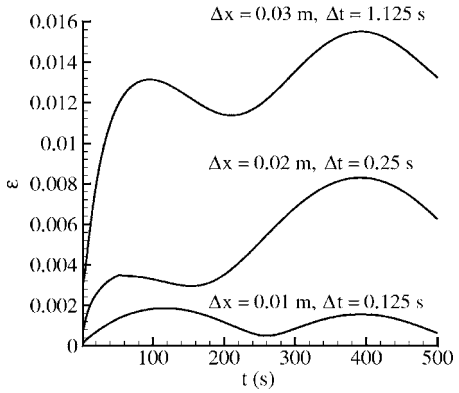

Fig. 4 Variations with time of average error for 36 interior test nodes corresponding to different grid spacings and time steps

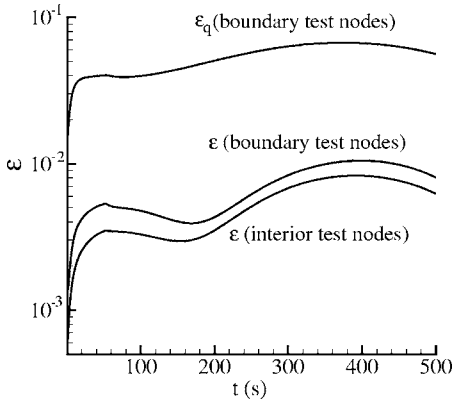

Fig. 6 Comparison of average error in computed temperatures for 36 interior test nodes, average error in computed temperatures for 6 boundary test nodes, and average error in computed heat flux for 18 boundary test nodes

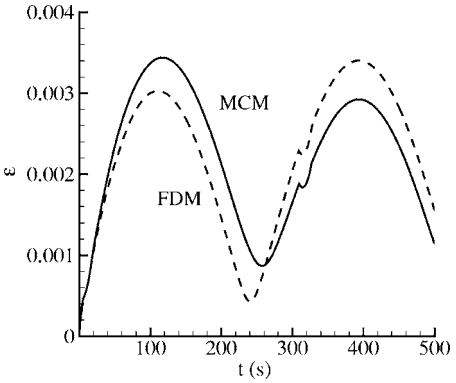

Fig. 7 Comparison of average errors for 121 interior test nodes by the multiquadric collocation method (MCM) and the finite difference method (FDM)

3.0 GHz Pentium 4 CPU indicated that the finite difference method was a little faster because it used less CPU time (116.95 s) than the multiquadric collocation method (134.55 s).

Conclusions

Heat conduction problems in materials of which thermal properties are temperature dependent can be solved by the multiquadric collocation method. Results show that the shape parameter of multiquadrics affects the accuracy of the solution. A value of the shape parameter that yields solutions of satisfactory accuracy is suggested. In addition, it is shown that the multiquadric collocation method is more accurate as grid spacing and time step decrease, a random arrangement of nodes does not affect the accuracy of the method significantly, average error in computed heat flux is about an order of magnitude larger than average error in computed temperatures, and solutions by the multiquadric collocation method and the finite difference method have comparable accuracy.

It has been accepted that meshless methods have advantages over the finite difference method and the finite element method in their ability to deal with domains of complex geometry without requiring mesh generation. Acceptance of these methods depends on more testing of these methods using nonlinear time-dependent problems. This paper has shown that the multiquadric collocation method has the potential to be an acceptable alternative numerical method for solving general partial differential equations.

Acknowledgment

The author would like to acknowledge the financial support from the Thailand Research Fund.

Nomenclature

a = coefficient
c = shape parameter
c_p = heat capacity, J/(kg.K)
d_1, d_2 = random numbers
k = thermal conductivity, W/(m.K)
N = number of nodes
n = normal coordinate or time level
q = heat flux, W/m^2
r = distance between two nodes, m
$\boldsymbol{r}$ = position vector of a boundary or an interior node
s = source function
T = temperature, K
t = time, s
u = Kirchhoff transformation variable, W/m
x = horizontal coordinate, m
y = vertical coordinate, m

Greek Symbols

Δ = grid spacing, m
Δt = time step, s
δ = tolerance number
ε = average error in computed temperature
ε_q = average error in computed heat flux
ϕ = multiquadrics
Γ_1 = Dirichlet boundary
Γ_2 = Neumann boundary
γ = reciprocal of thermal diffusivity, s/m^2
θ = relaxation parameter
ρ = density, kg/m^3
Ω = domain
$\boldsymbol{\xi}$ = position vector of a test node

Subscripts

0 = initial value
b = boundary
i = position index or interior
j = position index
r = reference
t = test

Superscript

n = time index

References

[1] Hardy, R. L., 1971, "Multiquadric Equations of Topography and Other Irregular Surfaces," J. Geophys. Res., **176**, pp. 1905–1915.
[2] Kansa, E. J., 1990, "Multiquadrics—A Scattered Data Approximation Scheme With Applications to Computational Fluid Dynamics II," Comput. Math. Appl., **19**, pp. 147–161.
[3] Leitao, V. M. A., 2001, "A Meshless Method for Kirchhoff Plate Bending Problem," Int. J. Numer. Methods Eng., **52**, pp. 1107–1130.
[4] Power, H., and Barraco, V., 2002, "A Comparison Analysis Between Unsymmetric and Symmertic Radial Basis Function Collocation Methods for the Numerical Solution of Partial Differential Equations," Comput. Math. Appl., **43**, pp. 551–583.
[5] Li, J., Cheng, A. H. D., and Chen, C. S., 2003, "A Comparison of Efficiency and Error Convergence of Multiquadric Collocation Method With Finite Element Method," Eng. Anal. Boundary Elem., **26**, pp. 205–255.
[6] Chantasiriwan, S., 2004, "Cartesian Grid Methods Using Radial Basis Functions for Solving Poisson, Helmholtz, and Diffusion–Convection Equations," Eng. Anal. Boundary Elem., **28**, pp. 1417–1425.
[7] Zerroukat, M., Power, H., and Chen, C. S., 1998, "A Numerical Method for Heat Transfer Problems Using Collocation and Radial Basis Functions," Int. J. Numer. Methods Eng., **42**, pp. 1263–1278.
[8] Wong, A. S. M., Hon, Y. C., Li, T. S., Chung, S. L., and Kansa, E. J., 1999, "Multizone Decomposition for Simulation of Time-Dependent Problems Using the Multiquadric Scheme," Comput. Math. Appl., **37**, pp. 23–43.
[9] Ferreira, A. J. M., Martins, P. A. L. S., and Roque, C. M. C., 2005, "Solving Time-Dependent Engineering Problems With Multiquadrics," J. Sound Vib., **280**, pp. 595–610.
[10] Sarra, S. A., 2005, "Adaptive Radial Basis Function Methods for Time Dependent Partial Differential Equations," Appl. Numer. Math., **54**, pp. 79–94.
[11] Hon, Y. C., and Mao, X. Z., 1998, "An Efficient Numerical Scheme for Burgers' Equation," Appl. Math. Comput., **95**, pp. 37–50.
[12] Incropera, F. P., and DeWitt, D. P., 1996, *Introduction to Heat Transfer*, Wiley, New York.
[13] Carlson, R. E., and Foley, T. A., 1991, "The Parameters R2 in Multiquadric Interpolation," Comput. Math. Appl., **21**, pp. 29–42.
[14] Kansa, E. J., and Carlson, R. E., 1992, "Improved Accuracy of Multiquadric Interpolation Using Variable Shape Parameters," Comput. Math. Appl., **24**, pp. 99–120.
[15] Fasshauer, G. E., 2002, "Newton Iteration With Multiquadrics for the Solution of Nonlinear PDEs," Comput. Math. Appl., **43**, pp. 423–438.

Effects of Gap Geometry and Gravity on Boiling Around a Constrained Bubble in 2-Propanol/Water Mixtures

Chen-Ii Sun[1]
Department of Mechanical Engineering,
National Taiwan University of Science and Technology,
43 Sec. 4 Keelung Rd.,
Taipei, 106, Taiwan
e-mail: clsun@mail.ntust.edu.tw

Van P. Carey
Department of Mechanical Engineering,
University of California,
Berkeley, Berkeley, CA 94720-1740
e-mail: vcarey@me.berkeley.edu

In this study, boiling experiments were conducted with 2-propanol/water mixtures in confined gap geometry under various levels of gravity. The temperature field created within the parallel plate gap resulted in evaporation over the portion of the vapor-liquid interface of the bubble near the heated surface, and condensation near the cold surface. Full boiling curves were obtained and two boiling regimes—nucleate boiling and pseudo-film boiling—and the transition condition, the critical heat flux (CHF), were identified. The observations indicated that the presence of the gap geometry pushed the nucleate boiling regime to a lower superheated temperature range, resulting in correspondingly lower heat flux. With further increases of wall superheat, the vapor generated by the boiling process was trapped in the gap to blanket the heated surface. This caused premature occurrence of CHF conditions and deterioration of heat transfer in the pseudo-film boiling regime. The influence of the confined space was particularly significant when greater Marangoni forces were present under reduced gravity conditions. The CHF value of x (molar fraction)=0.025, which corresponded to weaker Marangoni forces, was found to be greater than that of $x=0.015$ *with a* 6.4 mm *gap.* [DOI: 10.1115/1.2402178]

Keywords: confined gap, boiling, reduced gravity, binary mixtures

Introduction

Boiling under reduced gravity has significant applications in many aerospace engineering fields, including spacecraft thermal control designs that incorporate heat exchangers, heat pipes, microchannels, and cryogenic storage and transport systems. Many investigators have conducted intensive experimental research on pool boiling under various gravity levels, but none known to us has studied gravity effects on boiling in a confined space, which is frequently encountered in a wide variety of heat transfer applications, such as heat exchangers, pressurized water reactors, and electronic component cooling.

For pool boiling in the nucleate boiling regime, Straub [1] pointed out that the Rohsenow equation, which predicted that the heat flux at a specified superheat level diminished under reduced gravity, failed to predict the heat transfer for binary mixtures and pure organic fluids. On the contrary, a 20% enhancement of heat transfer was achieved even at low heat flux for some mixtures. This augmentation was also observed by Abe et al. [2], Oka et al. [3], and Lin et al. [4].

For critical heat flux (CHF), Shatto and Peterson [5] reported that the CHF for distilled water decreased with decreasing gravity, and even fell below the $g^{1/8}$ trend predicted by Lienhard and Dhir [6]. Nevertheless, Ahmed and Carey [7] found that by adding a proper amount of 2-propanol into water, the resulting Marangoni effect was able to sustain the boiling mechanism under reduced gravity. They observed that the CHF under reduced gravity was able to achieve the same order of magnitude as under the terrestrial condition with the aid of Marangoni forces.

Straub [8] compared several experimental results for cryogenic fluids in film boiling and found that the film boiling could be maintained by surface tension forces in microgravity. The heat transfer coefficient was gradually decreased with decreasing gravity, but remained constant for $a/g<0.01$. Alternatively, Liu et al. [9] proposed an analytical correlation for the film boiling of binary mixtures on a horizontal cylindrical heater. By taking the mass diffusion factor into account, their model suggested that the heat transfer coefficients were proportional to $g^{1/4}$.

There have been several studies focused on the influence of constrained space on boiling. The pioneering work by Ishibashi and Nishikawa [10] systematically examined the heat transfer of various saturated liquids while boiling in vertical annuli with the internal cylinder heated. Two different boiling characteristics were observed and thereafter referred to as the coalesced bubble regime and the isolated bubble regime. In the isolated bubble regime, many spherical bubbles were initiated from the heated surface, which then departed and rose upward. While in the coalesced bubble regime, large coalesced bubbles were fully grown in the confined space, which then departed and rose regularly at a low frequency. The coalesced bubble regime often occurred when the system pressure was low or a narrow gap was present. Similar boiling characteristics were observed by Akoi et al. [11] and Laser et al. [12] for vertical narrow annuli, and Bonjour and Lallemand [13] for narrow spaces between two vertical surfaces. Nevertheless, boiling phenomena in the horizontal confined geometry were expected to be distinct from the phenomena in the vertical confined geometry, especially under the Earth's gravity. Katto et al. [14] conducted boiling experiments of saturated water in a space bounded by two horizontal coaxial disks with a heated surface that faced upward. They found that decreasing the gap size augmented the heat transfer coefficient in the nucleate boiling regime but diminished the CHF. Furthermore, Katto and Kosho [15] extended the work to the boiling of R-113, ethyl alcohol, and benzene in horizontal confined geometries and proposed a correlation for CHF within ±15% agreement with the experimental data.

Despite the aforementioned investigations, no previous litera-

[1]Corresponding author.

Contributed by the Heat Transfer Division of ASME for publication in the JOURNAL OF HEAT TRANSFER. Manuscript received October 10, 2005; final manuscript received May 15, 2006. Review conducted by Ramendra P. Roy. Paper presented at the ASME Summer Heat Transfer Conference (HT2003), July 21–23, 2003, Las Vegas, Nevada.

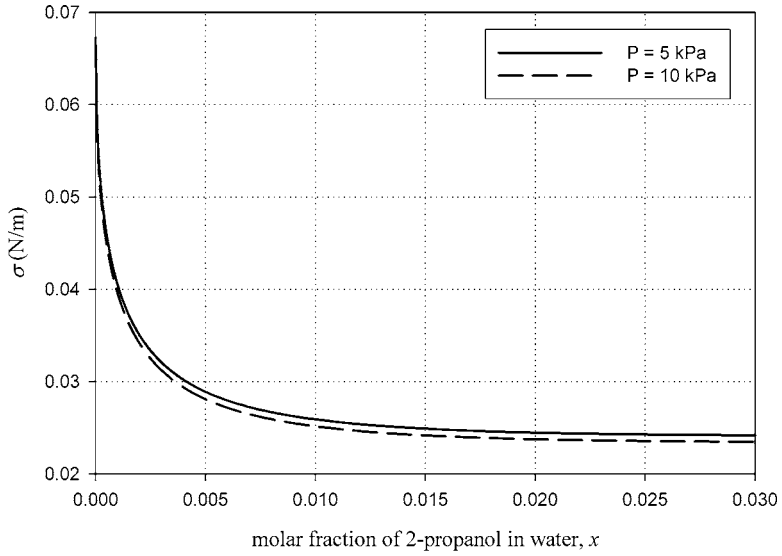

(*a*)

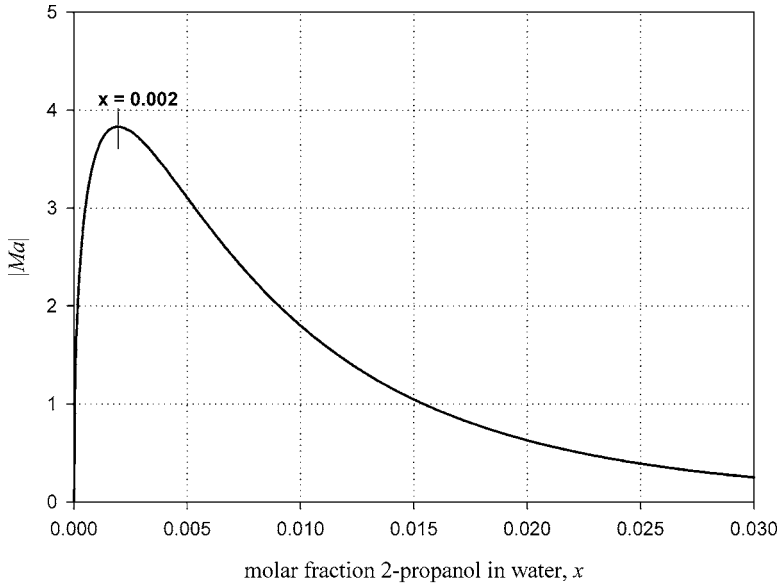

(*b*)

Fig. 1 (*a*) Surface tension versus molar fraction, (*b*) absolute value of the Marangoni parameter [16] versus molar fraction for 2-propanol/water mixtures at bubble point temperature, *P*=5 kPa

ture was found that documented studies of the boiling of binary mixtures in a horizontal confined geometry under various gravity levels. This study focused on the effects of an opposing subcooled wall and gravity levels on the boiling of a binary mixture on a small region of an otherwise adiabatic wall. Experiments were conducted with 2-propanol/water mixtures under various gravity levels and gap sizes. The heated region was 12.7 mm in diameter, and the two different sizes of the confined gap were 6.4 mm and 12.7 mm. During the experiments, the bulk liquid temperature varied from slightly subcooled to near saturation, and the cold plate temperature varied from 2 to 32 K subcooled in order to sustain the temperature gradient across the gap. Because the available electrical power onboard during the parabola flights was limited, the system pressure in the test section was kept in the subatmospheric range (3.7 kPa to 9.4 kPa) throughout the experiments. The mole fractions of 2-propanol in water for the experiments were 0 (distilled water), 0.015, and 0.025. The surface tension versus molar fraction is shown in Fig. 1(*a*) for 2-propanol/water mixtures at corresponding bubble point temperatures for $P = 5$ kPa and 10 kPa. The differences of surface tensions at $P = 5$ kPa and 10 kPa were less than 3% and could be assumed independent of pressure for the tested pressure range. According to Fig. 1(*a*), the surface tension decreased monotonically with the increasing addition of 2-propanol in water. To evaluate the strength of the Marangoni forces, the absolute value of the Marangoni parameter defined by McGillis and Carey [16] was used.

$$\mathrm{Ma} = \frac{1}{\sigma}\frac{\partial \sigma}{\partial x}(y - x) \tag{1}$$

where σ was the surface tension of the binary mixture, and y and x were the vapor and liquid molar fraction of the more volatile component (2-propanol), respectively. Figure 1(*b*) demonstrates how the Marangoni parameter was influenced by the addition of

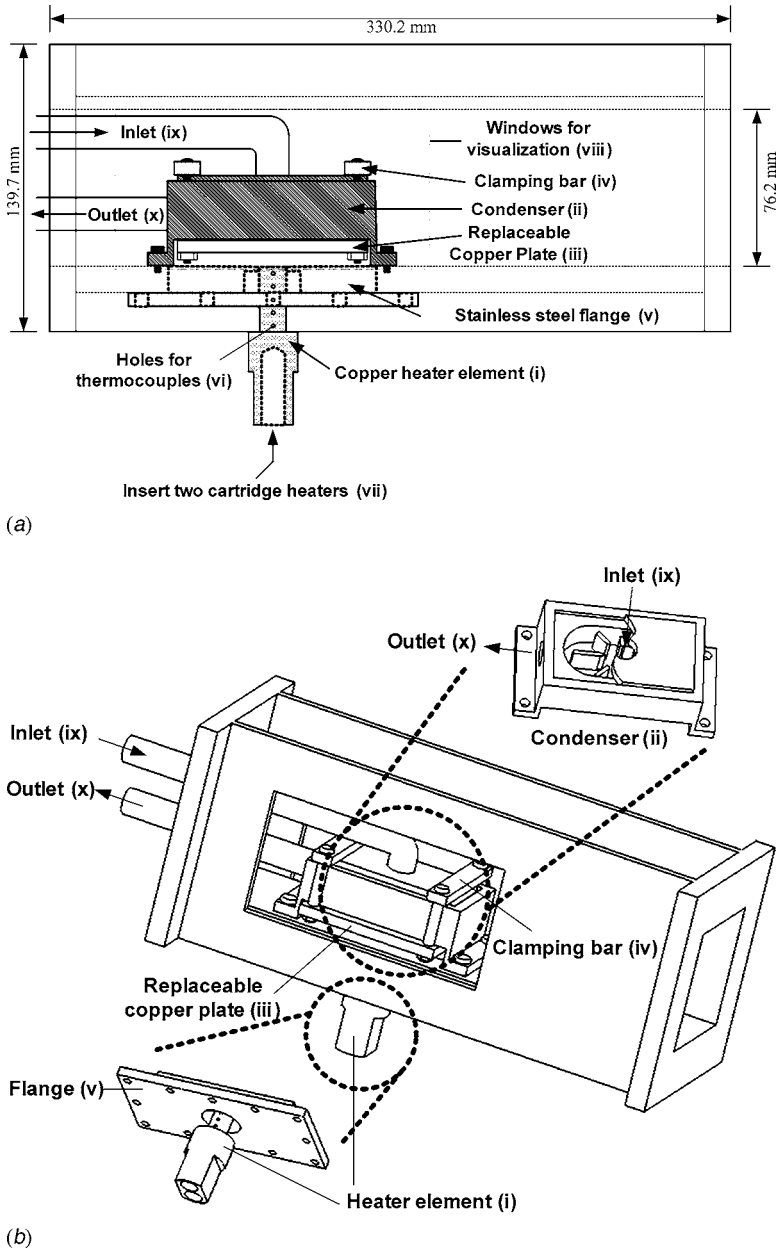

Fig. 2 Test section (*a*) side view, (*b*) 3D drawing

2-propanol in water for $x<0.03$. Despite the fact that Ma reached its maximum near $x=0.002$, larger molar fractions ($x=0.015$ and 0.025) were used in the experiments due to the restriction of blending. Therefore, $x=0.015$ corresponded to the maximal Marangoni effects among the tested molar fractions.

The current investigation aimed to clarify the interaction of the gap geometry with other mechanisms involved, which was largely unexplored. Although the reported experiments were limited to a few variations of gravity, gap geometry, and concentration, this investigation provided a valuable initial insight into the impacts of these parameters on the boiling process.

Experimental Setup

Figure 2 shows the test section with the heated surface piece (combination of (i) and (v)) and condenser (ii) installed. The heated surface piece consisted of a stainless steel holding flange (v) and a copper heater element (i) to accommodate the two electric cartridge heaters (vii), as shown in Fig. 2. The dimensions of the heater element (i) and holding flange (v) are shown in Figs. 3(*a*) and 3(*b*), respectively. The cartridge heaters were connected to a variable voltage controller to adjust the power input during the boiling experiments. To minimize heat loss, the top end of the heater element (i) was silver soldered to the holding flange (v) with minimum joint area, and the sidewall of the copper heater element (i) was insulated by a sheet of fiberglass. Only the top circular portion (12.7 mm in diameter) of the copper heater element was directly heated to localize the boiling process in the test section. The unheated portion of the surface extended laterally so that the effects of the aspect ratio of the space between the heated surface and the cold plate should be negligible. Five T-type thermocouples with a 6.4 mm pitch (vi) were embedded in the copper element (i) in order to estimate the heated surface temperature and the input heat flux by least-squares regression. The temperature profiles from thermocouples were checked to estimate the thermal time constant. Under terrestrial condition, the thermal time constant of the copper element (i) was approximately 0.5 s. Since the

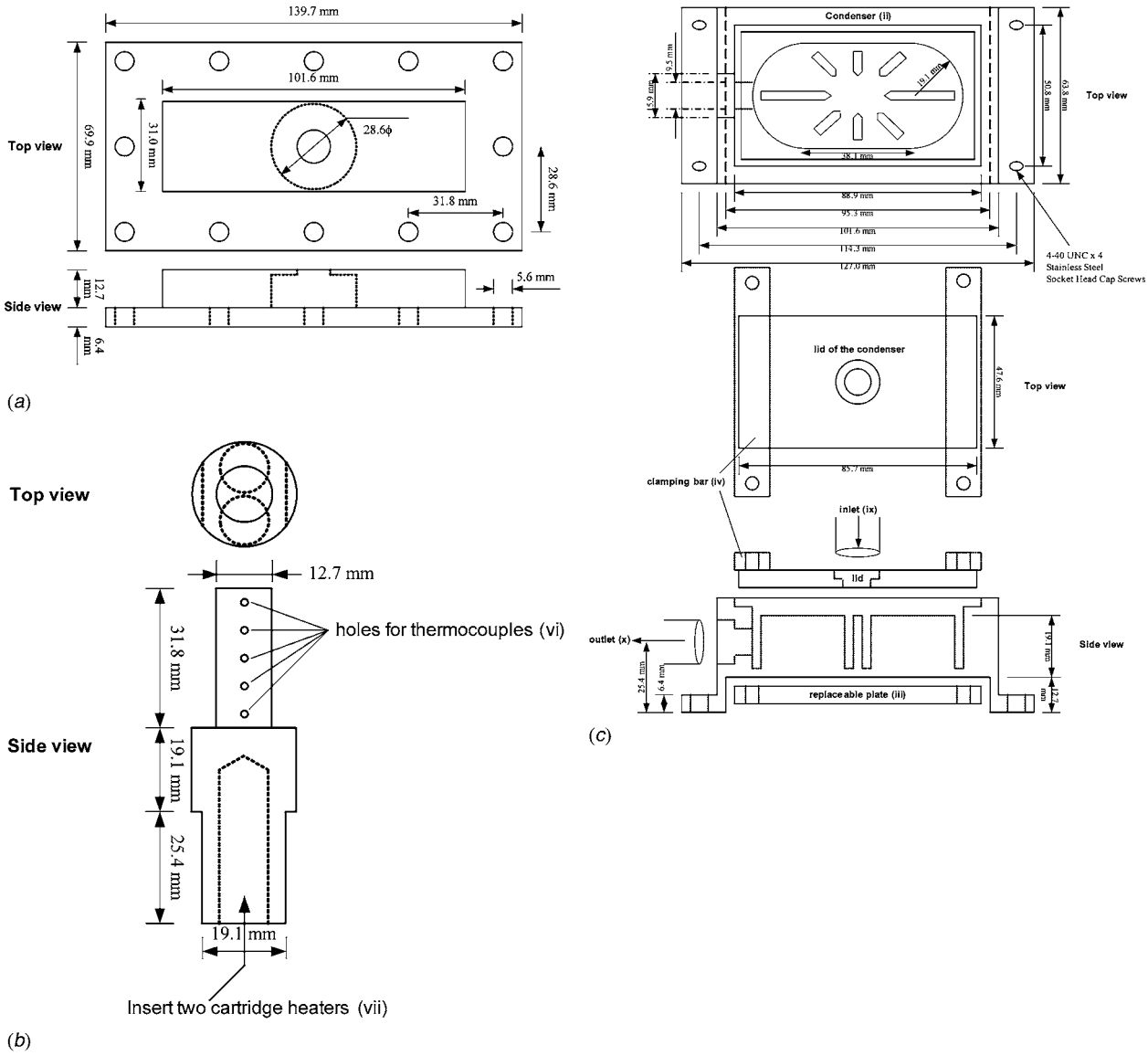

Fig. 3 Dimension of (*a*) holding flange (*v*), (*b*) heater element (*i*), (*c*) condenser (*ii*)

experimental results showed sudden alternations of the boiling regime when gravitational level was under transition, the same heat flux was maintained for two consecutive parabola maneuvers for bubble restabilization. Experimental data were taken during the second parabola maneuver when stable condition was retained.

The confined gap was formed by the space between the heated surface element ((i) and (v)) and the condenser (ii), as depicted in Fig. 2. The dimension of the condenser (ii) is shown in Fig. 3(*c*). The size of the gap geometry was adjustable by attaching the replaceable plate (iii) of varying thickness to the bottom of the copper condenser (ii). The condenser (ii) was placed close to the left end of the test section so that the length of the coolant circuit inside the test section was minimized. Cold water was circulated to impinge onto the center of the condenser bottom. The flow rate of the coolant was adjusted by a variable-speed centrifugal pump that connected to a Variac in addition to a bypass loop installed in the cooling circuit. The cold plate temperature was evaluated as the average of the inlet (ix) and outlet (x) temperatures of the condenser. During the experiments, the temperature difference of the coolant between inlet and outlet varied from 1 K to 11 K. The bulk liquid temperature inside the test section was measured by a T-type thermocouple probe.

Dissolved gas was reduced by preboiling at low pressure prior to the experiments. The reduced and high gravity experiments were carried out aboard a KC-135A aircraft at the NASA Glenn Research Center. The values of the physical properties of 2-propanol/water mixtures were evaluated based on the methods and information provided by Poling et al. [17], McGillis [18], and Daubert and Danner [19]. Ranges of system pressure, bulk liquid temperature, and subcooled temperature were summarized in Table 1 for each test condition (fixed molar fraction, gap size, and gravity level). The limited variations of gravity, concentration, and gap geometry were chosen as an initial exploration of the interaction of these mechanisms in the boiling process. It was noted that the superheated temperature increased drastically after the CHF condition was reached. Beyond CHF, the input heat flux was adjusted to prevent burnout and the flow rate of the coolant was modified accordingly in attempt to maintain stable superheated and subcooled temperatures.

Table 1 Ranges of pressure, bulk temperature, and subcooling for each test condition

x	Gap size (mm)	a/g	P (kPa)	T_{bulk} (K)	ΔT_c (K)
0	6.4	–0.10 to 0.16	5.3 to 6.7	26 to 36	10 to 25
0	6.4	1	4.3 to 4.7	22 to 24	18 to 24
0	6.4	1.5 to 1.92	5.8 to 6.7	22 to 37	12 to 26
0.015	6.4	–0.06 to 0.07	5.6 to 7.9	33 to 42	4 to 9
0.015	6.4	1	3.7 to 4.4	24 to 26	2 to 15
0.015	6.4	1.62 to 1.89	5.9 to 8.1	33 to 41	5 to 9
0.015	12.7	–0.06 to 0.04	5.5 to 7.1	26 to 43	15 to 31
0.015	12.7	1.56 to 1.85	6.0 to 8.6	24 to 40	16 to 32
0.025	6.4	–0.06 to 0.05	7.3 to 9.3	32 to 46	8 to 25
0.025	6.4	1.47 to 1.84	7.8 to 9.4	33 to 46	10 to 25

Table 2 lists the overall uncertainties of the measurements and calculated quantities in this study. The overall uncertainty of subcooled temperature was relatively high because the uncertainties of pressure (8.4%) and molar fraction (6.7%) were propagated through the calculations of bubble point temperature. The overall uncertainty of superheated temperature was similarly affected but the value was slightly higher than that of subcooled temperature. Since the heated surface temperature was determined by extrapolating the least-squares regression of temperature readings to the location of the heated surface, uncertainties of the thermocouple locations, i.e., the precision of machining, were also taken into account in the overall uncertainty of superheated temperature. The pressure transducer (Validyne DP-15 with a sensing diaphragm 3-42) was capable of measuring the differential pressure up to 140 kPa. The accuracy of DP-15 was ±0.2 kPa, and the random uncertainty was 0.06 kPa. Because system pressure was kept at subatmospheric range (5.5 kPa to 9.4 kPa), large fractional uncertainty of the pressure measurement (8.4%) was yielded.

Results

From the experiments, full boiling curves were obtained and two boiling regimes—nucleate boiling and pseudofilm boiling—and the transition condition, the critical heat flux, were identified. In the nucleate boiling regime, small bubbles were generated, which then condensed quickly in the bulk liquid. As the superheat level increased, bubbles coalesced to a large vapor slug that was constrained by the gap geometry. The maximum heat flux (i.e., the critical heat flux, CHF) was reached when the vapor bubble blanketed the heated surface. Further increasing the superheat level resulted in a slowly fluctuating bubble, where boiling only occurred at its base perimeter. The heated surface was completely dried out and this was called the pseudofilm boiling regime. The two boiling regimes and the CHF for 2-propanol/water mixtures with the gap constraint are depicted schematically in Fig. 4. Because the temperature gradient across the gap was influenced by the level of the subcooled temperature, thermocapillary force was evaluated to discuss the role of subcooling on the boiling of 2-propanol/water mixtures. Since the derivative of surface tension

Table 2 Overall uncertainties of measurements and calculated quantities

Quantity	Overall uncertainty
Superheated temperature, ΔT_h	3.3 K
Subcooled temperature, ΔT_c	2.9 K
Bulk temperature, T_{bulk}	1 K
Heat flux, q''	7.2%
System pressure, P	8.4%
Acceleration, a	0.007 g
Gap distance, L	0.5 mm
Molar fraction, x	6.7%
Heat transfer coefficient, α	12.3%

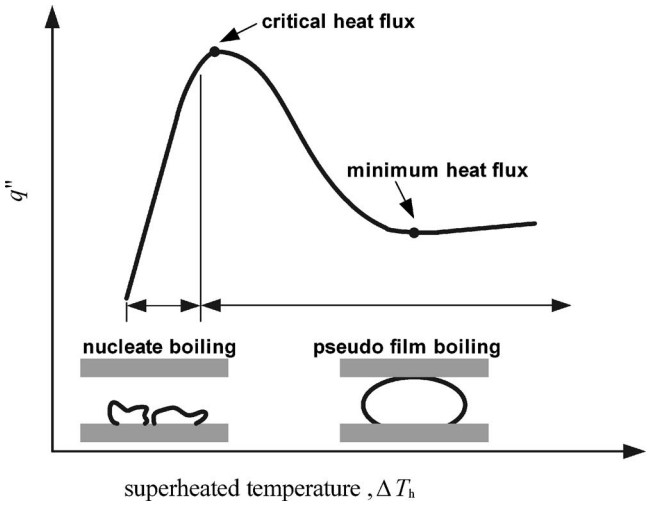

Fig. 4 Boiling regimes for 2-propanol/water mixtures with the gap constraint

with respect to molar fraction was very large for $x<0.01$, the ratio of surface tension differences caused by temperature gradient and concentration deviance was found to be in the order of 10^{-4} under our test conditions. This implied that the influences of subcooled temperature were relatively small comparing to the Marangoni effects.

The boiling curve for distilled water ($x=0$) inside the gap is shown in Fig. 5. For $\Delta T_h<20$ K under low gravity, nucleation was rarely observed. As the superheat levels increased, a large fluctuating bubble was sustained in the gap geometry and the boiling mode was directly transitioned into the pseudofilm boiling regime. The same phenomenon was also observed under terrestrial gravity. At $a/g=1$, a stable bubble was formed in the gap. The heated surface was mostly dried out when evaporation only occurred at the perimeter of the bubble base, with the top portion of the bubble attached to the cold plate. Because buoyancy tended to bring more vapor to the top wall, the contact area of the bubble with the cold plate was increased. Hence, the condensation effect was enhanced and a tiny liquid droplet was occasionally observed to hang from the center of the cold plate. Without the presence of buoyancy ($a/g=-0.10$ to 0.16), vapor-liquid interface became wavy and less stable. The nature of this instability created some mixing effects and resulted in better heat transfer under reduced gravity. Under high gravity ($a/g=1.50$ to 1.92), the nucleate boiling mode was the only one observed for distilled water. The bubbles fluctuated, merged, and released in a very rapid fashion at this gravity level. Embryos formed and coalesced but collapsed before growing to larger sizes. The chaotic nature of this process produced a strong mixing effect that made high heat transfer rates with low superheat levels possible.

For 2-propanol/water mixtures during the boiling process, different surface tensions along the bubble interface were produced, a phenomenon referred to as the concentration-induced Marangoni effect. For positive mixtures like 2-propanol/water mixtures, where the more volatile liquid has the lower surface tension, the difference of surface tension tended to draw liquids toward the heated surface, pushing bubbles away from each other. Hence, larger bubbles were harder to form and the boiling characteristics were different from those of distilled water.

The boiling curves for $x=0.015$ with a 6.4 mm gap under various gravity levels are shown in Fig. 6. The same level of heat flux was reached at a lower superheated temperature (ΔT_h) in the nucleate boiling regime under reduced gravity ($a/g=-0.06$ to 0.07) compared to under terrestrial and high gravity. Similar phenomena were also observed for the same concentration ($x=$

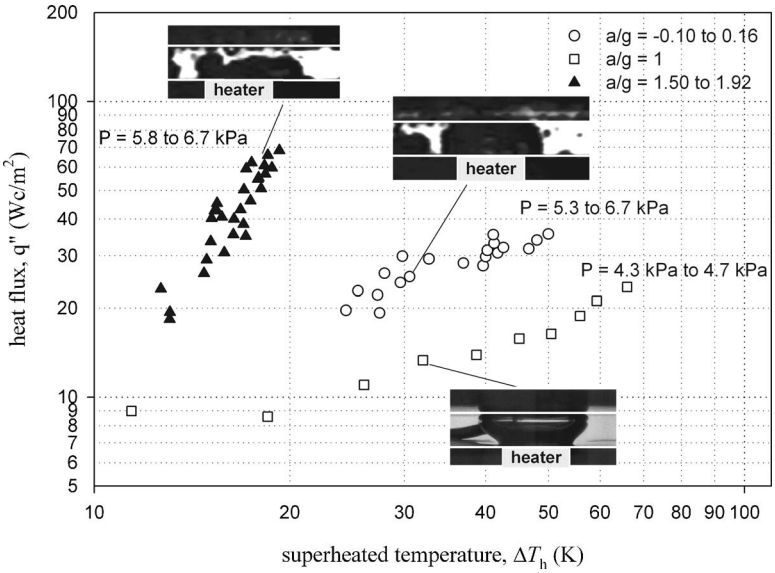

Fig. 5 Boiling curve of distilled water under various gravity levels, x=0, gap=6.4 mm (solid symbols represent the nucleate boiling regime, while open symbols represent the pseudofilm boiling regime)

0.015) with a 12.7 mm gap, as represented in Fig. 7. Nevertheless, the CHF under reduced gravity was greatly diminished to less than 50% of that under terrestrial gravity, and was also reached at a superheated temperature 10 K lower than that under terrestrial gravity for x=0.015 with a 6.4 mm gap. Due to the space constraint, a large vapor bubble blanketed the heated surface under reduced gravity and caused the CHF to decrease accordingly. As the gap size increased, the bubble had more space to grow and moved around. The CHF under low gravity for x=0.015 with a 12.7 mm gap was improved by more than 40% of that for the same concentration with a 6.4 mm gap. In the pseudofilm boiling regime, vapor bubble was squashed toward the cold plate under terrestrial gravity for x=0.015 with a 6.4 mm gap. The Marangoni forces induced a liquid flow against the direction of buoyancy, and vapor-liquid interface was highly fluctuated. Under reduced gravity, the bubble grew to a flat barrel shape and was more stable without the influence of buoyancy. This was contrary to the results for distilled water (x=0), for which the bubble was more stable with the presence of gravity.

For the same concentration (x=0.015) with a 12.7 mm gap, the vapor bubble became more unstable and rounder in the pseudofilm boiling regime, as shown in Fig. 7. Two trends of the boiling curve were observed beyond the CHF point for this particular condition. At the same superheat level, two different corresponding heat fluxes were found. In the lower heat flux region, a round bubble was observed with dry patches on the heated surface. In the high heat flux region, tiny embryos were observed that were more similar to the nucleate boiling mode. Nevertheless, pseudofilm boiling was difficult to maintain in both high and low heat

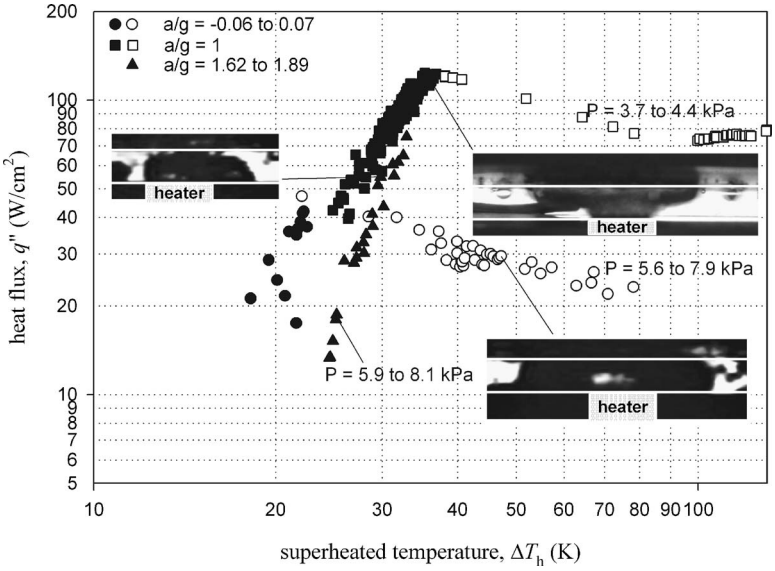

Fig. 6 Boiling curve of 2-propanol/water mixtures under various gravity levels, x=0.015, gap=6.4 mm (solid symbols represent the nucleate boiling regime, while open symbols represent the pseudo-film boiling regime)

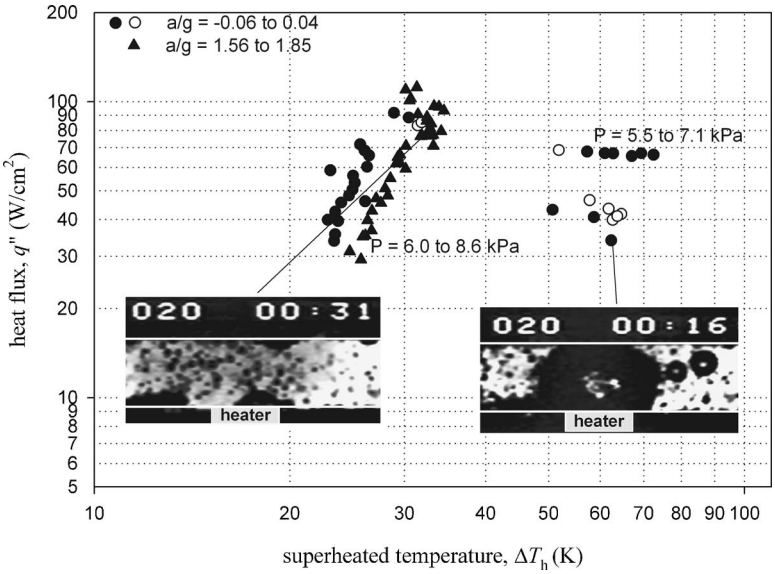

Fig. 7 Boiling curve of 2-propanol/water mixtures under various gravity levels, x=0.015, gap=12.7 mm (solid symbols represent the nucleate boiling regime, while open symbols represent the pseudo film boiling regime)

flux regions. With a 12.7 mm gap, the liquid occasionally flushed the bubbles away from the heated surface and the boiling mode jumped back to nucleate boiling.

For x=0.025, which corresponded to a weaker Marangoni influence, the boiling curves taken under reduced (a/g=−0.06 to 0.05) and high gravity (a/g=1.47 to 1.84) were nearly identical in the nucleate boiling regime, as indicated in Fig. 8. Among our test conditions, the only CHF found under high gravity was for x =0.025 with a 6.4 mm gap. Its CHF value was comparable to that under reduced gravity and the corresponding superheat discrepancy was less than 5 K. Pseudofilm boiling was reached under both reduced and high gravity for x=0.025 with a 6.4 mm gap. While bubbles became more stable near and beyond CHF (ΔT_h >30 K) under low gravity, it was not until ΔT_h>50 K that they stabilized at high gravity levels. Furthermore, the heat transfer under high gravity in this regime was 40% greater than that under reduced gravity.

Some interesting heat transfer characteristics were also observed in the transition period between low and high gravity during the KC-135A experiments. The transition between gravity levels occasionally caused switching from one regime to the other in a very short period of time. A rapid jump from pseudofilm boiling back to nucleate boiling changed the corresponding superheat by more than 10 K for a 6.4 mm gap (x=0, 0.015, 0.025), and 20 K for a 12.7 mm gap (x=0.015) during gravity transition. Since the input heat flux was fixed, the rapid temperature drop was primarily caused by the disappearance of the vapor blanket at high gravity levels. Reversely, rapid changing from nucleate boiling to

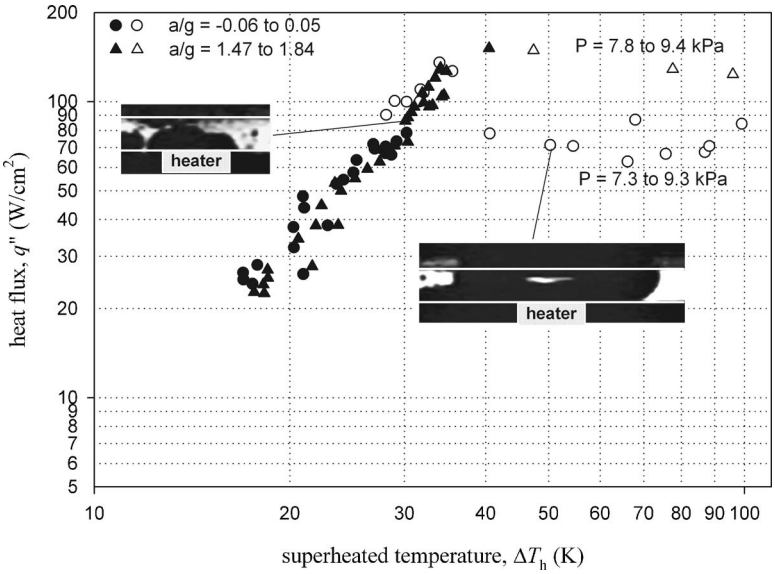

Fig. 8 Boiling curve of 2-propanol/water mixtures under various gravity levels, x=0.025, gap=6.4 mm (solid symbols represent the nucleate boiling regime, while open symbols represent the pseudo-film boiling regime)

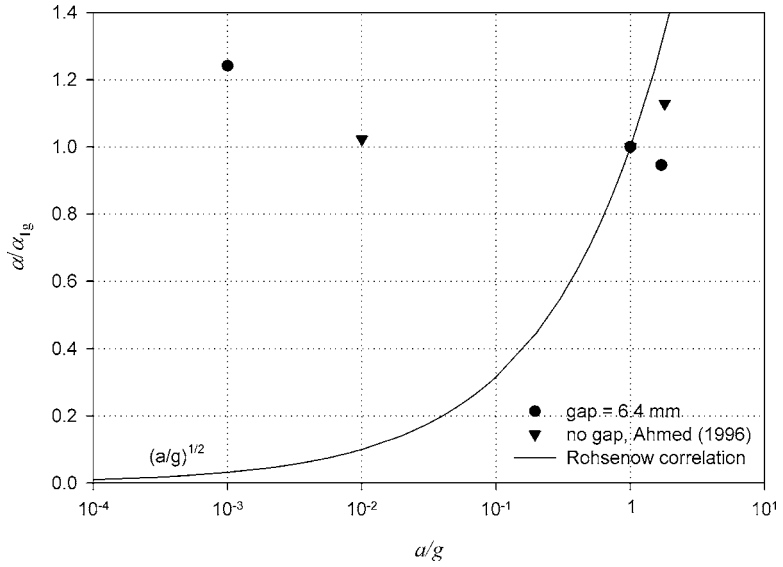

Fig. 9 Comparison of gravity dependency on heat transfer coefficients in nucleate boiling to the Rohsenow correlation (n=0.5 in Eq. (2)), x=0.015. Heat transfer coefficients were calculated at q''=40 W/cm^2 for gap =6.4 mm, and q''=250 W/cm^2 for pool boiling (no gap) from [22]

pseudofilm boiling was also observed during gravity transition. If the initial superheated temperature was high enough at the beginning of the gravity transition, the vapor blanket tended to stay on the heated surface, causing a switch to pseudofilm boiling under reduced gravity. The data points in pseudofilm boiling were carefully taken near the end of the reduced gravity period to ensure steady state was reached.

Discussions

Since there was no correlation available for the boiling of binary mixtures in a confined gap, conventional correlations for pool boiling were used to compare with our experimental results. In nucleate boiling, the dependency of heat transfer on gravity has been represented in the form of the power law by Straub [20]

$$\frac{\alpha}{\alpha_{1g}} = \left(\frac{a}{g}\right)^n \tag{2}$$

where $\alpha = q''/(T_h - T_{\text{bp}})$. In the Rohsenow [21] correlation, the exponent was equal to 0.5 in Eq. (2). This implied that the heat transfer coefficient was strongly reduced with decreasing gravity. In contrast, Ahmed [22] found that the heat transfer coefficients were nearly independent of gravity regardless of the concentration of the 2-propanol/water mixtures. Straub [1] also concluded that gravity and natural convection did not play a dominant role in pool boiling heat transfer. Nevertheless, Fig. 9 shows that gravity played an important role for x=0.015 with a gap constraint. With the gap geometry, the heat transfer coefficient under reduced gravity was enhanced by more than 20% compared to that under the Earth's gravity. This suggested that the gap geometry may alter the nature of the gravity dependency.

Regarding CHF, the Zuber correlation, derived from the hydrodynamic theory of film instability, indicated a $g^{1/4}$ dependency

$$q''_{\text{CHF,Zuber}} = 0.131 \rho_v h_{lv} \left[\frac{\sigma(\rho_l - \rho_v)g}{\rho_v^2}\right]^{-1/4} \tag{3}$$

However, this relationship was found to underestimate most of the experimental data under microgravity. For binary mixtures, Ahmed and Carey [7] reported that the CHF was nearly independent of gravity. Since the concentration-induced Marangoni effect was equally important to buoyancy, boiling was successfully sustained under reduced gravity. This was, however, found to contradict the results obtained with the gap geometry configuration. By extracting the CHF values from Fig. 6, Fig. 10 indicates that the CHF under low gravity was diminished to 40% of that under the Earth's gravity for x=0.015 with a 6.4 mm gap.

According to the above comparisons, the gap geometry was found to alter the characteristics of the heat transfer for 2-propanol/water mixtures. Under the Earth's gravity, the vapor bubble was restricted by the confining gap, and maintained a mushroom shape due to the influence of buoyancy. Under reduced gravity, the vapor grew isotropically in lateral directions. Combined with the compressive influence of the gap geometry, liquid film under the vapor was thinner, resulting in an increase of heat transfer. Under high gravity, the gap effect was less important because the departing diameter of bubbles was much smaller than the gap size due to the strong buoyancy. Conclusively, the confined geometry did not interfere with the evaporation process under high gravity, yielding a lower heat transfer rate in the nucleate boiling regime.

For laminar film boiling on a horizontal flat plate, the Berenson [23] correlation suggested that the heat transfer coefficient α was proportional to $g^{3/8}$

$$\alpha = 0.425\left\{\left[\frac{k_v^3 g \rho_v(\rho_l - \rho_v)h_{lv}}{\mu_v \Delta T_h}\right]\left[\frac{g(\rho_l - \rho_v)}{\sigma}\right]^{1/2}\right\}^{1/4} \tag{4}$$

where $\alpha = q''/(T_h - T_{\text{bp}})$. The experimental results of film boiling under reduced gravity were summarized by Straub [8]. He found that the gravity dependency of the heat transfer coefficients fell within $g^{0.16}$ to $g^{0.33}$ for $a/g > 0.01$. However, our results from the pseudofilm boiling regime did not follow these trends. As shown in Fig 11, the heat transfer coefficient under reduced gravity was diminished to less than 30% of that under terrestrial conditions for x=0.015 with a 6.4 mm gap ($\alpha/\alpha_{1g} \sim 0.25$), whereas it was almost doubled for x=0 with the same gap size ($\alpha/\alpha_{1g} \sim 2$).

The presence of the gap altered the dependencies of gravity and concentration on boiling. In the nucleate boiling regime, the effect of the gap geometry was limited. The heat transfer coefficients under reduced gravity were almost identical for x=0.015 and 0.025, similar to the observations from the DC-9 experiments reported by Ahmed [22] for pool boiling. It was not until the CHF condition was reached that the geometry constraint started to show a great influence on heat transfer. According to Ahmed [22],

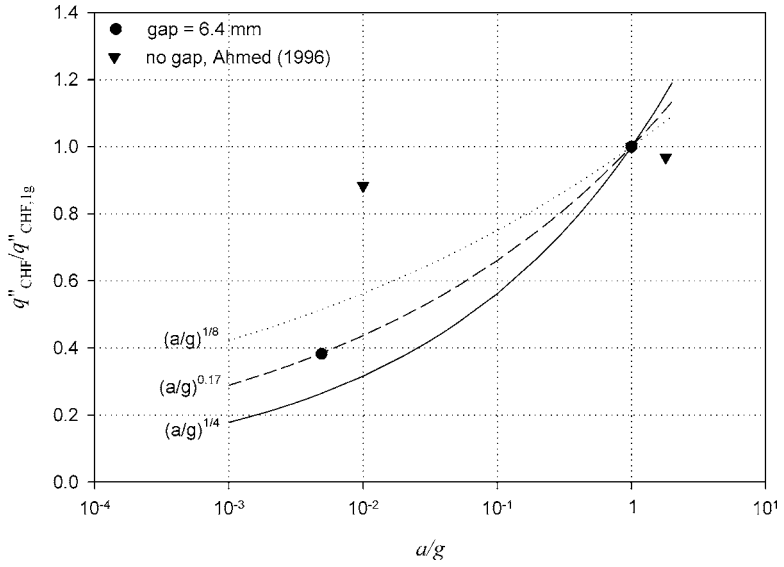

Fig. 10 Comparison of gravity dependency on CHF, x=0.015

the CHF that corresponded with the strongest Marangoni effect (x=0.015) was always the greatest among the tested concentrations for pool boiling, regardless of the gravity levels. However, the maximum CHF came to associate with a weaker Marangoni effect (x=0.025) when a gap geometry was installed into the apparatus. For positive mixtures such as 2-propanol/water, Marangoni forces tended to bring the liquid toward the heated surface in the wedge region. As a result, more liquid was brought to the heated surface for stronger Marangoni effects (x=0.015), and more vapor evaporated. Therefore, the CHF associated with stronger Marangoni effects was reached at a lower superheat level with the gap geometry. This deterioration in CHF did not occur in pool boiling because the vapor bubbles could freely depart from the heated surface and continue the nucleation process at higher superheat levels.

Concluding Remarks

In the presence of the gap geometry, the gravity dependency of heat transfer in the nucleate boiling regime was contrary to that predicted by the Rohsenow [21] correlation. For x=0.015 with a 6.4 mm gap, values of α/α_{1g} were 1.242 at low gravity and 0.946 at high gravity. The experimental results showed that heat transfer was diminished with the increase of gravity level, suggesting the gap geometry altered the nature of the gravity dependency.

Gravity was found to have a significant impact on the CHF condition when the gap geometry was in place. The maximum value of CHF was found for x=0.025 with a 6.4 mm gap within our test matrices under reduced gravity. The gravity dependency of the CHF for x=0.015 with a 6.4 mm gap was best approxi-

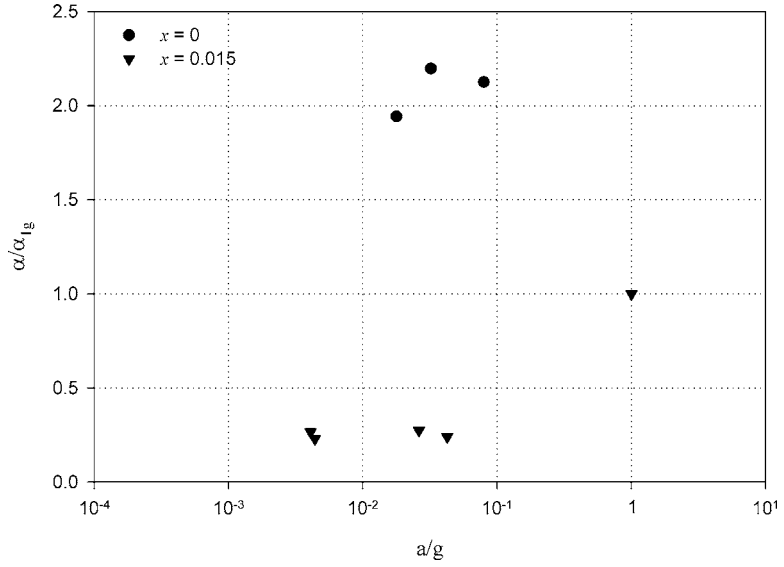

Fig. 11 Comparison of gravity dependency on heat transfer coefficients in pseudofilm boiling, gap=6.4 mm

mated by $g^{0.17}$, which fell between the $g^{1/4}$ and $g^{1/8}$ regression lines suggested by Shatto and Peterson [5] for pool boiling.

For film boiling, the Berenson [23] correlation predicted $\alpha/\alpha_{1_g}=0.23$ for $a/g=0.02$, which matched the pseudofilm boiling results to within 12% for $x=0.015$ with a 6.4 mm gap. However, it failed to indicate the heat transfer enhancement ($\alpha/\alpha_{1_g}=2.07$) for $x=0$.

The gravity remained a minor factor in the heat transfer mechanism within the nucleate and pseudo-film boiling regimes in this study. With the aid of concentration-induced Marangoni effects, boiling was not only maintained but also enhanced with the absence of gravity. However, a tradeoff occurred against a poorer heat transfer under microgravity during pseudofilm boiling regimes.

According to the observations of this study, the influence of the gap geometry became more significant in conjunction with the following conditions:

1. The reduction of the gap size
2. The decrease of the gravity level
3. Stronger Marangoni effects

Since the derivative of surface tension with respect to molar fraction was very large in the range of our tested conditions, thermocapillary forces induced by the thermal gradient across the gap were relatively small compared to the Marangoni effects. Hence, subcooling had a minor effect on the boiling process in this study. Conclusively, the influences of the gap sizes, gravity levels, and Marangoni effects on boiling heat transfer were not independent, but mutually interacted with one another. Although limited in scope, this study provided an initial exploration to illuminate the interaction of the gap geometry with gravity changes and Marangoni effects during a localized boiling process with an adjacent subcooled wall. The results suggested that the gap size can be optimized for a specific condition (boiling regime, concentration, gravity, pressure, and so forth) in order to reach the best heat transfer performance in the system.

Acknowledgment

This work was supported by the NASA Office of Life and Microgravity Sciences and Applications under Grant No. NAG3-2105. The authors would also like to express their gratitude to the staff at NASA Glenn Researcher Center for their assistance during the KC-135A flight experiments.

Nomenclature

a = system acceleration in vertical direction
Bo = Bond number, $\sqrt{gL^2(\rho_l-\rho_v)/\sigma}$
g = Earth gravitational acceleration, 9.8 m/s^2
h_{lv} = latent heat of vaporization
k = thermal conductivity
L = width of the gap (distance between heated surface and cold surface)
Ma = Marangoni parameter defined by [16], Ma $=1/\sigma\partial\sigma/\partial x(y-x)$
P = pressure
q'' = heat flux
ΔT_c = subcooled temperature, $T_{\mathrm{bp}}-T_c$
ΔT_{h} = superheated temperature, $T_{\mathrm{h}}-T_{\mathrm{bp}}$
T_c = cold plate surface temperature
T_h = heated plate surface temperature
x = liquid molar fraction of 2-propanol in water
y = vapor molar fraction of 2-propanol in water

Greek Symbols

α = heat transfer coefficient
μ = dynamic viscosity
ρ = density
σ = surface tension

Subscripts

bp = bubble point
bulk = bulk liquid in the test section
CHF = critical heat flux
l = liquid
v = vapor
1_g = Earth's gravity

References

[1] Straub, J., 1999, "Pool Boiling in Microgravity," *Proceedings of the Microgravity Fluid Physics and Heat Transfer: Proceedings of the International Conference on Microgravity Fluid Physics and Heat Transfer*, Oahu, HI, September 19–24, Begell House, Redding, CT, pp. 114–125.
[2] Abe, Y., Oka, T., Mori, Y. H., and Nagashima, A., 1994, "Pool Boiling of a Non-Azeotropic Binary Mixture Under Microgravity," Int. J. Heat Mass Transfer, **37**(16), pp. 2405–2413.
[3] Oka, T., Abe, Y., Mori, Y. H., and Nagashima, A., 1995, "Pool Boiling of N-Pentane, Cfc-113, and Water Under Reduced Gravity: Parabolic Flight Experiments With a Transparent Heater," J. Heat Transfer, **117**(2), pp. 408–417.
[4] Lin, L., Pisano, A. P., and Lee, A. P., 1991, "Microbubble Powered Actuator," *Proceedings of the 1991 International Conference on Solid-State Sensors and Actuators*, San Francisco, CA, June 24–27, IEEE International, New York, pp. 1041–1044.
[5] Shatto, D. P., and Peterson, G. P., 1999, "Pool Boiling Critical Heat Flux in Reduced Gravity," ASME J. Heat Transfer, **121**(4), pp. 865–873.
[6] Lienhard, J. H., and Dhir, V. K., 1973, "Hydrodynamic Prediction of Peak Pool-Boiling Heat Fluxes from Finite Bodies," J. Heat Transfer, **95**(2), pp. 152–158.
[7] Ahmed, S., and Carey, V. P., 1998, "Effects of Gravity on the Boiling of Binary Fluid Mixtures," Int. J. Heat Mass Transfer, **41**(16), pp. 2469–2483.
[8] Straub, J., 2001, "Boiling Heat Transfer and Bubble Dynamics in Microgravity," *Advances in Heat Transfer*, Vol. 35, J. P. Hartnett, and T. F. Irvine, Jr., eds., Academic Press, San Diego, CA, pp. 58–168.
[9] Liu, M., Yang, Y., and Maa, J., 1998, "A General Correlation for Pool Film Boiling Heat Transfer from a Horizontal Cylinder to Saturated Binary Liquid Mixtures," Int. J. Heat Mass Transfer, **41**(15), pp. 2321–2334.
[10] Ishibashi, E., and Nishikawa, K., 1969, "Saturated Boiling Heat Transfer in Narrow Spaces," Int. J. Heat Mass Transfer, **12**(8), pp. 863–893.
[11] Aoki, S., Inoue, A., Aritomi, M., and Sakamoto, Y., 1982, "Experimental Study on the Boiling Phenomena within a Narrow Gap," Int. J. Heat Mass Transfer, **25**(7), pp. 985–990.
[12] Laser, D., Shuhuai, Y., Chen, C.-H., Mikkelsen, J., Jr., Goodson, K., Santiago, J., and Kenny, T., 2001, "A Micromachined Silicon Low-Voltage Parallel-Plate Electrokinetic Pump," *Proceedings of the TRANSDUCERS '01. EUROSENSORS XV. 11th International Conference on Solid-State Sensors and Actuators*. Digest of Technical Papers, E. Obermeier, eds., Munich, Germany, June 10–14, Springer-Verlag, Berlin, Germany, **2**, pp. 920–923.
[13] Bonjour, J., and Lallemand, M., 1998, "Flow Patterns During Boiling in a Narrow Space between Two Vertical Surfaces," Int. J. Multiphase Flow, **24**(6), pp. 947–960.
[14] Katto, Y., Yokoya, S., and Teraoka, K., 1977, "Nucleate and Transition Boiling in a Narrow Space Between Two Horizontal, Parallel Disk-Surfaces," Bull. JSME, **20**(143), pp. 638–643.
[15] Katto, Y., and Kosho, Y., 1979, "Critical Heat Flux of Saturated Natural Convection Boiling in a Space Bounded by Two Horizontal Co-Axial Disks and Heated from Below," Int. J. Multiphase Flow, **5**(3), pp. 219–224.
[16] McGillis, W. R., and Carey, V. P., 1996, "On the Role of Marangoni Effects on the Critical Heat Flux for Pool Boiling of Binary Mixtures," J. Heat Transfer, **118**(1), pp. 103–109.
[17] Poling, B. E., Prausnitz, J. M., and O'Connell, J. P., 2001, *The Properties of Gases and Liquids*, McGraw-Hill, New York.
[18] McGillis, W. R., 1993, "Boiling from Localized Heat Sources in Pure and Binary Fluid Systems," Ph.D. thesis, University of California, Berkeley, CA.
[19] Daubert, T. E., and Danner, R. P., 1985, *Data Compilation Tables of Properties of Pure Compounds*, American Institute of Chemical Engineers, New York.
[20] Straub, J., 1995, "The Micro Wedge Model: A Physical Description of Nucleate Boiling without External Forces," *Proceedings of the 9th European Symposium on Gravity-Dependent Phenomena in Physical Sciences Materials and Fluids Under Low Gravity*, L. Ratke et al., eds., Berlin, Germany, May 2–5, Springer-Verlag, Berlin, Germany, pp. 351–359.
[21] Rohsenow, W., 1952, "A Method of Correlating Heat-Transfer Data for Surface Boiling of Liquids," Trans. ASME, **74**(2), pp. 969–976.
[22] Ahmed, S., 1996, "Marangoni Effects in the Boiling of Binary Fluid Mixtures," Ph.D. thesis, University of California, Berkeley, CA.
[23] Berenson, P. J., 1961, "Film-Boiling Heat Transfer from a Horizontal Surface," J. Heat Transfer, **83**(3), pp. 351–358.

An Efficient Localized Radial Basis Function Meshless Method for Fluid Flow and Conjugate Heat Transfer

Eduardo Divo
Department of Engineering Technology,
University of Central Florida,
Orlando, FL 32816-2450

Alain J. Kassab
Department of Mechanical, Materials, and
Aerospace Engineering,
University of Central Florida,
Orlando, FL 32816-2450
e-mail: kassab@mail.ucf.edu

A localized radial basis function (RBF) meshless method is developed for coupled viscous fluid flow and convective heat transfer problems. The method is based on new localized radial-basis function (RBF) expansions using Hardy Multiquadrics for the sought-after unknowns. An efficient set of formulae are derived to compute the RBF interpolation in terms of vector products thus providing a substantial computational savings over traditional meshless methods. Moreover, the approach developed in this paper is applicable to explicit or implicit time marching schemes as well as steady-state iterative methods. We apply the method to viscous fluid flow and conjugate heat transfer (CHT) modeling. The incompressible Navier–Stokes are time marched using a Helmholtz potential decomposition for the velocity field. When CHT is considered, the same RBF expansion is used to solve the heat conduction problem in the solid regions enforcing temperature and heat flux continuity of the solid/fluid interfaces. The computation is accelerated by distributing the load over several processors via a domain decomposition along with an interface interpolation tailored to pass information through each of the domain interfaces to ensure conservation of field variables and derivatives. Numerical results are presented for several cases including channel flow, flow in a channel with a square step obstruction, and a jet flow into a square cavity. Results are compared with commercial computational fluid dynamics code predictions. The proposed localized meshless method approach is shown to produce accurate results while requiring a much-reduced effort in problem preparation in comparison to other traditional numerical methods. [DOI: 10.1115/1.2402181]

Introduction

Established numerical methods such as finite element methods (FEM) and finite volume methods (FVM) that are routinely used to resolve complex multiphysics interactions require significant effort in mesh generation. In fact, for most models of geometrically intricate components commonly encountered in engineering analysis, mesh generation is very time consuming, far from automated, and most often the most taxing part of the modeling process. The term meshless methods refers to a class of numerical techniques that rely on global interpolation on nonordered spatial point distributions that, as such, offer the hope of reducing the effort devoted to model preparation. These techniques have been under much development over the past few years [1–8]. The approach finds its origin in classical spectral or pseudo-spectral methods [9–17] that are based on global orthogonal functions such as Legendre or Chebyshev polynomials requiring a regular nodal point distribution. In contrast, meshless methods use a nodal or point distribution that is not required to be uniform or regular in their spatial distribution due to the fact that most rely on global radial-basis functions (RBF) [18–20]. These interpolating functions have proved quite successful in their application to an earlier mesh reduction method, namely the dual reciprocity boundary element method (DRBEM) [21–23]. However, global RBF based meshless methods have some drawbacks including poor conditioning of the ensuing algebraic set of equations which can be addressed to some extent by domain decomposition and appropriate pre-conditioning. Moreover, care must be taken in the evaluation of derivatives in global RBF meshless methods. Although, very promising, these techniques can also be computationally intensive. Recently, local collocation meshless method [24,25] have been proposed to address many of the issues posed by global RBF meshless methods.

In this paper, we develop a localized meshless collocation method using the Hardy Multiquadrics RBF [26] and derive new and efficient set of formulae to compute the RBF interpolation for the variable and various derivatives in terms of vector products. We show that these interpolating can be precomputed at the problem preparation stage. The formulation thus provides a substantial computational savings over traditional meshless methods, including the newer localized meshless methods. Moreover, the approach developed in this paper is flexible in that it is applicable to explicit or implicit time marching schemes as well as steady-state iterative methods.

We apply the localized meshless RBF (LMRBF) technique to the solution of the conjugate heat transfer problem (CHT). The term conjugate heat transfer refers to the coupled interaction of convective heat transfer within a fluid with conduction in the solid in which it is in contact (see Fig. 1). A variety of schemes have been proposed to numerically resolve CHT, including coupled finite volume/boundary element algorithms [27–31]. To accelerate the solution of such problems, we also adopt a parallel iterative domain decomposition as developed in the context of pure heat transfer application for the boundary element method [32] and for meshless methods in heat conduction [33–36]. Unlike global RBF meshless methods where domain decomposition is necessary to reduce the conditioning number of the resulting algebraic set, domain decomposition is used here for LMRBF only as a means of accelerating the time to solution by effectively distributing the computational burden to multiple processors. Numerical examples are presented to validate the approach by comparing the meshless

Contributed by the Heat Transfer Division of ASME for publication in the JOURNAL OF HEAT TRANSFER. Manuscript received September 8, 2005; final manuscript received May 25, 2006. Review conducted by: N. K. Anand. Paper presented at the 2005 ASME International Mechanical Engineering Congress (IMECE2005), November 5–11, 2005, Orlando, FL.

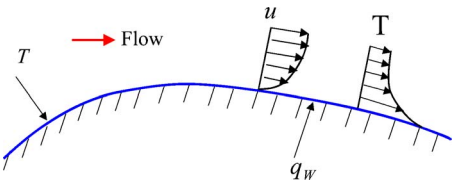

Fig. 1 CHT problem: external convective heat transfer coupled to heat conduction within the solid

solution to FVM solutions generated by a commercial computational fluid dynamics (CFD) solver (Fluent). We first review the solution algorithm for the Navier–Stokes equations, we then proceed to the localized RBF meshless collocation discretization, and we present numerical validation examples comparing predictions from our approach to those obtained by a commercial finite volume methods code.

Flow Solution by a Velocity Correction

Transient incompressible fluid flow is governed by the Navier–Stokes equations expressing the conservation of mass, linear momentum, and energy for a Newtonian fluid. In non-conservative form, these equations are

$$\nabla \cdot \mathbf{V} = 0 \tag{1a}$$

$$\rho \frac{\partial \mathbf{V}}{\partial t} + \rho(\mathbf{V} \cdot \nabla)\mathbf{V} = -\nabla p + \mu \nabla^2 \mathbf{V} + \rho \mathbf{f} \tag{1b}$$

$$\rho c \frac{\partial T}{\partial t} + \rho c(\mathbf{V} \cdot \nabla)T = k \nabla^2 T + \Phi \tag{1c}$$

Here, $\mathbf{V}$ is the flow velocity vector; ρ is the bulk density of the flow; p is the field pressure; μ is the absolute fluid viscosity; $\mathbf{f}$ is a specific body force; c is the fluid specific heat; T is the field temperature; k is the fluid thermal conductivity; and Φ is a nonlinear viscous dissipation term. All field variables are functions of space ($\boldsymbol{x}$) and time (t), in a fixed domain Ω surrounded by a closed boundary Γ. The explicit space–time dependency of each dependent variable has been omitted for simplicity of notation.

To arrive at an iterative solution algorithm for the fluid flow set of Eq. (1), a formulation must ensure coupled satisfaction of all the equations at convergence. Pressure correction or velocity correction schemes may be used to achieve this purpose in a time accurate manner or in a time-marching scheme to steady state where time stepping is then viewed and utilized as a relaxation procedure. We follow a velocity correction approach that was originally proposed by Harlow and Welch [37] in their MAC algorithm. The technique is closely related to alternative pressure-correction schemes [38]. We review the algorithm here for completeness.

The process starts from an initial velocity condition $\mathbf{V}^{(0)}$ that satisfies the continuity equation within the entire problem domain Ω, that is

$$\nabla \cdot \mathbf{V}^{(0)} = 0 \tag{2}$$

A new velocity field $\mathbf{V}^{(*)}$ may be estimated from the Navier–Stokes equations by positioning the space operators at the current time step as

$$\rho \frac{\partial \mathbf{V}^{(*)}}{\partial t} = \mu \nabla^2 \mathbf{V}^{(k)} - \nabla p^{(k)} - \rho(\mathbf{V}^{(k)} \cdot \nabla)\mathbf{V}^{(k)} \tag{3}$$

Notice that the body force term $\rho \mathbf{f}$ has been drop for simplicity. Equation (3) can also be recast in an implicit form by positioning the spatial operators at the new step (*) as

$$\mu \nabla^2 \mathbf{V}^{(*)} - \rho \frac{\partial \mathbf{V}^{(*)}}{\partial t} - \rho(\mathbf{V}^{(k)} \cdot \nabla)\mathbf{V}^{(*)} = \nabla p^{(k)} \tag{4}$$

Equations (3) or (4) can be advanced in time using a backward-difference approximation of the time derivative in a single step (first order) or multistep (second or higher order) scheme. The new velocity field $\mathbf{V}^{(*)}$ can then be determined by imposing a proper and complete set of boundary conditions generalized as

$$\alpha \frac{\partial \mathbf{V}^{(*)}}{\partial t} + \beta \frac{\partial \mathbf{V}^{(*)}}{\partial n} + \gamma \mathbf{V}^{(*)} = \sigma \tag{5}$$

As the solution of Eqs. (3) or (4) with the boundary conditions in Eq. (5) provides a velocity field that does not satisfy the continuity equation, that is

$$\nabla \cdot \mathbf{V}^{(*)} \neq 0 \tag{6}$$

Satisfaction of the continuity equation, may be accomplished by updating the velocity field $\mathbf{V}^{(*)}$ with a velocity variation field $\delta \mathbf{V}^{(k+1)}$ as

$$\mathbf{V}^{(k+1)} = \mathbf{V}^{(*)} + \delta \mathbf{V}^{(k+1)} \tag{7}$$

Furthermore, if the velocity variation field is required to be irrotational, that is

$$\nabla \times \delta \mathbf{V}^{(k+1)} = 0 \tag{8}$$

A Helmholtz potential (or velocity correction potential) $\phi^{(k+1)}$ can be defined as

$$\nabla \phi^{(k+1)} \equiv -\delta \mathbf{V}^{(k+1)} \tag{9}$$

Now, if the new velocity field is required to satisfy continuity, that is

$$\nabla \cdot \mathbf{V}^{(k+1)} = 0 \tag{10}$$

A relationship for the Helmholtz potential $\phi^{(k+1)}$ can be expressed in the form of a Poisson equation as

$$\nabla^2 \phi^{(k+1)} = (\nabla \cdot \mathbf{V}^{(*)}) \tag{11}$$

This Poisson equation for the Helmholtz potential can be solved by imposing a proper and complete set of homogeneous boundary conditions generalized as

$$\beta \frac{\partial \phi^{(k+1)}}{\partial n} + \gamma \phi^{(k+1)} = 0 \tag{12}$$

Once the Helmholtz Poisson problem is solved, the velocity field is updated and forced to satisfy continuity. An equation to update the pressure field can be easily obtained by taking the divergence of the momentum equation and applying the continuity equation where necessary to arrive at

$$\nabla^2 p^{(k+1)} = -\rho \nabla \cdot [(\mathbf{V}^{(k+1)} \cdot \nabla)\mathbf{V}^{(k+1)}] \tag{13}$$

This Poisson equation for the pressure field can be solved by imposing a proper and complete set of boundary conditions some of which can be derived directly from the Navier–Stokes equation and generalized as

$$\beta \frac{\partial p^{(k+1)}}{\partial n} + \gamma p^{(k+1)} = \sigma \tag{14}$$

With the updated velocity field, the temperature field can be solved from Eq. (1c) using an explicit scheme such as

$$\rho c \frac{\partial T^{(k+1)}}{\partial t} = k \nabla^2 T^{(k)} - \rho c(\mathbf{V}^{(k+1)} \cdot \nabla)T^{(k)} \tag{15}$$

or an implicit scheme as

$$k \nabla^2 T^{(k+1)} - \rho c \frac{\partial T^{(k+1)}}{\partial t} - \rho c(\mathbf{V}^{(k+1)} \cdot \nabla)T^{(k+1)} = 0 \tag{16}$$

Notice that in both cases the viscous dissipation term Φ has been dropped for simplicity. Equation (16) above is a linear differential

equation that can be time-march using a first- or higher-order scheme starting from an initial temperature field $T^{(0)}$ by imposing a proper and complete set of boundary conditions generalized as

$$\alpha\frac{\partial T^{(k+1)}}{\partial t}+\beta\frac{\partial T^{(k+1)}}{\partial n}+\gamma T^{(k+1)}=\sigma \tag{17}$$

Typical boundary conditions imposed to solve these equations are provided in the following list:

A. Boundary conditions for $\mathbf{V}$:

1. Wall (Dirichlet)

$$\mathbf{V}=0$$

2. Inlet (Dirichlet)

$$\mathbf{V}=\hat{V}$$

3. Outlet (nonreflective advective conditions) [39]

$$\frac{\partial \mathbf{V}}{\partial t}+V_n\frac{\partial \mathbf{V}}{\partial n}=0$$

B. Boundary conditions for p:

1. Wall (Neumann from *N-S* equation)

$$\frac{\partial p}{\partial n}=\left[\mu(\nabla^2\mathbf{V})-\rho\frac{\partial \mathbf{V}}{\partial t}\right]\cdot\hat{n}$$

2. Inlet (Dirichlet)

$$p=\hat{p}$$

3. Outlet (Neumann from *N-S* equation)

$$\frac{\partial p}{\partial n}=\left[\mu(\nabla^2\mathbf{V})-\rho\frac{\partial \mathbf{V}}{\partial t}-\rho(\mathbf{V}\cdot\nabla)V\right]\cdot\hat{n}$$

C. Boundary conditions for ϕ:

1. Wall (Neumann)

$$\frac{\partial \phi}{\partial n}=0$$

2. Inlet (Neumann)

$$\frac{\partial \phi}{\partial n}=0$$

3. Outlet (Dirichlet)

$$\phi=0$$

D. Boundary conditions for T:

1. Forced

$$T=\hat{T}$$

2. Natural

$$k\frac{\partial T}{\partial n}=-\hat{q}$$

3. Convective

$$k\frac{\partial T}{\partial n}=-\hat{h}(T-T_{\text{ref}})$$

where the notation $\hat{V}$, $\hat{p}$, $\hat{T}$, $\hat{q}$, and $\hat{h}$ signifies prescribed values; V_n is the normal velocity; and $\partial/\partial n$ denotes derivative with respect to the outward-drawn normal to a boundary, $\hat{n}$. We use the following fractional step method to time march to steady state

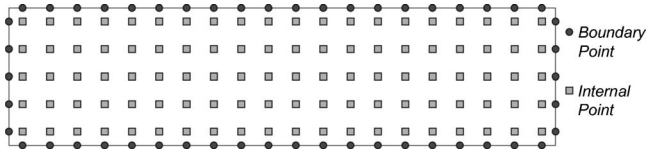

Fig. 2 Typical point collocation of data centers

$$f\left(t+\frac{\Delta t}{3}\right)=f(t)+\frac{\Delta t}{3}\left.\frac{\partial f}{\partial t}\right|_t$$

$$f\left(t+\frac{\Delta t}{2}\right)=f(t)+\frac{\Delta t}{2}\left.\frac{\partial f}{\partial t}\right|_{t+(\Delta t/3)}$$

$$f(t+\Delta t)=f(t)+\Delta t\left.\frac{\partial f}{\partial t}\right|_{t+(\Delta t/2)} \tag{18}$$

This method can be shown to be third-order accurate and when applied to the momentum equations leads to

$$\mathbf{V}^{(k+1/3)}=\mathbf{V}^{(k)}+\frac{\Delta t}{3}\left[\frac{\mu}{\rho}\nabla^2\mathbf{V}-(\mathbf{V}\cdot\nabla)\mathbf{V}\right]^{(k)}-\frac{\Delta t}{3\rho}\nabla p^{(k)}$$

$$\mathbf{V}^{(k+1/2)}=\mathbf{V}^{(k)}+\frac{\Delta t}{2}\left[\frac{\mu}{\rho}\nabla^2\mathbf{V}-(\mathbf{V}\cdot\nabla)\mathbf{V}\right]^{(k+1/3)}-\frac{\Delta t}{2\rho}\nabla p^{(k)}$$

$$\mathbf{V}^{(k+1)}=\mathbf{V}^{(k)}+\Delta t\left[\frac{\mu}{\rho}\nabla^2\mathbf{V}-(\mathbf{V}\cdot\nabla)\mathbf{V}\right]^{(k+1/2)}-\frac{\Delta t}{\rho}\nabla p^{(k)} \tag{19}$$

It is noted that the last update at $(k+1)$ is performed sequentially, with $\mathbf{V}^{(*)}$ computed first without the pressure gradient, and then $\mathbf{V}^{(k+1)}$ is updated with the velocity correction. These equations are iterated at each sublevel for time-accurate solutions or stepped once through if steady state is of interest. The pressure equation is subsequently updated by solving the Poisson equation and the energy equation is time-marched as well.

The use of the Helmholtz decomposition approach over the standard pressure-correction scheme [38] offers stability to the method by directly solving for the pressure field at every iteration step rather than correcting it. On the other hand, the computational efficiency of this approach is affected by the fact that two, instead of one, Poisson equations are solved at every step. This completes the review of the fluid flow solving algorithm, we now develop the localized RBF meshless collocation method.

Discretization in Space Using a Localized RBF Collocation

The meshless formulation begins by defining a set of data centers, *NC*, comprised of points on the boundary, *NB*, and points on the interior, *NI*. These data centers will serve as collocation points for the localized expansion of the different field variables in the domain Ω and on the boundary Γ (see Fig. 2).

A global interpolation for the field variables, $\phi(\boldsymbol{x})$ for instance, can be formulated by requiring

$$\phi(\boldsymbol{x})=\sum_{j=1}^{NB+NI}\alpha_j\chi_j(\boldsymbol{x}) \tag{20}$$

The expansion functions may be written in terms of radial-basis interpolation functions (RBF), in particular from the family of the so-called Hardy Multiquadrics [26] as

$$\chi_j(\boldsymbol{x})=[r_j^2(\boldsymbol{x})+c^2]^{n-(3/2)} \tag{21}$$

where n is a positive exponent parameter; c is a shape parameter; and $r_j(\boldsymbol{x})$ is the Euclidean distance from $(\boldsymbol{x})$ to $(\boldsymbol{x}_j)$. Several authors have shown [11,33–36] that a global interpolation of this type leads to large, fully populated, ill-conditioned coefficient ma-

trices for the unknown expansion coefficients. This behavior is exhibited even for small scale problems with a uniform distribution of data centers, and it affects the accuracy of the interpolation of the field variable, the accuracy of the approximation of the derivatives, and hence, the stability of the solution method. Several attempts have been made to mitigate this problem including preconditioning, domain decomposition [8], finite difference approximation of derivatives [36], and moving least-squares, among others.

A promising approach was recently proposed by Sarler et al. [24] and Sarler and Vertnik [25] to reduce the burden of the global interpolation by expanding the field variable locally around each data point to obtain its derivatives in an explicit time-marching scheme for the field variables. This approach yields the generation of a different but small interpolation matrix for each data point rather than the large and fully populated global interpolation matrix of the standard global RBF. This notion gives more leverage in the selection and distribution of points as well as in the choice of the free parameters for the RBF expansion functions. Moreover, since the approach consists of expanding known values of the field variables, it is applicable as long as an explicit time-marching scheme is formulated and inapplicable directly to steady problems.

A modification to the local formulation is now presented for its implementation to a general class of problems including the steady, Poisson-like problem encountered in the iterative solution of the Navier–Stokes equations of the previous sections, as well as explicit and implicit time marching schemes. For the development of the notions underlying the method, let us consider first the Poisson equation, Eq. (13), for the pressure update. This equation is recast in the following form

$$\nabla^2 p(\boldsymbol{x}) = f(\boldsymbol{x}) \tag{22}$$

and imposed with general boundary conditions given by

$$\beta(\boldsymbol{x})\frac{\partial p(\boldsymbol{x})}{\partial n} + \gamma(\boldsymbol{x})p(\boldsymbol{x}) = \sigma(\boldsymbol{x}) \tag{23}$$

A localized expansion based on the RBF multiquadric interpolation functions may be written as

$$p(\boldsymbol{x}) \approx \sum_{j=1}^{NF} \alpha_j \chi_j(\boldsymbol{x}) \tag{24}$$

where NF is the number of points of influence around and including the data center $\boldsymbol{x_i}$. Figure 3 shows typical collocation topologies for internal, boundary, and corner data centers. In this case, all of the topologies employ five points including the data center. However, this format can be modified to include, for example, the diagonal points. In addition, in order to form the connectivity of these topologies throughout the entire domain, a smart search algorithm must be formulated to account for irregularities in the geometry and/or point distribution.

The solution of the field variable p is initialized throughout the entire domain either with the initial condition, an initial guess, or, in this case, with the pressure field from the previous time step. The pressure at the data center of the collocation topology is constrained with the governing equation as

$$\nabla^2 p(\boldsymbol{x_i}) = \sum_{j=1}^{NF} \alpha_j \nabla^2 \chi_j(\boldsymbol{x_i}) = f(\boldsymbol{x_i}) \tag{25}$$

in the case where $\boldsymbol{x_i}$ is an internal data center, while

$$\sum_{j=1}^{NF} \alpha_j \left[\beta(\boldsymbol{x_i})\frac{l\chi_j}{\partial n}(\boldsymbol{x_i}) + \gamma(\boldsymbol{x_i})\chi_j(\boldsymbol{x_i}) \right] = \sigma(\boldsymbol{x_i}) \tag{26}$$

in the case where $\boldsymbol{x_i}$ is a boundary data center. The initial or current pressure field is imposed on the remaining points of the topology as

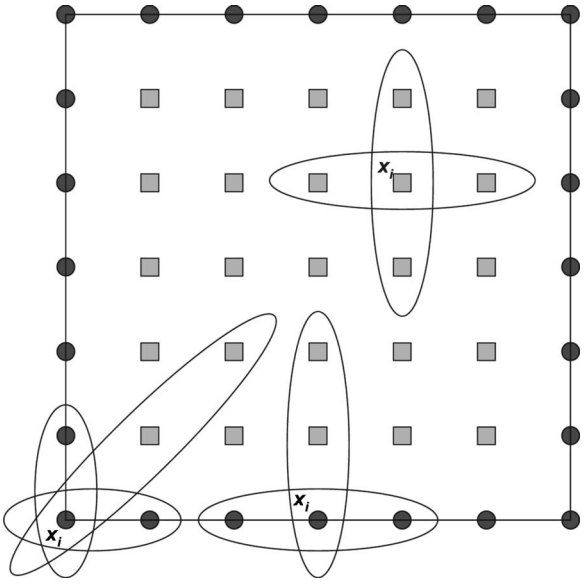

Fig. 3 Collocation topology for internal, boundary, and corner data centers

$$\sum_{j=1}^{NF} \alpha_j \chi_j(\boldsymbol{x_l}) = \hat{p}(\boldsymbol{x_l}) \tag{27}$$

where $l=2\ldots NF$. Equations (25) and (27) form a complete set of equations for the coefficients α at internal data centers while Eqs. (26) and (27) form a complete set of equations for the coefficients α at boundary data centers. This system of equations have the following form for the case of internal data centers

$$\begin{bmatrix} \nabla^2\chi_1(\boldsymbol{x_1}) & \cdots & \nabla^2\chi_{NF}(\boldsymbol{x_1}) \\ \chi_1(\boldsymbol{x_2}) & \cdots & \chi_{NF}(\boldsymbol{x_2}) \\ \vdots & \vdots & \vdots \\ \chi_1(\boldsymbol{x_{NF}}) & \cdots & \chi_{NF}(\boldsymbol{x_{NF}}) \end{bmatrix} \begin{pmatrix} \alpha_1 \\ \alpha_2 \\ \vdots \\ \alpha_{NF} \end{pmatrix} = \begin{pmatrix} f(\boldsymbol{x_1}) \\ \hat{p}(\boldsymbol{x_2}) \\ \vdots \\ \hat{p}(\boldsymbol{x_{NF}}) \end{pmatrix}$$

or in matrix-vector form

$$[C]\{\alpha\} = \{b\} \quad \text{or} \quad \{\alpha\} = [C]^{-1}\{b\} \tag{28}$$

A similar form can be obtained for boundary data centers. Combining the above with the localized expansion of the pressure p at the data center $\boldsymbol{x_i}$ yields

$$p_i = \{\chi_i\}^T\{\alpha\} = \{\chi_i\}^T[C]^{-1}\{b\} = \{g\}^T\{b\} \tag{29}$$

Therefore, evaluation of the pressure at the data center $\boldsymbol{x_i}$ is provided by a simple inner product of two vectors:$\{g\}$ which can be prebuilt and stored for every data center from the collocation matrix $[C]$ and the expansion functions $\chi_j(\boldsymbol{x_i})$ and $\{b\}$ which changes as the pressure field and/or right-hand side of the governing equation changes. Furthermore, the new pressure field may be underrelaxed with a parameter θ as

$$p^{(u+1)} = \theta p^{(\prime)} + (1-\theta)p^{(u)} \tag{30}$$

where (u) is the update step of the solution and $(\ ')$ stands for the estimated field from the localized meshless expansion. Once the pressure has been updated throughout the field, a direct interpolation with the same topology may be performed from the expression in Eq. (24) as

$$\{p\} = [\chi]\{\alpha\} \Rightarrow \{\alpha\} = [\chi]^{-1}\{p\} \tag{31}$$

Then, to estimate the field variable derivatives at the data center, any linear differential operator $\mathcal{L}$ can be applied over the localized expansion equation (24) as

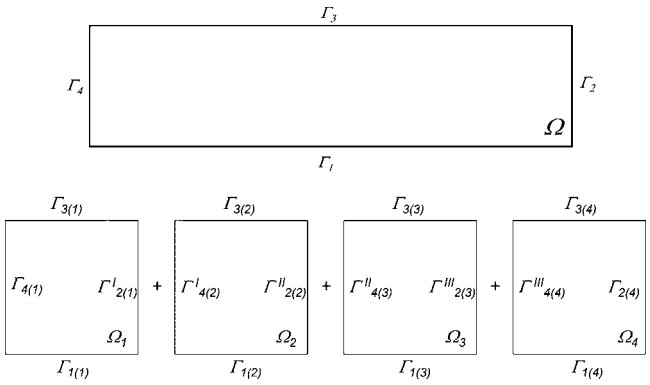

Fig. 4 Problem domain and typical decomposition

$$\mathcal{L}p(\boldsymbol{x}_i) \approx \sum_{j=1}^{NF} \alpha_j \mathcal{L}\chi_j(\boldsymbol{x}_i) \tag{32}$$

Thus, in matrix-vector form

$$\mathcal{L}p_i = \{\mathcal{L}\chi_i\}^T\{\alpha\} = \{\mathcal{L}\chi_i\}^T[\chi]^{-1}\{p\} = \{\mathcal{L}\}^T\{p\} \tag{33}$$

Therefore, evaluation of the field variable derivatives at everyone of the data centers $\boldsymbol{x}_i$ is again provided by a simple inner product of two vectors: $\{\mathcal{L}\}$ which can be prebuilt and stored and $\{p\}$ which is the updated pressure field within the topology of the data center $\boldsymbol{x}_i$. Notice that for the topologies considered herein, the length of the vectors $\{g\}$ and $\{\mathcal{L}\}$ is 5×1.

The particular feature of the localized collocation method that allows us to estimate the field variables and their derivatives by simple inner products of vectors that can be prebuilt and stored is precisely what makes this approach attractive. Notice that the Multiquadrics functions need only be evaluated at a setup stage when these vectors are being built reducing the CPU burden of having to evaluate fractional powers and complicated functions at every step of an iteration or time-marching scheme. In addition, the memory demands of this approach are minimal, as no global collocation matrix must be allocated [33], and, only very small vectors must be stored for every one of the data centers. This offers tremendous advantages in terms of data preparation over global RBF meshless methods. For example, to set up a 20,000 data point localized meshless methods problem, including establishing the topology and prebuilding all collocation vectors such as $\{g\}$ and $\{\mathcal{L}\}$, and storage of these onto disk takes less than 3 s on a 2.8 GHz P4 desktop computer with 1 GB of RAM. Thus, in addition to improved control and stability, the efficiency of the localized RBF method described in this paper is far superior to the global meshless methods reported in the literature. In the case of transient problems with moving boundaries this advantage is more pronounced in the sense that only affected topologies close to the boundary need to be recomputed as opposed to global meshless methods where the entire collocation matrix must be recomputed and stored.

Parallel Domain Decomposition Implementation

In order to further accelerate the solution process, a parallelization of the time-marching numerical algorithm is formulated and readily implemented in a parallel cluster environment. It is noted that unlike the necessity to adopt domain decomposition to reduce the conditioning number in global RBF approaches, parallel domain decomposition serves here only to reduce computing time by distributing computation to multiple processors.

The problem domain Ω is decomposed into multiple subdomains Ω_m separated by artificially created interfaces Γ^{I} (see [33–35] and Fig. 4). Each subdomain problem is rendered as a well-posed boundary value problem by imposing boundary conditions (starting from the initial conditions) at the artificially created interfaces. A simple iteration implementation can follow to force continuity conditions of the field variables and their derivatives at the interfaces. The boundary value problem will then be independently solved over each subdomain.

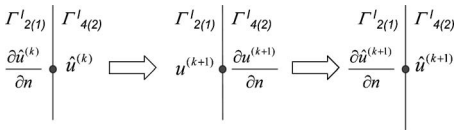

Fig. 5 Iteration process averaging across an interface

Once each boundary value problem is independently solved on each subdomain, an iteration scheme must follow to continuously ensure continuity of the field variables and their derivatives across the interfaces. This is accomplished by setting up a process in which each interface is treated differently on both sides: on one side the first kind of boundary condition is applied, while on the other side the second kind of boundary condition is applied. The resulting boundary values are then averaged with their corresponding values across the interfaces. This process is illustrated in Fig. 5 for a single point on the interface between subdomain Ω_1 and Ω_2 for the x component of the velocity field, u. In this case, the combination of boundary conditions at artificially created interfaces must be such that it ensures that each subdomain has at least one inlet (first kind) and one outlet (second kind) to satisfy physical requirements.

In Fig. 5 the imposed boundary conditions are $\partial\hat{u}^{(k)}/\partial n$ on the left-hand side of the interface and $\hat{u}^{(k)}$ on the right-hand side. After the solution of the boundary value problem on each subdomain, the resulting (provisional) values are $u^{(k+1)}$ on the left-hand side of the interface and $\partial u^{(k+1)}/\partial n$ on the right-hand side. These resulting values are averaged to generate the boundary conditions for the next time step as

$$\frac{\partial\hat{u}^{(k+1)}}{\partial n} = \frac{\partial\hat{u}^{(k)}}{\partial n} - \frac{1}{2}\left(\frac{\partial\hat{u}^{(k)}}{\partial n} + \frac{\partial u^{(k+1)}}{\partial n}\right)$$

$$\hat{u}^{(k+1)} = \frac{\hat{u}^{(k)} + u^{(k+1)}}{2} \tag{34}$$

ensuring continuity of the field variable and its normal derivative. Notice that in order to achieve truly time-accurate analysis, sublevel iterations must be performed at each time step. The iteration process may be stopped once steady state is achieved or at any time level. Steady state may be verified by defining a least-squares residual of the deviation from the satisfaction of the field equations and comparing it to that of the previous time step (k). Once the residual difference reaches a preset convergence criterion the iteration process may be stopped.

The domain decomposition formulation is implemented in a parallel computing environment: the algorithm has been coded and implemented in a 36-node 72 CPU 3.06–3.2 GHz Xeon Dell PowerEdge Cluster running Red Hat Linux 9.0 and the MPICH implementation of the MPI standards, and compiled using GNU FORTRAN 77. The parallel code collapses to serial computation if a single processor is assigned to the execution.

Upon launching the code under MPI, the processors are identified and given a rank. A small sample problem is solved on all processors to identify their relative performance. A load balancing routine is then performed to optimally assign domains to each processor by minimizing an objective function that contains information with regard to subdomain sizes and relative computational capability. This optimization is performed using a discrete genetic algorithm [32]. This completes the development of our numerical algorithm. We now proceed to present results from several numerical verification examples.

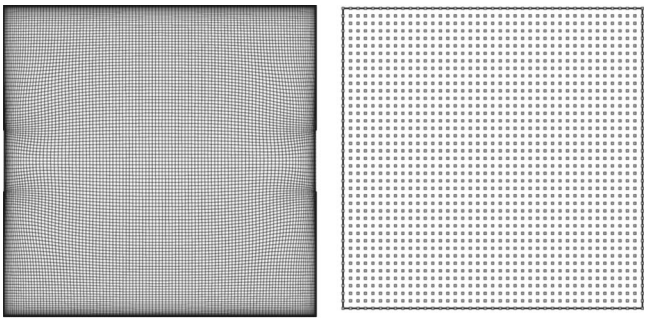

(*a*)

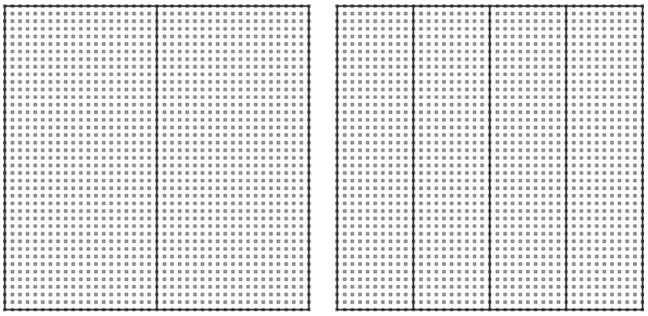

(*b*)

Fig. 6 FVM mesh and point collocation of cavity

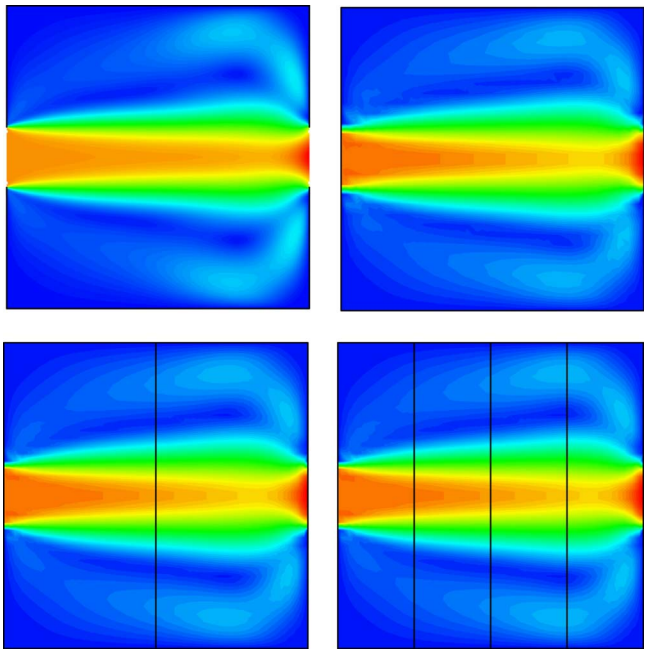

Fig. 7 FVM and meshless velocity contours

Numerical Verification

In all cases, we compare results predicted by our localized meshless RBF methods with those obtained by the commercial FVM computational fluid dynamics package Fluent 6.1. All cases considered here are laminar, and all FVM solutions are grid converged and carried out using the second-order upwinding scheme, unless otherwise stated. The efficiency of the localized meshless method is validated with these examples as the measured computational time per iteration is proportional to the ratio of data centers to FVM grid points for every case. Thus, with a much coarser meshless point distribution with respect to FVM grids, a significant improvement in computational time is obtained.

The first numerical test of the localized meshless method consists of a 1×1 m square cavity with a 20 cm air inlet at 0.01 m/s centered on the left-hand wall and a 20 cm outlet centered on the right-hand wall. The Prandtl number is taken as Pr=0.7 and the Reynolds number based on the cavity side length is Re_L=675. Here, the method will be tested for robustness by sequentially domain decomposing into one, two, and four regions. The meshless solution is provided by collocating 1681 (41×41) equally spaced data centers, while the FVM mesh contains 13,685 nodes as seen in Fig. 6. The velocity contours for the FVM solution as well as for the single and multiregion meshless solution is shown in Fig. 7 revealing accurate results.

The velocity profiles at x=0, 0.25, 0.5, 0.75, and 1.0 m are shown in Fig. 8 again revealing the accuracy of the localized meshless approach.

Next, the lid-driven square cavity problem is used as a benchmark to validate both the accuracy and efficiency of the localized meshless approach when compared to FVM solutions and results reported by Ghia et al. [40]. A square closed cavity is considered with the top wall moving at a constant speed. In addition, the bottom wall is kept at 323 K while the top wall is kept at 288 K.

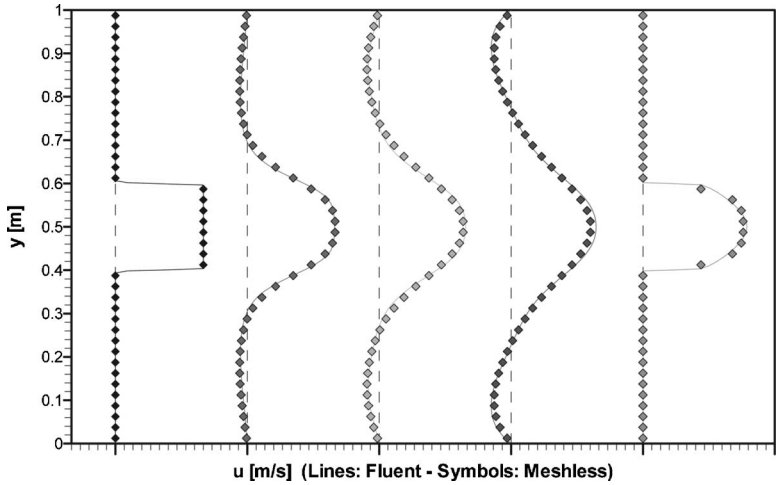

Fig. 8 FVM and meshless *x* velocity profiles at *x*=0, 0.25, 0.5, 0.75, and 1.0 m

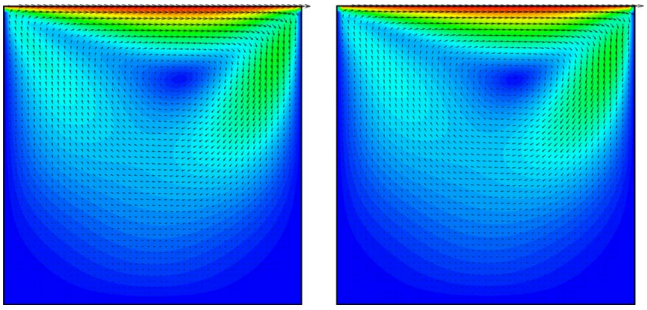

Fig. 9 FVM and meshless velocity vectors and magnitude contours for the lid-driven cavity

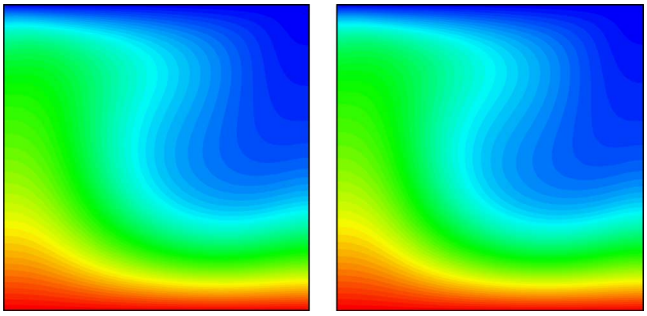

Fig. 10 FVM and meshless temperature contours for the lid-driven cavity

Table 1 Computation times for FVM and localized meshless solutions for different grid resolutions.

	FVM	Localized meshless		
Grid/Point distribution	Fluent 6.1 (1000 Δt)	Topology	RBF collocation	Solution (1000 Δt)
26×26	264 s	<1 s	<1 s	5.19 s
51×51	326 s	<2 s	<1 s	27.86 s
101×101	970 s	<8 s	<3 s	164.14 s

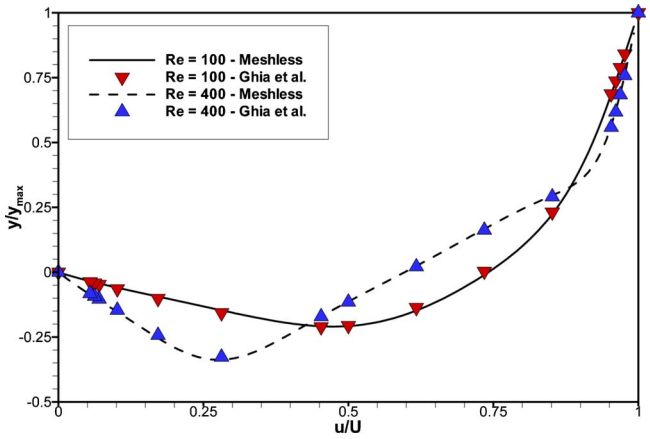

Fig. 11 FVM and meshless *x* velocity component at vertical center line

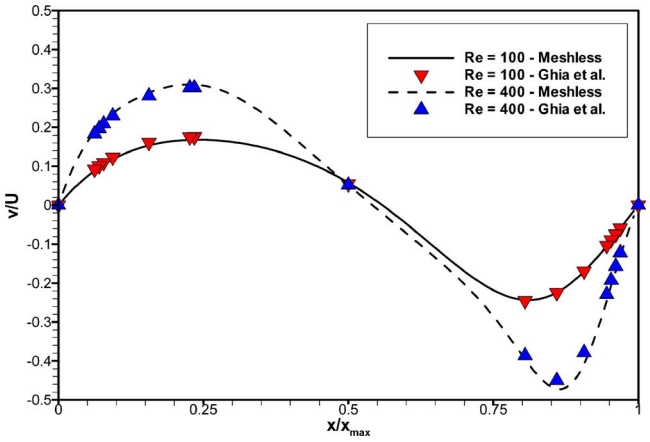

Fig. 12 FVM and meshless *y* velocity component at horizontal center line

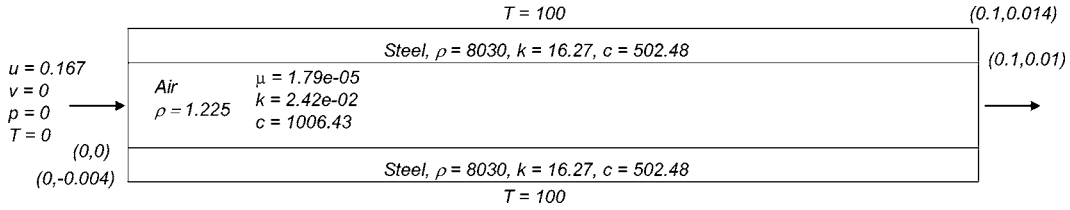

Fig. 13 Geometry and properties for parallel plates

Initially, FVM and meshless solutions are generated using three uniform point distributions $(26\times26, 51\times51, 101\times101)$ with a Reynolds number of 68 based on the side of the cavity and the Prandtl number is Pr=0.7. Qualitative comparison of the results are shown in Figs. 9 and 10 where FVM and meshless velocity vectors and magnitude contours, as well as temperature contours are displayed for the 51×51 grid and point distribution case. A measure of the efficiency of the localized meshless method com-

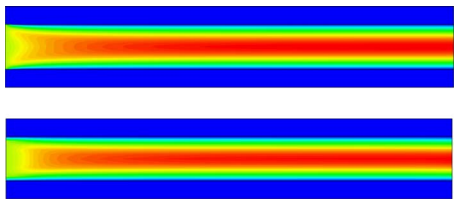

Fig. 14 FVM and meshless velocity contours

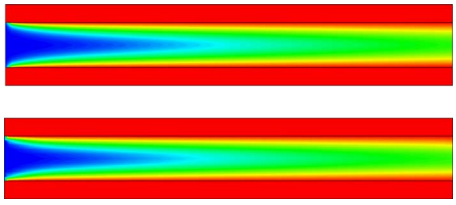

Fig. 15 FVM and meshless temperature contours

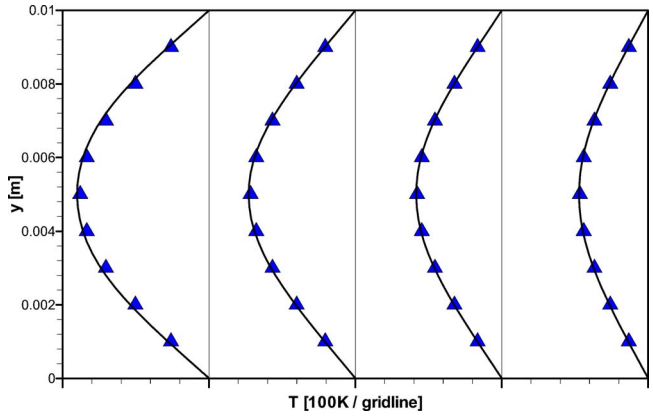

Fig. 16 FVM and meshless temperature profiles at 1/4, 1/2, 3/4, and 1/1 channel length

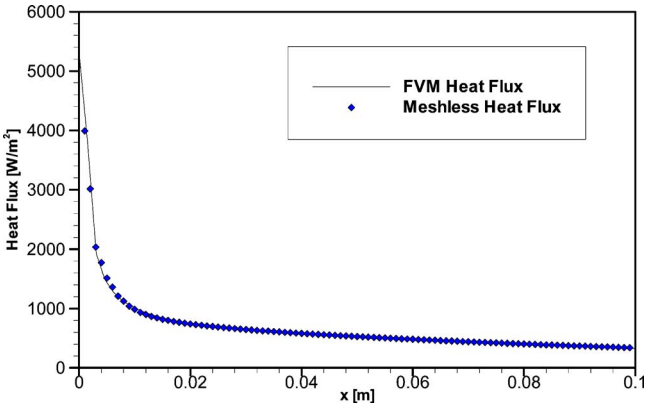

Fig. 17 FVM and meshless heat flux along interface

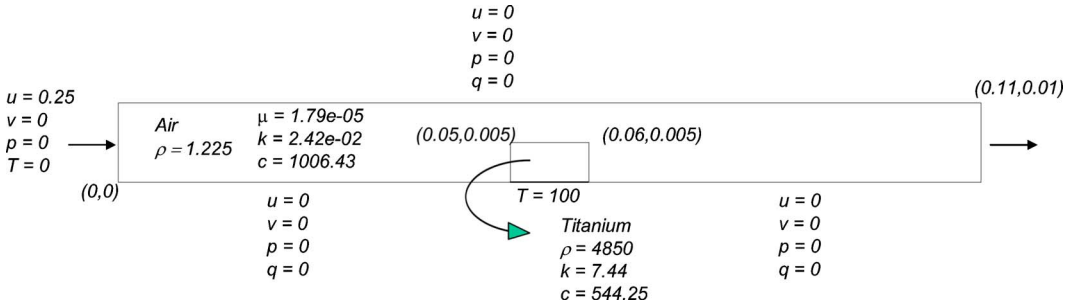

Fig. 18 Geometry and properties for square obstruction

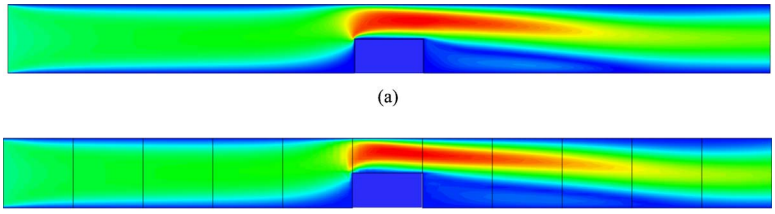

Fig. 19 Velocity contours: (*a*) FVM, and (*b*) meshless

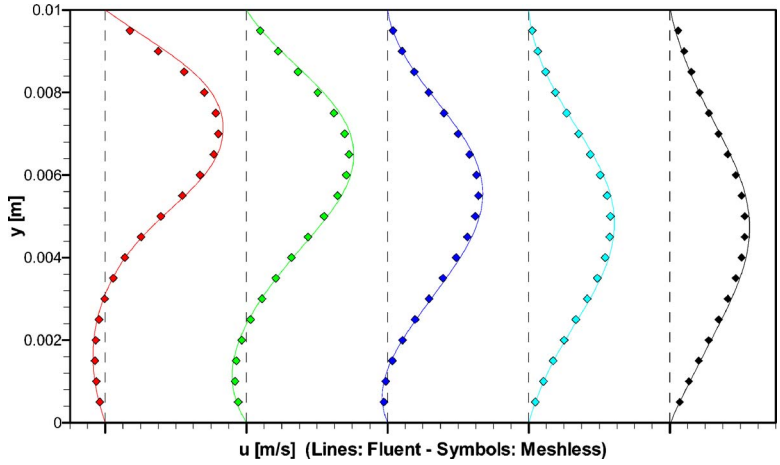

Fig. 20 FVM and meshless *x* velocity profiles at *x*=7, 8, 9, 10, and 11 cm

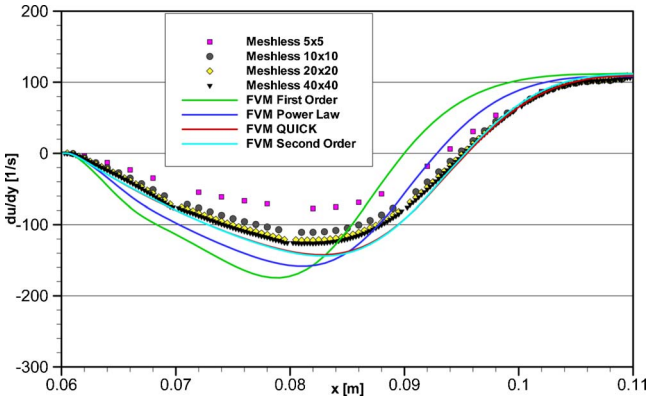

Fig. 21 FVM and meshless $\partial u/\partial y$ after the obstruction

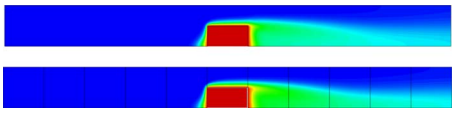

Fig. 22 FVM and meshless temperature contours

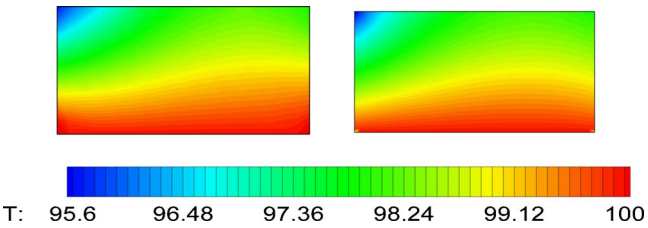

Fig. 23 Zoomed in FVM and meshless obstruction temperature contours in the square obstruction

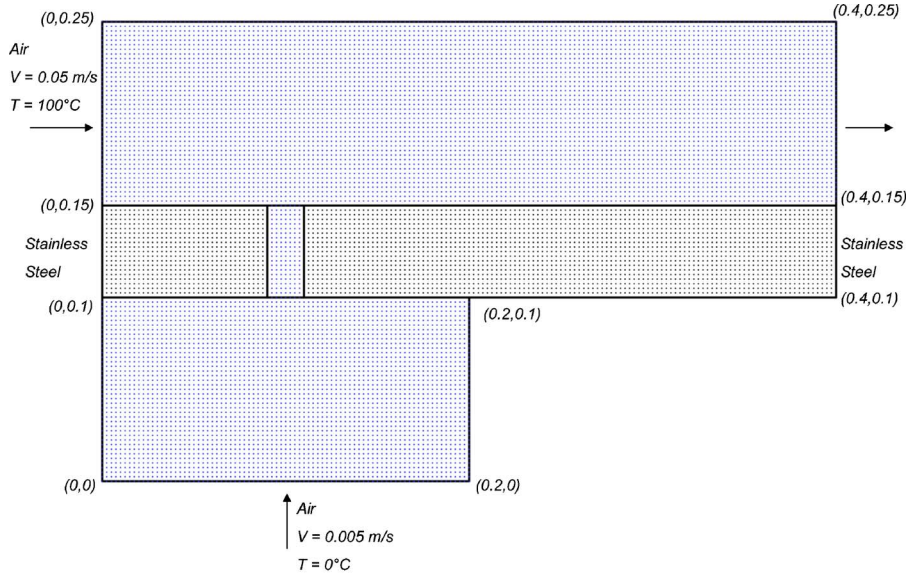

(a)

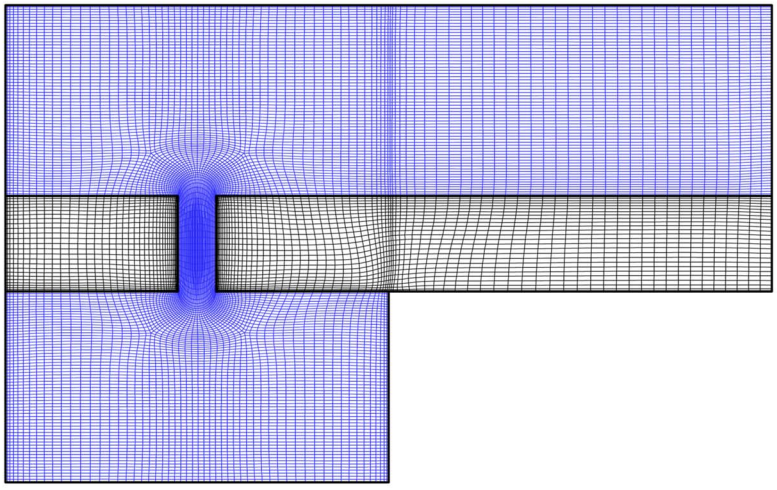

(b)

Fig. 24 Data center distribution and FVM mesh for cooling plenum, cooling hole (2 cm width), and main cooling channel:(*a*) meshless collocation (13,345 data centers) 2 cm cooling hole width and (*b*) finite volume mesh (14,859 finite volumes)

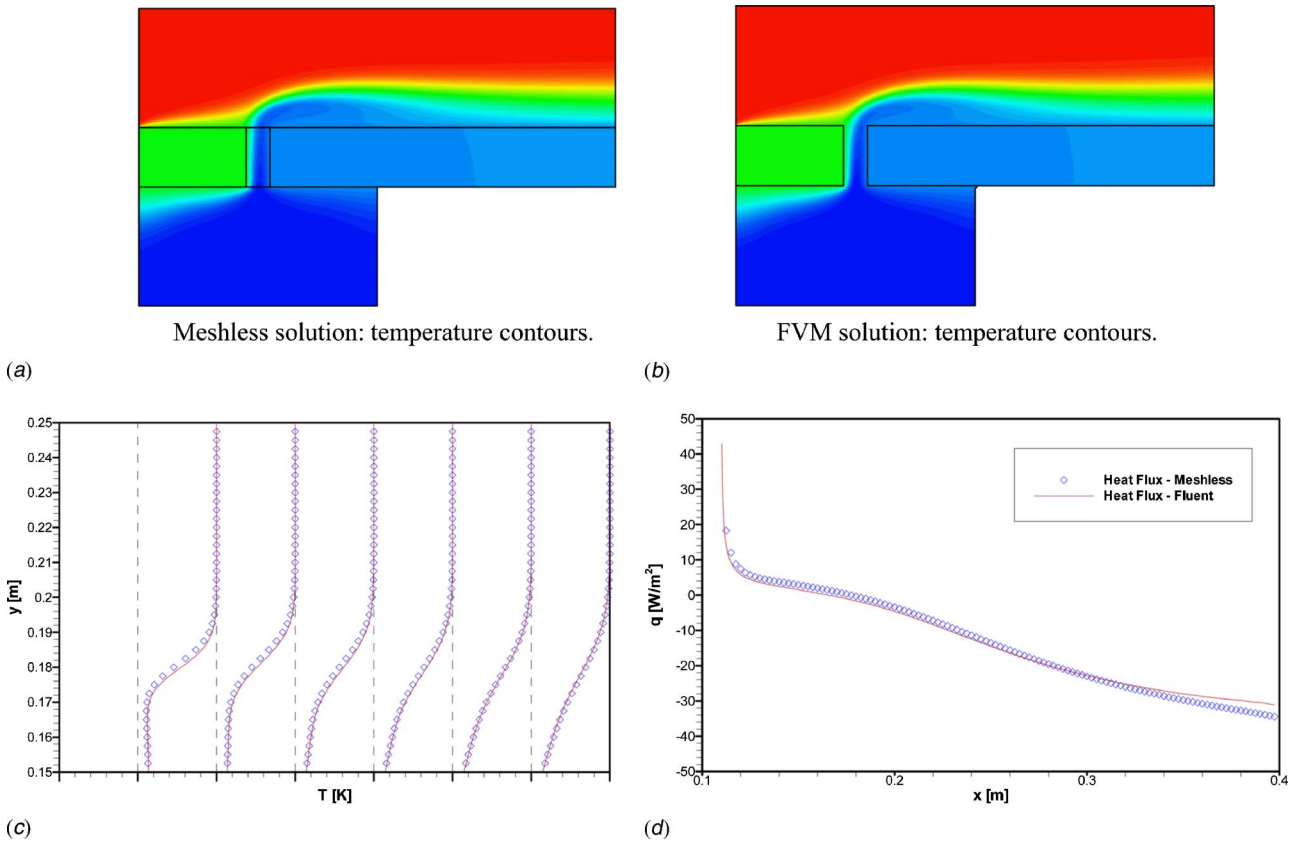

Fig. 25 Comparison of temperature distributions predicted by: (*a*) meshless and (*b*) FVM as well as (*c*) temperature profiles on top region at $x=0.15$, 0.2, 0.25, 0.3, 0.35, 0.4 m and (*d*) heat flux along top wall of stainless-steel block ($y=0.15$ m) after cooling hole

pared to FVM solutions processed in Fluent 6.1 are presented in Table 1. Here both FVM and meshless codes were implemented in the same platform (Single Xeon 64-bit, 3.2 GHz, 6 GB RAM) using the same grid and point distribution, respectively. Also, the settings of the FVM solution scheme were set to match those of the meshless solution scheme, i.e., explicit, coupled, unsteady with 1 sublevel iteration, $\Delta t=0.0001$ s. The values in Table 1 reveal that the localized meshless solution process is found to be more efficient than the FVM solution process implemented in Fluent 6.1 under the same conditions and scheme. The difference in performance is more noticable with the coarsest grid and point distribution which can be attributed to the amount of overhead involved in FVM computations. In addition to the average computation times over 1000 time steps, Table 1 also shows the localized meshless preprocessing time for generating the topologies and performing the RBF collocation and algebra, again revealing very little overhead at the startup of the process. It is worth mentioning that for this case the localized meshless topologies were configured to include up to 13 points each and despite this fact, this method was found to perform several times faster than Fluent 6.1 under the same conditions and platform.

In addition to the qualitative comparisons, the localized meshless results were compared along the geometrical center lines with those reported by Ghia et al. [40]. For this purpose, the Reynolds number was increased to 100 and 400 and the meshless resolution was increased to include 129×129 uniformly distributed points in order to match the resolution reported in Ref. [40]. Figures 11 and 12 display the x and y velocity components along the vertical and horizontal geometrical center lines respectively, revealing very close agreement between the meshless and reported benchmark FVM results.

Next, a conjugate solution is evaluated for developing air flow entering at 0°C and 0.167 m/s between parallel steel plates. The plates are 10 cm long and 1 cm apart. The plates have a finite thickness of 4 mm and the top and bottom are maintained at 100°C to test the effects of conjugate heat transfer. The geometry and thermophysical properties (in SI units) for the problem are shown in Fig. 13. The Prandtl number is taken as Pr=0.7, and the Reynolds number based on the hydraulic diameter is Re=225. The meshless solution was obtained by collocating 1919 (101×19) data centers while the FVM mesh contains 4091 nodes. The FVM and meshless velocity magnitude contours are shown in Fig. 14 while the temperature contours are shown in Fig. 15. A plot of the temperature profiles across the plates at 1/4, 1/2, 3/4, and 1 length of the plates is shown in Fig. 16 revealing high accuracy when compared to the FVM results. The heat flux along the interface wall between the air flow and the steel plates is shown in Fig. 17 again with very good agreement between the FVM and meshless solution. A heat balance analysis was carried out to show that the integrated heat rate into the fluid domain by conduction through the plates was $q_{\text{interface}}=-112.304$ W perfectly symmetric through top and bottom, while the heat rate removed by convection through the inlet and outlet based on the mass-flow-weighted average temperatures was $q_{\text{convection}}=111.797$ W, in addition to the axial conduction heat rate through inlet and outlet of $q_{\text{axial}}=1.425$ W, leading to a total heat rate imbalance of $q_{\text{imbalance}}=0.918$ W, or 0.82% of the total heat removed by convection, indicating remarkable precision in the analysis considering the coarseness of the point distribution.

The next numerical example examines air flowing through a channel with a titanium rectangular obstruction, all parameters are provided in the figure using SI units. The Prandtl number is taken as Pr=0.7, and the Reynolds number based on the hydraulic di-

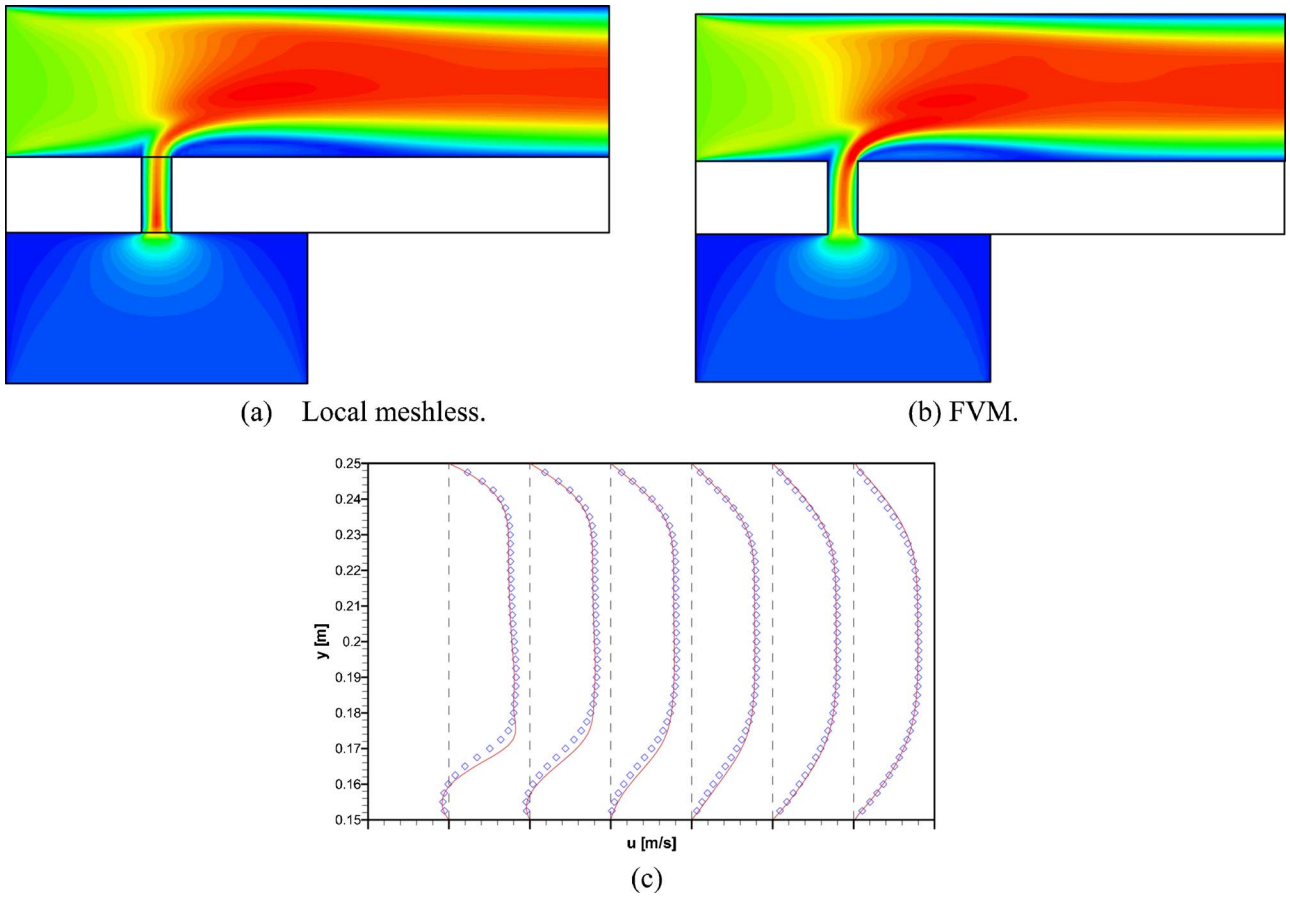

Fig. 26 Contours of velocity magnitude and velocity profiles: (*a*) LMRBF velocity contors; (*b*) FVM velocity contours; and (*c*) velocity profiles across the channel region at discrete locations $x=0.15$, 0.2, 0.25, 0.3, 0.35, and 0.4 m

ameter is Re=338. Again the effects of conjugate heat transfer will be tested as the bottom of the obstruction is kept at 100°C while the flow enters at 0°C with a velocity of 0.25 m/s. The channel is 10 cm long by 1 cm tall while the obstruction is 10 $\times$5 mm and is places 5 cm after the inlet as shown in Fig. 18. The meshless solution was obtained by collocation 4221 equally spaced data centers while the FVM mesh contains 9473 nodes. The FVM and meshless velocity contours are shown in Fig. 19. A plot of the velocity profiles after the obstruction at $x=7$, 8, 9, 10, and 11 cm is shown in Fig. 20 revealing very good agreement between the FVM and meshless solutions. A plot of the y derivative of the x velocity ($\partial u/\partial y$) on the bottom wall after the obstruction is presented in Fig. 21 showing FVM results generated using different upwinding schemes as well as meshless results provided by four different resolutions of data centers (5×5, 10×10, 20×20, and 40×40 points per region). Results reveal that the meshless method solution tends to converge with increased density of data centers and agrees closely with the second order and QUICK FVM upwinding schemes in trend, in magnitude, and in prediction of the reattachment point location. Finally, the FVM and meshless temperature contour plots are shown in Fig. 22 as well as a zoom of the plot on the titanium obstruction in Fig. 23 clearly showing the multidimensional temperature gradients across the solid.

The next example consists of a flow of colder air from a plenum through a stainless steel plate into a hotter incoming flow. The problem is conjugate and the boundary conditions are shown in Fig. 24 along with the meshless method and finite volume discretizations consisting of 13,345 data points and 14,859 FVM nodes, while temperature solutions are compared in Fig. 25. The flow solutions and flow profiles predicted by LMRBF and FVM are compared in Fig. 26.

The last numerical example presents results for a nonuniform data center distribution for meshless methods predictions of flow over a cylinder centered in rectangular channel. The cylinder of diameter d is enclosed between two parallel plates $3\cdot d$ apart by $10\cdot d$ long. The center of the cylinder is located at 1/3 of the length of the channel. A uniform flow field with an entrance Reynolds number of 10 based on the cylinder diameter enters the channel from the left boundary. This example serves the purpose of demonstrating the robustness of the localized meshless approach by applying it to a nonrectangular geometry using a nonuniform point distribution using methods for automated data center distribution described in Ref. [41]. The meshless results are compared to grid-converged FVM results provided by Fluent 6.1. The meshless results are obtained using a nonuniform distribution of 8989 points while the FVM results are obtained using a clustered mesh with 7872 quadrilateral cells adapted to 31,488 quadrilateral cells to verify grid convergence. Figure 27 displays a close up of the FVM grid and meshless point distribution around the cylinder clearly showing the clustering of the grid and the nonuniformity of the point distribution. Figure 28 shows the FVM and localized meshless contours of the velocity magnitude revealing close qualitative agreement. A quantitative comparison is presented in Figs. 29 and 30 where the FVM, adapted FVM, and localized meshless pressure coefficients and viscous stress coefficients (normalized magnitude of the traction vector) are displayed

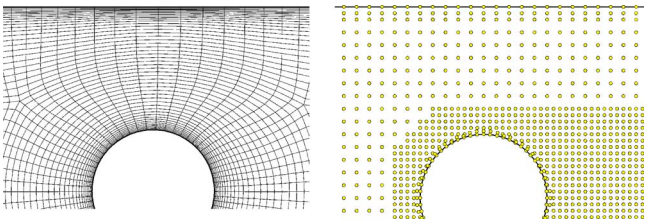

Fig. 27 FVM grid and meshless point distribution around the cylinder

around the top of the cylinder from leading edge to trailing edge, again revealing excellent agreement between grid-converged FVM results and localized meshless results.

Conclusions

In this paper we present a localized meshless method for the solution of coupled viscous fluid flow and convective heat transfer problems and implement it in parallel using domain decomposition. The method is based on localized RBF expansion using Hardy Multiquadrics for the sought-after unknowns. An efficient set of formulae are derived to compute the RBF interpolation in terms of vector products thus providing a substantial computational savings over traditional meshless methods. Moreover, the approach developed in this paper is applicable to explicit or implicit time-marching schemes as well as steady-state iterative methods. The incompressible Navier–Stokes set of equations for fluid flow and heat transfer in the fluid regions are solved using a standard time-marching scheme based on a Helmholtz potential decomposition. When conjugate heat transfer is considered, the simplified energy equation is solved in the solid regions using also a time-marching scheme.

Numerical results are presented and compared to results predicted by a commercial CFD code (Fluent) for several cases including a jet flow into a square cavity, conjugate analysis of a thick-walled channel flow, conjugate analysis of flow in a channel with a square step obstruction, and conjugate analysis of a plenum-cooled plate in contact with a hot freestream. Results consistently show the localized meshless method approach produces accurate results even when using a much coarser number of data centers versus FVM nodes. The approach is accurate and efficient while requiring a much-reduced effort in problem preparation as compared to FVM. The authors are investigating several extension of the method, including alterntive solutions schemes that lend themselves to parallel computation without resort to domain decomposition, application to natural convection and species transport, and extensions to three-dimensional and incorporation of turbulence models. These forthcoming results will be reported elsewhere in the literature.

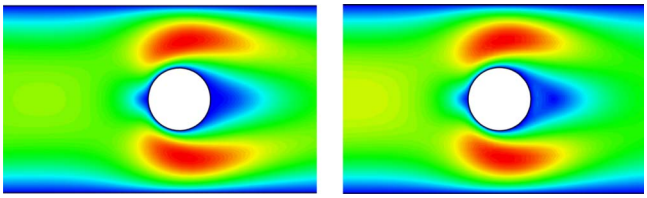

Fig. 28 FVM and meshless velocity magnitude contours around the cylinder

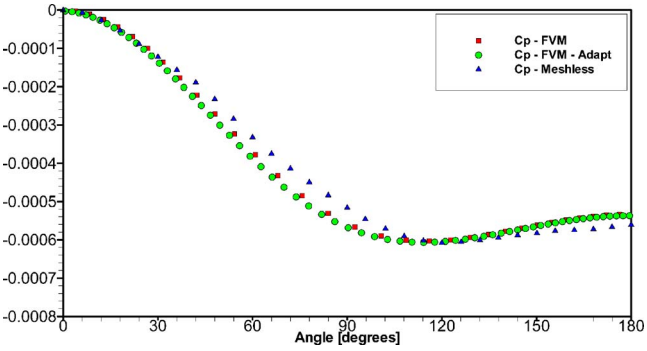

Fig. 29 Pressure coefficient around the cylinder

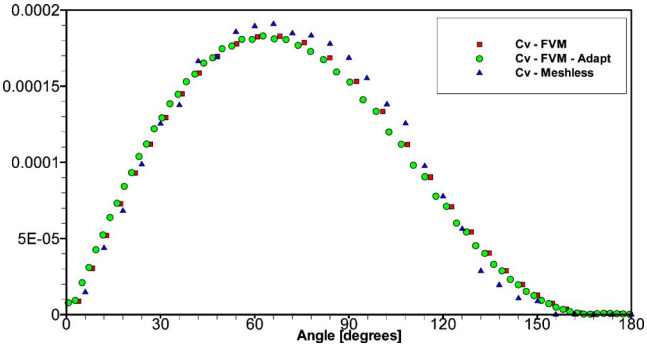

Fig. 30 Viscous stress coefficient around the cylinder

Nomenclature

$\mathbf{V}(\boldsymbol{x})$ = velocity field
$p(\boldsymbol{x})$ = pressure field
$T(\boldsymbol{x})$ = temperature field
$\phi(\boldsymbol{x})$ = Helmholtz potential
$\partial/\partial n$ = outward normal derivative
$\mathbf{f}$ = specific body force
ρ = density
μ = dynamic viscosity
k = thermal conductivity
c = specific heat
Φ = viscous dissipation
NC = number of data centers
NB = number of boundary collocation points
NI = number of internal collocation points
α_j = expansion coefficients
$\chi_j(x)$ = expansion functions
$r_j(x)$ = Euclidean distance to point j

References

[1] Belytscho, T., Lu, Y. Y., and Gu, L., 1994, "Element-Free Galerkin Methods," Int. J. Numer. Methods Eng., **37**, pp. 229–256.
[2] Atluri, S. N., and Shen, S., 2002, *The Meshless Method*, Tech. Science Press, Forsyth, GA.
[3] Atluri, S. N., and Zhu, T., 1998, "A New Meshless Local Petrov-Galerkin (MLPG) Approach in Computational Mechanics," Comput. Mech., **22**, pp. 117–127.
[4] Liu, G. R., 2003, *Mesh Free Methods*, CRC Press, Boca Raton, FL.
[5] Melenk, J. M., and Babuska, I., 1996, "The Partition of Unity Finite Element Method: Basic Theory and Application," Comput. Methods Appl. Mech. Eng., **139**, pp. 289–316.
[6] Kansa, E. J., 1990, "Multiquadrics—A Scattered Data Approximation Scheme With Applications to Computational Fluid Dynamics I—Surface Approximations and Partial Derivative Estimates," Comput. Math. Appl., **19**, pp. 127–145.
[7] Kansa, E. J., 1990, "Multiquadrics—A Scattered Data Approximation Scheme With Applications to Computational Fluid Dynamics II—Solutions to Parabolic, Hyperbolic and Elliptic Partial Differential Equations," Comput. Math. Appl., **19**, pp. 147–161.
[8] Kansa, E. J., and Hon, Y. C., 2000, "Circumventing the Ill—Conditioning Problem with Multiquadric Radial Basis Functions: Applications to Elliptic Partial Differential Equations," Comput. Math. Appl., **39**, pp. 123–137.
[9] Franke, R., 1982, "Scattered Data Interpolation: Test of Some Methods," Math. Comput., **38**, pp. 181–200.
[10] Mai-Duy, N., and Tran-Cong, T., 2002, "Mesh-Free Radial Basis Function Network Methods With Domain Decomposition for Approximation of Functions and Numerical Solution of Poisson's Equation," Eng. Anal. Boundary

Elem., **26**, pp. 133–156.
[11] Cheng, A. H.-D., Golberg, M. A., Kansa, E. J., and Zammito, G., 2003, "Exponential Convergence and H-c Multiquadric Collocation Method for Partial Differential Equations," Numer. Methods Partial Differ. Equ., **19**, pp. 571–594.
[12] Gottlieb, D., and Orzag, S. A., 1977, *Numerical Analysis of Spectral Methods: Theory and Applications*, Society for Industrial and Applied Mathematics, Bristol, UK.
[13] Maday, Y., and Quateroni, A., 1982, "Spectral and Pseudo-Spectral Approximations of the Navier-Stokes Equations," SIAM (Soc. Ind. Appl. Math.) J. Numer. Anal., **19**, pp. 761–780.
[14] Patera, A., 1984, "A Spectral Element Method of Fluid Dynamics: Laminar Flow in a Channel Expansion," J. Comput. Phys., **54**, pp. 468–488.
[15] Macaraeg, M., and Street, C. L., 1986, "Improvement in Spectral Collocation Discretization Through a Multiple Domain Technique," Appl. Numer. Math., **1989**, pp. 95–108.
[16] Hwar, C. K., Hirsch, R., Taylor, T., and Rosenberg, A. P., 1989, "A Pseudo-Spectral Matrix Element Method for Solution of Three Dimensional Incompressible Flows and its Parallel Implementation," J. Comput. Phys., **83**, pp. 260–291.
[17] Fasshauer, G., 2005, "RBF Collocation Methods as Pseudo-Spectral Methods," *Boundary Elements XVII*, A. Kassab, C. A. Brebbia, and E. Divo, eds., WIT Press, Southampton, UK, pp. 47–57.
[18] Powell, M. J. D., 1992, "The Theory of Radial Basis Function Approximation," *Advances in Numerical Analysis*, W. Light, ed., Oxford Science Publications, Oxford, Vol. II, pp. 143–167.
[19] Buhmann, M. D., 2003, *Radial Basis Functions: Theory and Implementation*, Cambridge University Press, Cambridge, MA.
[20] Dyn, N., Levin, D., and Rippa, S., 1986, "Numerical Procedures for Surface Fitting of Scattered Data by Radial Basis Functions," SIAM (Soc. Ind. Appl. Math.) J. Sci. Stat. Comput., **7**, pp. 639–659.
[21] Brebbia, C. A., Partridge, P., and Wrobel, L. C., 1992, *The Dual Reciprocity Boundary Element Method*, Computational Mechanics and Elsevier Applied Science, Southampton, UK.
[22] Golberg, M., Chen, C. S., and Bowman, H., 1999, "Some Recent Results and Proposals for the Use of Radial Basis Functions in the BEM," Eng. Anal. Boundary Elem., **23**, pp. 285–296.
[23] Rahaim, C. P., and Kassab, A. J., 1996, "Pressure Correction DRBEM Solution for Heat Transfer and Fluid Flow in Incompressible Viscous Fluids," Eng. Anal. Boundary Elem., **18**, pp. 265–272.
[24] Sarler, B., Tran-Cong, T., and Chen, C. S., 2005, "Meshfree Direct and Indirect Local Radial Basis Function Collocation Formulations for Transport Phenomena," *Boundary Elements XVII*, A. Kassab, C. A. Brebbia, and E. Divo, eds., WIT Press, Southampton, UK, pp. 417–428.
[25] Sarler, B., and Vertnik, R., 2005, "Local Explicit Radial Basis Function Collocation Method for Diffusion Problems," Comput. Math. Appl., **51**(8), pp. 1269–1282.
[26] Hardy, R. L., 1971, "Multiquadric Equations of Topography and Other Irregular Surfaces," J. Geophys. Res., **176**, pp. 1905–1915.
[27] Kassab, A., Divo, E., Heidmann, J., Steinthorsson, E., and Rodriguez, F., 2003, "BEM/FVM Conjugate Heat Transfer Analysis of a Three-Dimensional Film Cooled Turbine Blade," Int. J. Numer. Methods Heat Fluid Flow, **13**, pp. 581–610.
[28] Kassab, A. J., and Aliabadi, M. H., eds., 2001, *Advances in Boundary Elements: Coupled Field Problems*, WIT Press, Southampton, UK.
[29] Rahaim, C. P., Kassab, A. J., and Cavalleri, R., 2000, "A Coupled Dual Reciprocity Boundary Element/Finite Volume Method for Transient Conjugate Heat Transfer," AIAA J. Thermophys. Heat Transfer, **14**, pp. 27–38.
[30] He, M., Bishop, P., Kassab, A. J., and Minardi, A., 1995, "A Coupled FDM/BEM Solution for the Conjugate Heat Transfer Problem," Numer. Heat Transfer, Part B, **28**, pp. 139–154.
[31] Li, H., and Kassab, A. J., 1981, "A Coupled FVM/BEM Solution to Conjugate Heat Transfer in Turbine Blades," AIAA Paper No. 94–1981.
[32] Divo, E. A., Kassab, A. J., and Rodriguez, F., 2003, "Parallel Domain Decomposition Approach for Large-Scale 3D Boundary Element Models in Linear and Non-Linear Heat Conduction," Numer. Heat Transfer, Part B, **44**, pp. 417–437.
[33] Divo, E., Kassab, A. J., Mitteff, E., and Quintana, L., 2004, "A Parallel Domain Decomposition Technique for Meshless Methods Applications to Large-Scale Heat Transfer Problems," ASME Paper No. HT-FED2004-56004.
[34] Divo, E., and Kassab, A. J., 2005, "Effective Domain Decomposition Meshless Formulation of Fully-Viscous Incompressible Fluid Flows," *Boundary Elements XVII*, A. Kassab, C. A. Brebbia, and E. Divo, eds., WIT Press, Southampton, UK, pp. 67–77.
[35] Divo, E., and Kassab, A. J., 2005, "A Meshless Method for Conjugate Heat Transfer," *Proceedings of ECCOMAS Coupled Problems 2005*, M. Papadrakakis, E. Oñate, and B. Schrefler, eds., Santorini, Greece, April.
[36] Divo, E., and Kassab, A. J., 2005, "A Meshless Method for Conjugate Heat Transfer Problems," Eng. Anal., **29**, pp. 136–149.
[37] Harlow, F. H., and Welch, J. E., 1965, Numerical Calculation of Time Dependent Viscous Incompressible Flow of Fluids With a Free Surface, Phys. Fluids, **8**, pp. 2182–2189.
[38] Patankar, S. V., 1980, *Numerical Heat Transfer and Fluid Flow*, Hemisphere, Washington, DC.
[39] Orlanski, I., 1976, "A Simple Boundary Condition for Unbounded Hyperbolic Flows," J. Comput. Phys., **21**, pp. 251–269.
[40] Ghia, U., Ghia, K. N., and Shin, C. T., 1982, "High-RE Solutions for Incompressible-Flow Using the Navier Stokes Equations and a Multigrid Method," J. Comput. Phys., **48**(3), pp. 387–411.
[41] Mitteff, E., Divo, E., and Kassab, A. J., 2006, "Automated Point Distribution and Parallel Segmentation for Meshless Methods," *Proceedings of CIMENICS 2006, 8th International Congress of Numerical Methods in Engineering and Applied Sciences*, B. Gamez, D. Ojeda, G. Larrazabal, and M. Cerrolaza, eds., Sociedad Venezuelana de Methodos Numericos En Engineria, Valencia, Venezuela, Margarita Island, Venezuela, March 20–24, pp. 93–100.

A. Asias
Rafael Ltd,
P.O.B. 2250,
Haifa 31021, Israel

M. Shusser[1]
Faculty of Mechanical Engineering,
Technion,
Haifa 32000, Israel

A. Leitner

A. Nabi

Rafael Ltd,
P.O.B. 2250,
Haifa 31021, Israel

G. Grossman
Faculty of Mechanical Engineering,
Technion,
Haifa 32000, Israel

Instability of Heat Pipe Performance at Large Axial Accelerations

*To investigate the feasibility of using heat pipes in airborne systems, heat pipe performance at large axial accelerations in the range of 3–*12 g *was studied experimentally. The heat input chosen corresponded to the optimal heat pipe performance without acceleration. When applied against the direction of the liquid flow (unfavorable orientation) the accelerations were large enough to exceed the capillary limit, as was seen from the strong increase in the evaporator temperature. The influence of accelerations in the direction of the liquid flow (favorable orientation) was found to be more complicated. While at the acceleration of* 3 g *the heat pipe performance improved, at higher accelerations instability developed with resulting large-amplitude oscillations of the evaporator temperature. The instability found in these experiments is thought to be related to the geyser effect observed in thermosyphons.* [DOI: 10.1115/1.2402177]

Keywords: heat pipe, axial acceleration, instability, geyser effect, thermosyphon

1 Introduction

Thermal management of electronic components of airborne systems has become an important design issue as increased power output and miniaturization of the devices cause large heat dissipation and high local heat fluxes. Unless properly cooled, the equipment will be operating at high temperatures that could result in shorter life span or its failure. Hence, there is a growing interest in developing efficient cooling techniques to maintain the electronic components within their temperature limits.

Heat pipes have been proposed to be used for cooling in airborne systems. Due to its low weight, small dimensions, and very high thermal conductance, a heat pipe is especially suited to airborne requirements. However, traditionally heat pipes have been used in the environments free from large body forces such as inertia forces caused by large accelerations.

During combat, transient acceleration field of up to 9–10 g could be present on the aircraft [1,2]. Therefore, the knowledge of heat pipe performance under elevated acceleration field is important for proper design of electronic components in need of cooling.

Previous studies of heat pipe performance at large acceleration forces include Thomas and Yerkes [3] who studied the performance of a heat pipe subjected to transient accelerations, Thomas et al. [1] who investigated the influence of transverse accelerations and Zaghdoudi and Sarno [2] who considered the effects of body force environment (gravitation, vibration, acceleration) on flat heat pipes. Ochterbeck et al. [4] developed a model of the deprime and rewetting process in an arterial heat pipe undergoing externally induced accelerations and verified it using the experimental results obtained from acceleration tests conducted aboard the Space Shuttle. The review of earlier investigations can be found elsewhere [2].

It should be noted that when considering large acceleration forces the previous studies usually concentrated on the effects of unfavorable accelerations (opposite to the direction of the liquid flow) or vibrations and mostly ignored the influence of favorable accelerations (in the direction of the liquid flow). For example, while Zaghdoudi and Sarno [2] considered all heat pipe orientations (horizontal, unfavorable vertical, favorable vertical) when investigating the effects of gravitation, heat-pipe mounting was always unfavorable in their acceleration experiments.

The preference given by the investigators to the unfavorable accelerations follows from the fact that they are more dangerous. At sufficiently large unfavorable accelerations, the capillary limit [5,6] is reached and the heat pipe stops operating normally. On the other hand, favorable accelerations usually somewhat improve the heat pipe performance and therefore considered of lesser importance.

In the present work, we study experimentally the performance of a heat pipe at large axial accelerations with the emphasis on the favorable accelerations. We demonstrate that while small and moderate favorable accelerations indeed improve the heat pipe performance, large axial accelerations can cause instability with resulting strong oscillations in the heat pipe performance.

The plan of the paper is as follows. In the next section we briefly review the physical background and analyze possible behavior of a heat pipe subjected to axial accelerations. Experimental setup is described in Sec. 3 and the results are presented in Sec. 4.

2 Physical Background

The behavior of heat pipes subjected to axial accelerations against the direction of the liquid flow is very well understood [5,6]. In a heat pipe operating steadily the pressure at the vapor side of the liquid-vapor interface is always higher than at the liquid side, except at the point in the condenser (sometimes called the "wet point" [7]) where both pressures are equal. This pressure difference is balanced by the capillary pressure established by menisci that form at the interface. The smallest possible curvature radius of the meniscus (the effective capillary radius) determines the maximum capillary pressure that can be achieved in a given

[1]Corresponding author.

Contributed by the Heat Transfer Division of ASME for publication in the JOURNAL OF HEAT TRANSFER. Manuscript received October 9, 2005; final manuscript received April 9, 2006. Review conducted by Anthony M. Jacobi.

Table 1 Heat pipe specifications

Maximal heat flux[a]	Length[b]	Diameter[b]	Weight[b]	Wall material[b]	Working fluid[b]	Working fluid weight[b]
8 W	215 mm	3 mm	7.07 g	Copper	Water	0.31 g
Evaporator length[a]	Condenser length[a]		Vapor channel diameter[b]	Wick[b]	Particle diameter[b]	Porosity[b]
25 mm	30 mm		1.6 mm	Sintered copper	50–200 μm	0.8

[a]Provided by the manufacturer.
[b]Measured.

heat pipe. At a sufficiently high heat transfer rate the capillary pressure can no longer support the liquid flow. This failure causes the drying of the evaporator and ultimately causes the heat pipe to stop operating normally. This limit on the heat transfer rate is called the capillary limit.

Any body force acting against the direction of the liquid flow including the inertia force due to unfavourable axial acceleration increases the liquid pressure gradient and decreases the capillary limit. For a given heat transfer rate, at sufficiently large unfavourable acceleration, the capillary limit will be reached. The capillary limit will show itself as a sharp increase in the evaporator temperature.

Favorable axial accelerations that support the liquid flow in the wick decrease the liquid pressure gradient. Small favorable accelerations improve the heat pipe performance by decreasing the evaporator temperature for a given heat transfer rate. This effect is usually explained by the cooling of the evaporator by the additional flow of cold liquid from the condenser (see, e.g., [3]).

The effect of large favorable accelerations is more complicated. A detailed analysis of the influence of favorable body forces was done by Busse and Kemme [7] for gravity assisted heat pipes. They demonstrated that a sufficiently large body force completely changes the pressure distribution along the heat pipe. As the body force increases, the pressure drop in the liquid between the condenser and the evaporator decreases. As a result, the liquid-vapor pressure difference in the evaporator also decreases and will vanish if the body force is sufficiently high. Since the capillary pressure in the heat pipe cannot be negative (this would correspond to the liquid protruding from the wick into the vapor), any further increase in the body force will make the steady operation of the heat pipe with the wet point in the condenser impossible. The wet point will shift from the condenser to the evaporator where the liquid and vapor pressures will remain equal. It is emphasized by Busse and Kemme [7] that surplus liquid can form a pool at the lower end of the evaporator, as is often the case in gravity assisted heat pipes.

One can therefore conclude that at large favorable axial accelerations the heat pipe will operate with the wet point in the evaporator where the liquid can form a pool. Since the return of the condensate to the evaporator will be provided by the inertia force, the capillary force role being secondary, the heat pipe will essentially operate as a closed two-phase thermosyphon [6]. These devices often operate in the pool boiling regime [8], when the thermosyphon evaporator is flooded and boiling is sustained in it. We can therefore expect boiling in the evaporator when a heat pipe is subjected to large favorable accelerations. The boiling may in fact improve the heat pipe performance due to a larger value of the heat transfer coefficient in the evaporator.

There is instability of boiling in closed two-phase thermosyphons that is called the geyser effect [9,10]. When this instability occurs, instead of steady boiling, a large amount of the working fluid is periodically propelled from the evaporator to the condenser resulting in an oscillating heat transfer rate and large-amplitude oscillations of many characteristic variables, such as the evaporator wall temperature. Since this is a detrimental phenomenon, one would certainly want to know if this instability is possible in heat pipes at large favorable accelerations when their behavior is similar to that of thermosyphons. One of the goals of the present work was to verify this experimentally.

3 Experimental Setup

The heat pipe used in the experiments was manufactured by Thermacore, Inc. (Lancaster, PA). The heat pipe characteristics are given in Table 1. To obtain the information about the inner structure of the heat pipe, after the end of the experiments it was cut and the cross section studied under a microscope.

Power was supplied to the heat pipe by a heat source that consisted of two thermofoil heaters (HK538R15.7L12B, Minco Products, Inc., Minneapolis, MN) placed on two aluminum plates. The heat pipe evaporator was situated in a round groove that was drilled in the plates. The power was measured using the current and voltage readings. The current was calculated by measuring the voltage on a precision resistance of $1.1 \pm 1\%$ Ω.

To cool the heat pipe, the condenser was placed inside an aluminum heat sink of large thermal mass that was kept at a constant temperature. Thermal grease was applied to the contact areas to decrease the contact resistance between the heat pipe and the heat source and the heat sink. Since due to rotation the heat pipe was subjected to high air velocities, to reduce the convective heat losses from the exterior of the heat pipe, its exposed part was insulated with ceramic wool. Eight thermocouples (TTK-36, Ohmega Technologies, Inc., Culver City, CA) were used to monitor the heat source, heat sink, evaporator, and condenser temperatures.

The setup was mounted on a centrifuge table that had a radius of 3 m and was capable of producing accelerations in the range of 0–70 g. Two slip rings were used to transfer the measurement signals and the power to and from the centrifuge table. To control the acceleration, two piezoelectric acceleration gauges were added to the setup. The accelerometers were placed at the opposite ends of diameter in the middle cross section of the pipe. The acceleration profile was taken as the average of their readings.

Thermal resistance of the heat pipe R_t was defined as the ratio of the temperature drop between the evaporator and the condenser $T_{\text{evap}} - T_{\text{cond}}$ to the input heat power Q

$$R_t = \frac{T_{\text{evap}} - T_{\text{cond}}}{Q} \tag{1}$$

Using the standard uncertainty analysis [11] the maximum root-sum-square uncertainties for all of the measured and calculated values presented in this paper are given in Table 2.

A more detailed description of the experimental setup can be found elsewhere [12].

4 Results

To find the heat input corresponding to the optimal heat pipe performance, a series of steady-state experiments, with no acceleration applied, was carried out at the outset. The thermal resistance of the heat pipe was measured while varying the heat input

Table 2 Maximum uncertainties of measured and calculated values

Parameters	Values
Measured values	
Temperature	±0.5°C
Heater voltage	±1% of reading
Heater current	±2% of reading
Acceleration	±0.1 g
Calculated values	
Heat input	±3%
Thermal resistance	±15%

in the range of 0.5–10 W. To ensure steady-state conditions, after each change in the heat input the thermal resistance was calculated when the rate of temperature change in all the thermocouples dropped below 0.1°C/min. The experiment was repeated for four ambient temperatures between 25°C and 85°C. The results are shown in Fig. 1.

One sees from Fig. 1 that the heat pipe performance improves with increasing temperature and that for all the ambient temperatures the minimal thermal resistance of the heat pipe was reached for the heat input approximately in the range of 5–7 W. The acceleration experiments were therefore carried out when the heat input was kept constant and equal to 6 W.

In the acceleration experiments, the heat pipe was mounted on the centrifuge in both favorable (the acceleration in the direction of the fluid flow) and unfavorable (the acceleration against the direction of the fluid flow) orientations. In each run, the rotation speed of the centrifuge table increased for one minute, was kept constant for five minutes and decreased back to zero during the last minute of the run. Similar intervals of constant acceleration were used by Thomas et al. [1] in their stepwise acceleration profiles.

The evolution of the heater, evaporator, and condenser temperatures for unfavorable acceleration of 3 g is shown in Fig. 2. One sees from the increase in the heater and evaporator temperatures that such acceleration is sufficiently large to exceed the capillary limit and cause the evaporator dry out. However, after the acceleration is ceased to be applied the heat pipe successfully reprimed and resumed its normal operation. The maximum thermal resistance of the heat pipe in this experiment was 3.7 K/W which is about two times larger than during its normal operation (see Fig. 1).

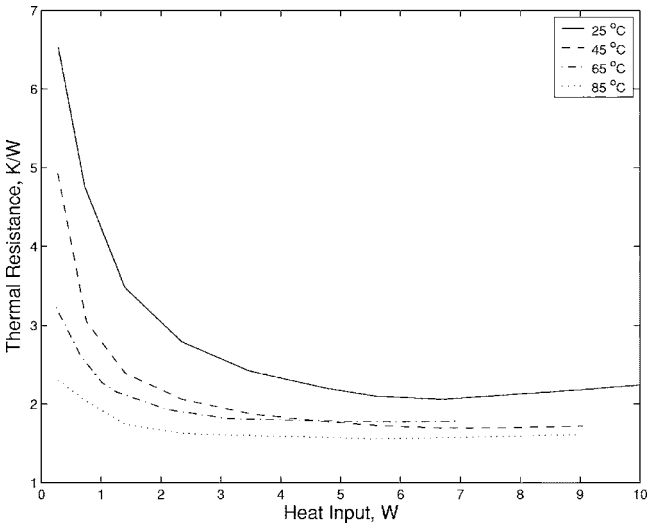

Fig. 1 Thermal resistance versus heat input. No acceleration.

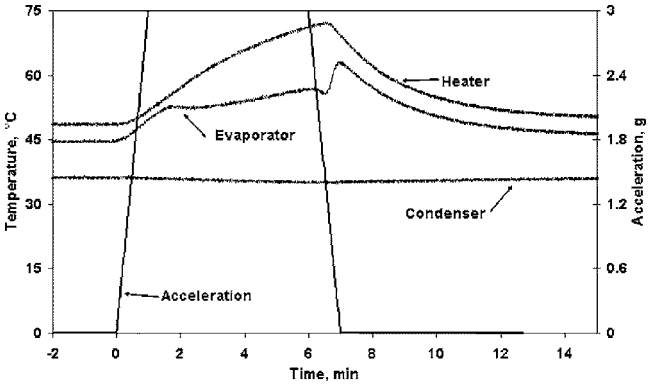

Fig. 2 Heater, evaporator, and condenser temperatures for unfavorable acceleration of 3 g

Since we were interested in large accelerations, all the experiments with the favorable orientation were conducted at accelerations of 3 g and higher.

Figure 3 shows the results for favorable acceleration of 3 g. As expected, favorable acceleration improved the heat pipe performance and the heater and evaporator temperatures were lower while the acceleration was applied.

An entirely different situation was observed when the favorable acceleration was increased to 6 g, as seen from Fig. 4. Instead of further improvement in the heat pipe performance, instability developed which caused large-amplitude oscillations (up to 25%) of the evaporator and heater temperatures and smaller perturbations of the condenser temperature. When the acceleration ended, the instability was suppressed and the heat pipe resumed its normal operation in about 1 min.

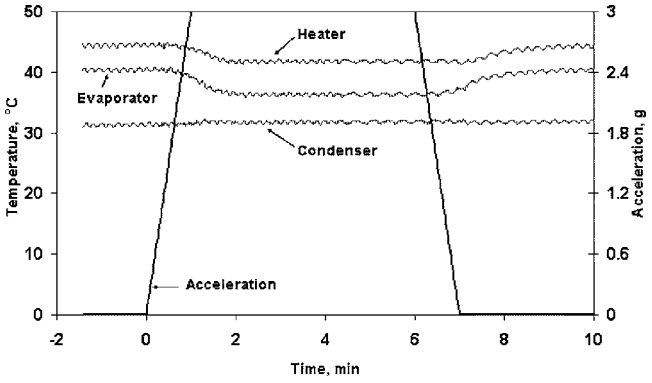

Fig. 3 Heater, evaporator, and condenser temperatures for favorable acceleration of 3 g

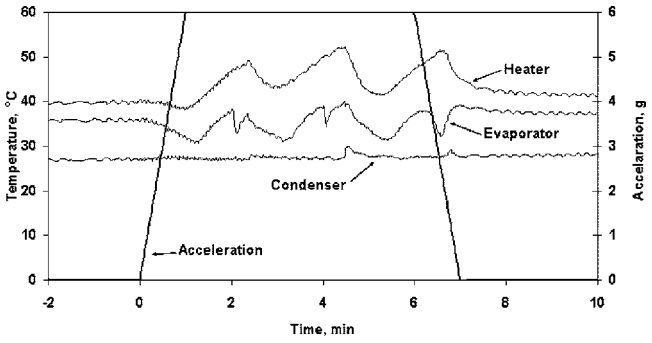

Fig. 4 Heater, evaporator, and condenser temperatures for favorable acceleration of 6 g

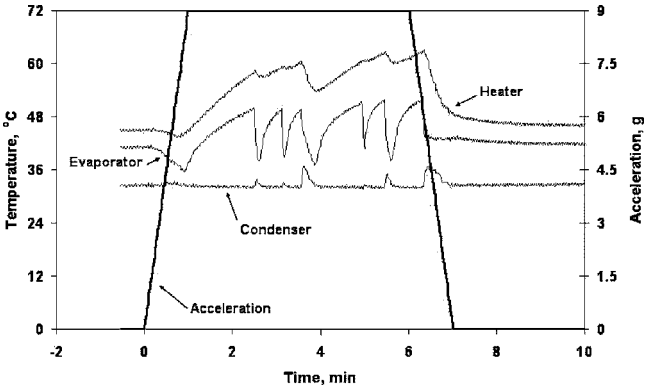

Fig. 5 Heater, evaporator, and condenser temperatures for favorable acceleration of 9 g

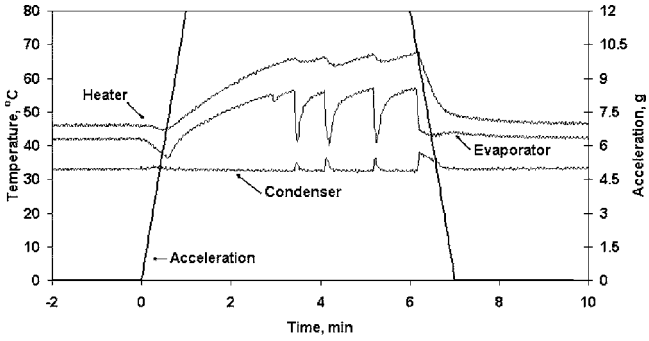

Fig. 6 Heater, evaporator, and condenser temperatures for favorable acceleration of 12 g

No instability was observed during the "transient" part of the acceleration profile (increasing acceleration). Both heater and evaporator temperatures decreased during the first minute and began increasing only after the acceleration reached its maximum value.

The results for higher favorable accelerations of 9 g and 12 g are shown in Figs. 5 and 6. One sees from these figures that the instability persists at higher accelerations. The oscillations of the evaporator temperature have now even larger amplitude and higher frequency. On the other hand, the heater temperature oscillates with smaller amplitude and increases while the acceleration is applied. At the acceleration of 12 g the time dependence of the heater temperature looks like that for the dried out evaporator (compare Fig. 6 with Fig. 2). We can conclude that probably the heat pipe cannot operate at this acceleration.

Since the acceleration is higher in this experiment, the instability starts developing earlier in the acceleration profile. One sees from Fig. 6 that the increase in the heater and evaporator temperatures began before the acceleration reached its maximum value.

5 Conclusions

We studied the performance of a heat pipe at large axial accelerations of 3–12 g. The accelerations were large enough to exceed the capillary limit and cause the evaporator dry out when applied against the direction of the liquid flow. The influence of accelerations in the direction of the liquid flow (favorable orientation) was found to be more complicated. At the acceleration of 3 g both evaporator and heater temperatures decreased showing that the heat pipe performance improved. On the other hand, at 6 g instability developed with resulting large-amplitude oscillations of the evaporator and heater temperatures. The instability persisted at higher accelerations though the heater temperature behavior changed from strong oscillations with an approximately constant average value to gradual increase with some oscillations imposed on it. At the acceleration of 12 g the time dependence of the heater temperature looked like that for the dried out evaporator suggesting that the heat transfer from the heat source to the heat sink at this acceleration is mainly by conduction through the heat pipe wall. In all the cases, when the acceleration ended, the instability was suppressed and the heat pipe resumed its normal operation.

Though only steady-state accelerations were considered in this paper it is plausible that this instability can also occur when the heat pipe is subjected to transient accelerations. Indeed, at the acceleration of 12 g the increase in the heater and evaporator temperatures began during the "transient" part of the acceleration profile before the acceleration reached its maximum value.

Since at large favorable axial accelerations the return of the condensate to the evaporator is provided by the inertia force, the capillary force role being secondary, the heat pipe essentially operates as a closed two-phase thermosyphon. It is therefore possible to suggest that the instability observed experimentally in this work is related to the instability of boiling in closed two-phase thermosyphons that is called the geyser effect. Both instabilities are characterized by oscillating heat transfer rate and large-amplitude oscillations of many characteristic variables. It is this instability that can cause large favorable acceleration to be as detrimental to heat pipe performance as large unfavorable acceleration.

References

[1] Thomas, S. K., Klasing, K. S., and Yerkes, K. L., 1998, "The Effects of Transverse Acceleration Induced Body Forces on the Capillary Limit of Helically Grooved Heat Pipes," J. Heat Transfer, **120**(2), pp. 441–451.

[2] Zaghdoudi, M. C., and Sarno, C., 2001, "Investigation on the Effects of Body Force Environment on Flat Heat Pipes," J. Thermophys. Heat Transfer, **15**(4), pp. 384–393.

[3] Thomas, S. K., and Yerkes, K. L., 1997, "Quasi-Steady-State Performance of a Heat Pipe Subjected to Transient Acceleration Loadings," J. Thermophys. Heat Transfer, **11**(2), pp. 306–309.

[4] Ochterbeck, J. M., Peterson, G. P., and Ungar, E. K., 1995, "Depriming Rewetting of Arterial Heat Pipes—Comparison with SHARE-II Flight Experiment," J. Thermophys. Heat Transfer, **9**(1), pp. 101–108.

[5] Chi, S. W., 1976, *Heat Pipe Theory and Practice*, Hemisphere, Washington, DC.

[6] Dunn, P. D., and Reay, D. A., 1994, *Heat Pipes*, 4th ed., Elsevier, New York.

[7] Busse, C. A., and Kemme, J. E., 1980, "Dry-Out Phenomena in Gravity-Assist Heat Pipes with Capillary Flow," Int. J. Heat Mass Transfer, **23**(5), pp. 643–654.

[8] Niro, A., and Beretta, G. P., 1990, "Boiling Regimes in a Closed Two-Phase Thermosyphon," Int. J. Heat Mass Transfer, **33**(10) pp. 2099–2110.

[9] Casarosa, C., Latrofa, E., and Shelginski, A., 1983, "The Geyser Effect in a Two-Phase Closed Thermosyphon," Int. J. Heat Mass Transfer, **26**(6), pp. 933–941.

[10] Lin, T. F., Lin, W. T., Tsay, Y. L., Wu, J. C., and Shyu, R. J., 1995, "Experimental Investigation of Geyser Boiling in an Annular Two-Phase Closed Thermosyphon," Int. J. Heat Mass Transfer, **38**(2), pp. 295–307.

[11] Baker, R. C., 2000, *Flow Measurement Handbook*, Cambridge University Press, Cambridge, England.

[12] Asias, A., 2005, "Heat Pipe for Airborne Systems," M.Sc. thesis, Technion-Israel Institute of Technology.

Ravi S. Prasher
Adjunct Professor
Intel Corporation,
CH5-157,
5000 W. Chandler Blvd.,
Chandler, AZ 85226
and
Department of Mechanical and Aerospace Engineering,
Arizona State University,
Tempe, AZ 85287
e-mail: ravi.s.prasher@intel.com

John Dirner

Je-Young Chang

Alan Myers

David Chau

Dongming He

Suzana Prstic

Intel Corporation,
CH5-157,
5000 W. Chandler Blvd.,
Chandler, AZ 85226

Nusselt Number and Friction Factor of Staggered Arrays of Low Aspect Ratio Micropin-Fins Under Cross Flow for Water as Fluid

Experimental results of the thermal and hydraulic performances of silicon-based, low aspect ratio micropin-fin cold plates under cross flow conditions are reported. The pins were both circular and square in shape with dimensions (diameter for circular and sides for square) ranging from 50 μm *to* 150 μm. *The test chip contained 20 integral* 75 $\times$75 μm *temperature sensors which were used to determine the thermal resistance* (K W^{-1}) *of the cold plates. The experiments were conducted using water, over a Reynolds number (Re) ranging from 40 to 1000. The data show that the average Nusselt number (Nu) based on the fin diameter varies as* $\mathrm{Re}^{0.84}$ *for* $\mathrm{Re}<100$ *and as* $\mathrm{Re}^{0.73}$ *for* $\mathrm{Re}>100$, *where Re is the Reynolds number based on maximum velocity and the fin diameter. Analysis of the Fanning friction factor* (f) *data shows that* f *varies as* $\mathrm{Re}^{-1.35}$ *for* $\mathrm{Re}<100$ *and as* $\mathrm{Re}^{-0.1}$ *for* $\mathrm{Re}>100$. [DOI: 10.1115/1.2402179]

Keywords: micropin fin, microscale heat exchanger, micropost, microchannel

1 Introduction

Since Tuckerman and Pease [1–3] introduced the concept of microchannels, there have been numerous experimental and theoretical studies of microchannels for heat transfer applications. Recently the semiconductor industry has started to seriously consider microchannel cooling with liquid coolant [4,5] because advanced microprocessors generate increasing heat fluxes and multiple hotspots [6]. Many review papers have been written on microchannels [7–9]. These review papers indicate that investigation of pin fins in the microscale regime is primarily absent from literature. Peles et al. [10], in a very recent paper, performed a systematic analytical study of micropin fins assuming a conventional long tube correlation for Nusselt number (Nu). Their study indicated that micropin fins can outperform microchannels in certain regimes. However, it is not established whether conventional correlations developed for macropin fins can be applied for micropin fins. The existing review papers on microcold plates [7–9] indicate a lack of attention to micropin-fin-based cold plates. Therefore, it is important to understand both the hydraulic and thermal performance of micropin fins for proper design and also for comparison with microchannels.

This paper reports the results of a systematic, experimental study of pressure drop and thermal resistance (K W^{-1}) for cold plates fabricated with a staggered array of circular and square micropin fins. The pin fin diameter (side length for the square) varied from 55 μm to 153 μm. The experiments were conducted using water at different flow rates. The experimental temperature measurement method is novel because 20 integral temperature sensors were fabricated on the heat generating die to adequately capture the thermal resistance of the micropin fin cold plate.

The paper is divided into six parts starting with the introduction. Section 2 is devoted to the literature review of previous work performed on micropin-fin cold plates. Sample fabrication is discussed in Sec. 3. Experimental setup is described in Sec. 4. Analysis of the data is covered in Sec. 5. Results and discussions are presented in Sec. 6.

2 Literature Review of Micropin-Fin Cold Plates Under Cross Flow

The available literature is very limited for investigations of micropin-fin cold plates under cross flow. Tuckerman and Pease [2] were first to evaluate the performance of silicon based micropin fins with water under cross flow conditions. In their study the fins were arranged in an in-line pattern. Details of the fabrication and pin dimensions are given in the thesis by Tuckerman [3]. Tuckerman and Pease [2] used mechanical sawing to fabricate the cold plate, and therefore could only fabricate square pin fins. The side of the square pin fins in this study ranged from 54 μm to 64 μm. The pressure drop was measured for three different designs of square pin fins, but the thermal resistance was measured only at one location on a single cold plate design at a single flow rate. For pin fins the thermal resistance varies with Reynolds number (Re). Therefore the study by Tuckerman and Pease does not provide a relationship between thermal resistance and Re. The pressure drop was modeled using a plate fin heat sink correlation, but the thermal resistance was not modeled.

Recently Peles et al. [10] and Kosar et al. [11] performed an experimental and analytical study of micropin fins. Peles et al. [10] performed an analytical study of the thermal performance of micropin-fin cold plates assuming the conventional long tube cor-

Contributed by the Heat Transfer Division of ASME for publication in the JOURNAL OF HEAT TRANSFER. Manuscript received August 30, 2005; final manuscript received April 13, 2006. Review conducted by Bengt Sunden.

relation for Nusselt number (Nu). They also performed experimental study with water as coolant on one design of silicon-based micropin fins where the diameter of the pin fin was 100 μm and the height of the pin fin was 243 μm. As in the work by Tuckerman [3] they only measured the thermal resistance for a single flow rate. Because of the low flow rate in the study (3.2 mL/min), the thermal resistance in their study was dominated by the flow resistance given by $1/\dot{m}c_p$ where $\dot{m}$ is the mass flow rate and c_p is the specific heat of liquid. They could not separate the convection resistance from the flow resistance. The 1 cm long heater in their study was also used as the temperature sensor, and in the calculation of thermal resistance from the experiments, they assumed the heater temperature accurately indicated the average wall temperature. Therefore their experiment had low spatial resolution for temperature measurement. The experimental study of thermal performance of micropin fin (MPF) cold plates by Peles et al. [10] also does not address the dependence of the convection resistance of MPF arrays on Re.

Koşar et al. [11] performed an extensive study of the hydraulic performance of various low aspect ratio MPF arrays with water as coolant. They considered four different designs of MPF arrays, three of which used circular fins and one with diamond shaped fins. Of the three circular fin designs, two were arranged in a staggered pattern and one was arranged in an in-line pattern. The Re based on the diameter of the fins and the maximum fluid velocity (v_{max}) varied from 6 to 128. They compared the experimental value of the friction factor (f) with various correlations in the literature valid for long and short fins, however none of the correlations closely predicted f. Thus they developed their own correlation based on experimental data. For the staggered array they used only two designs to develop the correlation, and for the in-line and diamond-shaped fins only one design was used to develop each correlation. Therefore it is not clear if their correlation is valid for different designs of MPF arrays and for larger values of Re.

Stephens et al. [12] performed MPF experiments using air as the fluid for thrust bearing applications under cross flow conditions. The pin fins were arranged in an in-line pattern, and fabricated using electrodeposition of nickel. Their experimental apparatus was very complicated compared to traditional cold plate applications because the geometry of the experimental structure mimicked a thrust bearing, and only thermal data were reported. Stephens et al. [12] also compared the conventional macropin-fin correlations with experimental data and found that for high porosity (97%) the correlation predictions were approximately 30% lower than the experimental results and for low porosity design (66%) the correlation predictions were approximately 500% higher than the experimental results.

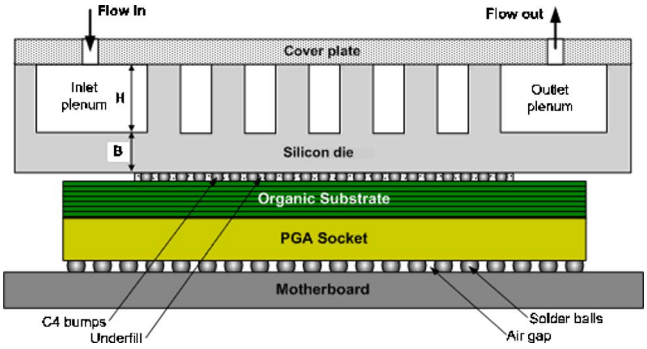

Fig. 1 Front view of micro-pin fin cold plate

Recently Marques and Kelly [13] performed experiments on pin fins of 500 μm in diameter in the staggered arrangement. The pin separation in their design was 1250 μm, making it questionable whether this was a true micropin-fin design. They performed the experiments with air in the high Reynolds number regime.

Overall, the review indicates that the available literature lacks a systematic study of both hydraulic and thermal performance of micropin-fin cold plates. A systematic study of both pressure drop and thermal resistance of MPF arrays is needed to address the following:

(1) The variation of Nu with Re for liquid as coolant.
(2) Friction factor for liquid as coolant for a large number of micropin-fin designs.
(3) The available literature [11] only investigates the hydraulic performance for Re up to 128, yet Re is expected to range between 10 and 1000 in micropin-fin applications [11]. It is important to know the performance of the MPF arrays at larger values of Re.
(4) Validation/development of correlations for both Nu and f as a function of geometry, shape and Re.

In response to the available literature, a systematic study of pressure drop and thermal resistance of square and round staggered micropin-fin cold plates was performed in this study. Tests were conducted at different flow rates using water as the cooling fluid. Thermal resistance of the pin-fin cold plate was determined using 20 integral temperature sensors on the silicon die.

3 Sample Fabrication

Figures 1 and 2 show the schematic of the test chip and nomenclature for different dimensions. The C4 bumps are solder bumps

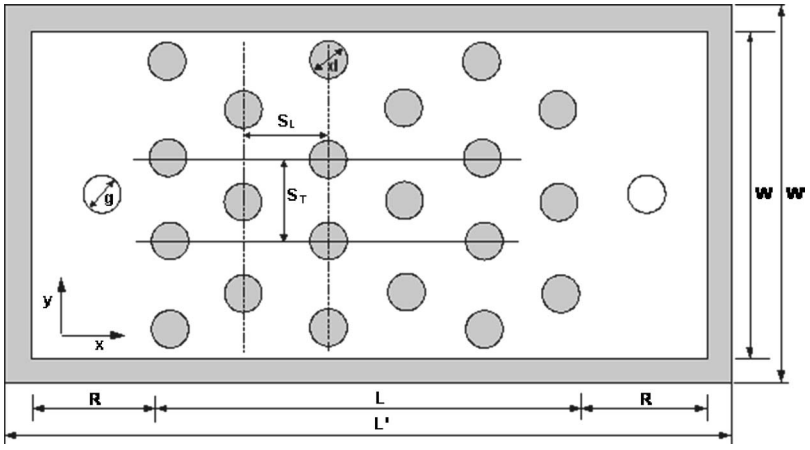

Fig. 2 Top view of micropin fin cold plate

Table 1 Dimension of the micropin-fin cold plate (see Fig. 2)

	W	W'	R	L	L'	g
Dimension (mm)	10	11	4	13	25	3.5

Note: W'=width of the micropin-fin cold plate, W=flow width of the micropin-fin cold plate, R=length of the plenum area, L'=length of the micropin-fin cold plate including the plenum area and the bounding walls, L=length of the finned area, g=diameter of the inlet and outlet holes.

for connecting the heater and temperature sensors to the substrate [14]. Underfill is a polymer that fills the space between the bumps for structural rigidity. PGA socket is a pin grid array socket. For details on the various components of the test setup as shown in Fig. 1 readers are advised to refer to Tummala [14]. The dimensions of the micropin-fin cold plates are given in Tables 1 and 2.

The first step in sample fabrication was fabrication of the heater and temperature sensors. Figure 1(*a*) shows the cross section of the test die. It has three built-up copper interconnect layers on the surface of bulk silicon substrate, each of which is fabricated using a typical copper damascene process [15].

Starting with the bulk silicon substrate, the first inter layer dielectric (ILD) was deposited, followed by the metal 1 trench etch, blank barrier layer, and copper seed layer sputtering. Copper was then electroplated and chemical mechanical polished (CMP) until barrier and seed layers were removed on top of the ILD surface. With almost the same procedure, via 1 and metal 2 was deposited and patterned. The difference between metal 2 / via 1 process and metal 1 process was that via 1 and metal 2 patterns were etched inside ILD by two patterning and etch steps, and then the barrier layer and copper were deposited and plated in one step to define both via and metal lines. This is referred to a dual-damascene process, whereas the metal 1 process is referred to as a single damascene process [15]. Via 2 and metal 3 were deposited using the same dual-damascene process as via 1 and metal 2. Finally, a passivation layer was deposited and patterned, followed by a flip chip bumping process including solder plating and reflow to fabricate solder balls [16].

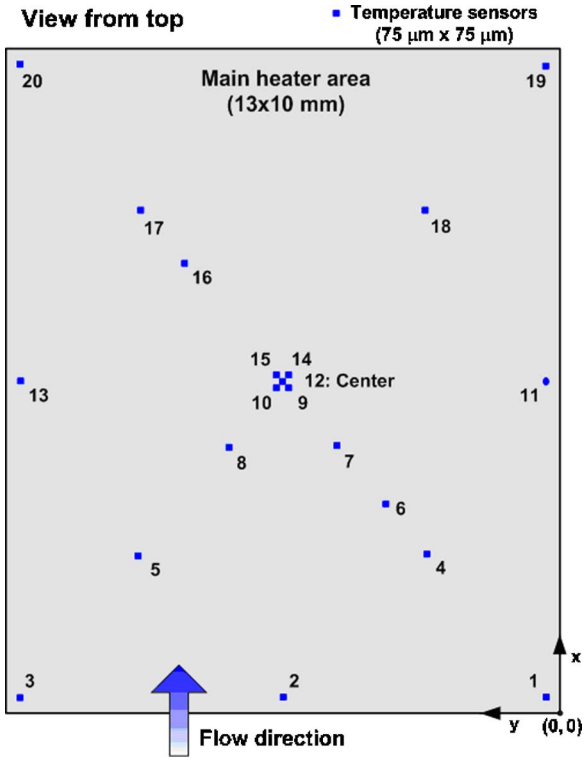

Fig. 3 Locations of heaters and thermal sensors

The main heater is uniformly distributed across the die in 10 mm × 13 mm area on metal 2 with linewidth and pitch on the order of a few microns. The main heater is divided into 16 legs which can be powered at the same time or separately. Detailed drawing of the heater is shown in a previous paper [17]. Twenty resistance temperature devices (RTD) are fabricated on the metal 1 layer with locations illustrated in Fig. 3. Heater and sensors

Table 2 Details of various micropin-fin designs (see Figs. 1 and 2)

Part number	Measured dimensions (μm)	Comments
SP3	H=310 d=125	Both thermal resistance and pressure drop
square	S_T=S_L=303	
	N_x=43 N_y=33	H/d=2.48
	B=365	S_T/d=S_L/d=2.4
RP3	H=310 d=125	Both thermal resistance and pressure drop
round	S_T=S_L=303	
	N_x=43 N_y=33	H/d=2.48
	B=365	S_T/d=S_L/d=2.4
RP1	H=155d=55	Both thermal resistance and pressure drop
round	S_T=S_L=200	
	N_x=66 N_y=50	H/d=2.8
	B=320	S_T/d=S_L/d=3.6
RP4	H=200 d=153	Only pressure drop
round	S_L=612 S_T=306	H/d=1.3
	N_x=22 N_y=33	S_n/d=2
	B=200	S_P/d=4
SP4	H=200 d=153	Only pressure drop
square	S_L=612 S_T=306	H/d=1.3
	N_x=22 Ny=33	S_T/d=2
	B=200	S_P/d=4

Note: H=pin height, d=pin diameter (side length for square pins), S_p=pitch in x direction, S_n=pitch in y direction, N_x=number of pins in x direction, N_y=number of pins in y direction, B=base thickness of the cold plate.

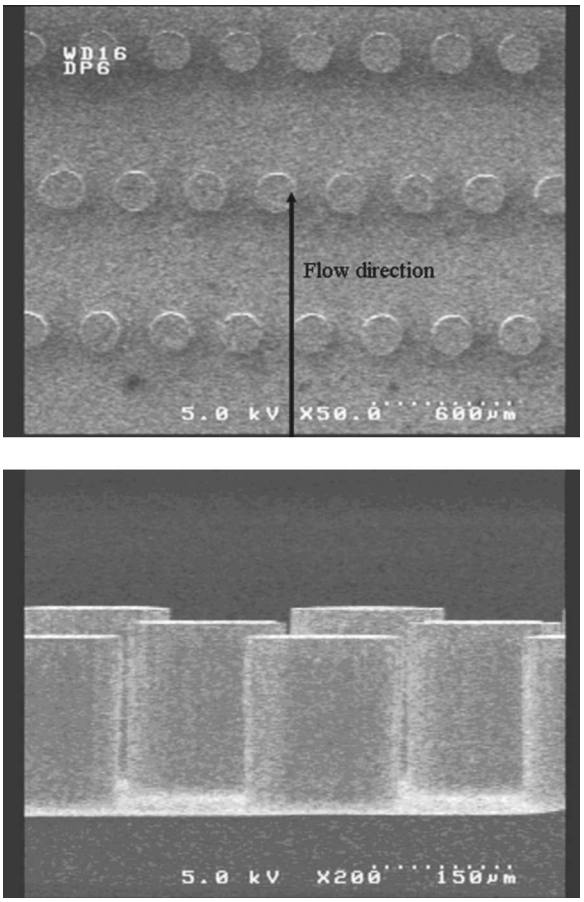

Fig. 4 SEM picture of RP4 micropin-fin cold plate. (*a*) Oblique view (*b*) side view.

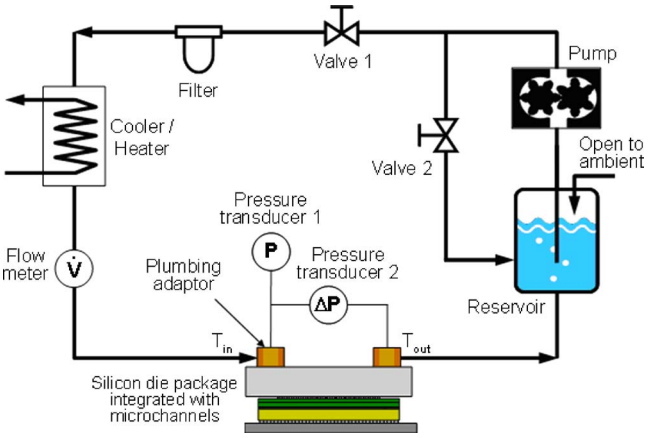

Fig. 5 Schematic of the experimental test setup

were fabricated only on SP3, RP3, and RP1 designs. Heater and sensors were not fabricated on RP4 and SP4 designs. Therefore thermal measurements were done only for SP3, RP3, and RP1 designs.

The pin fins shown in Fig. 2 were fabricated using the following procedure. First, a lithography process defined the pattern of the pin grids, inlet/outlet reservoirs, and device walls. The device side (heater and sensor side) of the wafer was protected by spinning a 13 μm thick coating of photoresist over the solder bumps and using the photoresist to act as a glue to bond the carrier silicon wafer to the device wafer. The bonded wafers were then baked in an oven for 30 min at 110°C in order to remove solvents from the resist and complete the bonding process. The "back-side" (pin-fin side) of the wafer was spin-coated with 7 μm of positive photoresist and baked in an oven at 90°C for 30 min. The wafer was then exposed to the pin-fin pattern through a chrome mask placed in hard contact with the photoresist.

A plasma deep reactive ion etch (DRIE) process was then used to etch the silicon to define the inlet/outlet reservoir, side walls, and the pin fins. The top of the pin fin cold plates were sealed by anodically bonding a 500 μm thick 7040 Pyrex glass to the top of the silicon wafer. The 3.5 mm diameter inlet and outlet holes were drilled in the Pyrex plate using an air impact drilling process, and were located above the reservoirs.

After the fabrication of the pin fin cold plate with integral heaters and temperature sensors, dimensional measurements of all the samples were performed using SEM (scanning electron microscopy). Figure 4 shows the SEM picture of the sample RP4. Dimensions given in Table 2 are based on SEM measurements.

4 Description of the Experimental Setup

The experimental setup for the micropin-fin cold plate was constructed to measure flow rate, pressure drop, and temperature. Figure 5 shows the schematic of the experimental setup. The cooling fluid (deionized water) was driven by a Micropump model GATT23 positive-displacement pump, and the flow rate through the micropin-fin cold plate was controlled using two manual needle valves. Fluid temperature upstream of the micropin-fin cold plate was controlled with a liquid-to-liquid heat exchanger plumbed in series with the micropin-fin unit. The heat exchanger transferred heat between the micropin-fin loop and an external liquid loop, the temperature of which was controlled by a Neslab RTE7 circulating chiller/heater. The flow meter, valve, and a 10 μm filter were also plumbed in series with the micropin-fin cold plate. Both branches in the loop, the bypass branch and the main branch, drained to a reservoir open to atmosphere, from which the pump drew water.

Flow rate was measured using a Flow Technology turbine flow meter. Pressure drop across the micropin-fin cold plate was measured with a Setra differential pressure transducer of range 0–172 kPa (0–25 psi). The pressure transducer ports were connected to the micropin-fin fluid inlet and outlet as shown in Fig. 5. The micropin-fin cold plate inlet and outlet were connected to the external tubing using copper adapters flush mounted to the cover plate with epoxy. Alignment pins were used to match the openings of the Cu blocks and the micropin-fin cover plate ports during the epoxy process. No leakage was observed during the testing. A Setra gauge pressure transducer with a pressure range 0–172 kPa (0–25 psi) was also connected to the micropin-fin fluid inlet. The voltage outputs of all three devices, flow meter, differential pressure transducer, and gauge pressure transducer, were recorded by a data logger.

Thermal resistance of the micropin-fin cold plate was calculated from the silicon die to the cooling fluid based on die temperature, fluid temperature, and die heater power. Die temperatures were measured using resistance temperature detectors (RTDs) fabricated directly on the die as mentioned earlier, and the fluid temperature was measured with fine-wire, K-type, thermocouples installed in the cold plate inlet and outlet reservoirs. The RTD and thermocouple measurements were taken with an Agilent data acquisition system. RTDs were calibrated in an isothermal liquid bath against a reference platinum resistance thermometer. The accuracy of RTD was ±0.1°C. This includes the standard deviation of the entire bath calibration process. The die RTD calibration did not change with time since all die RTDs were operated within the temperature limits of the bath calibration process. The system performed four-wire resistance measurements across each RTD and temperature measurements for each thermocouple. The four-wire

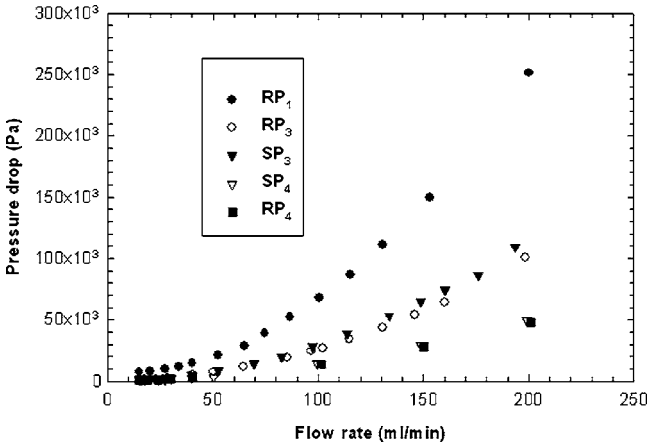

Fig. 6 Measured pressure drop versus flow rate for all micropin-fin arrays

resistance measurements were converted to temperatures by the data acquisition system based on a calibration performed at the start of each test.

5 Experimental Results and Data Reduction

In the first set of experiments, pressure drop was measured at varying flow rate without powering the heaters. The minimum flow rate in the experiment was 15 ml min^{-1} and the maximum flow rate was 200 ml min^{-1}. This range of flow rate was chosen in accordance with the capability of the flow meter. The fluid temperature was set at 50 °C using the liquid-to-liquid heat exchanger as shown in Fig. 5. Since the pressure transducers were connected to the inlet and outlet manifold, the measured pressure drop also includes the pressure drop associated with entrance and exit losses. The entrance and exit pressure drop losses were calculated using the correlations used by Qu and Mudawar [18], however they were found to be negligible compared to the measured pressure drop (less than one percent). Therefore measured pressure drop is same as the pressure drop thorough the pin fins.

Figure 6 shows the pressure drop of the MPF arrays as a function of flow rate. Figure 6 shows that RP1 has the highest pressure drop and RP4 and SP4 have the lowest pressure drop. This result is easily explained by the geometry of the cold plates, described in Table 2. RP1 has 66 pins, creating a greater flow restriction than RP4 and SP4, each of which have only 22 pins. Figure 6 also shows that pressure drop of square pins is somewhat higher than that of round pins at a given flow rate.

Two types of Reynolds number, friction factor, and Nusselt number are defined in this paper: (1) based on the pin diameter (2) based on channel/duct hydraulic diameter (D_h). Most of the data in the literature on pin fins have been analyzed based on the pin-fin diameter as the relevant length scale [19–34], however researchers have also analyzed the data by treating flow as flow through a duct [13,35]. For the present case H is the height, W is the width, and L is the length the duct.

Table 3 shows the porosity of the duct (ε), which is given by $\varepsilon=1-\pi N_x N_y d^2/(4WL)$ for the circular pins and $\varepsilon=1-N_x N_y d^2/(WL)$ for the square pins, where d is the diameter for round pins and side length for the square pins and N_x and N_y are the number of pins in the x and y directions, respectively. Table 3 shows that porosity of all the designs is very high. Therefore it might be possible that the presence of the pins has little effect on the pressure drop. The Fanning friction factor for a duct (f_c) is given by [19,21]

Table 3 Details of the dimensions based on channel/duct approach

Part number	Porosity (ε)	Enhanced area due for heat transfer due to presence of pins	Channel Hydraulic diameter (D_h) (μm)	$2H/d$
RP1	0.94	1.68	305	5.6
RP3	0.87	2.33	601	4.96
SP3	0.83	2.7	601	4.96
RP4	0.90	NA	392	2.6
SP4	0.87	NA	392	2.6

$$f_c = \frac{(\Delta p/L)D_h}{2\rho v_m^2} \tag{1}$$

where L is the length of the duct (length of the finned area) as shown in Fig. 2, Δp the pressure drop, ρ the density of the fluid, and v_m is the mean velocity of the fluid. v_m is given by $v_m=\dot{m}/(\rho HW)$. Realizing that $D_h=2HW/(H+W)$, the Reynolds number (Re_c) based on the channel hydraulic diameter is given by

$$\mathrm{Re}_c = \frac{v_m D_h \rho}{\mu} = \frac{2\dot{m}}{\mu(W+H)} \tag{2}$$

where μ is the viscosity of the fluid. Looking at Tables 1 and 2, it can be seen that $H \ll W$. Therefore the problem can be treated as flow through parallel plate. Therefore $D_h \approx 2H$ and

$$\mathrm{Re}_c \approx \frac{2\dot{m}}{\mu W} \tag{3}$$

Equation (3) shows that, by treating the system as parallel plates, Re_c is same for all the different designs for same flow rate, because W is same for all the designs.

Figure 7 shows the variation of f_c with Re_c. Although Re_c is same for all the designs for same $\dot{m}$, Fig. 7 shows that different designs have different f_c depending on the pin geometry and configuration. Another important point to notice is that although RP1 has the higher porosity than RP4 and SP4, the friction factor for RP1 is higher than both RP4 and SP4. Figure 7 also shows that

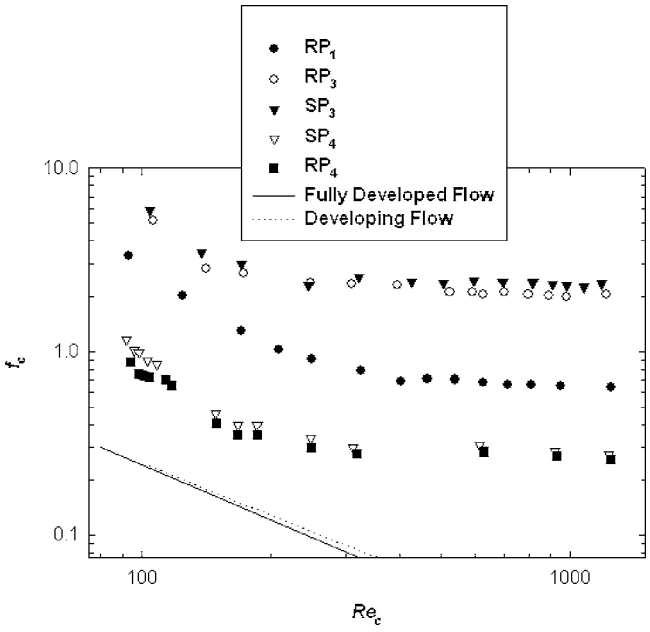

Fig. 7 Friction factor based on channel approach versus Reynolds number based on hydraulic diameter of the channel

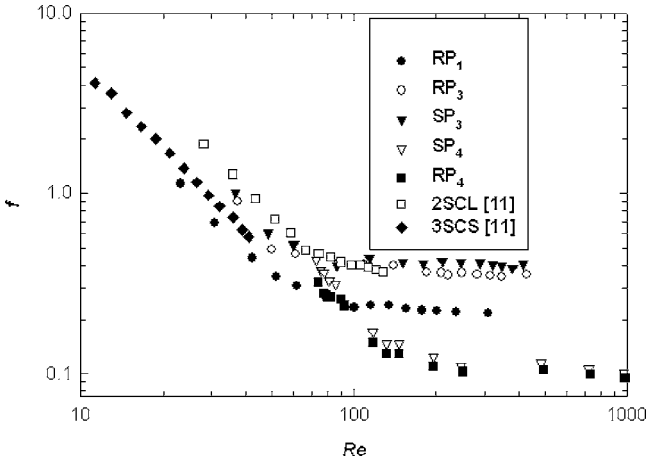

Fig. 8 Friction factor based on pin fin approach versus Reynolds number based on pin diameter

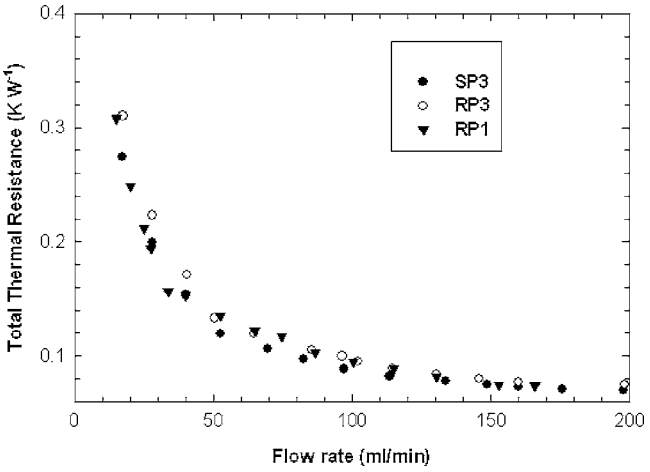

Fig. 9 Measured thermal resistance versus flow rate for different micropin-fin arrays

square pins lead to slightly higher f_c than circular pins. Figure 7 clearly shows that pins definitely affect the hydraulic performance of the micropin-fin array. The highest Re_c achieved in this study is approximately 1250, which means that from the parallel-plate point of view the flow is laminar [19,21]. The friction factor (f_0) for fully developed laminar flow through parallel plates is given by [19,36,37]

$$f_0 = \frac{24}{\mathrm{Re}_c} \tag{4}$$

Figure 7 shows that f_0 given by Eq. (4) is much smaller than the experimental data. Another question that should be asked is whether the flow is fully developed because length of the channel is only 13 mm. For the present case, the f_0 for developing flow through parallel plates is given by [37]

$$f_0 = \frac{1}{\mathrm{Re}_c} \times \left[24 + \frac{0.674\,\mathrm{Re}_c D_h}{4L} \right] \tag{5}$$

Figure 7 also shows f_0 calculated by using Eq. (5) and using the largest D_h from all designs (Table 3). Figure 7 shows that f_0 given by the fully developed case and developing case is almost identical. Therefore developing flow is also not the reason for discrepancy between the data and the theory of flow through parallel plates. Therefore it can be concluded that micropins are playing a very important and dominant role in deciding the friction factor because the friction factor from the experiments are one order of magnitude higher than can be expected from laminar flow in channels. Figure 7 also shows that the laminar flow theory of parallel plates does not predict the correct trend after some critical Re_c.

For the definition based on the pin diameter and pitch, the Fanning friction factor f is given by [19]

$$f = \frac{\Delta p}{2N_x \rho v_{\max}^2} \tag{6}$$

where $v_{\max}$ is the maximum velocity of the fluid between the pins. Figure 8 shows the variation of f with the Reynolds number (Re) based on the pin diameter (d). Re is given by

$$\mathrm{Re} = \frac{v_{\max} d}{\nu} \tag{7}$$

where ν is the kinemetic viscosity of water. Since Re depends on the pin diameter, it is different for different designs even for same $\dot{m}$.

Figure 8 shows there is a change in the relationship of f to Re around $\mathrm{Re}=100$. f is very sensitive to Re for $\mathrm{Re}<100$ and is less sensitive to Re for $\mathrm{Re}>100$. The data for a staggered array of circular pin fins from Koşar et al. [11] is also shown in Fig. 8, and it shows a similar trend. Koşar et al. [11] plotted their data on a linear scale. On the linear scale the change in the behavior of f with Re is not visible whereas on the log-log scale as shown in Fig. 8 the change in the behavior of f around $\mathrm{Re}=100$ is clearly visible.

For the thermal resistance experiments a current was applied to the metallic heater on the test chip to provide a constant power dissipation. The heat loss through the motherboard side was estimated by applying the energy conservation. The heat flow through the micropin-fin cold plate was calculated using $Q' = \dot{m} c_p (T_{\mathrm{out}} - T_{\mathrm{in}})$ where Q' is the heat transfer through the micropin-fin side, T_{out} is the outlet temperature of the water, and T_{in} is the inlet temperature of the water. The heat loss through the motherboard side was found to be less than 1%. This was expected considering the low thermal conductivity of the components on the motherboard side, most of which are made of polymer, and the lack of a cooling solution on the motherboard side. Total thermal resistance (R_T) between the heating surface and the fluid was calculated as

$$R_T = \frac{T_{\mathrm{Havg}} - T_{\mathrm{favg}}}{Q} \tag{8}$$

where T_{Havg} is the average temperature of the heating surface, $T_{\mathrm{favg}} = (T_{\mathrm{in}} + T_{\mathrm{out}})/2$ is the average temperature of the fluid, and Q is the power through the heater. T_{Havg} is the average of temperature readings of the 20 temperature sensors. Figure 9 shows the variation of R_T with flow rate for different samples. Figure 9 shows that R_T decreases with increasing flow rate. Figure 9 also shows the slightly lower R_T of the square pins compared to that of the circular pins, most likely caused by the larger area of the square pins. Area of the square pins $= 4/\pi$ times the area of the circular pins for the same nominal dimensions. R_T can be written as

$$R_T = R_c + R_{\mathrm{conv}} \tag{9}$$

where R_c is the conduction resistance through the silicon and R_{conv} is the effective convection resistance. In the thermal experiments the power was varied for different flow rates in order to keep the temperature rise of the water to about 5 °C.

The heat transfer from the heater to the fluid is assumed to be one-dimensional considering the geometry of the die and cold plate assembly. The base thickness is very small (320–365 μm) and the fins are located directly on top of the heater surface, creating primarily one-dimensional heat transfer. To validate this assumption a numerical simulation using ANSYS™ was conducted in which the reservoir was assigned a heat transfer coefficient of

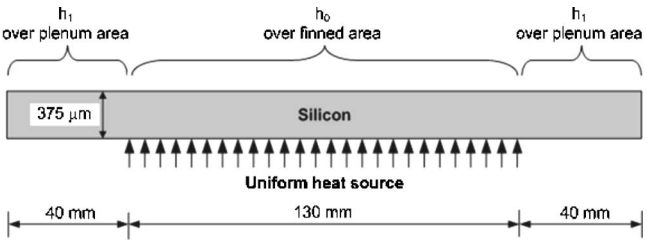

Fig. 10 Schematic of three-dimensional conduction model to estimate error in assuming one-dimensional heat transfer from the source to the cold plate (assuming $h_0=2.5\times10^4$ W/m^{2}K and $h_1=1\times10^3$ W/m^{2}K)

1000 W m^{-2} K^{-1}. This is very high considering the low water velocity in the reservoir. A heat transfer coefficient of 25000 W m^{-2} K^{-1} was assigned above the heater surface area, assuming the worst case thermal resistance of 0.31 K W^{-1} (the first data point in Fig. 9). Recall that 0.31 K W^{-1} also includes the conduction resistance, however this model assumed it was solely due to convection. The physical model is shown in Fig. 10. The base thickness of RP3 was used for the simulation because it is thicker than other designs considered in the thermal experiments (see Table 2). The thicker base gives more opportunity for heat spreading, therefore the simulation considered the worst-case scenario in evaluating the assumption of one-dimensional heat transfer. This worst case model showed that 98% of heat was transferred to the finned area, thereby validating the assumption of one-dimensional heat transfer.

The thermal data is also treated based on parallel-plate dimensions and pin-fin diameter. R_{conv} is calculated from the experimental data using Eq. (9). For the parallel-plate approach, the average heat transfer coefficient ($\bar{h}_c$) is given by $R_{conv}=1/(\bar{h}_c LW)$. The Nusselt number ($Nu_c$) based on the hydraulic diameter of the parallel plate is given by $Nu_c=\bar{h}_c D_h/k_l$, where k_l is the thermal conductivity of the liquid. Figure 11 shows the variation of Nu_c with Re_c. The Nusselt number (Nu_0) for fully developed flow in a parallel plate for one sided heating is [19,36,37] 5.385. If the flow is considered to be in a developing region, then Nu_0 is almost the same [37] as that for a developed flow if $(L/D_h)/(Re_c\,Pr)\geq 0.005$. Considering the best case situation for developing flow (largest D_h from all designs and largest Re_c of 1250) $(L/D_h)/(Re_c Pr)=0.005$. For all other cases $(L/D_h)/(Re_c Pr)>0.005$. Therefore Nu_0 is assumed 5.385 for all the cases considered here. Figure 11 shows that Nu_c is much larger than Nu_0.

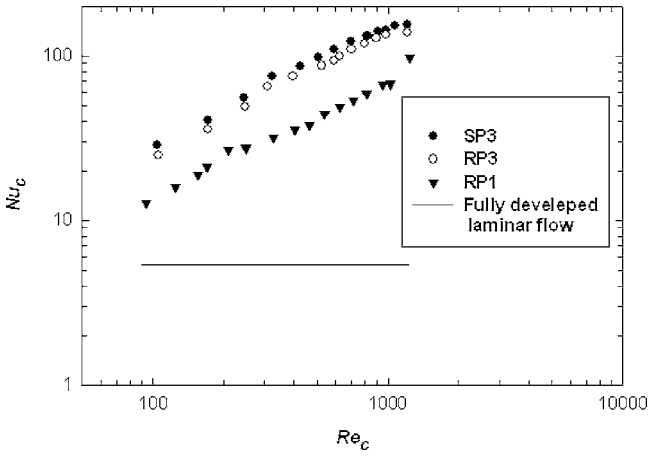

Fig. 11 Nusselt number based on channel approach versus Reynolds number based on hydraulic diameter of the channel

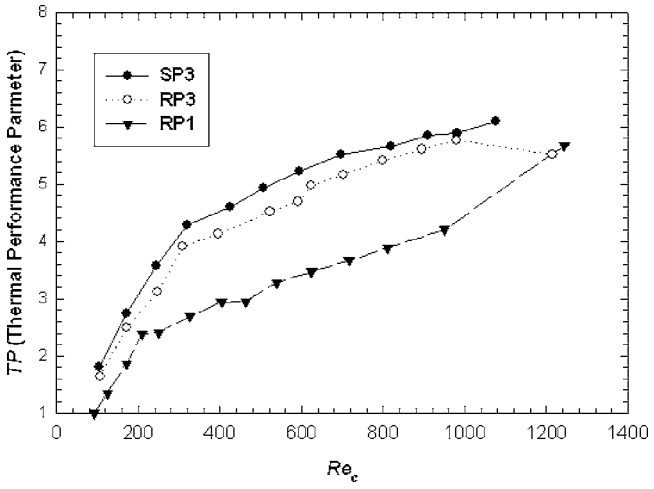

Fig. 12 Thermal performance parameter (Eq. (10)) versus Reynolds number based on hydraulic diameter of the channel

Figure 11 shows that depending on Re_c, the ratio, Nu_c/Nu_0 ranges from 5 to 25 for RP3 and RP4 and from 2.5 to 20 for RP1. Table 3 shows the enhancement in the heat transfer area due to the presence of the pins. The enhancement in the area is given by the expression $(\pi dHN_xN_y+WL)/(WL)$ for the circular pins and by $(4dHN_xN_y+WL)/(WL)$. The enhancement in the heat transfer area for the micropin-fin cold plate as compared to a parallel plate cold plate is 1.68, 2.33, and 2.7 for RP1, RP3, and SP3, respectively. Therefore major cause of enhancement in the heat transfer is not due to the increase in the area. Therefore it can be safely concluded that micropins are doing more than just increasing the area.

Since both the friction factor and Nusselt number for the micropin-fin cold plates are much higher than the friction factor and Nusselt number for a parallel plate cold plate, it is not clear if the addition of micropin-fin are really beneficial. To understand the impact of micropins, an overall thermal performance parameter TP is defined as [13,35]

$$TP=\frac{(Nu_c/Nu_0)}{(f_c/f_0)^{1/3}} \tag{10}$$

This ratio compares the heat transfer per unit pumping power for the test duct, with blockages [35], with that of a smooth channel with the same hydraulic diameter as the test channel. Figure 12 shows that TP is greater than 1 and increases with increasing Re_c. Therefore addition of micropin arrays to the parallel plate duct leads to a better cold plate.

For the analysis of the data based on pin diameter, the effect of the end wall is very important in short pin-fin cold plates as highlighted by several researchers [22,26,27]. Therefore for the calculation of the Nusselt number an average heat transfer coefficient ($\bar{h}$) is calculated using the experimental data and following the procedure for short pins in the literature [22,26]. The average heat transfer coefficient $\bar{h}$ is assumed to be the same for the finless area and the finned surface [26]. Therefore R_{conv} is given by

$$1/R_{conv}=\bar{h}[(L\times W-N_x\times N_y\times \pi/4\times d^2)+(P\times H\times \eta_f)] \tag{11}$$

where L is the length of the finned area, W the width of the finned area, P the perimeter of the pins, and η_f is the fin efficiency. η_f is given by [19]

$$\eta_f=\frac{\tanh(mH)}{mH} \tag{12}$$

where m is given by [19]

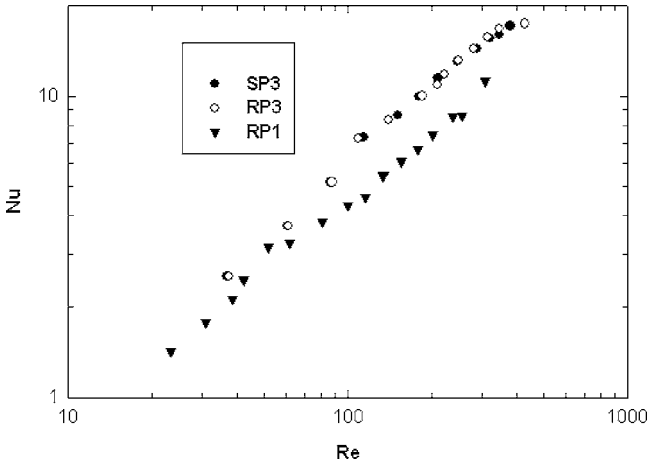

Fig. 13 Nusselt number based on pin fin approach versus Reynolds number based on pin diameter

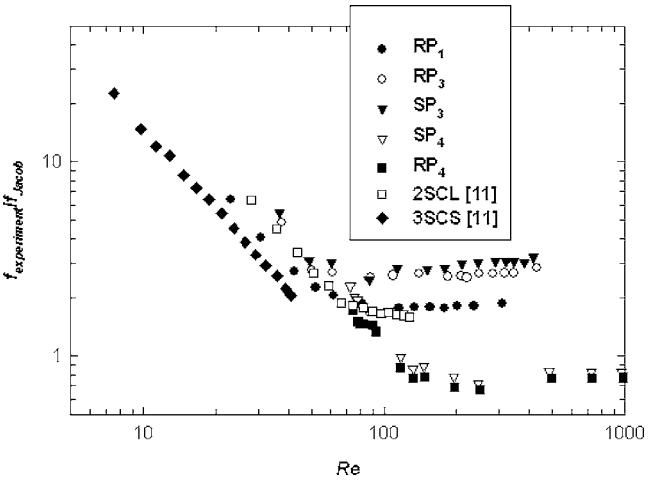

Fig. 14 Ratio of friction factor obtained from experiments and the correlation by Jacob [19] (Eq. (15))

$$m = \sqrt{\frac{\bar{h}P}{k_{Si}A}} \tag{13}$$

where k_{Si} is the thermal conductivity of Si and A is the cross-sectional area of the fins. Equation (11) is a transcendental equation. It is solved iteratively to obtain the value of $\bar{h}$.

The Nusselt number based on the diameter of the pins and $\bar{h}$ is given by

$$\mathrm{Nu} = \frac{\bar{h}d}{k_l} \tag{14}$$

For the thermal experiments all the properties of water were obtained at the average temperature of the water. Figure 13, a plot of Nu for different MPF arrays, shows the Nu for square and circular MPF arrays are identical. This result was also reported in the experimental study conducted by Chyu and Natarajan [28] for air in the macrogeometry. Nu does not show a strong transition with respect to Re as compared to f. This could be because Nu is defined based on $\bar{h}$. $\bar{h}$ is the average heat transfer coefficient that accounts for heat transfer from the end wall and the fins.

The uncertainties of measured values are given in Table 4. The uncertainties of the derived parameters R_T and f are obtained using the method developed by Kline and McClintock [38]. The error in R_T listed in Table 4 is the maximum value obtained from all the data collected. Similarly the error in f listed in Table 4 is the maximum value obtained from all the data collected.

6 Correlating the Data

The discussions in the previous section showed that the addition of the micropin fins have a dramatic effects on both the hydrodynamic and thermal behavior of the cold plate. Therefore the data has been correlated based on the pin-fin approach. Therefore the diameter of the pins is assumed to be the most important characteristic dimension.

Table 4 Uncertainty in different variables

Variable	Error
Flow rate	±0.5%
Pressure drop	±430 Pa
Friction factor (calculated)	±5%
Electrical power in the heater	±0.1 W
Temperature sensor	±0.1°C
Fluid temperature (thermocouple)	±0.25°C
R_T	±6% (maximum)

This section compares the experimental data obtained for f and thermal resistance with correlations based on those reported in the literature. The aspect ratio (H/d) of the fins evaluated in this study ranges between 1.3 and 2.8. Similarly, the aspect ratio of the fins in the staggered MPF array evaluated by Koşar et al. [11] was 1 and 2. Therefore correlations based on long tube [19,20] data are probably not valid for MPF cold plates. Short fins have been investigated very thoroughly in gas turbine cooling applications [22]. Armstrong and Whinstanley [22] compared various correlations with data on low aspect ratio pins for both Nu and f. For f they found that most of the data lay between the correlation developed by Holman [19] and correlation developed by Damerow et al. [23]. Note that both correlation by Jacob and Damerow et al. were developed for turbulent flow, however they have been used even in the laminar region with good success [20,22]. Both these correlations have been applied for $2 \leq S_T/d \leq 4.0$ for short pin-fin arrays. As seen from Table 2, S_T/d falls in this range for all the pin-fin designs considered in this study. Correlation by Holman is valid for long tubes whereas correlation by Damerow et al. [23] is valid for $2 \leq H/d \leq 4$. H/d falls in this range for all the designs except for SP4 and RP4.

Correlation for f by Jacob for staggered round pin fin arrangement is given by [19]

$$f = \left\{0.25 + \frac{0.118}{[(S_T - d)/d]^{1.08}}\right\}\mathrm{Re}^{-0.16} \tag{15}$$

Note that Kim et al. [20] found that above correlations agree within 8.8% of the more complex tube bank correlations of Zukaukas [24]. Figure 14 shows the ratio of experimental data and the correlation by Jacob. Figure 14 shows that this ratio is very different than one, which shows that correlation by Jacob does not predict the data well.

The friction factor by Armstrong and Winstanley [22] and Damerow et al. [23] is given by

$$f = [2.06(S_T/d)^{-1.1}]\mathrm{Re}^{-0.16} \tag{16}$$

Figure 15 shows the ratio of experimental data and the correlation by Damerow et al. Figure 15 shows that this ratio is very different than one, which shows that correlation by Damerow et al. does not predict the data well. Both the correlations by Holman and Damerow et al. do not depend on the aspect ratio of the pins, which may contribute to the failure of these correlations in predicting the data.

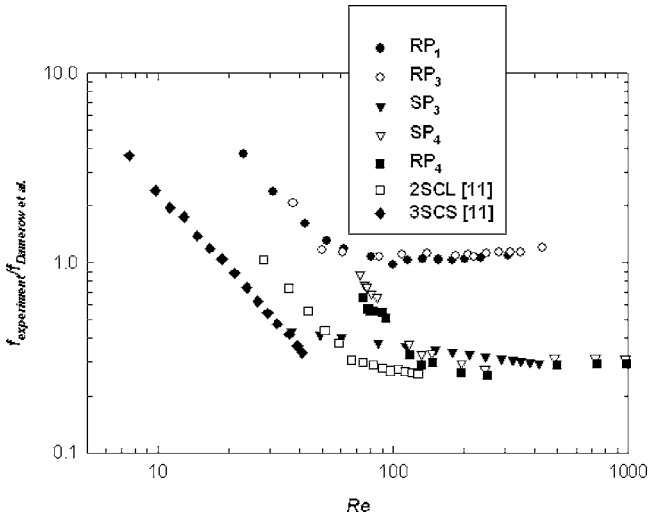

Fig. 15 Ratio of friction factor obtained from experiments and the correlations by Armstrong and Winstanley [22] and Damerow et al. [23] (Eq. (16))

Short et al. [25] performed a comprehensive study of friction factor of pin fin designs with air where they varied H/d, S_T/d, and S_L/d. They saw a transition in the behavior of f around Re $=1000$. Their data showed that f varied as $\mathrm{Re}^{-0.65}$ for $\mathrm{Re}<1000$ and as $\mathrm{Re}^{-0.08}$ for $\mathrm{Re}>1000$. Their correlation for $\mathrm{Re}<1000$ is given by

$$f = 35.1 \times (S_L/d)^{-1.3}(S_T/d)^{-0.78}(H/d)^{-0.55}\,\mathrm{Re}^{-0.65} \qquad (17)$$

Equation (17) shows that it includes all the pertinent length scales. Figure 16 shows the ratio of experimental data and Eq. (17), the correlation by Short et al. [25]. Figure 16 shows that this ratio is different than one for most data showing that Eq. (17) does not predict the data, however it shows a trend. Figure 16 shows that around Re=100 some type of transition is happening and the curves are symmetrical. This type of trend was missing from the correlations by Holman [19] and Damerow et al. [23] because

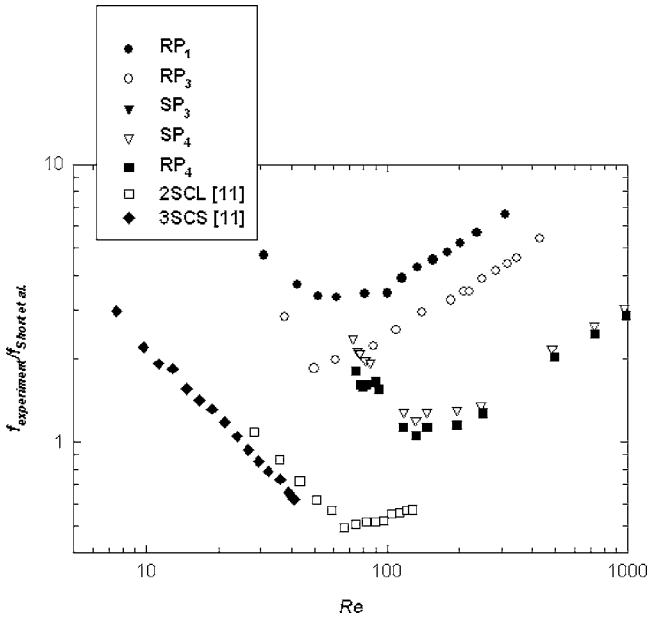

Fig. 16 Ratio of friction factor obtained from experiments and the correlation by Short et al. [25] (Eq. (17))

Table 5 Value of different factors in the correlations developed in this paper for low aspect ratio, staggered, micropin-fin array

Correlation	c	α_1	α_2	α_3	m
All data	3.5	0.724	−0.442	−0.245	0.58
Re<100	169.82	−0.640	−0.258	0.283	1.35
Re>100	0.295	1.249	−0.7	−0.36	0.1

both these correlations do not include all the relevant length scales.

Koşar et al. [11] compared their data with nine correlations from previous literature and they did not find a satisfactory match with any one. Readers are referred to the paper by Koşar et al. [11] for the details of the nine correlations used by them from the literature. Based on their own data Koşar et al. [11] proposed a correlation of the form

$$f = \frac{\psi_1(\text{geometry})}{\mathrm{Re}^{1.7}} + \frac{\psi_2(\text{geometry})}{\mathrm{Re}'} \qquad (18)$$

where Ψ_1 and Ψ_2 are functions of H/d, S_L/d, and S_T/d and Re′ is defined based on the compact heat exchanger approach [11]. Equation (18) shows that f is a strong function of Re, and referring to Fig. 8 it is clearly seen that f is a strong function of Re for Re approximately below 100. However, above Re=100, f is not very sensitive to Re. This is also the trend for the data from Koşar et al. [11] when plotted on a log-log scale as shown in Fig. 8, although the change in the behavior of f on their data takes place around Re=60. Since Koşar et al. [11] plotted their data on a linear scale, this trend was not observed, and their correlation under predicted f by a large margin for Re>100.

Considering the failure of the correlations from the previous literature, a correlation including all the relevant length scales was attempted. Friction factor data were first correlated assuming a single curve over the full range of Re. Taking the cue from the correlation by Holman [19] and correlation by Short et al. [25] the data were correlated assuming the following form:

$$f = c\left(\frac{H}{d}\right)^{\alpha_1}\left(\frac{S_L-d}{d}\right)^{\alpha_2}\left(\frac{S_T-d}{d}\right)^{\alpha_3}\mathrm{Re}^{-m} \qquad (19)$$

Values of c, α_1, α_2, α_3, and m obtained by a regression fit of Eq. (19) with data are given in Table 5. Figure 17 shows the comparison of Eq. (19) with experimental data. The trend in Fig. 17 is

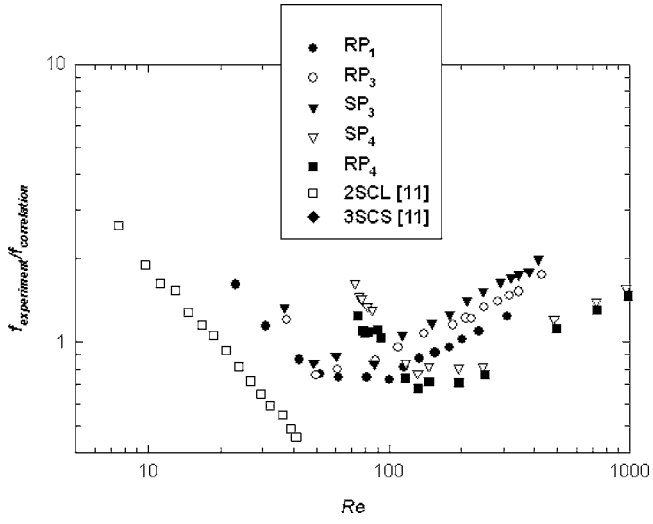

Fig. 17 Ratio of friction factor obtained from experiments and the correlation (Eq. (19)) developed by fitting all data

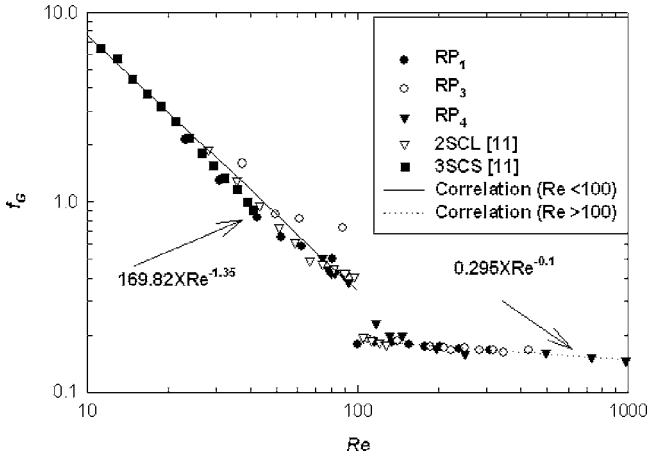

Fig. 18 Comparison between the friction factor obtained from experiments and the correlation (Eq. (19)) developed by fitting the data for Re<100 and Re>100 separately

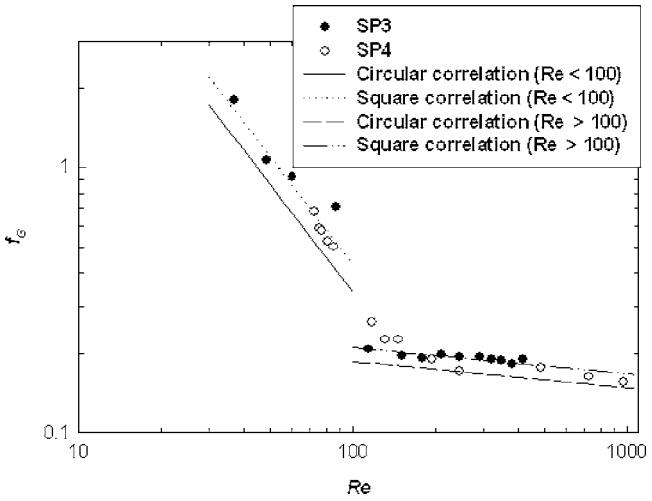

Fig. 19 Comparison between the proposed correlation (see text) and data from square pin fin array for friction factor

very similar to that in Fig. 16. This is expected because Eq. (19) is very similar in form to Eq. (17) by Short et al. [25]. Figure 17 also shows that there is some type of transition happening around Re = 100.

Considering the discussions in the previous paragraphs and the data from Fig. 17, it seems that a different correlation is needed for Re < 100 and for Re > 100. This idea was applied by Short et al. [25], in which a different correlation is developed for air for Re < 1000 and for Re > 1000. This two-part correlation based on Re resulted in a much better prediction of the friction factor. For the current study a similar approach is taken by applying separate regression fit for Re < 100 and Re > 100. Values of c, α_1, α_2, α_3, and m obtained by separate regression fit of Eq. (19) with data for Re < 100 and Re > 100 are given in Table 5. Regression fit of Eqs. (20) shows that $m=1.35$ for Re < 100 and $m=0.1$ for Re > 100. The huge discrepancy in the value of m between the two regimes was surprising at first, however a similar discrepancy was found by Short et al. [25] for air. Short et al. [25] found $m=0.65$ for Re < 1000 and $m=0.08$ for Re > 1000. The reason for this transition is not clear at this time, however $m=0.1$ for Re > 100 suggests turbulent flow behavior. Equation (19) is compared with the data by reducing the experimental data in the following form:

$$f_G = \frac{f_{\text{experiment}}}{\left(\frac{H}{d}\right)^{\alpha_1}\left(\frac{S_L-d}{d}\right)^{\alpha_2}\left(\frac{S_T-d}{d}\right)^{\alpha_3}} \tag{20}$$

where f_G is the geometry independent friction. Figure 18 shows the comparison between Eq. (19) and the experimental data. Figure 18 shows that by breaking the correlation into two parts for Re < 100 and Re > 100, the match with the data is very good. The data deviates slightly from the correlation in the range 60 < Re < 100. Looking at Fig. 8, it seems that transition is taking place for Re between 60 and 100.

The correlations developed in this study are based on the data from circular MPF arrays. Figure 19 shows the comparison between the data on square MPF arrays and Eq. (20). Figure 19 shows that friction factor f of square arrays is higher than that given by correlation developed for circular pins although the side of the square is the same as the diameter of the cylinder. This is expected for two reasons. First, for the same nominal dimension, square pins have a greater cross-sectional area leading to a higher volume fraction than circular pins (by a factor of $4/\pi$). Therefore there is less free space available in the square pin array compared to the circular pin array. Second, the square pin geometry alters the flow characteristics within the array compared to the circular array. To account for the difference in the volume fraction (volume fraction = 1 − porosity) between the circular and square pins arrays we found that $f_{\text{square}}=4/\pi f_{\text{circular}}$ for Re < 100 and $f_{\text{square}}=\sqrt{4/\pi} f_{\text{circular}}$ for Re > 100 matched the data very well for the square pins.

Figure 19 shows that alteration of f_{square} as given above matches well with the data. Although this transformation of f_{square} matches well with the data, it needs to be verified with other square pin fin designs to see if it is universal.

The conventional correlation for Nu for a tube bank is typically of the form [19,29]

$$\text{Nu} = C_1\,\text{Re}^n\,\text{Pr}^{1/3} \tag{21}$$

Recently Khan et al. [30] and Khan [31] proposed the following correlation for long pins:

$$\text{Nu}_{\text{fin}} = \frac{h_{\text{fin}}d}{k_l} = C_1\,\text{Re}_{\text{max}}^{1/2}\,\text{Pr}^{1/3} \tag{22}$$

where h_{fin} is the heat transfer coefficient due to the fins and

$$C_1 = \frac{0.61 S_T^{0.591} S_L^{0.053}}{(S_T-1)^{0.5}[1-2\exp(-1.09S_T)]} \tag{23}$$

Khan [31] showed Eq. (21) matched very well the data available for long tubes in the literature [32,33]. Figure 20 shows the ratio of the predictions of Eq. (21) and experimental data. Figure 20 shows that experimental Nu is substantially smaller than that predicted by long tube correlation. This is totally consistent with the conclusion drawn from previous studies on short pin fins in gas turbine cooling [22].

Armstrong and Winstanley [22] have compiled various correlations for Nu of short pin-fin arrays. Two of the of most widely used correlations for short pin-fin array are considered in this paper. First, VanFossen [26] conducted a comprehensive study on heat transfer in short pin fin array. The VanFossen (VF) correlation is given by [26]

$$\text{Nu}_{\text{VF}} = 0.153\,\text{Re}_{\text{VF}}^{0.685} \tag{24}$$

where Nu_{VF} is the VanFossen Nu and Re_{VF} is the VanFossen Re. The relation between Nu and Re as defined in this paper and Nu_{VF} and Re_{VF} is given by [22]

$$\text{Re} = \text{Re}_{\text{VF}}\frac{2(S_L-d)/d\times(S_T/d)+\pi[H/d-1/2]}{(H/d)[4(S_L-d)/d\times(S_T/d)-\pi]} \times \frac{(S_T/d)-\pi/4\times d/(S_T-d)}{(S_T/d-1)} \tag{25}$$

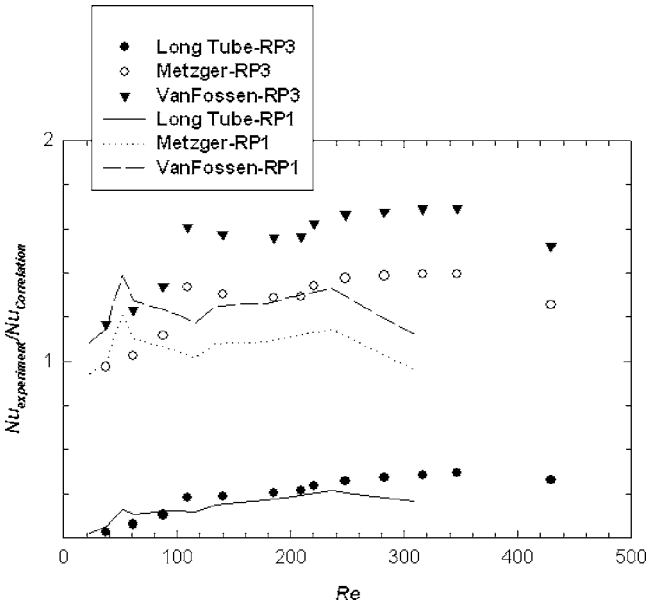

Fig. 20 Ratio of the Nusselt number obtained from experiments and that predicted from long and short fin correlation from the previous literature

$$\mathrm{Nu} = \mathrm{Nu}_{\mathrm{VF}} \frac{2(S_L - d)/d \times (S_T/d) + \pi[H/d - 1/2]}{(H/d)[4(S_L - d)/d \times (S_T/d) - \pi]} \tag{26}$$

Similarly Metzger et al. [34], based on a comprehensive experimental investigation, proposed a correlation of the form

$$\mathrm{Nu} = 0.135\left(\frac{S_L - d}{d}\right)^{-0.34} \mathrm{Re}^{0.69} \tag{27}$$

Both VanFossen and Metzger conducted their study using air as the cooling fluid, making their correlations valid only for air. For the current study using water, both the VF and Metzger correlations were modified to include the effect of Prandtl number by the following transformation [27]:

$$\frac{\mathrm{Nu}_{\mathrm{water}}}{\mathrm{Nu}_{\mathrm{air}}} = \left(\frac{\mathrm{Pr}_{\mathrm{water}}}{\mathrm{Pr}_{\mathrm{air}}}\right)^{0.36} \tag{28}$$

Figure 20 shows the ratio of the predictions from VF and Metzger correlations and the data. Figure 20 shows that both correlations predict smaller values of Nu than the experimental data for most of the Re range. For $\mathrm{Re} < 1000$, Short et al. [39] proposed a correlation of the form

$$\mathrm{Nu} = 0.76\left(\frac{S_L}{d}\right)^{0.16}\left(\frac{S_T}{d}\right)^{0.2}\left(\frac{L}{d}\right)^{-0.11} \mathrm{Re}^{0.33} \tag{29}$$

Figure 21 shows that ratio of Nu obtained from experiment and that obtained from Eq. (33). Figure 21 shows that Nu given by Eq. (30) does not predict the data both in magnitude and trend.

Considering the failure of the previous correlations, a new correlation was developed using the Metzger correlation as a base. The resulting correlation after regression fit leads to

$$\mathrm{Nu} = 0.132\left(\frac{S_L - d}{d}\right)^{-0.256} \mathrm{Re}^{0.84} \quad \text{for } \mathrm{Re} < 100 \tag{30}$$

$$\mathrm{Nu} = 0.281\left(\frac{S_L - d}{d}\right)^{-0.63} \mathrm{Re}^{0.73} \quad \text{for } \mathrm{Re} > 100 \tag{31}$$

The effect of H/d is not included in Eqs. (30) and (31) because thermal data were only collected for RP1, RP3, and SP3. Since RP3 and SP3 have the same H/d, there is not enough data to include all the length scales. However, Table 2 shows that H/d is similar for RP1, RP3, and SP3. The most notable difference between RP1 and RP3 is the fin pitch S_L/d. More comprehensive experiments with variations in all the length scales is needed to capture all the length dependencies. Figure 22 shows the comparison between the proposed correlation and the data. The experimental data is converted into geometry independent Nu (Nu_G) by

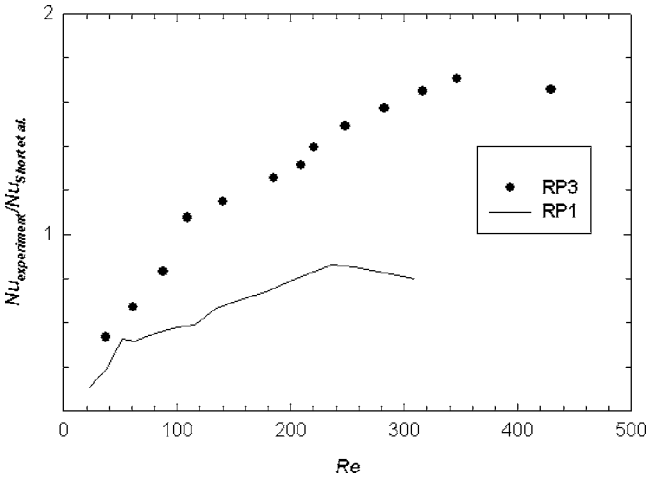

Fig. 21 Ratio of the Nusselt number obtained from experiments and that predicted from the correlation by Short et al. [39] (Eq. (3029))

$$\mathrm{Nu}_G = \frac{\mathrm{Nu}_{\mathrm{experiment}}}{\left(\frac{S_L - d}{d}\right)^{-0.256}} \quad \text{for } \mathrm{Re} < 100 \tag{32}$$

$$\mathrm{Nu}_G = \frac{\mathrm{Nu}_{\mathrm{experiment}}}{\left(\frac{S_L - d}{d}\right)^{-0.63}} \quad \text{for } \mathrm{Re} > 100 \tag{33}$$

Figure 22 shows that the proposed correlation matches very well with the data. The transition in Nu with respect to Re is not very strong as compared to the transition in f. This was also observed by Short et al. [25,39]. This could be because Nu is defined based on $\bar{h}$. $\bar{h}$ is the average heat transfer coefficient that accounts for heat transfer from the end wall and the fins.

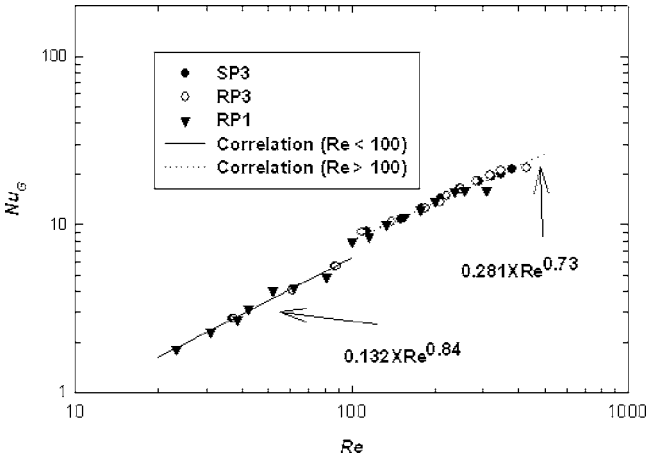

Fig. 22 Comparison between the Nusselt number obtained from experiments and the correlation developed by fitting the data for Re<100 and Re>100 separately

7 Conclusions

An experimental parametric study of both hydraulic and thermal performances of various micropin-fin arrays was performed. The main conclusions are as follows:

(1) The friction factor varies as $Re^{-1.35}$ for $Re < 100$ and as $Re^{-0.1}$ for $Re > 100$.
(2) The Nusselt number varies as $Re^{0.84}$ for $Re < 100$ and as $Re^{0.73}$ for $Re > 100$.
(3) Correlations available in the literature are unable to predict both f and Nu for the micropin-fin array.
(4) More studies are needed with variations in all the relevant length scales to understand the thermal and hydraulic performance of micropin-fin arrays.
(5) Flow visualization studies might be needed to understand the transition in the behavior of f around $Re = 100$ for water.

Nomenclature

c = empirical constant in various newly developed correlations for the friction factor
c_p = specific heat at constant pressure ($J\,kg^{-1}$)
C_1 = geometrical constant in long-tube Nu correlation
d = diameter of the fins (also the length of the side for square fins) (m)
f = fanning friction factor based on pin fin approach
f_c = fanning friction factor based on channel/duct approach
f_0 = friction factor for laminar flow through parallel plates
$f_{experiment}$ = friction factor obtained from experiments
$f_{Damerow}$ = friction factor obtained from Damerow [23] correlations
f_{Jacob} = friction factor obtained from Jacob correlation [19]
$f_{Short\ etal.}$ = friction factor obtained from correlation by Short et al. [25]
f_G = geometry independent friction factor
$\bar{h}$ = average heat transfer coefficient based on pin fin approach ($W\,m^{-2}\,K^{-1}$)
$\bar{h}_c$ = average heat transfer coefficient based on channel approach ($W\,m^{-2}\,K^{-1}$)
H = height of the fins or channel (m)
k_l = thermal conductivity of liquid ($W\,m^{-1}\,K^{-1}$)
L = length of the finned area (m)
m = empirical constants in various newly developed correlations for the friction
$\dot{m}$ = mass flow rate of water ($kg\,s^{-1}$)
MPF = micropin-fin
Nu = average Nusselt number based on diameter of the fins
Nu_c = average Nusselt number based on hydraulic diameter of the channel
Nu_G = geometry independent average Nusselt number
Nu_{VF} = VanFossen Nusselt number
N_x = number of fins in the x direction (stream wise direction)
N_y = number of fins in the y direction (transverse direction)
P = perimeter of the fins (m)
Pr = Prandtl number
Q = total heat input (W)
R_c = conduction resistance of the silicon ($K\,W^{-1}$)
R_{conv} = convection resistance ($K\,W^{-1}$)
Re = Reynolds number based on v_{max} and diameter of the fins
Re_c = Reynolds number based on v_m and hydraulic diameter of the channel
Re_{max} = maximum Reynolds number
Re_{VF} = VanFossen Reynolds number
R_T = total thermal resistance ($K\,W^{-1}$)
SEM = scanning electron microscopy
S_L = longitudinal (stream wise) pitch of the fins (center-to-center)
S_T = transverse pitch of the fins (center-to-center)
T_{favg} = average temperature of the fluid (K)
T_{Havg} = average temperature of the heating surface (K)
T_{in} = inlet temperature of water (K)
T_{out} = outlet temperature of water (K)
v_{max} = maximum velocity of the fluid ($m\,s^{-1}$)
v_m = mean velocity of the fluid based on channel dimensions ($m\,s^{-1}$)
W = width of the finned area or the channel (m)
Δp = pressure drop (Pa)

Greek Symbols

$\alpha_1, \alpha_2, \alpha_3$ = empirical constants in various newly developed correlations for the friction factor
ε = porosity of the pin fin channel
η_f = efficiency of the fins (defined in Eq. (12))
μ = viscosity ($N\,s\,m^{-2}$)
ν = kinematic viscosity ($m^2\,s^{-1}$)
ρ = density ($kg\,m^{-3}$)

References

[1] Tuckerman, D. B., and Pease, R. F. W., 1981, "High-Performance Heat Sinking for VLSI," IEEE Electron Device Lett., **2**(5), pp. 126–129.
[2] Tuckerman, D. B., and Pease, R. F. W., 1981, "Ultrahigh Thermal Conductance Microstructures for Cooling Integrated Circuits," *Proceedings 32nd Electronics Components Conference*, San Diego, CA, May 10–12, IEEE, Piscataway, NJ, pp. 145–149.
[3] Tuckerman, D. B., 1984, "Heat Transfer Microstructures for Integrated Circuits," Ph.D. thesis, Stanford University, Palo Alto, CA.
[4] Colgan, E. G., Furman, B., Gaynes, M., Graham, W., LaBianca, N., Polastre, R. J., Rothwell, M. B., Bezama, R. J., Choudhary, R., Marston, K., Toy, H., Wakil, J., Zitz, J., and Schimdt, R., 2005, "A Practical Implementation of Silicon Microchannel Coolers For High Power Chips," *21st IEEE SEMI-THERM Symposium*, San Jose, CA, March 15–17, IEEE, Piscataway, NJ.
[5] Chang, J-Y., Prasher, R., Chau, D., Myers, A., Dirner, J., Prstic, S., and He, D., 2005, "Convective Performance of Package Based Single Phase Microchannel Heat Exchanger," *Proc. of InterPack 2005*, San Francisco, CA, July 17–22, ASME, New York.
[6] Watwe, A., and Viswanath, R., 2003, "Thermal Implications of Non-Uniform Die Power and CPU Performance," *Proceedings of 2003 International Electronic Packaging Technical Conference and Expositions*, Maui, Hawaii, July 6–11, ASME, New York, Paper No. 2003-35044.
[7] Hassan, I., Phutthavong, P., and Abdelgawad, M., 2004, "Microchannel Heat Sinks: An Overview of the State-of-the-Art," Microscale Thermophys. Eng., **8**, pp. 183–205.
[8] Morini, G. L., 2004, "Single-Phase Convective Heat Transfer in Microchannels: A Review of Experimental Results," Int. J. Therm. Sci., **43**, pp. 631–651.
[9] Sobhan, C. B., and Garimella, S. V., 2001, "A Comparative Analysis of Studies on Heat Transfer and Fluid Flow in Microchannels," Microscale Thermophys. Eng., **5**, pp. 293–311.
[10] Peles, Y., Kosar, A., Mishra, C., Kuo, C-J., and Schneider, B., 2005, "Forced Convective Heat Transfer Across a Pin Fin Micro Heat Sink," Int. J. Heat Mass Transfer, **48**, pp. 3615–3627.
[11] Kosar, A., Mishra, C., and Peles, Y., 2005, "Laminar Flow Across a Bank of Low Aspect Ratio Mico Pin Fins," J. Fluids Eng., **127**, pp. 419–430.
[12] Stephens, L. S., Kelly, K. W., Kountouris, D., and McLean, J., 2001, "A Pin Fin Micro Heat Sink for Cooling Macroscale Conformal Surfaces Under the Influence of Thrust and Frictional Forces," J. Microelectromech. Syst., **10**(2), pp. 222–231.
[13] Marques, C., and Kelly, K. W., 2004, "Fabrication and Performance of a Pin Fin Micro Heat Exchanger," J. Heat Transfer, **126**, pp. 434–444.
[14] Tummala, R. R., 2001, *Fundamentals of Microsystems Packaging*, McGraw-Hill, New York.
[15] Verove, C., Descouts, B., Gayet, P., Guillermet, M., Sabouret, E., Spinelli, E., and Van der Vegt, E., 2000, "Dual Damascene Architectures Evaluation for the 0.18 μm Technology and Below," *Interconnect Technology Conference, Proceedings of the IEEE 2000 International*, San Diego, CA, June 5–7, IEEE, Piscataway, NJ, pp. 267–269.
[16] He, D., Srinivasan, S., Agraharam, S., Chandran, B., Mello, M., Sinha, P., and Atluri, V. 2004, "Test Vehicle to Characterize Silicon to Organic Flip Chip

Package Thermomechanical Interactions," *54th International Electronic and Component Technology Conference*, Las Vegas, June 1–4, IEEE, Piscataway, NJ, pp. 712–717.
[17] Chang, J-Y., Prasher, R., Chau, D., Myers, A., Dirner, J., Prstic, S., and He, D., 2005, "Convective Performance of Package-Based Microchannel Heat Exchanger," *Proceedings of InterPack 2005*, San Francisco, July 17–22, ASME, New York, Paper No. 2005-73126.
[18] Qu, W., and Mudawar, I., 2003, "Measurement and Prediction of Pressure Drop in Two-phase Micro-channel Heat Sinks," Int. J. Heat Mass Transfer, **46**, pp. 2737–2753.
[19] Holman, J. P., 1989, *Heat Transfer*, McGraw-Hill, New York.
[20] Kim, S. Y., Kim, N. H., Young, B., and Webb, R. L., 1999, "Air Side Heat Transfer and Friction Correlations for Plain Fin and Tube Heat Exchangers With Staggered Tube Arrangements," J. Heat Transfer, **121**, pp. 662–667.
[21] Incropera, F. P., and De Witt, D. P., 1990, *Fundamentals of Heat and Mass Transfer*, Wiley, New York.
[22] Armstrong, J., and Winstanley, D., 1988, "A Review of Staggered Array Pin Fin Heat Transfer for Turbine Cooling Applications," J. Turbomach., **110**, pp. 94–103.
[23] Damerow, W. P., Murtaugh, J. C., and Burgraf, F., 1972, "Experimental and Analytical Investigation of the Coolant Flow Characteristics in Cooled Turbine Airfoils," NASA CR-12088.
[24] Zukauskas, A., 1987, "Convective Heat Transfer in Cross flow," *Handbook of Single-phase Convective Heat Transfer*, Wiley-Interscience, New York.
[25] Short, B. E., Raad, P. E., and Price, D. C., 2002, "Performance of Pin Fin Cast Aluminum Coldwalls. Part 1: Friction Factor Correlations," J. Thermophys. Heat Transfer, **16**, pp. 389–396.
[26] VanFossen, G. J., 1982, "Heat-Transfer Coefficients for Staggered Arrays of Short Pin Fins," ASME J. Eng. Power, **104**, pp. 268–274.
[27] Moores, K. A., and Joshi, Y. K., 2003, "Effect of Tip Clearance on the Thermal and Hydraulic Performance of a Shrouded Pin Fin Array," J. Heat Transfer, **125**, pp. 999–1006.
[28] Chyu, M. K., and Natarajan, V., 1996, "Heat Transfer on the Base Surface of Three-dimensional Protruding Elements," Int. J. Heat Mass Transfer, **39**, pp. 2925–2935.
[29] Bejan, A., 1993, *Heat Transfer*, Wiley, New York.
[30] Khan, W. A., Culham, J. R., and Yovanovich, M. M., 2004, "Optimization of Pin Fin Heat Sinks Using Entropy Generation Minimization," *Ninth Intersociety Conference on Thermal and Thermomechanical Phenomena in Electronic Systems*, Las Vegas, NV, June 1–4, IEEE, Piscataway, NJ.
[31] Khan, W. A., 2004, "Modeling of Fluid Flow and Heat Transfer for Optimization of Pin-Fin Heat Sinks," Ph.D. thesis, University of Waterloo, Waterloo, Canada.
[32] Zukauskas, A., 1972, "Heat Transfer From Tubes in Cross flow," Discrete Contin. Dyn. Syst., **8**, pp. 93–160.
[33] Zukauskas, A., and Ulinskas, R., 1988, *Heat Transfer in Tube Banks in Cross Flow*, Hemisphere, Washington, DC.
[34] Metzger, D. E., Shepard, W. B., and Haley, S. W., 1986, "Row Resolved Heat Transfer Variations in Pin-fin Arrays Including Effects of Non-uniform Arrays and Flow Convergence," *Proc. of International Gas Turbine Conference and Exhibit*, Dusseldorf, Germany, June 8–12, ASME, New York.
[35] Moon, S. W., and Lau, S. C., 2003, "Heat Transfer Between Blockages With Holes in a Rectangular Channel," J. Heat Transfer, **125**, pp. 587–594.
[36] Bejan, A., 2004, *Convection Heat Transfer*, Wiley, Hoboken.
[37] Shah, R. K., and London, A. L., 1978, *Laminar Flow Forced Convection in Ducts*, Supplement 1 to Advances in Heat Transfer, Academic, San Diego, CA.
[38] Kline, S. J., and McClintock, F. A., 1953, "Describing Uncertainties in Single Sample Experiments," Mech. Eng. (Am. Soc. Mech. Eng.) **75**, pp. 3–8.
[39] Short, B. E., Raad, P. E., and Price, D. C., 2002, "Performance of Pin Fin Cast Aluminum Coldwalls. Part 2: Cilburn j-Factor Correlations," J. Thermophys. Heat Transfer, **16**, pp. 397–403.

Experimental Verification of a New Heat and Mass Transfer Enhancement Concept in a Microchannel Falling Film Absorber

Nitin Goel

D. Yogi Goswami
e-mail: goswami@ufl.edu

Mechanical and Aerospace Engineering Department,
Solar Energy and Energy Conversion Laboratory,
University of Florida,
P.O. Box 116300,
Gainesville, FL 32611-6300

This paper presents an experimental study of a new concept of using a screen mesh to enhance heat and mass transfer in a microchannel falling film absorber. Results of the experiments on the conventional and mesh-enhanced microchannel absorber designs are then reported. The experimental study shows that the absorber heat load for the mesh-enhanced design is about $17\% \pm 3.4\% - 26\% \pm 3.8\%$ *higher than a conventional microchannel design. The paper also presents a comparison of the experimental results with a numerical model. A finite difference scheme is used to model the heat and mass transfer processes in a falling film absorber. The numerical model agrees well with experimental results with some deviation at low temperature of coolant and high flow rate of weak solution.* [DOI: 10.1115/1.2402182]

Keywords: absorber, condenser, absorption, falling film

Introduction

Heat-driven absorption cycles provide refrigeration/air conditioning with environment friendly refrigerants, such as ammonia. The absorber is one of the critical components of such systems in terms of size, efficiency, and cost [1]. The key features of an efficient absorber design are high heat and mass transfer coefficients, and a large heat transfer surface area. Low-pressure drops for the liquid, vapor, and coolant flows are also desirable. Based on the vapor–liquid contacting arrangement, absorber design are divided into two broad categories, namely, those operating in falling film absorption mode and those in bubble absorption mode. Designs incorporating falling films mode over horizontal coolant tubes have been widely utilized in commercial absorption systems. This design has a low-pressure drop on the vapor-side, but also has a low heat transfer area and an unstable liquid distribution. Numerous heat and mass transfer enhancement techniques such as surface profiling/modification, miniaturization, extended fins, and use of surfactants have been extensively analyzed and studied by researchers.

Techniques such as sand blasting, surface patterning, scratching, and surface oxidation have been used to improve the wetting characteristics of liquid films. The effect of a porous surface on the enhancement of surface wettability was studied by Yang and Jou [2]. Benzeguir et al. [3] profiled the solution-side heat transfer surface by employing grooved and wire wound tubes to generate large mixing waves. Miller and Perez-Blanco [4] studied the effect of solution-side tubular surface with pin fins, grooves and twisted fins on the enhancement of mixing and uniformity of the falling film. Similar to the above concept of profiling the solution-side surface, Schwarzer et al. [5] used spiral steps on the inner periphery of the tubes. In addition, increasing fluid mixing, fins also act as obstructions in the vapor path that consequently induce turbulence in the flow. Constant curvature surfaces (CCS) were studied by Isshiki et al. [6] for the purpose of forming a uniformly thick falling film. Surfactants are also utilized to enhance mass transfer coefficient and wetting characteristics. The presence of surfactants causes local variation in the surface tension, which in turn induces turbulence at the liquid–vapor interface. Much research has been devoted to quantify and understand the effect of the surfactants [7–10].

Recently, Islam et al. [11] proposed a unique concept of periodically inverting the falling film while the liquid solution flows over the cooling surface. The liquid surface which was previously in contact with the cooled surface is directly exposed to the vapor by inverting the film. This design not only increases the mass flux but also induces mixing due to shear forces. However, the effective liquid–coolant surface area was reduced.

Another enhancement technique is the miniaturization of coolant sections. Very high heat transfer coefficients can be achieved for microchannels even in the laminar flow regime. It has shown promising improvements in application to heat transfer technology. In addition, the surface-to-volume ratio increases with the miniaturization of coolant sections, which provides larger falling film area. Garimella [12] proposed the application of small diameter coolant tubes in the falling film absorber. His group reported a high absorption heat duty (16 kW) in a compact microchannel absorber of size $0.178 \times 0.178 \times 0.508$ m^3 [13].

Goel and Goswami [14] proposed using a screen mesh/fabric stretched in between the small diameter horizontal tubes over which a liquid film can be easily formed. The schematics of the conventional horizontal tube type absorber and the addition of screen mesh over the design are shown in Figs. 1 and 2. The screen mesh will establish a double sided falling film rather then having liquid droplets in between the horizontal tubes. As the surface area of the droplets is much smaller than that of the falling film, the availability of a larger liquid–vapor contact area will lead to additional vapor absorption between the tubes. In addition to an increase in surface area, the mesh also enhances wetting conditions by preventing the coalescence of droplets on horizontal tubes. Fabrics have a natural tendency to soak liquid by capillary action, and this mechanism also helps in redistributing the liquid solution on the coolant tubes. The combined effect of increased

Contributed by the Heat Transfer Division of ASME for publication in the JOURNAL OF HEAT TRANSFER. Manuscript received September 16, 2005; final manuscript received May 26, 2006. Review conducted by Ramendra P. Roy.

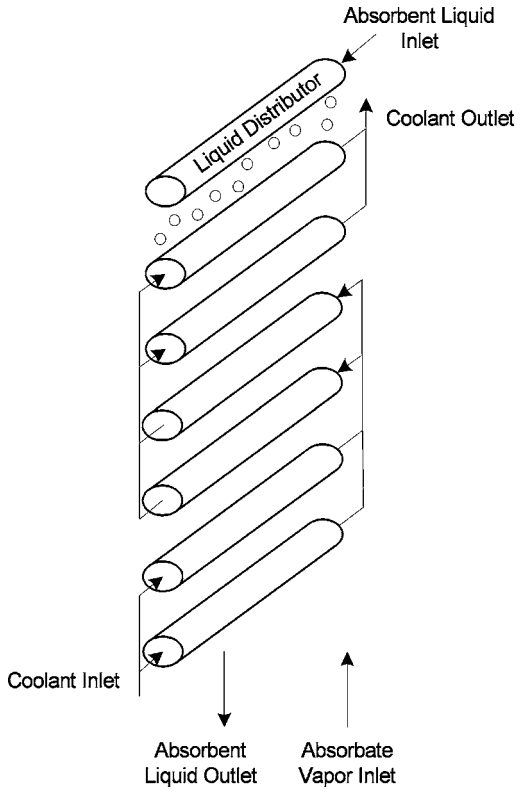

Fig. 1 Conventional horizontal tube type falling film absorber

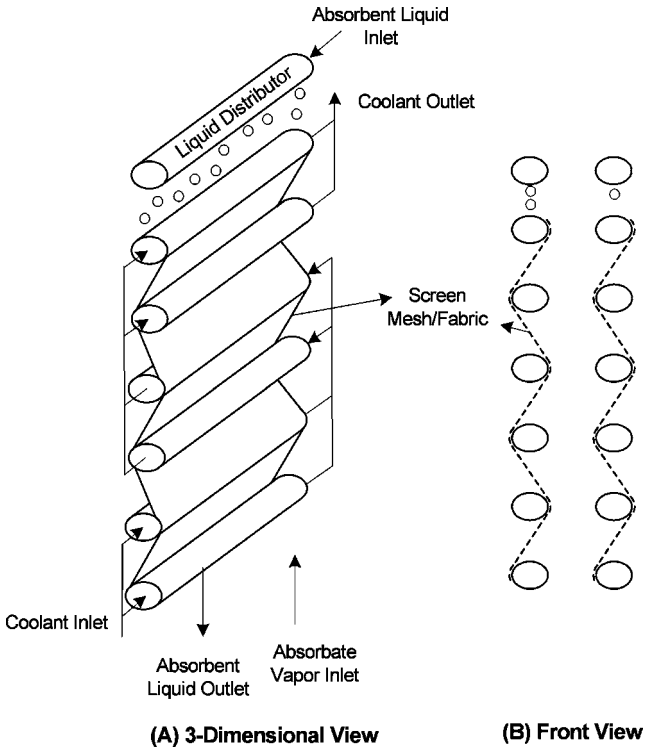

Fig. 2 Mesh-enhanced horizontal tube type falling film absorber

mass transfer area, and film stability will improve the absorption flux. Other phenomena associated with the new concept are the increase in liquid holdup and fineffect of the metallic mesh. These effects may also enhance the performance of a falling film absorber.

In this work, the effect of an aluminum screen mesh stretched between coolant tubes of a microchannel falling film absorber was experimentally investigated. As horizontal tube type absorbers with small diameter coolant tubes are very compact, this analysis will help in comparing the new concept with the current state-of-the-art absorber design.

Absorber Configuration

The coolant tubes used in this experimental study are stainless-steel tubing of 3.175 mm outer diameter and 0.4 mm wall thickness. The length of each horizontal tube is about 9.8 cm. The entire tube assembly consists of four columns each having 60 horizontal tubes with their ends brazed to stainless-steel headers of 12.7 mm outer diameter and 3 mm wall thickness. In a column, the tubes are connected in a parallel-series arrangement with 15 rows of tubes in parallel. The geometric dimensions of the coolant tube assembly are listed in Table 1. The entire tube assembly was fabricated in the laboratory by oxy-acetylene based nickel brazing. The top and bottom ends of all the four columns of tubular assembly are connected with manifolds to allow equal distribution of coolant between them. The coolant flows in cross-counter direction to the solution entering at the bottom and leaving at the top of the absorber. The instrumentation of coolant tube assembly to measure coolant temperature on a pass-by-pass basis was also considered. However, associated error in temperature measurements for pass-by-pass basis fails to provide any conclusive results. Thus, it was decided to measure the overall coolant temperature across the inlet and outlet coolant ports of the absorber. A thermopile assembly with an accuracy of $\pm 0.085^{\circ}$C was also installed between the inlet and outlet ports of coolant to accurately measure the temperature rise across the coolant loop.

The weak solution is distributed over the horizontal tubes by means of a drip tray arrangement. The drip tray has several perforations which are equidistant and located above the center axis of each column of horizontal tubes. It was made by punching a stainless-steel sheet, and the indentations/downward edges on the perforation caused by punching were not completely removed. However, the shape of the indentation was made uniform to prevent the coalescence of droplets from dripping through the tray. The drip tray and coolant tube assembly were screwed together to prevent any misalignment. In order to flow the entire amount of vapor over the horizontal tubes, the tubular assembly was enclosed in an aluminum case. The photographs of coolant assembly are shown in Fig. 3. The assembly was then housed in a pressure vessel of 15.24 cm inner diameter. A level gauge was also installed in the vessel to check the strong solution level in the absorber vessel. The level of strong solution was kept high enough to prevent the vapor from leaking through the bottom opening of the aluminum enclosure, whereas the top opening of the enclosure was open to the absorber vessel. The overall dimensions of the coolant assembly are approximately 6.35 cm $\times$ 12 cm $\times$ 63.5 cm, and the total surface area of the horizontal tubes is about 0.24 m^2.

Experiments were first conducted on the conventional microchannel absorber design, and then the same tubular assembly was modified by adding an aluminum woven wire mesh as described before, for the enhanced falling film experiments. The mesh had a

Table 1 Geometric dimensions of the coolant tube assembly

Tube outer diameter (mm)	3.175
Tube wall thickness (mm)	0.4
Tube material	316 stainless steel
Tube length (cm)	9.8
Number of tubes per row	4
Number of tube rows per pass	15
Tube vertical pitch (mm)	8
Tube traverse pitch (mm)	16

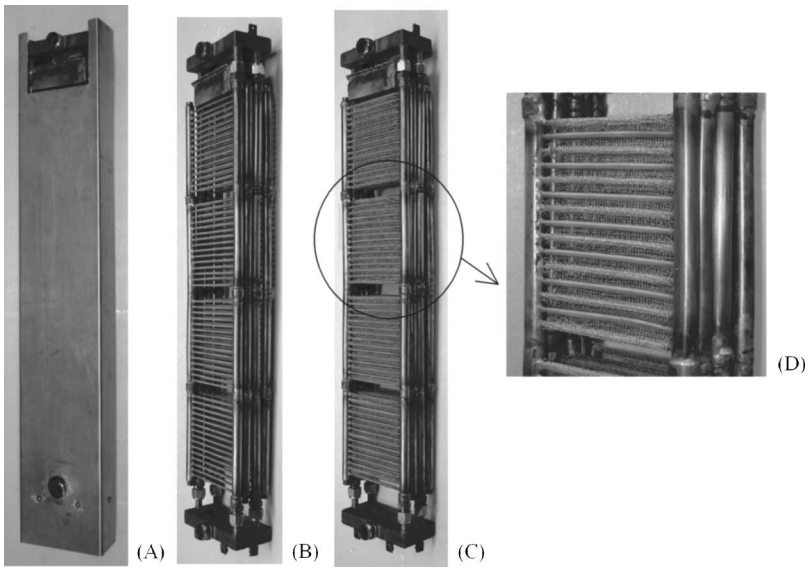

Fig. 3 Photographs of the coolant assembly: (*A*) external view of the tubular array housed in an aluminum casing; (*B*) internal view of the microchannel array; (*C*) internal view of the microchannel array with screen mesh; and (*D*) closer view of the screen mesh stretched in between the tubes

wire diameter of 0.2 mm with 16×16 meshes/in.^{2}. A close view of the screen mesh stretched in between the horizontal tubes is shown in Fig. 3. The wetting characteristics of the coolant tubes also play a major role in the formation of the falling film. The outer surface of the tubes was sand blasted to increase the roughness, and thereby wettability. The wetting characteristics of the aluminum mesh used in this study were enhanced by placing in hot water at about 80°C for a period of 30 min as recommended by Min and Webb [15].

Mathematical Model

A numerical model is developed to compare the performance of the mesh-enhanced microchannel absorber with the conventional microchannel absorber design. A detailed description of the mathematical model can be found in our previous paper [14]. The model is based on the application of continuity and energy balance at each differential segment of the absorber. It takes into account the mass transfer resistances in both the liquid and vapor phases, and uses empirical correlations to predict the heat and mass transfer coefficients. The model also considers the coupled nature of heat and mass transfer processes accompanying the falling-film absorption.

Goel and Goswami [14] considered the coolant-side heat transfer coefficient for a fully developed regime. However, it was found that developing laminar flow regime is present in current operating conditions. So, a modification was made to the empirical correlation of the coolant-side heat transfer coefficient. The correlation is based on the developing laminar flow conditions in the coolant tube, and the local Nusselt number for the uniform surface heat flux is of the form [16]

$$\frac{\mathrm{Nu}_D+1}{5.364[1+(\mathrm{Gz}/55)^{10/9}]^{3/10}}=\left(1+\left\{\frac{\mathrm{Gz}/28.8}{[1+(\mathrm{Pr}/0.0207)^{2/3}]^{1/2}[1+(\mathrm{Gz}/55)^{10/9}]^{3/5}}\right\}^{5/3}\right)^{3/10} \quad (1)$$

The mean value of Nusselt number for the coolant tube will be an average of local Nusselt number over the entire length of the tube.

Experimental Setup

A simplified schematic of the prototype of absorption cycle used in the experimental analysis is shown in Fig. 4 along with a representation of the various quantities that are measured. The

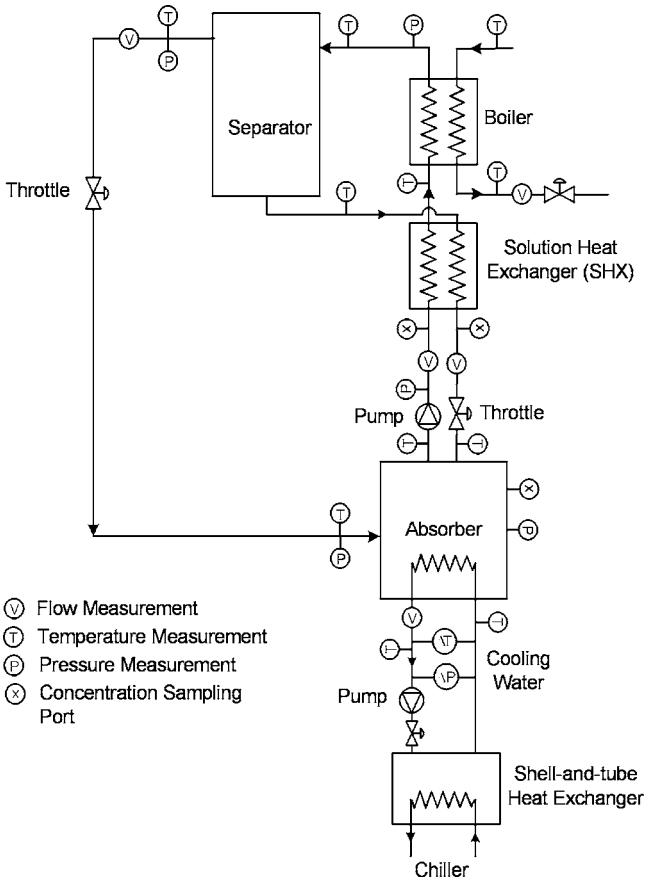

Fig. 4 Schematic of the experimental setup

strong solution is heated using hot water in a plate-type heat exchanger to produce the liquid–vapor mixture. The high pressure liquid–vapor mixture is subsequently brought into the separator. The low concentration ammonia solution is separated from the high concentration ammonia vapor by gravity, and settles at the bottom of the separator, while the vapor stream exits the separator and is adiabatically throttled by using a needle valve. The low-pressure vapor then flows into the absorber where it gets absorbed by the weak solution. The weak solution from the separator passes through the solution heat exchanger and then is throttled back to the absorber, where it is uniformly distributed on the outer surface of the horizontal coolant tubes. The vapor entering the absorber flows upward though the tubular assembly. The vapor and weak solution flow countercurrently leading to the absorption of vapor in the weak solution, thus forming the strong solution. The cooling water flows counter- and cross-currently to the falling film through small-diameter tubes. The absorption heat thus produced is rejected to the coolant to continue the absorption process. The cycle is completed by pumping back the strong solution through a rotary vane pump to the high-pressure side. Before entering the boiler, the strong solution recovers heat from the weak solution in a counter-current plate-type solution heat exchanger.

Water is circulated in a closed loop through the absorber coolant tubes to remove the heat of absorption. The temperature of the water entering the absorber in this loop is regulated using an external 50/50 mixture of ethylene glycol/water supply and a shell-and-tube heat exchanger installed in the cooling water loop. The cooling water flow is controlled by a centrifugal pump and a ball valve, whereas its temperature is controlled by varying the flow rate of a 50/50 mixture of ethylene glycol/water circulating across the chiller. The heat source for the test facility is a 5 kW electric water heater whose capacity is augmented by using phase change thermal energy storage. The thermal storage tank was pressurized to about 80 psig with city water, which allows the temperature of hot water to exceed 100°C. A centrifugal pump was used to circulate a controlled amount of hot water between thermal storage and plate type heat exchanger of the test facility. A ball valve was also installed between suction and discharge ports of the pump to control the amount of liquid flowing back into the pump, and thereby regulating the flow of hot water into the test facility.

Experimental Procedure and Analysis

The experimental analysis is primarily based on the conditions encountered in a single stage ammonia–water absorption system [17]. The experiments were first conducted on the conventional microchannel falling film absorber design. The experiments on the mesh-enhanced microchannel absorber were then conducted by stretching an aluminum screen mesh in the tubular array used in the conventional microchannel absorber. The temperature, vapor flow rate and pressure measurements were recorded through a PC-based data acquisition system. The initial warmup of the test facility and steady state operation required about 2 h. The occurrence of steady state was determined based on variation of measured values displayed from the data acquisition system, flow meters, and the level of strong solution in the absorber with time. Achievement of negligible change in the readings with respect to time was considered as the steady state condition. Measurements for each experiment were averaged values of the data recorded at a rate of 100 Hz for a period of 5 min. The experiments were repeated by re-establishing the operating conditions after a period of at least 6 h.

The analysis of both designs is based on the baseline conditions listed in Table 2. The weak solution flow rate and inlet coolant temperature were also individually varied to study their influence on the performance of both designs. The weak solution flow rate was varied from 11.1 g/s±0.424 g/s to 17.8 g/s±0.424 g/s, whereas the inlet temperature of the coolant was in the range of 20°C±0.5°C to 30°C±0.5°C. Limitations of the test facility necessitated a lower concentration (~96%) of the vapor entering the absorber in comparison to a commercial absorption system where vapor enters the absorber at >99.5%. The computational models developed by Goel and Goswami [18], Kim [19], and Perez-Blanco [20] predicted that the liquid-phase transfer resistance controls the overall mass transfer process. Thus, a slightly lower concentration of vapor phase will have a negligible effect in representing the performance of commercial absorption systems.

Table 2 Baseline experimental conditions of the conventional and mesh-enhanced microchannel absorber designs

Absorber pressure (bar)	2.81±0.02
Coolant medium	Water
	Absorber inlet conditions
Coolant mass flow rate (g/s)	88.7±1.7
Inlet coolant bulk temperature (K)	27.0±1.0
Weak solution mass flow rate (g/s)	14.46±0.424
Weak solution bulk temperature (°C)	43.0±1.0
Weak solution concentration (kg/kg)	0.30±0.015
Vapor bulk temperature (°C)	58.0±1.0
Vapor concentration (kg/kg)	0.956±0.004

The parameters selected to assess the performance of both designs are absorber heat duty, and product of the overall heat transfer coefficient and wetted-tube surface area. The absorber heat duty is the amount of heat rejected to the coolant in order to continue the vapor absorption into the weak solution at a steady state. Its value can be determined by conducting an energy balance across either the solution side or the coolant side of the absorber. At steady state the loss of energy by the solution side is equal to the gain in energy by the coolant side. The mass flow rate and enthalpy of each fluid stream exiting/entering the absorber are thus required to conduct an energy balance over the absorber.

The volumetric flow rates of the weak solution and vapor were measured by a rotameter and a turbine flow meter, respectively. The weak solution concentration was measured using a gas chromatograph, whereas the vapor concentration was determined by the application of vapor–liquid equilibrium correlations on the measured temperature and pressure of vapor stream. The liquid solution is extracted from the test facility through septum ports using a syringe. The syringe is cooled prior to the sampling to ensure liquid sample temperature remains below its bubble point. It should also be pumped a few times before drawing a liquid solution from the septum port to prevent any dead volume with the desired sample. The liquid sample is then transported to the gas chromatograph in a locked syringe. The syringe is finally cleaned with de-ionized water for the next sample. The measurements for the vapor stream were taken at the vapor exit of the separator section, which ensures that the vapor is at saturated equilibrium conditions. Thermodynamic property correlations were finally used to compute the density of liquid and vapor phases at the given temperature, pressure, and concentration. The enthalpies of the liquid and vapor streams were then estimated by thermodynamic property correlations. The heat duty of the absorber was calculated for both coolant and solution loops to confirm an energy balance between them.

The overall heat transfer coefficient U can be estimated from the given absorber heat duty, coolant tube wetted-surface area, and log mean temperature difference (LMTD) between the coolant and solution sides. The LMTD is based on the assumption of constant specific heat of both heat transfer fluids. However, in the case of absorbers, the specific heat of solution changes as it absorbs the vapor phase. The approach of estimating the overall heat transfer coefficient on the basis of LMTD is thus an approximation to a complex analysis. However, this approach has been widely used to present the performance of an absorber [21–23]. The wetted surface area of the coolant tube is unknown, and thereby the value of U cannot be reasonably estimated. Therefore, it was decided to estimate the value of UA, which represents the

Table 3 Experimental comparison of the conventional and mesh-enhanced microchannel absorber designs for the representative test at baseline operating conditions

	Mesh-enhanced microchannel absorber	Conventional microchannel absorber
Absorber heat duty (coolant side) (kW)	4.085±0.084	3.378±0.072
Absorber heat duty (solution side) (kW)	3.878±0.127	3.218±0.127
Overall heat transfer coefficient × wetted-tube surface area UA (W/K)	483±42	334±26
Absorber pressure (bar)	2.797±0.02	2.795±0.02
Weak solution mass flow rate (g/s)	14.461±0.424	14.450±0.424
Weak solution bulk temperature (°C)	43.3±0.5	43.7±0.5
Weak solution concentration (kg/kg)	0.298±0.015	0.302±0.015
Strong solution mass flow rate (g/s)	16.513±0.535	15.995±0.535
Strong solution bulk temperature (°C)	39.6±0.5	40.0±0.5
Strong solution concentration (kg/kg)	0.381±0.015	0.370±0.015
Vapor mass flow rate (g/s)	2.061±0.023	1.774±0.021
Vapor bulk temperature (°C)	59.4±0.5	57.1±0.5
Vapor concentration (kg/kg)	0.956±0.0018	0.959±0.0015

effective thermal performance of a falling film. The uncertainties in indirect measurements were also estimated to determine the confidence in the experimental results. It was estimated by ascertaining the sensitivity of various directly measured parameters through the perturbation method.

Experimental Results and Discussion

A comparison of both designs for a representative experiment conducted at the baseline operating conditions is presented in Table 3. The heat duties of both coolant and solution sides are within the estimated limits of error, which validates energy balance over both absorbers. The coolant side heat load for the mesh-enhanced microchannel absorber is 4.085 kW±0.084 kW, whereas the conventional microchannel absorber has a heat load of 3.378 kW±0.072 kW. The difference between the two designs is due to the inclusion of an aluminum mesh in the new microchannel absorber design. The experiments on both absorber designs were conducted on same coolant assembly with the same coolant flow rates, and thus all coolant side conditions for the two designs are the same. The presence of screen mesh increases the heat duty of the absorber by about 20.5% ±3.6% for the representative experiment considered. The higher heat load for the proposed design is primarily due to an increase in the mass transfer, area, and an enhancement in the turbulence, and wettability of the falling film. However, increase in the residence time of the liqui–vapor contact and heat conduction through the metallic screen mesh are some of the other reasons that cannot be neglected. The higher heat load of the proposed design can also be confirmed by the requirement of higher vapor flow rate. The mass flow rate and concentration measurements of the strong solution were also higher for the proposed design than the conventional microchannel absorber design. The value of *UA* is found to increase by more than 45% ±16.8% with the proposed design. It is not possible to conclude as to the exact reason for the observed results without more detailed experimental data as well as flow visualization. However, increased mixing and tube wetting due to the introduction of wire roughness over the coolant tubes are the possible reasons for this increase. Repetition of experiments at the same baseline operating conditions also provided similar results.

The influence of the weak solution flow rate and the coolant inlet temperature on both designs was also studied experimentally. These two parameters were alternatively varied for the baseline operating conditions listed in Table 2. The volumetric flow rate of weak solution was varied in the range of 0.2 gpm±0.00076 gpm to 0.32 gpm±0.00076 gpm with incremental steps of 0.02 g/min, which correspond to the variation in mass flow rate in between 11.1 g/s±0.424 g/s and 17.8 g/s± 0.424 g/s. The mass flow rate of weak solution is calculated after the application of density correlations to compute the density of liquid and vapor phases at the given temperature, pressure, and concentration.

Figure 5 illustrates the variation in absorber heat duty with weak solution flow rate. For the given operating conditions, the absorber heat duty of both designs increases as the weak solution flow rate is increased. It translates into higher vapor absorption rates with increasing weak solution flow rate. The enhancement in turbulence, mass transfer coefficients, and wetting characteristics with increasing flow rate causes higher vapor absorption rates [24]. The coolant side conditions were kept constant in these experiments, and it suggests that the absorption process in falling film absorber is controlled by the liquid mass transfer process. The computational models developed by Goel and Goswami [18], Kim [19], and Perez-Blanco [20] also predicted that the liquid-phase transfer resistance controls the overall mass transfer process. There is a consistent enhancement in absorber heat duty with the mesh-enhanced microchannel absorber. The heat load of the mesh-enhanced microchannel absorber is found to be about 17% ±3.4% –26% ±3.8% higher than the conventional microchannel absorber.

The effect of weak solution flow rate on *UA* (product of the overall heat transfer coefficient and wetted-tube surface area) is illustrated in Fig. 6. The value of *UA* is relatively constant over

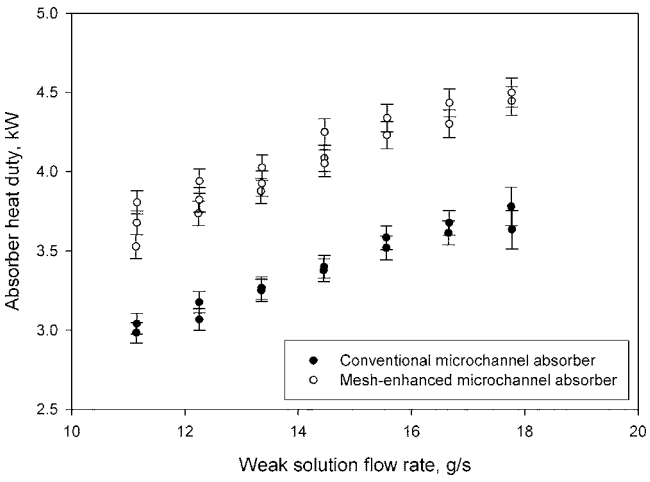

Fig. 5 Absorber heat duty with the variation in weak solution flow rate

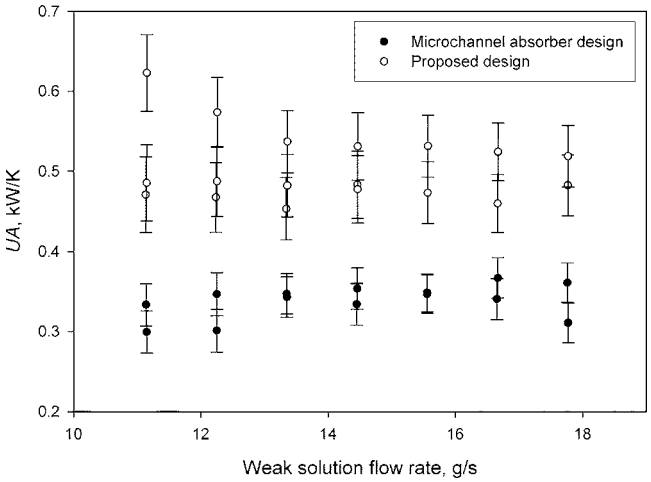

Fig. 6 Variation of *UA* with the weak solution flow rate

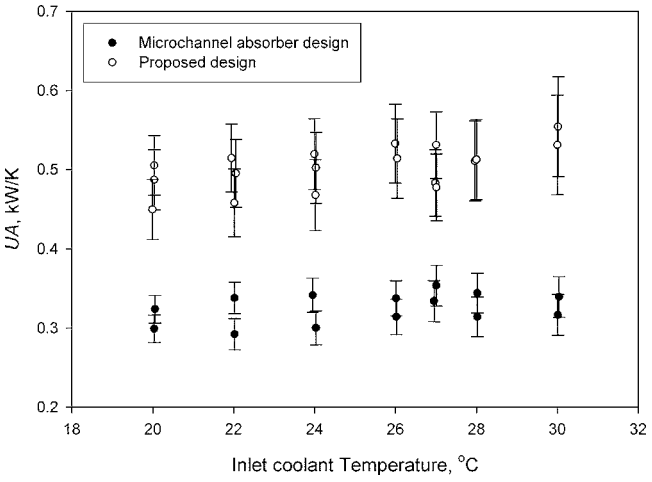

Fig. 8 Variation of *UA* with the inlet coolant temperature

the operating range of weak solution flow rate. Its average values are 0.34 kW/K and 0.5 kW/K, respectively, for the microchannel and proposed absorber designs. In the case of proposed design, some experiments at low weak solution flow rates (11.1 g/s±0.424g/s–12.25 g/s±0.424 g/s) show a relatively high value of *UA* 0.62 kW/K±0.048 kW/K, while other experiments at the same flow rates show lower value of *UA* 0.48 kW/K±0.048 kW/K. We do not have an explanation for these differences. However, our speculation is that the instability in wetting conditions at the low flow rates might have resulted in the large variation in values of *UA* for these experiments. The average increase in the *UA* value for the proposed design is about 49%±17% in comparison to the microchannel design for all the experiments conducted at various weak solution flow rates.

Figure 7 shows the effect of the inlet coolant temperature on the absorption capacity of both designs. The temperature range was selected as 20°C±0.5°C–30°C±0.5°C (68°F–86°F), which covers typical thermal conditions for the cooling towers. As expected, a decrease in the inlet coolant temperature results in an increase in the absorber heat duty for both designs. The effect is very prominent and can be utilized in places where the option of lower inlet coolant temperature is viable. The absorber heat duty of the proposed design is consistently higher (17%±3.4%–25%±3.7%) than the microchannel absorber design. The variation of *UA* with the coolant inlet temperature is shown in Fig. 8. The value of *UA* is essentially not affected by the coolant temperature. Its average values are 0.32 kW/K and 0.5 kW/K, respectively, for the microchannel and proposed absorber designs. A consistent enhancement in *UA* was noticed with the introduction of the metallic screen mesh. The average increase in the *UA* value for the proposed design is found to be about 55%±18% higher in comparison to the microchannel design.

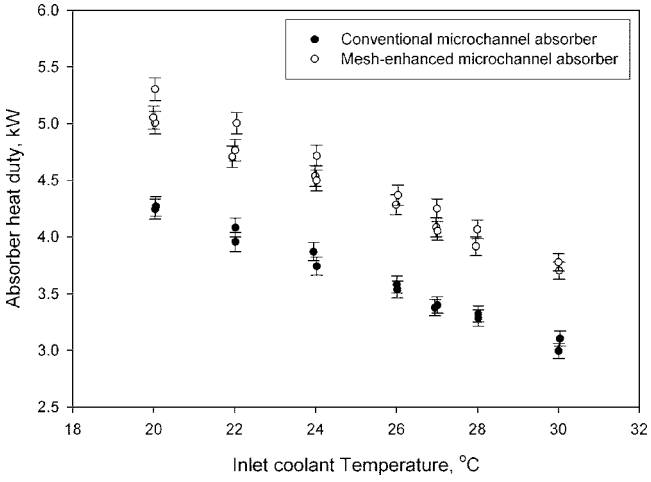

Fig. 7 Absorber heat duty with the variation in inlet coolant temperature

Comparison of Numerical and Experimental Analysis

As described earlier, the experimental analysis was performed on the conventional and mesh-enhanced microchannel absorber designs. The coolant assembly consists of a fixed number of 240 horizontal small-diameter tubes, which was created by stacking four columns of 60 tubes each. The experiments were conducted at various inlet coolant temperatures, and weak solution flow rates. For each experiment, the vapor flow rate was varied until a pressure of about 2.81 bar was achieved in the absorber vessel. The given absorber size was thus sufficient to accomplish complete vapor absorption at the corresponding experimental conditions.

A finite difference numerical model was developed to predict the minimum absorber size needed to accomplish complete absorption in both designs. A comparison between numerical and experimental results was then performed to determine the validity of the numerical model. Numerical simulations were run for each experiment to find the theoretical minimum number of rows of tubes needed to accomplish complete absorption. The input parameters of the numerical simulation were obtained from the corresponding experiment which includes temperature, pressure, concentration, and flow rates of the weak solution, vapor, and coolant. The predicted number of rows was then compared with the actual number of rows used in the experimental analysis.

An assessment of the uncertainty associated with the numerical analysis is also required when a comparison between experimental and numerical results is done. The major reasons for deviation include the errors in the theoretical representation of a physical phenomenon, the errors in their numerical implementation, and the uncertainty of the input parameters of the numerical analysis. The errors in numerical implementation are primarily due to the mathematical approximation of a three-dimensional system with a one-dimensional analysis at a set of discrete locations in space, and the roundoff error from the computer. An uncertainty analysis was performed on the numerical model to account the effect of the uncertainty of the input parameters. The measured experimental values of temperature, pressure, concentration, and flow rates of weak solution, vapor, and coolant are input into the numerical model. Thus, uncertainties in these measurement results in uncer-

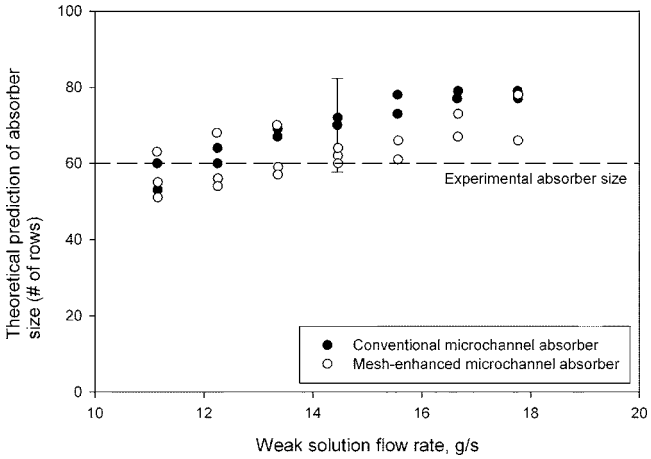

Fig. 9 Comparison of numerical and experimental results for the variation in weak solution flow rate

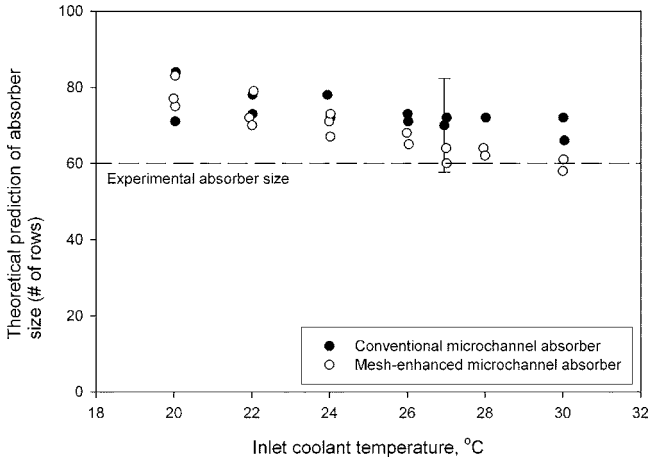

Fig. 10 Comparison of numerical and experimental results for the variation in inlet coolant temperature

tainty in the numerical results. The dimensional parameters are also the input in the numerical model. However, the uncertainties in dimensional parameters are quite small, and their effect on the overall uncertainty in predicting the absorber size is negligible. Perturbation method was used to estimate the sensitivity of predicted number of rows to uncertainties in various input parameters. The uncertainty in the prediction of absorber size for a representative test at the baseline conditions was estimated to be ±12.3 rows of tubes for both designs.

Figures 9 and 10 show the deviation of the size predicted by the numerical model from the actual absorber size in the experimental investigation. The numerical and experimental results compare well with some deviation at low temperature of coolant and high flow rate of weak solution. If an uncertainty of ±12.3 rows of tubes is assumed to hold for all the experiments conducted for various weak solution flow rates and coolant inlet temperatures, 58% and 79% of the total experiments on conventional and mesh-enhanced microchannel absorber designs, respectively, show a good agreement with the experimental results. The standard deviation of numerical predictions from experimental absorber size is about eight and seven tube rows for conventional and mesh-enhanced microchannel absorber designs, respectively at various weak solution flow rates. In the case of varying coolant inlet temperature, its value is about four and seven tube rows for conventional and mesh-enhanced microchannel absorber designs, respectively.

As shown in Figs. 9 and 10, the numerical model mostly overpredicts the size for both designs. This trend is more pronounced in the case of the conventional microchannel absorber than the mesh-enhanced microchannel absorber. This trend is expected as the current numerical analysis completely neglects the adiabatic absorption of vapor that takes place between the horizontal tubes of the microchannel absorber. The transfer of weak solution between the horizontal tubes of the conventional microchannel absorber occurs in the form of droplets, and the surfaces of these newly formed droplets provide extra areas for vapor absorption.

The over prediction of absorber size in the case of mesh-enhanced microchannel absorber design may be largely due to the non consideration of heat conduction from the coolant tubes to the metallic mesh in the numerical model. The screen mesh used in this experimental investigation is made of aluminum, which is a highly thermally conductive material with conductivity of about 200 W/m K. As the screen mesh is mechanically stretched around the horizontal tubes, the thermal resistance between the coolant tubes and screen mesh was assumed to be very large, and thus heat conduction was neglected in the numerical analysis. However, the metallic screen mesh can dissipate heat through conduction by acting as a fin.

There is also a visible trend in the deviation between the predicted and the actual sizes with the variation of the weak solution flow rate. As the flow rate of weak solution is increased, the deviation of the numerical model increases in the positive direction for both designs. The correlation used to estimate the heat transfer coefficient of a falling film, and the assumption of complete wetting conditions can lead us to the possible explanation behind this trend. The correlation used for estimating the falling heat transfer coefficient [25] is based on simple convective heating of a laminar falling film over the vertical flat plates. The unavailability of the correlation for the falling film over horizontal tubes led to the use of the heat transfer correlation for wetted wall columns. The correlation predicts a decrease in the falling film heat transfer coefficient with the increase in the flow rate of the falling film. The assumption of complete wetting of the coolant tubes will therefore cause a decrease in the *UA* product with an increase in the flow rate of the falling film. However, the experimental results for *UA* show that its value is unaffected by the weak solution flow rate. This discrepancy is due to the estimation of falling film heat transfer coefficient and assumption of complete wetting conditions of the falling film, which can lead to an over-prediction of the absorber size with the increase in the weak solution flow rate.

As evident from Fig. 10, a similar increase in the extent of over prediction of the absorber size is observed with a decrease in the inlet temperature of the coolant stream. A reason behind this deviation is unknown. The coolant tubes are brazed to stainless steel headers of 12.7 mm outer diameter and 3 mm wall thickness. The headers in the current experimental study were not insulated. The heat transfer due to forced convection between the metallic header and vapor was neglected in the numerical model, which could be a possible reason behind the increase in over prediction of absorber size with the decrease in inlet coolant temperature.

Conclusion

The experimental verification of a new concept of forming a falling film in between the horizontal coolant tubes by a flow guidance medium like a screen mesh/fabric is presented. The design utilizes the unused vertical spacing between the coolant tubes to form a double sided falling film which consequently leads to an increase in the mass transfer area. The experiments conducted on the conventional and mesh-enhanced microchannel absorbers shows that the absorber heat load of the mesh-enhanced microchannel absorber design is about 17% ±3.4% –26% ±3.8% higher than the conventional microchannel design. The *UA* value is found to increase by about 50% ±17% with the introduction of the screen mesh. This is attributable to the fact that the screen mesh enhances both mass transfer area and wetting conditions of

the liquid film. Some other phenomena associated with the mesh-enhanced microchannel absorber design are the increase in liquid holdup, improvement of wetting characteristics, prevention of satellite droplets, and fineffect of the metallic mesh. These effects may also contribute in enhancing the performance of the new absorber design. Comparison between the experimental and the numerical results shows a good agreement. The results further shows the effect of satellite droplets is insignificant in comparison to the effect of forming double sided falling film in between the tubes. However, a detailed experimental is required to study the importance of satellite droplets.

Nomenclature

b^+ = dimensionless position for developing flow, $b/(D_I \mathrm{Re}_{D_I} \mathrm{Pr})$
b = axial coordinate, m
C_P = specific heat, kJ/kg K
D = diameter of the coolant tube, m
Gz = Graetz number, $\pi/(4b^+)$
h = heat transfer coefficient, $\mathrm{kW/m^2\,K}$
k = thermal conductivity, W/m K
Nu_D = Nusselt number, hD_I/k
Pr = Prandtl number, $\mu C_p/k$
Re_{D_I} = Reynolds number for flow in the coolant tube, $\rho u D_I/\mu$
U = Overall heat transfer coefficient in the path of heat flow between the weak solution and coolant, $\mathrm{kW/m^2\,K}$
UA = product of the overall heat transfer coefficient and wetted-tube surface area, kW/K
u = Velocity, m/s

Greek Symbols

μ = dynamic viscosity, kg/m s
ρ = density, $\mathrm{kg/m^3}$

Subscripts

C = coolant
I = inside

References

[1] Killion, J. D., and Garimella, S., 2001, "A Critical Review of Models of Coupled Heat and Mass Transfer in Falling-Film Absorption," Int. J. Refrig., **24**, pp. 755–797.
[2] Yang, R., and Jou, D., 1995, "Heat and Mass Transfer of Absorption Process for the Falling Film Flow Inside a Porous Medium," Int. J. Heat Mass Transfer, **38**, pp. 1121–1126.
[3] Benzeguir, B., Setterwall, F., and Uddholm, H., 1991, "Use of a Wave Model to Evaluate Falling Film Absorber Efficiency," Int. J. Refrig., **14**, pp. 292–296.
[4] Miller, W. A., and Perez-Blanco, H., 1993, "Vertical-Tube Aqueous LiBr Falling Film Absorption Using Advanced Surfaces," *Proceedings ASME Transaction of International Absorption Heat Pump Conference*, Vol. 31, ASME, New York, pp. 185–202.
[5] Schwarzer, B., Rahbar, M. S., and LeGoff, P., 1993, "A Novel Type of Falling Film Heat and Mass Exchanger," *Proceedings ASME Transaction of International Absorption Heat Pump Conference*, Vol. 31, ASME, New York, pp. 179–183.
[6] Isshiki, N., Ogaka, K., and Sasaki, K., 1988, "Studies on Mechanism and Enhancement of Absorption Heat and Mass Transfer," *Absorption Heat Pumps, Proceedings of Workshop by Commission of the European Communities*, Luxembourg, pp. 399–408.
[7] Kashiwagi, T., 1988, "Basic Mechanism of Absorption Heat and Mass Transfer Enhancement by the Marangoni Effect," Newsletter, IEA Heat Pump Center, 6, pp. 2–6.
[8] Hozawa, M., Inoue, M., Sato, J., and Tsukada, T., 1991, "Marangoni Convection During Steam Absorption Into Aqueous LiBr Solution with Surfactant," J. Chem. Eng. Jpn., **24**, pp. 209–214.
[9] Kim, K. J., Berman, N. S., and Wood, B. D., 1996, "The Interfacial Turbulence in Falling Film Absorption: Effects of Additives," Int. J. Refrig., **19**, pp. 322–330.
[10] Kulankara, S., and Herold, K. E., 2000, "Theory of Heat/Mass Transfer Additives in Absorption Chillers," HVAC&R Res., **6**, pp. 369–380.
[11] Islam, R. Md., Wijeysundera, N. E., and Ho, J. C., 2003, "Performance Study of a Falling-Film Absorber with a Film-Inverting Configuration," Int. J. Refrig., **26**, pp. 909–917.
[12] Garimella, S., 2000, "Microchannel Components for Absorption Space-Conditioning Systems," ASHRAE Trans., **106**, pp. 453–462.
[13] Meacham, J. M., and Garimella, S., 2003, "Modeling of Local Measured Heat and Mass Transfer Variations in a Microchannel Ammonia-Water Absorber," ASHRAE Trans., **109**, pp. 412–422.
[14] Goel, N., and Goswami, D. Y., 2005, "A Compact Falling Absorber," J. Heat Transfer, **127**, pp. 957–965.
[15] Min, J., and Webb, R. L., 2002, "Long-Term Wetting and Corrosion Characteristics of Hot Water Treated Aluminum and Copper Fin Stocks," Int. J. Refrig., **25**, pp. 1054–1061.
[16] Churchill, S. W., and Ozoe, H., 1973, "Correlations for Laminar Forced Convection with Uniform Heating in Flow Over a Plate and in Developing and Fully Developed Flow in a Tube," ASME J. Heat Transfer, **95**, pp. 78–84.
[17] Herold, K. E., Radermacher, R., and Klein, S. A., 1996, *Absorption Chillers and Heat Pumps*, CRC Press, New York.
[18] Goel, N., and Goswami, D. Y., 2005, "Analysis of a Counter-Current Vapor Flow Absorber," Int. J. Heat Mass Transfer, **48**, 1283–1292.
[19] Kim, B., 1998, "Heat and Mass Transfer in a Falling Film Absorber of Ammonia-Water Absorption Systems," Heat Transfer Eng., **19**, pp. 53–63.
[20] Perez-Blanco, H. A., 1988, "A Model of an Ammonia-Water Falling Film Absorber," ASHRAE Trans., **94**, pp. 467–483.
[21] Lee, K. B., Chun, B. H., Lee, J. C., Hyun, J. C., and Kim, S. H., 2002, "Comparison of Heat and Mass Transfer in Falling Film and Bubble Absorbers of Ammonia-Water," Exp. Heat Transfer, **15**, pp. 191–205.
[22] Sujatha, K. S., 1999, "Experiments on a Bubble Absorber," Int. Commun. Heat Mass Transfer, **26**, pp. 975–984.
[23] Jeong, S., Lee, S. K., and Koo, K., 1998, "Heat Transfer Performance of a Coiled Tube Absorber with Working Fluid of Ammonia/Water," ASHRAE Trans., **104**, pp. 1577–1583.
[24] Killion, J. D., and Garimella, S., 2003, "A Review of Experimental Investigations of Absorption of Water Vapor in Liquid Films Falling Over Horizontal Tubes," HVAC&R Res., **9**, pp. 111–136.
[25] Yih, S. M., 1986, "Modeling Heat and Mass Transport in Falling Liquid Films," *Handbook of Heat and Mass Transfer: Mass Transfer and Reactor Design*, N. P. Cheremisinoff, ed., Gulf Publishing Company, Houston, TX, pp. 111–120.

Mixed Convection in a Vertical Parallel Plate Microchannel

Mete Avcı

Orhan Aydın[1]
e-mail: oaydin@ktu.edu.tr

Department of Mechanical Engineering,
Karadeniz Technical University,
61080 Trabzon, Turkey

In this study, fully developed mixed convective heat transfer of a Newtonian fluid in an open-ended vertical parallel plate microchannel is analytically investigated by taking the velocity slip and the temperature jump at the wall into account. The effects of the mixed convection parameter, Gr/Re, the Knudsen number, Kn, and the ratio of wall temperature difference, r_T, on the microchannel hydrodynamic and thermal behaviors are determined. Finally, a $\mathrm{Nu}=f(\mathrm{Gr}/\mathrm{Re},\mathrm{Kn},r_T)$ *expression is developed.* [DOI: 10.1115/1.2422741]

Keywords: microfluidics, vertical microchannel, mixed convection, temperature jump, velocity slip

1 Introduction

The microfluidics have attracted an important research interest in recent years due to the rapid growth of novel techniques applied in microelectromechanical systems (MEMS) and biomedical applications such as drug delivery, DNA sequencing, and bio-MEMS. Readers are referred to see recent excellent reviews related to transport phenomena in microchannels by Ho and Tai [1], Palm [2], Sobhan and Garimella [3], Obot [4], Rostami et al. [5,6], Gad-el-Hak [7], Guo and Li [8,9], and Morini [10].

Aydin and Avci [11–14] theoretically studied forced convective heat transfer in two different microgeometries, mainly microtube and microduct between two parallel plates, both for the fully developed and for the developing cases.

Although there are many studies on forced convection in microchannels, there are only a few studies regarding natural or mixed convection. In a recent study, Chen and Weng [15] analytically studied the fully developed natural convection in an open-ended vertical parallel plate microchannel with asymmetric wall temperature distributions. The effects of rarefaction and fluid–wall interaction were shown to increase the volume flow and to decrease the heat transfer rate. Khadrawi et al. [16] analytically investigated the transient hydrodynamics and thermal behaviors of fluid flow in an open-ended vertical parallel-plate microchannel under the effect of the hyperbolic heat conduction model. Haddad et al. [17] numerically investigated the developing hydrodynamical behaviors of free convection gas flow in a vertical open-ended parallel-plate microchannel filled with porous media.

The purpose of the present study is to analytically investigate mixed convection of rarefied gas in a vertical asymmetrically heated microchannel between two parallel plates. To the authors' best knowledge, this is the first study on mixed convection in microchannels. The effects of the mixed convection parameter, Gr/Re, the Knudsen number, Kn, and the ratio of wall temperature difference, r_T, on the temperature profile and subsequently on the Nusselt number are determined.

2 Analysis

Consider internal mixed convection in a microchannel between two parallel plates held at different uniform temperatures as shown in Fig. 1. The flow is assumed to be fully developed both hydrodynamically and thermally. Steady, laminar flow having constant properties is considered. The axial heat conduction in the fluid and in the wall is assumed to be negligible. It is shown that fluid flow and heat transfer at microscale differ greatly from those at macroscale. At macroscale, classical conservation equations are successfully coupled with the corresponding wall boundary conditions, usual no slip for the hydrodynamic boundary condition, and no-temperature jump for the thermal boundary condition. These two boundary conditions are valid only if the fluid flow adjacent to the surface is in thermal equilibrium. However, they are not valid for gas flow at microscale. For this case, the gas no longer reaches the velocity or the temperature of the surface and therefore a slip condition for the velocity and a jump condition for the temperature should be adopted. In this study, the usual continuum approach is coupled with the two main characteristics of the microscale phenomena, the velocity slip and the temperature jump. Velocity slip is defined as [18]

$$u_s = -\frac{2-F}{F}\lambda \left.\frac{\partial u}{\partial y}\right|_{y=W} \tag{1}$$

where u_s is the slip velocity; λ is the molecular mean free path; and F is the tangential momentum accommodation coefficient, and the temperature jump is defined as [18]

$$T_s - T_w = -\frac{2-F_t}{F_t}\frac{2\gamma}{\gamma+1}\frac{\lambda}{\mathrm{Pr}} \left.\frac{\partial T}{\partial y}\right|_{y=W} \tag{2}$$

where T_s is the temperature of the gas at the wall; T_w is the wall temperature; and F_t is the thermal accommodation coefficient. For the rest of the analysis, F and F_t will be shown by F and assumed to be 1.

In a sufficient long channel, the velocity and the temperature profiles will cease to change with distance along the channel, i.e., a fully developed flow will exist [19]. Assuming hydrodynamically fully developed flow, the transverse velocity v becomes equal to zero. Then, the continuity equation drops to $\partial u/\partial x = 0$. Using the Boussinesq approximation, ignoring viscous dissipation (assuming a low speed flow of a low Pr fluid [15]), and substituting the above condition into the governing equations of the heat and fluid flow, we obtain

$$0 = -\frac{dp}{dx} + \mu\frac{\partial^2 u}{\partial y^2} \pm \beta g\rho(T - T_0) \tag{3}$$

$$u\frac{\partial T}{\partial x} = \left(\frac{k}{\rho c_p}\right)\frac{\partial^2 T}{\partial y^2} \tag{4}$$

The pressure, p, is thus measured relative to that which would exist at the same elevation in the stagnant fluid if it were at a uniform temperature of T_0. The positive sign in front of the buoyancy term applies to the buoyancy-assisted flow and the negative one applying to the buoyancy-opposed flow [20].

The boundary conditions for these equations are

[1]Corresponding author.

Contributed by the Heat Transfer Division of ASME for publication in the JOURNAL OF HEAT TRANSFER. Manuscript received February 16, 2006; final manuscript received April 19, 2006. Review conducted by Gautam Biswas.

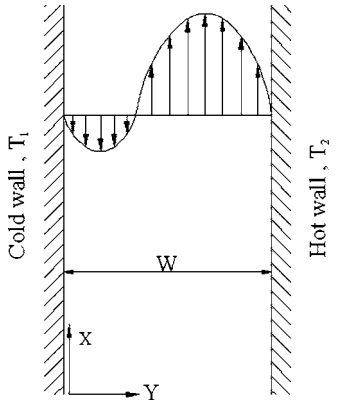

Fig. 1 Schematic diagram of the flow domain

$$u = u_{s1} \quad \text{at } y = 0$$

$$u = u_{s2} \quad \text{at } y = W$$

$$T = T_{s1} \quad \text{at } y = 0$$

$$T = T_{s2} \quad \text{at } y = W \tag{5}$$

By introducing the following nondimensional quantities

$$Y = \frac{y}{W}, \quad \theta = \frac{T - T_0}{T_2 - T_0}, \quad U = \frac{u}{u_0}, \quad \mathrm{Kn} = \frac{\lambda}{W},$$

$$\beta_v = \frac{2 - F}{F}, \quad \beta_t = \frac{2 - F_t}{F_t}\frac{2\gamma}{\gamma + 1}\frac{1}{\mathrm{Pr}}$$

$$X = \frac{x}{\mathrm{Re}\, W}, \quad P = \frac{p}{\rho u_0^2}, \quad \mathrm{Gr} = \frac{\beta g (T_2 - T_0) W^3}{\upsilon^2}, \quad \mathrm{Re} = \frac{u_0 W}{\upsilon} \tag{6}$$

Eqs. (3) and (4) can be written as

$$0 = -\frac{dP}{dX} + \frac{d^2U}{dY^2} + \frac{\mathrm{Gr}}{\mathrm{Re}}\theta \tag{7}$$

$$0 = \frac{d^2\theta}{dY^2} \tag{8}$$

Note that the term on the left-hand side of Eq. (4) is dropped since the fully developed temperature profile is characterized by $\partial\theta/\partial X = 0$ [15,19].

In terms of the dimensionless variables introduced in Eq. (6), the boundary conditions given in Eq. (5) can be shown as

$$U = \beta_v\, \mathrm{Kn}\frac{dU}{dY} \quad \text{at } Y = 0$$

$$U = -\beta_v\, \mathrm{Kn}\frac{dU}{dY} \quad \text{at } Y = 1$$

$$\theta = \frac{T_{s1} - T_0}{T_2 - T_0} = r_T + \beta_T\, \mathrm{Kn}\frac{d\theta}{dY} \quad \text{at } Y = 0$$

$$\theta = \frac{T_{s2} - T_0}{T_2 - T_0} = 1 - \beta_T\, \mathrm{Kn}\frac{d\theta}{dY} \quad \text{at } Y = 1 \tag{9}$$

where

$$r_T = \frac{T_1 - T_0}{T_2 - T_0} \tag{10}$$

Equation (8) indicates that the dimensionless temperature varies linearly across the duct. Integrating Eq. (8) and applying the boundary conditions gives

$$\theta = A_0 + A_1 Y \tag{11}$$

where A_0 and A_1 are

$$A_0 = r_T + \frac{(1 - r_T)\beta_T\, \mathrm{Kn}}{(1 + 2\beta_T\, \mathrm{Kn})}, \quad A_1 = \frac{1 - r_T}{1 + 2\beta_T\, \mathrm{Kn}} \tag{12}$$

Substituting Eq. (11) into the momentum equation, Eq. (7) gives

$$U = -\frac{\mathrm{Gr}}{\mathrm{Re}}\left(A_0\frac{Y^2}{2} + A_1\frac{Y^3}{6}\right) + \frac{dP}{dX}\frac{Y^2}{2} + A_2 Y + A_3 \tag{13}$$

where A_2 and A_3 are

$$A_2 = \frac{-\dfrac{\mathrm{Gr}}{\mathrm{Re}}\dfrac{A_1}{4}\left(\beta_v\, \mathrm{Kn} + \dfrac{1}{6}\right) + 3(1 + 2\beta_v\, \mathrm{Kn})}{\dfrac{1}{2} + 4\beta_v\, \mathrm{Kn} + 6\beta_v^2\, \mathrm{Kn}^2},$$

$$A_3 = \frac{-\dfrac{\mathrm{Gr}}{\mathrm{Re}}\dfrac{A_1}{4}\left(\beta_v\, \mathrm{Kn} + \dfrac{1}{6}\right) + 3(1 + 2\beta_v\, \mathrm{Kn})}{4 + \dfrac{1}{2\beta_v\, \mathrm{Kn}} + 6\beta_v\, \mathrm{Kn}} \tag{14}$$

At any cross section in the channel, the dimensionless mean velocity, U_m, can be written as

$$U_m = \int_0^1 U\, dY = 1 \tag{15}$$

Substituting Eq. (13) into this equation then gives

$$\frac{dP}{dX} = \frac{\mathrm{Gr}}{\mathrm{Re}}\left(A_0 + \frac{A_1}{4}\right) - 3A_2 - 6A_3 + 6 \tag{16}$$

Substituting Eq. (16) back into Eq. (13) gives

$$U = -\frac{\mathrm{Gr}\, A_1}{\mathrm{Re}}\left(\frac{Y^3}{6} - \frac{Y^2}{8}\right) - A_2\left(\frac{3Y^2}{2} - Y\right) - A_3(3Y^2 - 1) + 3Y^2 \tag{17}$$

The dimensionless mean/bulk temperature is defined as

$$\theta_m = \frac{\displaystyle\int_0^1 U\theta\, dY}{\displaystyle\int_0^1 U\, dY} \tag{18}$$

Substituting Eqs. (11) and (17) into the above equation, Eq. (18) gives

$$\theta_m = \frac{T_m - T_0}{T_2 - T_0} = A_0 + A_1\left(-\frac{\mathrm{Gr}}{\mathrm{Re}}\frac{A_1}{480} - \frac{A_2}{24} - \frac{A_3}{4} + \frac{3}{4}\right) \tag{19}$$

The convective heat transfer coefficient is given as follows

$$h = \frac{-k\left.\dfrac{\partial T}{\partial y}\right|_{y=W}}{T_2 - T_m} = \frac{-\dfrac{k}{W}\left.\dfrac{\partial\theta}{\partial Y}\right|_{Y=1}}{1 - \theta_m} \tag{20}$$

which is obtained from the following Nusselt number

$$\mathrm{Nu} = -\frac{A_1}{1 - \left[A_0 + A_1\left(-\dfrac{\mathrm{Gr}}{\mathrm{Re}}\dfrac{A_1}{480} - \dfrac{A_2}{24} - \dfrac{A_3}{4} + \dfrac{3}{4}\right)\right]} \tag{21}$$

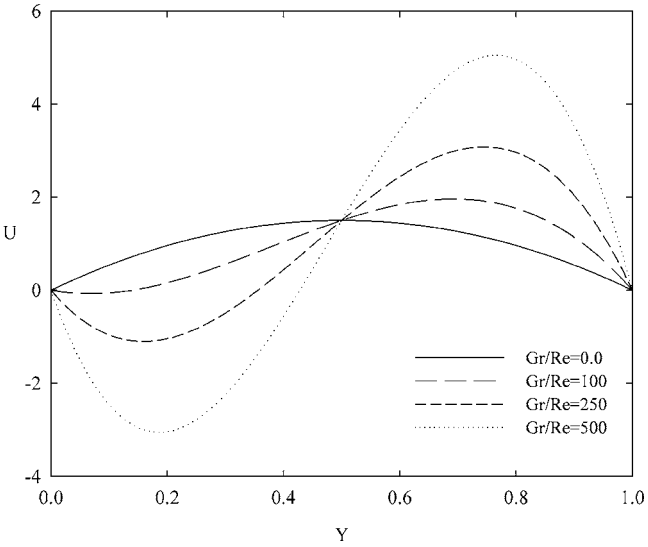

Fig. 2 Velocity distribution as a function Gr/Re for Kn=0 and r_T=0

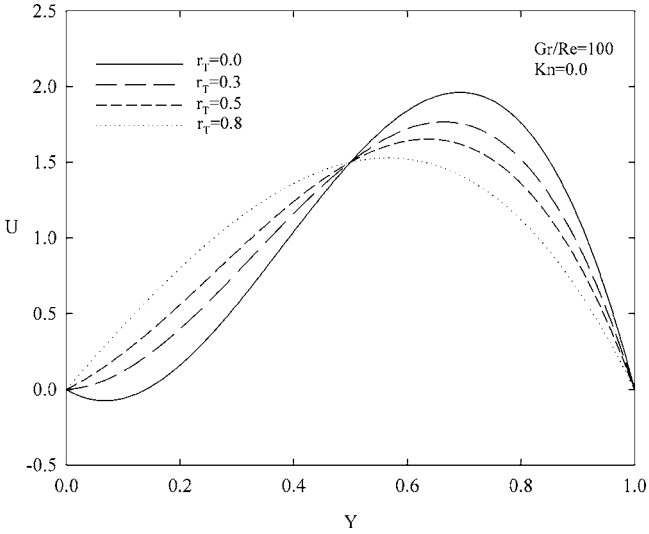

Fig. 3 Velocity distribution as a function r_T for Kn=0 and Gr/Re=100

3 Results and Discussion

In this study, we investigate the interactive effects of the mixed convection number, Gr/Re, the Knudsen number, Kn, and the ratio of wall temperature difference, r_T, on heat and fluid flow in a microchannel between two parallel plates with asymmetrical heating for both hydrodynamically and thermally fully developed cases. The Knudsen number, Kn, is the ratio of the gas mean free path, λ, to the characteristic dimension in the flow field, W, and, it determines the degree of rarefaction and the degree of the validity of the continuum approach. As Kn increases, rarefaction become more important, and eventually the continuum approach breaksdown. In this study, we examined Knudsen number values in the range of $0 \leqslant \mathrm{Kn} \leqslant 0.1$. In the range of $0.001 \leqslant \mathrm{Kn} \leqslant 0.1$, the slip-flow regime (slightly rarefied) is disclosed to exist [11]. We covered the following values of the mixed convection parameter: Gr/Re=0, 100, 250, and 500.

As it is mentioned earlier, the Boussinesq approximation has been used in this study. It should be noted here that there are two separate groups in the existing literature on the consideration of density gradient in the flow field [21]. For example, in the rarefied gas, Chen and Weng [15] assumed the Boussinesq approximation is valid while Tzeng and Liu [22] reported that it is not.

At first, we validated our analysis by comparing two limiting results with those available in the existing literature. For Kn=0, the velocity and temperature distributions given in Eqs. (17) and (11) are exactly identical to those given by Aung and Worku [19]. For the microscale case, Eq. (13) represents the free convection flow when dP/dX is zero. The velocity distribution obtained for this free convection case is exactly the same as that given by Chen and Weng [15].

At Kn=0, representing the macroscale or the continuum case, Fig. 2 shows the streamwise velocity profile for different values of Gr/Re. Increasing Gr/Re results in the increasingly skewed velocity profiles as observed by Aung and Worku [19]. At Gr/Re=0, there is only forced convection flow with axisymmetrical velocity profile. The buoyancy establishes an upward free convection flow near the hot wall and a downward one near the cold wall. In the mixed convection case, the natural convection currents superimpose on the forced convection flow. Therefore, in the right half of the microchannel, the hot side, the buoyancy has an aiding effect on the forced flow, while having an opposing effect in the left half of the microchannel, the cold side. With an increase at Gr/Re, both the velocities and the velocity gradient near the hot wall increase. However, near the cold wall, increasing Gr/Re leads to decreased velocities. For larger values of Gr/Re, there exists a reversed flow region with negative velocity values. Further increase at Gr/Re broadens this reversed flow region. The limiting value of Gr/Re leading to the flow reversal can be found by setting

$$\left(\frac{dU}{dY}\right)_{Y=0} < 0 \tag{22}$$

Applying this condition to Eq. (17), we obtain

$$\frac{\mathrm{Gr}}{\mathrm{Re}} = \frac{72}{1 - r_T}(1 + 2\beta_T \,\mathrm{Kn}) \tag{23}$$

For Kn=0 and r_T=0, the point beyond which the flow reversal is obtained can be determined as Gr/Re=72, which is clear from Fig. 2.

For a constant value of the mixed convection parameter, Gr/Re=100, the effect of the ratio of the wall temperature difference, r_T, on the velocity profile, is shown in Fig. 3. Increasing r_T decreases both the velocities and the velocity gradient near the hot wall, but increases velocities near the cold wall. From Eq. (23),

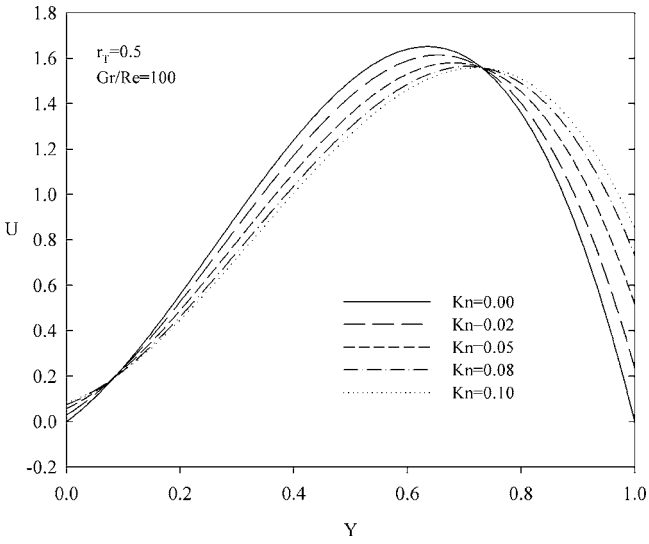

Fig. 4 Velocity distribution as a function Kn for r_T=0.5 and Gr/Re=100

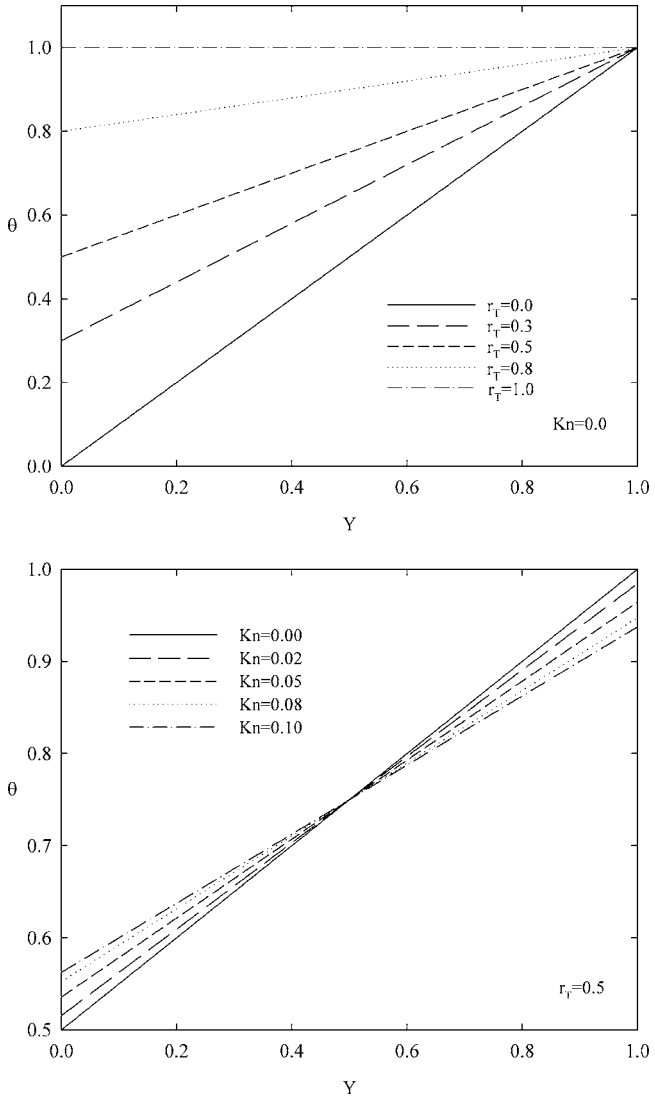

Fig. 5 Temperature distribution as a function Kn and r_T

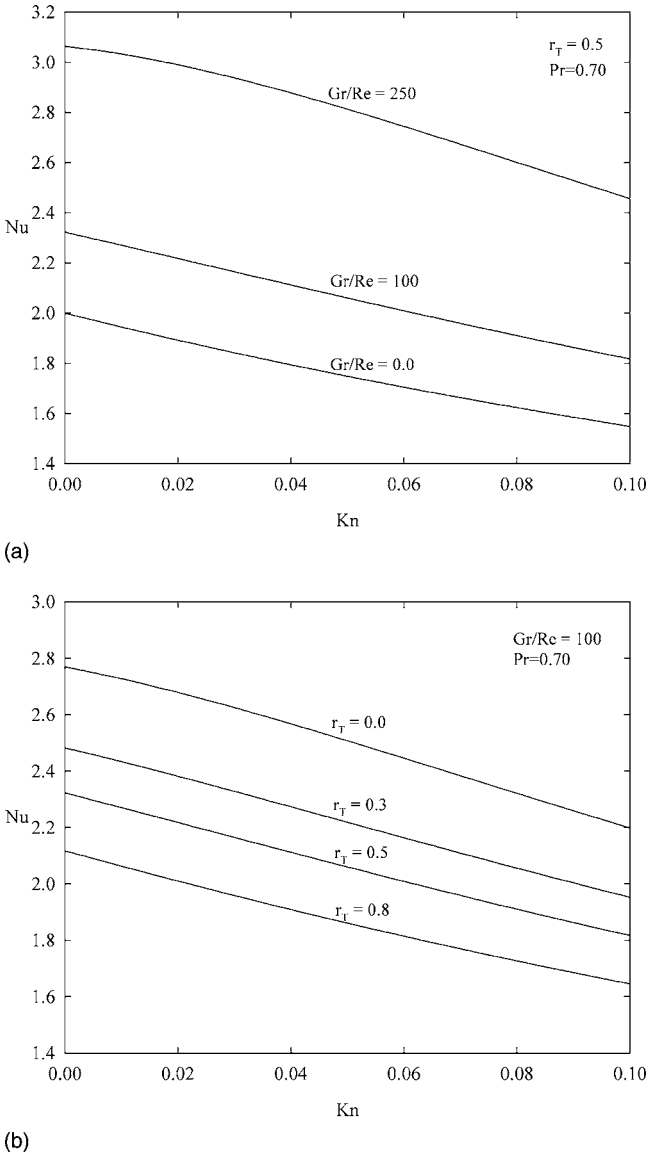

Fig. 6 The variation of the Nu with Kn at different values of Gr/Re (*a*) and r_T (*b*)

one can observe that with increase at r_T the limiting point moves Gr/Re to higher values. This is why we do not see any flow reversal for r_T=0.,3, 0.5, and 0.8 at Gr/Re=100 in Fig. 3.

For constant values of Gr/Re and r_T, the influence of the Knudsen number, Kn, on the velocity profile is illustrated in Fig. 4. It can be seen that increasing Kn increases velocity slips at the walls. With an increase at Kn, the maximum velocity decreases and its position shifts toward the right hot wall. Similarly, the influence of Kn on the temperature profile can be seen from Fig. 5.

Finally, we can plot the variation of Nu with Kn using Eq. (21) (see Fig. 6). As seen, increasing Kn decreases Nu. From this figure, it is also clear that increasing Gr/Re increases Nu while an increase at r_T decreases Nu.

4 Conclusions

Analytical solutions have been obtained for the fully developed mixed convective heat transfer of a Newtonian fluid in an open-ended vertical parallel plate microchannel. Both the velocity slip and the temperature jump conditions have been included in the formulations. The mixed convection parameter, Gr/Re, the Knudsen number, Kn, and the ratio of wall temperature difference, r_T, have been the main parameters studied and their effects on the heat and fluid flow phenomena have been determined. The Nusselt number is found to decrease as Kn or r_T increased, whereas it increased as Gr/Re increased.

Acknowledgment

The authors greatly acknowledge the financial support of this work by the Scientific and Technological Research Council of Turkey (TUBITAK) under Grant No. 104M436.

Nomenclature

c_p = specific heat at constant pressure
g = gravitational acceleration
Gr = Grashof number $=g\beta(T_2-T_1)W^3/\upsilon^2$
F = tangential momentum accommodation coefficient
F_t = thermal accommodation coefficient
h = convective heat transfer coefficient
k = thermal conductivity
Kn = Knudsen number$=\lambda/W$
Nu = Nusselt number

p = pressure difference $= p' - p''$
p' = static pressure
p'' = hydrostatic pressure
Pr = Prandtl number
Re = Reynolds number $= u_m W/\upsilon$
r_T = ratio of wall temperature differences, Eq. (10)
T = temperature
u = axial velocity
U = dimensionless axial velocity
W = channel width
x, y = axial and transverse coordinate
X, Y = dimensionless axial and transverse coordinate

Greek Symbols

α = thermal diffusivity
β = thermal expansion coefficient
β_v, β_t = dimensionless variables, Eq. (6)
γ = specific heat ratio
λ = molecular mean free path
μ = dynamic viscosity
ρ = density
υ = kinematic viscosity
θ = dimensionless temperature, Eq. (8)

Subscripts

0 = inlet properties of the fluid (i.e., at x=0)
1 = value on the cool wall (i.e., at y=0)
2 = value on the hot wall (i.e., at y=W)
m = mean value
s = fluid properties on the walls
s_1 = fluid properties on the cool wall
s_2 = fluid properties on the hot wall
w = wall

References

[1] Ho, C. M., and Tai, C. Y., 1998, "Micro-Electro-Mechanical Systems (MEMS) and Fluid Flows," Annu. Rev. Fluid Mech., **30**, pp. 579–612.
[2] Palm, B., 2001, "Heat Transfer in Microchannels," Microscale Thermophys. Eng., **5**, pp. 155–175.
[3] Sobhan, C. B., and Garimella, S. V., 2001, "A Comparative Analysis of Studies on Heat Transfer and Fluid Flow in Microchannels," Microscale Thermophys. Eng., **5**, pp. 293–311.
[4] Obot, N. T., 2002, "Toward a Better Understanding of Friction and Heat/Mass Transfer in Microchannels-A literature review," Microscale Thermophys. Eng., **6**, pp. 155–173.
[5] Rostami, A. A., Saniei, N., and Mujumdar, A. S., 2000, "Liquid Flow and Heat Transfer in Microchannels: A Review," Heat Technol., **18**, pp. 59–68.
[6] Rostami, A. A., Mujumdar, A. S., and Saniei, N., 2002, "Flow and Heat transfer for Gas Flowing in Microchannels: A Review," Heat Mass Transfer, **38**, pp. 359–367.
[7] Gad-el-Hak, M., 2001, "Flow Physics in MEMS," Méchanique & Industries, **2**, pp. 313–341.
[8] Guo, Z. Y., and Li, Z. X., 2003, "Size Effect on Microscale Single-Phase Flow and Heat Transfer," Int. J. Heat Mass Transfer, **46**, pp. 59–149.
[9] Guo, Z. Y., and Li, Z. X., 2003, "Size Effect on Single-Phase Channel Flow and Heat Transfer at Microscale," Int. J. Heat Fluid Flow, **24**(3), pp. 284–298.
[10] Morini, G. L., 2004, "Single-Phase Convective Heat Transfer in Microchannels: A Review of Experimental Results," Int. J. Therm. Sci., **43**, pp. 631–651.
[11] Aydın, O., and Avcı, M., 2006, "Heat and Fluid Flow Characteristics of Gases in Micropipes," Int. J. Heat Mass Transfer, **49**, pp. 1723–1730.
[12] Aydın, O., and Avcı, M., 2007, "Analsysis of Micro-Graetz Problem in a Microtube," Nanoscale and Microscale Thermopysical Engineering, accepted.
[13] Aydın, O., and Avcı, M., 2007, "Analysis of Laminar Heat Transfer in Micro-Poiseuille Flow," Int. J. Therm. Sci., **46**, pp. 30–37.
[14] Aydın, O., and Avcı, M., 2006, "Thermally Developing Flow in Microchannels," J. Thermophys. Heat Transfer, **20**, pp. 628–632.
[15] Chen, C. K., and Weng, H. C., 2005, "Natural Convection in a Vertical Microchannel," J. Heat Transfer, **127**, pp. 1053–1056.
[16] Khadrawi, A. F., Othman, A., and Al-Nimr, M. A., 2005, "Transient Free Convection Fluid Flow in a Vertical Microchannel as Described by the Hyperbolic Heat Conduction Model," Int. J. Thermophys., **26**(3), pp. 905–918.
[17] Haddad, O. M., Abuzaid, M. M., and Al-Nimr, M. A., 2005, "Developing Free-Convection Gas Flow in a Vertical Open-Ended Microchannel Filled With Porous Media," Numer. Heat Transfer, Part A, **48**, pp. 693–710.
[18] Gad-el-Hak, M., ed., 2001, *The MEMS Handbook*, CRC Press, New York.
[19] Aung, W., and Worku, G., 1986, "Theory of Fully Developed, Combined Convection Including Flow Reversal," J. Heat Transfer, **108**, pp. 485–488.
[20] Oosthuizen, P. H., and Naylor, D., 1999, *Introduction to Convective Heat Transfer Analysis*, McGraw-Hill, New York, pp. 158–167.
[21] Stefanov, S., and Roussinov, V., 2002, "Rayleigh-Benard Flow of a Rarefied Gas and its Attractors. I. Convection Regime," Phys. Fluids, **14**(7), pp. 2255–2269.
[22] Tzeng, P. Y., and Liu, M. H., 2005, "Direct-Simulation Monte Carlo Modelling on Two-Dimensional Rayleigh-Benard Instabilities of Rarefied Gas," Numer. Heat Transfer, Part A, **47**, pp. 805–823.

Localized Heat Transfer in Buoyancy Driven Convection in Open Cavities

Wilson Terrell, Jr.[1]
Department of Engineering Science,
Trinity University,
One Trinity Place,
San Antonio, TX 78212-7200
e-mail: wilson.terrelljr@trinity.edu

Ty A. Newell
Air Conditioning and Refrigeration Center,
Department of Mechanical and Industrial Engineering,
University of Illinois at Urbana-Champaign,
140 MEB, MC-244,
1206 West Green Street,
Urbana, IL 61801

Background. An experimental study of buoyancy driven convection heat transfer in an open cavity was conducted. Method of Approach. Test cavities were constructed with calorimeter plates bonded to Styrofoam insulation. The inside of the cavities was heated and then exposed to ambient air for approximately thirty minutes. Different size cavities were examined at inclination angles of 0, 45, and 90 deg. *The heat transfer coefficient was determined from an energy balance on each calorimeter plate. The cavity's plate temperatures varied spatially due to the transient nature of the tests. A parameter describing the nonisothermal cavity wall temperature variation was defined in order to compare with isothermal cavity heat transfer results. Results. Results showed that the cavity Nusselt number, based on a cavity averaged temperature, was insensitive to the transient development of nonisothermal conditions within the cavity. Comparison of cavity-average Nusselt number for the current study, where the Rayleigh number ranged from* 5×10^6 *to* 2×10^8*, to data from the literature showed good agreement. Cavity-average Nusselt number relations for inclination angles of 0, 45, and* 90 deg *in the form of* $\mathrm{Nu}_{H,\mathrm{cav}}=C\mathrm{Ra}^{1/3}$ *resulted in coefficients of 0.091, 0.105, 0.093, respectively. The* 45 deg *inclination angle orientation yielded the largest Nusselt numbers, which was similar to previous literature results. Trends in the local plate Nusselt numbers were examined and found similar to data from the literature.* [DOI: 10.1115/1.2401615]

Keywords: open cavities, experimental, natural convection, buoyancy-driven flows

Introduction

Refrigerator manufacturers have made substantial gains in energy efficiency over the last two decades. The gains have been based on several small, but cumulative effects including improved compressors, controls, heat exchangers, and cabinets. Continued improvement of refrigerators is dependent on tracking down all manners in which energy is transferred into a cabinet. Boughton et al. [1] investigation concluded that the basic conduction of heat through a cabinet's walls and door was the primary contributor to the cabinet load. For closed-door conditions, Williams et al. [2] studied natural convection inside the refrigerator while Stein et al. [3] investigated moisture transport into the refrigerator cabinet.

The present study is an investigation of buoyancy driven convection related to refrigerator cabinet loads when the refrigerator door is opened. Alissi et al. [4] found that refrigerator door openings increased energy usage by as much as 32% above closed-door conditions. When a refrigerator door is opened, the refrigerator can be represented as a cavity with one side opened to the ambient. The purpose of this work is the development of heat transfer prediction relations for estimating refrigerator cabinet door opening loads and to provide more general information related to buoyancy driven cavity heat transfer.

Investigations of cavity heat transfer have focused on variety of configurations of heated walls, inclination angles (θ) and aspect ratios (H/L) (see Fig. 1).

Chan and Tien [5] studied numerically square cavities with the back wall heated, while the other walls were considered adiabatic. Angirasi et al. [6] conducted a 2D numerical study of transient and steady state laminar flows in open cavities with the backwall heated. The Prandtl number was varied and the Rayleigh number varied from 1.75×10^1 to 1×10^8. Angirasi concluded that the outside cavity boundary condition as well as at the cavity opening did not have heavy influence on the flow inside the cavity. Elsayed et al. [7] conducted a 2D numerical analysis of natural convection in fully open tilted square cavities with the backwall heated. The inclination angle ranged from 90 to −60 deg and Grashof numbers varied from 10^2 to 10^5. From the model results, Elsayed developed a correlation to determine the Nusselt number based on the Grashof number and cavity inclination angle.

LeQuere et al. [8] developed a 2D numerical model for an open cavity with the top, bottom, and back walls held at a uniform temperature. In the study, the Grashof number and the inclination angle were varied. Cha and Choi [9] conducted an experimental study on open cavities with the top, back, and bottom plates held at a constant temperature. Unlike other studies on open cavities, two intermediate temperature strips were placed next to the top and bottom plates to provide a gradual temperature change from the inner cavity to the adjacent adiabatic walls. A double exposure, holographic technique was used to view the temperature profile inside the cavity to determine the Nusselt number. Skok et al. [10] experimentally and numerically studied natural convection on open cavities with an aspect ratio of 1.5. Water-glycerol mixtures of different compositions were used as the working fluid immersed inside the cavity to vary the Rayleigh number from 3.5×10^6 to 1.2×10^9. From the experimental and numerical data, a correlation was developed for the cavity-average Nusselt number. Showole et al. [11] conducted both experimental and numerical analysis of upward-facing inclined open cavities with bottom, back, and top walls heated. The aspect ratio varied from 0.25, 0.5, and 1.0 while the tilt angle varied from 30, 45, 60, and 90 deg. Correlations for the experimental cavity-average Nusselt number were determined, with a standard deviation ranging from 9% to 13%. The numerical correlation for an inclination angle of 90 deg was determined with a standard deviation of ±7%.

[1]Corresponding author.

Contributed by the Heat Transfer Division of ASME for publication in the JOURNAL OF HEAT TRANSFER. Manuscript received January 27, 2005; final manuscript received August 16, 2006. Review conducted by Jay M. Khodadadi.

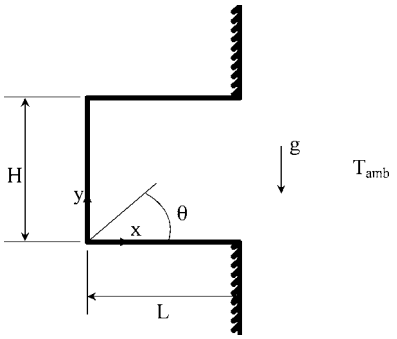

Fig. 1 Open cavity geometry and orientation

Most numerical studies of natural convection on open cavities have focused on modeling 2D flow, neglecting the effects of the sidewalls. Sezai and Mohamad [12] conducted 3D simulation of natural convection in an open cavity with the backwall heated. The results of the 3D and 2D model was compared for various lateral aspect ratios (H/W) to examine the effects of the sidewalls for Rayleigh numbers of 10^3–10^6. The study found for H/W greater than unity and Rayleigh numbers less than 10^5, differences in the 2D and 3D model results were not significant.

The present study examines localized heat transfer characteristics on five heated walls in an open cavity during transient cooling of a cavity. Clausing et al. [13], Laleman et al. [14], and Knackstedt et al. [15] utilized a similar transient technique using the interior of a refrigerator cabinet. This study extends the results of these authors and provides more detailed information related to the transient development of nonisothermal walls during the cavity heat transfer process. Local plate Nusselt numbers determined from this study provides useful information for numerical modelers interested in 3D buoyancy driven simulations.

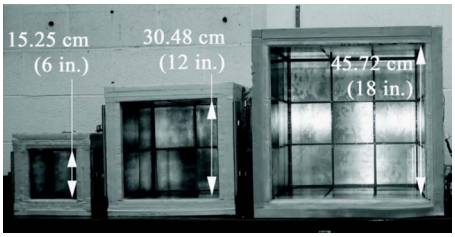

Fig. 2 Photos of various test cavities (from left to right): one-plate per wall, four-plate per wall, and nine-plate per wall

Experimental Apparatus

Test Section and Apparatus. Test cavities were constructed with polished 0.3175 cm (1/8 in.) thick 6061-T6 aluminum plates acting as cavity walls and calorimeters. The square plates were 15.24 cm (6 in.) in length. Two holes were drilled close to the center of each plate at a 45 deg angle. Thermocouple wire (25 gauge copper-constantan) was inserted in each hole for two temperature readings. Thermal epoxy was placed over each wire to hold the thermocouple bead in place and ensure good thermal contact. During the tests, differences between a single plate's two thermocouple temperatures were generally within 0.5 °C, due in part to the epoxy and positioning of the thermocouples. Three-square cavities were designed of different sizes (see Fig. 2). The calorimeter plates were bonded to 2 in. thick Styrofoam insulation with a thin layer of silicone gel. Plates were placed 0.635 cm (1/4 in.) apart to ensure no physical contact with each other. Gaps between adjacent plates were sealed and leveled with silicone gel.

A cover was placed over the cavity at the start of each test. Incandescent lights and fans were positioned on the inside cover to provide uniform heating of the aluminum plates. The cover was removed when the cavity reached the desired temperature and the cavity was then exposed to the ambient air. The cavity was located away from the room door and minimum air movement was maintained in the room to ensure no significant air currents near the cavity. The room was large enough that the ambient room temperature was unaffected by the warm cavity plates. Four thermocouples were used to determine the ambient temperature. These thermocouples were placed far from the cavity to ensure no influence from the cavity. The average room ambient temperature was constant during a test, typically deviating less than 0.5 °C.

Tests ended when the time elapsed reached the thermal time constant (τ_t) for each plate. The thermal time constant was expressed as the time when Eq. (1) was satisfied

$$\frac{T_{\text{plate}} - T_{\text{amb}}}{T_{\text{plate},i} - T_{\text{amb}}} = e^{-1} = 0.368 \tag{1}$$

Typical thermal time constants for tests ranged from 25 to 30 min. The cavity's angle of inclination was varied (see orientations in Fig. 3) to compare results with other studies.

Data Reduction

Estimation of Convective Heat Transfer Coefficient. Each aluminum plate on the test cavity walls was used as a calorimeter. The general energy balance assumed for each plate is given in Eq. (2)

$$m_{\text{plate}} c_{p,\text{AL}} \frac{dT_{\text{plate}}}{dt} = q_{\text{conv}} + q_{\text{rad}} + q_{\text{cond}} \tag{2}$$

The convective heat transfer was determined using Eq. (3)

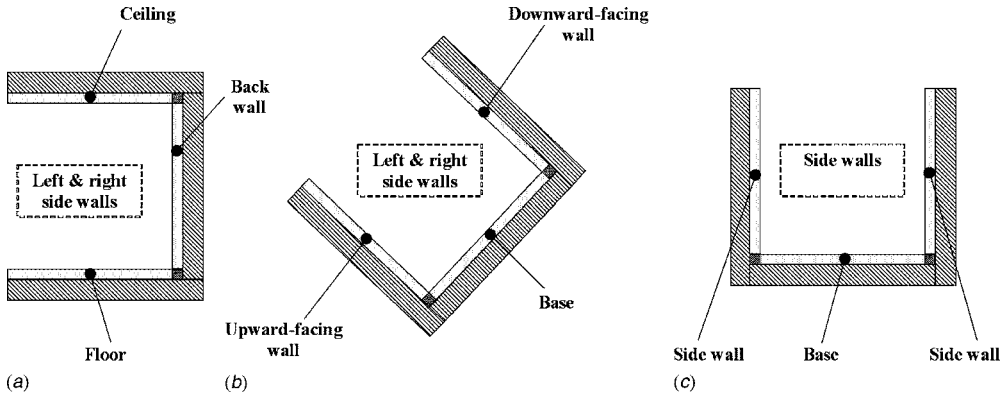

Fig. 3 Nomenclature of wall descriptions at various inclination angles (*a*) 0, (*b*) 45, and (*c*) 90 deg

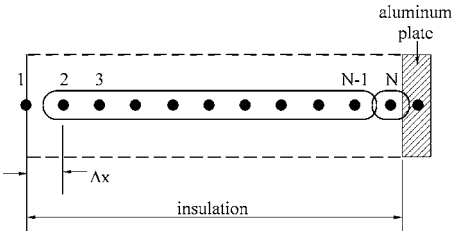

Fig. 4 Schematic of network representation used to examine thermal effects of the insulation

$$q_{\text{conv}} = hA_{\text{plate}}(T_{\text{amb}} - T_{\text{plate}}) \tag{3}$$

The ambient surrounding was treated as a blackbody surface while the aluminum plates were assumed to be diffuse, gray surfaces. The net radiation transfer rate for each plate was determined from Eq. (4)

$$q_{\text{rad}} = \sum_{j=1}^{N} \frac{J_i - J_j}{(A_i F_{ij})^{-1}} \tag{4}$$

The radiosity (J_i) was determined from Eq. (5) by solving the simultaneous set of equations for the surfaces

$$\frac{E_{bi} - J_i}{(1-\varepsilon_i)/\varepsilon_i A_i} = \sum_{j=1}^{N} \frac{J_i - J_j}{(A_i F_{ij})^{-1}} \tag{5}$$

The view factors were determined with expressions from Ehlert et al. [16]. A transient explicit 1D finite difference method similar to Laleman et al. [14] was developed to estimate the insulation's energy storage effects. A schematic of the conduction network can be seen in Fig. 4.

Thermophysical properties of the aluminum plate and insulation are given in Table 1. The conductive heat transfer from aluminum to the insulation was determined with Eq. (6).

$$q_{\text{cond}} = \frac{A_{\text{plate}}}{\left(\frac{\Delta x_w/2}{k_w}\right)}(T_N - T_{\text{plate}}) \tag{6}$$

The aluminum plate temperatures and outside insulation temperature were used as boundary conditions for the simulation. Since the plate temperatures were measured at 30-s intervals, Δx_W was chosen to ensure numerical stability and accuracy. Five nodes across the insulation were found to be adequate. Numerical simulations included the time when the plates were heated to the desired initial temperature, and the 25–30 minutes when the cavity was exposed to the ambient.

Significant Parameters. The Nusselt number is a dimensionless ratio comparing the convective heat transfer to that of a conducting fluid layer with a defined thickness. The Nusselt number was determined from Eq. (7).

$$Nu_{L_c} = \frac{hL_c}{k} \tag{7}$$

Using Eqs. (2)–(8), the local plate convective heat transfer coefficient (h) was determined from the plate temperature data, which was collected every thirty seconds. The transient change of plate temperatures (dT_{plate}/dt) at each interval was computed by taking the slope of a least-square curve fit of the temperature measurements. The Rayleigh number was determined from Eq. (8).

$$\text{Ra}_{L_c} = \frac{g\beta(T_{\text{plate}} - T_{\text{amb}})L_c^3}{\nu\alpha} \tag{8}$$

L_c is the characteristic length, and was chosen as the cavity height, H. The Nusselt and Rayleigh number was determined every 30 s throughout the test.

Uncertainty Analysis. An uncertainty analysis was conducted in accordance with ASHRAE Standard 2-1986 [17]

$$w_r = \sqrt{\left(\frac{\partial R}{\partial v_1}w_1\right)^2 + \left(\frac{\partial R}{\partial v_2}w_2\right)^2 + \ldots + \left(\frac{\partial R}{\partial v_n}w_n\right)^2} \tag{9}$$

A computer code utilizing Engineering Equation Solver (Klein and Alvarado [18]) was used to determine the relative uncertainty of experimental measurements and property parameters (see Table 2). A summary of the uncertainty results can be seen in Table 3. The relative uncertainty of the convective heat transfer coefficient and the Nusselt number was examined at the beginning and end of tests. Generally, tests operated at higher cavity temperatures had a lower relative uncertainty due to higher temperature differences between the cavity and surrounding ambient.

Table 1 Physical properties of materials used in test cavities

Property	Aluminum	Styrofoam insulation
Specific heat, c_p	0.876 kJ kg^{-1} K^{-1}	1.5 kJ kg^{-1} K^{-1}
Density, ρ	2707 kg m^{-3}	24 kg m^{-3}
Thermal conductivity, k	157.5 W m^{-1} K^{-1}	0.027 W m^{-1} K^{-1}

Table 2 Uncertainty of various measurements and parameters from current experimental tests

Variable	Uncertainty
Dimensions (length, width, height)	±2 mm
Temperature	Greater of 0.5°C or 0.75%
Time (clock reading)	0.01% of elapsed time
Plate emissivity	10%

Results and Discussion

Nonuniformity of Plate Temperatures During Testing. Cavity walls were nearly isothermal at the beginning of a test. As the cavity was exposed to the ambient air, the variation of the internal wall heat transfer resulted in nonisothermal walls. The sensitivity of the Nusselt number to this variation in cavity plate temperature was examined. To quantify the spatial temperature deviation of a cavity at any given time during an experiment, the spatial deviation parameter, Γ_T, was defined with Eq. (10)

$$\Gamma_T = \frac{T_{\text{plate,max}} - T_{\text{plate,min}}}{T_{\text{cav}} - T_{\text{amb}}} \tag{10}$$

Γ_T is the ratio of the difference between maximum and minimum

Table 3 Results from uncertainty analysis of current experimental tests

	Relative uncertainty at beginning of test (%)	Relative uncertainty at end of test (%)
h	3.3–7.8	7.5–24.0
Nu_H	2.7–6.9	7.2–24.0
Ra_H	3.2–4.8	3.8–9.0

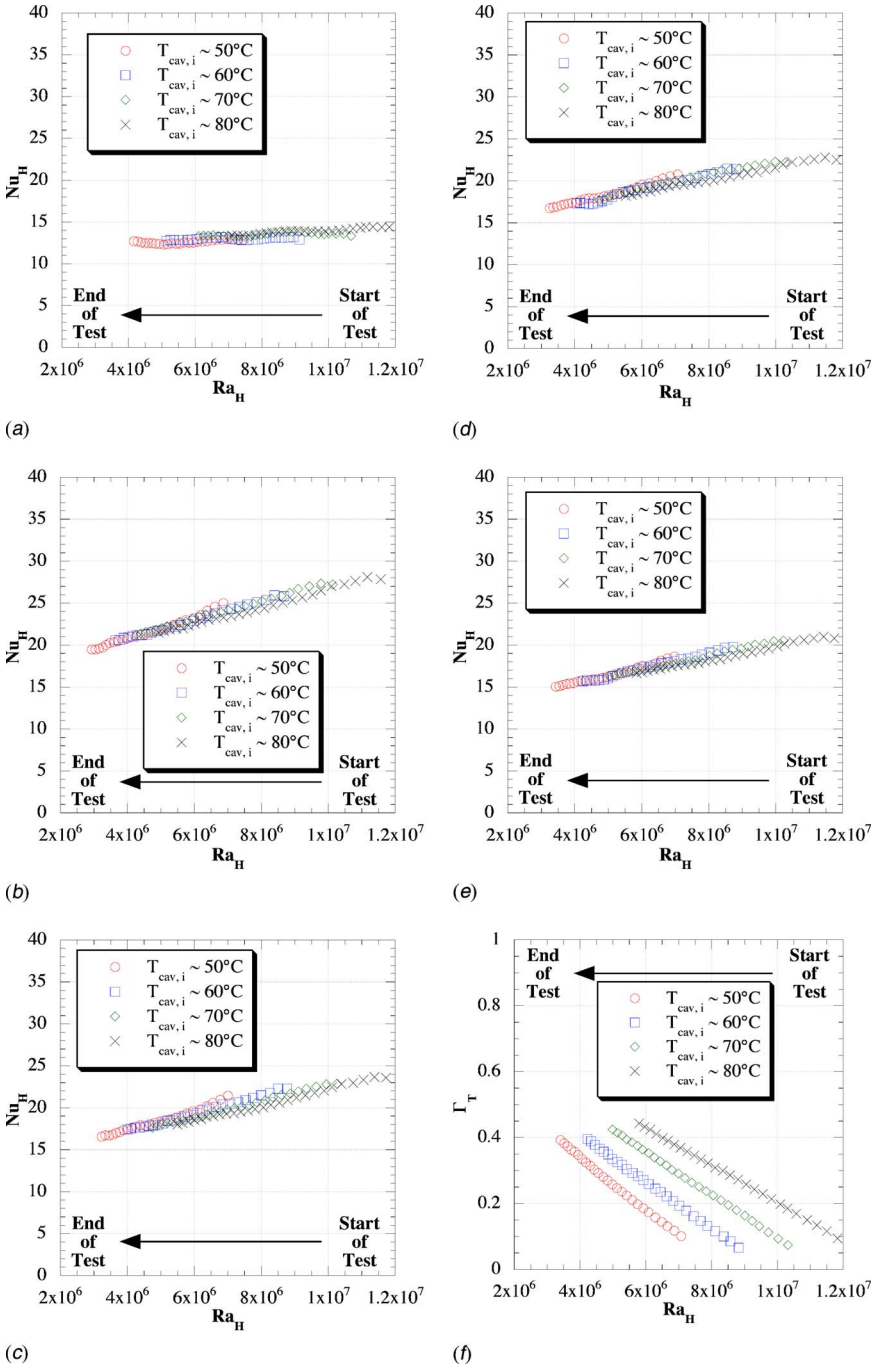

Fig. 5 Plate Nusselt numbers: one-plate per wall cavity with different initial cavity temperatures ($T_{cav,i}$) at 0 deg inclination angle: (*a*) plate-1 (ceiling), (*b*) plate-2 (floor), (*c*) plate-3 (left wall), (*d*) plate-4 (right wall), (*e*) plate-5 (backwall), and (*f*) spatial temperature deviation of a cavity, Γ_T

plate temperature relative to the difference between the cavity temperature (T_{cav}) and the ambient temperature (T_{amb}). The cavity temperature was averaged from all the plate temperatures. The plate Nusselt number was insensitive to the initial cavity average temperature over the range of measured Rayleigh numbers, as seen in Figs. 5(*a*)–5(*e*) for a 1-plate per wall cavity. Variations between the Nusselt number of the cavity with an initial temperature of 80°C when it reached a Rayleigh number of tests with an initial temperature of 70 and 60°C ranged from 0.41% to 7.42%. The spatial temperature deviation parameter at those Rayleigh numbers varied significantly as shown in Fig. 5(*f*). The trends seen in Fig. 5 are consistent with the other cavities tested. Therefore, for buoyancy driven convection in cavities tested for these experimental conditions, the average cavity wall temperature may be used to determine the cavity heat transfer with an isothermal cavity heat transfer relation.

Cavity-Average Nusselt Numbers. The current results and results from other investigations in which cavity wall temperatures were constant have been compared. Good agreement can be seen between current study and studies for similar Rayleigh numbers for 0 deg cavity inclination angle (see Fig. 6). Cavity-average

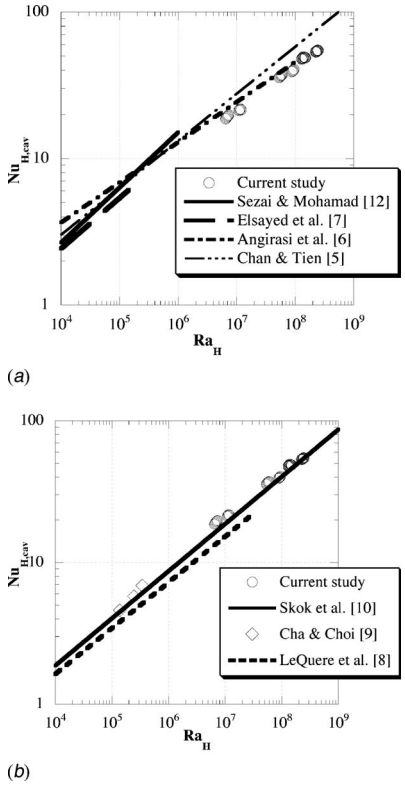

Fig. 6 Cavity-average Nusselt numbers 0 deg inclination angle: (*a*) current study compared to investigators with studies of open cavities with backwall heated and (*b*) current study compared to investigators with studies of open cavities with bottom, back, and top walls heated

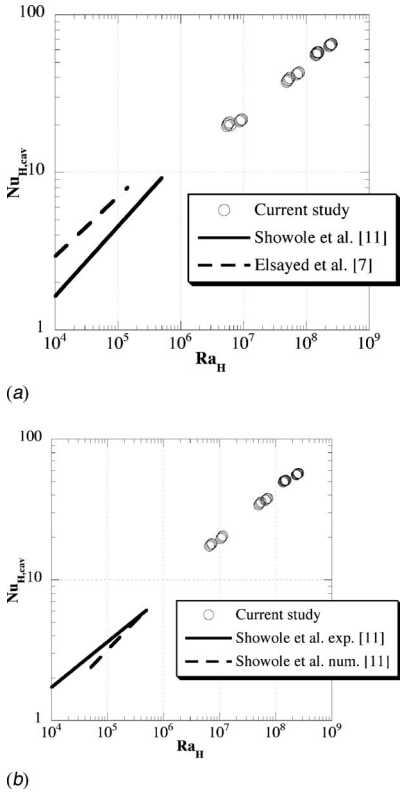

Fig. 7 Cavity-average Nusselt numbers for inclination angles (*a*) 45 deg and (*b*) 90 deg

Nusselt numbers from the current study and results from other investigators for 45 and 90 deg inclination angles can be seen in Fig. 7. Although the Rayleigh number in the present study differs by one to three orders of magnitude compared to other studies, the comparison indicates reasonable trends in the current data.

A least square fit to the experimental data of the cavity-average Nusselt number for various inclination angles was determined in the form of Eq. (11)

$$\mathrm{Nu}_{H,\mathrm{cav}} = C\mathrm{Ra}_H^{1/3} \tag{11}$$

The 1/3 power from Eq. (11) was based on Skok et al. [10]. The least squares fit, standard deviation, and average deviation for the current data can be seen in Table 4. The 45 deg inclination angle produced slightly higher Nusselt numbers than at 0 and 90 deg, and this trend was also seen in Elsayed et al. [7] and Showole et al. [11].

Local Wall Nusselt Numbers. The wall Nusselt number of each calorimeter plate was determined and allowed for the local variation of heat transfer throughout a cavity to be examined. A relation for the hydraulic boundary layer to the thermal boundary layer is given by Eq. (12) and is assumed if turbulent mixing of flow is not prevalent [19]

$$\frac{\delta}{\delta_t} \approx \mathrm{Pr}^n \tag{12}$$

Since the working fluid for the current study was air (Pr $\sim$0.7), the hydraulic boundary layer can be approximated with the thermal boundary layer. The trends seen in the local plate Nusselt numbers for the current data help relate the air flow in the cavity. For parallel laminar flow over a heated flat plate, the highest local Nusselt number occurs at the wall's leading edge, where the ambient air is first exposed to the plate. As the thermal and hydraulic boundary layer grows along the wall, the temperature gradient at the wall decreases, resulting in a decrease in the local heat transfer coefficient, and thus a decrease in the local Nusselt number.

For the small cavity with one calorimeter plate per wall at 0 deg inclination angle, the floor and ceiling surfaces have the highest and lowest Nusselt numbers, respectively (see Fig. 8). Flow enters the bottom of the cavity, travels around the cavity walls, and then exits from the ceiling. The left wall had a slightly higher Nusselt number than the right wall which was unexpected due to symmetry of the walls. Both sidewalls have slightly higher Nusselt number than the backwall, most likely due to the sidewall proximity to the cavity opening. The relatively low Nusselt number for the ceiling was most likely due to air that was warmed by the surrounding bottom and sidewalls. This effect has been seen in other studies in which the bottom, back and top walls were heated [8,10,20]. Cha and Choi [9] had slightly different results due in part to pre-heating the air entering the cavity, which caused their bottom plate to exhibit lower Nusselt numbers relative to the other heated plates in the cavity. When the four-plate and nine-plate per wall cavities were examined (see Figs. 9 and 10), the trends in wall averaged Nusselt numbers were similar to that of the one-plate per wall cavity. More detail in local Nusselt numbers was observed with these larger cavities because of the multiple plate calorimeters on each wall. For the nine-plate per wall cavity, simi-

Table 4 Least squares fit to cavity average Nusselt numbers from current study

Inclination angle (deg)	Curve fit of data	Standard deviation of data to curve fit	Average deviation of data to curve fit (%)
0	$\mathrm{Nu}_H=0.091\mathrm{R}_H^{1/3}$	±1.72	4.67
45	$\mathrm{Nu}_H=0.105R_H^{1/3}$	±1.22	2.86
90	$\mathrm{Nu}_H=0.093\mathrm{Ra}_H^{1/3}$	±1.25	2.22

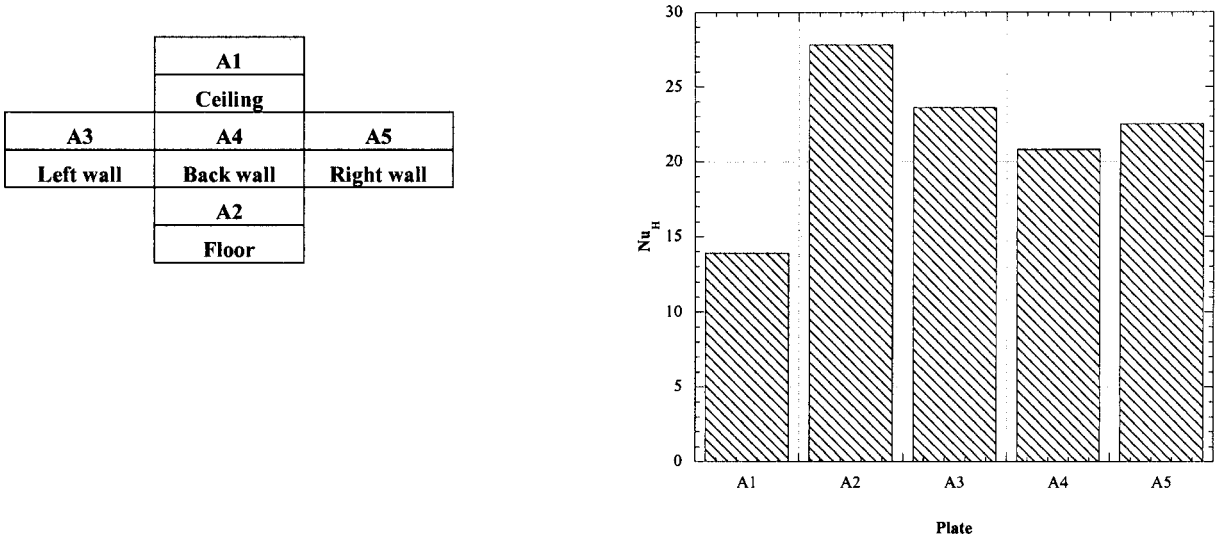

Fig. 8 Plate Nusselt numbers: one-plate per wall cavity at 0 deg inclination angle ($Ra_H \sim 1.18 \times 10^7$)

lar Nusselt numbers were observed in the plates along the lateral direction for the bottom, back, and top walls, which showed that the effect of the heated sidewalls on the other walls was not significant. The sidewall plate Nusselt number decreased as air traveled up the wall due most likely to the growing boundary layer. The plate in the upper front corner of the sidewalls exhibited a higher Nusselt number than the other plates along the row since there was a larger temperature difference from the outside air.

For the 45 deg cavity inclination angle (see Figs. 11–13) the base and upward-facing walls have similar Nusselt numbers, with the upward-facing wall being slightly higher. The downward-facing wall has lower Nusselt number than all other walls in the cavity. Trends in the current study were similar to Showole et al.'s results [11]. Showole contributed the low heat transfer for the downward-facing wall to inhibiting the flow rising due to buoyancy forces. The sidewalls' Nusselt numbers were similar, showing more symmetry than the sidewalls at 0 deg inclination angle. The sidewalls' Nusselt number at 45 deg inclination angle was slightly lower than the sidewalls at 0 deg due to possibly to the ambient air entering the cavity to the upward-facing and base walls first, then traveling from those walls up over the sidewalls. The four-plate per wall and nine-plate per wall cavity local Nusselt numbers help show the trend in more detail. The Nusselt number in the lower corner of the sidewalls has the highest Nusselt number, then the Nusselt numbers decrease along the walls. For the nine-plate per cavity walls, the base, upward-facing wall, and downward facing walls varied along the lateral position, which suggest a greater effect due to the sidewalls.

For 90 deg inclination angle (see Figs. 14–16) the sidewalls exhibited similar Nusselt numbers, due to symmetry, while the base had slightly higher Nusselt number. These results were similar to the Cha and Choi [9] study results. Showole et al. [11] results showed the base having significantly lower Nusselt number than the sidewalls. Showole's numerical simulation showed air entering the cavity past the sidewalls, turning toward the base, and then exiting the cavity. When Nusselt numbers in the nine-plate per wall cavity were examined for the same inclination angle, similar trends were observed as the one-plate per wall and four-plate per wall cavity. The middle of the base has the largest Nusselt number in the cavity, due the ambient air entrance flow to the cavity. The Nusselt number decreased significantly away from the center as the boundary layer grows. The symmetry seen in Figs. 16(*a*)–16(*e*) suggested a large effect of the sidewalls and 3D nature of the flow patterns in the base. The corners exhibit the lowest

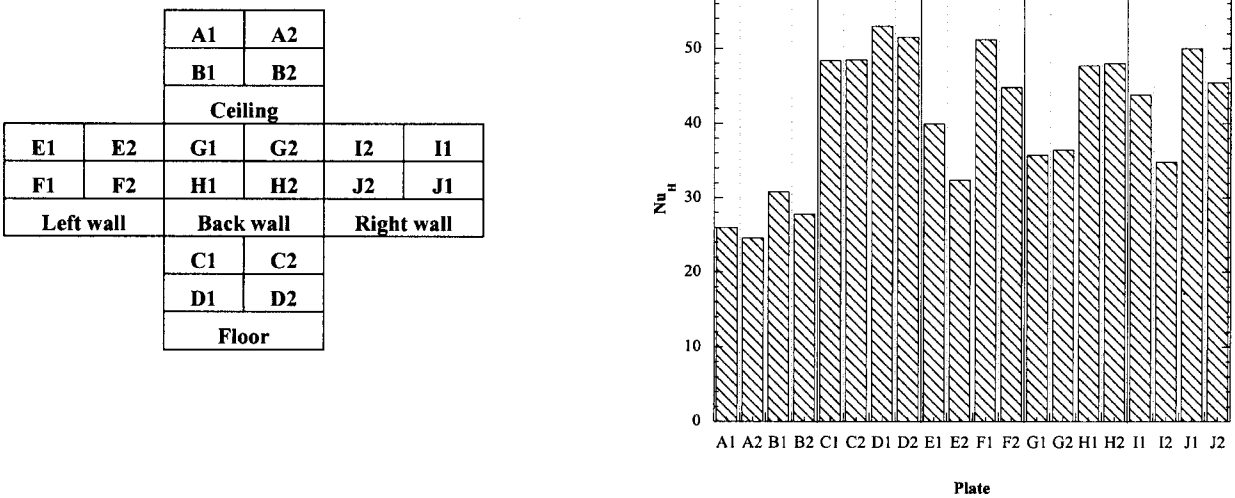

Fig. 9 Plate Nusselt numbers: four-plate per wall cavity at 0 deg inclination angle ($Ra_H \sim 9.45 \times 10^7$)

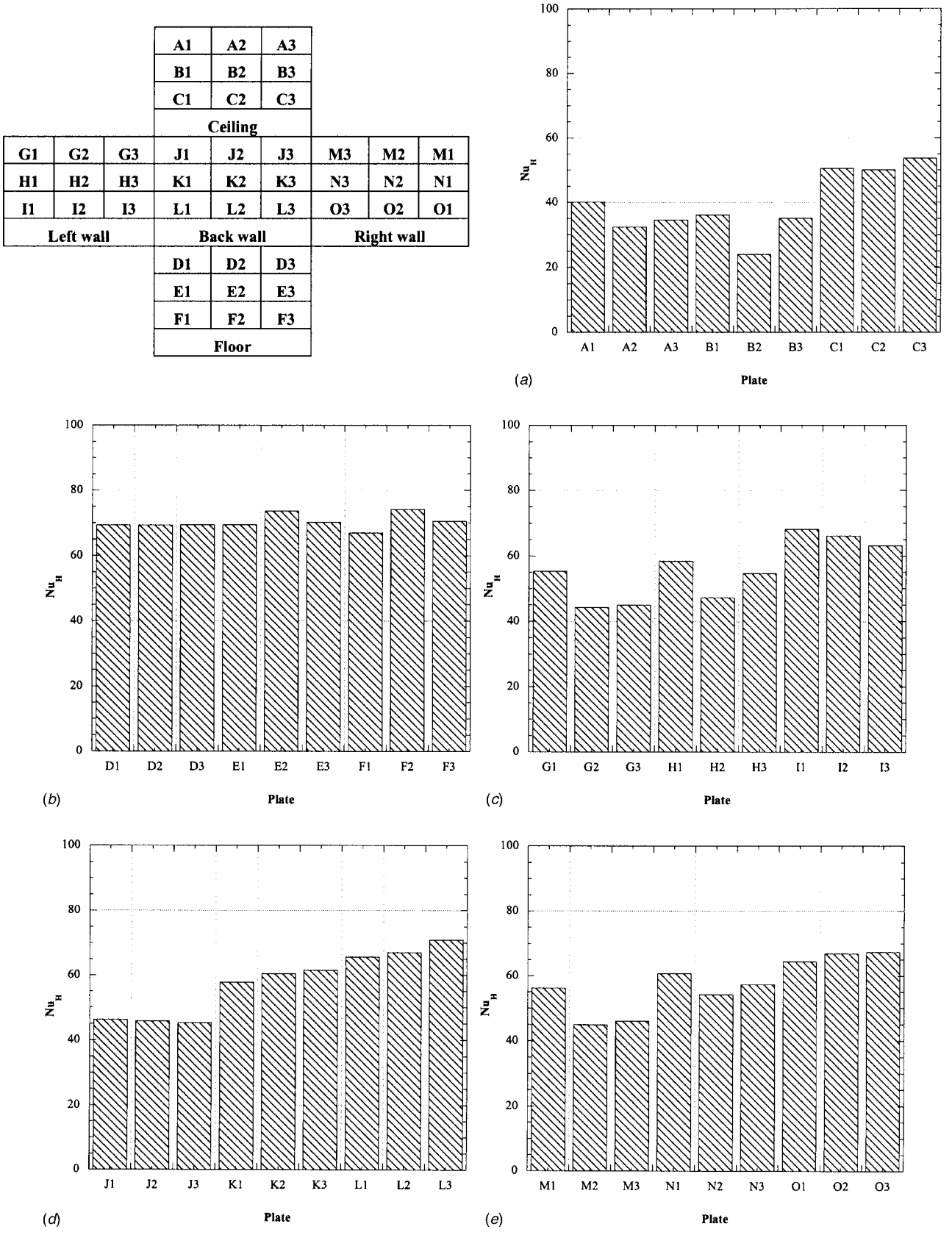

Fig. 10 Plate Nusselt numbers: nine-plate per wall cavity at 0 deg inclination angle ($Ra_H \sim 2.46 \times 10^8$): (*a*) ceiling, (*b*) floor, (*c*) left wall, (*d*) backwall, and (*e*) right wall

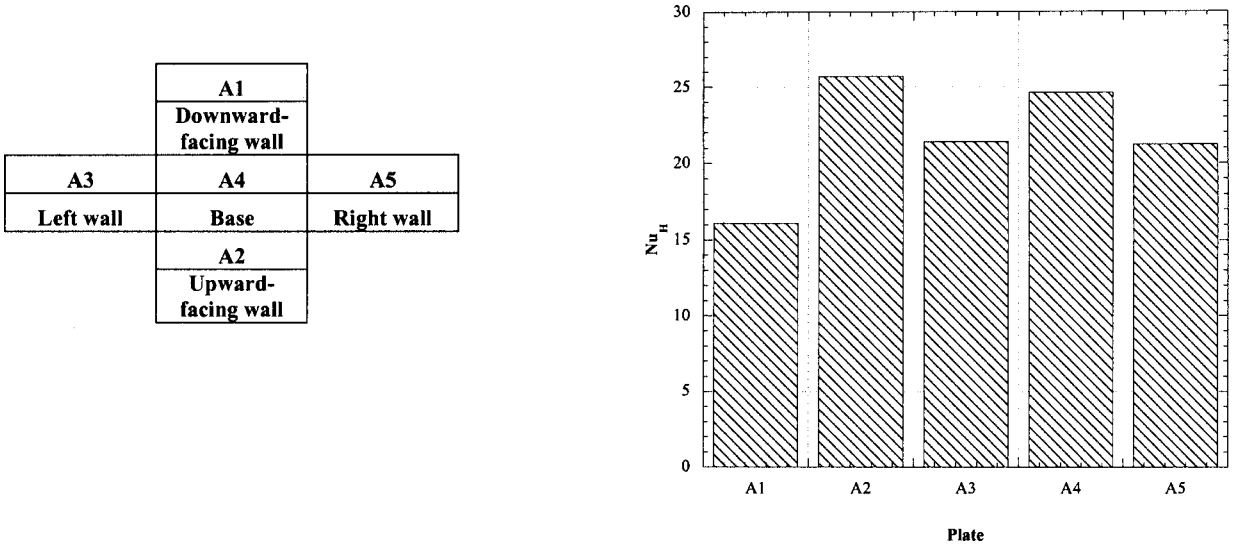

Fig. 11 Plate Nusselt numbers: one-plate per wall cavity at 45 deg inclination angle ($Ra_H \sim 9.41 \times 10^6$)

Nusselt numbers of the base due in part to the sidewalls. On the lower plates of the sidewalls, the Nusselt number grew due in part to either reformation of the boundary layer from air flowed over from the base. Future flow visualization could help determine if the multiple cell flows exist, and even if recirculation occurred between those cells. The Nusselt number decreased significantly as the air traveled up the sidewalls as the boundary layer grows. The effects of the adjacent sidewalls can be seen by the variation in Nusselt number along the row of plates on the walls.

The general flow patterns in a cavity at the various inclination angles are shown in Fig. 17. These patterns were based on the trends seen in the local plate Nusselt numbers for the cavities at various angles, and applying relationships between the local Nusselt number and boundary layer for parallel flow over a flat plate. The patterns show good agreement with streamlines from various studies in the literature.

Conclusions

Buoyancy driven heat transfer from open cavities has been investigated for a variety of cavity sizes, initial inner wall temperatures, and inclination angles. The transient heat transfer process caused spatial temperature variations among the cavity walls that were quantified with a nondimensional parameter Γ_T. Results showed that the nonisothermal cavity heat transfer was similar to that of an isothermal cavity with the same average Rayleigh number. Comparison of cavity-average Nusselt number for current study to data from the literature, in which the cavity wall temperature was held constant, showed good agreement. The cavity-average Nusselt number results were correlated using a relation in the form of $Nu_{H,cav} = C Ra^{1/3}$ for Rayleigh numbers ranging from 5×10^6 to 2×10^8 for inclination angles of 0, 45, and 90 deg. The cavities inclined at an angle of 45 deg yielded larger cavity average Nusselt numbers than cavities inclined 0 or 90 deg. The local wall Nusselt number was examined at various inclination angles. Highest local Nusselt numbers were seen at the entrance of the floor when the cavity was inclined at 0 deg, the corners of the upward facing and base walls when the cavity was inclined at 45 deg, and the middle of the base when the cavity was inclined at 90 deg. As the cavity was inclined, the influence of the sidewalls on the other cavity walls increased and suggest greater influence

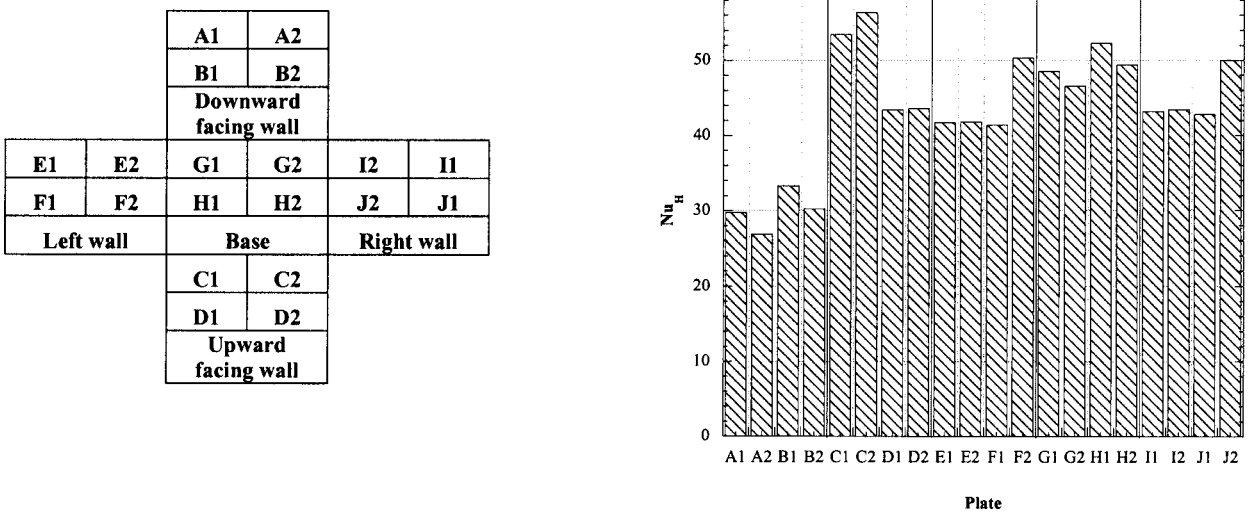

Fig. 12 Plate Nusselt numbers: four-plate per wall cavity 45 deg inclination angle ($Ra_H \sim 7.61 \times 10^7$)

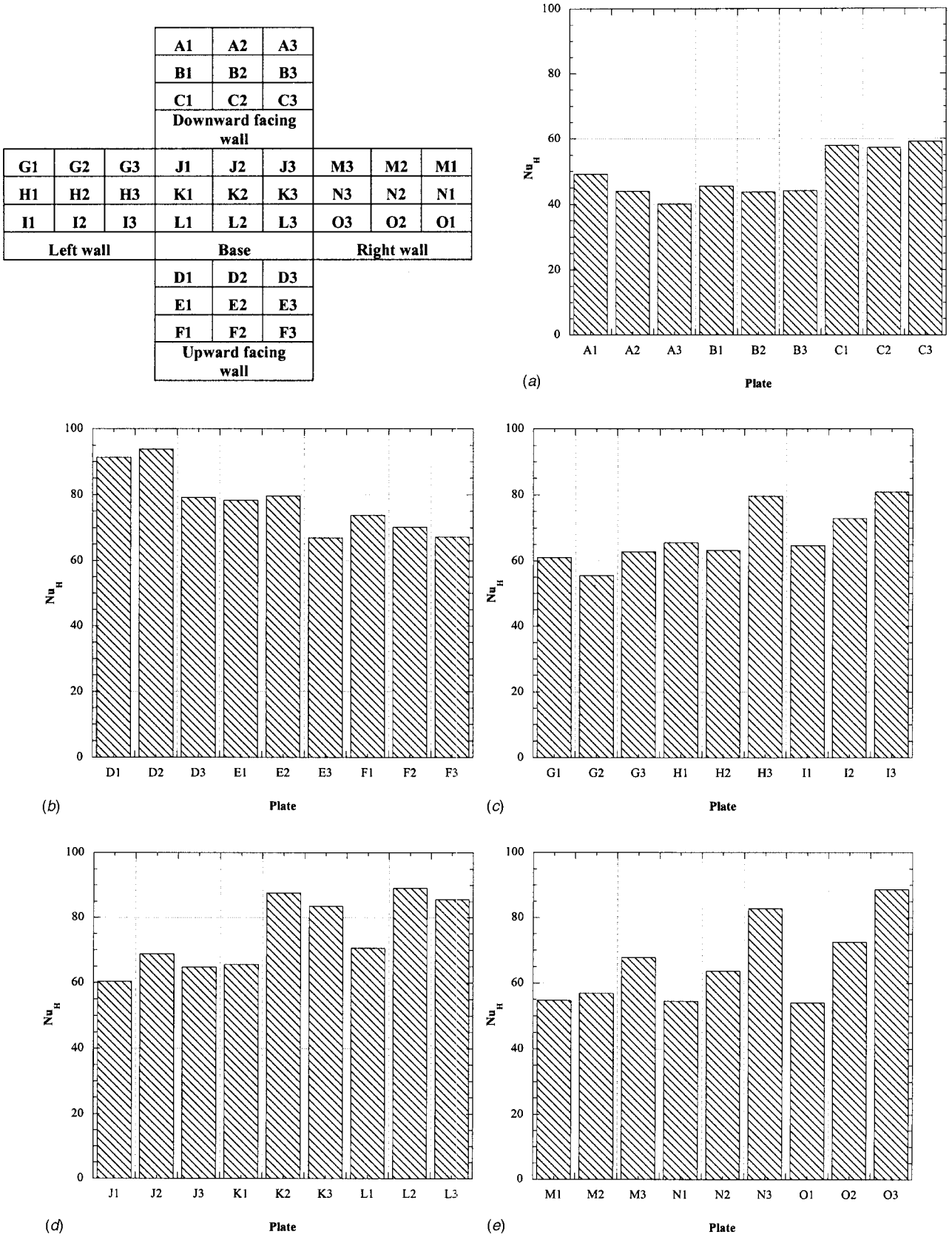

Fig. 13 Plate Nusselt numbers: nine-plate per wall cavity at 45 deg inclination angle ($Ra_H \sim 2.53 \times 10^8$): (*a*) downward-facing wall, (*b*) upward-facing wall, (*c*) left wall, (*d*) base, and (*e*) right wall

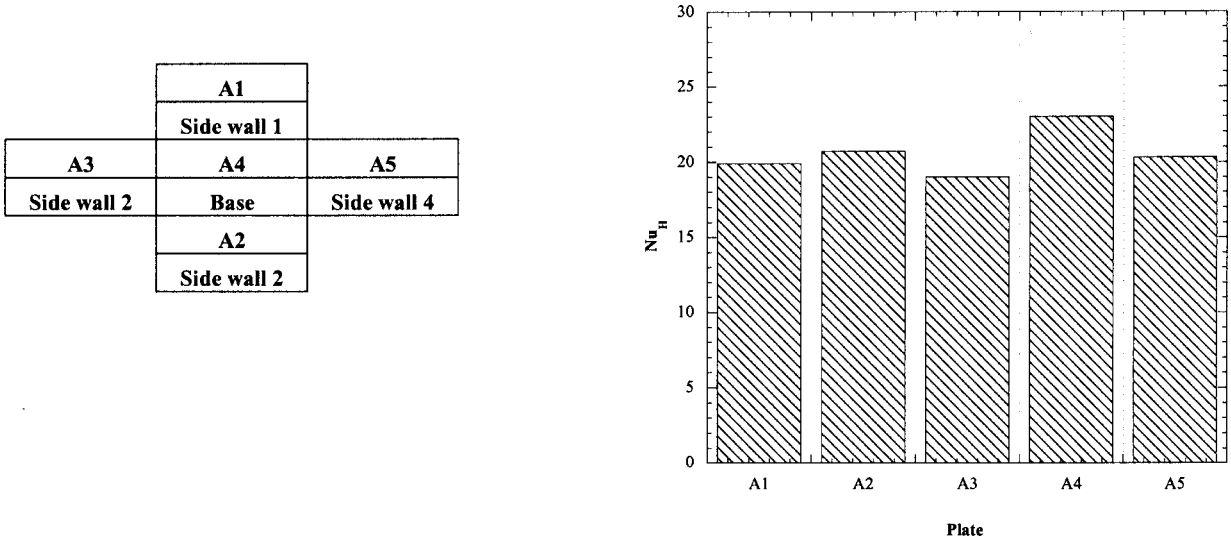

Fig. 14 Plate Nusselt numbers: one-plate per wall cavity at 90 deg inclination angle ($Ra_H \sim 1.13 \times 10^7$)

by the boundary layer. The trends in local Nusselt numbers as well as postulated flow patterns, based on the parallel flow over a heated flat plate, were in good agreement with the literature.

Acknowledgment

Financial support for this project was provided by the industrial partners of the Air Conditioning and Refrigeration Center at the University of Illinois at Urbana-Champaign and Trinity University's William Liston-Zander Junior Faculty Fellowship.

Nomenclature

A = area, m^2
AR = aspect ratio
c_p = specific heat, kJ kg^{-1} K^{-1}
E_{bi} = total emissive power of a blackbody, W m^{-2}
F_{ij} = view factor between surfaces i and j
g = acceleration of gravity (9.81), m s^{-2}
Gr = Grashof number, $g\beta(T_{plate}-T_{amb})L_c^3/\nu^2$
h = heat transfer coefficient, W m^{-2} K^{-1}
H = height of cavity, m
k = thermal conductivity, W m^{-1} K^{-1}
J_i, J_j = radiosity, W m^{-2}
L = length of cavity, m
L_c = characteristic length, m
m = mass, kg
Nu = Nusselt number, Eq. (7)
Pr = Prandtl number, ν/α
q = heat transfer rate, W
R = dependant variable
Ra = Rayleigh number, Eq. (8)
t = time, s
T = temperature, °C
v_i = independent variable
w = uncertainty, Eq. (9)
W = width of cavity, m
x = x-component coordinate
y = y-component coordinate

Greek Symbols

α = thermal diffusivity, m^2 s^{-1}

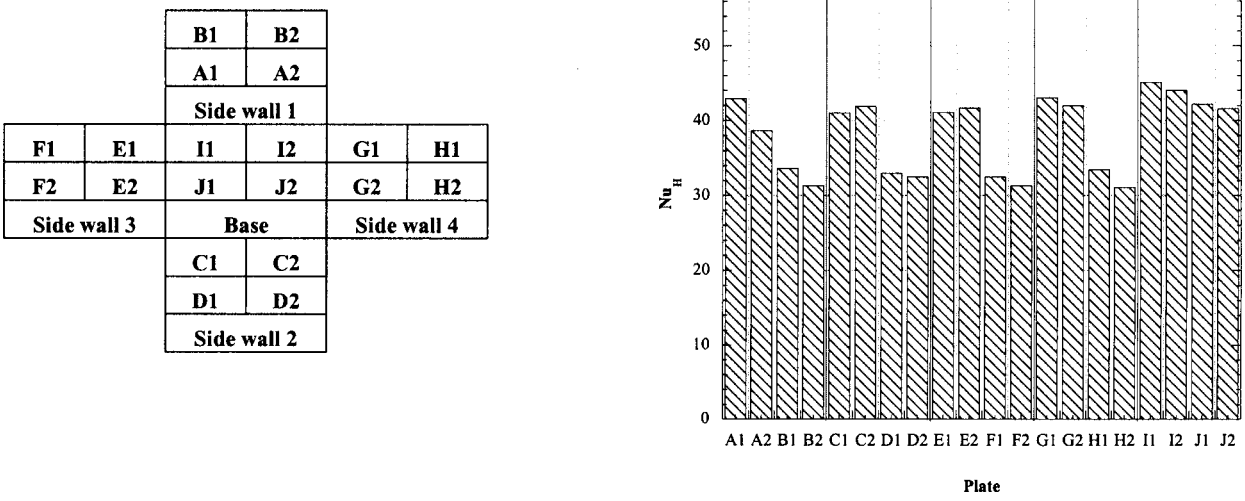

Fig. 15 Plate Nusselt numbers: four-plate per wall cavity at 90 deg inclination angle ($Ra_H \sim 7.27 \times 10^7$)

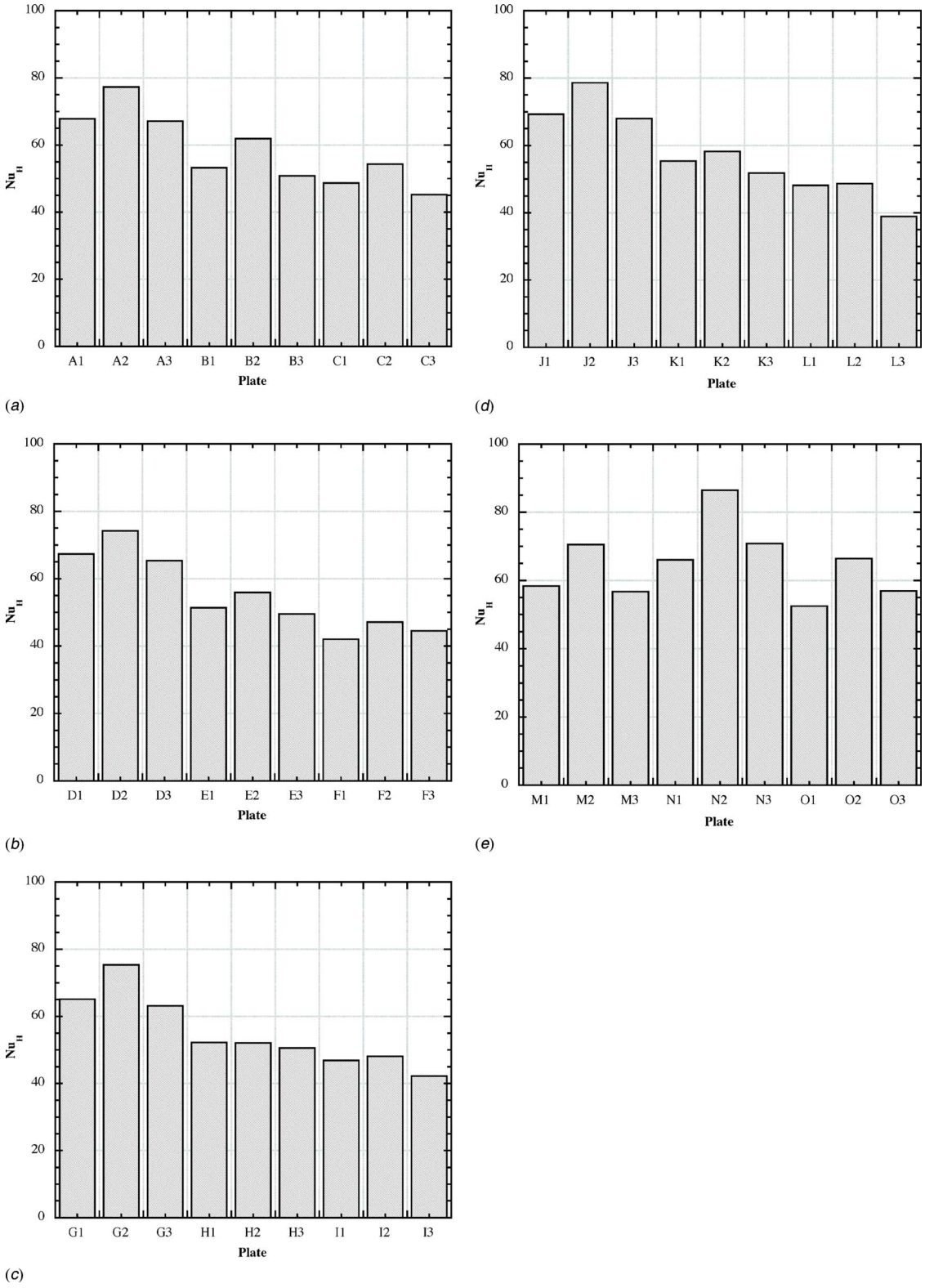

Fig. 16 Plate Nusselt numbers: nine-plate per wall cavity at 90 deg inclination angle ($Ra_H \sim 2.57 \times 10^8$): (*a*) sidewall 1, (*b*) sidewall 2, (*c*) sidewall 3, (*d*) sidewall 4, and (*e*) base

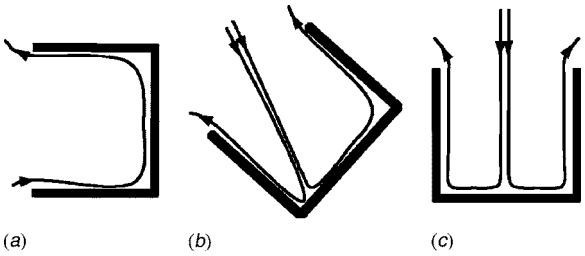

Fig. 17 Possible flow patterns in cavity, based on local Nusselt numbers of the current study, for various inclination angles: (*a*) 0 deg, (*b*) 45 deg, and (*c*) 90 deg

β = thermal expansion coefficient, K^{-1}
Γ_T = spatial temperature deviation parameter, Eq. (10)
δ = hydraulic boundary layer, m
δ_t = thermal boundary layer, m
Δ = difference
ε = emissivity
θ = inclination angle, deg
ν = kinematic viscosity, $m^2\,s^{-1}$

Subscripts

AL = aluminum
amb = ambient
cav = cavity
cond = conduction
conv = convection
i = initial
max = maximum
min = minimum
plate = aluminum plate
rad = radiation
w = foam wall (or thickness) through which heat is being conducted

References

[1] Boughton, B. E., Clausing, A. M., and Newell, T. A., 1996, "An Investigation of Household Refrigerator Cabinet Thermal Loads," HVAC&R Res., **2**(2), pp. 135–148.
[2] Williams, T. L., Clausing, A. M., and Newell, T. A., 1994, "An Experimental Investigation of Natural Convection Heat Transfer in a Refrigerator During Closed Door Conditions," ACRC TR-54, Air Conditioning Refrigeration Center University of Illinois, Urbana, IL.
[3] Stein, M. A., Bullard, C. W., and Newell, T. A., 2000, "Moisture Transport, Frost Visualization, and Dual Evaporator Modeling in Domestic Refrigerators," ACRC CR-28, Air Conditioning Refrigeration Center University of Illinois, Urbana, IL.
[4] Alissi, M. S., Ramadhyani, S., and Schoenthals, R. J., 1988, "Effects of Ambient Temperature, Ambient Humidity, and Door Openings on Energy Consumption of a Household Refrigerator-Freezer," ASHRAE Trans., **94**(2), pp. 1713–1735.
[5] Chan, Y. L., and Tien, C. L., 1985, "A Numerical Study of Two-Dimensional Natural Convection in Square Open Cavities," Numer. Heat Transfer, **8**, pp. 65–80.
[6] Angirasa, D., Pourquie', M. J. B. M., and Nieuwstadt, F. T. M., 1992, "Numerical Study of Transient and Steady Laminar Buoyancy-Driven Flows and Heat Transfer in a Square Open Cavity," Numer. Heat Transfer, Part A, **22**, pp. 223–239.
[7] Elsayed, M. M., Al-Najem, N. M., El-Refaee, M. M., and Noor, A. A., 1999, "Numerical Study of Natural Convection in Fully Open Tilted Cavities," Heat Transfer Eng., **20**(3), pp. 73–85.
[8] Le Quere, P., Humphrey, J. A. C., and Sherman, F. S., 1981, "Numerical Calculation of Thermally Driven Two-Dimensional Unsteady Laminar Flow in Cavities of Rectangular Cross Section," Numer. Heat Transfer, **4**, pp. 249–283.
[9] Cha, S. S., and Choi, K. J., 1989, "An Interferometric Investigation of Open-Cavity Natural-Convection Heat Transfer," Exp. Heat Transfer, **2**, pp. 27–40.
[10] Skok, H., Ramadhyani, S., and Shoenals, R. J., 1991, "Natural Convention in a Side-Facing Open Cavity," Int. J. Heat Fluid Flow, **12**(1), pp. 36–45.
[11] Showole, R. A., and Tarasuk, J. D., 1993, "Experimental and Numerical Studies of Natural Convection With Flow Separation in Upward-Facing Inclined Open Cavities," ASME J. Heat Transfer, **115**(3), pp. 592–605.
[12] Sezai, I., and Mohamad, A. A., 1998, "Three-Dimensional Simulation of Natural Convection in Cavities With Side Opening," Int. J. Numer. Methods Heat Fluid Flow, **8**(7), pp. 800–813.
[13] Clausing, A. M., 1983, "Convective Losses From Cavity Solar Receivers—Comparison Between Analytical Predictions and Experimental Results," ASME J. Sol. Energy Eng., **105**, pp. 29–33.
[14] Laleman, M. R., Newell, T. A., and Clausing, A. M., 1992, "Sensible and Latent Energy Loading on a Refrigerator During Open Door Conditions," ACRC TR-20, Air Conditioning Refrigeration Center University of Illinois., Urbana, IL.
[15] Knackstedt, L. N., Newell, T. A., and Clausing, A. M., 1995, "A Study of Convective Heat and Mass Transfer in a Residential Refrigerator During Open Door Condition," ACRC TR-71, Air Conditioning Refrigeration Center University of Illinois, Urbana, IL.
[16] Ehlert, J. R., and Smith, T. F., 1993, "View Factors for Perpendicular and Parallel Rectangular Plates," J. Thermophys. Heat Transfer, **7**(1), pp. 173–175.
[17] "Guide for Engineering Analysis of Experimental Data," 1986, ASHRAE Guide, ANSI/ASHRAE 2–1986.
[18] Klein, S. A., and Alvarado, F. L., 2002, EES: Engineering Equation Solver, F-Chart Software, Middleton WI.
[19] Incropera, F. P., and DeWitt, D. P., 2002, *Fundamentals of Heat and Mass Transfer*, Wiley, New York, Chap. 6, p. 6.
[20] Penot, F., 1982, "Numerical Calculation of Two-Dimensional Natural Convection in Isothermal Open Cavities," Numer. Heat Transfer, **5**, pp. 421–437.

On the Role of Coriolis Force in a Two-Dimensional Thermally Driven Flow in a Rotating Enclosure

Nadeem Hasan
Research Scholar
Department of Applied Mechanics,
IIT Delhi,
New Delhi, INDIA-110016
e-mail: nadhasan@gmail.com

Sanjeev Sanghi[1]
Associate Professor
Department of Applied Mechanics,
IIT Delhi,
New Delhi, INDIA-110016
e-mail: sanghi@am.iitd.ernet.in

In this work the role of Coriolis forces in the evolution of a two-dimensional thermally driven flow in a rotating enclosure of arbitrary geometry is discussed. Contrary to the claims made in some of the studies involving such class of flows that there is an active involvement of the these forces in the dynamics of the flow, it is shown that the Coriolis force does not play any role in the evolution of the velocity and temperature fields. This is theoretically demonstrated by recognizing the irrotational character of the Coriolis force in such class of flows. It is further shown that the presence of the irrotational Coriolis force affects only the pressure distribution in the rotating enclosure. The theoretical deductions apply quite generally to any geometry and thermal boundary conditions associated with the enclosure. The numerical results for the problem of two-dimensional thermally driven flow of air (Pr=0.71) *in a circular rotating enclosure provide direct evidence of the theoretical deductions.* [DOI: 10.1115/1.2402176]

Keywords: Boussinesq, Coriolis, enclosure, irrotational, rotating

1 Introduction

The problem of thermally driven flow in a steadily rotating enclosure is important from both fundamental as well as the application point of view. Thermal energy storage in rotating systems, cooling systems for rotating machinery, and space applications are some of the areas of relevance of such a class of flows. From the fundamental point of view such flows are important as they represent flow systems driven by multiple body forces. A rich dynamical behavior is expected as the relative magnitudes of these forces is varied.

The fluid in a steadily rotating enclosure is in a state of solid-body rotation. If a temperature variation is imposed on the walls of the enclosure, fluid motion relative to the solid-body rotation will be induced under the action of thermally introduced density gradients on the fields of gravity and/or centrifugal accelerations. The fluid motion relative to the solid-body rotation is conveniently studied using a frame attached to the rotating enclosure. The usage of a noninertial frame introduces the centrifugal buoyancy and the Coriolis body forces in addition to the gravitational buoyancy force. The non-dimensional parameters that are often employed to characterize such class of flows are (1) gravitational Rayleigh number (Ra_g), (2) rotational Rayleigh number (Ra_Ω), (3) Taylor number (Ta), and (4) Prandtl number (Pr). These numbers are defined as

$$\mathrm{Ra}_g = \frac{g\beta\Delta T S_1^3}{\nu\kappa}, \quad \mathrm{Ra}_\Omega = \frac{\Omega^2\beta\Delta T S_1^4}{\nu\kappa}, \quad \mathrm{Ta} = \frac{\Omega^2 S_1^4}{\nu^2}, \quad \mathrm{Pr} = \frac{\nu}{\kappa}$$

In the above definitions, S_1 is the length scale of the problem, and ν and κ are the kinematic viscosity and thermal diffusivity of the fluid, respectively. The acceleration due to gravity is denoted as g, while β is the coefficient of volume expansion of the fluid. The scale of the imposed temperature variation is denoted as ΔT and Ω is the steady rotation rate of the enclosure. Literature survey on the subject reveals that efforts aimed at investigating the thermally driven flows in rotating enclosures can be broadly split into two categories on the basis of geometrical configuration. The two categories are (1) rotating cylinders with differential heating at its ends, and (2) rotating rectangular boxes with differential heating across a pair of opposite faces. Most of the studies on a circular cylinder involve rotation of the cylinder along its longitudinal axis aligned parallel to the gravity vector [1–7]. Similarly, a significant amount of research has been done on rotating rectangular containers with rotation axis aligned parallel to the gravity vector [8,9]. The configurations having either the gravity or its component perpendicular to the axis of rotation have been far less explored. The thermally driven flow in such configurations is driven by an unsteady gravitational buoyancy force as a result of changing orientation of the gravity vector with respect to the frame attached with the rotating enclosure. Studies by Ker and Lin [10], Hamady et al. [11], Baig and Masood [12], and Hasan and Sanghi [13] are the few isolated works on configurations involving a time-periodic gravitational buoyancy force. The study in [10] involves a numerical and experimental investigation of three-dimensional flow in a tilted air filled differentially heated cubic cavity.

The study in [11] deals with an experimental and numerical investigation of two-dimensional thermally driven flow of air in a rotating square enclosure. The investigation was carried out at low enough rotation rates so that the centrifugal buoyancy effects could be safely ignored. Therefore, it was argued that the dynamics of the flow were controlled by the gravitational buoyancy force and the Coriolis force. It was conjectured that the Coriolis force aids in setting up a clockwise circulation relative to a counterclockwise rotating enclosure.

The study in [12] involves a numerical investigation of the two-dimensional convection of air in a rotating square enclosure. Some of the features of the flow observed in the numerical experiments were attributed to the Coriolis force. In particular it was concluded that the effect of the Coriolis force is to create convective motion in the core of the cavity. It was also reasoned that the

[1]Corresponding author.

Contributed by the Heat Transfer Division of ASME for publication in the JOURNAL OF HEAT TRANSFER. Manuscript received October 25, 2005; final manuscript received August 15, 2006. Review conducted by Phillip M. Ligrani.

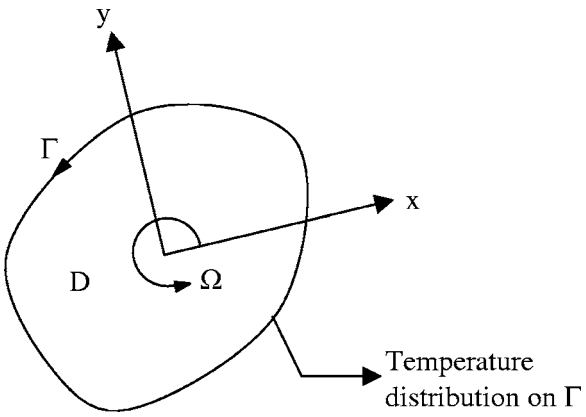

Fig. 1 Generic configuration of two-dimensional thermally driven flow in an arbitrary cross-sectional rotating enclosure

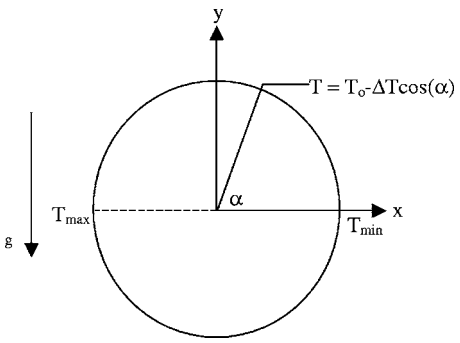

Fig. 2 Geometry and thermal boundary conditions of the problem in Ref. [18]

stratification in the core became unstable and a reversal of the flow in the core was observed whenever coriolis forces dominated the flow.

In a recent study conducted by the authors [13], a two-dimensional thermally driven flow of air in a steadily rotating horizontal cylinder was investigated. In this numerical investigation, a spatially periodic temperature variation was imposed on the circular wall of the cylinder. The investigation was carried out in a Cartesian rotating frame of reference. The changes in the spatial and temporal structure of the unsteady flow, at a fixed $Ra_g = 10^5$ and Pr=0.71, as Ra_Ω was varied from 10^2 to 10^7 were studied. In order to obtain physically realizable solutions, the Taylor number (Ta) was varied simultaneously along with the variation in Ra_Ω. It was pointed out in [10] that (Ta) and Ra_Ω cannot be assigned arbitrary values. Rather they must be made to conform to the fact that the ratio $Ta/Ra_\Omega = 1/(\beta \Delta T\, Pr)$. It was argued in [13] that for commonly occurring fluids like air and water, the ratio is $O(10^2)$. Thus a fixed ratio of 100 was utilized in the study. It was recognized in this study that the Coriolis force has an irrotational character in such a class of two-dimensional flows. The earlier studies had failed to recognize this important fact [11,12]. However, even though the irrotational character of the Coriolis force was recognized in [13], the role of the Coriolis force was incorrectly interpreted. Similar, to the conjecture made in [11], it was argued that for $Ta \sim Ra_g$, the Coriolis forces assisted gravity in maintaining a clockwise circulation in the enclosure and preventing flow reversal during certain phase of the rotating gravity vector. This was believed to be the reason of enhancement of heat transfer at low rotation rates.

The present work attempts to examine the role of Coriolis forces in two-dimensional thermally driven flows in rotating enclosures of an arbitrary cross section. The effort is motivated by the fact that some of the earlier studies dealing with such a class of flows have apparently not recognized the irrotational character of the coriolis force. This has led to the misinterpretation of the role of the Coriolis force in such a class of flows.

The paper is organized in five sections. The governing equations for the problem of thermal convection in a steadily rotating arbitrary shaped enclosure are presented in Sec. 2. Section 3 briefly describes the numerical scheme employed. Since the numerical scheme is the same as the one employed in [13], the details of the scheme are omitted. The role of the Coriolis force is examined theoretically in Sec. 4. This section also presents some numerical results for the problem considered in [13], with and without the Coriolis force, clearly indicating the role of the Coriolis force in such a class of flows. Finally, the results are summarized and conclusions are drawn in Sec. 5.

2 Governing Equations

Figure 1 shows the generic geometry of a rotating enclosure of an arbitrary cross section. It is assumed that the enclosure has been rotating steadily for a long time so that the fluid inside is in a state of solid-body rotation. If a temperature variation is imposed on the boundary Γ of the enclosure, the fluid motion relative to the rotating enclosure would be generated under the combined influence of gravitational and centrifugal buoyancy force. Such a motion is most conveniently studied using a frame of reference rotating with the enclosure. For the sake of simplicity let us consider a Cartesian rotating frame of reference. The equations governing the fluid motion are the mass, momentum, and energy equations subject to Boussinesq approximation [13]. The dimensionless forms of the equations are

$$\text{Mass:} \quad \nabla \cdot \vec{V} = 0 \tag{1}$$

$$\text{Momentum:} \quad \frac{D\vec{V}}{D\tau} = -\nabla p_m - Ra_\Omega\, Pr\, \theta \hat{n}_g - Ra_\Omega\, Pr\, \theta \vec{r} - 2\, Ta^{1/2}\, Pr(\hat{k} \times \vec{V}) + Pr\, \nabla^2 \vec{V}. \tag{2}$$

$$\text{Energy equation:} \quad \frac{D\theta}{D\tau} = \nabla^2 \theta \tag{3}$$

The vector $\hat{n}_g$ in Eq. (2) is the unit vector indicating the instantaneous direction of the rotating gravity vector and is defined as

$$\hat{n}_g = -\hat{i} \sin(Ta^{1/2}\, Pr\, \tau) - \hat{j} \cos(Ta^{1/2}\, Pr\, \tau).$$

The length, time, and velocity scales employed to transform the equations to their dimensionless forms are R, R^2/κ, and κ/R, respectively. The scales utilize the cylinder radius R and the thermal diffusivity of the fluid κ. The term p_m in Eq. (2) is the dimensionless change in pressure over the pressure in the solid-body rotation state under isothermal conditions. This is the rotational analogue of piezometric pressure. The temperature in the governing equations appears in the form of a dimensionless change over the isothermal conditions that prevail prior to the application of temperature perturbation at the wall. The formal definitions of p_m and θ are

$$p_m = \frac{(P - P_o)R^2}{\rho_o \kappa^2}, \quad \theta = \frac{(T - T_o)}{\Delta T} \tag{4}$$

In the solid-body rotation state, the fluid is taken to be at a uniform temperature T_o and density ρ_o. The amplitude of the periodic temperature perturbation is represented as ΔT. The dimensional pressure P_o in a state of rest with respect to the rotating frame under isothermal conditions is given by the momentum equation as

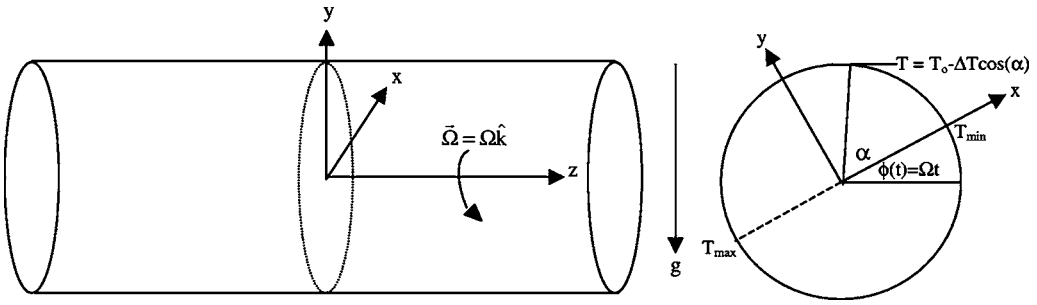

Fig. 3 Geometry of the problem of two-dimensional thermally driven flow in a rotating horizontal cylinder

$$\nabla P_o = \rho_o(\vec{g} - \vec{\Omega} \times \vec{\Omega} \times \vec{r}) \tag{5}$$

In Eq. (5), $\vec{\Omega}=\Omega\hat{k}$ is the steady rotation rate of the frame attached to the rotating cylinder. Equations (1)–(3) together with the no-slip boundary conditions for the velocity and the specified temperature perturbation on Γ (Fig. 1), govern the motion of the fluid relative to the rotating frame.

3 Numerical Scheme

A two-step predictor-corrector semiexplicit scheme is the same as employed in [13]. For the sake of completeness, a brief description of the scheme is given here. A two-step predictor-corrector, semiexplicit scheme is employed to numerically integrate Eqs. (1)–(3) on a Cartesian structured colocated mesh. In the predictor step, Eqs. (2) and (3) are integrated explicitly using first-order Euler integration. A first-order accurate temperature field is obtained in this step. The velocity field obtained in this step does not satisfy continuity. In order to correct this provisional velocity field, a semiexplicit corrector step is introduced. In this corrector step, the provisional velocity field is corrected through irrotational velocity corrections obtained through a pressure correction field. The pressure correction field is obtained by solving the pressure

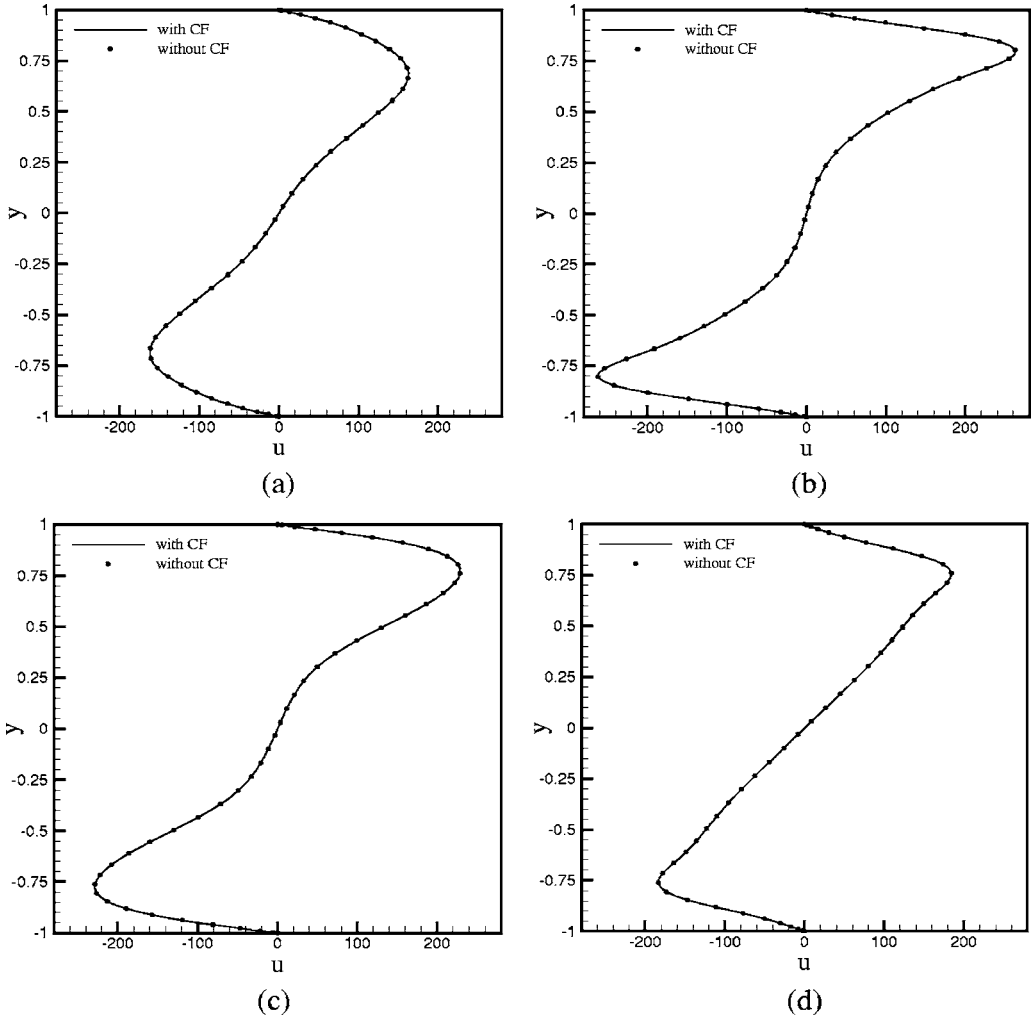

Fig. 4 Profiles of *u* velocity along the vertical diameter (*x*=0) for ($Ra_\Omega=10^3$, $Ta=10^5$) at (*a*) $\phi_g=3\pi/2$, (*b*) $\phi_g=\pi$, (*c*) $\phi_g=\pi/2$, and (*d*) $\phi_g=0$

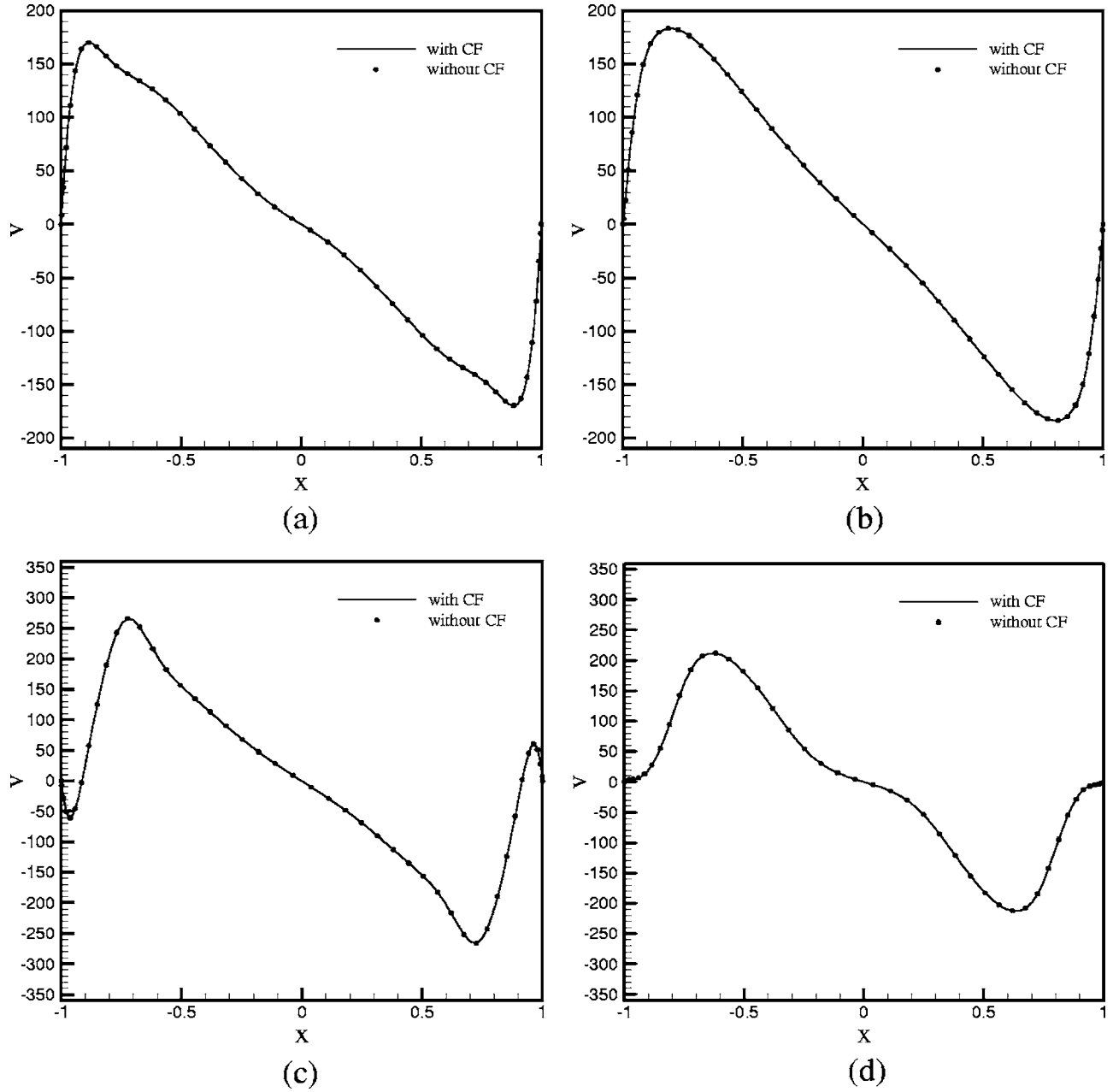

Fig. 5 Profiles of v velocity along the horizontal diameter ($y=0$) for ($Ra_\Omega=10^3$,$Ta=10^5$) at (*a*) $\phi_g=3\pi/2$, (*b*) $\phi_g=\pi$, (*c*) $\phi_g=\pi/2$, and (*d*) $\phi_g=0$

correction Poisson's equation (PCPE) which implicitly enforces continuity. The scheme closely resembles the (SMAC) scheme originally proposed by Amsden and Harlow [14].

A finite difference type of discretization has been employed. A fourth-order central differencing in the interior and a second-order central differencing for the nodes adjacent to the boundary has been employed for the diffusion terms. For the interior nodes, a third order upwinding or a fourth-order central differencing has been employed for the convective terms. The choice between upwinding and central differencing is based on the local cell Peclet number (Pe). The central differencing is employed if $-2<\mathrm{Pe}<2$, otherwise upwinding is utilized. For grid points adjacent to the boundary, a second-order central differencing is employed for the convective terms. The pressure gradients are discretized using a second-order central scheme.

The discretization of PCPE on a colocated grid requires care as improper discretization can lead to spurious pressure oscillations [15,16]. A compact discretization together with momentum interpolation procedure helps to achieve a discretization that maintains the pressure-velocity coupling at a grid point on a colocated structured mesh [15,17]. The details of the discretization of the PCPE can be seen in [13]. The discretized PCPE has a five-point molecule and is solved using a (SIP) procedure [16]. The PCPE is solved subject to zero normal gradient of the pressure correction field at the solid wall [13,15]. Once the velocity and pressure fields have been corrected in the interior, the wall pressure is obtained by applying the normal momentum equation.

For the purpose of validation of the scheme, the problem of two-dimensional thermally driven flow of air (Pr=0.71) in a fixed circular enclosure, subject to a spatially periodic temperature variation around the periphery (Fig. 2), was considered in [13]. Xin et al. [18] carried out a detailed numerical investigation of this flow. The distribution of wall normal heat flux over the wall

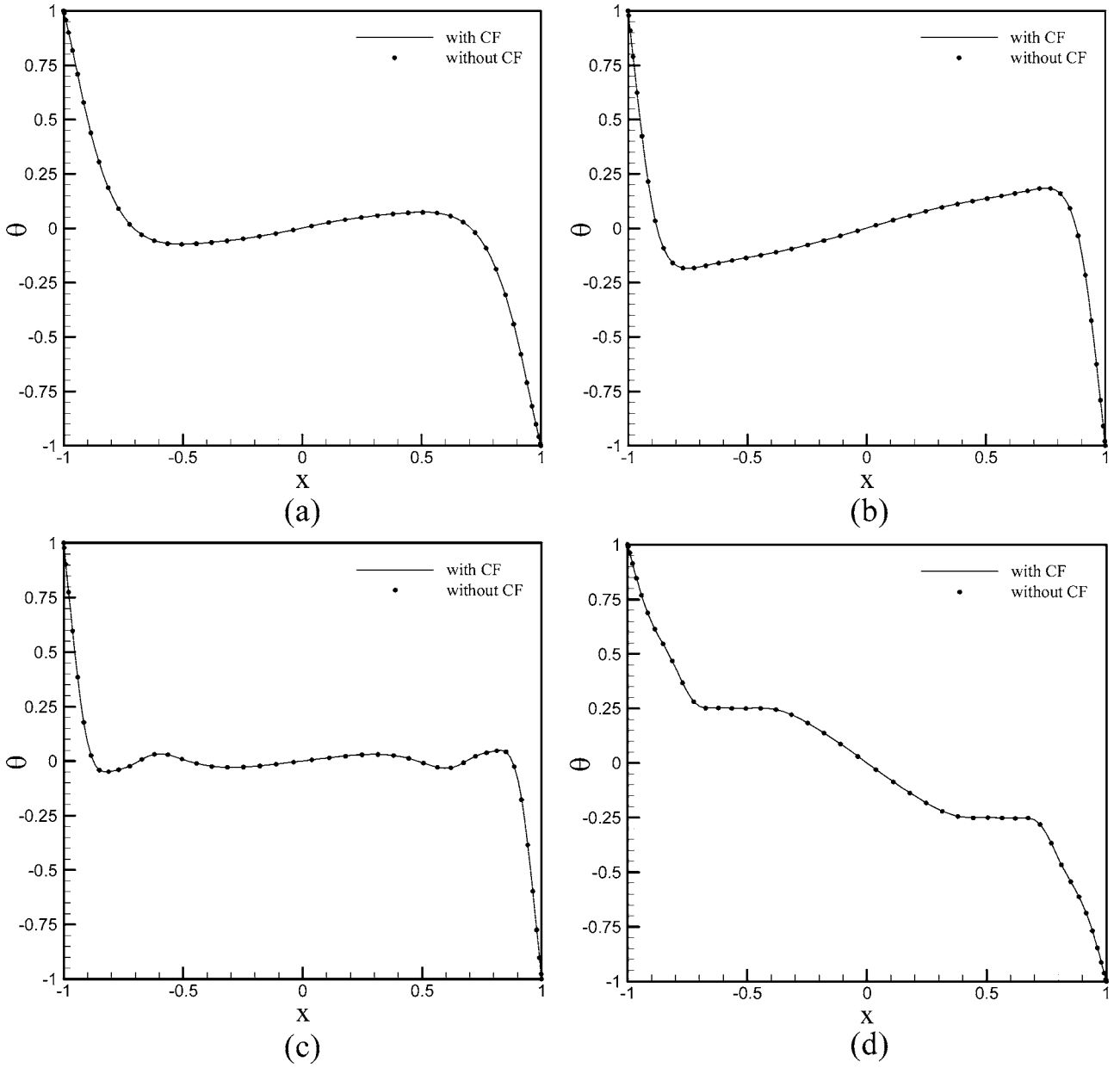

Fig. 6 Profiles of θ along the horizontal diameter ($y=0$) for ($Ra_\Omega=10^3, Ta=10^5$) at (*a*) $\phi_g=3\pi/2$, (*b*) $\phi_g=\pi$, (*c*) $\phi_g=\pi/2$, and (*d*) $\phi_g=0$

and the heat transfer over the heated portion of the circular enclosure were compared with the numerical data in [18]. Comparisons were made at $Ra_g=1\times10^4$, 5×10^4, 1×10^5, and 5×10^5. As shown in [18] these Ra_g correspond to the steady regime. Excellent agreement with the numerical data in [18] was demonstrated in [13]. The details of the validation can be seen in [13].

4 Role of the Coriolis Force

In this section the role of the Coriolis force in two-dimensional thermally driven flow in a rotating enclosure of arbitrary geometry is examined. The irrotational character of the Coriolis force in this class of flows is demonstrated. Theoretical arguments on the basis of irrotational character are presented. The inference drawn from the theoretical considerations is supported through numerical experiments on thermally driven two-dimensional flow in a rotating circular enclosure. This problem has already been investigated by the present authors in [13] for a fixed $Pr=0.71$ and $Ra_g=10^5$.

4.1 Theoretical Analysis. The equations governing the two-dimensional thermally driven flow in a rotating enclosure of arbitrary cross section in primitive variables were presented in Sec. 2. In order to demonstrate the irrotational nature of the Coriolis force, the curl of the term respresenting the Coriolis force in Eq. (2) is expressed as

$$(2\,\mathrm{Ta}^{1/2}\,\mathrm{Pr})(\nabla\times\hat{k}\times\vec{\mathrm{V}})=(2\,\mathrm{Ta}^{1/2}\,\mathrm{Pr})\left\{(\nabla\,.\,\vec{\mathrm{V}})\hat{\mathrm{k}}-\frac{\partial\vec{\mathrm{V}}}{\partial z}\right\} \quad (6)$$

The right-hand side of Eq. (6) is identically zero for the type of flow under consideration. Thus the Coriolis force is irrotational in character. The irrotational nature of Coriolis force stems from two basic assumptions (1) Boussinesq approximation leading to the solenoidal velocity field and (2) the two-dimensional approximation of the flow.

The irrotational nature of the Coriolis force has an important implication which is illuminated by the following considerations.

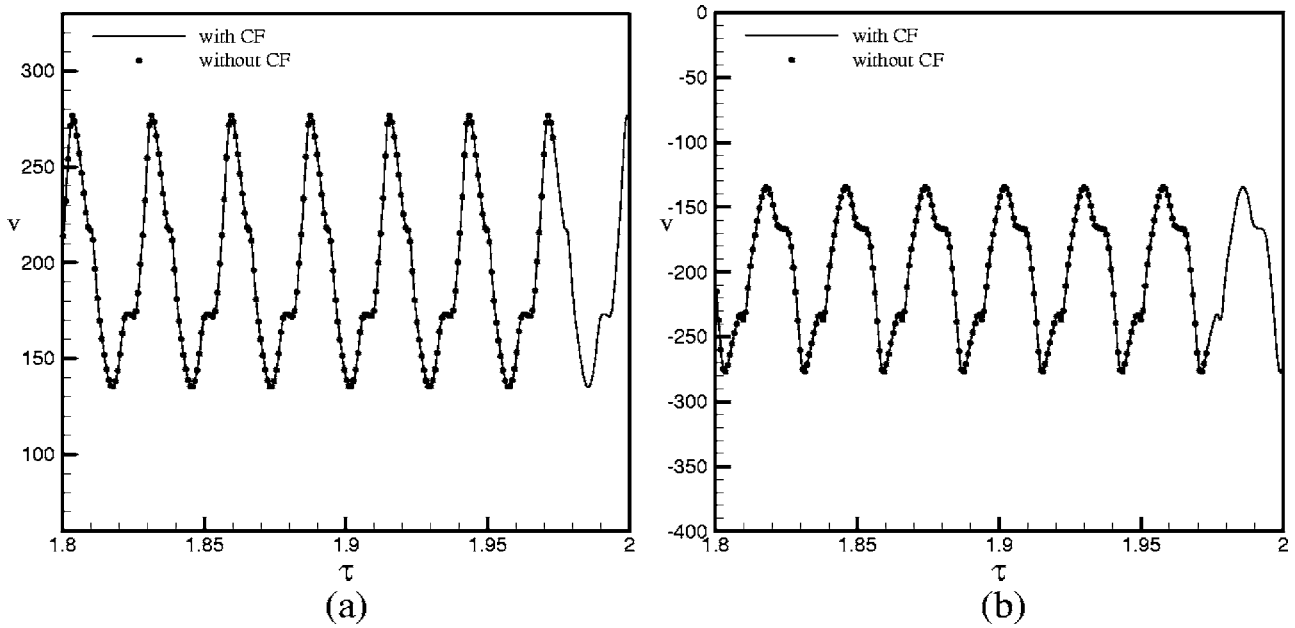

Fig. 7 Time histories of *v* velocity for ($Ra_\Omega = 10^3, Ta = 10^5$) at (*a*) (−0.72,0) and (*b*) (0.72,0)

Any irrotational force field can be mathematically represented as a gradient of a scalar field. Such a scalar field ϕ_c is related to the velocity field as

$$\hat{k} \times \vec{V} = \nabla \phi_c \tag{7a}$$

$$\text{or } u = \frac{\partial \phi_c}{\partial y}, \quad v = -\frac{\partial \phi_c}{\partial x} \tag{7b}$$

Thus, the Coriolis force in Eq. (2) with the aid of Eq. (7*a*), can be combined with the pressure force to form an effective pressure in the flow field. In fact all the irrotational forces can be combined in a similar manner to form a single force field whose presence in the (NS) equations is expressed as a gradient of a scalar field. Mathematically, the effective pressure can be expressed as

$$P_{\text{eff}} = p_m + 2\,\text{Ta}^{1/2}\,\text{Pr}\,\phi_c \tag{8}$$

Thus, Eqs. (1)–(3) do not actually sense the pressure and the Coriolis force separately but in the form of the gradient of the effective pressure. Initially, $p_m = 0$ everywhere in the flow domain and the gradients of ϕ_c are also absent. This implies that *no gradients* of effective pressure are *imposed* on the flow. The fluid motion, relative to the rotating observer, develops under the action of gravitational and centrifugal buoyancy forces. As the flow evolves, the gradients of effective pressure develop. Thus, whether the coriolis force is present or absent, the same distribution of P_{eff} would be developed for a given set of parameters (Ra_g, Ra_Ω, Ta, and Pr). These arguments imply that the velocity and thermal fields evolve independently of the Coriolis force. Further, the presence of the Coriolis force modifies the actual pressure p_m. It is worth mentioning that while Coriolis forces do not affect the velocity and thermal fields, the parameter Ta is still important as it appears in Eq. (2) explicitly through the rotating unit vector $\hat{n}_g$. It is clear that the above remarks apply quite generally to any geometrical configuration as well as the choice of thermal boundary conditions. However, it is to be remembered that departures from the Boussinesq approximation and/or the two-dimensional approximation would render the conclusions regarding the role of the Coriolis force meaningless.

The theoretical arguments presented clearly indicate that the Coriolis force does not play any role in the evolution of velocity and temperature fields. Further it is also shown that the presence of Coriolis force would simply affect the pressure distribution in the rotating enclosure. Thus it is incorrect to attribute any observed flow feature or characteristic related to the velocity and thermal fields to the coriolis force.

4.2 Numerical Experiments. In order to test the conclusions obtained via theoretical arguments in the previous section, the problem of thermally driven flow of air in a rotating circular enclosure is considered. This is the same problem considered earlier in [13]. For the benefit of the readers the problem is described in brief in this section. Figure 3 shows the geometry of the problem together with the thermal boundary conditions employed. The governing equations for the problem are Eqs. (1)–(3) in primitive variables. In order to demonstrate that the conclusions regarding Coriolis force obtained in Sec. 4.1 are valid, the simulations are carried out by simply ignoring the coriolis force. The no-slip condition for the velocity and known values of the dimensionless temperature at the wall provide the necessary boundary conditions.

A nonuniform 91×91 Cartesian mesh identical to the one employed in [13] has been utilized. The grid has a minimum and maximum dimensionless spacing of 5×10^{-4} near the wall and 0.038 near the center in the x and y directions, respectively. It was shown in [13] that this grid yields grid independent solutions. Hence it has been utilized for the numerical experiments. A time step of 0.4×10^{-6} is utilized for all the numerical experiments.

In order to support the theoretical deductions regarding the role of Coriolis force, the spatial and temporal structure of the flow obtained by neglecting the Coriolis force is compared with that of the flow simulated with the full set of equations. The spatial structure of the velocity and temperature fields are compared at four time instants marked by four different orientation or phase "ϕ_g" of the rotating gravity vector. The phase angle ϕ_g is measured from the positive direction of the x axis in the counter-clockwise direction. As in [13], the four values of ϕ_g selected are $3\pi/2$, π, $\pi/2$, and 0. The time histories of v velocity at (−0.72,0) and (+0.72,0) are also compared. In the numerical simulations, Ra_g and Pr were kept fixed at 10^5 and 0.71, respectively. The numerical simulations are carried out at ($Ra_\Omega = 10^3, Ta = 10^5$), ($Ra_\Omega = 1.7 \times 10^3, Ta = 1.7 \times 10^5$), and ($Ra_\Omega = 1.9 \times 10^3, Ta = 1.9 \times 10^5$). These values have been deliberately chosen, as for these sets of param-

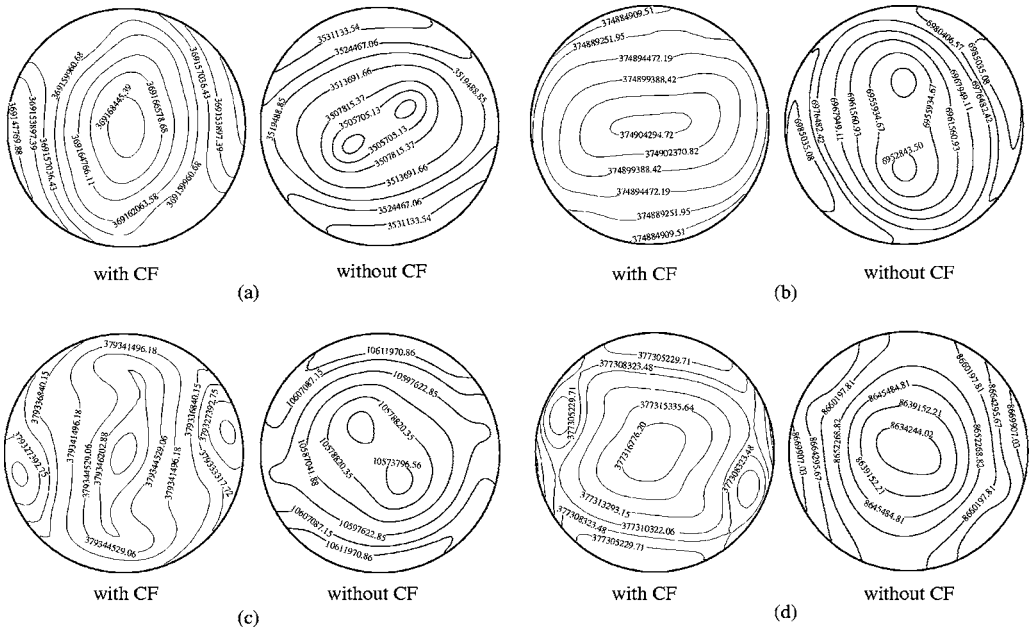

Fig. 8 Pressure distributions with and without coriolis force for ($Ra_\Omega = 10^3, Ta = 10^5$) at (*a*) $\phi_g = 3\pi/2$, (*b*) $\phi_g = \pi$, (*c*) $\phi_g = \pi/2$, and (*d*) $\phi_g = 0$

eters, the Coriolis force is comparable to the gravitational buoyancy force. In the earlier studies it was argued that for $Ta \approx Ra_g$ the Coriolis forces assist the gravitational buoyancy in maintaining a clockwise circulation in the enclosure [11,13]. In order to test these claims, runs are taken by neglecting the Coriolis forces, specifically for $Ta \approx Ra_g$.

Figures 4(*a*)–4(*d*) compare the evolving structure of u velocity obtained with and without Coriolis forces. It is clearly seen that the data obtained without the Coriolis forces matches exactly with the results from the simulations using the full set of Eqs. (1)–(3). Similarly, Figs. 5(*a*)–5(*d*) and Figs. 6(*a*)–6(*d*) compare the structure of v velocity and temperature θ at different values of ϕ_g. Figures 7(*a*) and 7(*b*) compare the time histories of v velocity obtained by neglecting the Coriolis force with those obtained from the full set of equations at $(-0.72, 0)$ and $(0.72, 0)$, respectively. It is again observed that the two trajectories exactly overlap. These figures confirm the theoretical prediction that the Coriolis force does not affect the evolution of the velocity and the temperature fields.

To demonstrate the effect of Coriolis force on pressure, the distribution of pressure with and without Coriolis force is compared at different values of ϕ_g in Figs. 8(*a*)–8(*d*). The difference in the pressure distribution is very obvious from the contour plots. It is now of interest to examine the distribution of effective pressure (P_{eff}) as defined in Eq. (8). Figure 9(*a*) shows the effective pressure (P_{eff}) distributions in the enclosure obtained by taking the Coriolis force into consideration and by simply ignoring them in the governing equations. The figure confirms that the effective pressure evolves as a function of the velocity and temperature fields and is therefore unaffected by dropping the Coriolis force. Figure 9(*b*) compares the distribution of the magnitude of the force generated due to the effective pressure with and without the Coriolis force. The contours represent isovalues of magnitude of ∇P_{eff}. Again, as predicted by the theoretical considerations, the Coriolis force does not affect the effective pressure force.

Similar results are found for $(Ra_\Omega = 1.7 \times 10^3, Ta = 1.7 \times 10^5)$ and $(Ra_\Omega = 1.9 \times 10^3, Ta = 1.9 \times 10^5)$. The time histories of v velocity at $(-0.72, 0)$ and $(0.72, 0)$ are compared for these set of parameters in Figs. 10 and 11. These figures also show that the Coriolis force does not play any role in the evolution of velocity and temperature fields.

5 Conclusions

It has been shown that in a *two-dimensional* thermally driven flow in a rotating enclosure of arbitrary geometry subject to

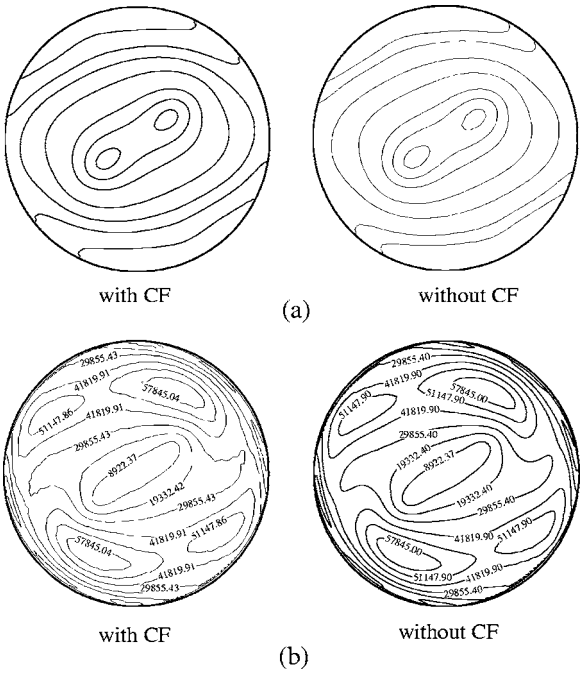

Fig. 9 Distribution of (*a*) P_{eff} and (*b*) magnitude of gradient of P_{eff} with and without coriolis force for ($Ra_\Omega = 10^3, Ta = 10^5$) at $\phi_g = 3\pi/2$

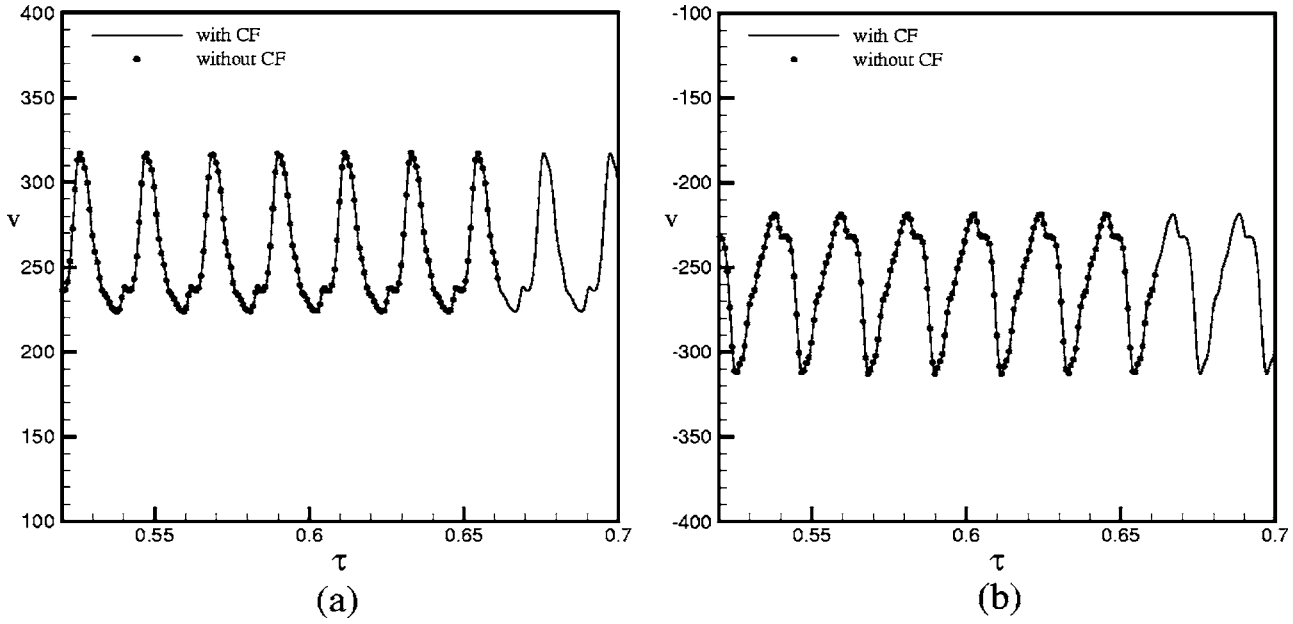

Fig. 10 Time histories of *v* velocity for ($Ra_\Omega = 1.7\times10^3$, $Ta = 1.7\times10^5$) at (*a*) (−0.72, 0) and (*b*) (0.72, 0)

Boussinesq approximation, the Coriolis forces are irrotational in character. The irrotational Coriolis force combines with the irrotational force of pressure to form an effective pressure (P_{eff}). The momentum equations only sense the gradients of the irrotational effective pressure force. Owing to the fact that no effective pressure gradients are imposed on the flow, the effective pressure develops as a *function of* the velocity and the temperature fields which are governed by the inertia, viscous, and the buoyancy forces of gravity and centrifugal acceleration fields. Therefore a change in the magnitude of the Coriolis force would alter the pressure p_m in the enclosure leaving the effective pressure unaltered. The irrotational character is responsible for the insensitivity of the velocity and temperature fields to the Coriolis force in such class of flows.

Direct numerical evidence supporting the theoretical prediction of the role of Coriolis force, in the class of flows under consideration in the present study, has been provided through numerical simulations of two-dimensional thermally driven flow of air (Pr = 0.71) in a rotating circular enclosure. Computations carried out by simply ignoring the Coriolis force reveal no change in the unsteady velocity and temperature fields. However, the pressure distribution was altered in the absence of Coriolis forces.

The earlier studies involving two-dimensional thermally driven flows in a rotating enclosure subject to Boussinesq approximation, with the exception of the work in [13], have failed to recognize the irrotational character of the coriolis force. In virtually all the earlier studies, all the workers including the present authors, have

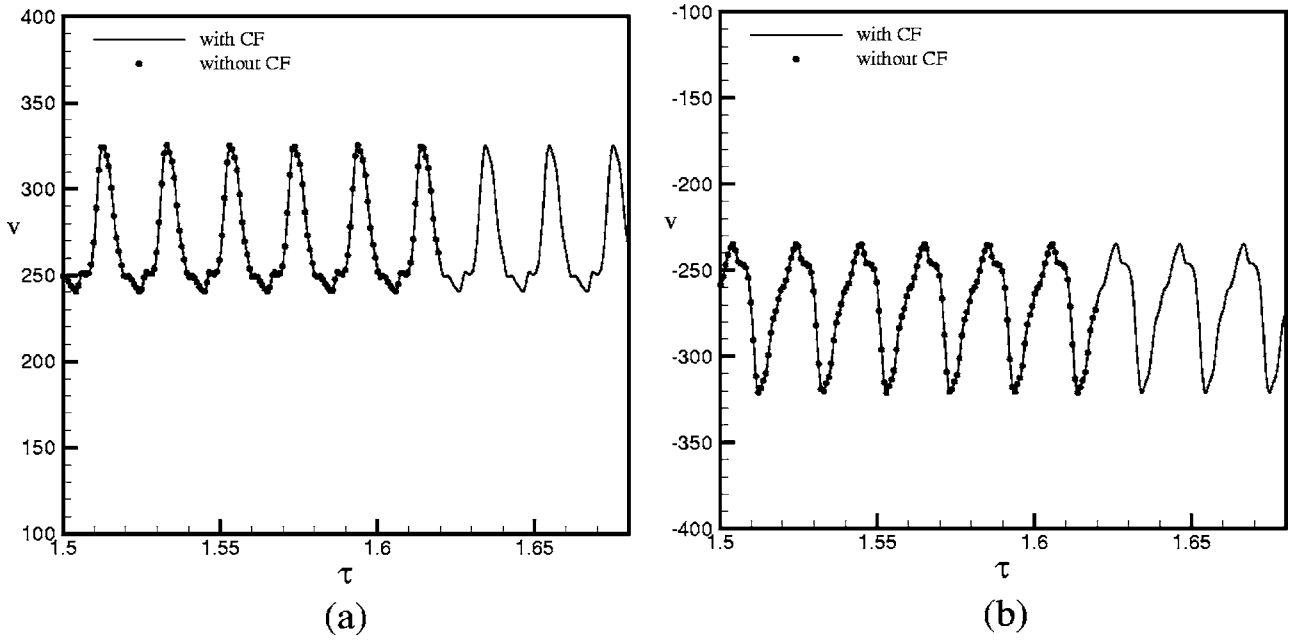

Fig. 11 Time histories of *v* velocity for ($Ra_\Omega = 1.9\times10^3$, $Ta = 1.9\times10^5$) at (*a*) (−0.72, 0) and (*b*) (0.72, 0)

misinterpreted the role of the Coriolis force. This work highlights the error in the earlier works. The correct role of the Coriolis force, in the class of flows focused upon in this work, has been deduced using theoretical reasoning. The theoretical deductions are backed up by direct evidence in the form of computing of an "apparently Coriolis assisted flow" without any Coriolis forces.

It is worth mentioning that the arguments presented and conclusions reached can be extended to any flow in a rotating reference frame where the Coriolis forces are irrotational. In any such flow situation, the Coriolis force will not play any role in the evolution of the velocity field. The role of this force would be to redistribute the pressure.

Acknowledgment

The authors would like to thank Professor K. V. Pagalthivarthi, Department of Applied Mechanics, I.I.T Delhi, New Delhi, for the useful discussions on this topic.

References

[1] Homsy, G. M., and Hudson, J. L., 1969, "Centrifugally Driven Thermal Convection in a Rotating Cylinder," J. Fluid Mech., **35**, Part 1, pp. 33–52.
[2] Hudson, J. L., Tang, D., and Abell, S., 1978, "Experiments on Centrifugally Driven Thermal Convection in a Rotating Cylinder," J. Fluid Mech., **86**, Part 1, 147–159.
[3] Tang, D., and Hudson, J. L., 1983, "Experiments on a Rotating Fluid Heated From Below," Int. J. Heat Mass Transfer, **26**(6), 943–949.
[4] Somerville, R. C. J., 1971, "Bénard Convection in a Rotating Fluid," Geophys. Fluid Dyn., **2**, 247–262.
[5] Somerville, R. C. J., and Lipps, F. B., 1973, "A Numerical Study in Three Space Dimensions of Bénard Convection in a Rotating Fluid," J. Atmos. Sci., **30**, 590–596.
[6] Buell, J. C., and Catton, I., 1983, "Effect of Rotation on the Stability of a Bounded Cylindrical Layer of Fluid Heated From Below," Phys. Fluids, **26**(4), 892–896.
[7] Ker, Y. T., Li, Y. H., and Lin, T. F., 1998, "Experimental Study of Unsteady Thermal Characteristics and Rotation Induced Stabilization of Air Convection in a Bottom Heated Rotating Vertical Cylinder," Int. J. Heat Mass Transfer, **41**(11), 1445–1458.
[8] Bühler, K., and Oertel, H., 1982, "Thermal Cellular Convection in Rotating Rectangular Boxes," J. Fluid Mech., **114**, 261–282.
[9] Abell, S., and Hudson, J. L., 1975, "An Experimental Study of Centrifugally Driven Free Convection in a Rectangular Cavity," Int. J. Heat Mass Transfer, **18**, 1415–1423.
[10] Ker, Y. T., and Lin, T. F., 1996, "A Combined Numerical and Experimental Study of Air Convection in a Differentially Heated Rotating Cubic Cavity," Int. J. Heat Mass Transfer, **39**(15), 3193–3210.
[11] Hamady, F. J., Lloyd, J. R., Yang, K. T., and Yang, H. Q., 1994, "A Study of Natural Convection in a Rotating Enclosure," J. Heat Transfer, **116**, 136–143.
[12] Baig, M. F., and Masood, A., 2001, "Natural Convection in a Two-Dimensional Differentially Heated Square Enclosure Undergoing Rotation," Numer. Heat Transfer, Part A, **40**, 181–202.
[13] Hasan, N., and Sanghi, S., 2004, "The Dynamics of Two-Dimensional Buoyancy Driven Convection in a Horizontal Rotating Cylinder," J. Heat Transfer, **126**, 963–984.
[14] Amsden, A. A., and Harlow, F. H., 1970, "The SMAC Method: A Numerical Technique for Calculating Incompressible Fluid Flows," *Los Alamos Scientific Rep.* LA 4370.
[15] Cheng, L., and Armfield, S., 1995, "A Simplified Marker and Cell Method for Unsteady Flows on Non-Staggered Grids," Int. J. Numer. Methods Fluids, **21**, 15–34.
[16] Ferziger, J. H., and Peric, M., 1996, "*Computational Methods for Fluid Dynamics*," Springer-Verlag, Berlin, Chap. 5, p. 95.
[17] Rhie, C. M., and Chow, W. L., 1983, "Numerical Study of the Turbulent Flow Past an Airfoil With Trailing Edge Separation," AIAA J., **21**, 1525–1532.
[18] Xin, S., Quéré, P. L., and Daube, O., 1997, "Natural Convection in a Differentially Heated Horizontal Cylinder: Effects of Prandtl Number on Flow Structure and Instability," Phys. Fluids, **9**(4), 1014–1033.

Shyy Woei Chang
Professor
Thermal Fluids Laboratory,
National Kaohsiung Marine University,
No. 142 Haijhuan Road,
Nanzih District,
Kaohsiung City 81143,
Taiwan, Republic of China
e-mail: swchang@mail.nkmu.edu.tw

Tong-Minn Liou
Professor

Jui-Hung Hung
Ms Student

Department of Power Mechanical Engineering,
National Tsing Hua University,
300 Hsinchu,
Taiwan, Republic of China

Wen-Hsien Yeh
Ms Student
Department of Marine Engineering,
National Kaohsiung Marine University,
No. 142 Haijhuan Road,
Nanzih District,
Kaohsiung City 81143,
Taiwan, Republic of China

Heat Transfer in a Radially Rotating Square-Sectioned Duct With Two Opposite Walls Roughened by 45 Deg Staggered Ribs at High Rotation Numbers

This paper describes an experimental study of heat transfer in a radially rotating square duct with two opposite walls roughened by 45 deg *staggered ribs. Air coolant flows radially outward in the test channel with experiments to be undertaken that match the actual engine conditions. Laboratory-scale heat transfer measurements along centerlines of two rib-roughened surfaces are performed with Reynolds number (Re), rotation number (Ro), and density ratio* $(\Delta\rho/\rho)$ *in the ranges of 7500–15,000, 0–1.8, and 0.076–0.294. The experimental rig permits the heat transfer study with the rotation number considerably higher than those studied in other researches to date. The rotational influences on cooling performance of the rib-roughened channel due to Coriolis forces and rotating buoyancy are studied. A selection of experimental data illustrates the individual and interactive impacts of Re, Ro, and buoyancy number on local heat transfer. A number of experimental-based observations reveal that the Coriolis force and rotating buoyancy interact to modify heat transfer even if the rib induced secondary flows persist in the rotating channel. Local heat transfer ratios between rotating and static channels along the centerlines of stable and unstable rib-roughened surfaces with Ro varying from 0.1 to 1.8 are in the ranges of 0.6–1.6 and 1–2.2, respectively. Empirical correlations for periodic flow regions are developed to permit the evaluation of interactive and individual effects of ribflows, convective inertial force, Coriolis force, and rotating buoyancy on heat transfer.* [DOI: 10.1115/1.2409988]

Keywords: high rotating number, turbine rotor blade cooling

1 Introduction

The advanced gas turbine engine takes the thermodynamic advantage by operating the turbine entry temperatures at extremely high levels that are often above the melting temperatures of blade materials. It is essential to adopt the internal air cooling for turbine rotor blades, even though the consumption of air flow is treated as a loss of engine efficiency. In order to effectively manage the air flow inside a turbine rotor blade, the coolant channels are interconnected in the multipass manner. The air coolant can flow in the radially outward and inward directions with the interchannel bends needed. A variety of techniques for heat transfer augmentation is adopted for these coolant channels. The surface devices such as ribs, fins, and pins are often used to promote the local heat transfer coefficients. As a result, the cooling passages inside the turbine rotor blade become extremely complex. When the film and transpiration cooling methods are used, the cooling air is bleeding from these internal coolant channels via the tiny holes drilled through the blade. The complicate cooling network makes the prediction of the three-dimensional flow and heat transfer phenomena inside the coolant channels to be a difficult task. Because the coolant inside the cooling channel rotates with the turbine rotor blade, the rotation gives rise to Coriolis and centrifugal forces that modify the flow fields inside the nonrotational channel. The Coriolis forces create secondary flows in the plane perpendicular to the channel axis, acting as a source term to generate the vorticity. These secondary flows driven by the Coriolis force generate the peripheral heat transfer variation around the rotating channel that cause heat transfer enhancement and impediment relative to the nonrotating reference over the destabilized and stabilized surfaces, respectively. The interaction of centrifugal force and density variation of coolant produces the buoyancy effect that affects the mainstream flow and Coriolis secondary flow. These two physical manifestations of rotation, namely the Coriolis and rotating-buoyancy effects, also modify the structure of turbulence so that the evaluation of flow and heat transfer inside the rotating channel becomes extremely difficult. However, the internal cooling of turbine rotor blade has been a standard design feature for over 40 years.

The heat transfer in a rotating channel with cooling application to gas turbine rotor blade has motivated a large amount of laboratory-scale experimental studies using simplified models of the real blade cooling geometry [1–25]. The geometries of rotating channels relevant to the cooling network in the gas turbine rotor blade, such as the surface ribs [6–10], cross-sectioned shape [11–13], channel orientation [14–17], wall heating condition [18,19], multipass channel [20–22], and pin-fin duct [23] at various test conditions have been examined to study their effects on heat transfer in these rotating channels. There are intercorrelative influences between the various test geometries, such as the cross-sectioned shape with surface ribs [24] and the wall heating conditions with channel orientation [25] that additionally modify the rotational impacts on heat transfer. For a set of specific channel geometries, the heat transfer coefficient in the rotating channel is controlled by forced convection, Coriolis forces, and rotating

Contributed by the Heat Transfer Division of ASME for publication in the JOURNAL OF HEAT TRANSFER. Manuscript received January 3, 2006; final manuscript received May 2, 2006. Review conducted by Minking Chyu.

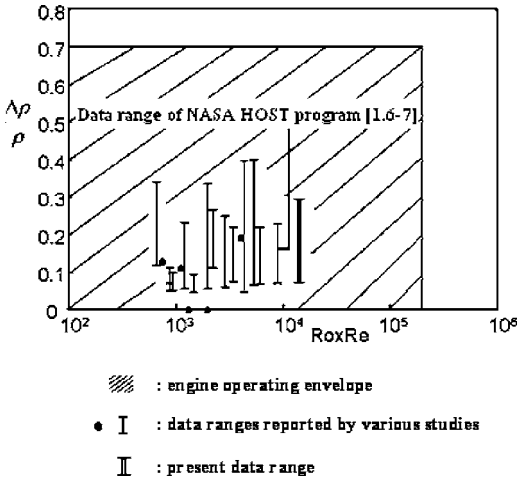

Fig. 1 $\Delta\rho/\rho$ versus Ro×Re

buoyancy. This technical society has agreed that the Reynolds (Re) and rotation (Ro) numbers characterize the forced convection and the Coriolis-force induced secondary flows in their own rights with the buoyancy impact to be indexed by density ratio $\Delta\rho/\rho$. The density difference, $\Delta\rho$, is customarily referred to as the coolant's density variation from the reference density, ρ, at a selected temperature datum. This density ratio is conveniently defined as $\beta(T_w\text{-}T_b)$ where β, T_w, and T_b are the thermal expansion coefficient of coolant, the local wall, and flow-bulk temperatures, respectively. Although the buoyancy parameter in terms of $\Delta\rho/\rho$ has been widely adopted to index the buoyancy level inside a rotating channel, the centrifuge is not taken into account by this density ratio ($\Delta\rho/\rho$). The combination of density ratio with relative centrifuge constructs the nondimensional group of $\beta(T_w - T_b)\mathrm{Ro}^2(R/d)$. This dimensionless group (Bu) can physically reflect the relative strength of rotating buoyancy force. The simulation of real engine condition for a rotating coolant channel in the laboratory condition requires matching the nondimensional groups of Re, Ro, and $\Delta\rho/\rho$. It is a strategic decision to extend the experimental data to emulate more closely realistic engine conditions.

The typical gas turbine engine speed is in the range of 3000–20,000 rpm with maximum Re of 100,000 for coolant channel flow in the turbine blade [2]. To acquire the laboratory scale simulations with Re, Ro, and $\Delta\rho/\rho$ simultaneously matching the realistic engine conditions is under the constant pursuit. This is illustrated by converting the typical range of geometric, flow, rotational speed, and temperature parameters of the real engine blade cooling channels [2] into Re, Ro, and $\Delta\rho/\rho$ that gives the operational $\mathrm{Re}\times\mathrm{Ro}$ and $\Delta\rho/\rho$ envelope as shown in Fig. 1. The previous data ranges [1–25] marked in Fig. 1 are limited in the ranges of $\mathrm{Re}\times\mathrm{Ro}<10{,}000$ and $\Delta\rho/\rho<0.4$, which cannot cover the so-called engine worse-case scenarios [2]. The experimental data in the range of $\mathrm{Re}\times\mathrm{Ro}>10{,}000$ and $\mathrm{Ro}>1$ has considerably extended the past data experience that is attainable by conducting the high pressure tests with the simulated coolant channel of large hydraulic diameter. In Fig. 1, it is interesting to depict the regions where the experimental data has been acquired by the present study and by the most extensive research activities undertaken by NASA HOST program [1,6,7]. As the radius of rotation (R) is included in the accountancy of centrifugal accelerations, the buoyancy parameter in terms of $\beta(T_w-T_b)\mathrm{Ro}^2(R/d)$ needs to consider the match of R/d ratio. The strategic aim of the present study is to generate the heat transfer results that are closely approaching the engine worse-case scenarios. The local heat transfer data along the centerlines of two opposite heated walls roughened by 45 deg staggered ribs has been generated and analyzed by the present study. The heat transfer physics in association with the individual and interactive effects of convective inertial force, Coriolis force and rotating buoyancy force are illustrated during which the empirical heat transfer correlation is developing. This set of empirical heat transfer correlations derived from the present experimental data, which could uncouple the individual but mutually interactive effects of Coriolis and rotating buoyancy forces, provides the physical and numerical consistencies between the correlative results and actual measurements. An engineering methodology in the research phase, which generates the heat transfer correlation that is applicable to the design of coolant channel in the gas turbine rotor blade and for validating the numerical result, is demonstrated by present study.

2 Rotating Facility and Heat Transfer Test Module

The design philosophy of the rotating test rig involved the creation of a rotating platform on which the assorted simulated blade cooling passages could be mounted and tested. The layout of the rotating rig that has been designed and constructed to perform the high pressure tests is illustrated in Fig. 2. The rotor assembly consists of a hollow shaft: (1) connected to a rotating test platform (2), which is supported by two main bearings (3). The heat trans-

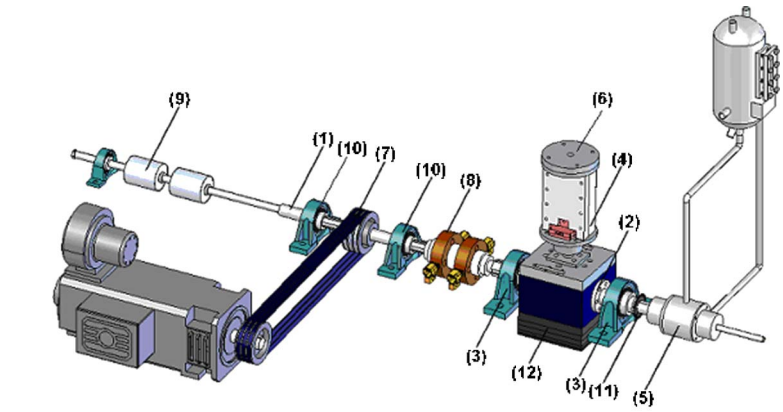

Fig. 2 Rotating test facility

fer test module (4) is mounted on the rotating test platform (2). The rotating radius (R) between the center of rotation and the midspan section of the heated test duct is 370 mm which is equivalent to 12.33 hydraulic diameters of test duct. A pair of bent blindholes is bored through the platform to communicate with each of the blind holes running through the center of the shaft. The right-hand side of shaft as indicated in Fig. 2 has a centrally located blind bore to permit pressurized air up to 10 bar entering the shaft via an EKK high pressure rotary seal assembly (5). For the test section with multipass channels, the pressurized air can be channeled through the test section and returns to a centrally located blind hole bored on the left-hand side of the shaft. In the present single-pass test channel, the test air enters the rotor and passes through the test section that exits through a convergent nozzle (6) installed at the exit end of test section. The adjustment of pressure level in the test channel is achieved by replacing the exit nozzle with different throat areas so that the tested Re and Ro numbers can be controlled at the predefined values. The pressure levels are controlled in the range of 2.8–3.5 bars for the present study in order to cover the full test matrix.

The entire rotor system is driven by a variable-speed dc motor via a pulley system using three V belts (7). The electrical power for heating the test section is transmitted to the rotor by means of two sets of power slip rings (8) that are capable of conveying the electrical current up to 200 A from a Variac transformer to the test section. Electrical wiring needed to run heating power to the rotating test platform is laid in a pair of diametrically opposite keyways milled on the outer surface of shaft. The instrumentation slip ring unit (9) transfers the electrical signals from the thermocouples attached to the heated surface of test section to the computer for data storage and processing via the Fluke Net-Daq 2640A data logger. This slip ring unit consists of 72 silver/silver graphite ring and brush pairs. The thermocouple leads are soldered to the terminals fitted to the slip-ring unit and the rotor-borne wiring is secured on the outer surface of shaft. The rotor system that consists of power slip rings, driven pulley, and instrument slip rings is supported by two secondary bearings (10). The speed of rotor is measured using an optical pick-up and encoder unit (11) attached to the shaft. The rotor assembly is dynamically balanced by the counter weight (12) secured on the back of the rotating platform. The balance weight is adjusted via trimming shims to provide the satisfied overall dynamic balance performance.

Prior to entering the rotating test rig, the test coolant, air, is pressurized by IWATA SC 175C screw-type compressor unit after which the flow is dehumidified and cooled to the ambient temperature through a refrigerating system. The air coolant is then channeled into the rotor assembly through a dryer, a pressure regulator and filter, a pressure transducer, a Tokyo Kesio mass flow meter, and a needle valve for the control of the mass flow rate of coolant. The nominal through flow Reynolds number is controlled by adjusting the mass flow rate of coolant measured at 15 m upstream of the rotating rig. As the properties of coolant, such as viscosity and density, vary with the local fluid temperatures, the mass flow rate of coolant is adjusted to compensate the variations of fluid properties. The variations of Re and Ro at the flow entrance of test section are controlled with in ±1% of the targeting values.

The heat transfer test module with airflow in the radially outward direction is shown as (4) in Fig. 2 with more enlarged details in Fig. 3. The test section itself is square in cross section and made up of leading (1) and trailing (2) heated walls, together with two tufnol side walls (3). The material of tufnol used is polytetrafluoroethylene, which can sustain 250°C with the thermal conductivity of 0.5 W m^{-1} K^{-1}. The leading, trailing, and side walls are physically held together by means of a series of axial bolts to form the square-sectioned test channel with hydraulic diameter, d, of 30 mm. the heat transfer measurements and electrical heating are only provided over the rib-roughened leading (4) and trailing (5) foils. Each of the two rib-roughened heating foils (4)(5) are produced by forging a continuous 30-mm-wide, 0.1 mm-thick stainless-steel foil. Each of these heating foils gives an active heating length of 240 mm. The surface ribs with the attack angle of 45 deg are arranged in the staggered manner along each side of the two opposite heating walls. The surface areas of all the skewed ribs are taken into account for the heating area in order to evaluate the realistic heat flux. The high-current, low-voltage dc electrical power is connected in series to heat two ribbing foils (4)(5) that generates the uniform heat flux heating conditions on two opposite rib-roughened walls. The thermal boundary condition simulated by this heating method is different from those generated by using the heating foil underneath the rib-roughened plate. For the present test-section simulation, the distributions of heat flux are also uniform over the top and two side surfaces of each skewed ribs. The different thermal boundary condition over the present rib-roughened surface can result in the different degrees of rotating buoyancy effect on heat transfer from those reported in the open literature [1,6–9,14–17,19,23–25].

The source of electrical heating power is supplied via a Variac transformer with the power consumption measured by a Wattmeter. Adjusting the heating power varies the relative strength of buoyancy level at each tested flow condition. The rib-roughened heating foils (4)(5) are clamped between the top tufnol flange (6) and two bottom copper plates (7) to secure their positions in the test channel. Under the top tufnol flange (6), a 3-mm-thick copper plate is sandwiched between the top flange (6) and the heating foils (4)(5) to complete the electrical circuit. Along the centerline of each rib-roughened surface, 15 K-type thermocouples (8) with equal intervals are sparkle-welded on the back of the stainless-steel heating foil to measure the centerline wall temperatures. The coordinate system and the locations of these thermocouples with respect to the rib and midrib locations are indicated in Fig. 3. The ceramic cement is inserted at each thermocouple junction to secure its position on the heating foil. The thermocouple wires are taken out of the test section through the grooves machined on the tufnol leading and trailing walls. These grooves are filled with high-temperature sealant to inhibit air leakage. The thermocouple and heater wire harness is taken from the test section and then connected to the instrumentation and power slip rings via the grooves machined on the keyways of rotating shaft. It is worth noting that the peripheral heat transfer variation across the width of each rib-roughened surface that reflects the impacts of Coriolis secondary flows and 45 deg rib-induced vortical flows is expected. However, the present study is limited by the available channels of instrumentation slip-ring unit so that the peripheral heat transfer variation over each rib-roughened surface is not investigated.

The geometric features of the single-pass square sectioned test channel are specified in Fig. 3. The rib-roughened surface is characterized in terms of four dimensionless parameters as: rib angle of attack, α, =45 deg; rib height, e(3 mm)/channel hydraulic diameter, d(30 mm)=0.1; rib pitch, P(30 mm)/rib hight, e(3 mm) =10; and rib land, l(3 mm)/rib height e(3 mm)=1,

A two-part cylindrical plenum chamber (9) consolidates with the end flange (10). At the entrance of the rib-roughened channel, several layers of fine mesh (11) are installed. The complete set of the test section is tightened between the end and top flanges (6)(10) by four draw bolts (12). Air leakage from each jointed surface is prevented by means of a series of internal O ring seals.

The temperature of entry air is measured by a type K thermocouple (13) penetrating into the entry plenum chamber. The fluid properties required to evaluate Re and Ro are calculated based on the measured air inlet temperature. At the exit plane of the rotating channel, three type K thermocouples (14) penetrate into the test channel at three different spanwise locations as indicated in Fig. 3. The flow bulk temperature at the exit plane of the test channel is obtained by averaging these three temperature measurements detected from these thermocouples (14). There is no thermocouple

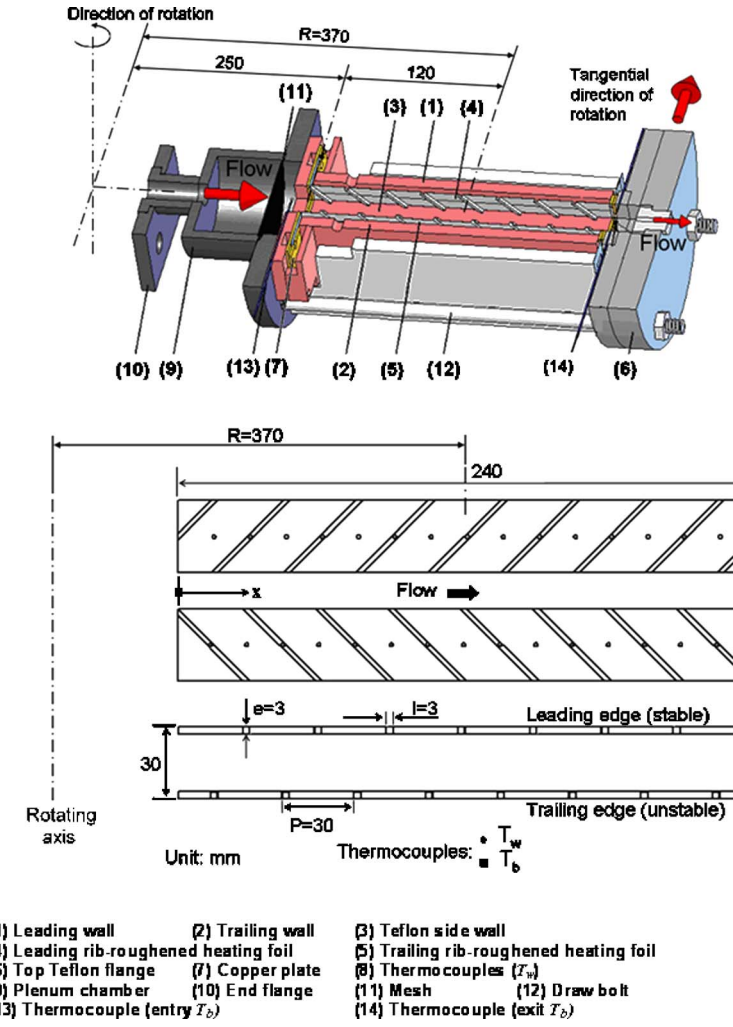

Fig. 3 Details of heat transfer test module

penetrating into the heated flow passage to measure the streamwise distribution of flow bulk temperature in order to avoid the disturbance of flow field by penetrating the thermocouples into the flow passage. The enthalpy balance method is employed to evaluate the flow bulk temperatures corresponding to the axial locations where T_w are detected. The evaluated flow bulk temperature at the exit plane is checked with the actual measurement. The agreement between the evaluated and measured flow bulk temperatures at the exit plane can confirm the accuracy of instrumentation. The experimental raw data are accepted for the subsequent data processing when the difference between the evaluated and measured flow bulk temperatures at the exit plane is less ±10%. The fiber-glass thermal insulation material is packed on the outer surface of the test module in order to minimize the external heat loss. The extent and characteristics of external heat loss are acquired by means of the series of static and rotating heat loss calibrations tests that are individually performed. The builtup heat transfer test module is vertically mounted onto the rotating platform.

3 Experimental Details

3.1 Strategy. The variation of any governing dimensionless group, such as Re, Ro, Pr or Bu for a set of predefined channel and heating geometries results in the different flow and temperature fields in the rotating test channel. The heat convective capability in the rotating channel is accordingly varied. Such heat transfer variation attributed from the systematic change of each of the governing flow parameters reflects the heat transfer impacts in association with each varying parameter. Within the present tested T_b range of 302.3–342.8 K, the maximum variation in Prandtl number (Pr) of tested coolant is negligible about 1.34%. Therefore the strategic approach of this experimental study is to disclose the functional relationship of

$$\mathrm{Nu} = \Psi\{\mathrm{Re}, \mathrm{Ro}, \mathrm{Bu}, X\} \tag{1}$$

where the experimentally defined Nusselt number, Nu, is calculated as

$$\mathrm{Nu} = \frac{qd}{k(T_w - T_b)} \tag{2}$$

The convective heat flux, q, in equation (2) is obtained by subtracting the external heat loss from the total heat flux supplied.

A set of precalibration heat loss test runs aimed at revealing the functional relationships of external heat-loss flux with the wall-to-ambient temperature difference and the rotating speed is performed. When the heat loss experiment is performed, the flow is blocked and the coolant passage is filled with wool. The supplied heating power is balanced with the external heat loss at the steady wall-to-ambient temperature difference. The proportionality between the heat loss flux and the wall-to-ambient temperature difference increases with the increase of rotational speed of the test section. These heat loss proportionalities are correlated as the

Table 1 Range of experimental nondimensional parameters

Nondimensional parameter		Range	
Reynolds number [Re]		7500–15000	
Rotation number [Ro]		0–1.8	
Buoyancy number [Bu=$\beta(T_w$-$T_b)$Ro$^2(r/d)$]		0.0986–8.789	
Density ratio [$\Delta\rho/\rho$]		0.073–0.296	
Tested Reynolds numbers for each rotation number			
Ro	Re	Ro	Re
1.8	7500	1	7500, 10,000, 12,500
1.4	7500, 10,000	0.7, 0.5, 0.3, 0.1	7500, 10,000, 12,500, 15,000

function of rotational speed of the test channel, whose function is incorporated into the data processing program in order to evaluate the local heat loss flux. For this class of experimentation, the maximum heat loss is about 9.63% of the total heat flux supplied, taking place at the highest speed and Re tested. Having defined the local convective heat flux, q, at each axial spot where T_w is measured, the local enthalpy balance is accounted for at each measurement location to determine the flow bulk temperature, T_b. All the fluid properties used to define the dimensionless parameters in eq. (1) are evaluated at the local T_b value.

High rotational speeds of a gas turbine engine propose the extreme difficulty to attempt a full coverage of the engine conditions depicted in Fig. 1 for any rig simulation. The present approach for rig simulation is to reduce the mean flow velocity, W_m, with the coolant mass flow rate unchanged by increasing the pressure of flow inside the rotating test channel. This approach increases Ro and Bu by reducing the mean through flow velocity at any specified Reynolds number. Table 1 summarizes the present range of experimental nondimensional parameters. The maximum Re and Ro in Table 1 are not simultaneously attainable. The present Ro and Bu ranges are considerably extended from the past research experiences [1–25].

3.2 Program. Initially the static duct flow conditions are examined to generate the database against which the rotating heat transfer results are compared. The static tests are followed by a series of rotating experiments. In the ranges of nondimensional parameters simulated by the present test rig as shown in Table 1, this set of rotating data is produced at fixed Re and Ro by adjusting the rotational speed and the pressure level of test channel. To investigate the rotating buoyancy effect, four ascending heater powers to raise the highest T_w levels to 348, 373, 393, and 413 K are used for each selected Re–Ro combination. The flow and heater power are generally kept for about 30 min in order to assure the flow reaches the steady state after varying the coolant-flow-rate or the heating power. The steady-state condition is assumed when the temporal wall temperature variations for several successive scans are less than ±0.3 °C. The time interval between such successive scans is about 60 s. The relevant steady state measurements are processed into the dimensionless groups defined in Eq. (1), with the fluid properties calculated from the local flow bulk temperature.

The dimensionless data generated in the phase of rotating experiments is subsequently analyzed to determine the individual and interactive impacts of Re, Ro, Bu on heat transfer. The empirical heat transfer correlation is derived, which permits the individual and interactive effects of through-flow inertia, Coriolis force and rotating buoyancy on heat transfer in the repeated rib flow region to be evaluated. The systematic variation of each one variable in Eq. (1) with the remaining variables unchanged reveals the individual impact of the varying variable on heat transfer. The individual impact in association with the varying variable is separated from the remaining variables in Eq. (1). However, the evaluation of experimental heat transfer data requires the finite wall-to-fluid temperature difference. The heat transfer data generated in the series of rotational tests involves certain degrees of buoyancy impact. The separation of Re or Ro impact from Bu interaction is performed by extrapolating the rotational heat transfer data into the limiting condition of Bu=0. This regression measure enables the determination of heat transfer results without buoyancy interaction so that the analysis of Re and Ro effects on heat transfer can be performed.

The result of uncertainty analysis reveals that the most of the experimental uncertainties in calculating the dimensionless parameters are attributed from the temperature measurements because the fluid properties are estimated using the equations with T_b as the dependent variable. Also indicated by the uncertainty analysis is the improved accuracy for the tests with the higher heating power and Reynolds number. Based on the method of estimating the experimental uncertainty recommended by the editorial board of ASME J. Heat Transfer [26], with the wall to bulk-flow temperature differences varying in the range of 31.02–93.147 K, the estimated maximum uncertainties for Nu, Re, Ro and Bu are about 10.6%, 8.2%, 4.2%, and 6.3% respectively.

4 Results and Discussion

4.1 Static Results. With zero rotation, wall temperature measurements along the centerlines of leading and trailing surfaces do not exhibit significant differences but only reflect the differences at the rib and midrib locations. At each heat flux tested, the axial wall temperature distributions show patterns of streamwise zigzag variation with the lower wall temperature develops at the rib location relative to its adjacent downstream midrib spots. The experimental heating conditions on two rib-roughened surfaces correspond closely to uniform heat flux. The flow bulk temperatures in the channel increase linearly in the direction of flow. The axial Nu_0 variation reassembles the zigzag pattern of wall temperature

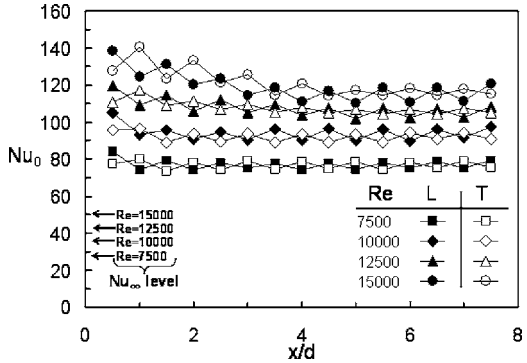

Fig. 4 Local Nusselt number distributions along leading and trailing edges at various Re for Ro=0

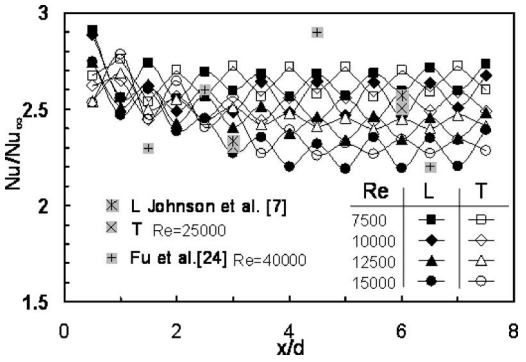

Fig. 5 Axial variation of Nusselt number ratio along leading and trailing edges for Ro=0

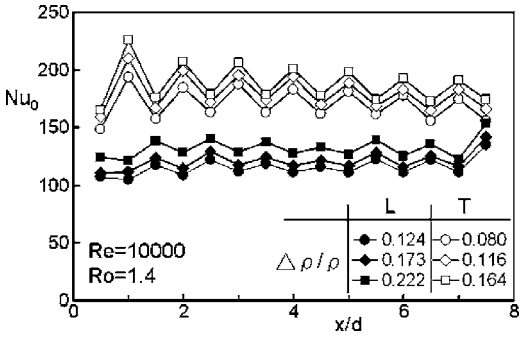

Fig. 6 Typical variation of local rotational Nusselt number along trailing and leading edges with three density ratios

distribution. Figure 4 shows the axial variations of Nu_0 for all the Reynolds numbers tested at zero Ro. The extent of data scatters at each x/d location, driven by varying $\Delta\rho/\rho$ value in the tested range is small, indicating the negligible buoyancy impact on Nu_0 in static channel. The general trend of streamwise Nu_0 variation for all Re tested is described as follows. An initial entry region with relatively high heat transfer coefficient decays into a relatively regular zigzag pattern after the flow traverses about five ribs. The tendency for the so-called zigzag *repeated rib* type of Nu variation takes place after the fifth rib. This region corresponds to a pseudo-developed flow region with relatively high heat transfer coefficients at the rib locations. By way of normalizing Nu_0 with a Dittus–Boelter Nusselt number (Nu_∞) [27], the heat transfer enhancement in the static rib-roughened channel is unraveled as shown in Fig. 5. Over the present Re range of 7500–15000, the Nusselt number ratio, Nu_0/Nu_∞ varies in the range of 2.2–2.9. This Nusselt number ratio falls as Re increases. The systematic reduction of Nu_0/Nu_∞ with the increased Re indicates that the correlation of Nu_0 is no longer followed by the $Re^{0.8}$ relationship but the exponent of Re is less than 0.8 in the present rib-roughened channel. The relative heat transfer enhancement attributed from 45 deg surface ribs is Re dependent. The dependence of Nu_0 on Re at each measurement spot is individually examined. As the variation of Pr is negligible over the temperature range covered by this series of experiments, the functional structure of Nu_0 is expressed as:

$$Nu_0 = A(x/d) \times Re^{n(x/d)} \tag{3}$$

The coefficients A and n vary with the axial location, x/d, to reflect the influence of boundary layer development and rib induced secondary flows on heat transfer. Table 2 summarizes the correlated coefficients A and n along the centerlines of rib-roughened leading and trailing surfaces. As the rotating. Figure 5 shows the comparable data of Johnson et al. [7] and Fu et al. [24] that share the similar geometries of test channel and rib-roughened surfaces. The selection of available data [7,24] suggests that the heat transfer enhancement in ducts fitted with 45 deg staggered ribs tends to fall in the range of 2–3.6 times the Dittus–Boelter level [27] for a given Reynolds number. The present data also fall in this cited range. The heat transfer data acquired by the present investigation is deemed to be satisfactory. Consequently the static heat transfer correlation based on these results is taken as the benchmark for assessing the effect of rotation on heat transfer in this particular rib-roughened channel.

4.2 Rotational results. The immediate rotational effect on the heated channel using uniform heat flux is that the axial wall temperature profiles are no longer axisymmetric. For each of the heat flux settings at any Re–Ro combination, the leading edge constantly operates at the higher temperature than the trailing edge. This result illustrates the presence of a cross-stream secondary flow driven by Coriolis forces that convects the relatively cool fluid from the duct core toward the trailing edge. The leading-to-trailing wall temperature differences cause the relatively high local Nusselt number along the centerline of trailing wall as demonstrated in Fig. 6. In this figure with Re=10,000 and Ro=1.4, three sets of distinguishable axial Nu distributions obtained with three buoyancy levels along the leading and trailing centerlines demonstrate the existence of buoyancy effect. Justified by the upward Nu trend driven by the ascending $\Delta\rho/\rho$ value as shown in Fig. 6, the rotating buoyancy effect in isolation enhances local heat transfer for the present test geometries. Driven by the increase of density ratio ($\Delta\rho/\rho$), the higher increasing rates of Nus-

Table 2 Correlative coefficients *A* and *n* for stationary Nusselt number, Nu_0

	Leading edge		Trailing edge		
Axial location	x/d	$A(x/d)$	$n(x/d)$	x/d	$A(x/d)$	$n(x/d)$
Rib 1	0.5	0.02218	0.9102	1	0.01673	0.9321
Rib 2	1.5	0.1211	0.7184	2	0.3381	0.6094
Rib 3	2.5	0.2383	0.6427	3	0.769	0.524
Rib 4	3.5	0.4433	0.5787	4	0.5128	0.567
Rib 5	4.5	0.5318	0.5684	5	0.5811	0.5535
Rib 6	5.5	0.5302	0.5635	6	0.5411	0.5622
Rib 7	6.5	0.5334	0.5608	7	0.5368	0.5603
Midrib 1-2	1	0.032	0.8603	0.5	0.0098	0.9958
Midrib 2-3	2	0.1118	0.7179	1.5	0.01591	0.9353
Midrib 3-4	3	0.267	0.6269	2.5	0.369	0.5973
Midrib 4-5	4	0.2712	0.6281	3.5	0.994	0.4937
Midrib 5-6	5	0.563	0.5574	4.5	0.5101	0.5533
Midrib 6-7	6	0.5538	0.5512	5.5	0.5216	0.5518
Midrib 7-8	7	0.56	0.5563	6.5	0.5198	0.5523

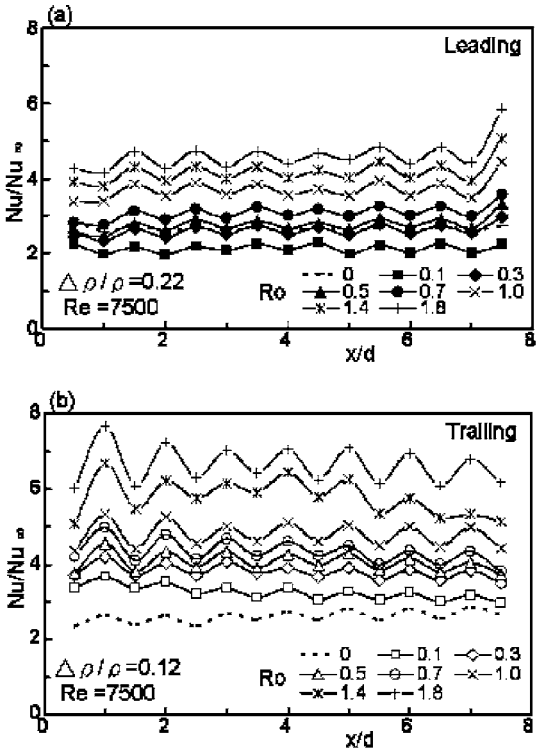

(c) Illustrative data set with $Re = 10000$, $Ro = 1$

x/d	Ω (rad/s)	T_i (in) (°C)	T_i (°C)	$T_{\infty o}$ (°C)	$T_{\infty i}$ (°C)	Mass flow rate (kgs^{-1})	Pressure (bar)	Heating power Current (A)	Heating power Voltage (V)	Heat flux (Wm^{-2})	Heat loss (Wm^{-2})	E/I
4	378	45	56.7	133	113	0.005819	3.189	25.68	6.64	8689.4	798	12.3

R/d represents the local ratio at the measurement spot of x/d = 4

Fig. 7 Axial distributions of rotational Nusselt number ratio along: (*a*) leading; and (*b*) trailing edges at various Ro; and (*c*) illustrative data set of rotational tests

selt numbers (Nu) along the trailing edge of the rotating test duct from their leading-edge counterparts are depicted in Fig. 6, whose result indicates the stronger rotating buoyancy impacts on heat transfer along the trailing edge. The clear evidence of relatively high Nu along the trailing edge is detected for all the rotational results, as typified in Fig. 6. It is interesting to note the amplified zigzag Nu range along the trailing edge. After reviewing all the rotating test results, the amplified zigzag Nu range along the trailing edge is enhanced as Ro increases. The amplified zigzag Nu range on the trailing wall in the entry flow region is evident but gradually decays toward the repeated-rib pattern. This amplified zigzag Nu variation on the trailing wall in the entry region of the present rotating channel suggests the interactive influences of Coriolis and rib-induced secondary flows on the heat transfer in this flow region.

By way of comparison with Nu_∞, the heat transfer enhancements in the rotating rib-roughened channel at rotational numbers of 0, 0.1, 0.3, 0.5, 0.7, 1, 1.4, and 1.8 at the Reynolds number of 7500 are compared in Figs. 7(*a*) and 7(*b*) for the leading and trailing walls. The averaged density ratios along the leading and trailing centerlines are selected as 0.22 and 0.12, respectively, for all the results compared in Fig. 7. For each of the density ratio tested, there is a systematic tendency for the trailing-edge heat transfer to increase as Ro increases. The leading-edge heat transfer is initially decreased from the zero-rotational reference as Ro increases from 0 to 0.1 but recovers by way of increasing Ro to 0.3. The further increase of Ro from 0.3 to 1.8 incurs a systematic increase of local heat transfer along the leading edge. Over the entire heating length, the minimum heat transfer coefficients on the leading edge are consistently developed at the rotation number of 0.1 for all the buoyancy levels tested. However, the rotation numbers after which the leading-edge Nu levels turn to be higher than the zero speed references vary with the rib and midrib locations. This will be further illustrated in the section dealing with the parametric analysis of rotational heat transfer. The Ro impact along leading and trailing edges demonstrated in Fig. 7 is consistent with the heat transfer results in the rotating channels that operate at high rotation numbers of $Ro > 0.45$ [1,4–8,13]. A similar Ro impact on heat transfer along the leading and trailing edges is detected for all the heat flux settings tested.

Chang and Morris [8] have demonstrated that the Re effect in Eq. (1) for the rotating channel fitted with in-line transverse ribs is similar to that of static heat transfer, which is the $n(d/d)$ power term. This concept for isolating Re impact from the influences of Ro and Bu on heat transfer is testified by comparing several sets of normalized heat transfer data in terms of $Nu/Re^{n(x/d)}$. This set of $Nu/Re^{n(x/d)}$ results are obtained with different Re with a fixed Ro. Figure 8 illustrates this verification. The axial distributions of $Nu/Re^{n(x/d)}$ along the centerlines of leading and trailing walls are shown for four representative cases of Ro=0.1, 0.3, 0.5, and 0.7 in Fig. 8. At each selected Ro, four sets of $Nu/Re^{n(x/d)}$ data obtained at different Re of 7500, 10,000, 12,500, and 15,000 are compared at a similar $\Delta\rho/\rho$ ratio. These four sets of data, generated with four different Re at a fixed Ro, gradually collapse into a tight data band as the flow enters the repeated-rib region. The data scatters are detected in the developing flow region on both leading and trailing walls which suggests that the simplifying assumption of isolating Re impact from Eq. (1) using $Nu/Re^{n(x/d)}$ structure is not completely valid in the developing flow region. Referring to the

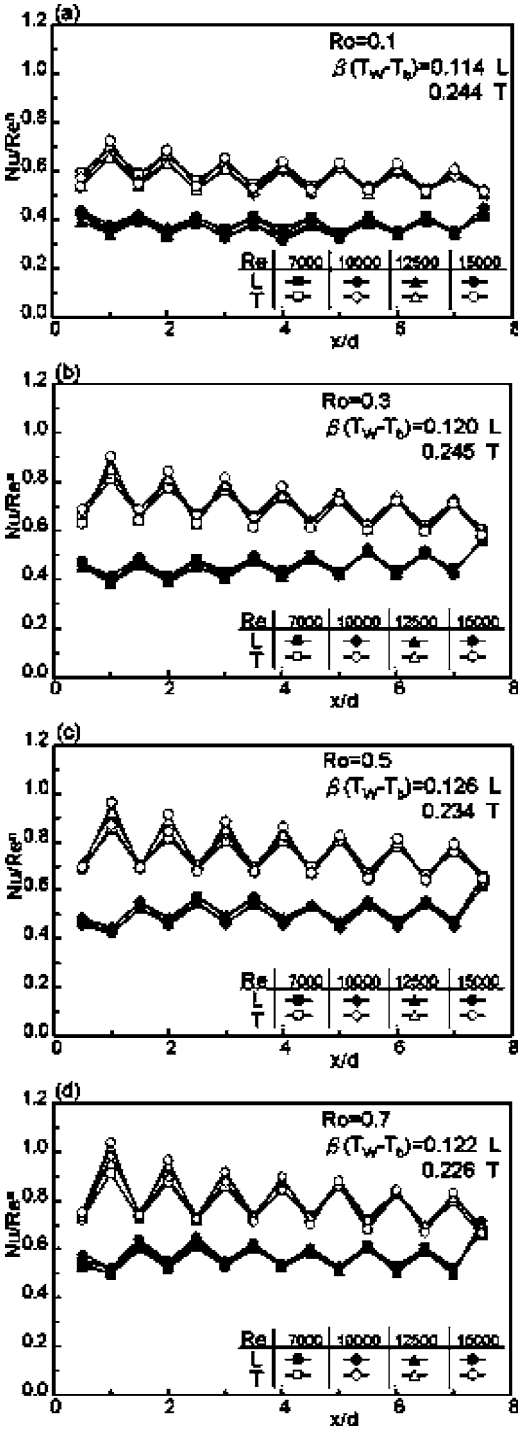

Fig. 8 Axial distributions of normalized rotational Nusselt number at various Re for Ro= (*a*) 0.1; (*b*) 0.3; (*c*) 0.5; and (*d*) 0.7

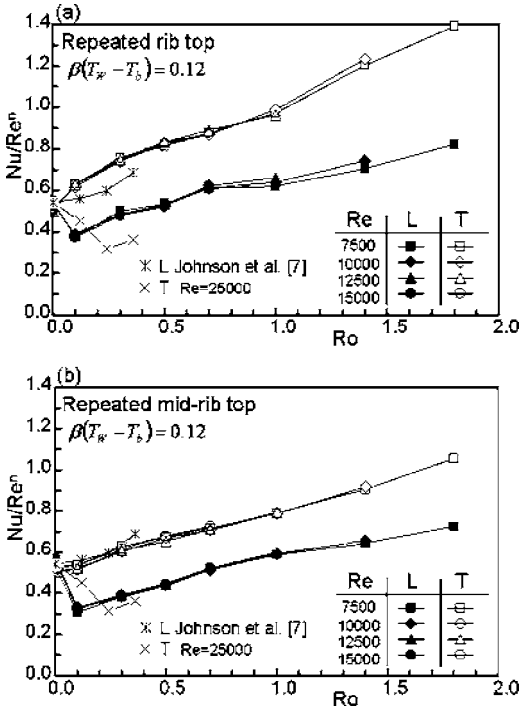

Fig. 9 Variation of normalized rotational Nusselt number with rotation number at repeated: (*a*) rib top; and (*b*) midrib location

amplified zigzag Nu variations in the entry region as shown in Fig. 6, the cause of entry-region data scatter in Fig. 8 is deemed to be the interactive Ro–Re impact on heat transfer. Nevertheless, Fig. 8 does demonstrate the feasibility to isolate Re impact from the influences of Ro and Bu on heat transfer using $\mathrm{Nu}/\mathrm{Re}^{n(x/d)}$ structure for the flow in the repeated-rib flow region.

The uncoupled rotational influence on heat transfer is subsequently examined using $\mathrm{Nu}/\mathrm{Re}^{n(x/d)}$ data in the repeated-rib flow region, covering the measurements downstream of the fifth midrib locations. Fig. 9 illustrates the Coriolis force effect at a selected buoyancy level on local heat transfer in the repeated-rib flow region. The satisfactory data convergence for four sets of data at different Reynolds numbers tested is again demonstrated in Fig. 9. Here, the trailing edge heat transfer consistently increases from the zero-rotation reference as Ro increases. Initially the leading edge heat transfer is reduced relative to the zero-rotation condition but, as Ro increases from 0.3, the local heat transfer is recovered with a region of enhanced heat transfer in the parametric range of $\mathrm{Ro}>0.7$. This Ro controlled effect is consistent with the results reported by other workers with different surface geometries but operate at high rotational numbers [1,4–8,13]. Also shown in Fig. 9 is the comparable data acquired by Johnson et al. [7] under the constant wall temperature heating condition. The heat transfer data reported by Johnson et al. [7] is re-evaluated into the present scaled Nusselt number form. As seen in Fig. 9, the general agreement between the results obtained from these two research groups are confirmed. There is considerable extension of Ro range from the past experience for the present data. Nevertheless, as the heat transfer data acquired from the locations of the fifth rib and onward shows the repeated-rib fashion, the heat transfer measurements in this repeated-rib flow region are sorted into two groups of repeated *rib* and *midrib* locations for subsequent data analysis.

Although the heat transfer behavior in the present rotating channel is described in Fig. 9, the separation of Ro impact from Bu interaction is not practical. The heat transfer data at the limiting case of $\beta(T_w-T_b)=0$ but $\mathrm{Ro}\neq 0$, which simulates the rotating channel with zero-buoyancy scenario, is generated using the regression analysis. For a set of geometric configurations and axial location, the plot of $\mathrm{Nu}/\mathrm{Re}^{n(x/d)}$ against $\mathrm{Ro}^2\beta(T_w-T_b)(R/d)$ is a meaningful way to unravel the rotating buoyancy effect. The regression-type curve fitting for each series of data trend with a finite rotation number can lead to the limiting heat transfer solution at zero $\beta(T_w-T_b)$. This is attempted in Fig. 10 to produce the rotational zero-buoyancy heat transfer data by extrapolating a series of $\mathrm{Nu}/\mathrm{Re}^{n(x/d)}$ data collected from a fixed Ro toward the asymptotic value corresponding to zero Bu. The linear-like increase of $\mathrm{Nu}/\mathrm{Re}^{n(x/d)}$ with the increase of Bu is evident for each

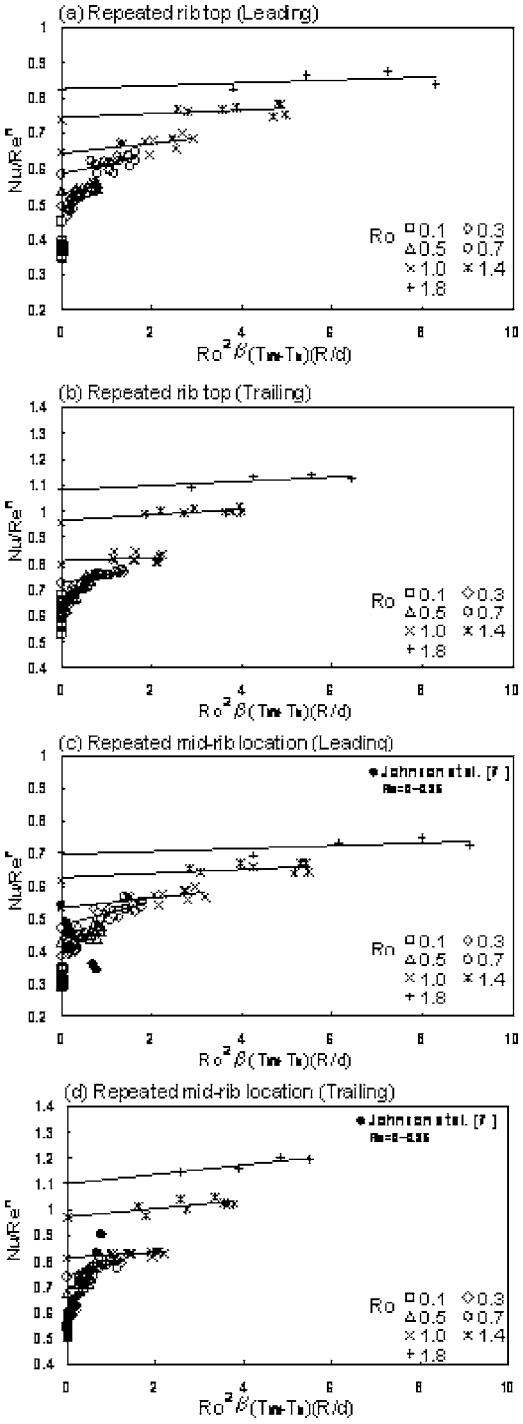

Fig. 10 Variation of normalized rotational Nusselt number with buoyancy number for various Ro at repeated: (*a*) rib top(*L*); (*b*) rib top(*T*); (c) midrib location(*L*); and (*d*) midrib location (*T*)

Ro controlled data series. The rotational heat transfer at each rib or midrib location in the repeated-rib flow region can accordingly be correlated by the equation of

$$\frac{\mathrm{Nu}_{L,T}}{\mathrm{Re}^n} = \phi_1\{\mathrm{Ro}\} + \phi_2\{\mathrm{Ro}\} \times \mathrm{Ro}^2\beta(T_w - T_b)(R/d) \tag{4}$$

In Eq. (4), ϕ_1 and ϕ_2 are functions of Ro that vary with rib and midrib locations in the repeated-rib flow region. Functional values of ϕ_1 at various rotation numbers account for the rotational zero-buoyancy heat transfer data. The different slopes for these correlating lines shown in Fig. 10, as indexed by ϕ_2 functions, indicate the various degrees of buoyancy impact on heat transfer. The data trend, which shows ϕ_2 value decreases as Ro increases from 0.1 to 1.8, is followed by all the data series at the repeated-rib and midrib locations. Although ϕ_2 values always remain positive in the range of $0.1 \leqslant \mathrm{Ro} \leqslant 1.8$, which suggests the rotational buoyancy effect improves heat transfer, the reduction of ϕ_2 value with the increased Ro reflects the weakened heat transfer enhancement due to rotating buoyancy. If such reduction trend in the ϕ_2 value is followed as Ro increases further, the Bu impact can yield from enhancing to impeding heat transfer. Also shown in Fig. 10 is the experimental data obtained by Johnson et al. [7]. In order to make the comparison, the results cited by these workers are converted along the lines described above with the present study. The R/d ratios for the present study and that used by Johnson et al. [7] are 12.33 and 50.2 respectively. Also the present rib is square sectioned while the rib adopted by Johnson et al. [7] is in the circular shape. The selection of this set of available data suggests a similar trend of buoyancy impact with an agreeable comparison. As ϕ_2 values appear to be function of Ro, the existence of coupling effect between Coriolis force and rotational buoyancy is confirmed. The data convergence seen in Figs. 8–10 reconfirms the applicability of scaling out Re dependency on the rotational Nusselt number by presenting heat transfer data in terms of $\mathrm{Nu}/\mathrm{Re}^n$. However, as the higher Reynolds numbers ($\mathrm{Re} > 25{,}000$) preclude the transitional range of $3000 < \mathrm{Re} < 20{,}000$, a further confirmation to ensure the independency of $\mathrm{Nu}/\mathrm{Re}^n$ data with Re is necessary to perform using the data generated with $0 < \mathrm{Ro} < 2$ and $\mathrm{Re} \geqslant 25{,}000$ is necessary.

The variations of evaluated zero-buoyancy heat transfer data against Ro in the repeated-rib flow region are shown in Fig. 11. Acting by the Coriolis force alone, the heat transfer differences between leading and trailing edges continuously increase as Ro increases. This result is consistent with the growing strength of Coriolis secondary flow when Ro increases. In general, the data trends shown in Fig. 11 follow the results typified in Fig. 9. Leading edge heat transfer coefficients turn out to be higher than the zero speed references as $\mathrm{Ro} > 0.5$ and $\mathrm{Ro} > 0.7$ at the repeated-rib and midrib locations, respectively. As the rotating buoyancy impacts improve heat transfers under the present test conditions, increases of density ratios ($\Delta\rho/\rho$) reduce the rotation numbers required to turn the leading-edge heat transfers from impediments to improvements from the heat transfer references at zerospeed. This is demonstrated in Fig. 9 by the data generated with nonzero buoyancy levels.

As shown by Fig. 11 in the range of $\mathrm{Ro} \geqslant 0.1$, the linear function can correlate the scaled Nusselt number data well. Evidence of this has been typified in Fig. 11 that the lines shown are linear regressions of the evaluated zero-buoyancy data. The variation manner of ϕ_2 value with Ro is shown in Fig. 12, which follows the general trend of exponential decay. In combination with the regression results unraveled in Figs. 11 and 12, the heat transfer correlations at rib and midrib locations on leading and trailing walls in the repeated-rib flow region are obtained as

$$\mathrm{Nu}_L = \mathrm{Re}^{0.5654} \times \{(0.2427 \times \mathrm{Ro} + 0.3971) + [0.00795 + 1.34 \times \mathrm{Exp}(-6.76 \times \mathrm{Ro}) \times \beta(T_w - T_b)\mathrm{Ro}^2(R/d)]\} \tag{5}$$

at rib location on leading wall,

$$\mathrm{Nu}_L = \mathrm{Re}^{0.5731} \times \{(0.1958 \times \mathrm{Ro} + 0.3434) + [0.00789 + 0.278 \times \mathrm{Exp}(-4.37 \times \mathrm{Ro}) \times \beta(T_w - T_b)\mathrm{Ro}^2(R/d)]\} \tag{6}$$

at midrib location on leading wall,

$$\mathrm{Nu}_T = \mathrm{Re}^{0.5654} \times \{(0.3274 \times \mathrm{Ro} + 0.5006) + [0.024 + 8.3 \times \mathrm{Exp}(-10.5 \times \mathrm{Ro}) \times \beta(T_w - T_b)\mathrm{Ro}^2(R/d)]\} \tag{7}$$

at rib location on trailing wall,

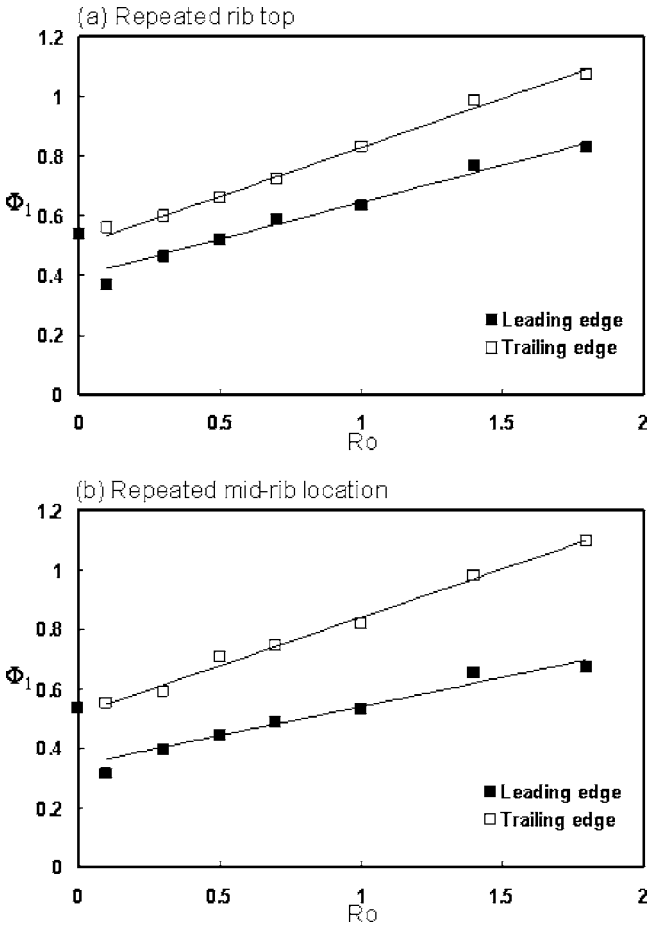

Fig. 11 Variations of evaluated zero-buoyancy heat transfer ϕ_1 with rotation number at repeated: (*a*) rib top; and (*b*) midrib location

$$\mathrm{Nu}_T = \mathrm{Re}^{0.5731} \times \{(0.325 \times \mathrm{Ro} + 0.5135) + [0.0276 + 3.9 \times \mathrm{Exp}(-10.6 \times \mathrm{Ro}) \times \beta(T_w - T_b)\mathrm{Ro}^2(R/d)]\} \quad (8)$$

at midrib location on trailing wall.

The set of empirical heat transfer correlations has been derived following an experimental approach to resolve the influences of Re, Ro, and $\mathrm{Ro}^2\beta(T_w - T_b)(r/d)$ on rotational Nusselt number. With the new correlation generated, the heat transfer coefficient

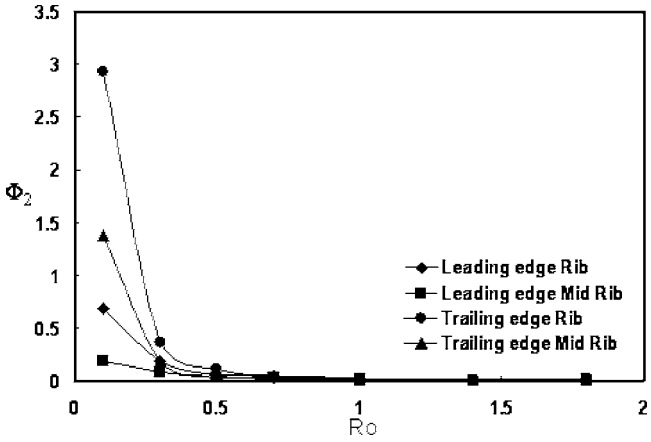

Fig. 12 Variations of ϕ_2 with rotation number for repeated rib flow region

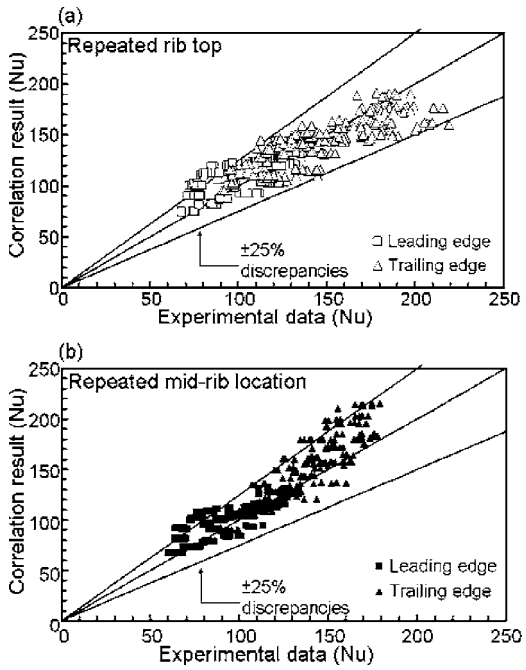

Fig. 13 Comparison of experimental data with correlation results at repeated: (*a*) rib top; and (*b*) midrib location

can be obtained with each controlling parameter such as Re, Ro, or Bu varied individually or simultaneously. The correlation can now be used to generate the plots of Nusselt number versus the individual parameters of Re, Ro, and Bu. The comparison of all the experimental measurements with the correlative predictions is performed to review the overall success of the present experimental proposal. Over the entire range of parametric conditions examined, 92% of the present experimental data are found to agree within +25% of the correlation proposed. The correlation is most sensitive to the variables of Ro and Bu. Figure 13 typifies this comparison of experimental data with the correlative results that demonstrates the reasonably well agreements. Considering the complexities induced by the surface ribs, Coriolis force, and rotating buoyancy, this set of heat transfer correlation can offer the more realistic reference for the design of internal cooling channels in the gas turbine rotor blade. The relative heat transfer modification from the zero rotational speed condition is also examined in terms of $\mathrm{Nu}/\mathrm{Nu}_0$. The review of the entire set of rotational heat transfer data generated indicates that the local Nusselt number ratios between the rotating and static channels ($\mathrm{Nu}/\mathrm{Nu}_0$) are, respectively, in the ranges of 0.6–1.6 and 1–2.2 along the centerlines of leading and trailing edges. Nevertheless, the extrapolation of Eqs. (5)–(8) beyond the present testing conditions can give rise to the uncertainties as usual. But the methodology developed by this study remains applicable to attack this type of heat transfer problem.

5 Conclusions

A general rotating facility that is constructed to examine the influence of rotation on heat transfer inside the cooling passages of the gas turbine rotor blade at near engine conditions is commissioned using a square-sectioned duct with two opposite walls roughened by 45 deg staggered ribs. The experiments undertaken have generated the rotational heat transfer results with considerable extension of previous test conditions that are compatible with the published data in this specialized field. The net result of the present study has been a set of correlations embodied in Eqs. (5)–(8), which may be used to estimate the rotational Nusselt numbers at the repeated rib and midrib locations on the leading

and trailing edges of a rotating rib-roughened square duct. The heat transfer results obtained from the present study have demonstrated that:

1. The present surface ribs have generated the overall heat transfer augmentation in the range of 2.2–2.9 times the Dittus–Boelter level with Re varied from 7500 to 15,000 in the static channel. The axial distribution of Nu_0 exhibits the zigzag pattern with a region of relatively high heat transfer at the rib location.
2 The Re impact on rotational heat transfer is similar to that of forced convection in the static channel, which is indexed by the n exponent in Eq. (3). The isolation of Re impact from the influences of Ro and Bu on heat transfer using $Re^{n(x/d)}$ is satisfactory for flow in the repeated rib flow region.
3 Acting with Coriolis force effect alone, the trailing edge heat transfer consistently increases from the zero-rotation reference as Ro increases. The leading edge heat transfer is initially reduced from the zero-rotation level but is recovered as Ro increases from 0.3 with which the increasing trend can lead to a region of enhanced heat transfer from the static-channel level as $Ro > 0.7$.
4 Within the present parametric range examined, the rotating buoyancy effect improves local heat transfer along the leading and trailing edges. The degree of heat transfer enhancement attributed from the rotating buoyancy effect decreases rapidly as Ro increases so that the existence of coupling effect between Coriolis force and rotating buoyancy is demonstrated.
5 A set of heat transfer correlations is developed to calculate local Nusselt numbers at the repeated rib and midrib locations that permits the evaluations of individual and interactive effects of Re, Ro and Bu on rotational Nusselt number, Nu.

Acknowledgment

This research project was financially supported by National Science Council, Taiwan, under Grant No. NSC 93-2611-E-022-004.

Nomenclature

A, n = coefficient
Bu = buoyancy number=$Ro^2\beta(T_w-T_b)(R/d)$
C_p = specific heat of fluid (J kg^{-1} K^{-1})
d = hydraulic diameter of test duct (m)
e = rib height (m)
k = thermal conductivity of fluid (W m^{-1} K^{-1})
l = rib land (m)
Nu = rotational Nusselt number=$qd/[k(T_w-T_b)]$
Nu_0 = stationary Nusselt number
Nu_∞ = Nusselt number value for stationary developed turbulent duct flow
P = rib pitch (m)
Pr = Prandtl number=$\mu C_p/k$
q = convective heat flux (W m^{-2})
Re = Reynolds number=$\rho W_m d/\mu$
R = rotating radius at midspan of test duct from rotating axis (mm)
Ro = rotating number=$\Omega d/W_m$
T_b = fluid bulk temperature (K)
T_w = wall temperature of test duct (K)
W_m = mean through flow velocity (m s^{-1})
x = axial location (m)
X = Dimensionless axial location=x/d

Greek Symbols

α = rib angle of attack (deg)
β = thermal expansion coefficient of fluid (K^{-1})
ρ = fluid density (kg m^{-3})
μ = fluid dynamic viscosity (kg s^{-1} m^{-1})
Ω = rotating speed of test duct (rad s^{-1})
Ψ, ϕ_1, ϕ_2 = unknown functions

Subscripts

L = centerline of rotating leading edge
T = centerline of rotating trailing edge
0 = nonrotating situation

References

[1] Wagner, J. H.Johnson, B. V., and Hajek, T. J., 1991, "Heat Transfer in Rotating Passage with Smooth Walls and Radial Outward Flow," ASME J. Turbomach., **113**, pp. 42–51.
[2] Morris, W. D., 1996, "A Rotating Facility to Study Heat Transfer in the Cooling Passage of Turbine Blades," Power Eng. J., **210**, pp. 55–63.
[3] Dutta, S., Andrew, M. J., and Han, J. C., 1996, "On Flow Separation With Adverse Rotational Buoyancy," ASME J. Heat Transfer, **118**, pp. 977–979.
[4] Morris, W. D., and Chang, S. W., 1997, "An Experimental Study of Heat Transfer in a Simulated Turbine Cooling Passage," Int. J. Heat Mass Transfer, **40**, (15), pp. 3703–3716.
[5] Morris, W. D., and Chang, S. W., 1998, "Heat Transfer in a Radially Rotating Smooth-Walled Tube," Aeronaut. J., **102**, (1015), pp. 277–285.
[6] Wagner, J. H., Johnson, B. V. Graziani, B. A., and Yeh, F. C., 1992, "Heat Transfer in Rotating Serpentine Passages With Trips Normal to the Flow," ASME J. Turbomach., **114**, pp. 847–857.
[7] Johnson, B. V., Wagner, J. H., Steuber, G. D., and Yeh, F. C., 1994, "Heat Transfer in Rotating Serpentine Passages with Trip Skewed to the Flow," ASME J. Turbomach., **116**, pp. 113–123.
[8] Chang, S. W., and Morris, W. D., 2003, "Heat Transfer in a Radially Rotating Square Duct Fitted With In-line Transverse Ribs," Int. J. Therm. Sci., **42**, pp. 267–282.
[9] Taslim, M. E., Bondi, L. A., and Kercher, D. M., 1991, "An Experimental Investigation of Heat Transfer in an Orthogonally Rotating Channel Roughened With 45 Deg Criss-Cross Ribs on Two Opposite Walls," ASME J. Turbomach., **113**, pp. 346–353.
[10] Liou, T-M., Chen, M-Y., and Wang, Y-M., 2003, "Heat Transfer, Fluid Flow and Pressure Measurements Inside a Rotating Two-Pass Duct With Detached 90-Deg Ribs," ASME J. Turbomach., **125**, pp. 565–574.
[11] Clifford, R. J., Morris, and W. D., Harasgama, S. P., 1984, "An Experimental Study of Local and Mean Heat Transfer in a Triangular Sectioned Duct Rotating in the Orthogonal Mode," ASME J. Eng. Gas Turbines Power, **106**, pp. 661–667.
[12] Morris, W. D., and Harasgama, S. P., 1988, "The Influence of Rotation on the Heat Transfer Characteristics of Circular, Triangular and Square-Sectioned Coolant Passages of Gas Turbine Rotor Blades," ASME J. Turbomach., **110**, pp. 44–50.
[13] Chang, S. W., and Morris, W. D., 1998, "A Comparative Study of Heat Transfer Between Rotating Circular Smooth-Walled and Rib-Roughened Ducts With Cooling Application for Gas Turbine Rotator Blades," JSME Int. J., Ser. B, **41**, (2), pp. 302–315.
[14] Dutta, S., and Han, J. C., 1996, "Local Heat Transfer in Rotating Smooth and Ribbed Two-Pass Square Channels With Three Channel Orientations," ASME J. Heat Transfer, **118**, pp. 578–584.
[15] Al-Hadhrami, L., and Han, J. C., 2002, "Effect of Rotation on Heat Transfer in Two-Pass Square Channels with Five Different Orientations of 45° Angled Rib Turbulators," Int. J. Heat Mass Transfer, **46**, pp. 653–669.
[16] Parson, J. A., Han, J. C., and Zhang, Y. M., 1995, "Effects of Model Orientation and Wall Heating Condition on Local Heat Transfer in a Rotating Two-Pass Square Channel with Rib Turbulators," Int. J. Heat Mass Transfer, **38**(7), pp. 1151–1159.
[17] Park, C. W., Yoon, C., and Lau, S. C., 2000, "Heat (Mass) Transfer in a Diagonally Oriented Rotating Two-Pass Channel with Rib-Roughened Walls," ASME J. Heat Transfer, **122**, pp. 208–211.
[18] Han, J. C., Zhang, Y. M., and Kalkuehler, K, 1993, "Uneven Wall Temperature Effect on Local Heat Transfer in a Rotating Two-Pass Square Channel With Smooth Walls," ASME J. Heat Transfer, **115**, pp. 912–920.
[19] Parsons, J. A., Han, J. C., and Zhang, Y. M., 1994, "Wall Heating Effect on Local Heat Transfer in a Rotating Two-Pass Square Channel with 90° Rib Turbulators," Int. J. Heat Mass Transfer, **37**(9), pp. 1411–1420.
[20] Liou, T.-M., and Chen, C. C., 1999, "Heat Transfer in a Rotating Two-Pass Smooth Passage With a 180° Rectangular Turn," Int. J. Heat Mass Transfer, **42**, pp. 231–247.
[21] Hwang, G. J., Tzeng, S. C., and Mao, C. P., 1999, "Heat Transfer of Compressed Air Flow in a Spanwise Rotating Four-Pass Serpentine Channel,"

ASME J. Heat Transfer, **121**, pp. 583–591.
[22] Iacovides, H., Jackson, D. C., Ji, H., Kelemenis, G., Launder, B. E., and Nikas, K., 1998, "LDA Study of Flow Development Through an Orthogonally Rotating U-Bend of Strong Curvature and Rib-Roughened Walls," ASME J. Turbomach., **108**, pp. 386–391.
[23] Willett, F. T., and Bergles, A. E., 2002 "Heat Transfer in Rotating Narrow Rectangular Pin-Fin Ducts," Exp. Therm. Fluid Sci., **25**, pp. 573–582.
[24] Fu, W.-L., Wright, L. M., and Han, J. C., 2005, "Buoyancy Effects on Heat Transfer in Five Different Aspect-Ratio Rectangular Channels With Smooth Walls and 45-Degree Ribbed Walls," Proceeding ASME Turbo Expo 2005: Power for Land, Sea and Air, Reno-Tahoe, NV, June 6–9, GT2005-68493.
[25] Parsons, J. A., Han, J. C., and Zhang, Y., 1995, "Effect of Model Orientation and Wall Heating Condition on Local Heat Transfer in a Rotating Two-Pass Square Channel with Rib Turbulator," Int. J. Heat Mass Transfer, **38**, pp. 1151–1159.
[26] JHT Editorial Board of ASME J. Heat Transfer, 1993, Journal of Heat Transfer Policy on Reporting Uncertainties in Experimental Measurements and Results, Int. J. Heat Mass Transfer, **115**, pp. 5–6.
[27] Dittus, F. W., and Boelter, L. M. K., 1930, *Publications in Engineering*, Vol. 2, University of California Press, Berkeley, CA, P. 443.7.

Air Flow and Heat Transfer in Louver-Fin Round-Tube Heat Exchangers

H. L. Wu[1]
e-mail: hailingwu_02@yahoo.com

Y. Gong

X. Zhu

Advanced Heat Transfer LLC,
1715 Aaron Brenner Drive,
Suite 726,
Memphis, TN 38120

Experimental investigations were conducted to understand the air flow and heat transfer in louver-fin round-tube two-row two-pass cross-counterflow heat exchangers. The Colburn factor j and friction factor f were obtained by using the ε-NTU approach. A three-dimensional computational fluid dynamics model was developed based on a representative unit cell with periodical and symmetric boundary conditions. Analysis of tube-side circuiting effect has been conducted and showed improvement by applying overall nonlinear tube-side fluid temperature boundary conditions. Comparison of heat transfer rate of the first and second rows showed that the first row was much more effective, achieving 68–53% *of the total heat transfer rate, when air velocity changes from* 1.02 m/s to 2.54 m/s. *A dimensionless parameter, F, was introduced to describe the louver interaction for different fin designs with various louver angles. Using* $j'/f^{1/3}$ *as a criterion to evaluate the heat transfer and pressure loss performance, an optimal F was predicted around 0.62.* [DOI: 10.1115/1.2402180]

Keywords: louver fin, round tube, low-Re airflow, louver interaction

1 Introduction

Louver-fin round-tube heat exchangers are widely used in residential and commercial air-conditioning systems. To improve the overall heat exchanger performance, fin surface enhancement is critical because the air-side thermal resistance is about 80% of the total thermal resistance [1,2]. An enhanced fin surface provides opportunity for the reduction in heat exchanger size, weight, material cost, and increase in energy efficiency. Louver-fin heat exchangers, which have been widely used in recent years, proved to be effective in thermal enhancement. Furthermore, development of air conditioning systems shows a tendency of lower air flow rate operating conditions to reduce noise and energy consumption.

In the past 20 years, there were extensive studies on louver fin enhancement both experimentally and numerically. However, most of the previous relevant studies were for louvered-fin flat-tube heat exchanger applications, which featured two-dimensional geometry and flow characteristics. Achaichia and Cowell [3] numerically modeled the flow through the louver fin array. Their study showed that the flow structure was a function of Re, which was based on louver pitch and face velocity, the louver-to-fin-pitch ratio P_L/P_F, and the louver angle α. Webb and Trauger [1] experimentally investigated the influence of the louver geometrical configuration (including α, P_F, P_L) and Re on the flow structure in the louver bank in automotive applications. They introduced "flow efficiency" to describe the mean flow direction relative to the louver direction, and developed a correlation to predict flow efficiency. Suga and Aoki [4] performed a two-dimensional numerical study on automotive louver-fin heat exchangers to determine the optimum combinations of several geometrical parameters. The numerical results showed the existence of an optimal ratio of fin-to-louver-pitch for various louver angles. It was concluded that the control of the thermal wake formed behind louvers was critical for optimization of louver fins. For louver angles in the range between 20 deg and 30 deg smaller louver angle showed superior performance from the viewpoint of both heat transfer performance and pumping power consumption. Kim et al. [5] tested 12 serpentine flat-tube and brazed aluminum louver-fin heat exchangers for air-conditioning applications. They found that heat transfer was mainly affected by fin pitch rather than louver angle, whereas pressure loss was mainly affected by louver angle rather than fin pitch. They identified an optimal $j/f^{1/3}$ value exists with α around 20 deg–25 deg. Jacobi et al. [6] summarized optimal louver fin geometric parameters from two-dimensional numerical simulation results. Using j/f as a criterion in the design of a compact heat exchanger, they recommended two geometries for $\mathrm{Re}<120$ and $\mathrm{Re}>120$, respectively, where Re was based on louver pitch and face velocity.

Although most of the associated investigations handled simplified two-dimensional configurations, there were a few on round-tube louver-fin heat exchangers. Wang et al. [7–9] tested several louver-fin and plain-fin round-tube heat exchangers, varying the tube size, fin pitch, and number of rows. They reported different influences of fin pitch on heat transfer performances for $\mathrm{Re}<1000$ and $\mathrm{Re}>1000$, where Re was based on tube diameter and face velocity. Improved heat transfer performance and decreased pressure drop were observed for smaller tubes, especially when the inlet air velocity $u_{\mathrm{in}}<1.5$ m/s. The reason was the ineffective region behind the smaller tube was smaller. Based on the experimental data, correlations to calculate j and f were developed for louver-fin and plain-fin heat exchangers.

Flow pattern in a louver bank is critical for the flow and heat transfer performance of louver fin heat exchangers. Flow efficiency was used to describe the extent of the fluid flowing along the louver direction [1,10–12]. Low flow efficiency means dominant intra-fin flow, or to say "tunnel flow," and high efficiency means dominant inter-fin flow guided by louvers. Some researchers showed the relationship between flow efficiency and heat transfer performance [10,11]. However, further investigations are necessary to understand the influence of the louver interaction on the flow and heat transfer behavior.

To evaluate heat exchanger air-side performance, different criteria were applied for various applications. The selection of appropriate performance criteria requires tradeoff between improved heat transfer rate and increased pressure drop. One of the most commonly used criteria is the flow area goodness factor defined as

[1]Corresponding author.

Contributed by the Heat Transfer Division of ASME for publication in the JOURNAL OF HEAT TRANSFER. Manuscript received September 9, 2005; final manuscript received May 21, 2006. Review conducted by Satish G. Kandlikar.

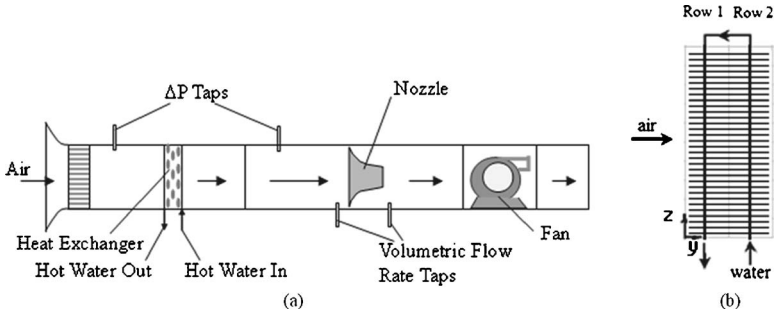

Fig. 1 Experimental facility: (*a*) sketch 3map of the test facility; and (*b*) circuiting

the ratio of the Colburn factor j to friction factor f, j/f [13]. Other criteria include: (1) $j/f^{1/3}$ [5]; (2) JF ratio defined as $JF = j/j_R/(f/f_R)^{1/3}$, where subscript R refers to a reference design [14]; (3) heat transfer rate per unit fin volume at unit pumping power [15]; and (4) heat transfer rate based on equal pumping power [4]. More detailed discussions were summarized in Ref. [16].

In the present study, a three-dimensional computational fluid dynamics (CFD) model was developed for a two-row louver-fin round-tube air-conditioning condenser. The numerical method was validated by experimental data. Airflow and heat transfer behavior were analyzed to explore the effects of fin and tube geometries and tube-side circuiting. The influence of louver interaction was studied to understand the mechanism of heat transfer enhancement under different flow patterns. Two criteria were discussed to evaluate the heat transfer and pressure loss performance of heat exchangers.

2 Experiments

2.1 Experimental Apparatus. The wind-tunnel test facility employed is shown in Fig. 1(*a*). It was built in accordance with ANSI/ASHRAE Standard 33-2000. The range of air-side face velocity u_{in} was 1.02–2.54 m/s. During the experiment, u_{in} was changed to desired values until steady-state conditions prevailed. Special attention was paid to relatively low-Re flows with u_{in} = 1.02 m/s, which is typical in low-noise air conditioning applications. The temperature and pressure at the inlets and outlets of both water side and air side of the heat exchanger were measured. The air volumetric flow rate was measured downstream of the heat exchanger. The energy balances between air and water sides were used to ascertain the performance of the test apparatus. The energy balances were within 4% based on the deviation from the mean heat transfer rate.

The air-side and water-side temperatures were measured by thermocouples having an uncertainty of ±0.1 °C. The differential pressure transducers measuring the pressure drop across the heat exchanger had an uncertainty of ±0.2%. The air flow rate was obtained by measuring the pressure drop across an ASME standard flow nozzle, with the pressure transducer having an uncertainty of ±0.1%. A gauge repeatability and reproducibility study was performed to provide information on wind tunnel performance by using ratios of measurement variation and parameter (temperature, pressure, velocity, etc.) fluctuation gathered from multiple tests and operator measurements [17].

The test heat exchanger was a commercially available aluminum-louver-fin, copper-round-tube heat exchanger with two-row two-pass cross-counterflow circuiting. Hot water in an inlet header was evenly distributed into 30 tubes in Row 2. Each circuit passed through the heat exchanger, which was cooled outside by cross-flowing air, as shown in Fig. 1(*b*). Then the cooled water in all the circuits was collected by an outlet header. A sample core section of the heat exchanger is shown in Fig. 2.

The heat exchanger air-side face area was 0.762 m in height (X axis) and 0.864 m in width (Z axis). The fin and tube geometric parameters are listed in Table 1. The heat transfer area density β, defined as heat transfer area per unit volume, is 1574.6 m^2/m^3

$$\beta = A_o/V \tag{1}$$

where A_o is the air-side total heat transfer area; and V the volume of the heat exchanger. A heat exchanger is considered compact when $\beta > 700$ m^2/m^3 [18]. In Fig. 2, the collars mating with the tube were punched from the fin base sheets, and were used to conveniently assemble fins along the tube. There are edge ripples at the front and rear edge of the fin, which is typical to resist damage.

2.2 Data Reduction. In a properly manufactured heat ex-

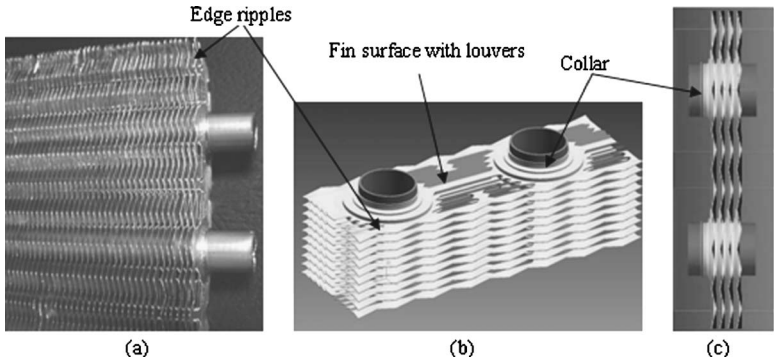

Fig. 2 Fin configurations: (*a*) core section; (*b*) isometric view; and (*c*) side view

Table 1 Geometric dimensions of the tested heat exchanger

D_c	P_F	$P_{T,X}$	$P_{T,Y}$	P_L	θ_T	θ_F	α
0.0085	0.0013	0.0254	0.0159	0.0019	0.0003	0.00011	37

changer, the contact heat transfer resistance between the tube and the collar is negligible and can be ignored. Therefore, the air-side heat transfer coefficient h_0 could be derived by

$$\frac{1}{UA_o} = \frac{1}{\eta_o h_o A_o} + \frac{1}{h_i A_i} + \frac{\theta_T}{\lambda_T A_i} + \frac{\theta_F}{\lambda_F A_1} \tag{2}$$

where U is the overall heat transfer coefficient, η_o the fin surface effectiveness, and h_i the tube-side heat transfer coefficient calculated by applying the Gnielinski correlation [19]

$$h_i = \frac{\lambda_i}{D_i} = \frac{(f_i/2)(\mathrm{Re}_i - 1000)\mathrm{Pr}_i}{1 + 12.7(f_i/2)^{1/2}(\mathrm{Pr}_i^{2/3} - 1)} \tag{3}$$

where $f_i = [1.58 \ln(\mathrm{Re}_i) - 3.28]^{-2}$, and the characteristic fluid temperature was the average temperature of inlet and outlet.

The overall heat transfer coefficient U was obtained from the ε-NTU approach [18], following the procedure as below:

1. Obtain the heat exchanger effectiveness by

$$\varepsilon = \dot{Q}_{\mathrm{HX}}/\dot{Q}_{\mathrm{HX,max}} \tag{4}$$

2. Calculate the NTU by using appropriate ε-NTU relationships for two-row two-pass cross-counterflow circuiting. Typical louver-fin round-tube heat exchangers usually have less than six rows, therefore the effect of row number or/and pass number should be considered. Kays and London [20] presented ε-NTU relationships for a multipass cross-counterflow heat exchanger with fluid unmixed between passes for $C^* = 1$. However, the relationships need to be developed for various C^* because C^* is far less than 1 in the present study. According to the comparison of ε-NTU relationship curves and the comments in [20], "there is no great difference between three sets of curves for multipass cross-counterflow heat exchangers with both fluids mixed between passes, with one fluid mixed between passes and the other fluid unmixed, and with both fluids unmixed between passes." Therefore, solutions in a much simpler algebraic form for multipass cross counterflow with fluids mixed between passes could be applied for our case

$$\varepsilon = \frac{[(1 - \varepsilon_p C^*)/(1 - \varepsilon_p)]^N - 1}{[(1 - \varepsilon_p C^*)/(1 - \varepsilon_p)]^N - C^*} \tag{5}$$

where N is the number of the identical passes in the cross-counterflow arrangement; and ε_p the effectiveness of each pass as in a single-row crossflow circuiting. Taken from the ESDU [21], the corresponding ε_p-NTU relationships for single-row unmixed/unmixed crossflow are applied as

$$\varepsilon_p = \frac{1}{C^*}[1 - e^{-C^*(1 - e^{-\mathrm{NTU}})}] \tag{6}$$

Substituting Eq. (6) into Eq. (5), the obtained ε-NTU relationsips for two-row two-pass cross counterflow with various C^* are shown in Fig. 3.

3. Then, obtain U from

$$U = \mathrm{NTU}^* C_{\min}/A_o \tag{7}$$

The fin surface effectiveness η_o in Eq. (2) was calculated from the fin efficiency η

$$\eta_o = 1 - \frac{A_2}{A_o}(1 - \eta) \tag{8}$$

where η was calculated by using Schmidt approximation [22]

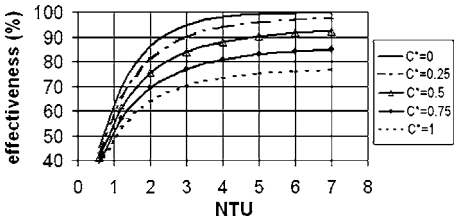

Fig. 3 ε-NTU relationships for two-row two-pass cross counterflow heat exchangers

$$\eta = \frac{\tanh(mr\phi)}{mr\phi} \tag{9}$$

where $r = 0.5D_c$, $m = \sqrt{2h_o/\lambda_f \delta_f}$ for thin sheet fin, $\phi = (R-1)(1 + 0.35\ln(R))$, $R = 1.27(X_M/r)[(X_L/X_M) - 0.3]^{0.5}$, $X_L = \sqrt{(P_{t,X}/2)^2 + P_{t,Y}^2}/2$, and $X_M = P_{t,X}/2$. Because h_o was needed to determine η, iterations were conducted as follows to obtain the converged solution of h_o:

1. An initial h_o^0 is obtained by Eq. (2) by assuming $\eta = \eta^0 = 1$;
2. Calculate η_o^1 from Eqs. (8) and (9) with $h_o = h_o^0$;
3. Calculate h_o^1 by Eq. (2) with $\eta_o = \eta_o^1$; and
4. If the difference between h_o^1 and h_o^0 is greater than 1%, set $h_o^0 = h_o^1$, and repeat Steps 2 and 3. Otherwise, $h_o = h_o^1$.

The Colburn factor j was used to describe the heat transfer performance

$$j = \mathrm{St} \cdot \mathrm{Pr}^{2/3} \tag{10}$$

where

$$\mathrm{St} = \frac{h_o}{\rho c_p u_c} \tag{11}$$

The friction factor f was used to describe the pressure loss characteristics [20]

$$f = \frac{A_c}{A_o}\frac{\bar{\rho}}{\rho_{\mathrm{in}}}\left[\frac{2\rho_{\mathrm{in}}\Delta P}{G_c^2} - (1 + \sigma^2)\left(\frac{\rho_{\mathrm{in}}}{\rho_{\mathrm{out}}} - 1\right)\right] \tag{12}$$

where $\sigma = A_c/A_f$.

2.3 Experimental Results. The air-side and water-side inlet temperatures were maintained constantly at 299.8 K and 355.4 K, respectively. The operating conditions are listed in Table 2. The air-side Reynolds number Re_o was defined as $\mathrm{Re}_o = \rho u_c D_c/\mu$, which was used in the previous works of Wang et al. [7–9]. The Reynolds numbers based on another definition, $\mathrm{Re}_{o,Dh} = \rho u_{\mathrm{in}} D_h/\mu$, are also applied for comparison. For both definitions, the characteristic air temperature was defined as $\bar{T}_o = T_{o,\mathrm{in}} + T_{o,\mathrm{out}}/2$. The tube-side heat transfer coefficient h_i was calculated by Eq. (3).

Figure 4 shows the distribution of the Colburn factor j and friction factor f for all cases. The results obtained by the correla-

Table 2 Operating parameters

Case No.	u_{in} (m/s)	Re_o	$\mathrm{Re}_{o,Dh}$	h_i (w/(m$_2$ K))
1	1.02	738	108	9086
2	1.27	928	136	9035
3	1.52	1131	165	8997
4	1.78	1320	193	8952
5	2.03	1515	222	8915
6	2.29	1713	251	8903
7	2.54	1916	280	8883

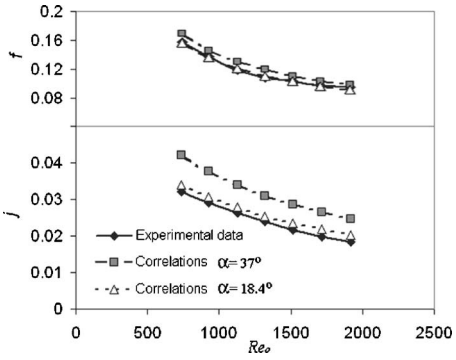

Fig. 4 The Colburn factor *j* and friction factor *f* versus Re_o

tions of Wang et al. [8] are also shown for comparison. It is observed that *j* predicted by Wang et al.'s correlations is about 30% higher than the experimental data. However, if the louver angle is 18.4 deg, the correlation results show good agreement with the measurement. In Ref. [8], the maximum louver angle was 30 deg, and considerable scattering was observed in their experimental data when $Re_o < 1000$. Furthermore, Wang et al. correlations indicate better heat transfer performance when α increases from 18.4 deg to 37.0 deg. However, our study in Sec. 5.2 shows $\alpha = 18.4$ deg obtains better heat ransfer performance because its louver alignment results in better interaction bwteewn fins and the bulk flow.

In the present study, the percentages of both tube and collar conductive heat transfer resistance are less than 0.2% of the overall heat transfer resistance. The percentage of the air-side heat transfer resistance ranges from 87% to 82% when the air face velocity increases from 1.02 m/s to 2.54 m/s.

3 Numerical Method and Model Validation

3.1 Computational Domain and Boundary Conditions. Figure 5 shows the computational domain, a three-dimensional representative unit cell containing one fin pitch (in the *Z* axis direction). In the heat exchanger under investigation, the number of unit cells is 40,800. Fluid–solid conjugated heat transfer was modeled. The contact heat transfer resistance between the tube and the collar was ignored. The airflow inlet is located $0.2D_o$ upstream of the leading edge of the fin, and the outlet is located $2.7D_o$ downstream of the rear edge of the fin. Uniform air velocity and temperature profiles were applied at the airflow inlet. Zero relative pressure was applied at the airflow outlet, which was beyond the possible recirculation region downstream of the tube and louver bank.

In the spanwise direction (*X* axis), symmetric boundary condition was applied. In the tube axial direction (*Z* axis), periodical boundary condition was applied at the boundary pair above and below the fin, as indicated in Fig. 5(*b*). In order to adapt to the fin geometry, the periodical boundary was composed of three parts: (*a*) a higher annular part close to the tube; (*b*) a lower peripheral part containing the louver region; and (*c*) a frustum-side transition connecting parts (*a*) and (*b*). At the tube-side wall boundaries, a convective heat transfer boundary condition was applied, with the tube-side convective heat transfer coefficient h_i specified as listed in Table 2. For the tube-side fluid temperatures, two methods were applied to investigate the influence of tube-side circuiting. Method one assumed a constant water temperature profile for both rows, with $\bar{T}_i = (T_{i,\text{in}} + T_{i,\text{out}})/2$. Method two was based on an overall linear profile assumption, with water temperature in Row 1 set as $(\bar{T}_i + T_{i,\text{out}})/2$ and water temperature in Row 2 set as $(T_{i,\text{in}} + \bar{T}_i)/2$.

An unstructured tetrahedral grid was applied. For regions near the fin, the grid had a mesh interval size of about the fin thickness, and for the regions at periodic boundaries, the average mesh interval size was about 0.15 mm. The distance of the center of the mesh element immediately adjacent to the wall surface decreased with higher air inlet velocity. The typical meshes near louver corners are displayed in Fig. 5(*c*).

3.2 Numerical Method. The numerical simulation was conducted by applying the CFD software FLUENT Version 6.2 based on a control-volume method [23]. A double precision solver was applied to solve the continuity and Navier–Stokes equations sequentially. A node-based derivative evaluation was used to discretize the convection and diffusion terms of the governing equations, which has a second-order spatial accuracy. The value of the variables at the interface of adjacent cells for the convective terms was interpolated using a second-order upwind scheme. The diffusion terms were central differenced having second-order spatial accuracy. Pressure–velocity coupling was obtained by the SIMPLEC algorithm [24]. The W-cycle algebraic multigrid method with one prerelaxation sweep was applied to improve the conver-

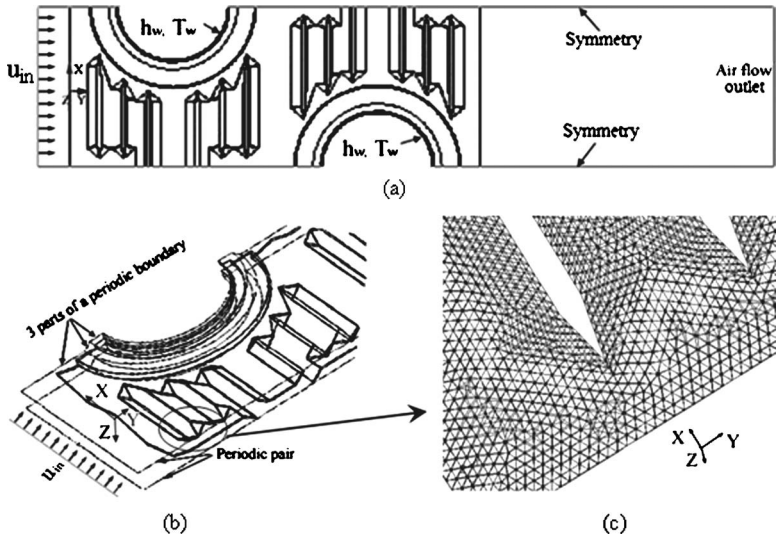

Fig. 5 Computational domain and grids: (*a*) computational domain (top view); and (*b*) fin geometry and periodical boundary; and (*c*) meshes near louver corners

Table 3 CFD grid dependency (Case 1)

Grid	Element number	$\dot{Q}$ (W)	ΔP (Pa)
1	565,800	0.9200	23.84
2	820,000	0.9182	23.75
3	1,148,000	0.9159	23.60
4	1,573,400	0.9156	23.27

gence. The convergence criteria required the scaled residuals R^{ϕ} [23] of 10^{-3} for the continuity and momentum equations and 10^{-8} for the energy equation. To ensure the balance of energy, the integrated heat flux from the water side was checked to be equal to that from the air-side heat transfer surface, and also equal to that gained by airflow through the heat exchanger. In all the equations solved, the thermophysical properties of air were defined as variables dependent of air temperature.

3.3 Validation. Four sets of grid were investigated, and the number of mesh elements were 565,800, 820,000, 1,148,000, and 1,573,400, respectively. Taking Case 1 as an example, the heat transfer rate of the unit cell $\dot{Q}$ and air-side pressure drop ΔP obtained from four grid sets are compared in Table 3. The results indicate asymptotically decrease from the sparsest Grid 1 to the finest Grid 4, and no distinct difference between Grid 3 and Grid 4. However, with larger numbers of mesh elements, the computational cost will increase because of more difficulties in the iteration convergence and stability, as well as increased memory and CPU time. Therefore, Grid 3 was chosen as an appropriate grid size for this investigation.

To validate the fidelity of the modeling method, Table 4 lists a comparison of computational results and experimental data in two aspects, air-side pressure drop ΔP and heat transfer rate $\dot{Q}$. For ΔP, the results obtained by both methods of the T_i definition show a negligible difference, and the CFD predictions deviate from the experimental data by −5.8–−0.5%. For $\dot{Q}$, the CFD results deviate from the experimental data by 6.3–11.8% with T_i using Method 1, and by 9.7–17.3% with T_i using Method 2. Generally, the comparison between the CFD prediction and the measurements indicates reasonable agreement.

It is observed that the overprediction of $\dot{Q}$ increases with the increase in air velocity. Furthermore, though Method 1 assumes a simplified uniform water temperature for both rows, it results in a better system level agreement with the experimental data. However, to evaluate the local heat transfer performance in each row, results by using Method 2 may be more credible because it includes tube-side circuiting information. Improvement of Method 2 may be obtained by a more practical T_i profile. This will be further analyzed in Sec. 3.4.

Table 4 Comparison of measured and calculated data

	U_{in} (m/s)	Exp. data	Method 1[a] Cal.	Method 1[a] Dev. (%)	Method 2[b] Cal.	Method 2[b] Dev. (%)
$\dot{Q}$ (W)	1.02	0.86	0.92	6.3	0.95	9.7
	1.27	1.01	1.08	6.8	1.12	10.8
	1.52	1.13	1.22	8.0	1.27	12.5
	1.78	1.22	1.34	10.4	1.40	15.2
	2.03	1.31	1.45	10.5	1.51	15.6
	2.29	1.39	1.54	11.0	1.62	16.2
	2.54	1.46	1.63	11.8	1.71	17.3
ΔP (Pa)	1.02	22.67	22.01	−2.9	22.08	−2.6
	1.27	30.89	29.52	−4.4	29.52	−4.4
	1.52	38.36	37.82	−1.4	37.82	−1.4
	1.78	47.33	47.10	−0.5	47.10	−0.5
	2.03	58.79	57.11	−2.9	57.11	−2.9
	2.29	70.24	68.07	−3.1	68.07	−3.1
	2.54	84.94	80.05	−5.8	80.05	−5.8

[a]Using a constant water temperature profile for both rows.
[b]Using an overall linear profile.

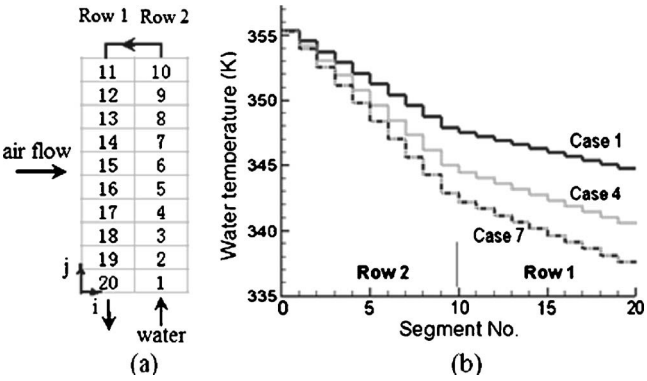

Fig. 6 Water temperature profiles along the circuit: (*a*) circuiting; and (*b*) water temperature profiles

3.4 Influence of Tube-Side Circuit. Although Table 4 shows reasonable agreement between numerical results and test data, the heat capacity is generally overpredicted and the deviation from the experimental data increases with higher air velocities. This may be caused by the tube-side water temperature boundary condition. Instead of the simplified uniform or overall-linear profile assumptions, overall-nonlinear water temperature profiles are considered in this section.

In order to analyze the influence of tube-side circuiting, or water temperature on the heat transfer behavior, a simplified heat exchanger model was built to estimate the water temperature profile. The model assumed that air flowed through the heat exchanger in the i direction ($i=0,1,2$) with a given uniform velocity, and ignored the air heat transfer in the j direction ($j=1-10$) due to air temperature gradient. The diagram of circuiting and airflow are illustrated in Fig. 6(*a*), where the tube is divided into 20 segments along the two-pass flow passage. For each segment, the energy conservation equations were applied to calculate the water and air temperatures

$$c_{p,f}\dot{m}_f(T_{f,1,j+1}-T_{f,1,j}) = c_{p,a}\dot{m}_a(T_{a,1,j}-T_{a,0,j}) = U_{i,j}A_{i,j}(T_{f,1,j}-T_{a,0,j}) \quad \text{for Row 1} \tag{13a}$$

$$c_{p,f}\dot{m}_f(T_{f,2,j}-T_{f,2,j+1}) = c_{p,a}\dot{m}_a(T_{a,2,j}-T_{a,1,j}) = U_{i,j}A_{i,j}(T_{f,2,j}-T_{a,1,j}) \quad \text{for Row 2} \tag{13b}$$

where $T_{f,i,j}$ is the water temperature in Segment (i,j); $T_{a,i,j}$ the air temperature in segment (i,j) after the air–water heat exchange; $U_{i,j}$ is the overall heat transfer coefficient in segment (i,j); and $A_{i,j}$ is the heat transfer surface area in segment (i,j). $U_{i,j}$ was assumed as to be constant for all segments and was to be determined by iterations, until the calculated heat transfer rate matches the experimental measurement.

The boundary conditions are

$$T_{a,0,j}=T_{a,\text{in}}, \quad T_{f,2,1}=T_{f,\text{in}}, \quad T_{f,1,10}=T_{f,2,10} \tag{14}$$

Taking Case 1, 4, and 7 as examples, the calculated water temperature profiles along the circuit are presented in Fig. 6(*b*). The water temperature shows a linear profile in each row, but the temperature gradient of Row 1 is less than that of Row 2, resulting in an overall-nonlinear profile. The gradient difference is small at

Table 5 Deviation of heat transfer rate $\dot{Q}$ using three methods of T_i definition

Case No.	u_{in} (m/s)	Method 1 (%)	Method 2 (%)	Method 3 (%)
1	1.02	6.3	9.7	7.2
2	1.27	6.8	10.6	7.7
3	1.52	8.0	12.5	9.1
4	1.78	10.4	15.2	11.3
5	2.03	10.5	15.6	11.3
6	2.29	11.0	16.2	11.6
7	2.54	11.8	17.3	12.3

low air velocity, showing approximate overall linear profile. However, the difference becomes larger at higher air velocity, showing a continuous deviation from an overall linear profile. This explains the reason for increasing deviation of heat transfer rate $\dot{Q}$ with increasing air velocity when Method 2 was used.

To consider the practical water temperature profile, Method 3 was applied to specify T_i, which used the average water temperature of each row based on the overall nonlinear profile obtained by the simplified model above. All cases were simulated again by using Method 3 and the comparison of heat transfer prediction among the three methods is listed in Table 5. The deviation of $\dot{Q}$ from the experimental data by applying Method 3 is 7.2–12.3%. The deviation of ΔP is almost the same as using either Method 1 or Method 2.

The heat transfer rate of an individual row was also calculated to compare the heat transfer contribution of the two rows. Using Method 2 or 3 of the T_i definition, the heat transfer contribution percentage of Row 1 is 68–53% of the total heat transfer rate, while using Method 1, it is 77–63%.

As a summary of the three methods of T_i definition, all of them show good agreement in ΔP with experimental data; Method 3 shows the best prediction of either system level or local level heat transfer; Method 2 shows consistency with Method 3 concerning the heat transfer contribution percentage of each row, but the system level prediction becomes worse when air velocity increases; Method 1 shows good prediction of $\dot{Q}$ in a system level, however it overpredicts the heat transfer rate in Row 1. Therefore, the tube-side overall nonlinear T_i profiles is helpful in considering the influence of the tube-side circuiting, especially when the nonlinear feature becomes significant. The following analyses and discussions are based on the results by applying Method 3.

4 Flow and Heat Transfer Behavior

4.1 Stagnant Flow Behind the Tube. Figure 7 shows the top view of streamline pattern by tracking the fluid trajectories released from Line *MN* in the midplane between two fins. The oncoming flow is reoriented by the tube, detouring and accelerating at the convex tube wall. A stagnant flow region exists behind the round tube. This results in locally diminished convective heat transfer, which is demonstrated by the distribution of the local heat flux (Fig. 8(*a*)) and the wall temperature contours at the fin surface (Fig. 8(*b*)).

For the highest air velocity condition (Case 7, with $Re_o=1916$), a recirculation region appears downstream of the fin region, as shown in Fig. 7(*b*). This may indicate the origination of possible flow instability caused by boundary layer vortex shedding from the round tube and the fin surface. Tafti et al. [25] pointed out that flow instability might be induced by perturbation of louvers on the bulk flow in a two-dimensional multilouver fin array. Those flow instabilities cannot be simulated by the present steady-state model with symmetric boundary conditions. However, the simulation results still show good agreement with the experimental data. It implies that, in the present operating range, those downstream instabilities have little influence on the heat transfer behavior in the upstream fin region, so the present model is appropriate and descriptive. For higher Re flows, a transient flow model with a larger computational domain may be necessary to consider the effect of the flow instabilities.

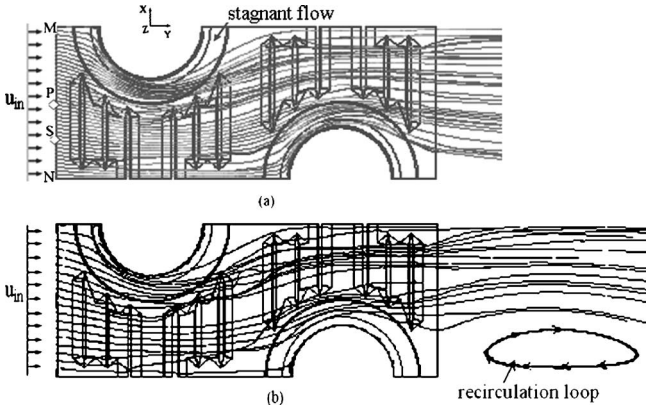

Fig. 7 Top views of streamlines released from line *MN* in the midplane between two fins (Note: higher u_{in} produces recirculation loop): (*a*) case 1, $u_{in}=1.017$ m/s; and (*b*) case 7, $u_{in}=2.542$ m/s

4.2 Louver-Directed Flow. For all cases, the flow in the louver region presents louver-directed flow characteristics, with strong interfin mass transport through the louver openings. Figure 9 shows typical side view streamline pattern in Row 1 and Row 2 for Case 1. Figure 9(*a*) shows the side view of streamline pattern by fluid trajectories released from the line where the plane $X=0$ intersects the front surface (as marked by Point *P* in Fig. 7). Figure 9(*b*) shows the streamlines in representative parts of louvers in Row 1 and Row 2. The louver segments in Row 1 are in the plane $X=-P_{T,X}/8$, where Point *S* is located in Fig. 7, and those in Row 2 are in the plane $X=P_{T,X}/8$. The wavy flow penetration in the tube axial direction reaches about $3-3.4P_F$. Comparison of flow in Row 1 and that in Row 2 (Fig. 9(*b*)) shows that the streamlines are more uniform in Row 1. When developing downstream in Row 2, they gradually approach the center of the "wavy" flow passage confined by the louver alignment. Combination of Figs. 7 and 9 provides a visual three-dimensional vision of flow in louver-fin and round-tube heat exchangers.

4.3 Leading Edge Effect. As shown in Fig. 8, the most intensive heat flux on the fin surface occurs at the frontal part of the fin, especially near the leading edge. It is assumed that this enhancement is caused by the splitting and initial disturbance of the oncoming flow, and the very thin boundary layer therein. This is termed the "leading edge effect." In order to examine the heat transfer behavior along the flow direction, the computational domain was divided into 32 parallel narrow strips, or segments, aligning along the streamwise direction, as illustrated in Fig. 10(*a*) with segment 17 as an example. The profile of segment-area-averaged heat flux along the flow direction is presented in Fig. 10(*a*). The profile shows a maximum at the leading edge of the fin, and rapid attenuation downstream, and then much lower values in the second row. As mentioned before, the contribution percentage of Row 1 is 68–53% of the total heat transfer rate, indicating that heat transfer in the second row is less effective.

Figure 10(*b*) presents a segment-area-averaged heat transfer coefficient, $h_{o,\text{seg}}$, which is defined by

$$h_{o,\text{seg}}=\frac{q_{w,\text{seg}}}{(\bar{T}_{w,\text{seg}}-\bar{T}_{o,\text{seg}})} \tag{15}$$

where $q_{w,\text{seg}}$ is the segment-area-averaged heat flux; $\bar{T}_{w,\text{seg}}$ the segment-area-averaged wall temperature; and $\bar{T}_{o,\text{seg}}$ the segment-

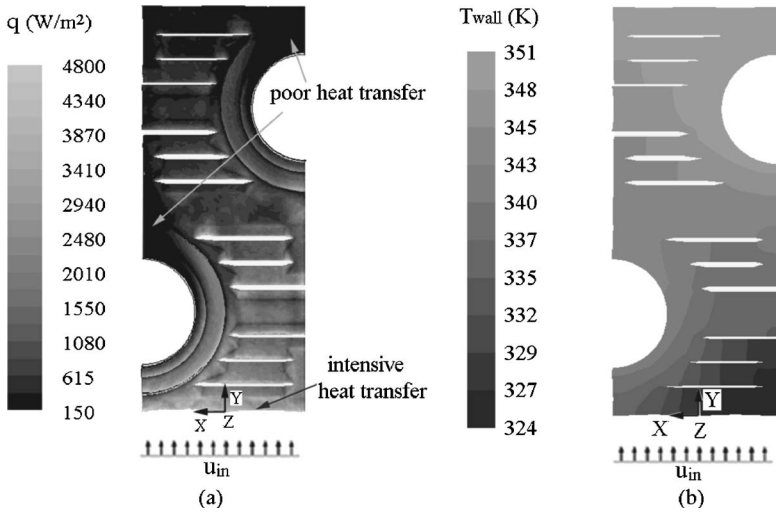

Fig. 8 Contours of heat flux and wall temperature: (*a*) heat flux; and (*b*) wall temperature

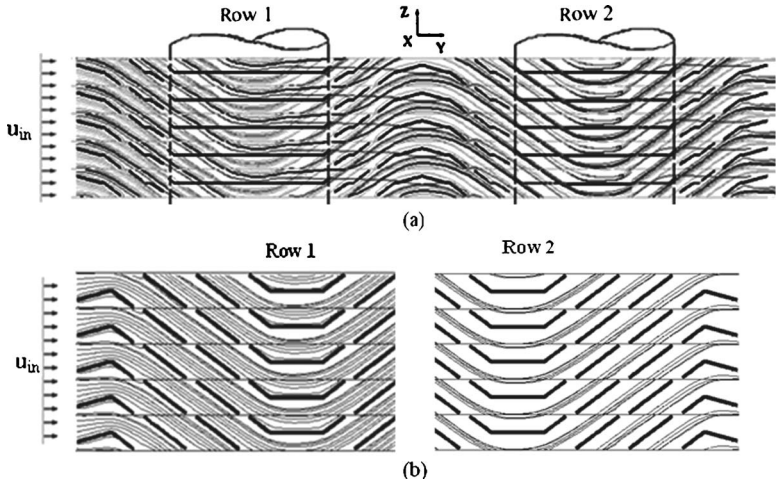

Fig. 9 Flow pattern through louver fins (Case 1): (*a*) side view of streamline pattern; and (*b*) streamlines in representative louver sections (two rows shown)

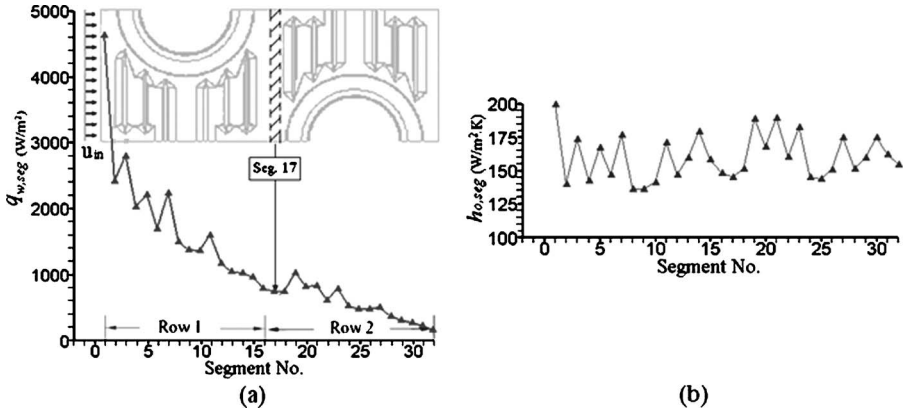

Fig. 10 Profiles of: (*a*) segment-area-averaged heat flux $q_{w,\mathrm{seg}}$; and (*b*) segment-area-averaged heat transfer coefficient $h_{o,\mathrm{seg}}$

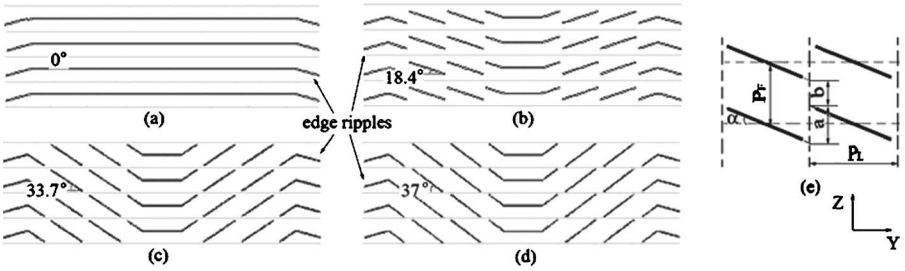

Fig. 11 The four fin designs and geometric parameters: (*a*) Fin A; (*b*) Fin B; (*c*) Fin C; (*d*) Fin D; and (*e*) geometric relationship.

volume-averaged fluid temperature. Although the definition of $h_{o,\mathrm{seg}}$ is different than the experimentally measured h_o, it may be a variable useful to represent the local heat transfer characteristics.

Figure 10(*b*) shows a maximum $h_{o,\mathrm{seg}}$ near the leading edge of the fin. Besides, there is also minor local heat transfer enhancement at the leading edge of the louvers, shown as local impulses in Fig. 10(*b*). This indicates that the louvers serve as a disturbance of the flow, especially at the leading edge of the louvers where the air stream is split. The heat transfer coefficient in the second row shows similar variation and values to that in the first row. This implies that it is the temperature difference between the wall and fluid, rather than the heat transfer coefficient, that dominates the heat transfer contribution.

5 Discussion

5.1 Contribution of Primary and Secondary Heat Transfer Area. The air-side heat transfer surface area consists of two parts: A_1 and A_2. A_1 is the primary heat transfer surface area, which is the outer cylindrical surface of the collar. A_2 is secondary heat transfer surface area A_2, which is the fin surface area exposed to the air flow, including the top, bottom, and end-edge surfaces of the fin and the cutting-edge surfaces of the louvers. The heat transfer area ratio χ, defined by Eq. (16), is about 23.3

$$\chi = A_2/A_1 \tag{16}$$

By integrating the heat flux on A_1 and A_2, the ratio of the convective heat transfer from A_2 over that from A_1 could be calculated as

$$\xi = \frac{\int\int_{A_2} q_w \, dA}{\int\int_{A_1} q_w \, dA} \tag{17}$$

Calculated from Eq. (17), the value of ξ is 81.2, which is about 3.48 times the heat transfer area ratio χ, indicating that convective heat transfer from A_2 is more efficient than that from A_1. Apparently, the fin surface plays a most significant role in such compact heat exchangers.

5.2 Influence of Louver Interaction. The louver alignment has important influence on the flow pattern and heat transfer behavior. Further investigations were conducted with three more fin designs. The geometries of those fin designs are the same as the one studied above, except for the louver angle α. The four fin geometries are illustrated in Fig. 11 and described in Table 6. Fin A is a fin without louver or with $\alpha=0$ deg (Fig. 11(*a*)); Fin B has evenly staggered louver alignment with $\alpha=18.4$ deg (Fig. 11(*b*)); Fin C has precisely in-line louver alignment with $\alpha=33.7$ deg (Fig. 11(*c*)); and Fin D is the tested fin design with $\alpha=37.0$ deg (Fig. 11(*d*)). Fin D is the baseline for comparison. Special attention was paid to Case 1, which is typical for low-noise air conditioning applications. The flow patterns were examined for the four fin designs. Fin A shows pure tunnel flow; Fin B presents a transition case of tunnel flow to louver-directed flow; and Fin C and Fin D shows typical louver-directed flows.

Based on the geometric configuration illustrated in Fig. 11(*e*), a dimensionless parameter, F, was introduced to describe the louver interaction with bulk flow

$$F = P_L \tan(\alpha)/P_F \tag{18}$$

Two aspects were considered in the definition of F. The first one is louver interaction for tunnel flow pattern, where most fluid goes through the flow "tunnel" between two adjacent fins. In this case, louvers serve as disturbance on the bulk flow. The degree of such louver disturbance can be estimated by the ratio of louver height $P_L \tan(\alpha)$ over fin pitch P_F. Consequently, F presents intrafin louver interaction. The second aspect is louver interaction for louver-directed flow pattern, where interfin louver interaction is important. In this flow pattern, the flow is dependent upon the discharge of fluid from the louver openings upstream. The louver interaction is closely associated with the frequency of louver appearance along the louver direction, which is almost the flow direction for typical louver-directed flow pattern. This can be described by $[P_L/\cos(\alpha)]/[P_F/\sin(\alpha)]$, turning out to be the same definition as F.

Though the Colburn factor j and friction factor f are commonly used to characterize the performance of heat exchangers, it is difficult to obtain j from the numerical simulation. To compare the performance of the different fin designs, an equivalent Colburn factor j' was introduced, with the same definition as Eq. (10), but with h_0 replaced by

$$h_0' = \frac{\dot{Q}}{(\overline{T_i} - \overline{T_0}) \int\int_{A_o} dA_o} \tag{19}$$

j' indicates the overall heat transfer performance including air and water sides. However, because the tube-side fluid temperature and heat transfer coefficient are fixed in the fin comparison study, j' could reflect the difference of air-side heat transfer performance.

The results of j' and f of the four fin designs are compared in

Table 6 Description of four fin designs

Fin	Description	α (deg)	F
A	No louvers, with $a=0$, $b=P_F$	0	0.0
B	Evenly staggered louver alignment with $a=b=0.5P_F$	18.4	0.50
C	In-line louver alignment with $a=P_F$, $b=0$	33.7	1.00
D	Slightly zigzagged louver alignment with $a=1.13\ P_F$, $b=-0.13\ P_F$	37.0	1.13

Table 7 Comparison of j and f of the four fin designs (baseline: Fin D)

Fin type	F	j'	f	$j'/f^{1/3}$	j'/f	Improvement (%) $j'/f^{1/3}$	Improvement (%) j'/f
A	0.0	0.0378	0.101	0.081	0.374	–9.2	21.8
B	0.50	0.0490	0.152	0.0918	0.322	2.72	4.88
C	1.00	0.0484	0.153	0.0897	0.313	0.42	2.11
D	1.13	0.0482	0.157	0.0893	0.307	0	0

Table 7 and Fig. 12. A maximum j' exists when F reaches about 0.65. The profile of f presents a more complex feature. It increases when F varies from 0 to 0.5, sustains when F increases to 1.0, and mounts up again when F is greater than 1.0. The last period implies a significant increase of pressure drop caused by fluid impingement on the louvers when the louver angle increases.

An appropriate criterion is needed to evaluate the heat tranfer and pressure loss performance of heat exchangers. Here two criteria, j'/f or $j'/f^{1/3}$, were considered. The latter was derived based on heat transfer coefficient and friction power consumption [14]. It was recommended for low-Re flow operating conditions in compact heat exchangers, where the heat transfer performance is more critical than pressure drop. As illustrated in Table 7 and Fig. 12, Fin B has the best performance among the four fin designs according to the criterion $j'/f^{1/3}$. An optimal F was predicted around 0.62, with the corresponding louver angle of 22.5 deg. However, according to the criterion j'/f, Fin A possesses the best performance. Practically this is not true. So j'/f is not appropriate for such low-Re flow applications.

To further understand the influence of louver interaction, Fig. 13 compares the contours of static pressure distribution and streamlines through the louver region of Fin B and Fin C. The trajectories are tracked by fluid released from the perpendicular line located at Point S marked in Fig. 7. Fin C displays little mass transport through the small gaps between the in-line louvers. A barely disturbed flow passage is formed in such in-line louver alignment. The downstream louvers are well in the flow and thermal wake of the upstream louvers, which mitigates the refreshment of the downstream fin surface with bulk fluid. Contrarily, Fin B shows bulk flow periodically splitting at the staggered louver front and merging in the louver wake, with the downstream louvers located far away from the thermal wake of the upstream ones, resulting in improved performance.. Furthermore, the pressure distributions in Fig. 13(a) show local increase at the leading edge of each louver. This local heat transfer enhancement is caused by the impingement of the oncoming stream.

In previous investigations on flow and heat transfer in two-dimensional louver-fin arrays [1,10–12], "flow efficiency" was used to describe the flow in a louver bank. It was defined as the ratio of the actual transverse distance traveled by the flow through the louver array over the ideal transverse distance defined by the louver direction [12], and was determined by the streamlines obtained from flow visualization experiments. In the present study, flow efficiency was obtained based on the simulated streamlines in the louver region. The result indicates that better performance (based on the criterion of $j'/f^{1/3}$) is obtained with higher flow efficiency.

6 Conclusions

Investigations on flow and heat transfer in louver-fin round-tube heat exchangers were conducted by experimental study and numerical simulations. The air-side heat transfer coefficients were obtained by the ε-NTU approach with appropriate relationships

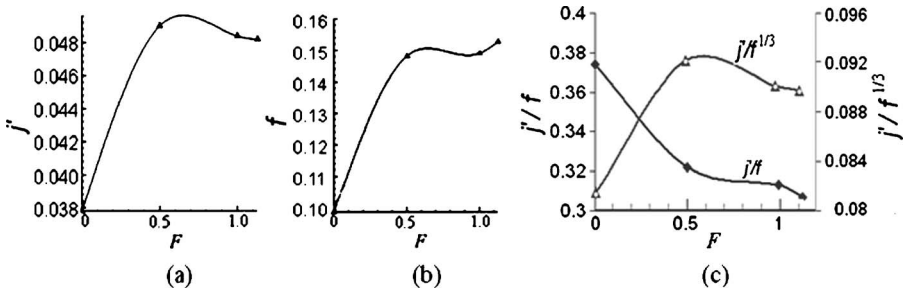

Fig. 12 Performance of the four fin designs: (a) j' versus F; (b) f versus F; and (c) j'/f^x (x=1/3,1) versus F

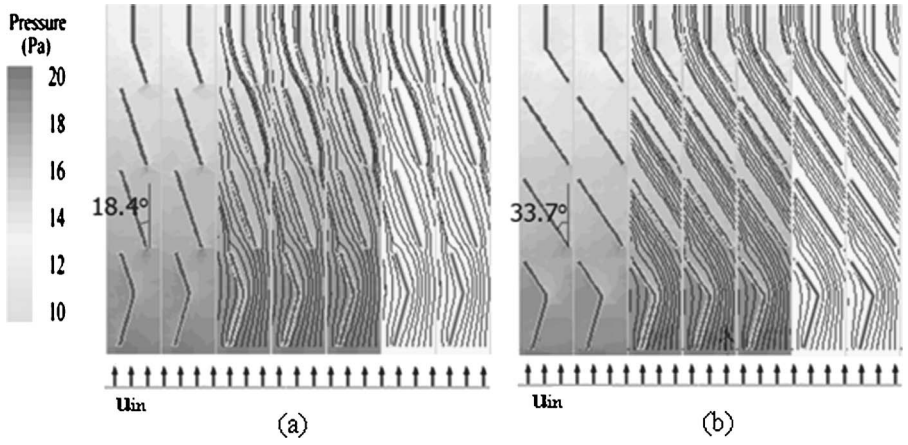

Fig. 13 Influence of louver interaction on pressure field and streamline pattern: (a) Fin B; and (b) Fin C

for the two-pass cross-counterflow heat exchangers. The Colburn factor j and friction factor f were compared with Wang et al. correlations [8].

In the CFD model, influence of tube-side circuiting was analyzed by different tube-side fluid temperature profiles. Overall nonlinear profiles show good prediction of heat transfer performance both in a system level and in a local level for the individual row, especially at high air face velocity conditions.

Stagnant flow exists behind the round tube, with diminished local heat transfer. The flow pattern shows louver-directed flow, with strong interfin mass transfer through the louver openings. The most intensive heat flux on the fin surfaces occurs at the leading edges of the fin. Row 1 contributes 68–53% of the total heat transfer rate when air velocity changes from 1.02 m/s to 2.54 m/s. Local heat transfer enhancement of the louvers presents due to disturbance of the developing flow and splitting of the bulk stream. The temperature difference between the wall and air serves as a dominant factor for the heat transfer contribution in the heat exchanger. Convective heat transfer from secondary heat transfer surface area A_2 is more effective than that from primary heat transfer surface area A_1.

Four fin designs with different louver angles were analyzed to investigate the influence of louver interaction, with flow patterns from pure tunnel flow to louver-directed flow. A dimensionless parameter F was introduced to describe the louver interaction. The heat transfer and pressure loss performance were evaluated by applying criterion $j'/f^{1/3}$ and j'/f. The latter is not suitable for low-Re flows. Fin B presents the best performance, with bulk flow periodically splitting at the staggered louver front and merging in the louver wake. An optimal F was predicted at around 0.62.

Acknowledgment

This work was supported by Advanced Heat Transfer LLC ⟨http://www.advancedheattransfer.com⟩. A special thank you goes to Dr. Steve Wayne, the CEO of AHT, for his valuable input and encouragement.

Nomenclature

A_o = air-side total heat transfer area, m^2
A_c = minimum free flow area, m^2
A_f = frontal area, m^2
A_1 = primary heat transfer area, $A_1=\pi D_c(P_F-\theta_F)$, m^2
A_2 = secondary heat transfer area, $A_2=A_o-A_1$, m^2
C = the capacity rate, $C=\dot{m}c_p$, W/K
$C_{\min}C_{\max}$ = the smaller or greater of the air-side and tube-side capacity rates, W/K
C^* = $C^*=C_{\min}/C_{\max}$
c_p = specific heat, J/(kg K)
D_h = hydraulic diameter, m
D_i = tube inner diameter, m
D_c = collar outer diameter, m
F = parameter of louver interaction
f = friction factor
G_c = mass flux of air based on A_c, $G_c=\rho u_c$, $kg/(m^2\,s)$
h = convective heat transfer coefficient, $W/(m^2\,K)$
j = the Colburn factor, $j=\mathrm{St}\cdot\mathrm{Pr}^{2/3}$
j' = the equivalent Colburn factor
U = overall heat transfer coefficient, $W/(m^2\,K)$
L = length of heat exchanger along flow direction, m
$\dot{m}$ = mass flow rate, kg/s
N = number of the identical passes
NTU = number of transfer unit, $UA_o/C_{\min}$
Nu = Nusselt number
P_F = fin pitch, m
$P_{T,X}$ = longitudinal tube pitch (in X direction), m
$P_{T,Y}$ = transverse tube pitch (in Y direction), m
P_L = louver pitch, m
Pr = Prandtl number
q = heat flux, W/m^2
$\dot{Q}$ = heat transfer rate, W
$\dot{Q}_{\max}$ = maximum possible heat transfer rate of the heat exchanger, $\dot{Q}_{\max}=C_{\min}(T_{i,\mathrm{in}}-T_{o,\mathrm{in}})$, W
R^ϕ = scaled residual
Re_i = tube-side Reynolds number, $\mathrm{Re}_i=\rho u_i D_i/\mu$
Re_o = air-side Reynolds number, $\mathrm{Re}_o=\rho u_c D_c/\mu$
St = Stanton number, $\mathrm{St}=h_0/\rho c_P u_c$
t = characteristic time scale, $t=L/u_c$, s
T = temperature, K
$\overline{T}$ = average air temperature, $\overline{T_o}=(T_{o,\mathrm{in}}+T_{o,\mathrm{out}})/2$, K
$\overline{T_i}$ = average water temperature, $\overline{T_i}=T_{i,\mathrm{in}}+T_{i,\mathrm{out}}/2$, K
u = velocity, m/s
u_c = mean velocity at the minimum cross section A_c, m/s
u_{in} = air-side face velocity at the inlet, m/s
V = enveloping volume of a heat exchanger, m^3
X,Y,Z = coordinate axis, m
α = louver angle, deg
β = heat transfer area density, m^2/m^3
χ = heat transfer area ratio
ε = heat exchanger effectiveness, $\varepsilon=\dot{Q}_{\mathrm{HX}}/\dot{Q}_{\mathrm{HX,max}}$
ε_p = heat exchanger effectiveness of single-pass crossflow circuiting
η = fin efficiency
η_o = fin surface effectiveness
λ = heat conductivity, W/(m K)
μ = viscosity, kg/(m s)
θ = thickness, m
ρ = mass density, kg/m^3
σ = the ratio of the minimum free flow area to the frontal area, $\sigma=A_c/A_f$
ξ = ratio of convective heat transfer from A_2 over that from A_1
ΔP = air-side pressure drop, Pa

Subscripts

F = fin
f = tube side fluid
HX = heat exchanger
i = tube side
in = inlet
o = air side
out = outlet
seg = segment
T = tube
w = wall

References

[1] Webb, R. L., and Trauger, P., 1991, "Flow Structure in the Louvered Fin Heat Exchanger Geometry," Exp. Therm. Fluid Sci., **4**, pp. 205–217.
[2] Chang, W. R., Wang, C. C., Tsi, W. C., and Shyu, R. J., 1995, "Airside Performance of Louver Fin Heat Exchanger," *Proceedings ASME/JSME Thermal Engineering Conference*, Vol. 4, L. S. Fletcher and T. Aihara, eds., Maui, HI, March 19–25, pp. 367–372.
[3] Achaichia, A., and Cowell, T. A., 1988, "Heat Transfer and Pressure Drop Characteristics of Flat Tube and Louvered Plate Fin Surfaces," Exp. Therm. Fluid Sci., **1**, pp. 147–157.
[4] Suga, K., and Aoki, H., 1995, "Numerical Study on Heat Transfer and Pressure Drop in Multilouvered Fins," J. Enhanced Heat Transfer, **2**, pp. 231–238.
[5] Kim, J. H., Yun, J. H., and Lee, C. S., 2004, "Heat-Transfer and Friction Characteristics for the Louvered-Fin Heat Exchanger," J. Thermophys. Heat Transfer, **18**, pp. 58–64.
[6] Jacobi, A. M., Park, Y., Tafti, D., and Zhang, X., 2001, "An Assessment of the State of the Art, and Potential Design Improvements, For Flat Tube Heat

Exchangers in Air Conditioning and Refrigeration Applications—Phase I," University of Illinois, Technical Report ARTI-21CR/20020–01.
[7] Wang, C. C., Chi, K. Y., and Chang, Y. J., 1998, "An Experimental Study of Heat Transfer and Friction Characteristics of Typical Louver Fin-and-Tube Heat Exchangers," Int. J. Heat Mass Transfer, **41**, pp. 817–822.
[8] Wang, C. C., Lee, C. J., Chang, C. T., and Lin, S. P., 1999, "Heat Transfer and Friction Correlation for Compact Louvered Fin-and-Tube Heat Exchangers," Int. J. Heat Mass Transfer, **42**, pp. 1945–1956.
[9] Wang, C. C., Chi, K. Y., and Chang, C. J., 2000, "Heat Transfer and Friction Characteristics of Plain Fin-and-Tube Heat Exchangers, Part II: Correlation," Int. J. Heat Mass Transfer, **43**, pp. 2693–2700.
[10] DeJong, N. C., and Jacobi, A. M., 2003, "Flow, Heat Transfer and Pressure Drop in the Near-Wall Region of Louvered-fin Arrays," Exp. Therm. Fluid Sci., **27**, pp. 237–250.
[11] DeJong, N. C., and Jacobi, A. M., 2003, "Localized Flow and Heat Transfer Interactions in Louvered-Fin Arrays," Int. J. Heat Mass Transfer, **46**, pp. 443–455.
[12] Zhang, X., and Tafti, D. K., 2002, "Flow Efficiency in Multi-Louvered Fins," University of Illinois, Technical Report ACRC TR-197.
[13] London, A. L., 1964, "Compact Heat Exchanger, Part 2: Surface Geometry," Mech. Eng. (Am. Soc. Mech. Eng.), **86**, pp. 31–34.
[14] Yun, J. Y., and Lee, K. S., 2000, "Influence of Design Parameters on the Heat Transfer and Flow Friction Characteristics of the Heat Exchanger with Slit Fins," Int. J. Heat Mass Transfer, **43**, pp. 2529–2539.
[15] Stephan, R. A., 2002, "Heat Transfer Measurements and Optimization Studies Relevant to Louvered Fin Heat Exchangers," Master thesis, Virginia Polytechnic and State University, Blacksburg, VA.
[16] Shah, R. K., and Sekulic, D. P., 2003, *Fundamentals of Heat Exchanger Design*, Wiley, New York.
[17] Breyfogle F. W., III, 2003, *Implementing Six Sigma: Smarter Solutions Using Statistical Methods*, 2nd ed., Wiley, New York.
[18] Bejan, A., 1993, *Heat Transfer*, Wiley, New York.
[19] Kakac, S., Shah, R. K., and Aung, W., 1987, *Handbook of Single-Phase Convective Heat Transfer*, Wiley, New York.
[20] Kays, W. M., and London, A. L., 1998, *Compact Heat Exchangers*, 3rd ed., Krieger, Malabar, FL.
[21] ESDU 86018, 1991, "Engineering Science Data Unit 86018 with Amendment A," ESDU International plc, London, pp. 92–107.
[22] Schmidt, Th. E., 1957, "Heat Transfer Calculations for Extended Surfaces," Refrig. Eng., **57**, pp. 351–357.
[23] Fluent Inc., 2005, *Fluent 6.2 User Guide Manual*, Lebanon, NH.
[24] Vandoormaal, J. P., and Raithby, G. D., 1984, "Enhancements of the SIMPLE Method for Predicting Incompressible Fluid Flows," Numer. Heat Transfer, **7**, pp. 147–163.
[25] Tafti, D. K., and Zhang, X., 2001, "Geometry Effects on Flow Transition in Multilouvered Fins—Onset, Propagation, and Characteristic Frequencies," Int. J. Heat Mass Transfer, **44**, pp. 4195–4210.

Enhancement of Convective Heat and Mass Transfer From Two Bubbles at High Reynolds Number

Abdullah Abbas Kendoush
Department of Mechanical and Aerospace Engineering,
University of Florida,
P.O. Box 116300,
Gainesville, FL 32611-6300
e-mail: kendoush@ufl.edu

Analytical solutions to the heat convection from two bubbles were obtained. These solutions were applied to the two bubbles with the flow along their line of centers and perpendicular to their line of centers. The method of images has been used to give a solution to the velocity distribution around the two bubbles. The derived solutions apply to fluid spheres. In general the derived solutions were compared well with the other available analytical and numerical results. Some avenues for further research were pointed out. [DOI: 10.1115/1.2402183]

Keywords: hydrodynamics, heat convection, two bubbles, potential flow

1 Introduction

Convective heat and mass transfer from bubbles rising in fluids occurs in many engineering industries, technologies, and scientific applications. Among these are: drying, adsorption, extraction, fixed and fluidized beds, cloud physics, and combustion of fuel droplets. Although an individual spherical bubble is rarely found in practical systems, most of the information of the scientific literature deals with studies of an individual bubble.

The problem of a two, three, and multibubble system is now being addressed by a number of research workers, e.g., Ruzicka [1]. Ramachandran et al. [2] solved the forced convective heat transfer to a linear array of three spheres by using the finite element method. In general, an increased rate of convective heat or mass transfer was obtained in systems of either dilute or concentrated particles [3].

Bispherical coordinates were used by Yuan and Prosperetti [4] and Aminzadeh et al. [5] to obtain the solution of the velocity around the two bubbles. The form of the velocity field was not convenient for the solution of the energy equation analytically, but may provide an alternative method for the solution numerically.

The heat and mass transfer to the two bubbles are governed by two opposite effects: first, diffusion of heat or mass from one bubble moderates the gradient of temperature or concentration around the other bubble and thus Nu or Sherwood numbers, respectively, are decreased with the separation distance between bubbles, respectively. This phenomenon is encountered in low Re number flow (e.g., Ramachandran and Kleinstreuer [6]). Second, the velocity profile around the two bubbles might intensify mixing and viscous stresses and thus Nu or Sherwood is increased with decreased separation distance, respectively. This is encountered in high Re flow (e.g., Ref. [2]).

Tal et al. [7] solved the Navier–Stokes and energy equations numerically for a pair of drops in tandem. The shape of their local Nu number distribution was totally altered on the downstream drop, as the location of the maximum Nu number was no longer at the front stagnation point—it was shifted to the equator region. Chen and Tong [8] also solved the Navier–Stokes and the energy equations numerically for three spherical droplets in tandem. Their finite difference solutions were for a Reynolds number range of 10–200. They obtained solutions in terms of local and overall Nu numbers.

Chiang and Kleinstreuer [9] solved a system of momentum and energy equations in a tandem of three spherical droplets. They showed that the leading and second droplets have the strongest interaction effects.

A comprehensive treatment of the convection and hydrodynamic effects on spheres, drops, and bubbles is found in Ref. [10]. Irrotational and inviscid flow assumptions were adopted successfully by Paidoussis et al. [11] and Balsa [12] to predict the flow interaction effects in cylinder arrays. They believed that the presence of adjacent cylinders seems to deflect fluid into the wake of upstream cylinders, minimizing the regions of rotational flow and producing potential flow configurations.

The following conclusions were deduced from the literature review:

1. A confusion exists as to the increase or decrease of heat transfer with bubble spacing at a particular value of Reynolds number flow (e.g., Ref. [13]).
2. The majority of the theoretical research was confined to the numerical solution of the conservation equations of mass, momentum, and energy.
3. Two-bubble interactions were not treated experimentally, except for the fluid dynamics works of Katz and Meneveau [14], Kok [15], and Sanada [16] as far as the present author is aware.
4. Neither experimental nor theoretical investigations were reported in the literature on heat or mass transfer from two bubbles as far as the present author is aware.

The ideal case of the present paper serves the purpose of modeling analytically practical situations of convective flow of heat in a system of two bubbles. In this paper analytical solutions are presented for the heat or mass transfer around two bubbles moving in line and with their line of centers perpendicular to the direction of the flow. The two-bubble analysis can be considered as the lowest-order effect of thermal interaction of multibubbles in a swarm. Potential flow around bubbles was assumed. The present analyses were confined to low Prandtl number and high Reynolds number flow. The range of Reynolds number covered by the present work is $1 < \mathrm{Re} < 1000$. Bubbles remain spherical in shape in this range provided that $10^{-2} < Eo < 1$ (Ref. [17], p. 27).

Contributed by the Heat Transfer Division of ASME for publication in the JOURNAL OF HEAT TRANSFER. Manuscript received October 7, 2005; final manuscript received April 13, 2006. Review conducted by Louis C. Burmeister.

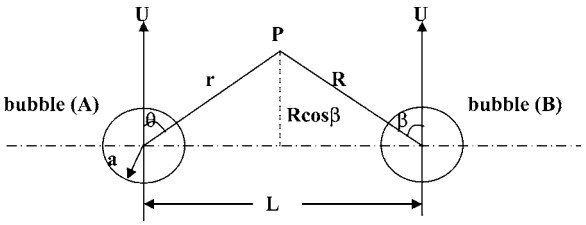

Fig. 1 Two bubbles horizontally side by side in a flow field

2 Theory

This section deals with the analysis of the pattern of fluid flow adjacent to the surface of two bubbles in their motion perpendicular to the line of centers and along their line of centers. This study is motivated by a desire to determine the velocity distribution, based on potential flow, around two bubbles by using the method of images. The derived velocity vectors were then inserted into the energy equation to get the convective heat transfer from the two bubbles.

2.1 Two Horizontally Side-by-Side Bubbles in a Potential Flow

2.1.1 Solution Method for the Flow Field. Consider two bubbles A and B as shown in Fig. 1. The method of images has been used to give solution to the velocity distribution around two bubbles situated such that their line of centers is perpendicular to the flow [18]. As shown in Fig. 1, a is the radius of both bubbles and L is the distance between their centers.

Initially, we assume that the two bubbles move with velocity U in a fluid, otherwise at rest, and we are going to add a velocity vector to the final velocity expression to obtain the solution for the flow past two bubbles. Bubble (A) is situated within the (r,θ) coordinates while bubble (B) is situated within the (R,β) coordinates. The two systems of coordinates are connected by the distance L.

This velocity potential ϕ should satisfy the following Laplace's equation

$$\frac{\partial}{\partial r}\left(r^2\frac{\partial\phi}{\partial r}\right)+\frac{\partial}{\sin\theta\,\partial\theta}\left(\sin\theta\frac{\partial\phi}{\partial\theta}\right)=0 \tag{1}$$

in the (r,θ) coordinates. A similar expression to this can be obtained in the (R,β) coordinates as shown in Fig. 1.

The radial and tangential velocity components of the flow are obtained from $\mathbf{V}=\nabla\phi$ as follows

$$V_r=-\frac{\partial\phi}{\partial r},\quad V_R=-\frac{\partial\phi}{\partial R} \tag{2}$$

and

$$V_\theta=-\frac{1}{r}\frac{\partial\phi}{\partial\theta},\quad V_\beta=-\frac{1}{R}\frac{\partial\phi}{\partial\beta} \tag{3}$$

Referring to the above coordinate system, when each bubble alone in the fluid produces the same effect as a doublet, the boundary conditions to be satisfied are

$$\frac{\partial\phi_A}{\partial r}=-U\cos\theta\quad\text{over bubble (A)}$$

$$-\frac{\partial\phi_{\mathrm{A}}}{\partial\mathrm{R}}=0\quad\text{over bubble (B)}$$

$$-\frac{\partial\phi_{\mathrm{B}}}{\partial\mathrm{r}}=0\quad\text{over bubble (A)}$$

$$\frac{\partial\phi_{\mathrm{B}}}{\partial\mathrm{R}}=-U\cos\beta\quad\text{over bubble (B)} \tag{4}$$

If bubble (A) was alone in the fluid, moving with velocity U, we should have a velocity potential

$$\phi_{A1}=\frac{U}{2}\frac{a^3}{r^2}\cos\theta \tag{5}$$

which would make $\partial\phi_A/\partial r|_{r=a}=-U\cos\theta$ over bubble (A) and, therefore, satisfying the first boundary condition in Eqs. (4). Now, near bubble (B), $r=L$ and $r\cos\theta=R\cos\beta$, Eq. (5) becomes the following

$$\phi_{A1}=\frac{U}{2}\left(\frac{a}{L}\right)^3R\cos\beta \tag{6}$$

giving a normal velocity over bubble (B) equals to $U/2(a/L)^3\cos\beta$. This normal velocity might be canceled by the addition of a velocity potential

$$\phi_{A2}=\frac{U}{4}\left(\frac{a}{L}\right)^3\frac{a^3}{R^2}\cos\beta \tag{7}$$

and the value of this term near bubble (A) is

$$\phi_{A2}=\frac{U}{4}\left(\frac{a}{L}\right)^6r\cos\theta \tag{8}$$

giving a normal velocity over bubble (A) equal to $(-U/4)\times(a/L)^6\cos\theta$. This normal velocity can be canceled by the addition of a velocity potential

$$\phi_{A3}=\frac{U}{8}\left(\frac{a}{L}\right)^6\frac{a^3}{r^2}\cos\theta \tag{9}$$

and so on.

This process can be continued until the order of approximation is acceptable. For the above terms

$$\phi_A=\phi_{A1}+\phi_{A2}+\phi_{A3}$$

or

$$\phi_A=\frac{U}{2}\frac{a^3}{r^2}\cos\theta+\frac{U}{4}\left(\frac{a}{L}\right)^6r\cos\theta+\frac{U}{8}\left(\frac{a}{L}\right)^6\frac{a^3}{r^2}\cos\theta \tag{10}$$

The level of approximation is, therefore, dependent on $L\gg a$. To obtain a similar approximation for ϕ_B, the same procedure is followed but with respect to position (B), that is

$$\phi_B=\frac{U}{2}\frac{a^3}{R^2}\cos\beta+\frac{U}{4}\left(\frac{a}{L}\right)^6R\cos\beta+\frac{U}{8}\left(\frac{a}{L}\right)^6\frac{a^3}{R^2}\cos\beta \tag{11}$$

To find the radial and tangential velocity component for the flow past the two bubbles, a velocity vector $(-U\cos\theta)$ was added to (V_r) and a velocity vector $(U\sin\theta)$ to (V_θ) so that the two bubbles were brought to rest in the stream and the fluid would pass around them. This is a common practice in hydrodynamics. Hence

$$V_r=-U\cos\theta\left[1-\left(\frac{a}{r}\right)^3+\frac{1}{4}\left(\frac{a}{L}\right)^6-\frac{1}{4}\left(\frac{a}{L}\right)^6\left(\frac{a}{r}\right)^3\right] \tag{12}$$

and

$$V_\theta=U\sin\theta\left[1+\frac{1}{2}\left(\frac{a}{r}\right)^3+\frac{1}{4}\left(\frac{a}{L}\right)^6+\frac{1}{8}\left(\frac{a}{L}\right)^6\left(\frac{a}{r}\right)^3\right] \tag{13}$$

2.1.2 Heat Convection to Two Side-by-Side Bubbles. Consider two bubbles with their surface temperatures kept at T_a. The analytical treatment of heat transfer to the two bubbles starts by solving the energy equation which, in spite of its linearity, cannot be solved in closed form. Therefore, a boundary layer approximation has to be made as shown below.

Assuming $y/a=(r-a)/a\ll1$ over the surface of bubble (A) in

the presence of bubble (B). Therefore V_r and V_θ from Eqs. (12) and (13) become the following after the approximations given in the Appendix

$$V_r = -3Ub(y/a)\cos\theta \tag{14}$$

where

$$b = \left[1 + \frac{1}{4}\left(\frac{a}{L}\right)^6\right]$$

and

$$V_\theta = (3/2)Ub\sin\theta \tag{15}$$

The steady-state equation of heat transport in spherical coordinates is given by the following

$$V_r\frac{\partial T}{\partial r} + \frac{V_\theta}{r}\frac{\partial T}{\partial \theta} = \alpha\left[\frac{1}{r^2}\frac{\partial}{\partial r}\left(r^2\frac{\partial T}{\partial r}\right) + \frac{1}{r^2\sin\theta}\left(\sin\theta\frac{\partial T}{\partial \theta}\right)\right] \tag{16}$$

By neglecting the conductive transfer of heat in the direction tangent to the surface of the bubble we get

$$V_r\frac{\partial T}{\partial r} + \frac{V_\theta}{r}\frac{\partial T}{\partial \theta} = \alpha\left(\frac{\partial^2 T}{\partial r^2} + \frac{2}{r}\frac{\partial T}{\partial r}\right) \approx \alpha\frac{\partial^2 T}{\partial r^2} \tag{17}$$

This equation can be further simplified by boundary layer considerations into the following (Kendoush [19])

$$V_r\frac{\partial T}{\partial r} + \frac{V_\theta}{a}\frac{\partial T}{\partial \theta} = \alpha\frac{\partial^2 T}{\partial r^2} \tag{18}$$

Substitution of V_r and V_θ from Eqs. (14) and (15) into the above reduced energy equation yields

$$-2y\cos\theta\frac{\partial T}{\partial y} + \sin\theta\frac{\partial T}{\partial \theta} = M\frac{\partial^2 T}{\partial y^2} \tag{19}$$

where

$$M = \frac{2a\alpha}{3bU}$$

Utilizing the following two independent variables in the energy equation

$$S = y\sin^2\theta \tag{20}$$

and

$$J = \int_0^\theta \sin^3\theta\, d\theta = \frac{1}{3}\cos^3\theta - \cos\theta + \frac{2}{3} \tag{21}$$

and substituting their derivatives into Eq. (19) gives

$$\frac{\partial T}{\partial J} = M\frac{\partial^2 T}{\partial S^2} \tag{22}$$

The general solution of the above equation is

$$T = T_a\,\mathrm{erfc}\left(\frac{S}{2\sqrt{MJ}}\right) \tag{23}$$

Substituting the values of S, J, and M into Eq. (23) gives

$$T = T_a\,\mathrm{erfc}\left[\frac{y\sin^2\theta}{2\left[\frac{2a\alpha}{3bU}\left(\frac{1}{3}\cos^3\theta - \cos\theta + \frac{2}{3}\right)\right]^{1/2}}\right] \tag{24}$$

In order to find the heat transfer coefficient, we start by calculating the angular heat flux q_θ as follows

$$q_\theta = -k\left(\frac{\partial T}{\partial y}\right)_{y=0} = -k\left(\frac{\partial T}{\partial S}\right)\left(\frac{\partial S}{\partial y}\right)_{y=0} = \frac{kT_a\sin^2\theta}{(\pi MJ)^{1/2}} \tag{25}$$

Newton's law of cooling (that is, $q_\theta = h_\theta T_a$) together with Eq. (25) gives the following

$$h_\theta = \frac{k\sin^2\theta}{\sqrt{\pi}\left[M\left(\frac{1}{3}\cos^3\theta - \cos\theta + \frac{2}{3}\right)\right]^{1/2}} \tag{26}$$

and consequently the local Nu number becomes

$$\mathrm{Nu}(\theta) = \frac{3\sin^2\theta\sqrt{b}(\mathrm{Pe})^{1/2}}{\sqrt{\pi}(\cos^3\theta - 3\cos\theta + 2)^{1/2}} \tag{27}$$

Proceed to calculate the average heat flux on the bubble surface as follows

$$q = \frac{1}{4\pi a^2}\int_0^\pi q_\theta 2\pi a^2\sin\theta\, d\theta \tag{28}$$

The integration from 0 to π in the above equation is justified by the fact that the separation zone of the boundary layer around the bubble is quite narrow. Durst et al. [20] did not notice any identifiable separation flow regions behind spherical gas bubbles in their laser Doppler experiments, but recent experiments by De Varies et al. [21] and the computations by Mougin and Magnaudet [22] indicated the presence of a well defined wake region behind bubbles at high Re number. Substituting Eq. (26) into Eq. (28) gives

$$q = \frac{kT_a}{2\sqrt{\pi M}}\int_0^\pi \frac{\sin^3\theta}{\sqrt{J}}d\theta \tag{29}$$

therefore the average Nu number over bubble (A) is given by

$$(\mathrm{Nu})_A = \frac{2}{\sqrt{\pi}}\sqrt{b}(\mathrm{Pe})^{1/2} \tag{30}$$

as $L\to\infty$; $\sqrt{b}\to 1$. Equation (30) reduces to the single bubble equation of Boussinesq [23], that is

$$(\mathrm{Nu})_s = \frac{2}{\sqrt{\pi}}(\mathrm{Pe})^{1/2} \tag{31}$$

The ratio of the two-bubble Eq. (30) to the above single-bubble equation is the following

$$\frac{(\mathrm{Nu})_A}{(\mathrm{Nu})_s} = \sqrt{b} = \left[1 + \frac{1}{4}\left(\frac{a}{L}\right)^6\right]^{1/2} \tag{32}$$

Now we shall find the heat transfer to bubble (B) by calculating the following velocity components using Eq. (11)

$$V_R = -\frac{\partial\phi_B}{\partial R} = -U\cos\beta\left[1 - \left(\frac{a}{R}\right)^3 + \frac{1}{4}\left(\frac{a}{L}\right)^6 - \frac{1}{4}\left(\frac{a}{L}\right)^6\left(\frac{a}{R}\right)^3\right] \tag{33}$$

and

$$V_\beta = -\frac{1}{R}\frac{\partial\phi_B}{\partial\beta} = U\sin\beta\left[1 + \frac{1}{2}\left(\frac{a}{R}\right)^3 + \frac{1}{4}\left(\frac{a}{L}\right)^6 + \frac{1}{8}\left(\frac{a}{L}\right)^6\left(\frac{a}{R}\right)^3\right] \tag{34}$$

Assuming that $(y/a) = (R-a)/a \ll 1$ over the surface of bubble (B) and using the procedure of the Appendix, we get

$$V_R = -3Ub(y/a)\cos\beta \tag{35}$$

and

$$V_\beta = (3/2)Ub\sin\beta \tag{36}$$

The steady-state equation of heat convection in (R,β) spherical coordinates is given by the following

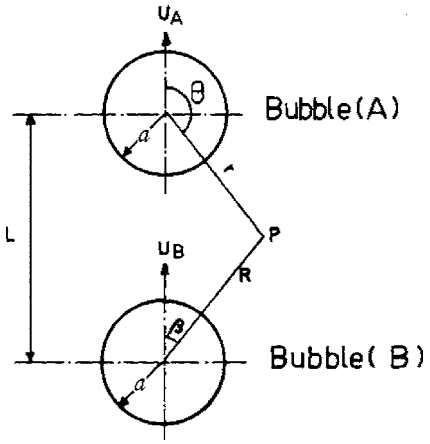

Fig. 2 Two bubbles vertically one above the other in a flow field

$$V_R\frac{\partial T}{\partial R}+\frac{V_\beta}{R}\frac{\partial T}{\partial \beta}=\alpha\left[\frac{1}{R^2}\frac{\partial}{\partial R}\left(R^2\frac{\partial T}{\partial R}\right)+\frac{1}{R^2\sin\beta}\left(\sin\beta\frac{\partial T}{\partial \beta}\right)\right] \tag{37}$$

Following the same approximations outlined for bubble (A), we get

$$V_R\frac{\partial T}{\partial R}+\frac{V_\beta}{a}\frac{\partial T}{\partial \beta}=\alpha\frac{\partial^2 T}{\partial R^2} \tag{38}$$

Substituting V_R and V_β from Eqs. (35) and (36) into Eq. (38) yields

$$-2y\cos\beta\frac{\partial T}{\partial y}+\sin\beta\frac{\partial T}{\partial \beta}=M\frac{\partial^2 T}{\partial y^2} \tag{39}$$

The equations from Eqs. (30)–(39) are applied to the case of bubble (B) with the replacement of every angle θ by β until we get the following

$$(\mathrm{Nu})_B=\frac{2}{\sqrt{\pi}}\sqrt{b}(\mathrm{Pe})^{1/2} \tag{40}$$

which represents the heat convection from bubble (B). Ruzicka [1] stated that the steady drag force acting on a pair of bubbles is the mean drag of the pair. The similarity between momentum and heat transfer allows us to use the same averaging process to determine the mean value of heat convection of the two bubbles rising side by side as follows

$$\mathrm{Nu}=(1/2)[(\mathrm{Nu})_A+(\mathrm{Nu})_B] \tag{41}$$

Substituting Eqs. (30) and (40) into Eq. (41) gives

$$\mathrm{Nu}=\frac{2}{\sqrt{\pi}}\sqrt{b}(\mathrm{Pe})^{1/2} \tag{42}$$

2.2 Two Bubbles Vertically Above One Another in a Potential Flow

2.2.1 Solution Method for the Flow Field. The same method of solution used previously is adopted here. The two bubbles under consideration are shown in Fig. 2, but we cannot assume the two bubbles move with the same velocity as the wake of the leading bubble certainly affects the rise of the trailing bubble. Clift et al. ([17], p. 172) report that the bubble wake extends no more than two diameters downstream. Hence we assume that bubble (A) moves with velocity U_A and bubble (B) moves with velocity U_B in a fluid otherwise at rest. Referring to the coordinate systems shown in Fig. 2, the boundary conditions are the following

$$\frac{\partial \phi_A}{\partial r}=-U_A\cos\theta \quad \text{over bubble (A)}$$

$$-\frac{\partial \phi_A}{\partial R}=0 \quad \text{over bubble (B)}$$

$$-\frac{\partial \phi_B}{\partial r}=0 \quad \text{over bubble (A)}$$

$$\frac{\partial \phi_B}{\partial R}=-U_B\cos\beta \quad \text{over bubble (B)} \tag{43}$$

If bubble (A) was alone in the fluid, moving with velocity U_A we should have a velocity potential

$$\phi_{A1}=\frac{U_A}{2}\frac{a^3}{r^2}\cos\theta \tag{44}$$

which would make $\partial\phi_A/\partial r=-U_A\cos\theta$ over bubble A, thus satisfying the first boundary condition of Eq. (43). Milne-Thomson [18] derived the following approximation, from considerations of spherical harmonics, to move from R,β coordinates to r,θ coordinates

$$\frac{r\cos\theta}{r^3}=-\frac{1}{L^2}\left(1+\frac{2R}{L}\cos\beta+\cdots\right) \tag{45}$$

Therefore, near bubble (B) and using Eqs. (44) and (45), it follows that

$$\phi_{A1}=-\frac{U_A}{2}\frac{a^3}{L^2}\left(1+\frac{2R\cos\beta}{L}\right) \tag{46}$$

This produces a normal velocity over bubble $(B)=-(a/L)^3U_A\cos\beta$. This normal velocity might be canceled by the addition of a velocity potential

$$\phi_{A2}=\frac{U_A}{2}\left(\frac{a}{L}\right)^3\frac{a^3}{R^2}\cos\beta \tag{47}$$

The value of this term near bubble (A) is

$$\phi_{A2}=\frac{U_A}{2}\frac{a^3}{L^2}\left(1+\frac{2r\cos\theta}{L}\right) \tag{48}$$

This gives a normal velocity over bubble $(A)=-(a/L)^3U_A\cos\theta$. Again this normal velocity might be canceled by the addition of a velocity potential

$$\phi_{A3}=\frac{U_A}{2}\left(\frac{a}{L}\right)^3\frac{a^3}{r^2}\cos\theta \tag{49}$$

and so on.

To this order of approximation we have to calculate the velocity potential around bubble (A) as follows

$$\phi_A=\phi_{A1}+\phi_{A2}+\phi_{A3}+\cdots \tag{50}$$

or the following

$$\phi_A=\frac{U_A}{2}\frac{a^3}{r^2}\cos\theta+\frac{U_A}{2}\frac{a^3}{L^2}\left(1+\frac{2r\cos\theta}{L}\right)+\frac{U_A}{2}\left(\frac{a}{L}\right)^3\frac{a^3}{r^2}\cos\theta \tag{51}$$

This function satisfies the first boundary condition in Eq. (43). To obtain a similar approximation for ϕ_B, the same procedure is followed but with respect to position B, that is

$$\phi_B=\frac{U_B}{2}\frac{a^3}{R^2}\cos\beta+\frac{U_B}{2}\frac{a^6}{L^5}\left(1+\frac{2R\cos\beta}{L}\right)+\frac{U_B}{2}\left(\frac{a}{L}\right)^6\frac{a^3}{R^2}\cos\beta \tag{52}$$

From the velocity potential of Eq. (51) we find the velocity components (V_r) and (V_θ) then we add the velocity vector

$(-U_A \cos\theta)$ and $(U_A \sin\theta)$ to them, respectively, in order to fix the two bubbles in the stream. Thus

$$V_r = U_A \cos\theta[-1 + (a/r)^3 - (a/L)^3 + (a/L)^3(a/r)^3] \quad (53)$$

and

$$V_\theta = U_A \sin\theta[1 + 0.5(a/r)^3 + (a/L)^3 + 0.5(a/L)^3(a/r)^3] \quad (54)$$

2.2.2 Heat Convection to the Two Bubbles Rising in Tandem. The same method of solution used previously is adopted here but with V_r and V_θ from Eqs. (53) and (54) approximated as follows

$$V_r \approx -3U_A H \frac{y}{a}\cos\theta \quad (55)$$

and

$$V_\theta \approx \frac{3}{2}U_A H \sin\theta \quad (56)$$

where

$$H = [1 + (a/L)^3]$$

Introducing the above equations into the simplified energy equation and solving it we finally get the local Nu number as follows

$$\mathrm{Nu}(\theta) = \frac{3\sqrt{H}\sin^2\theta([\mathrm{Pe}]_A)^{1/2}}{\sqrt{\pi}(\cos^3\theta - 3\cos\theta + 2)^{1/2}} \quad (57)$$

and the average Nu number is given by

$$(\mathrm{Nu})_A = \frac{2}{\sqrt{\pi}}\sqrt{H}([\mathrm{Pe}]_A)^{1/2} \quad (58)$$

as $L \to \infty$; $\sqrt{H} \to 1$. Equation (58) reduces to the single sphere equation of Boussinesq (that is, Eq. (31)).

The ratio of the two-bubble equation (58) to the single sphere Eq. (31) is

$$\frac{(\mathrm{Nu})_A}{(\mathrm{Nu})_s} = \sqrt{H} \quad (59)$$

Now we shall find the heat transfer to bubble (B) by calculating the following velocity components and by using Eqs. (2), (3), and (52)

$$V_R = U_B \cos\beta[-1 + (a/L)^3 - (a/L)^6 + (a/L)^6(a/L)^3] \quad (60)$$

and

$$V_\beta = U_B \sin\beta[1 + 0.5(a/R)^3 + (a/L)^6 + 0.5(a/L)^6(a/R)^3] \quad (61)$$

In a method similar to above, we get

$$(\mathrm{Nu})_B = \frac{2}{\sqrt{\pi}}\sqrt{G}([\mathrm{Pe}]_B)^{1/2} \quad (62)$$

where

$$G = \left[1 + \left(\frac{a}{L}\right)^6\right]$$

as $L \to \infty$; $\sqrt{b} \to 1$. Equation (62) reduces to the single bubble equation of Boussinesq (that is, Eq. (31)). The mean value of heat convection of the two bubbles rising in line is given by Eq. (41) as follows

$$\mathrm{Nu} = \frac{1}{2}\left[\frac{2}{\sqrt{\pi}}\sqrt{H}([\mathrm{Pe}]_A)^{1/2} + \frac{2}{\sqrt{\pi}}\sqrt{G}([\mathrm{Pe}]_B)^{1/2}\right] \quad (63)$$

Note that the heat convection from the trailing bubble (B) is smaller than that of the leading bubble (A) when the Pe number is kept at the same value. This comparison is clearly seen as follows by taking the ratio of Eq. (58) to Eq. (62)

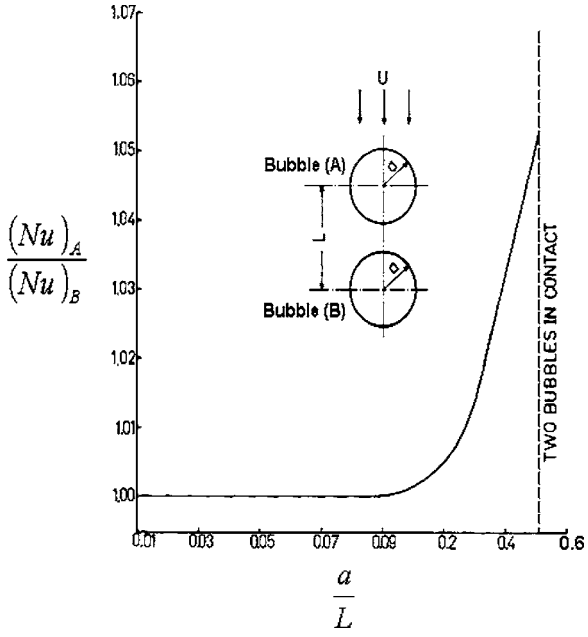

Fig. 3 The ratio of heat convection from the leading bubble (A) to that of the trailing bubble (B) versus (*a*/*L*) according to Eq. (64)

$$\frac{(\mathrm{Nu})_A}{(\mathrm{Nu})_B} = \sqrt{\frac{H}{G}} \quad (64)$$

The reduction of heat transfer to bubble (B) as compared to bubble (A) is attributed to the fact that bubble (A) encounters fresh liquid as it rises, then this liquid would acquire a lower temperature gradient. When this liquid flows over bubble (B), less heat will transfer from it.

3 Discussion and Validation of Results

The adoption of potential flow for the fluid outside the bubble excludes the momentum boundary layer effects. It should be noted that the bubble shape might depart from the sphere that is assumed in the present analysis.

The variation of the ratio $(\mathrm{Nu})_A/(\mathrm{Nu})_B$ given by Eq. (64) with the separation of the two tandem bubbles is shown in Fig. 3. The increase of the ratio of heat transfer from the leading bubble to that of the trailing bubble is in qualitative agreement with the following authors:

1. Chen and Tong [8] as shown in their Fig. 7. Quantitatively, the ratio of Nu from the first droplet to that from the second droplet ranged from 1.1 to 1.7 at droplet separation of $a/L = 0.333$. These values were too high in comparison to the results of Fig. 3.
2. Kleinstreuer and Chiang [24]. Both authors dealt with tandem of droplets. Their ratio ranged from 1.2 to 1.6 at a range of droplet separation of 0.08–0.333.

The high values reported by the above two references were mainly due to their numerical solution of tandem of droplets of fuel in a heated gas stream. Unlike the present solution, there exists a well defined boundary layer separation in the wake of the droplet.

The ratio of the heat convection from the leading bubble in in-line arrangement to the single bubble given by Eq. (59) and the same ratio for bubble (A) given by Eq. (32) are shown plotted in Fig. 4. The hydrodynamic interaction and subsequently the convection of heat is higher in the case of the two bubbles in tandem than that of the two bubbles with the flow perpendicular to their line of centers. This can also be envisaged intuitively as the wake

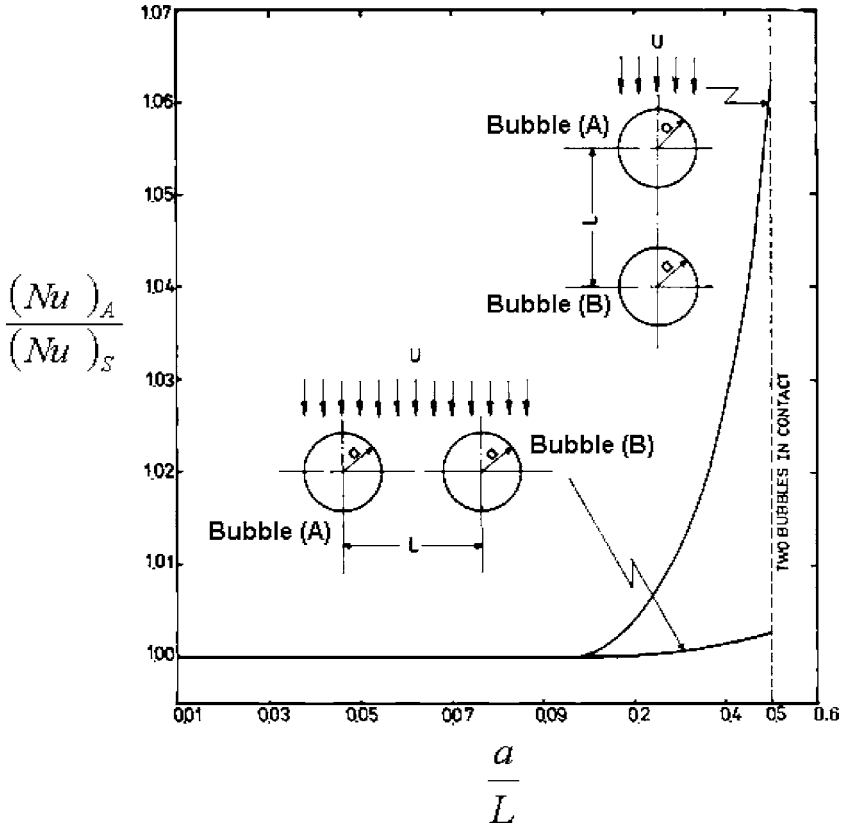

Fig. 4 The ratio of heat convection from the leading bubble (A) in the tandem orientation to that of bubble (A) in the side-by-side orientation versus (*a*/*L*) according to Eqs. (32) and (59)

length between the tandem bubbles influences the flow field more than that in the case of the two side-by-side bubbles. In both cases the thermal interaction between the two bubbles vanishes at $a/L < 0.1$ where the two-bubble transport conditions approach those of the single bubble. Figure 4 also shows how heat convection from the two bubbles increases when the bubbles separation distance gets smaller. This comes in conformity with earlier theoretical results by the author [25] who found that the Nu number increases with the increase of the volume fraction of vapor bubbles ε in a mixture of liquid and bubbles (that is, $\mathrm{Nu} = 2[\mathrm{Pe}/\pi(1-\varepsilon)]^{1/2}$).

Harper [26] derived the following equation for the tangential velocity of the two bubbles flowing along their line of centers

$$\frac{V_\theta}{U_A} = \frac{3}{2}\sin\theta\left[1 - \left(\frac{a}{L}\right)^3 + 5\left(\frac{a}{L}\right)^4\cos\theta + \frac{1}{2}\left(\frac{a}{L}\right)^5(7 + 35\cos^2\theta)\right] \tag{65}$$

This velocity was taken at the leading bubble surface. At $r=a$ and $\theta=60$ deg the present Eq. (54) is modified to suit Harper's equation as follows

$$\frac{V_\theta}{U_A} = \frac{3}{2}\sin 60\left[1 + \left(\frac{a}{L}\right)^3\right] \tag{66}$$

Figure 5 shows a comparison between Eq. (65) of Harper after we made $\theta=60$ deg in it and the present solution (Eq. (66)). This comparison was done for the purpose of validating the derived velocity field by the present author.

Figure 6 shows satisfactory agreement between Eq. (58) of the average Nu number of the leading bubble in the tandem arrangement and the first droplet in an array of three droplets of the numerical solution of Tong and Chen [27].

Ramachandran et al. [2] dealt numerically with three droplets aligned at different spacing and found the local Nu number distributions for Re number ranging from 20 to 200, Pr number ranging from 0.7 to 200, and different separation distances between two droplets of $L/2a=2$ and 4. Figure 7 shows comparisons between the present Eq. (57) and the numerical solution of Ramachandran et al. [2]. Figure 8 also shows a comparison between Eq. (58) and numerical solution of Ramachandran et al. for the average Nu numbers at Pr=0.7 and different droplet separation distances.

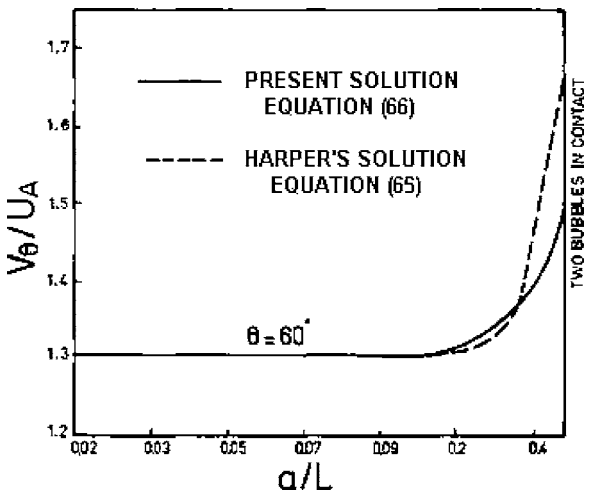

Fig. 5 Comparison between the present solution (Eq. (66)) (—) and the solution of Harper [26] (Eq. (65)) (-------)

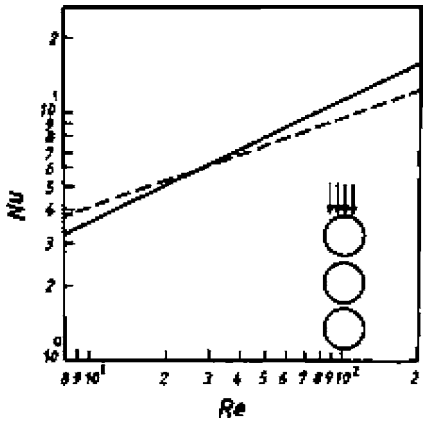

Fig. 6 Comparison between the present solution (Eq. (58)) (—) and the numerical solution of Tong and Chen [27] (-------) for $a/L=1/3$ and Pr=1

These results are important in the analysis of spray combustion of fuel droplets. It seems that the present results of two bubbles are about the same as those of the three droplets of Ramachandran et al. [2].

The enhancement of the heat transfer coefficient at high Re number flow is based on hydrodynamic considerations because the velocity components around any two bubbles, that is

$$V_r = -3Ub\frac{y}{a}\cos\theta$$

and

$$V_\theta = \frac{3}{2}Ub\sin\theta$$

are higher than those around a single bubble by the value of b or H of Eqs. (55) and (56) which are greater than unity.

For low Re number flow or at the limiting case of zero fluid velocity, a reduction in the Nu number occurs as a result of the temperature gradient becoming less steep adjacent to the two bubbles. The comparison between the high and low Re number cases is illustrated in Fig. 9. The molecular conduction of heat from the two spheres is derived by the author and given as follows:

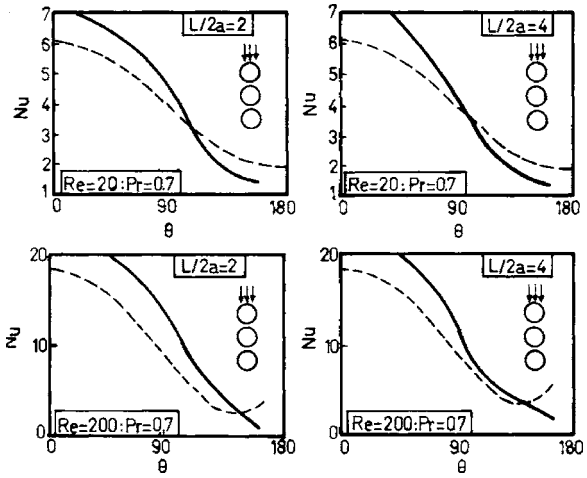

Fig. 7 Comparison between the present solution (Eq. (57)) (—) and the numerical solution of Ramachandran et al. [2] (– – –)

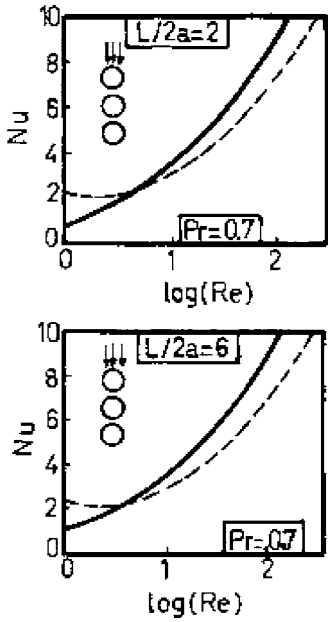

Fig. 8 Comparison between the present solution (Eq. (58)) (—) and the numerical solution of Ramachandran et al. [2] (– – –)

$$\frac{\mathrm{Nu}}{(\mathrm{Nu})_s} = \sum_{n=0}^{\infty} \frac{(-1)^n \sinh\cosh^{-1}\left(\frac{L}{2a}\right)}{\sinh(n+1)\cosh^{-1}\left(\frac{L}{2a}\right)} \tag{67}$$

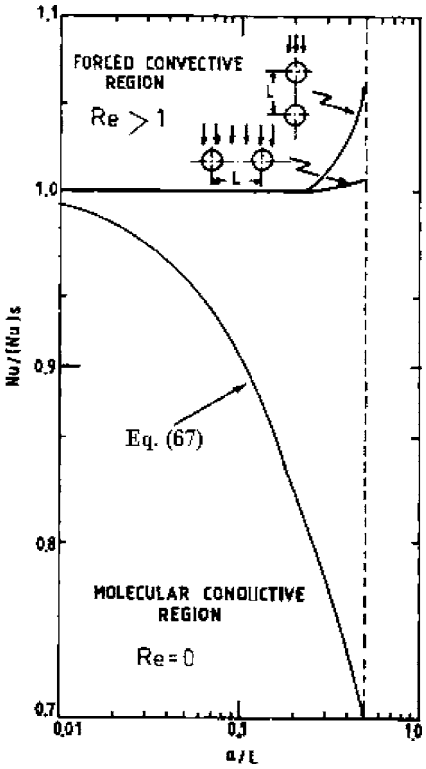

Fig. 9 Comparison between the convective and the conductive heat transfer to the two bubbles according to Eqs. (42), (63), and (67)

The corresponding mass transfer problem is analogous to the previously discussed heat transfer, particularly when viscous heating is ignored in the latter. One needs only to replace temperature by concentration and the Nu number by Sherwood number and Pe number by Re number times the Schmidt number in Eqs. (27), (30)–(32), (40), (42), (57), (58), (62)–(64), and (67).

When the lift coefficient is negative, any two bubbles moving side by side would attract each other and vice versa. The attraction force is stronger the closer the two bubbles are until coalescence occurs [28]. For any two bubbles rising in line, it was found experimentally by Katz and Meneveau [14] and Sanada [16] that the trailing bubble moves faster than the leading bubble. This relative motion continues during the rise of the two bubbles and the distance between them diminishes until they coalesce with each other.

The above discussion reveals that the motion of the two bubbles (in both their configurations) is transient in nature. This motivated the present author to look for a suitable solution to the virtual mass coefficient of two rising bubbles ([29]).

The present solution ignores gas or vapor circulation inside the bubble. Heat convection from the liquid phase to the bubble either causes gas to heat up or it may cause evaporation from the internal surface of the bubble and vapor formation. In all these circumstances, the heat flux on the liquid side of the bubble will transfer through the boundary layer. This heat flux is equal to $k_f(dT/dr)_f$. The heat flux on the gas side inside the bubble, assuming gas circulation and a boundary layer there, would be equal to $k_g(dT/dr)_g$. Simple calculations show that the heat flux from the bubble exterior is many orders of magnitude higher than that of the bubble interior in addition to the heating caused by the internal viscous effects in the liquid of the bubble exterior. These two modes of heat transfer justify the neglect of gas circulation inside the bubble.

4 Conclusions

New solutions were derived in this investigation for heat convection to two bubbles in their motion along their line of centers and perpendicular to their line of centers.

The present paper revealed and proved analytically the following phenomena:

1. The heat convection is higher for the two bubbles moving along their line of centers than those moving perpendicular to their line of centers as shown in Fig. 3.
2. Heat convection from two bubbles increases as the bubbles approach one another as shown in Figs. 3, 4, and 9.
3. There are two distinct behaviors of heat transfer to the two bubbles at low and high Re number as shown in Fig. 9.

Acknowledgment

I wish to thank the University of Florida, Department of Mechanical and Aerospace Engineering, Thermal Science and Fluid Dynamics Group and the Institute of International Education, Scholar Rescue Fund for their continuing support of my work.

Nomenclature

a = radius of the bubble, mσ
E_o = Eotvos number $(\rho(2a)^2 g/\sigma)$
g = acceleration due to gravity (ms^{-2})
h = average convective heat transfer coefficient, $(W\,m^{-2}\,K^{-1})$
h_θ = local convective heat transfer coefficient, $(W\,m^{-2}\,K^{-1})$
k = thermal conductivity of the fluid $(W\,m^{-1}\,K^{-1})$
L = the distance between centers of two bubbles (m)
$Nu(\theta)$ = local Nusselt number $(2ah_\theta/k)$
Nu = average Nusselt number $(2ah/k)$
Pe = Peclet number (Re Pr)
Pr = Prandtl number (ν/α)
q = average heat flux on the bubble surface $W\,m^{-2}$
q_θ = angular heat flux $(W\,m^{-2})$
r, R = radial coordinates (m)
Re = Reynolds number $(2a\rho U/\mu)$
T = temperature (K)
T_a = temperature of the bubble surface (K)
U = main velocity of the fluid, $(m\,s^{-1})$
$V_{r,\theta}$ = velocity component of the fluid in r and θ directions, respectively (ms^{-1})
y = radial distance from the bubble surface, (m)

Greek Symbols

α = thermal diffusivity, $m^2\,s^{-1}$
β, θ = spherical coordinates
ε = volume fraction of bubbles
ϕ = velocity potential, $m^2\,s^{-1}$
μ = dynamic viscosity, $Ns\,m^{-2}$
ν = kinematic viscosity, $m^2\,s^{-1}$
ρ = density of the fluid, $kg\,m^{-3}$
σ = surface tension, $N\,m^{-1}$

Subscript

A, B = bubble (A) and bubble (B), respectively
f = liquid
g = gas
s = single bubble
θ = local

Appendix: The Boundary Layer Approximation of the Flow Field

The assumption of a thin layer around the bubble of thickness y is given as follows

$$\frac{y}{a} = \frac{r}{a} - 1 \ll 1 \tag{A1}$$

Applying the approximation to Eq. (12) and substituting for every r/a by Eq. (A1) as follows

$$V_r = -U\cos\theta\left[1 - \left(1+\frac{y}{a}\right)^{-3} + \frac{1}{4}\left(\frac{a}{L}\right)^6 - \frac{1}{4}\left(\frac{a}{L}\right)^6\left(1+\frac{y}{a}\right)^{-3}\right] \tag{A2}$$

By taking the first two terms of the expansion series, yields

$$\left(1+\frac{y}{a}\right)^{-3} = 1 - 3\frac{y}{a} + \cdots \tag{A3}$$

Substituting this equation into Eq. (A2), would recover the form of Eq. (14).

References

[1] Ruzicka, M. C., 2000, "On Bubbles Rising in Line," Int. J. Multiphase Flow, **26**, pp. 1141–1181.
[2] Ramachandran, R. S., Kleinstreuer, C., and Yang, T.-Y., 1989, "Forced Convection Heat Transfer of Interacting Spheres," Numer. Heat Transfer, Part A, **15**, pp. 471–487.
[3] Zydney, A. L., and Colton, C. K., 1988, "Augmented Solute Transport in the Shear Flow of a Concentrated Suspension," PCH, PhysicoChem. Hydrodyn., **10**, pp. 77–96.
[4] Yuan, H., and Prosperetti, A., 1994, "On the In-Line Motion of Two Spherical Bubbles in a Viscous Fluid," J. Fluid Mech., **278**, pp. 325–349.
[5] Aminzadeh, K., Al-Taha, T. R., and Cornish, A. R. H., 1974, "Mass Transport Around Two Spheres at Low Reynolds Numbers," Int. J. Heat Mass Transfer, **17**, pp. 1425–1436.
[6] Ramachandran, R. S., and Kleinstreuer, C., 1985, "Mass Transfer with Chemical Reaction in Two Interacting Drops," Chem. Eng. Commun., **36**, pp. 197–210.
[7] Tal, R., Lee, D. N., and Sirignano, W. A., 1984, "Heat and Momentum Transfer Around a Pair of Spheres in Viscous Flow," Int. J. Heat Mass Transfer, **27**, pp. 1953–1962.
[8] Chen, W. C., and Tong, A. Y., 1987, "Numerical Study on Hydrodynamic and

Heat Transfer of Droplets Arrays Using Grid Generation," AIChE Symp. Ser., **83**, pp. 230–236.
[9] Chiang, H., and Kleinstreuer, C., 1992, "Computational Analysis of Interacting Vaporizing Fuel Droplets on a One-Dimensional Trajectory," Combust. Sci. Technol., **86**, pp. 289–309.
[10] Leal, L. G., 1992, *Laminar Flow and Convective Transport Processes*, Butterworth-Heinemann, Boston.
[11] Paidoussis, M. P., Mavriplis, D., and Price, S. J., 1984, "A Potential Flow Theory for the Dynamics of Cylinder Arrays in Cross-Flow," J. Fluid Mech., **146**, pp. 227–240.
[12] Balsa, T. F., 1977, "Potential Flow Interactions in an Array of Cylinders in Cross-Flow," J. Sound Vib., **50**, pp. 285–303.
[13] Mulholand, J. A., Srivastava, R. K., and Wendt, J. O. L., 1988, "Influence of Droplet Spacing on Drag Coefficient in Nonevaporating, Monodisperse Streams," AIAA J., **26**, pp. 1231–1245.
[14] Katz, J., and Meneveau, C., 1996, "Wake-Induced Relative Motion of Bubbles Rising in Line," Int. J. Multiphase Flow, **22**, pp. 239–245.
[15] Kok, J. B. W., 1993, "Dynamics of a Pair of Gas Bubbles Moving Through Liquid. Part I. Theory," Eur. J. Mech. B/Fluids, **12**, pp. 515–540.
[16] Sanada, T., 2005, "Interaction and Coalescence of Bubbles in Quiescent Liquid," Ph.D. thesis, Kyushu University, Japan.
[17] Clift, R., Grace, R. J., and Weber, M. E., 1978, *Bubbles, Drops and Particles*, Academic, New York.
[18] Milne-Thomson, L. M., 1972, *Theoretical Hydrodynamics*, Macmillan, London.
[19] Kendoush, A. A., 1995, "Low Prandtl Number Heat Transfer to Fluids Flowing Past an Isothermal Spherical Particle," Int. J. Heat Fluid Flow, **16**, pp. 291–297.
[20] Durst, F., Schonung, B., Selanger, K., and Winter, M., 1988, "Bubble-Driven Liquid Flow," J. Fluid Mech., **170**, pp. 53–82.
[21] de Varies, A. W. G., Biesheuvel, A., and van Wijngaarden, L., 2002, "Notes on the Path and Wake of a Gas Bubble Rising in Pure Water," Int. J. Multiphase Flow, **28**, pp. 1823–1835.
[22] Mougin, J., and Magnaudet, J., 2002, "Path Instability of a Rising Bubble," Phys. Rev. Lett., **88**, pp. 14–19.
[23] Boussinesq, M. J., 1905, "Calcul du pouvoír refroídissant des courants fluides," J. Math. Pures Appl., **1**, pp. 285–390.
[24] Kleinstreuer, C., and Chiang, H., 1993, "Convection Heat Transfer of Closely-Spaced Spheres With Surface Blowing," Waerme- Stoffuebertrag., **28**, pp. 285–293.
[25] Kendoush, A. A., 1989, "The Delay Time During Depressurization of Saturated Water," Int. J. Heat Mass Transfer, **32**, pp. 2149–2157.
[26] Harper, J. F., 1970, "On Bubbles Rising in Line at Large Reynolds Numbers," J. Fluid Mech., **41**, pp. 751–758.
[27] Tong, A. Y., and Chen, S. J., 1986, "Heat Transfer Correlations for Vaporizing Liquid Droplet Array in a High Temperature Gas at Intermediate Reynolds Number," Proceedings Fall Technical Meeting, Eastern Section of the Combustion Institute, San Juan, Puerto Rico.
[28] Legendre, D., Magnaudet, J., and Mougin, G., 2003, "Hydrodynamic Interactions Between Two Spherical Bubbles Rising Side by Side in a Viscous Liquid," J. Fluid Mech., **497**, pp. 133–166.
[29] Kendoush, A. A., 2006, "The Virtual Mass of Two Spheres Moving in Fluids," ASME J. Fluids Eng., submitted.

Journal of Heat Transfer

Technical Briefs

Conjugate Heat Transfer Study of a Two-Dimensional Laminar Incompressible Wall Jet Over a Backward-Facing Step

P. Rajesh Kanna[1]
e-mail: prkanna@gmail.com

Manab Kumar Das[2]
e-mail: manab@iitg.ernet.in

Department of Mechanical Engineering,
Indian Institute of Technology Guwahati,
Guwahati-781 039, India

Steady-state conjugate heat transfer study of a slab and a fluid is carried out for a two-dimensional laminar incompressible wall jet over a backward-facing step. Unsteady stream function-vorticity formulation is used to solve the governing equation in the fluid region. An explicit expression has been derived for the conjugate interface boundary. The energy equation in the fluid, interface boundary and the conduction equation in the solid are solved simultaneously. The conjugate heat transfer characteristics, Nusselt number are studied with flow property (Re), fluid property (Pr), and solid to fluid conductivity ratio (k). *Average Nusselt number is compared with that of the nonconjugate case. As k is increased, average Nusselt number is increased, asymptotically approaching the non-conjugate value.* [DOI: 10.1115/1.2424235]

Keywords: plane wall jet, step flow, conjugate heat transfer, interface temperature, Nusselt number

1 Introduction

A plane jet was defined by Glauert [1] as a stream of fluid blown tangential along a plane wall. Similarity solution for a plane wall jet as well as a radial wall jet for both the laminar and the turbulent cases were presented with the introduction of a Glauert constant F. Schwarz and Caswell [2] have investigated the heat transfer characteristics of a 2D laminar incompressible wall jet. They have found an exact solutions for both the constant wall temperature and the constant heat flux cases. In addition, they have solved for a variable starting length of the heated section at a constant wall temperature. The solution was derived with the plate and the jet regimes as nonconjugated. The experimental study on the laminar plane wall jet is presented in Bajura and Szewczyk [3]. Based on jet exit Reynolds number, they have reported the laminar wall jet results up to Re=770.

Angirasa [4] has studied the laminar buoyant wall jet and reported the effect of velocity and the width of the jet during convective heat transfer from the vertical surface. Seidel [5] has done a numerical work to find the effect of high amplitude forcing on the laminar and the turbulent wall jet over a heated flat plate. Seidel has used DNS for the laminar case and RANS for the turbulent wall jet. Recently, Bhattacharjee and Loth [6] have simulated the laminar and transitional cold wall jets. They have investigated the significance of three different inlet profiles viz. parabolic, uniform, and ramp. They have presented the detailed results of a time-averaged wall jet thickness and temperature distribution with RANS approach for higher Reynolds number and DNS approach for a three-dimensional wall jet. They have reported that the early transition begins at about Re=700 for the plane wall jet.

Recently Kanna and Das [7] have studied the conjugate heat transfer of plane wall jet flow and reported a closed-form solutions for the conjugate interface temperature, the local Nusselt number distribution and the average Nusselt number. In another study, Kanna and Das [8] have investigated the conjugate heat transfer from a plane laminar offset jet. The bottom of the slab is maintained at a constant higher temperature. Effect of the variations of offset geometry, Re, Pr, and slab geometry have been presented in details.

The flow emanating from a two-dimensional plane wall jet over backward-facing step is shown in Fig. 1(a) where the main features and regions of interest are depicted. Fluid is discharged from a slot along the horizontal wall into the ambient near a horizontal solid boundary parallel to the inlet jet direction. The jet flow features are different in various regions. In the near-field up to step from the point of discharge, the jet behaves like a plane wall jet. Further downstream, the jet expands over the step. From the step to the reattachment point, it is called a recirculation region. After this point, the jet has an effect of impingement and it is called an impingement region. The fluid flow structure rearranges and a wall jet behavior is observed after some distance. This is called a wall jet region. Wall jet over step flow occurs in many engineering applications such as environmental discharges, heat exchangers, fluid injection systems, cooling of combustion chamber wall in a gas turbine, automobile demister, and others. In electronics cooling, the prediction of Nusselt number distribution along the step as conjugate situation is very important from the thermal design point of view.

Although many studies on the nonconjugate and conjugate heat transfer have been conducted on wall jet, the available literature suggests that theoretical simulation of the wall jet over backward-facing step as conjugate case has not been carried out by any researcher. In the present configuration, the step length and the step height considered are 2 and 1, respectively. The bottom wall

[1]Present address: Post-Doctoral Fellow, Department of Mechanical Engineering, National Taiwan University of Science and Technology, Taipei, Taiwan.

[2]Corresponding author.

Contributed by the Heat Transfer Division of ASME for publication in the JOURNAL OF HEAT TRANSFER. Manuscript received February 27, 2006; final manuscript received July 15, 2006. Review conducted by Yogesh Jaluria.

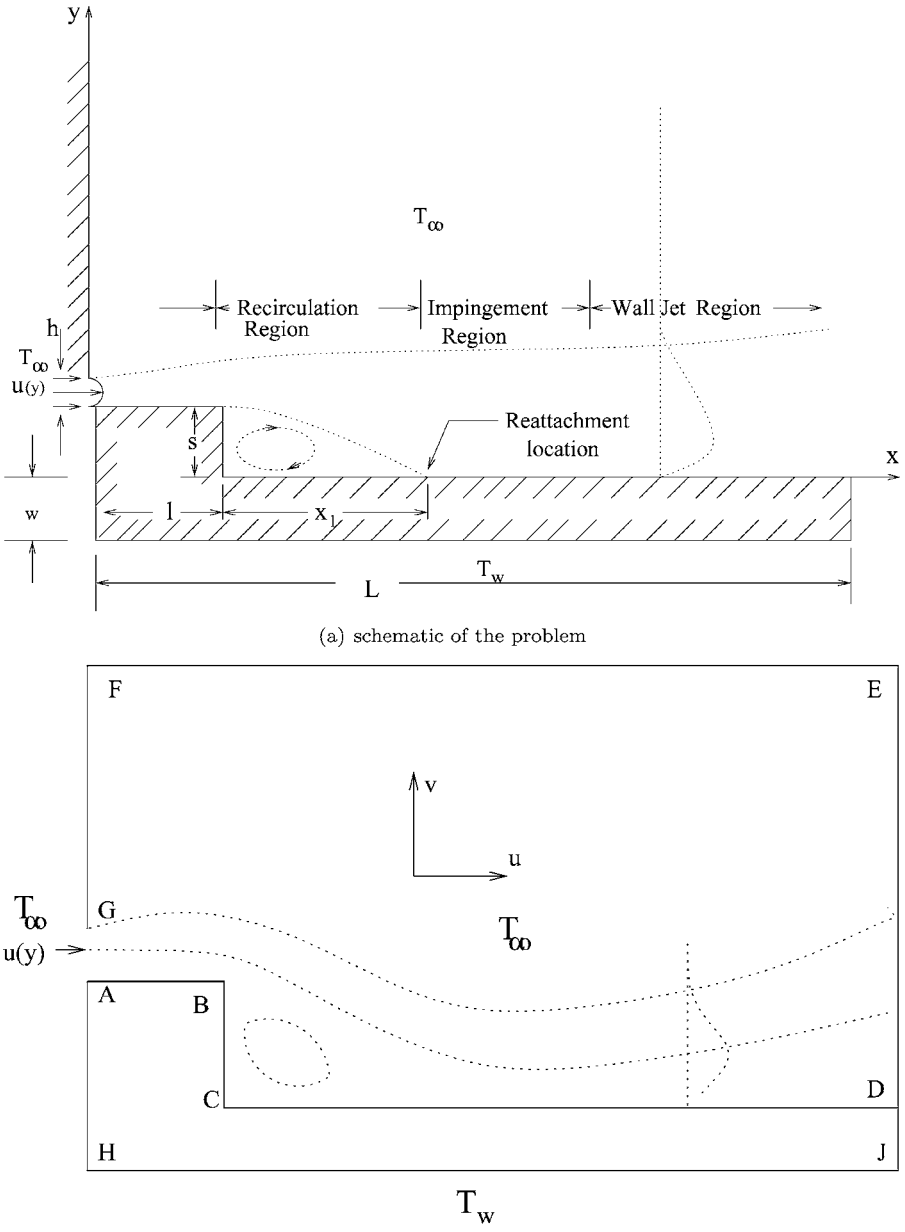

Fig. 1 Schematic diagram and boundary conditions in a wall jet over backward-facing step problem: (*a*) schematic of the problem and (*b*) computational domain

is maintained at a constant higher temperature whereas the wall jet is at ambient temperature. The temperature at the interface (separating fluid from the slab) is obtained by satisfying the conjugate boundary condition criteria. The interface temperature, Nusselt number and average Nusselt number variations are studied for a range of Re, Pr, and conductivity ratio (k). The present study is restricted to fall within the laminar Reynolds number range.

2 Mathematical Formulation

An incompressible 2D laminar plane wall jet is considered. For the sake of simplicity, the jet inlet temperature is assumed to be isothermal and to have the same density and temperature as the ambient fluid. Also, the velocity profile at the jet inlet is taken as parabolic. The solid slab bottom is kept at constant temperature, and the sidewalls of the slab are insulated.

The governing equations for incompressible laminar flow are solved by the stream function-vorticity formulation. The transient nondimensional governing equations in the conservative form are

Stream function equation

$$\nabla^2\psi = -\omega \tag{1}$$

Vorticity equation

$$\frac{\partial\omega}{\partial t} + \frac{\partial(u\omega)}{\partial x} + \frac{\partial(v\omega)}{\partial y} = \frac{1}{\mathrm{Re}}\nabla^2\omega \tag{2}$$

Energy equation in the fluid region

$$\frac{\partial\theta_f}{\partial t} + \frac{\partial(u\theta_f)}{\partial x} + \frac{\partial(v\theta_f)}{\partial y} = \frac{1}{\mathrm{Re\,Pr}}\nabla^2\theta_f \tag{3}$$

Energy equation in the solid region

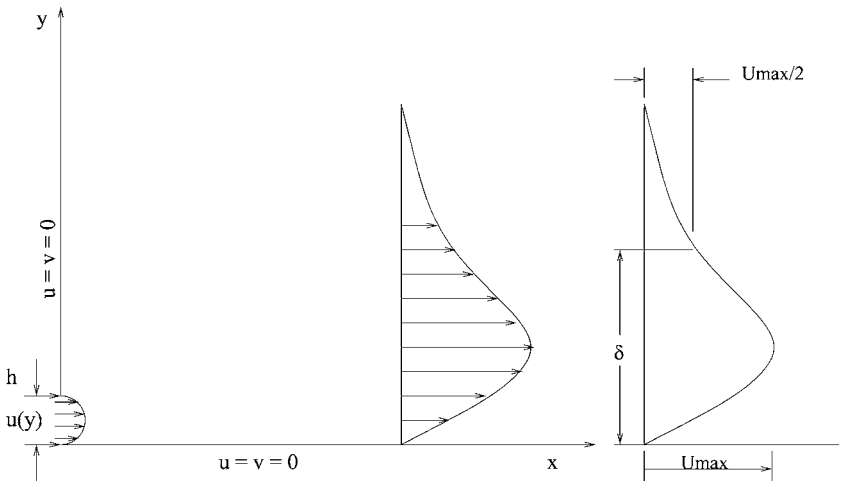

Fig. 2 Schematic diagram and boundary conditions in a wall jet problem

$$\frac{\partial \theta_s}{\partial t} = \frac{k}{\mathrm{Re\,Pr}} \nabla^2 \theta_s. \tag{4}$$

where $u=\partial\psi/\partial y$, $v=-\partial\psi/\partial x$, $\omega=\partial v/\partial x-\partial u/\partial y$, and $k=k_s/k_f$.

The variables are scaled as $u=\bar{u}/\bar{U}$; $v=\bar{v}/\bar{U}$; $x=\bar{x}/h$; $y=\bar{y}/h$; $\omega=\bar{\omega}/(\bar{U}/h)$; $t=(\bar{t}/h)/\bar{U}$, $\theta=(T-T_\infty)/(T_w-T_\infty)$ with the overbar indicating a dimensional variable and $\bar{U}, h$ denoting the average jet velocity at nozzle exit and the jet width, respectively.

The slab energy equation is written in the transient nondimensionalised form. The point to note here is that the term on the right hand side of Eq. (4) contains k, Re, and Pr. A similar form of the equation has been considered by Chiu et al. [9]. The boundary conditions needed for the numerical simulation have been prescribed. For an offset jet with entrainment, the following dimensionless conditions have been enforced as shown in Fig. 1(*b*). The inlet slot height is assumed as 0.05.

At the jet inlet, along AG (Fig. 1(*b*)),

$$u(y) = 120y - 2400y^2; \quad \omega(y) = 4800y - 120;$$

$$\psi(y) = 60y^2 - 800y^3 \tag{5}$$

Along AB, BC, CD, and FG due to no-slip condition

$$u = v = 0 \tag{6}$$

Along entrainment boundary FE

$$\frac{\partial v}{\partial y} = 0 \tag{7}$$

Along HJ

$$\theta = 1 \tag{8}$$

Along AH, DJ, and FG (adiabatic condition)

$$\frac{\partial \theta}{\partial x} = 0 \tag{9}$$

Along FE and AG, ambient condition is assumed for θ. At downstream boundary, the condition of zero first derivative has been applied for velocity components. This condition implies that the flow has reached a fully developed condition. Thus, at DE

$$\frac{\partial u}{\partial x} = \frac{\partial v}{\partial x} = \frac{\partial \theta}{\partial x} = 0 \tag{10}$$

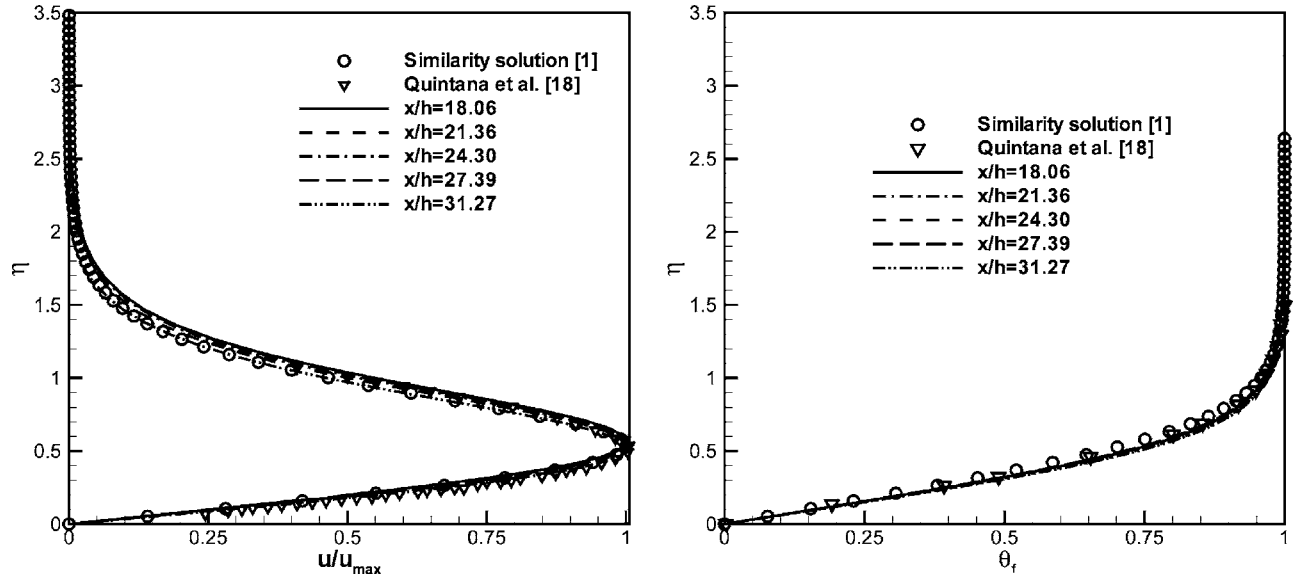

Fig. 3 Laminar wall jet results. Re=500, Pr=1.4 (*a*) *u*-velocity and (*b*) temperature.

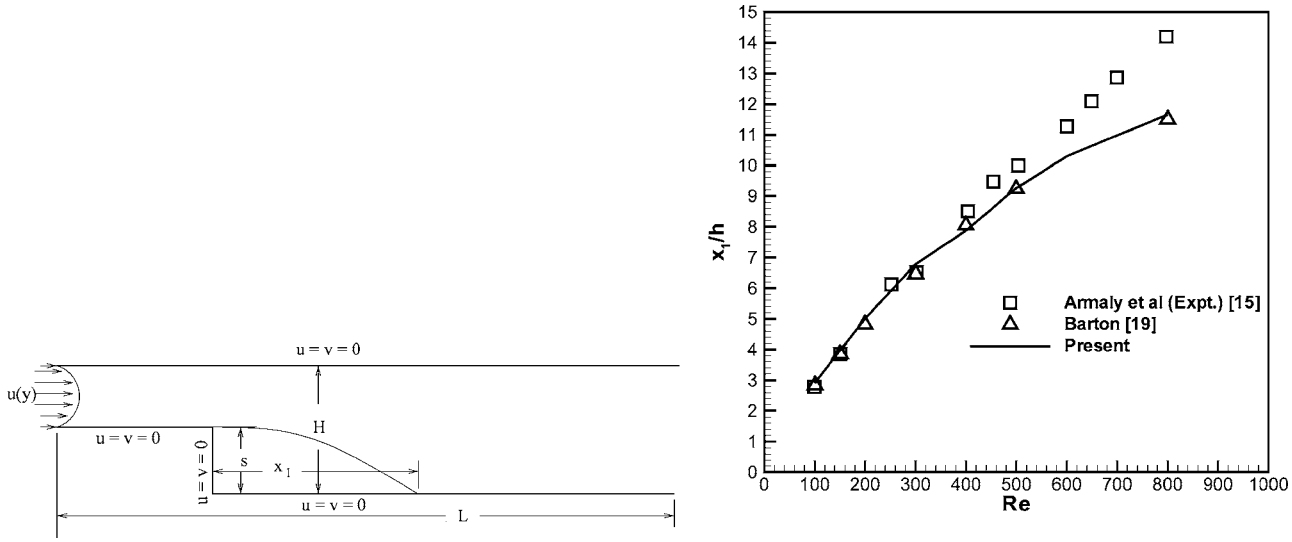

Fig. 4 Backward-facing step flow with upstream channel problem. (*a*) Schematic diagram. and (*b*) Reattachment length for different Reynolds number.

Interface Boundary Condition. The conjugate boundary condition along AB

$$k_s\left(\frac{\partial \theta_s}{\partial y}\right)_{\text{solid}} = k_f\left(\frac{\partial \theta_f}{\partial y}\right)_{\text{fluid}} \quad \text{and}$$

$$\theta_f = \theta_s \text{ at interface } y = 1,\ 0 < x \leqslant 2 \tag{11}$$

The conjugate boundary condition along CD

$$k_s\left(\frac{\partial \theta_s}{\partial y}\right)_{\text{solid}} = k_f\left(\frac{\partial \theta_f}{\partial y}\right)_{\text{fluid}}$$

$$\text{and} \quad \theta_f = \theta_s \text{ at interface } y = 0,\ 2 < x \leqslant 25 \tag{12}$$

The conjugate boundary condition along BC

$$k_s\left(\frac{\partial \theta_s}{\partial x}\right)_{\text{solid}} = k_f\left(\frac{\partial \theta_f}{\partial x}\right)_{\text{fluid}}$$

$$\text{and} \quad \theta_f = \theta_s \text{ at interface } x = 2,\ 0 < y \leqslant 1 \tag{13}$$

The Nusselt number expressions are given by, along AB

$$\text{Nu}(x) = -\left.\frac{\partial \theta}{\partial y}\right|_{y=1} \tag{14}$$

along CD

$$\text{Nu}(x) = -\left.\frac{\partial \theta}{\partial y}\right|_{y=0} \tag{15}$$

along BC

$$\text{Nu}(y) = -\left.\frac{\partial \theta}{\partial x}\right|_{x=2} \tag{16}$$

The average Nusselt number is given by

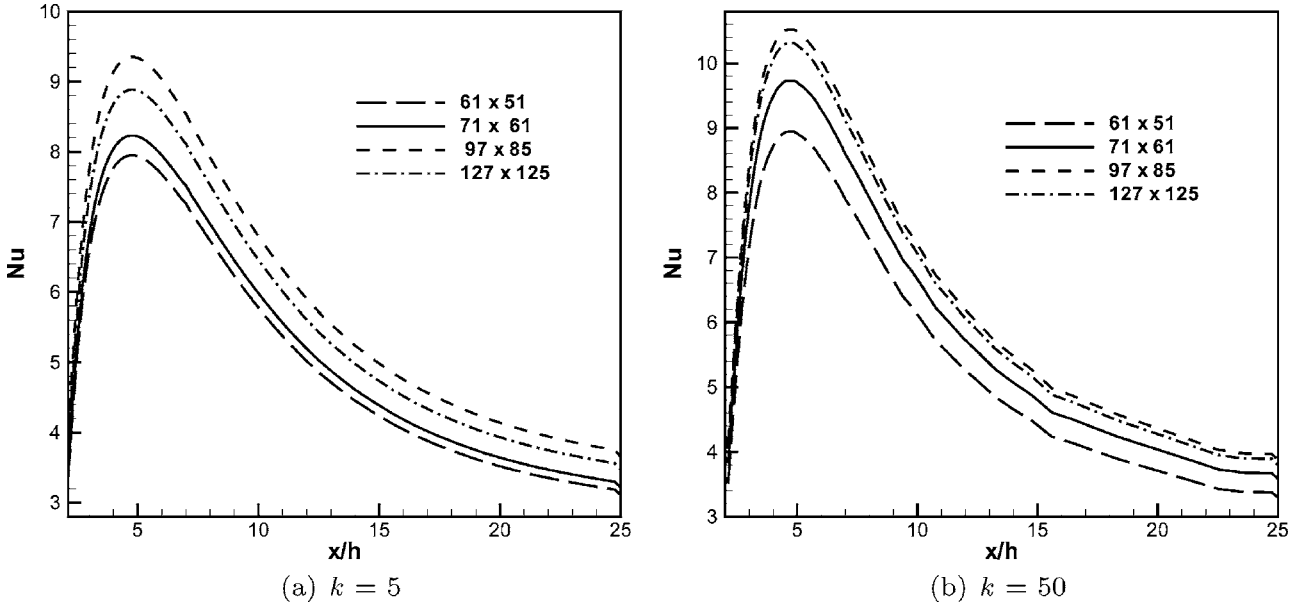

Fig. 5 Grid independence study. Variation of Local Nu for *k*=5 and 50. (*a*) *k*=5. (*b*) *k*=50.

$$\overline{\mathrm{Nu}} = \frac{1}{AB + BC + CD}\left\{\int_A^B \mathrm{Nu}(x)dx + \int_C^B \mathrm{Nu}(y)dy + \int_C^D \mathrm{Nu}(x)dx\right\} \tag{17}$$

3 Numerical Procedure

The computational domain considered here is a clustered cartesian grid. For unit length, the grid space at the ith node is (Kuyper et al. [10])

$$x_i = \left[\frac{i}{i_{\max}} - \frac{\kappa}{\vartheta}\sin\left(\frac{i\vartheta}{i_{\max}}\right)\right] \tag{18}$$

where ϑ is the angle and κ is the clustering parameter. $\vartheta = 2\pi$ stretches both end of the domain whereas $\vartheta = \pi$ clusters more grid points near one end of the domain. κ varies between 0 and 1. When it approaches 1, more points fall near the end.

The unsteady vorticity transport equation (Eq. (2)) and the energy equation (Eq. (3)) in time are solved by an alternate direction implicit scheme. The central differencing scheme is followed for both the convective as well as the diffusive terms (Roache [11]). The Poisson Eq. (1) is solved explicitly by the five point Gauss–Seidel methods. Thom's vorticity condition has been used to obtain the wall vorticity as given below

$$\omega_w = -\frac{2(\psi_{w+1} - \psi_w)}{\Delta n^2} \tag{19}$$

where Δn is the grid space normal to the wall. It has been shown by Napolitano et al. [12] and Huang and Wetton [13] that convergence in the boundary vorticity is actually second order for steady problems and for time-dependent problems when $t > 0$. Roache [11] has reported that for a Blausius boundary-layer profile, numerical test verify that this first-order form is more accurate than second-order form.

Solution approaches steady-state asymptotically while the time reaches infinity (a very large value). The energy equations in fluid regime and solid regime are solved simultaneously. For the computation, time step of 0.01 is used for Pr=1.0, 100.0, whereas for Pr=0.01, time step of 0.0001 is used. Steady state is obtained when the sum of temperature error from consecutive time marching steps (Eq. (20)) is reduced to either the convergence criteria ε or a large total time is elapsed.

$$\sum_{i,j=1}^{i_{\max},j_{\max}} \left[(\theta_{si,j}^{t+\Delta t} - \theta_{si,j}^{t}) + (\theta_{fi,j}^{t+\Delta t} - \theta_{fi,j}^{t})\right] < \varepsilon \tag{20}$$

For Pr=0.01, the convergence criteria ε is set as 10^{-4} and for higher Pr, it is set as 10^{-6}.

Table 1 Grid independence study: Value of $\overline{\mathrm{Nu}}$ (Re=400, Pr=1, $l=2h$, $s=1h$, $w=1h$)

Grids	$\overline{\mathrm{Nu}}(k=5)$	$\overline{\mathrm{Nu}}(k=50)$
61×51	3.5293	5.4823
71×61	4.8012	6.740125
97×85	7.64481	8.269212
127×125	7.55307	8.153443

4 Validation of the Code

To validate the developed code, the 2D lid-driven square-cavity flow problem (Ghia et al. [14]) and the backward-facing flow problem (Armaly et al. [15], Gartling [16], and Dyne and Heinrich [17]) have been solved. Excellent agreement has been obtained with the benchmark solutions and reported elsewhere [7]. The laminar plane wall jet problem (Fig. 2) has been solved and the computed velocity profiles are compared with the similarity solutions of Glauert [1] and the experimental results of Quintana et al. [18] in a similar way as represented by Seidel [5] (Fig. 3). To validate the present numerical procedure, backward-facing step flow with upstream channel is solved and the primary vortex reattachment length is compared with Barton [19] (Fig. 4). The fluid flow solution of the present problem has been reported by Kanna and Das [20]. The heat transfer study of the present problem has been reported also by Kanna and Das [21].

5 Grid Independence Study

The domain has been chosen as $25\times h$ in the streamwise direction from the step and $20\times h$ in the normal direction. A systematic grid refinement study is carried out with the grids in the fluid

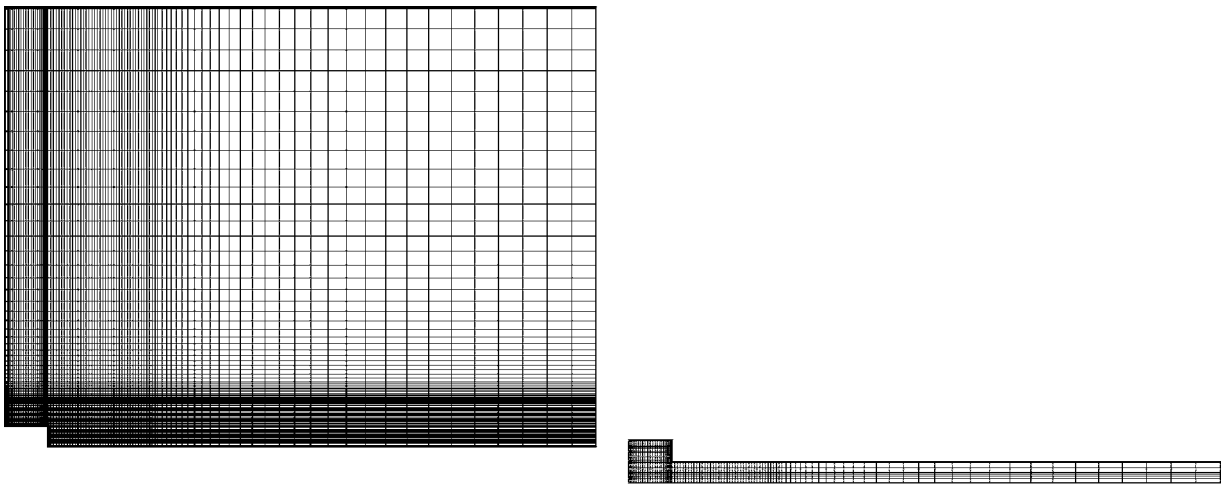

(a) Fluid region (b) Solid region

Fig. 6 Clustered grids used for the computation. (*a*) Fluid region. (*b*) Solid region.

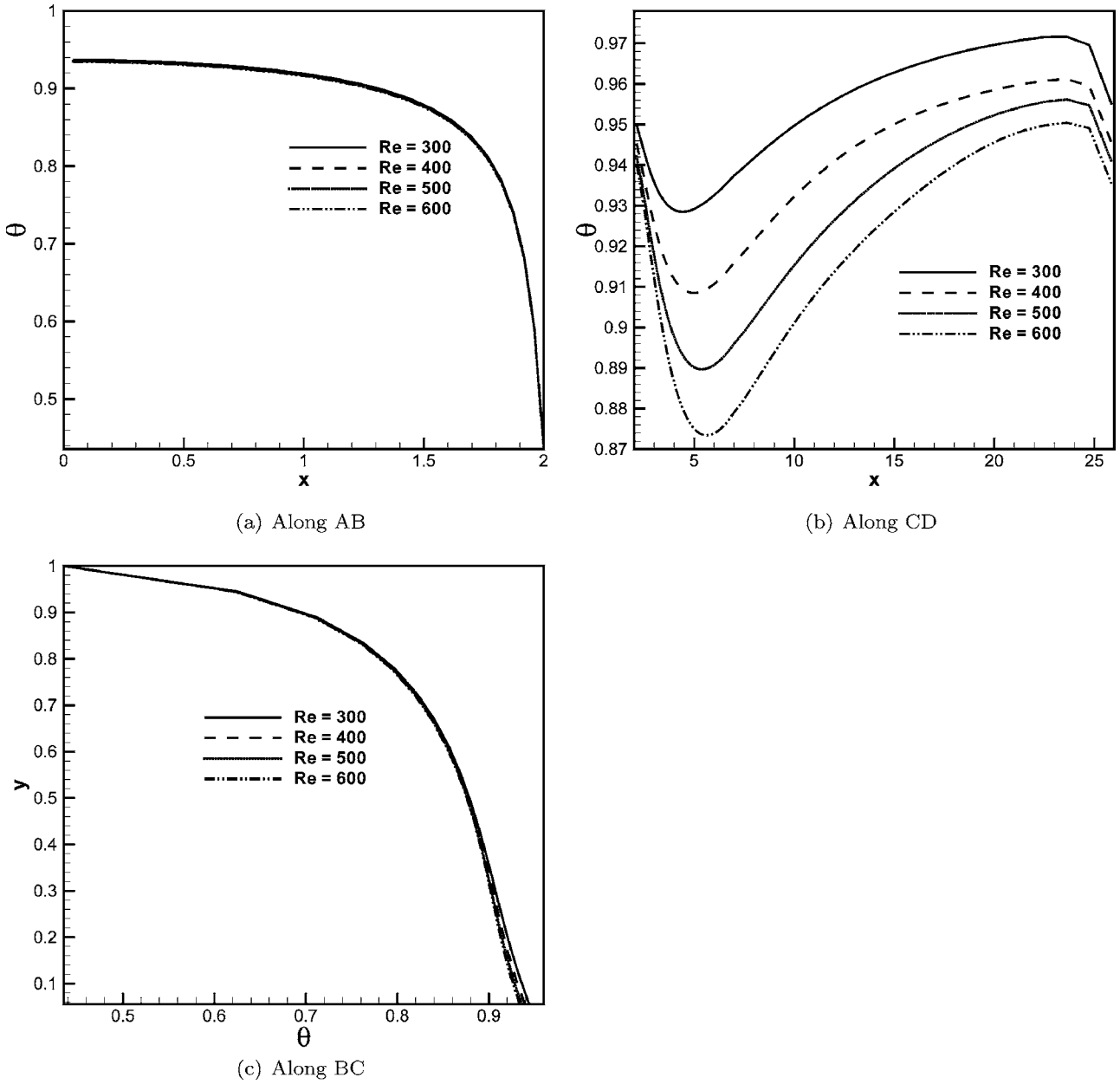

Fig. 7 Conjugate interface temperature: Effect of Re (Pr=1, k=5, l=2h, s=1h, w=1h). (*a*) Along AB. (*b*) Along CD. (*c*) Along BC.

region as 61×51, 71×61, 97×85, and 127×125. The variations of the local Nu for $k=5$ and 50 are shown in Fig. 5. Rao et al. [22] have used maximum interface temperature and the average skin friction coefficient as the criteria for grid independent study for conjugate mixed convection problem. When presented in a similar way, it has been observed that the variation in $\overline{\text{Nu}}$ is less than 1.5% between the last two grid system (Table 1). So a grid of 97×85 is used for the entire computation. Within the solid slab, 36 grid points are arranged in the normal direction. The grids are clustered in the streamwise direction whereas in the normal direction up to $3\times h$ height, grids are arranged uniformly and above this region, they are clustered. Typical grids are shown in Fig. 6.

6 Results and Discussion

The conjugate heat transfer study has been carried out with three parameters considered here. They are Re, Pr, and conductivity ratio (k). Results are presented for values of Re=300, 400, 500, and 600, Pr=(0.01,1,100), and k=(1,5,10,20,50). The detailed conjugate heat transfer results are presented in terms of the conjugate interface temperature, Nusselt number (Nu) and average Nusselt number ($\overline{\text{Nu}}$) for the above cases.

Conjugate Interface Temperature. The conjugate interface temperature for sections AB, BC, and CD are presented in Figs. 7–9. The influence of Re on the interface temperature is presented in Figs. 7(*a*)–7(*c*). Along AB, the interface temperature decreases nonlinearly. It is observed that this is less sensitive to Re. Along BC (in the positive y direction), interface temperature is reduced nonlinearly. This is attributed to the large recirculation near the step. The influence of Re on the interface temperature is very significant along CD. It decreases to a minimum value and further increases leading to a fully developed profile (Fig. 7(*b*)). The decrement in the temperature is attributed by the recirculation eddy. The minimum value is located downstream of the reattachment point. It shifts further when Re is increased. When Re increases,

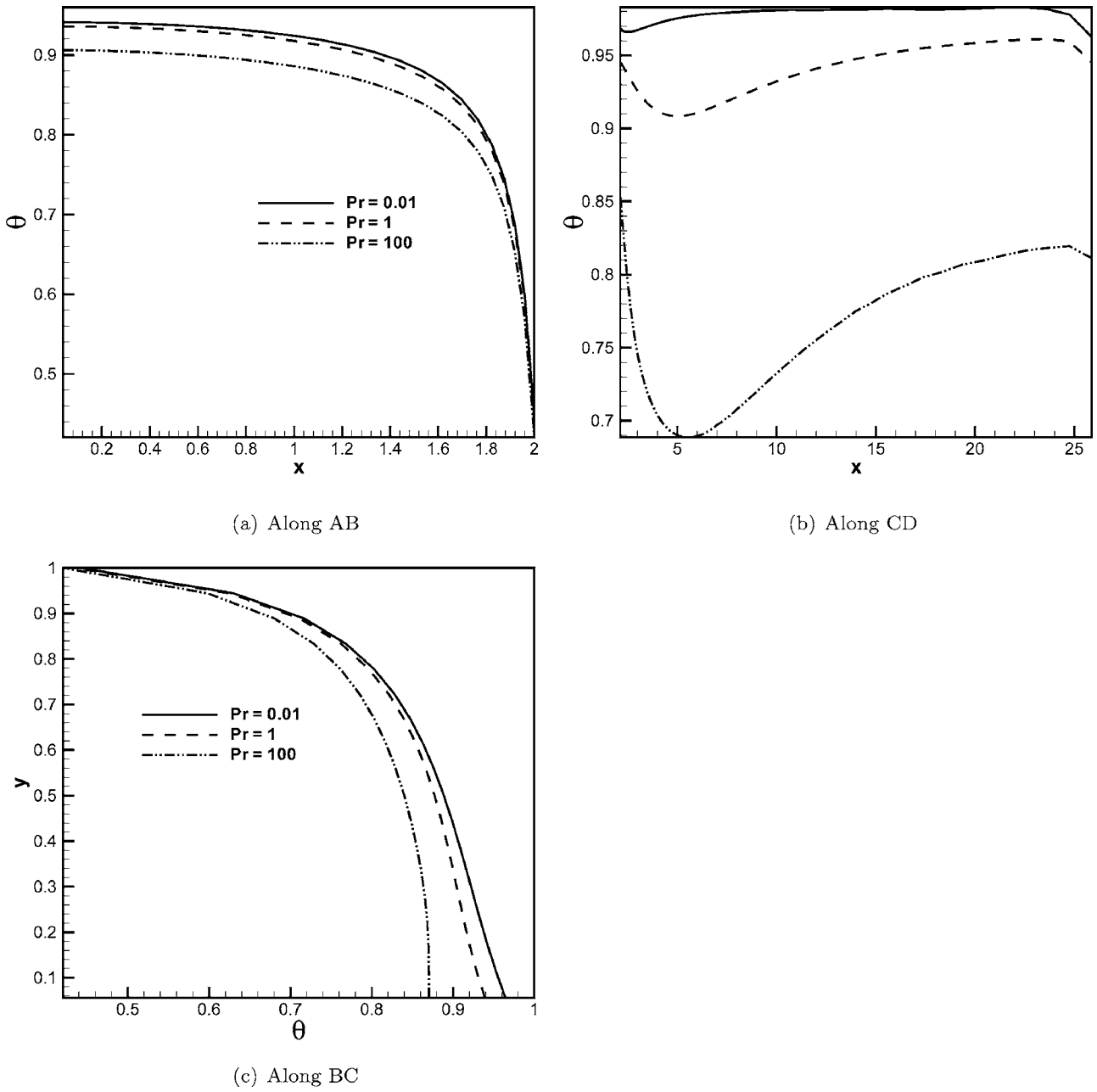

Fig. 8 Conjugate interface temperature: Effect of Pr (Re=400, k=5, l=2h, s=1h, w=1h). (*a*) Along AB. (*b*) Along CD. (*c*) Along BC.

the temperature value is decreased in the entire downstream direction. The effect of Pr on interface temperature is presented in Fig. 8. The interface temperature decreases along AB. When Pr increases from 0.01 to 100, the temperature values are decreased. Along CD the interface temperature reduces to a minimum value and further it increases leading to a fully developed profile. At low Pr, these variations are very less and are significant when Pr increases (Fig. 8(*b*)). It is observed that the location of minimum temperature value occurs in CD and is shifted in the downstream direction when Pr is increased. Along BC, the interface temperature value is decreased in the normal direction. BC is laid between the recirculation eddy and the solid slab. This situation causes the conduction to be dominant mode of heat transfer which leads to higher interface value for low Pr (Fig. 8(*c*)). The influence of conductivity ratio on the interface temperature is presented in Fig. 9. It is observed that k is sensitive to the entire interface. Along AB, the interface temperature is increased nonlinearly to k. However, it is noticed that the increment rate is reduced at higher k values. Along CD, the interface temperature value is decreased to a minimum value and further increases. At high k, it becomes almost constant value (Fig. 9(*b*)). Along BC, the interface temperature value is decreased in the positive y direction. It is noticed that with increasing k, the interface temperature value is increasing.

Nusselt Number. The local Nusselt number distribution is presented in details in Figs. 10–12. The influence of Re is shown in Fig. 10. Along AB, due to entrainment, the Nu value is large near the inlet and further it decreases in the downstream direction. When Re increases, Nu is increased due to the increment in the thermal gradient (Fig. 10(*a*)). Along CD, Nu is increased to a maximum value and further decreases to a steady value. It is observed that the peak Nu is falling downstream of the reattachment location and it shifts down when Re is increased (Fig.

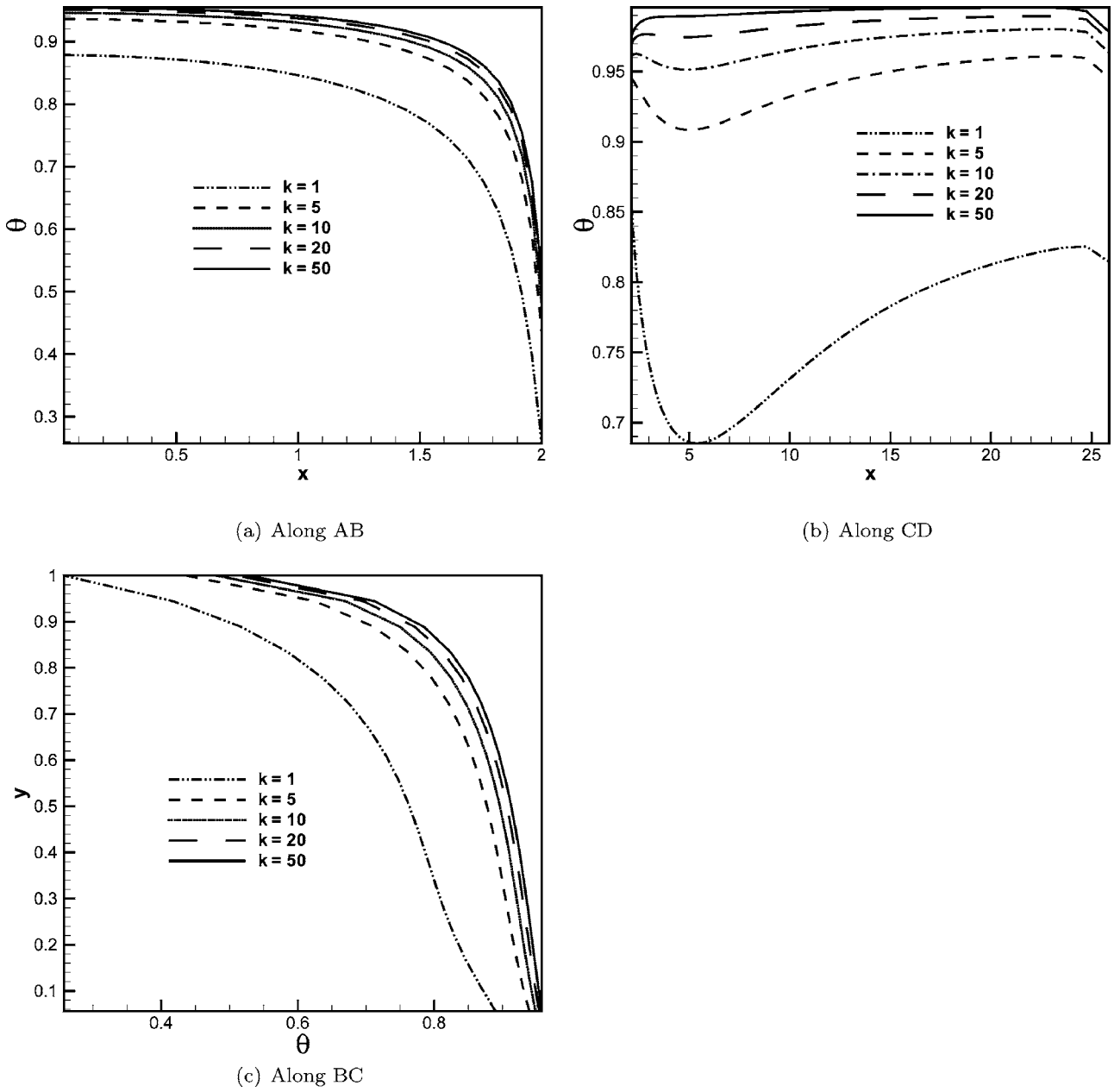

Fig. 9 Conjugate interface temperature: Effect of *k* (Re=400, Pr=1, *l*=2*h*, *s*=1*h*, *w*=1*h*). (*a*) Along AB. (*b*) Along CD. (*c*) Along BC.

10(*b*)). Along BC, the Nusselt number increases to a maximum value and further it decreases to a small value followed by an increase (Fig. 10(*c*)). This trend in Nusselt number is attributed to the conjugate effect between recirculation eddy and solid wall near the corner. The effect of Pr is presented in Fig. 11. Along AB, convection is dominant in the region due to the jet entry as well as ambient entrainment. This results in high Nu for high Pr (Fig. 11(*a*)). Along CD, Nu increases to a maximum and decreases to a fully developed profile in the downstream direction (Fig. 11(*b*)). The peak Nusselt number occurs due to recirculation. Along BC, Nu increases to a maximum value and decreases followed by an increase. Due to recirculation, the Nusselt number is increased for high Pr (Fig. 11(*c*)). The effect of *k* on local Nusselt number is shown in Fig. 12. The thermal resistance in the solid wall can be overcome with high *k*. A nonconjugate isothermal interface heat transfer study is compared to validate this point. Along AB, when *k* is increasing, Nu is increased (Fig. 12(*a*)). It approaches the nonconjugate value at downstream. Near the corner, a kink is observed. Along CD, the Nu distribution is shown in Fig. 12(*b*). It increases to a peak value and decreases further downstream. It is observed that at high *k* value, the Nusselt number distribution along CD is higher than that of the nonconjugate case. In downstream direction (for the nonconjugate case) the jet expands and bottom wall is isothermal whereas in conjugate case the wall temperature is variant (Fig. 9(*b*)). Along BC, Nu is increasing to maximum value and further reduces and increases in the normal direction.

Average Nusselt Number. The variations of average Nusselt number ($\overline{\text{Nu}}$) with Re, Pr, and *k* are shown in Tables 2–4. The influence of Re is shown in Table 2. For Re=300, $\overline{\text{Nu}}$=5.81 and for Re=600, $\overline{\text{Nu}}$=10.34. Conjugate values are always less than the nonconjugate average Nusselt number. For Re=300, the difference is 9.81% and for Re=600, it is 12.12%. Effect of Pr is shown

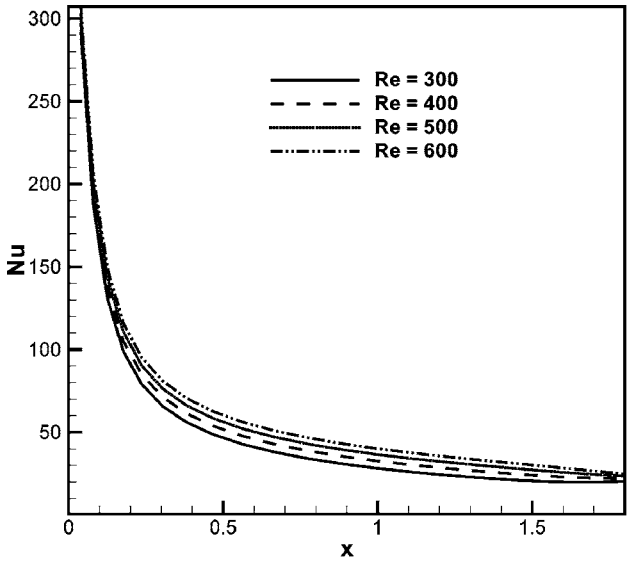

(a) Along AB

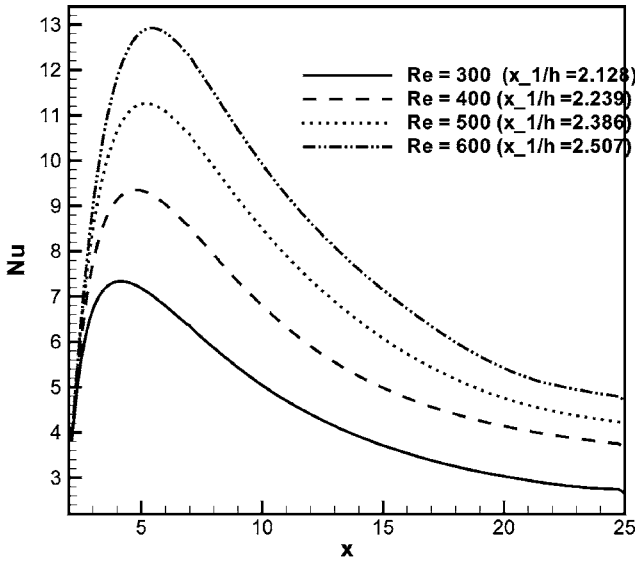

(b) Along CD

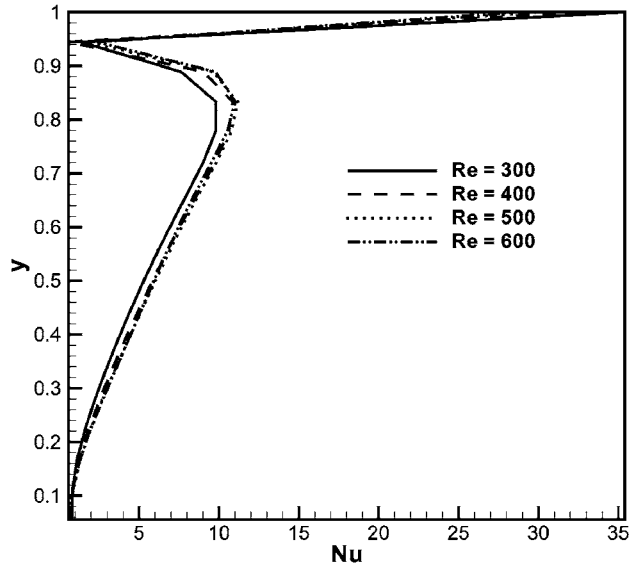

(c) Along BC

Fig. 10 Local Nusselt number: Effect of Re (Pr=1, k=5, l=2h, s=1h, w=1h). (*a*) Along AB. (*b*) Along CD. (*c*) Along BC.

in Table 3. For Pr=0.01, $\overline{\text{Nu}}$=2.16 and for Pr=100, $\overline{\text{Nu}}$=30.72. When compared with the nonconjugate values, it is observed that at low Pr, the nonconjugate $\overline{\text{Nu}}$ is less than the conjugate case. For Pr=0.01, the nonconjugate case is less by −26.33% whereas for Pr=100, it is higher by 26.6%. In conjugate case, heat transfer in solid is coupled with the fluid heat transfer. For low Pr, the thermal boundary layer is large. There is a higher $\overline{\text{Nu}}$ than the nonconjugate $\overline{\text{Nu}}$. Where as for high Pr, the thermal boundary layer is thin and the $\overline{\text{Nu}}$ is high for the nonconjugate case compared to the conjugate case. It is observed that when k increases, $\overline{\text{Nu}}$ value is increased (Table 4). At higher k value, it approaches the nonconjugate value. When k=50, the difference between the two cases is 3% only. It is important to note that though the local Nusselt number distribution for conjugate case at higher k along BC is higher than the nonconjugate (Fig. 12), the average Nusselt number of the nonconjugate is higher than the conjugate case. This is mainly due to the entrainment near the inlet and the recirculation eddy.

7 Concluding Remarks

Conjugate heat transfer study of two-dimensional incompressible nonbuoyant wall jet under backward-facing step problem is carried out by solving the stream function vorticity equations and energy equations in fluid and solid regions. Heat transfer characteristics are systematically studied for flow property (Re), fluid property (Pr), and the conductivity ratio (k) and the following conclusions are made.

The conjugate interface temperature value decreases along the step length and height. After expansion from the step, its value is reduced to a minimum followed by an increase. The minimum Nu falls after the reattachment location. The interface temperature value decreases when Re is increased. Also, it decreases for higher Pr. However, the interface temperature increases for higher k. The local Nusselt number has a peak value near the inlet due to the entrainment and a second peak occurs after the reattachment of the jet. Increment in Re, Pr, and k increases $\overline{\text{Nu}}$. At low Pr nonconjugate $\overline{\text{Nu}}$ is smaller than the conjugate $\overline{\text{Nu}}$.

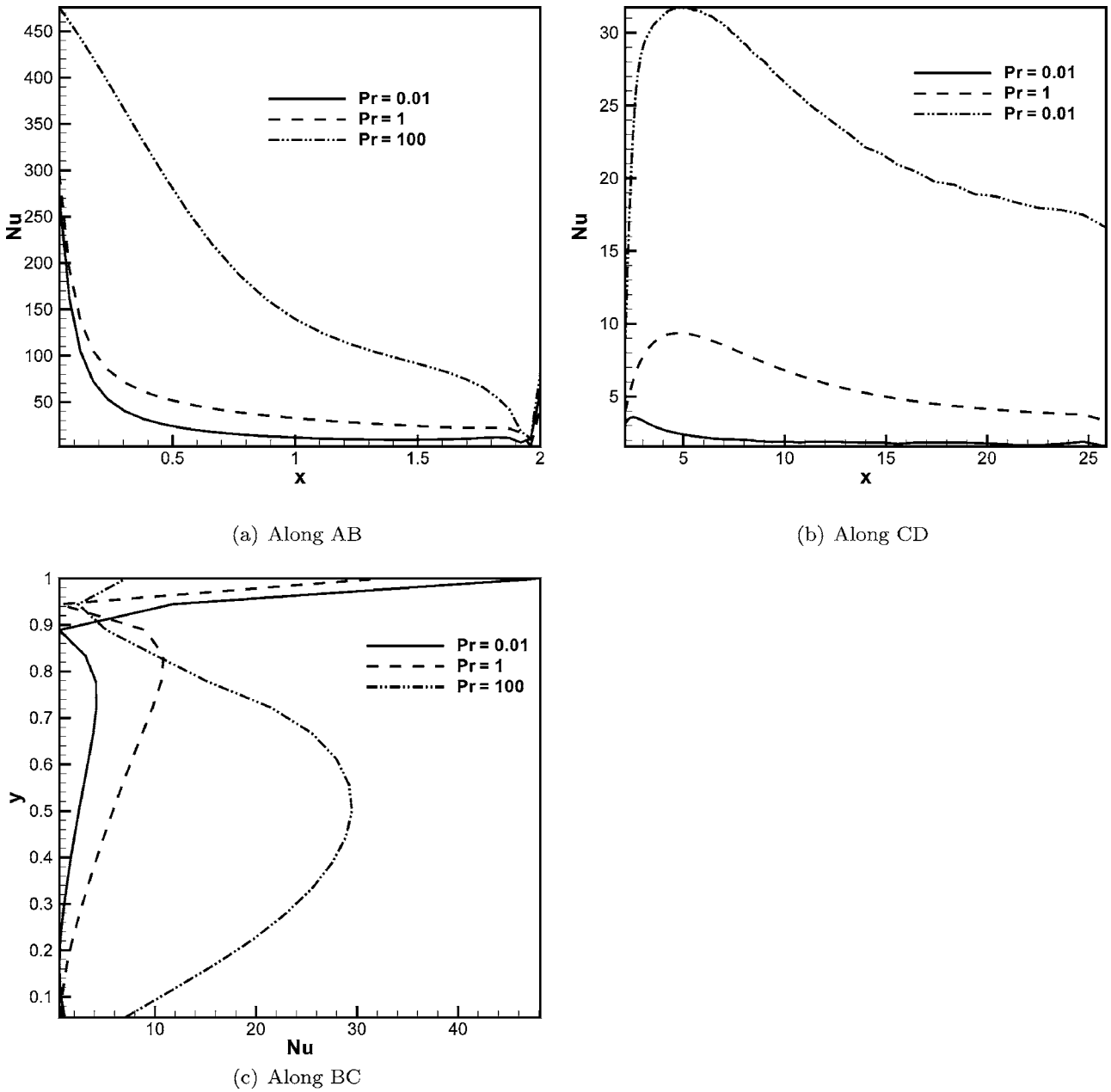

Fig. 11 Local Nusselt number: Effect of Pr (Re=400, k=5, l=2h, s=1h, w=1h). (*a*) Along AB. (*b*) Along CD. (*c*) Along BC.

$\overline{\text{Nu}}$ for the nonconjugate case is 12.12% higher compared to the conjugate case for Re=600. For low Pr (=0.01), $\overline{\text{Nu}}$ for the nonconjugate case is lower by −26.33%. whereas for high Pr (=100), the trend reverses and it is higher by 26.6%. As k is increased, $\overline{\text{Nu}}$ for conjugate case behavior is close to that of the nonconjugate case and the difference is 3%.

Acknowledgment

The authors are thankful to the reviewers for various suggestions on the manuscript. The authors are thankful to the associate editor of the paper.

Nomenclature

h = inlet slot height
k = thermal conductivity ratio, k_s/k_f
n = normal direction
Nu = local Nusselt number (Eq. (2))
$\overline{\text{Nu}}$ = average Nusselt number (Eq. (17))
Pr = Prandtl number, ν/α
Re = Reynolds number for the fluid, $\overline{U}h/\nu$
s = height of the step, m
T = dimensional temperature, °C
$\bar{t}$ = dimensional time, s
t = nondimensional time
$\bar{u},\bar{v}$ = dimensional velocity components along (x,y) axes, m/s
u,v = dimensionless velocity components along (x,y) axes
$\overline{U}$ = inlet mean velocity, m/s
w = solid wall thickness
$\bar{x},\bar{y}$ = dimensional Cartesian coordinates along and normal to the plate, m
x,y = dimensionless Cartesian coordinates along and normal to the plate

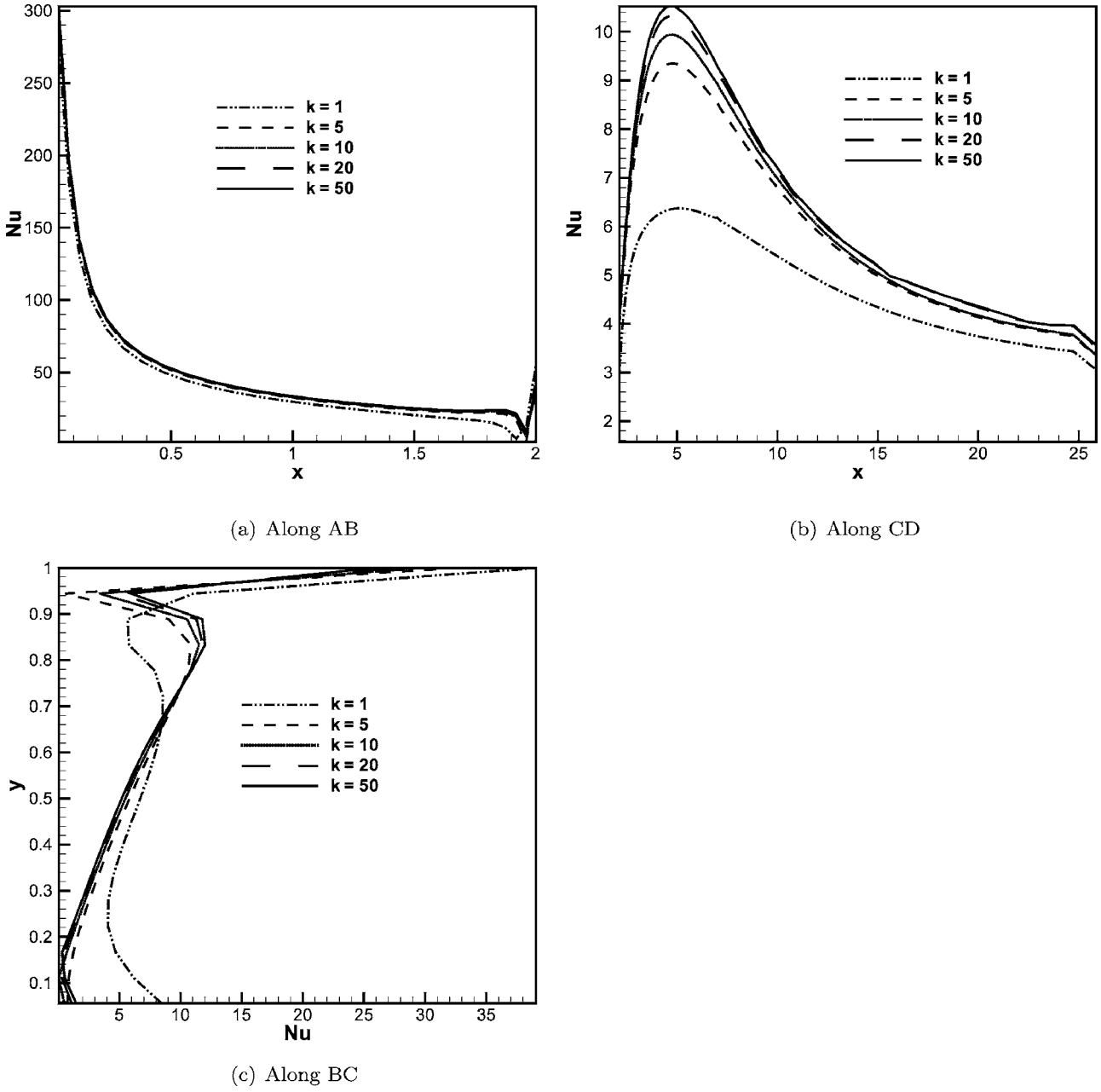

(a) Along AB

(b) Along CD

(c) Along BC

Fig. 12 Local Nusselt number: Effect of *k* (Re=400, Pr=1, *l*=2*h*, *s*=1*h*, *w*=1*h*). Nonconjugate case. (*a*) Along AB. (*b*) Along CD. (*c*) Along BC.

Greek Symbols

ε = convergence criterion
θ = dimensionless temperature
θ_b = dimensionless average boundary temperature
κ = clustering parameter
ν = kinematic viscosity
ψ = dimensionless stream function
ω = dimensionless vorticity

Subscripts

f = fluid

Table 2 Average Nusselt number: Effect of Re (Pr=1, *k*=5, *l*=2*h*, *s*=1*h*, *w*=1*h*)

Re	$\overline{\text{Nu}}$	Nonconjugate	% difference from nonconjugate
300	5.808317	6.441137	9.82
400	7.644812	8.524984	10.32
500	9.079950	10.212431	11.09
600	10.341680	11.767634	12.12

Table 3 Average Nusselt number: Effect of Pr (Re=400, *k*=5, *l*=2*h*, *s*=1*h*, *w*=1*h*)

Pr	$\overline{\text{Nu}}$	Nonconjugate	% difference from nonconjugate
0.01	2.165427	1.714043	−26.33
1	7.644812	8.524984	10.32
100	30.719183	41.852650	26.60

Table 4 Average Nusselt number: Effect of k (Re=400, Pr=1, l=2h, s=1h, w=1h)

k	$\overline{\text{Nu}}$
1	5.968452
5	7.644812
10	7.913072
20	8.179786
50	8.269212
Nonconjugate	8.524984

max = maximum
s = solid
w = wall
∞ = ambient condition

References

[1] Glauert, M. B., 1956, "The Wall Jet," J. Fluid Mech., **1**, pp. 1–10.
[2] Schwarz, W. H., and Caswell, B., 1961, "Some Heat Transfer Characteristics of the Two-Dimensional Laminar Incompressible Wall Jet," Chem. Eng. Sci., **16**, pp. 338–351.
[3] Bajura, R. A., and Szewczyk, A. A., 1970, "Experimental Investigation of a Laminar Two-Dimensional Plane Wall Jet," Phys. Fluids, **13**, pp. 1653–1664.
[4] Angirasa, D., 1999, "Interaction of Low-Velocity Plane Jets With Buoyant Convection Adjacent to Heated Vertical Surfaces," Numer. Heat Transfer, Part A, **35**, pp. 67–84.
[5] Seidel, J., 2001, "Numerical Investigations of Forced Laminar and Turbulent Wall Jets Over a Heated Surface," Ph.D. thesis, Faculty of the Department of Aerospace and Mechanical Engineering, The Graduat College, The University of Arizona, Tucson, AZ.
[6] Bhattacharjee, P., and Loth, E., 2004, "Simulations of Laminar and Transitional Cold Wall Jets," Int. J. Heat Fluid Flow, **123**, pp. 32–43.
[7] Kanna, P. R., and Das, M. K., 2005, "Conjugate Forced Convection Heat Transfer from a Flat Plate by Laminar Plance Wall Jet Flow," Int. J. Heat Mass Transfer, **48**, pp. 2896–2910.
[8] Kanna, P. R., and Das, M. K., 2005, "Conjugate Heat Transfer Study of Two-Dimensional Laminar Incompressible Offset Jet Flows," Numer. Heat Transfer, Part A, **48**, pp. 671–691.
[9] Chiu, W. K. S., Richards, C. J., and Jaluria, Y., 2001, "Experimental and Numerical Study of Conjugate Heat Transfer in a Horizontal Channel Heated From Below," ASME J. Heat Transfer, **123**, pp. 688–697.
[10] Kuyper, R. A., Van Der Meer, Th. H., Hoogendoorn, C. J., and Henkes, R. A. W. M., 1993, "Numerical Study of Laminar and Turbulent Natural Convection in an Inclined Square Cavity," Int. J. Heat Mass Transfer, **36**, pp. 2899–2911.
[11] Roache, P. J., 1998, *Fundamentals of Computational Fluid Dynamics*, Hermosa, Albuquerque, NM, Chap. 3.
[12] Napolitano, M., Pascazio, G., and Quartapelle, L., 1999, "A Review of Vorticity Conditions in the Numerical Solution of the $\zeta-\psi$ Equations," Comput. Fluids, **28**, pp. 139–185.
[13] Huang, H., and Wetton, B. R., 1996, "Discrete Compatibility in Finite Difference Methods for Viscous Incompressible Fluid Flows," J. Comput. Phys., **126**, pp. 468–478.
[14] Ghia, U., Ghia, K. N., and Shin, C. T., 1982, "High Re Solutions for Incompressible Flow Using the Navier-Stokes Equations and Multigrid Method," J. Comput. Phys., **48**, pp. 387–411.
[15] Armaly, B. F., Durst, F., Pereira, J. C. F., and Schonung, B., 1983, "Experimental and Theoretical Investigation of Backward-Facing Step Flow," J. Fluid Mech., **127**, pp. 473–496.
[16] Gartling, D. K., 1990, "A Test Problem for Outflow Boundary Conditions-Flow Over a Backward-Facing Step," Int. J. Numer. Methods Fluids, **11**, pp. 953–967.
[17] Dyne, B. R., and Heinrich, J. C., 1992, "Flow Over a Backward-Facing Step: A Benchmark Problem for Laminar Flow With Heat Transfer," *Benchmark Problems for Heat Transfer Codes*, ASME, New York, **HTD-V 222**, pp. 73–76.
[18] Quintana, D. L., Amitay, M., Ortega, A., and Wygnanski, I. J., 1997, "Heat Transfer in the Forced Laminar Wall Jet," ASME J. Heat Transfer, **119**, pp. 451–459.
[19] Barton, I. E., 1997, "The Entrance Effect of Laminar Flow over a Backward-Facing Step Geometry," Int. J. Numer. Methods Fluids, **25**, pp. 633–644.
[20] Kanna, P. R., and Das, M. K., 2006, "Numerical Simulation of Two-Dimensional Laminar Incompressible Wall Jet Flow Over Backward-Facing Step," J. Fluids Eng., **128**, pp. 1023–1035.
[21] Kanna, P. R., and Das, M. K., 2006, "Heat Transfer Study of Two-Dimensional Laminar Incompressible Wall Jet Over Backward-Facing Step," Numer. Heat Transfer, Part A, **50**, pp. 165–187.
[22] Rao, C. G., Balaji, C., and Venkateshan, S. P., 2001, "Conjugate Mixed Convection With Surface Radiation From a Vertical Plate With a Discrete Heat Source," ASME Trans. J. Heat Transfer, **123**, pp. 698–702.

Thermal Conductivity and Compressive Strain of Aerogel Insulation Blankets Under Applied Hydrostatic Pressure

Erik R. Bardy
Department of Mechanical Engineering,
Grove City College,
100 Campus Drive,
Grove City, PA 16127-2104
e-mail: erbardy@gcc.edu

Joseph C. Mollendorf
e-mail: molendrf@buffalo.edu

David R. Pendergast
e-mail: dpenderg@buffalo.edu

Department of Mechanical and Aerospace Engineering,
State University of New York at Buffalo,
318 Jarvis Hall,
Buffalo, NY 14260-2000;
Department of Physiology and Biophysics Center for Research and Education in Special Environments,
State University of New York at Buffalo,
124 Sherman Hall,
Buffalo, NY 14214-3005

Aerogel is among the best solid thermal insulators. Aerogel is a silica gel formed by supercritical extraction which results in a porous open cell solid insulation with a thermal conductivity as low as 0.013 W/m K. *Aerogels have a wide range of uses such as insulation for windows, vehicles, refrigerators/freezers, etc. Usage for aerogel can be extended for use where flexibility is needed, such as apparel, by embedding it into a polyester batting blanket. These aerogel blankets, although flexible, have little resistance to compression and experience a residual strain effect upon exposure to elevated pressures. It was suggested, by Aspen Aerogels Inc., that a prototype aerogel blanket would have increased resistance to compression and minimized residual strain upon exposure to elevated pressures. Samples of prototype and normal product-line aerogel insulating blankets were acquired. These materials were separately tested for thermal conductivity and compressive strain at incremental pressure stops up to* 1.2 MPa. *The compressive strain of the prototype aerogel blanket reached a level of* 0.25 mm/mm *whereas the product-line aerogel blanket compressed to* 0.48 mm/mm *at* 1.2 MPa. *Before compression, the thermal conductivity of the prototype aerogel blanket was slightly higher than the product-line aerogel blanket. During compression the thermal conductivity increased 46% for the product-line aerogel blanket whereas it increased only 13% for the prototype aerogel blanket at* 1.2 MPa. *The total thermal resistance decreased 64% for the product-line aerogel blanket at* 1.2 MPa *and remained at that value upon decompression to atmospheric pressure. The total thermal resistance of the prototype aerogel blanket decreased 33% at* 1.2 MPa *and returned to within 1% of its initial value upon decompression to atmospheric pressure. It was found that the prototype aerogel blanket has approximately twice as much resistance to hydrostatic compression to a pressure of* 1.2 MPa *and also recovers to its original state upon decompression. The thermal resistance of the prototype aerogel blanket remained 37% higher than the product-line aerogel blanket at* 1.2 MPa. *This resistance to compression and the ability to recover to its original state upon decompression from elevated pressures makes the prototype aerogel blanket suitable for applications where high insulation, resistance to compression, and recovery after a compression cycle is needed.* [DOI: 10.1115/1.2424237]

Keywords: aerogel, thermal conductivity, compressive strain, hydrostatic pressure

1 Background

Silica aerogels are among the best solid thermal insulating materials [1]. Aerogels are formed by sol-gel processes and dried by supercritical extraction [2,3]. This process leaves a porous medium which has pore sizes of approximately 10 nm which is about eight times smaller than the mean free path of air [4]. The porosity can be as high as 90% [5,6]. The overall effective thermal conductivity can be as low as 0.013 W/m K for aerogels with a density of 120 kg/m^3 [1].

Aerogels have a wide range of use, such as insulation for cryogenic applications, space launch applications, solar collectors, as well as windows, refrigerators/freezers, water boilers, and vehicle heat accumulators [1,7–11]. Aerogels can also be modified for use in applications where flexibility is needed such as for thermal protective clothing, acoustic insulation, and also in part for prototype wetsuit insulation [12–14]. This is done by mixing aerogel in granular or dust form into a flexible matrix resulting in an insulating aerogel blanket. These aerogel blankets can vary in composition yielding different thermal properties. Table 1 gives the thermal conductivity and composition of several commercially available aerogel blankets.

Recently, Aspen Aerogels has developed a prototype aerogel blanket (proprietary microstructure, patent pending) as an improvement to the trade name product "spaceloft" that can be used for high compression applications. This prototype aerogel blanket has an increased resistance to compressive loading and returns to its original thickness after a high pressure application. Normal product-line aerogel blankets experience a residual strain when compressed, which results in the material not recovering to its original thickness.

The purpose of this study is to compare the thermal conductivity and compressive strain under hydrostatic pressure of this newly developed prototype aerogel blanket to that of a product-line aerogel blanket ("spaceloft"). An investigation of the microstructure of the aerogel blanket is beyond the scope of this study. It was hypothesized that the prototype aerogel blanket would compress less and maintain a lower thermal conductivity at elevated hydrostatic pressure compared to the product-line aerogel blanket; and that the prototype aerogel blanket would recover to its original state upon decompression.

2 Methods

2.1 Experimental Setup. The experimental setup used in this study consisted of a thermal conductivity meter (Anter Corp model Quickline 16) custom modified to operate at elevated hydrostatic pressures. This meter was placed in a hyperbaric chamber as shown in Fig. 1. All connections were made by means of penetrations through the hyperbaric chamber. The thermal conductivity meter (further referenced as "thermal meter") works on the principle of the heat flow metering method (in accordance with ASTM C518 and ISO DIS 8301).

A test specimen (30.5 cm × 30.5 cm) is placed between two flat

Contributed by the Heat Transfer Division of ASME for publication in the JOURNAL OF HEAT TRANSFER. Manuscript received November 1, 2005; final manuscript received April 21, 2006. Review conducted by Ranga Pitchumani.

Table 1 Thermal conductivity of various commercially available aerogel blankets

Trade name	Thermal conductivity (W/m K)	Matrix composition
Spaceloft[a]	0.0141–0.0135	Silica gel, Copolyolefin Poly (ethylene terephthalate)
Spaceloft[a]	0.013	Silica gel, carbon black Poly (ethylene terephthalate)
Pyrogel[a]	0.0147	Silicon dioxide, Zircon Silica gel (trimethylsilyated) Amophous silica fiber felt
Pyrogel[a]	0.0157	Silica gel Oxidized polyacrylonitrile
Nanogel[b]	0.020	Treated precipitated silica/silica gel (trimethylsilylated) blend with copolyolefin bicomponent fiber with nylon cover.

[a]Aspen Aerogels, Inc. ⟨www.aerogel.com.⟩.
[b]Cabot Corporation ⟨w1.cabot-corp.com.⟩.

plates controlled to be at different temperatures. The upper plate is set at 30°C and the lower plate is set at 10°C. Due to the temperature difference, heat flows from the upper plate to the lower plate. The amount of heat flow depends on the thickness and thermal conductivity of the test specimen. When thermal equilibrium is reached, i.e., when all temperatures are steady, the thermal conductivity of the test specimen can be estimated by using Fourier's law

$$\lambda = \Phi^* d/(T_{\text{hot}} - T_{\text{cold}}) \quad (1)$$

where λ is thermal conductivity (W/m K); Φ is the heat flux (W/m^2), d is the thickness of the test sample (m); T_{hot} is the temperature of the upper plate (30°C), and T_{cold} is the temperature of the lower plate (10°C).

The amount of heat flowing through the sample is measured with a heat flow meter placed between the sample and the upper plate. Equation (1) relies on the assumption that the heat flow through the test specimen is linear (one dimensional). Heat exchange between the edge of the test specimen and the surrounding environment was minimized using 5 cm of fibrous board insulation (k=0.0328 W/m K at 20°C) placed around the perimeter of the test specimen. It is further noted that the actual heat flow measurement is limited to a 10 cm×10 cm area in the center of the 30.5 cm×30.5 cm test specimen.

The temperatures of the upper and lower plates are measured by using type K thermocouples located in the plate surfaces. It is assumed that the temperature across the interface between the plates and the test specimen is constant. This assumption is only valid for test specimens that have and overall thermal resistance greater than 0.08 m^2K/W (*User's Manual Quickline 16, Heat Flow Meter Thermal Conductivity Instrument, Version 1.0*). If the thermal resistance of the sample falls below this minimum, the temperature difference across the interface between the plates and the test specimen cannot be ignored. All samples tested in this study have thermal resistances above 0.08 m^2K/W.

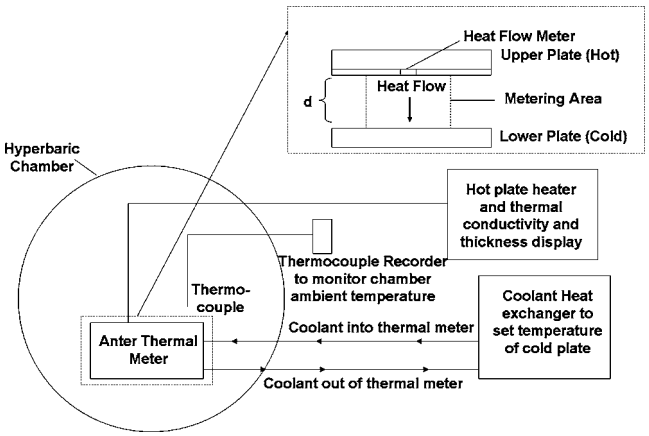

Fig. 1 Schematic of experimental setup

The thickness (d) of a test specimen is determined during testing by using a linear potentiometer located on the upper plate that measures the distance between the upper plate and the lower plate.

The thermal meter was calibrated under atmospheric pressure, in accordance with the manufacturer's recommendation, using a fibrous glass board (NIST SRM 1450b) having a thermal conductivity of 0.0328 W/m K at a temperature of 20°C. Before using the calibration sample it was conditioned, according to recommended protocol, in an oven at 90°C for 1 h to drive out any residual moisture. The linear potentiometer was calibrated by using a brass ring of known thickness (25.5 mm) and a thin sheet of brass of known thickness (0.2 mm). The linear potentiometer was calibrated to the thickness of the plastic ring and the brass sheeting. After proper calibration and when equilibrium conditions were reached, the manufacturer's estimate for the measuring accuracy of the thermal conductivity is 5% with a reproducibility of 1% (Anter Corp., 83/04-97).

2.2 Testing Protocol. A 5-mm-thick 30.5 cm×30.5 cm sheet of a prototype aerogel blanket and a product-line aerogel blanket (Aspen Aerogel product AR3103) were each separately encapsulated in a mylar bag (PAKVF4D, Impak Corp.) at atmospheric pressure. Since aerogel is an open-cell insulation, the mylar bag serves as a nonloading membrane allowing the aerogel to experience the force of increased hydrostatic pressure. The mylar bag was heat sealed at atmospheric pressure while being held between two flat plates to minimize the amount of trapped air. Leaks in the mylar bag were checked by immersing the sample in water. The encapsulated sample was then placed in the Anter thermal meter within the hyperbaric chamber. Thermal conductivity and thickness readings were taken at incremental pressure stops at 0.10 MPa, 0.18 MPa, 0.25 MPa, 0.41 MPa, 0.56 MPa, 0.71 MPa, 0.95 MPa, and 1.20 MPa during compression and 0.72 MPa, 0.41 MPa, 0.25 MPa, and 0.10 MPa during decompression. One compression/decompression cycle was performed on each sample. A compression rate of 0.03 MPa/min was chosen to simulate isothermal compression. During compression to an incremental stop, cool air was circulated in the hyperbaric chamber by air blowers to minimize air temperature change. The temperature change of the air inside the hyperbaric chamber was monitored by using a thermocouple suspended above the thermal meter. When a given pressure level was reached, and the chamber air temperature reached within two degrees of room temperature, the air blowers were turned off. Once the blowers were turned off, thermal conductivity readings were taken from a display located outside the chamber. Readings were taken about every 2 min until the displayed value changed less than 1%, typically within 10 min. This was assumed to be steady state in accordance with the manufacturer's operating instructions. Thermal conductivity and thickness measurements were then recorded for that pressure.

3 Results and Discussion

The variation of the compressive strain of both aerogel blankets with increasing hydrostatic pressure is shown in Fig 2. It can be seen that the strain of the product-line aerogel blanket increased to a value of about 0.48 mm/mm at 1.2 MPa and remained essentially constant upon decompression. The prototype aerogel blanket increased to a total strain of about 0.25 mm/mm at 1.2 MPa and then returned to its initial thickness upon decompression. During the decompression phase, the compressive strain experienced by

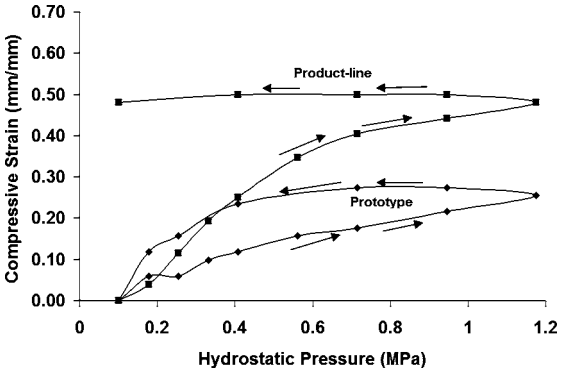

Fig. 2 Variation of the compressive stain of aerogel blanket samples with hydrostatic pressure. Arrows indicate direction of pressure change during the experiment.

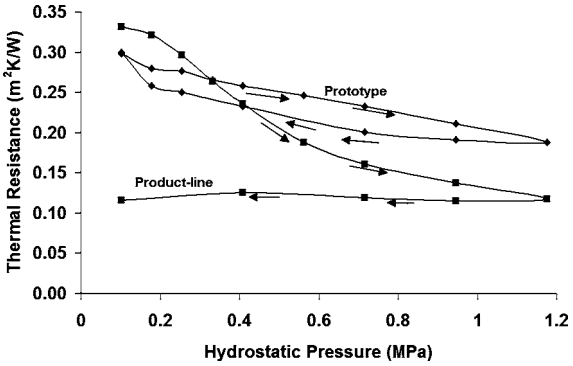

Fig. 4 Variation of the thermal resistance of the aerogel blanket samples with hydrostatic pressure. Arrows indicate direction of pressure change during the experiment.

the prototype aerogel blanket remained 50%–100% greater than the strain experienced by the same sample during the compression phase. When atmospheric pressure was reached the compressive strain of the prototype aerogel blanket returned to 0 mm/mm.

Figure 3 shows the corresponding variation of the thermal conductivity of both aerogel blankets with hydrostatic pressure. It can be seen that the thermal conductivity of the prototype aerogel blanket was 0.016 W/m K at atmospheric pressure, whereas the product-line aerogel blanket was about 0.018 W/m K. During compression, the thermal conductivity of both aerogel blankets increased. Upon reaching a pressure of 1.2 MPa the thermal conductivity of the product-line aerogel blanket reached about 0.023 W/m K; slightly surpassing the prototype aerogel blanket value of about 0.020 W/m K. Upon decompression, the thermal conductivity of the product-line aerogel blanket decreased slightly, but again rose to and remained at about 0.020 W/m K at atmospheric pressure. This corresponds to an increase in thermal conductivity of approximately 46% for the product-line aerogel blanket at atmospheric pressure after one compression cycle. The prototype aerogel blanket returned to within 1% of its initial thermal conductivity.

The variation of the overall thermal resistance of each aerogel blanket with hydrostatic pressure is shown in Fig. 4. The thermal resistance of the product-line aerogel blanket started at approximately 0.33 m^2 K/W and decreased by about 64% at a pressure of 1.2 MPa and remained essentially at that value upon decompression to atmospheric pressure. The thermal resistance of the prototype aerogel blanket was approximately 0.30 m^2 K/W at atmospheric pressure and decreased by about 37% but returned to its initial value when atmospheric pressure was reached. In addition the thermal resistance of the prototype aerogel blanket remained about 58% higher than the product-line aerogel blanket at a pressure of 1.2 MPa. It appears that the prototype aerogel blanket has increased elasticity in the direction of compression which permits the aerogel blanket to return to very close to its initial state upon decompression. The resistance to compression and recovery property of the prototype aerogel blanket makes it desirable for applications where resistance to pressure and recovery to its original thickness after compression is desirable.

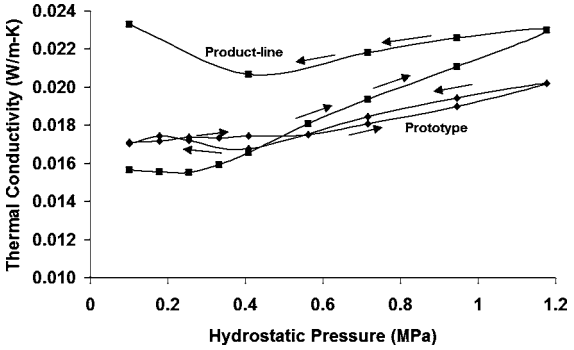

Fig. 3 Variation of the thermal conductivity of aerogel blanket samples with hydrostatic pressure. Arrows indicate direction of pressure change during the experiment.

4 Conclusions

It was found that the prototype aerogel blanket has approximately twice as much resistance to hydrostatic compression at a pressure of 1.2 MPa (170.5 psia) and recovers to its original thickness upon decompression. The thermal conductivity of the prototype aerogel was slightly higher than the product-line aerogel blanket before the compression cycle was performed. The overall thermal resistance of the prototype aerogel blanket remained about 37% higher than the product-line aerogel blanket at 1.2 MPa. Upon decompression to atmospheric pressure, both the thermal conductivity and compressive strain of the product-line aerogel blanket were permanently increased to the values measured at 1.2 MPa, whereas the prototype aerogel blanket returned to its initial state as measured before the compression cycle was performed.

This resistance to compression and the ability to recover to its original state upon decompression from elevated pressures makes the prototype aerogel blanket desirable for applications where high insulation, resistance to compression, and recovery is needed.

Acknowledgment

This research was supported by ONR Grant No. N00014-01-0278. In addition we would like to thank all the technicians at the Center for Research and Education in Special Environments for operating the hyperbaric chamber. We would also like to thank Aspen Aerogels, Inc. for providing their prototype aerogel blanket products for testing.

Nomenclature

T_{hot} = hot plate temperature
T_{cold} = cold plate temperature
d = sample thickness
λ = thermal conductivity of the test sample
Φ = heat flux through sample

References

[1] Lu X., et al., 1992, "Thermal Conductivity of Monolithic Organic Aerogels," Science, **255**(5047), pp. 971–972.
[2] Hrubesh, L. W., and Pekala, R. W., 1994, "Thermal Properties of Organic and

Inorganic Aerogels," J. Mater. Res., **9**(3), pp. 731–738.
[3] Hrubesh, L. W., and Poco, J. F., 1995, "Thin Aerogel Films for Optical, Thermal, Acoustic and Electronic Applications," J. Non-Cryst. Solids, **188**, pp. 46–53.
[4] Zeng, S. Q., Hunt, A. J., and Grief, R., 1995, "Mean Free Path and Apparent Thermal Conductivity of a Gas in a Porous Medium," J. Heat Transfer, **117**, pp. 758–761.
[5] Scheuerpflug, P., Hauck, M., and Fricke, J., 1992, "Thermal Properties of Silica Aerogels Between 1.4 and 300 K," J. Non-Cryst. Solids, **145**, pp. 196–201.
[6] Scheuerpflug P., et al., 1991, "Low-Temperature Thermal Transport in Silica Aerogels," J. Phys. D, **24**, pp. 1395–1403.
[7] Fricke, J. et al., 1987, "Thermal Loss Coefficients of Monolithic and Granular Aerogel Systems," Sol. Energy Mater., **16**, pp. 267–274.
[8] Herrmann, G. H., Bednarek, H., Reichert, H., Stephans, R., and Strahle, R., 1995, "Aerogels the Leading Edge in Thermal Insulation," H & V Engineer, **68**(725), pp. 8–11.
[9] Fesmire, J. E., 2006, "Aerogel Insulation Systems for Space Launch Applications," Cryogenics, **46**(2–3), pp. 111–117.
[10] Jensen, K. I., Schultz, J. M., and Kristiansen, F. H., 2004, "Development of Windows Based on Highly Insulating Aerogel Glazings," J. Non-Cryst. Solids, **350**, pp. 351–357.
[11] Reim, M., et al., 2005, "Silica Aerogel Granulate Material for Thermal Insulation and Daylighting," Sol. Energy, **79**(2), pp. 131–139.
[12] Abu Obaid, A., Anderson, S., Gillespie, Jr., J. W., Vaidyanathan, R., and Studley, A., 2005, "Investigation of Thermal and Acoustic Performance of Aerogel-Based Glass Fiber Composites," *Proceedings 50th International SAMPE Symposium and Exhibition*, Vol. 50, Long Beach, CA.
[13] Gibson, P., and Lee, C., 2004, "Application of Nanofiber Technology to Nonwoven Thermal Insulation," Proceedings of the 14th Annual International TANDEC Nonwovens Conference, Knoxville, TN.
[14] Bardy, E., Mollendorf, J., and Pendergast, D., 2005, "Thermal Conductivity and Compressive Strain of Foam Neoprene Insulation under Hydrostatic Pressure," J. Phys. D, **38**(20), pp. 3832–3840.

Analytical Formulation for the Temperature Profile by Duhamel's Theorem in Bodies Subjected to an Oscillatory Heat Source

Jun Wen

M. M. Khonsari[1]
Dow Chemical Endowed Chair in Rotating Machinery
Fellow ASME
e-mail: Khonsari@me.lsu.edu

Department of Mechanical Engineering,
Louisiana State University,
2508 CEBA,
Baton Rouge, LA 70803

An analytical technique is presented for treating heat conduction problems involving a body experiencing oscillating heat flux on its boundary. The boundary heat flux is treated as a combination of many point heat sources, each of which emits heat intermittently based on the motion of the flux. The working function of the intermittent heat source with respect to time is evaluated by using the Fourier series and temperature profile of each point heat source is derived by using the Duhamel's theorem. Finally, by superposition of the temperature fields over all the point heat sources, the temperature profile due to the original moving heat flux is determined. Prediction results and verification using finite element method are presented for an oscillatory heat flux in a rectangular domain. [DOI: 10.1115/1.2424236]

Keywords: oscillating heat flux, point heat source, Fourier series, Duhamel's theorem

1 Introduction

Many heat conduction problems are concerned with a moving heat source traversing along over one of the boundaries, for example, as a result of a solid sliding back and forth on another body. The heat generated within the contact region is due to friction, whose magnitude is dependent on the friction coefficient, sliding velocity, and pressure in the contact area. Depending on the thermomechanical properties of the bodies, part of the interfacial heat transfers to the sliding body and the rest conducts into the stationary solid. Thus relative to the respective coordinate systems attached to each body, the sliding body is subject to a fixed heat source, and the stationary body is subject to a moving heat source. The temperature rise at the interface has a significant effect on the tribological behavior of the contact materials, causing the materials to distort, which in turn affects the contact geometry, pressure distribution, and the temperature. In some applications, depending on the operating conditions, a positive feedback loop develops where the contact pressures and temperature become exceedingly high leading to gross surface damage and ultimately failure of the system. Thus, an efficient methodology for prediction of the temperature field as a function of time is needed at the design stage.

Pioneering work on the moving heat source problems was reported by Blok [1] with particular interest in the meshing of gear teeth giving rise to the concept of flash temperature. The work was later extended by Jaeger [2] who expressed the surface temperature of each solid in terms of heat flux. Tian and Kennedy [3] analyzed the surface temperature rise for a semi-infinite body due to different moving heat sources for the entire range of Peclet number using a Green's function method. Ju and Farris [4] and Gao and Lee [5] developed a transient temperature model based on the fast Fourier transform method, respectively. Qiu and Cheng [6] did a numerical simulation of the temperature rise for a three-dimensional rough surface sliding against a smooth surface in mixed lubricated contact by the moving grid method. Hirano and Yoshida [7] analyzed the surface temperature of semi-infinite body subjected to a rectangular heat source with reciprocating motion. Greenwood and Greiner [8] presented an analysis of surface temperature in fretting contact by assuming the source remains stationary. Additional references about the models for flash temperature can be found in Ref. [9], where the difference of the predicted temperature among the models is investigated. With the exception of Ref. [8,9], most of the papers focused their attention on a unidirectional, moving heat source.

In this paper Duhamel's theorem is used to analytically determine the temperature in a rectangular domain subjected to oscillating heat source on its boundary, extending the semi-analytical treatment of the problem as developed by Krishnamurthy [10].

The approach to this paper is as follows. The moving heat flux is considered to consist of many intermittent point heat sources and their working function $f(\xi,t)$ with respect to time is evaluated by using the Fourier series. The temperature field $T_\xi(x,y,t)$ of each point heat is derived by using Duhamel's theorem. Then, the superposition of $T_\xi(x,y,t)$ over all the heat sources yields the desired solution for $T(x,y,t)$ of the original problem. The mathematical formulation is illustrated in Sec. 2.

2 Mathematical Formulation

Referring to Fig. 1, consider a rectangular domain of width L and height h on which an oscillating heat flux of magnitude q'' is acting over a contact width $l(l<L/2)$. The oscillation velocity is v. The other three sides are at constant temperature T_0, and the initial temperature of the domain is T_i. Along the top surface, the local coordinate ξ denotes the location of a point heat source. The heat flux extending over the width l is treated as a combination of many point heat sources. Without the loss of generality, it is assumed that the oscillation starts from the left side.

2.1 Working Function $f(\xi,t)$ of a Time-Dependent Point Heat Source. Each point heat source on the top surface emits heat intermittently. Referring to Fig. 2, the working function $f(\xi,t)$ for a point heat source at $x=\xi(y=h)$ within one cycle is a periodic square wave function with magnitude of 1 (on) or 0 (off).

The oscillation period and the angular frequency are $T=2(L-l)/v$ and $\omega=2\pi/T=\pi v/(L-l)$, respectively. The function $f(\xi,t)$ can be treated as an even function. Its Fourier series is given by

$$f(\xi,t)=a_0+\sum_{n=1}^{\infty}a_n\cos(n\omega t) \tag{1a}$$

where

$$a_0=\frac{2}{T}\int_0^{T/2}f(\xi,t)dt \tag{1b}$$

[1]Corresponding author.

Contributed by the Heat Transfer Division of ASME for publication in the JOURNAL OF HEAT TRANSFER. Manuscript received December 31, 2005; final manuscript received July 5, 2005. Review conducted by A. Haji-Sheikh.

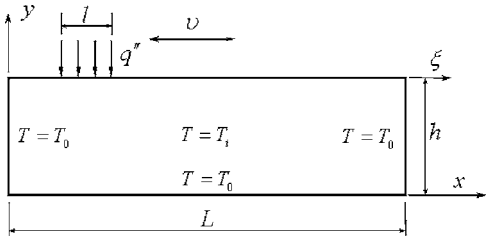

Fig. 1 A rectangular domain subject to oscillatory heat flux on its top boundary

$$a_n = \frac{4}{T}\int_0^{T/2} f(\xi,t)\cos(n\omega t)dt \tag{1c}$$

Then for the interval $0<\xi\leqslant L$, the Fourier series of $f(\xi,t)$ is

$$f(\xi,t)=\begin{cases} f_1(\xi,t) & \text{if } 0<\xi\leqslant l \\ f_2(\xi,t) & \text{if } l<\xi\leqslant L-l \\ f_3(\xi,t) & \text{if } L-l<\xi\leqslant L \end{cases} \tag{2a}$$

where

$$f_1(\xi,t)=\frac{\xi}{L-l}+\frac{2}{\pi}\sum_{n=1}^{\infty}\frac{1}{n}\sin\left(\frac{n\pi\xi}{L-l}\right)\cos\left(\frac{n\pi\nu t}{L-l}\right) \tag{2b}$$

$$f_2(\xi,t)=\frac{l}{L-l}+\frac{2}{\pi}\sum_{n=1}^{\infty}\frac{1}{n}\left[\sin\left(\frac{n\pi\xi}{L-l}\right)-\sin\left(\frac{n\pi(\xi-l)}{L-l}\right)\right]\cos\left(\frac{n\pi\nu t}{L-l}\right) \tag{2c}$$

$$f_3(\xi,t)=\frac{L-\xi}{L-l}-\frac{2}{\pi}\sum_{n=1}^{\infty}\frac{1}{n}\sin\left[\frac{n\pi(\xi-l)}{L-l}\right]\cos\left(\frac{n\pi\nu t}{L-l}\right) \tag{2d}$$

2.2 Temperature Profile $T_\xi(x,y,t)$ of a Time-Dependent Point Heat Source. The governing equation for time-dependent heat conduction is

$$\frac{\partial^2 T_\xi(x,y,t)}{\partial x^2}+\frac{\partial^2 T_\xi(x,y,t)}{\partial y^2}=\frac{1}{\alpha}\frac{\partial T_\xi(x,y,t)}{\partial t} \quad \text{in } 0<x<L,\ 0<y<h,\ t>0 \tag{3a}$$

where $T_\xi(x,y,t)$ is the transient temperature field of a time-dependent point heat source at location (ξ,h), k is the thermal conductivity of the material, and α represents the thermal diffusivity.

The boundary conditions are

$$T_\xi = T_0 \quad \text{at } x=0,\quad x=L,\quad t>0 \tag{3b}$$

$$T_\xi = T_0 \quad \text{at } y=0,\quad t>0 \tag{3c}$$

$$k\frac{\partial T_\xi}{\partial y}=q''\delta(x-\xi)f(\xi,t) \quad \text{at } y=h,\quad t>0 \tag{3d}$$

where $\delta(x-\xi)$ represents the Dirac delta function defined as

$$\delta(x-\xi)=\begin{cases}\infty & \text{if } x=\xi \\ 0 & \text{if } x\neq\xi\end{cases} \tag{3e}$$

with

$$\int_{\xi-\varepsilon}^{\xi+\varepsilon}\delta(x-\xi)dx=1 \tag{3f}$$

for $\varepsilon>0$, and the following property for any function $g(x)$

$$\int\delta(x-\xi)g(x)dx=g(\xi) \tag{3g}$$

The initial condition is

$$T_\xi = T_i \quad \text{at } t=0,\quad \text{in } 0\leqslant x\leqslant L,\quad 0\leqslant y\leqslant h \tag{3h}$$

Let

$$T_\xi(x,y,t)=\phi_1(x,y,t)+\phi_\xi(x,y,t) \tag{4}$$

the solution of problem (3) becomes the superposition of the following two problems

$$\frac{\partial^2\phi_1}{\partial x^2}+\frac{\partial^2\phi_1}{\partial y^2}=\frac{1}{\alpha}\frac{\partial\phi_1}{\partial t} \quad \text{in } 0<x<L,\quad 0<y<h,\quad t>0$$

$$\phi_1 = T_0 \quad \text{at } x=0,\quad x=L,\quad t>0$$

$$\phi_1 = T_0 \quad \text{at } y=0,\quad t>0$$

$$\frac{\partial\phi_1}{\partial y}=0 \quad \text{at } y=h,\quad t>0$$

$$\phi_1 = T_i \quad \text{at } t=0 \tag{5}$$

and

$$\frac{\partial^2\phi_\xi}{\partial x^2}+\frac{\partial^2\phi_\xi}{\partial y^2}=\frac{1}{\alpha}\frac{\partial\phi_\xi}{\partial t} \quad \text{in } 0<x<L,\quad 0<y<h,\quad t>0$$

$$\phi_\xi = 0 \quad \text{at } x=0,\quad x=L,\quad t>0$$

$$\phi_\xi = 0 \quad \text{at } y=0,\quad t>0$$

$$k\frac{\partial\phi_\xi}{\partial y}=q''\delta(x-\xi)f(\xi,t) \quad \text{at } y=h,\quad t>0$$

$$\phi_\xi = 0 \quad \text{at } t=0 \tag{6}$$

It can be shown that the Green's function for the problem is

$$G(x,y,t|x',y',\tau)=\frac{4}{Lh}\sum_{m=1}^{\infty}\sum_{p=1}^{\infty}e^{-\alpha(\beta_m^2+\eta_p^2)(t-\tau)}\times\sin(\beta_m x)\sin(\eta_p y)\sin(\beta_m x')\sin(\eta_p y') \tag{7}$$

Then the solution for problem (5) can be obtained by use of the Green's function as

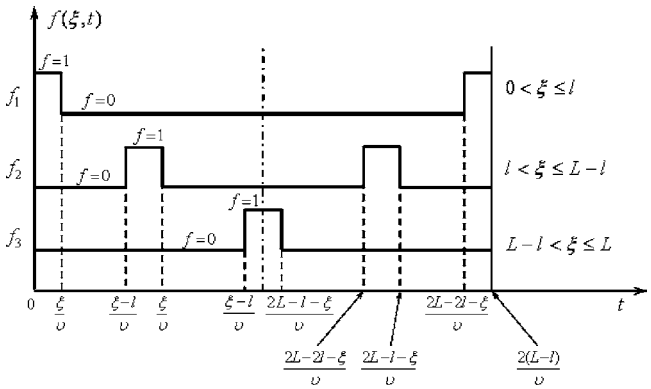

Fig. 2 Periodic square wave of working function of the point heat source

$$\phi_1 = T_0 + \frac{4(T_i - T_0)}{Lh}\sum_{m=1}^{\infty}\sum_{p=1}^{\infty}\frac{1-(-1)^m}{\beta_m \eta_p} e^{-\alpha(\beta_m^2+\eta_p^2)t}\sin(\beta_m x)\sin(\eta_p y) \tag{8a}$$

where

$$\beta_m = \frac{m\pi}{L} \quad (m = 1,2,\cdots,\infty) \tag{8b}$$

$$\eta_p = \frac{(2p-1)\pi}{2h} \quad (p = 1,2,\cdots,\infty) \tag{8c}$$

To solve problem (6) using Duhamel's theorem, the auxiliary problem is defined as follows:

$$\frac{\partial^2\theta_\xi}{\partial x^2} + \frac{\partial^2\theta_\xi}{\partial y^2} = \frac{1}{\alpha}\frac{\partial\theta_\xi}{\partial t} \quad \text{in } 0 < x < L, \quad 0 < y < h, \quad t > 0$$

$$\theta_\xi = 0 \quad \text{at } x = 0, \quad x = L, \quad t > 0$$

$$\theta_\xi = 0 \quad \text{at } y = 0, \quad t > 0$$

$$k\frac{\partial\theta_\xi}{\partial y} = \delta(x-\xi) \quad \text{at } y = h, \quad t > 0$$

$$\theta_\xi = 0 \quad \text{at } t = 0 \tag{9}$$

Then by Duhamel's theorem the solution to problem (6) is written as

$$\phi_\xi(x,y,t) = \int_{\tau=0}^{t} q'' f(\xi,\tau)\frac{\partial\theta_\xi(x,y,t-\tau)}{\partial t}d\tau \tag{10}$$

Application of the same Green's function as that in Eq. (7) yields the solution for the auxiliary problem (9)

$$\theta_\xi(x,y,t) = \frac{4}{Lhk}\sum_{m=1}^{\infty}\sum_{p=1}^{\infty}\frac{(-1)^{p+1}\sin(\beta_m\xi)}{\beta_m^2+\eta_p^2} \times(1-e^{-\alpha(\beta_m^2+\eta_p^2)t})\sin(\beta_m x)\sin(\eta_p y) \tag{11}$$

where β_m, η_p are the same as those in Eqs. (8*b*) and (8*c*), respectively.

Introducing Eq. (11) to Eq. (10), the solution to problem (6) is obtained as

$$\phi_\xi(x,y,t) = q''\frac{4\alpha}{Lhk}\sum_{m=1}^{\infty}\sum_{p=1}^{\infty}(-1)^{p+1} \times\sin(\beta_m x)\sin(\eta_p y)\sin(\beta_m\xi)\int_{\tau=0}^{t} f(\xi,\tau)e^{-\alpha(\beta_m^2+\eta_p^2)(t-\tau)}d\tau \tag{12}$$

Substituting Eqs. (8*a*) and (12) into Eq. (4), temperature profile of a time-dependent point heat source at location (ξ,h) with working function $f(\xi,t)$ is obtained as

$$T_\xi(x,y,t) = T_0 + \frac{4(T_i-T_0)}{Lh}\sum_{m=1}^{\infty}\sum_{p=1}^{\infty}\frac{1-(-1)^m}{\beta_m\eta_p} \times e^{-\alpha(\beta_m^2+\eta_p^2)t}\sin(\beta_m x)\sin(\eta_p y) + q''\frac{4\alpha}{Lhk}\sum_{m=1}^{\infty}\sum_{p=1}^{\infty}(-1)^{p+1}\sin(\beta_m x)\sin(\eta_p y)\sin(\beta_m\xi)\int_{\tau=0}^{t} f(\xi,\tau)e^{-\alpha(\beta_m^2+\eta_p^2)(t-\tau)}d\tau \tag{13}$$

2.3 Transient Temperature Profile $T(x,y,t)$ for the Entire Domain. In Eq. (13) the last term, i.e.,$\phi_\xi(x,y,t)$, is the only term that accounts for the contribution of a point heat source at location (ξ,h) to the entire domain temperature. The temperature profile $T(x,y,t)$ due to all the point heat sources is determined by integrating the last term in Eq. (13) over the top surface of the domain as

$$T(x,y,t) = \phi_1(x,y,t) + \int_{\xi=0}^{L}\phi_\xi(x,y,t)d\xi \tag{14}$$

Substituting Eqs. (8*a*) and (12) into Eq. (14) and performing the indicated operations yields the following solution for the transient field temperature of the entire domain

$$T(x,y,t) = T_0 + \frac{4(T_i-T_0)}{Lh} \times\sum_{m=1}^{\infty}\sum_{p=1}^{\infty}\frac{1-(-1)^m}{\beta_m\eta_p}e^{-\lambda_{mp}t}\sin(\beta_m x)\sin(\eta_p y) + q''\frac{4\alpha}{Lhk}\sum_{m=1}^{\infty}\sum_{p=1}^{\infty}(-1)^{p+1}\sin(\beta_m x) \times\sin(\eta_p y)\cdot\left[\frac{1-(-1)^m}{\lambda_{mp}\beta_m^2(L-l)}\sin(\beta_m l)(1-e^{-\lambda_{mp}t}) + \sum_{n=1}^{\infty}S_n\frac{\mu_n\sin(\mu_n t)+\lambda_{mp}\cos(\mu_n t)-\lambda_{mp}e^{-\lambda_{mp}t}}{\mu_n^2+\lambda_{mp}^2}\right] \tag{15a}$$

where

$$\mu_n = \frac{n\pi\nu}{L-l} \tag{15b}$$

$$\lambda_{mp} = \alpha(\beta_m^2+\eta_p^2) \tag{15c}$$

$$S_n = \begin{cases} \dfrac{1-(-1)^{n+m}}{n\pi}\sin(\beta_m l)\left(\dfrac{1}{\beta_m-\mu_n/\nu}-\dfrac{1}{\beta_m+\mu_n/\nu}\right) & \text{if } \beta_m-\mu_n/\nu \neq 0 \\ \dfrac{1-(-1)^{n+m}}{n\pi}\sin(\beta_m l)\left(-\dfrac{1}{\beta_m+\mu_n/\nu}\right)+\dfrac{L-l}{n\pi}\left[1-\cos\left(\dfrac{n\pi l}{L-l}\right)\right] & \text{if } \beta_m-\mu_n/\nu = 0 \end{cases} \tag{15d}$$

β_m, η_p are determined from Eqs. (8*b*) and (8*c*), respectively.

3 Results and Discussion

In this section, simulations are done using Eq. (15). Table 1 shows the input parameters. In the simulations, the truncation error is set to be 10^{-5}, and thus the maximum numbers of the terms for the infinite series in Eq. (15) are $m=50$, $p=48$, and $n=7$. A finite element model, shown in Fig. 3, was also developed to verify the results. The top surface is divided into 30 elements. The flux traverses from the left to the right side after 20 steps and then oscillates back to the left. The step time $\Delta t=L/30/v=0.00833$ s. The user-defined subroutine DFLUX is used to apply the thermal load of the oscillatory flux. The simulations are done using the ABAQUS on a 3.2 GHz Pentium 4 computer. It takes about 11 h to perform 2000 s of simulations for the oscillatory heat flux. In contrast, the computations of the analytical solution take only a few minutes on the same computer. The temperature contour at the steady state is shown in Fig. 4.

Figure 5 shows a comparison between the predicted analytical results and ABAQUS simulations for the temperature rise at locations $(L/2,h)$, $(L/6,h)$, $(5L/6,h)$, and $(L/2,h/2)$ specified in Fig. 3. The analytical and numerical results are in excellent agreement. In the analytical solution, the temperature rise at $(L/6,h)$ is slightly higher than that at $(5L/6,h)$. The reason is that although the geometry of the domain is symmetric along the center line in the y direction, the motion of the flux is not exactly symmetric because of our assumption that the flux begins to oscillate from the left. If we assume the beginning location is at the center of the top surface, the difference will disappear. The analytical solution provides a direct and efficient methodology for problems involving oscillatory heat flux.

Table 1 Parameters used in the simulations

Width of the domain L (m)	0.3
Height of the domain h (m)	0.1
Length of heat flux l (m)	0.1
Heat flux q'' (W/m^2)	50,000
Velocity of oscillation v (m/s)	1.2
Thermal conductivity k (W/m K)	52
Thermal diffusivity α (m^2/s)	10^{-5}
Boundary temperature T_0 (C°)	25
Initial temperature T_i (C°)	25

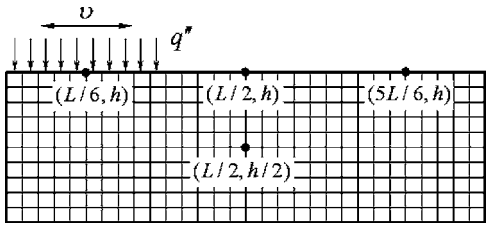

Fig. 3 Model of finite element method

4 Concluding Remarks

In this paper, an analytical method for treating heat conduction problems involving a body subjected to oscillating heat flux on one of its boundaries is developed. The method can be easily applied to the problem where the working function and fundamental solution are easily determined. Otherwise, the semi-analytical treatment of the problem reported in Ref. [10] can be used. Prediction results by the analytical solution and verification using the finite element method are also presented. The analysis demonstrates that the result can efficiently predict the field temperature of such moving boundary problems or be used to verify the solution from other methods. The method can be readily extended to three-dimensional problems as well as problems involving other types of periodic heat flux on a boundary.

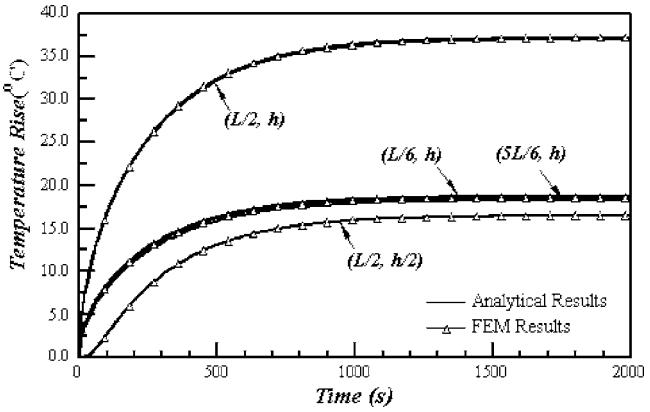

Fig. 5 Comparison of temperature rise obtained analytically and by the finite element method at locations $(L/2,h)$, $(L/6,h)$, $(5L/6,h)$, and $(L/2,h/2)$

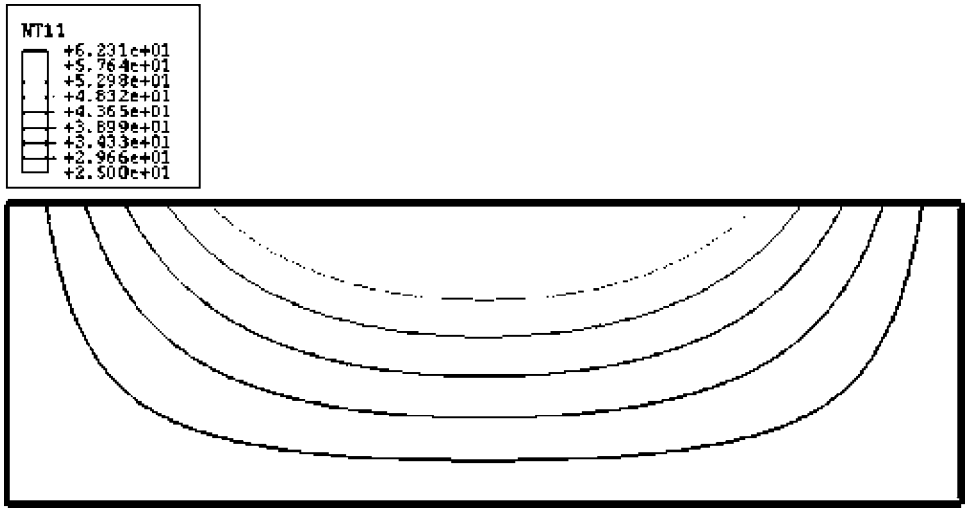

Fig. 4 Temperature contour at steady state

References

[1] Blok, H., 1937, "Theoretical Study of Temperature Rise at Surfaces of Actual Contact under Oiliness Conditions," *Proceeding Inst. of Mechanical Engineers General Discussion of Lubrication*, Vol. 2, London, October 13–15, Inst. of Mech. Engineers, London, pp. 222–235.

[2] Jaeger, J. C., 1942, "Moving Sources of Heat and the Temperature at Sliding Contacts," J. Proc. R. Soc. N. S. W., **20**, pp. 203–224.

[3] Tian, X., and Kennedy, F. E., 1994, "Maximum and Average Flash Temperature in Sliding Contacts," ASME J. Tribol., **116**, pp. 167–174.

[4] Ju, Y. and Farris T. N., 1997, "FFT Thermoelastic Solutions for Moving Heat Source," ASME J. Tribol., **119**, pp. 156–162.

[5] Gao, J., Lee S. C., Ai, X., and Nixon, H., 2000, "An FFT-Based Transient Temperature Model for General Three-Dimensional Rough Surface Contacts," ASME J. Tribol., **122**, pp. 519–523.

[6] Qiu, L., and Cheng, H., 1998, "Temperature Rise Simulation of Three-Dimensional Rough Surfaces in Mixed Lubricated Contact," ASME J. Tribol., **120**, pp. 310–318.

[7] Hirano, F., and Yoshida, S., 1966, "Theoretical Study of Temperature Rise at Contact Surface for Reciprocating Motion," Am. Inst. Chem. Eng., 4, pp. 127–132.

[8] Greenwood, J. A., and Alliston-Greiner, A. F., 1992, "Surface Temperature in a Fretting Contact," Wear, **155**, pp. 269–275.

[9] Kalin, M., and Vižintin, J., 2001, "Comparison of Different Theoretical Models for Flash Temperature Calculation under Fretting Conditions," Tribol. Int., **34**, pp. 831–839.

[10] Krishnamurthy, H., 2003, "Application of Duhamel's Theorem to Problem Involving Oscillating Heat Source," MS thesis, Louisiana State University, Baton Rouge, LA.

Semiconductor Crystal Growth by the Vertical Bridgman Process With Transverse Rotating Magnetic Fields

X. Wang
Graduate Research Assistant
Mem. ASME

N. Ma[1]
Assistant Professor
e-mail: nancy_ma@ncsu.edu

Department of Mechanical and Aerospace Engineering,
North Carolina State University,
Campus Box 7910,
Raleigh, NC 27695

During the vertical Bridgman process, a single semiconductor crystal is grown by the solidification of an initially molten semiconductor contained in an ampoule. The motion of the electrically conducting molten semiconductor can be controlled with an externally applied magnetic field. This paper treats the flow of a molten semiconductor and the dopant transport during the vertical Bridgman process with a periodic transverse or rotating magnetic field. The frequency of the externally applied magnetic field is sufficiently low that this field penetrates throughout the molten semiconductor. Dopant distributions in the crystal are presented.
[DOI: 10.1115/1.2352790]

1 Introduction

Since molten semiconductors are excellent electrical conductors, an externally applied magnetic field can be used to control the flow of the molten semiconductor (melt) in order to control the dopant distribution in the crystal, which depends on the convective and diffusive transport of the dopant in the melt. Devices are fabricated on wafers sliced from single crystals and the performance of a device is directly proportional to the compositional uniformity of the wafer on which it is produced.

Recently, rotating magnetic fields (RMFs) have been applied to semiconductor crystal growth and have revealed a promising flow phenomenon in many situations. Dold and Benz [1] reviewed the literature on the use of RMFs during semiconductor crystal growth. Salk et al. [2] and Fiederle et al. [3] conducted experimental investigations with RMFs and produced much better crystals with less segregation. A RMF is a periodic transverse magnetic field which rotates in the azimuthal direction about the centerline of the melt. A RMF is produced by a number of magnet poles which are placed at equally spaced azimuthal positions around the crystal-growth furnace and which are connected to successive phases of a multiphase electric power source. A RMF has a constant magnetic field pattern which rotates in the azimuthal direction with an angular velocity ω. Previous studies [4–6] have modeled melt motion in cylindrical or Bridgman-like geometries without solidification. In the present study, we treat a RMF with two poles so that the field is uniform and rotates one time per power cycle and we investigate the dopant segregation for the crystal growth.

[1]Corresponding author.

Contributed by the Heat Transfer Division of ASME for publication in the JOURNAL OF HEAT TRANSFER. Manuscript received October 25, 2005; final manuscript received May 14, 2006. Review conducted by Ranga Pitchumani.

2 Formulation of the Problem

This paper treats the unsteady, axisymmetric species transport of germanium in a silicon melt during the vertical Bridgman process with an externally applied, periodic, transverse magnetic field where $\hat{\mathbf{r}}$, $\hat{\theta}$, and $\hat{\mathbf{z}}$ are the unit vectors for the cylindrical coordinate system, as shown in Fig. 1. Our dimensionless problem is sketched in Fig. 1. All lengths and coordinates are normalized by R. The crystal-melt interface moves at a constant growth rate $U_g = \alpha U_c$ where the α is the dimensionless growth rate and $U_c = \mu/\rho R$ is the characteristic velocity, while μ and ρ are the melt's dynamic viscosity and density, respectively. The planar crystal-melt interface lies along $z=-b$, where the instantaneous dimensionless melt depth $b(t)=a-\alpha t$ decreases during growth. Here, a is the dimensionless melt depth at the beginning of growth and time t is normalized by R/U_c. The dimensionless time to grow the entire crystal is a/α.

This spatially uniform, transverse RMF actually produces a periodic, nonaxisymmetric body force in addition to the steady, axisymmetric, azimuthal body force but the frequency of the nonaxisymmetric body force is two times that of the axisymmetric body force. Witkowski et al. [4] proved that the inertia of the melt precludes any response to such a high-frequency oscillatory body force, so we neglect the nonaxisymmetric body force.

With the Boussinesq approximation, the equations governing the melt motion are

$$\frac{\partial \mathbf{v}}{\partial t} + (\mathbf{v}\cdot\nabla)\mathbf{v} = -\nabla p + T_m f_\theta \hat{\theta} + \frac{\mathrm{Ra}}{\mathrm{Pr}} T\hat{\mathbf{z}} + \nabla^2 \mathbf{v} \tag{1a}$$

$$\nabla\cdot\mathbf{v} = 0 \tag{1b}$$

$$\mathrm{Pr}\left(\frac{\partial T}{\partial t} + \mathbf{v}\cdot\nabla T\right) = \nabla^2 T \tag{1c}$$

where the melt velocity $\mathbf{v}$ is normalized by U_c, p is the deviation of the pressure from the hydrostatic pressure normalized by $\mu^2/\rho R^2$, and T is the deviation of the temperature from the furnace's hot-zone temperature, normalized by the characteristic temperature difference. In Eq. (1*a*), f_θ is the body force due to the RMF normalized by $\sigma\omega R B^2$, and is given by a separation-of-variables solution derived by Walker et al. [6]. For Eq. (1*c*), in certain situations, the Thomson, Peltier, and Seebeck effects are important [7–10]. However, the electric current densities that cross the interface, i.e., the crystal-melt interface are small enough that the heat source or sink associated with the Thomson and Peltier effects are negligible compared to the heat transfer imposed on the system by the external power source [10]. In addition, the thermoelectric current generated by the temperature gradient along the interfaces is negligible compared to the electric currents in the melt [10]. The dimensionless parameters in Eqs. (1*a*) and (1*c*) are the magnetic Taylor number $\mathrm{T}_m = \rho\sigma\omega B^2 R^4/\rho\mu^2$, the Rayleigh number $\mathrm{Ra}=\mathrm{g}\rho^2 c_p \beta(\Delta T)R^3/\mu k$, and the Prandtl number $\mathrm{Pr}=\mu c_p/k$. Here, k, c_p, β are the thermal conductivity, the specific heat, and the thermal volumetric expansion coefficient, respectively. The magnetic flux density of the RMF is B while gravitational acceleration is $g=9.81\ \mathrm{m}^2/\mathrm{s}$. The no-slip and no-penetration conditions are applied at the ampoule walls and the crystal-melt interface. We use the same thermal conditions applied by Wang and Ma [11] for the vertical Bridgman process.

At the beginning of crystal growth, the melt concentration is at uniform initial concentration $C(r,z,t=0)=1$. This is a standard initial condition that is utilized until experimental conditions are better understood [12]. The dopant transport is governed by the species conservation equation. The characteristic ratio of the convective to diffusive species transport in the melt is the mass Péclet number $\mathrm{Pe}_m = U_c R/D$, where D is the diffusion coefficient for the dopant in the molten semiconductor. For germanium in a silicon

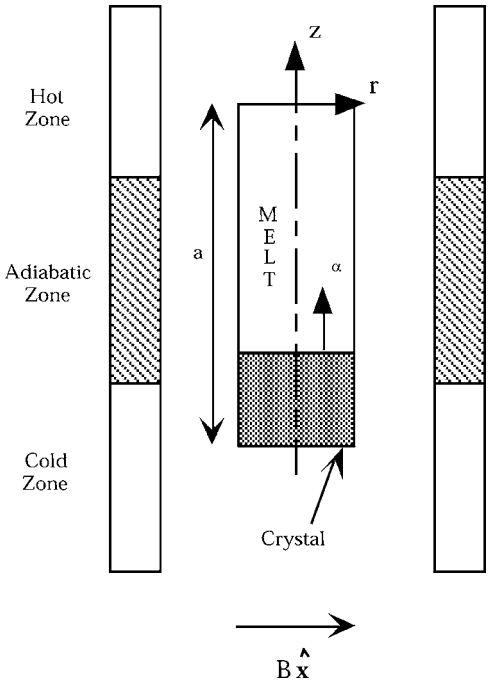

Fig. 1 Vertical Bridgman ampoule with a spatially uniform, transverse, rotating magnetic field and with coordinates normalized by the crucible's inner radius

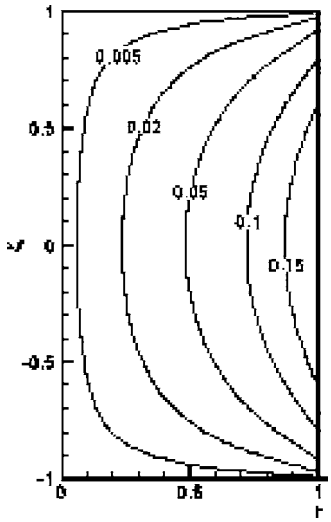

Fig. 2 Dimensionless, azimuthal electromagnetic body force f_θ at initial state for $b=1$

melt, the segregation coefficient k_s is equal to 0.406. The crystal absorbs silicon upon solidification and rejects germanium. The surfaces of the ampoule are impermeable. These equations are presented in a previous investigation [11]. Assuming that there is no diffusion of dopant in the solid crystal, the dopant distribution in the crystal $C_s(r,z)$ normalized by the initial uniform dopant concentration in the melt is $C_s(r,z)=k_sC(r,z=-b,t=z/\alpha)$.

We use a highly accurate Chebyshev spectral collocation method with Gauss-Lobatto collocation points in r and ζ. For the time derivatives in the governing equations, we use a second-order implicit time integration scheme to integrate from $t=0$ to a t that is slightly less than a/α. We use a sufficient number of collocation points and a large enough number of time steps so that the results do not change by increasing these numbers. This investigation represents an effort toward the fundamental understanding of dopant segregation in a system with a RMF. Future research will compare numerical predictions with measurements of dopant concentration in the crystal.

3 Results

We present results for silicon doped with germanium in a typical crystal growth process, for which $\omega=376.99$ rad/s, $U_g=23$ μm/s, $U_c=45.33$ μm/s, $\alpha=0.5074$, Pr=0.01284, $\mathrm{Pe}_m=10$, Ra=643.28, and $T_m=4.8942\times10^9B^2$ with B in Tesla. For $a=1$, the dimensionless time to grow the crystal is $a/\alpha=1.971$.

We investigated a RMF ranging from 0 mT to 4 mT. The isotherms for all cases are very similar to those in Wang and Ma [11] because the heat transfer is dominated by conduction for this small value of Pr. The thermal gradients are concentrated in a region of the melt near the crystal-melt interface because this region of the ampoule is adjacent to the furnace's thermal-gradient zone. These gradients alone drive a thermal buoyant convection that is counterclockwise in the melt, which decreases as the melt depth decreases.

We study the influence of a RMF on the flow. An RMF induces currents in the melt, and the currents interact with RMF to generate an azimuthal electromagnetic (EM) body force in the melt. This EM body force can stir the melt to control the fluid flow and dopant transport. Figure 2 shows the electromagnetic body force produced by RMF. In Fig. 2, $\zeta=1+2z/b$ is a rescaled axial coordinate so that $1\leqslant\zeta\leqslant+1$ for all time. It is evident that the maximum density of the body force is in the middle of the melt's height. The end effect of the bounding walls decreases the body force to zero near the bottom and top walls of the ampoule, where the current and the magnetic field are in the same direction. The EM body force decreases as the melt depth decreases.

We present results for $B=0.3$ mT, for which $T_m=440.475$. This azimuthal flow drives an additional meridional flow, or electromagnetic (EM) stirring, which opposes the buoyant convection. The meridional melt motion still produces an entirely counterclockwise circulation in the melt, so that the flow is radially outward along the crystal-melt interface. This convective transport produces a crystal which has relatively little radial segregation. The dopant concentration increases with z due to the rejection of dopant along the crystal-melt interface. The constant-concentration curves in the crystal are presented in Fig. 3.

When we increase the field to $B=3.0$ mT, for which $T_m=44047.5$, the EM body force is much stronger than that for $B=0.3$ mT. The meridional melt motion due to the EM stirring has become strong enough to cause some of the melt to reverse its flow direction. An upper circulation still remains counterclockwise. However, a significant clockwise circulation emerges in the lower half of the melt. This causes the flow to be radially inward

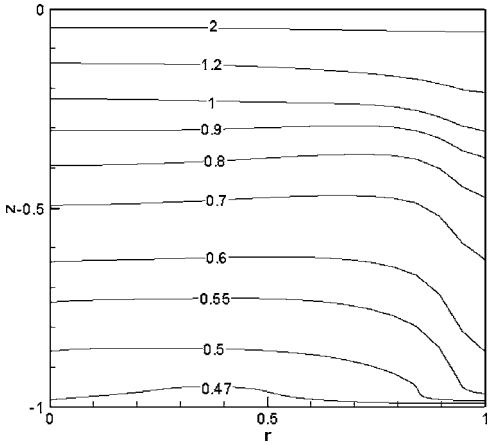

Fig. 3 Contours of concentration in the crystal $C_s(r,z)$ for $B=0.3$ mT, $U_g=23$ μm/s, and $a=1$

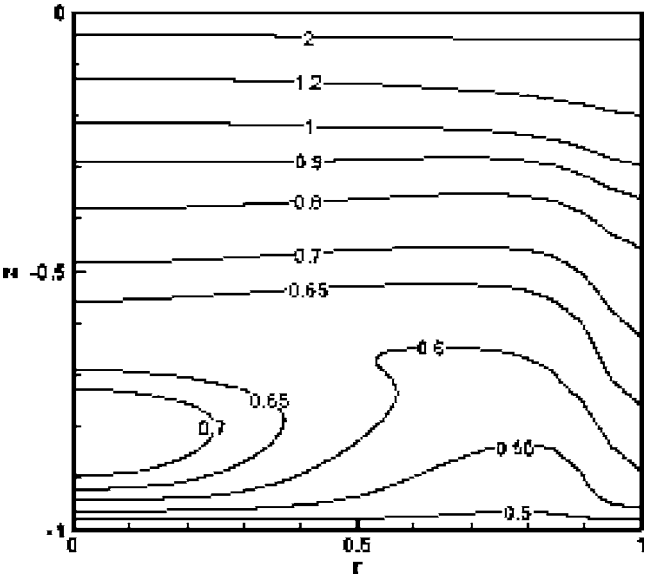

Fig. 4 Contours of concentration in the crystal $C_s(r,z)$ for B =3.0 mT, U_g=23 μm/s, and a=1

near the centerline and radially outward near the periphery along the crystal-melt interface. This explains the large radial segregation in the bottom of the crystal, as reflected in Fig. 4. For the last part of the crystal which solidified near $z=0$, the crystal has a relatively radially uniform composition because both the EM stirring and the buoyant convection has become weak. The buoyant convection is much stronger than the EM stirring, so that the flow is radially outward along the entire crystal-melt interface which decreases segregation. The dopant concentration in the crystal increases with z due to the rejection of dopant along the crystal-melt interface.

4 Conclusions

We have developed a numerical model that can treat the unsteady transport in the melt and predict the dopant transport in the crystal for Bridgman process with a RMF. With a very weak RMF less than 2 mT, there is only radially outward flow along the crystal-melt interface and the crystal solidifies with relatively little radial segregation. When field strength increases from 2 mT, the flow structure is very different. Along the crystal-melt interface, there exists both radially inward flow near the centerline and radially outward flow near periphery of the ampoule, which leads to severe segregation in both the melt and in the crystal.

Acknowledgment

This research was supported by the U. S. Air Force Office of Scientific Research under Grant No. FA9550-04-1-0249. The calculations were performed on the Cray X1 provided by the DoD High Performance Computing Modernization Program under Grant No. AFSNH2487.

Nomenclature

a = dimensionless length of the ampoule
b = dimensionless depth of the melt
B = magnetic flux density
c_p = specific heat of the melt
C = dimensionless concentration of the dopant in the melt
C_s = dimensionless concentration in the crystal
D = diffusion coefficient for the solute in the molten semiconductor
f_θ = electromagnetic body force
k = thermal conductivity of the melt
k_s = segregation coefficient for aluminum antimonide in gallium antimonide
p = dimensionless pressure
Pe_m = mass transport Péclet number
Pr = Prandtl number
r = dimensionless radial coordinate in the melt
$\hat{\mathbf{r}}$ = unit vector in the radial direction for the cylindrical coordinate system
R = crystal radius or inner radius of ampoule
Ra = Rayleigh number
t = dimensionless time
T = dimensionless temperature in the melt
T_m = magnetic Taylor number
U_c = characteristic velocity of the melt
U_g = growth rate or velocity of the crystal-melt interface
$\mathbf{v}$ = dimensionless velocity in the melt
z = dimensionless axial coordinate in the melt
$\hat{\mathbf{z}}$ = unit vector in the axial direction for the cylindrical coordinate system

Greek Symbols

(ΔT) = characteristic temperature difference
α = dimensionless growth rate or dimensionless velocity of the crystal-melt interface
β = thermal coefficient of volumetric expansion
μ = dynamic viscosity of the melt
$\hat{\theta}$ = unit vector in the azimuthal direction for the cylindrical coordinate system
ρ = density of the melt
σ = electrical conductivity of the melt
ω = angular velocity of the rotating magnetic field
ζ = dimensionless rescaled axial coordinate

References

[1] Dold, P., and Benz, K. W., 1999, "Rotating Magnetic Fields: Fluid Flow and Crystal Growth Applications," *The Role of Magnetic Fields in Crystal Growth, Progress in Crystal Growth and Characterization*, edited by K. W. Benz, Elsevier, Oxford, UK, Vol. 38, pp. 7–38.
[2] Salk, M., Fiederle, M., Benz, K. W., Senchenkov, A. S., Egorov, A. V., and Matioukhin, D. G., 1994, "CdTe and $CdTe_{0.9}Se_{0.1}$ Crystals Grown by the Travelling Heater Method Using a Rotating Magnetic Field," J. Cryst. Growth, **138**, pp. 161–167.
[3] Fiederle, M., Eiche, C., Joerger, W., Salk, M., Senchenkov, A. S., Egorov, A. V., Ebling, D. G., and Benz, K. W., 1996, "Radiation Detector Properties of $CdTe_{0.9}Se_{0.1}$:Cl Crystals Grown Under Microgravity in a Rotating Magnetic Field," J. Cryst. Growth, **166**, pp. 256–260.
[4] Witkowski, L. M., Walker, J. S., and Marty, P., 1999, "Nonaxisymmetric Flow in a Finite-Length Cylinder With a Rotating Magnetic Field," Phys. Fluids, **11**, pp. 1821–1826.
[5] Ma, N., Walker, J. S., Lüdge, A., and Riemann, H., 2001, "Combining a Rotating Magnetic Field and Crystal Rotation in the Floating Zone Process With a Needle Eye Induction Coil," J. Cryst. Growth, **230**, pp. 118–124.
[6] Walker, J. S., Volz, M. P., and Mazuruk, K., 2004, "Rayleigh-Bénard Instability in a Vertical Cylinder With a Rotating Magnetic Field," Int. J. Heat Mass Transfer, **47**, pp. 1877–1887.
[7] Sellers, C. C., Walker, J. S., Szofran, F. R., and Motakef, S., 2000, "Melt Motion Due to Peltier Marking During Bridgman Crystal Growth With an Axial Magnetic Field," Flow, Turbul. Combust., **64**, pp. 197–214.
[8] Khine, Y. Y., Walker, J. S., and Szofran, F. R., 2000, "Thermoelectric Magnetohydrodynamic Flow During Crystal Growth With a Moderate or Weak Magnetic Field," J. Cryst. Growth, **212**, pp. 584–596.
[9] Walker, J. S., Cröll, A., and Szofran, F. R., 2001, "Thermoelectromagnetic Convection in Floating Zone Silicon Growth With a Nonaxisymmetric Temperature and a Magnetic Field," J. Cryst. Growth, **223**, pp. 73–82.
[10] Landau, L. D., and Lifshitz, E. M., 1984, *Electrodynamics of Continuous Media*, Pergamon, New York.
[11] Wang, X., and Ma, N., 2005, "Numerical Model for Bridgman-Stockbarger Crystal Growth With a Magnetic Field," J. Thermophys. Heat Transfer, **19**, pp. 406–412.
[12] Ma, N., and Walker, J. S., 1997, "Dopant Transport during Semiconductor Crystal Growth With Magnetically Damped Buoyant Convection," J. Cryst. Growth, **172**, pp. 124–135.